

https://dspace.org/

Constraints on the genesis of orbicular granites and sulphide mineralization in the Koperberg Suite, South Africa and the Diana's Pool area, Zimbabwe

Dumisa, Senamile Siyaya

2024
University of the Witwatersrand, Johannesburg
https://hdl.handle.net/10539/41826

Dumisa, Senamile Siyaya. (2024). Constraints on the genesis of orbicular granites and sulphide mineralization in the Koperberg Suite, South Africa and the Diana's Pool area, Zimbabwe [PhD thesis, University of the Witwatersrand, Johannesburg]. WireDSpace. https://hdl.handle.net/10539/41826

Downloaded from a DSpace repository. https://dspace.org/

Constraints on the genesis of orbicular granites and sulphide mineralization in the Koperberg Suite, South Africa and the Diana's Pool area, Zimbabwe.

By

Senamile Siyaya Dumisa

A thesis submitted in fulfilment of the requirements for the degree of Doctor of Philosophy

Faculty of Science, University of the Witwatersrand, Private Bag 3, Johannesburg, 2050, South Africa.



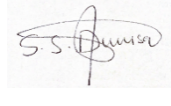


WITS
UNIVERSITY



Declaration

I declare that this thesis is my own, unaided work. It is being submitted for the Degree of Doctor of Philosophy at the University of the Witwatersrand, Johannesburg. It has not been submitted before for any degree or examination at any other University.



_____ _____

____11 January 2024_____

Abstract

This work tackles a long-standing problem in petrology, the formation of orbicular granitoids. These bodies occur as entire facies or as areas enriched in orbicules within distinct facies of plutons. Some European examples are highly prized for their decorative qualities. However, their origin is a matter of much debate going back to times when the origins of granitoids themselves were not obvious and are confused by topics such as 'granitization' and over-exaggeration of metasomatic effects. Here, poorly studied outcrops of orbicular rocks from the Matopos granite batholith in the Diana's Pool area, Zimbabwe and the Koperberg Suite, South Africa are tackeld. Enzman (1953) and Garvie (1969; 1971) studied the Koperberg Suite and the Diana's Pool orbicules, respectively and employed field observations and petrography to examine and characterize the genesis of these rocks. However, there is little evidence presented to confirm their theories on how these rocks formed as previous work lacks detailed geochemical, mineral chemistry and isotope data to support Enzman and Gravie's conclusions on the genesis of these rocks. Furthermore, there is no connection between the metallogenesis of the sulphide mineralization and the origin of orbicular rocks, which is a unique characteristic of particular orbicule sites in the Koperberg Suite.

This study focuses on four different orbicular bodies (Orbicule Koppie, Henderson South, Henderson North and Hoogkraal Lease) from the Koperberg Suite, hosted in lithologies ranging from diorite to pyroxenite compositions. The orbicules from different orbicular share similar characteristics. Coarse-grained felsic cores, fine-grained and alternating ferromagnesian and feldspathic shells, and coarse-grained to pegmatitic matrices characterize them. The orbicules are generally spherical to ellipsoidal in shape, however, some appear to be abraded and deformed (e.g., Orbicule Koppie). The compositions and grain sizes of cores and the matrix are comparable in all localities. Both the matrix and the cores are medium- to coarse-grained and dominated by plagioclase (the matrix probably in slightly lesser proportions), microcline (in variable proportions, and seemingly absent in some cores), quartz, biotite, magnetite and orthopyroxene (in the case of Hoogkraal Lese, Henderson North and Henderson South). Contrary to the cores and matrix, shells are fine-grained and exhibit polygonal textures. In addition to this, the shells are dominated by biotite and orthopyroxene.

Plagioclase in the Henderson North and Henderson South orbicules is more calcic than plagioclase in Hoogkraal Lease and Orbicule Koppie orbicules. Biotite in the Henderson North and the Orbicule Koppie orbicules is more magnesian than those at Henderson South and Hoogkraal Lease orbicules. Plagioclase in the Henderson North orbicules are characterized by elevated and radiogenic initial $^{87}Sr/^{86}Sr$ ratios than the other orbicule localities. There is also a variation in $^{87}Sr/^{86}Sr$ ratios within the individual orbicular structures (cores, shells and matrices) in individual localities. The orbicules at Henderson South, Orbicule Koppie and the Jubilee Pit host a bornite-dominated sulphide assemblage where disseminated chalcopyrite and bornite grains are characterized by granular textures and chalcopyrite is replaced by magnetite and bornite. Bismuth, Ni and Se in these sulphides appear to partition into bornite while Ag, In, Cd, Sn, Mn, Ge and Co partition into chalcopyrite.

Diana's Pool orbicular samples exhibit closely packed orbicules in a granitic matrix characterized by different types of orbicules containing coarse-grained felsic cores, fine-grained and alternating ferromagnesian and feldspathic shells, and a coarse-grained to pegmatitic matrix. The orbicules are

generally spherical to ellipsoidal in shape, however, some appear to be abraded and deformed. The compositions and grain sizes of cores and the matrix are comparable. Both the matrix and the cores are medium- to coarse-grained and dominated by plagioclase (the matrix probably in slightly lesser proportions), microcline (in variable proportions, and seemingly absent in some cores), quartz, biotite and accessory hornblende and magnetite. Contrary to the cores and matrix, shells are fine-grained and exhibit polygonal textures. In addition to this, the shells are dominated by biotite and magnetite; however, they do not contain hornblende. Plagioclase in cores, shells and matrices shows an almost complete overlap of An contents. Biotite composition in the shells is significantly less magnesian than in core and matrix, whose compositions overlap. Initial $^{87}Sr/^{86}Sr$ ratios from plagioclase in shells are slightly more radiogenic than in the matrix and cores.

Formation of both the Koperberg Suite and Diana's Pool orbicules has been attributed to metasomatic processes. However, modelling of the Koperberg Suite orbicules using the Magma Chamber Simulator and a variety of textural and geochemical constraints rules out a metasomatic origin. The quartz + biotite-dominated diorite (Orbicule Koppie) and the pyroxene-diorites (Hoogkraal Lease, Henderson South, Henderson North), together with more felsic anorthosite and the more mafic pyroxenites, are all produced by progressive AFC + recharge processes, where the magma was most likely anatectic melts of the country rocks that were at granulite grade. In both Diana's Pool and the Koperberg Suite, cores are autoliths, which are plagioclase-rich, cumulate, or rim fragments reworked by new magma inputs or injections. Heterogeneous nucleation leading to the formation of orbicular shells around the cores is attributed to adiabatic decompression of magma pulses ascending in dykes leading to superheating and resorption of early solids, and volatile exsolution, inducing undercooling, supersaturation, and shell crystallization. An alternative process that triggered superheating is magma mixing (e.g., Henderson South and Henderson North). The coarse-grained matrix crystallized later, after the orbicules formed, creating the groundmass, and locking the orbicules in place. The deformation of shells and cores (e.g., Orbicule Koppie and Diana's Pool) suggests that the orbicules continued to evolve in the presence of a melt (matrix material) until they were emplaced at their present setting.

The *in* situ sulphide assemblages in the Koperberg Suite have been reassessed in view of recent research on sulphide behavior. The bornite-chalcopyrite assemblage is atypical of the intermediate solid solution (*iss*) assemblage (chalcopyrite and pyrrhotite) observed in most Cu-Ni magmatic sulphide deposits. The high concentrations of trace elements that are incompatible with monosulphide solid solution and the depletion of Ni and Co in the sulphides are consistent with the derivation of sulphides from a Cu-rich sulphide melt that separated from a Ni-rich sulphide melt prior to magma emplacement and orbicule formation. The oxidation and Cu-enrichment of a sulphide melt that formed the mineralization in the orbicules and Koperberg Suite more generally began prior to the emplacement of the silicate Koperberg Suite magmas that formed the orbicules, suggesting no link between orbicule genesis and sulphide metallogenesis.

Acknowledgements

The DSI-NRF-CIMERA is to be commended for sponsoring this initiative. I owe a great deal to my supervisors, Professors Grant Bybee and Paul Nex, for their assistance, counsel, and encouragement during this study. I value the time spent in meetings and talks very much. I owe Koos Beukes a sincere debt of gratitude since without him; we would not have been able to locate the many orbicular outcrops and samples required for this study. Mr Caiphus Majola and Mr Samuel Tshabalala prepared the thin sections, for which I am thankful. I appreciate the help with the EPMA, LA-ICMPS, micro-XRF and ICP-MS analyses that I received from Prof. Alexander Ziegler, Ms Henriette Ueckermann, Deshenthree Chetty and Ms Riana Rossouw, respectively. I also want to express my gratitude to Dr Loic Le Bras and Dr Leoidas Vonopartis for always being willing to help me understand and interpret my data. I would also like to thank Dr. Bibi Ayesha Jogee, Mr Peace Zowa, Ms Thoriso Lekoetje, Ms Busisiwe Khoza, Miss Phumele Mashele, Dr. Khulekani Khumalo, Miss Snegugu Ziqubu, Miss Obehi Atita, Dr Mpofana Sihoya, and Miss Lenah Mtiyane for their invaluable assistance and suggestions. I would like to thank my parents Bongani and Nobuhle Dumisa, and my siblings, to whom I am forever grateful for providing the support, guidance and encouragement to pursue my goals, through these many years. Thank you to everyone who was engaged in any manner, no matter how small.

Table of Contents **Page**

1. Introduction 1

1.1. Petrology of Orbicular rocks 3

1.1.1. Magmatic models 4

1.1.2. Metamorphic and metasomatic models 5

1.1.2.1. Origin by active diffusion and granitization 5

1.1.2.2. Influx of Na^{+1} ions and outward diffusion of Ca^{2+} , Mg^{2+}, and Fe^{2+} 6

1.2. Aims (s) 6

1.3. Key research questions 6

1.4. Objectives 7

2. Geological Setting(s) 9

2.1. Regional Namaqualand Metamorphic Complex 9

2.1.1. Structure 8

2.1.2. Metamorphism 9

2.2. Koperberg Suite 9

2.2.1. Petrography and mineral compositions 10

2.2.2. Sulphide mineralization 10

2.2.3. Isotope studies 14

2.2.4. The genesis of the Koperberg Suite 15

2.2.4.1. Field relationships and emplacement models 15

2.2.4.2. Petrogenic models of the Koperberg Suite 16

2.2.5. Orbicular Rocks in the Koperberg Suite 18

2.3. Matopos granite and the Diana's Pool area 20

3. Methodology 23

3.1.1. Sample collection and preparation 23

3.1.2. Micro- XRF 23

3.1.3. Petrographic analyses 23
3.1.4. Tescan Integrated Mineral Analyzer (TIMA) Analyses 24
3.1.5. Electron Probe Micro Analyses (EPMA) 24
3.1.6. Sr isotope Analyses 24
3.1.7. Geochronology 25
3.1.8. Trace Element analyses in sulphides 25
3.1.9. Modelling using the Magma Chamber Simulator (MCS) 26
4. Diana's Pool Orbicules 30
4.1. Hand sample descriptions 30
4.2. Petrography 32
4.3. Geochemistry 43
4.3.1. *In-situ* compositions of mineral phases 43
4.3.1.1. Plagioclase 43
4.3.1.2. Biotite 47
4.3.2. Initial $^{87}Sr/^{86}$ Sr isotopes ratios in plagioclase 51
5. The Koperberg Suite orbicules 54
5.1. Field Observations 54
5.1.1. Country Rock: Nababeep Gneiss and the Concordia Granite 54
5.1.2. Koperberg Suite host rocks to orbicular granites: Anorthosite and Diorite 54
5.1.3. Orbicules in the Koperberg Suite 56
5.1.3.1. The Orbicule Koppie orbicules 56
5.1.3.2. The Hoogkraal Lease orbicules 58
5.1.3.3. The Henderson North orbicules 60
5.1.3.4. The Henderson South orbicules 62
5.1.4. Summary of Field observations 64
5.2. Petrographic Observations 65

5.2.1. Country Rock: Nababeep Gneiss and the Concordia Granite 65
5.2.2. The Koperberg Suite anorthosite 66
5.2.3. The Koperberg Suite diorite 69
5.2.4. Orbicules 72
5.2.4.1. Orbicule Koppie 72
5.2.4.2. Hoogkraal Lease 83
5.2.4.3. Henderson North 95
5.2.4.4. Henderson South 105
5.2.5. Summary of the petrographic observations 114
5.3. Geochemistry 115
5.3.1. Regional *in-situ* compositions of mineral phases 115
5.3.2. Intra-locality *in-situ* major element mineral chemistry 120
5.3.2.1. Orbicule Koppie 120
5.3.2.2. Hoogkraal Lease 124
5.3.2.3. Henderson North 129
5.3.2.4. Henderson South 134
5.3.3. *In-situ* $^{87}Sr/^{86}$ Sr ratios 137
5.3.4. Mineral chemistry summary 142
6. Geochronology 143
7. Sulphide Mineralization 147
7.1. Microscopic descriptions 147
7.2. Chemistry 149
7.2.1. EPMA analyses 149
7.2.1.1. Chalcopyrite 150
7.2.1.2. Bornite 150
7.2.2. LA-ICP-MS Trace Element analyses 151

8. Discussion 155

8.1. Comparing Koperberg Suite and Diana's Pool orbicules with global occurrences 155

8.2. A magmatic vs a metasomatic origin? 155

8.3. Diana's Pool vs the Koperberg Suite orbicules: Similarities, differences and implications 158

8.4. Petrogenesis of the Koperberg Suite orbicules 159

8.4.1. Localized processes and the magma source (s) of the Koperberg Suite orbicules 160

8.4.2. Modelling Recharge-Assimilation-Fractional Crystallization (RAFC) 163

8.4.2.1. A conclusion on modelling 175

8.5. Formation of orbicules in the Koperberg Suite and the Diana's Pool area 175

8.5.1. Formation of Koperberg Suite and Diana's Pool orbicular cores 177

8.5.2. The formation of the Koperberg Suite and Diana's Pool shell (s) 177

8.5.3. The Formation of the Koperberg Suite and Diana's Pool matrices 182

8.6. Mineralization in the Koperberg Suite orbicules 183

8.6.1. The metallogenesis of sulphides in the Koperberg Suite orbicules 183

8.7. The link between the genesis of orbicular rocks and sulphide metallogenesis in the Koperberg Suite 188

9. Conclusions 189

10. Recommendations for future research 190

11. References 191

List of Figures

Figure 1: Photographs showing different orbicular textures: (a) a heterogeneous orbicular sample from Finland (Lahti et al., 2005).(b) A sample showing orbicules characterized by multiple shells hosted in a granitic matrix taken from Orbicule Koppie, Koperberg Suite. (c) A sample showing combined radial and concentric orbicular textures (Lahti et al., 2005). In general, orbicules are spherical to ellipsoidal in shape; however, some orbicules are deformed, possibly resulting from

indentation on interaction with other orbicules. In addition, the shapes observed in 2D with respect to the cores, are not erosional surfaces but they are observed on a variety of surfaces, suggesting that they are 3D as opposed to 2D. 1
Figure 2: World map showing some of the orbicule localities (black circles) and the studied Koperberg Site and Diana's Pool orbicules (red circles), after Leveson (1966). 2
Figure 3: Images showing a classification of the internal structure of orbicules: (a) schematic diagram showing the core, mantle, shell and matrix classification (Enzman, 1953). (b) Field photograph of an orbicule showing the different parts of an orbicule taken from the Henderson North outcrop, Namaqualand.....3
Figure 4: Simplified geological map showing the regional tectonic setting of the Namaqua-Natal Province: (a) A map of Namaqualand showing different domains, sub provinces and the study area (red rectangle) modified after Cornell et al. (2006). (b) Geological map of the O'okiep Copper District modified after Lombaard et al. (1986).....7
Figure 5: An example of a steep structure from the Klondike east area showing a Koperberg Suite dyke (red dotted line) intruded in the central part of the steep structure (black dotted line) from Marima (2021). 19
Figure 6: A Google Earth image showing the location of some of the orbicular localities mapped by Enzman (1953).....19
Figure 7: Geological map of Zimbabwe and Diana's Pool area: (a) Geological map of Zimbabwe modified after Broderick and Hubbard (2016) and the red square shows where Diana's Pool is located. (b) Simplified geological sketch map of the orbicular granite outcropping 400 m downstream of Diana's Pool modified after Garson (1995). The Matopos granite porphyry to the north, east and south and a 13 m wide NW trending dolerite dyke to the west surround the orbicular granite.....21
Figure 8: Orbicular granite samples from the Diana's Pool area: (a) A sample showing the general appearance of Diana's Pool orbicules. These spherical to ellipsoidal orbicules make up approximately 70% of the rock volume and are characterized by felsic and medium-grained cores dominated by feldspars and patches of dark hornblende surrounded by alternating mafic and felsic shells in a pegmatitic and granitic host matrix. (b) Closely packed orbicules surrounded by a pegmatitic matrix. The red dotted lines show the sharp contacts between orbicules and the host matrix. (c, d) Pegmatitic matrix crosscutting the mafic orbicular shells and the felsic cores. (e)

Inclusions of the granitic host matrix material (blue arrow) in mafic shells creating a “saddle reef”. The coin is 23 mm in diameter. 31
Figure 9: Element maps of the Diana’s Pool sample BM 14780B: (a) A mosaic showing the mapped area in white rectangle. (b) A composite of selected elements (Al-dark blue, Si-green, Ca-pink, Fe- yellow and K-light blue) and their distribution shown in a full orbicule sample. (c) Element map showing uniform distribution of Al throughout the sample. However, the dark patches in central cores and some places in shells and matrices do not contain Al. (d) Element map showing uniform distribution of Si in cores and the matrix however, high intensities of Si are observed in the pegmatitic matrix. (e) Element map showing high distribution and intensities of Fe in shells, matrix and some parts of the cores. (f) Element map showing the distribution and concentrations of Zr in different parts of the orbicules. (g) Element map showing the highest concentrations and intensities of K in the matrix, the granitic matrix between the shells (red-dotted area), and some parts of the cores. (h) Element map showing the distribution and concentrations of Ca in different parts of the orbicules.....33
Figure 10: Element maps of the Diana’s Pool sample BM 14780A: (a) A mosaic showing the mapped area in white rectangle. (b) A composite of selected elements (Al-green, Si-dark blue, Ca-orange, Ti-light blue, and K-neon) and their distribution shown in a full orbicule sample. (c) Element map showing uniform distribution of Al in sample with dark patches containing no Al. (d) Element map showing the highest distribution and intensities of Si in the core and the matrix. (e) Element map showing the distribution and high intensities of Fe in shells, matrix and in the dark patches in the core. 34
Figure 11: Full thin section photomicrographs of the orbicule samples and corresponding TIMA image: (a) Plane–polarized (left) and cross-polarized light (right) full thin section images of sample BM14780F. (b) TIMA image of orbicule sample BM14780F showing a medium-grained core predominated by feldspars, quartz and hornblende; fine-grained and alternating mafic and felsic shells predominated by feldspars, biotite, magnetite, and a pegmatitic matrix predominated by feldspars and hornblende. 35
Figure 12: Full thin section photomicrographs and TIMA image of the Diana’s Pool orbicular core: (a) Plane–polarized (left) and cross-polarized light (right) full thin section images of sample BM14780D. (b) TIMA image of orbicule sample BM14780D showing a medium-grained core comprising feldspars, quartz, biotite and chlorite. 36

Figure 13: Photomicrographs showing mineral phases and textures in orbicular cores taken from Diana's Pool orbicules: (a, b) Subhedral plagioclase grains occurring adjacent to quartz and biotite. (c, d) Subhedral plagioclase grains occurring adjacent to quartz. Plagioclase is altered to sericite. (e, f) Interstitial microcline enveloping large plagioclase grains that occur adjacent to hornblende. (g, h) Large hornblende grains adjacent to plagioclase and quartz.....37
Figure 14: Reflected light image showing radiating grains of magnetite (yellow arrows) within a shell of sample BM1478F. (a) and (b) are the full thin section photomicrographs of the orbicule sample and corresponding TIMA image of sample BM14780F showing the location of the reflected light image.....38
Figure 15: Full thin section photomicrographs of Diana's Pool orbicule sample BM14780H: (a) Plane–polarized (left) and cross-polarized light (right) full thin section images of sample BM14780H. (b) TIMA image of orbicule sample BM14780H showing fine-grained shells crosscut by a pegmatitic and granitic matrix.....39
Figure 16: Photomicrographs showing mineral phases and textures in Diana's Pool orbicular shells: (a, b) Equigranular grains of feldspars, quartz and magnetite occurring close to each other and forming granoblastic textures. (c, d) Mafic shells comprising biotite containing poikilitic inclusions of quartz and magnetite adjacent to smaller plagioclase and quartz grains.(e, f) Felsic shells characterized by less biotite and more quartz and feldspars with poikilitic inclusions of magnetite. (g, h) Equigranular grains of plagioclase and quartz forming T- junctions (120 ^{o}; red arrow). Plagioclase contains poikilitic inclusions of magnetite and elongate biotite. 40
Figure 17: Full thin section photomicrographs of the Diana's Pool matrix: (a) Plane–polarized (left) and cross-polarized light (right) full thin section images of sample BM14780A. (b) TIMA image of the Diana's Pool orbicule sample BM14780A showing a coarse-grained to pegmatitic and granitic matrix comprising feldspars, quartz, biotite and chlorite as predominant phases. 41
Figure 18: Photomicrographs showing mineral phases and textures in the Diana's Pool matrix: (a) large grain of anhedral hornblende that grows into feldspars and quartz. Hornblende contains small poikilitic inclusions of quartz and grows adjacent to biotite (b) Microcline and quartz grains adjacent to each other. Granophyric textures are observed where microcline and quartz grow together. (c) Sharp contact between a coarse-grained matrix and a medium to fine- grained shell. (d) Interstitial hornblende enveloping touching grains of feldspars. (e) Poikilitic inclusions of

quartz in feldspars. (f) Granoblastic textures where touching quartz grains form T-junctions (white arrows).....42
Figure 19: Chemical variation diagrams showing the variation of different oxides in plagioclase from the Diana's Pool orbicular cores, shells and matrices plotted against SiO2 (wt.%). 44
Figure 20: A classification of feldspars from Diana's Pool orbicules on a ternary albite-anorthite-orthoclase diagram. 45
Figure 21: The graph showing the An content in plagioclase from Diana's Pool orbicular core, shells and matrix from orbicule sample BM14780F (representative of a full orbicule with a core, shells and a matrix). The graph shows little variation in the An contents in the core and matrix, however, the shells have slightly low An contents. The two sigma represent the minimum and maximum values, the box represents the interquartile range, x represents the mean, and the middle straight line represents the median.....46
Figure 22: Chemical variation diagrams showing variation of different oxides in biotite from the Diana's Pool orbicular cores, shells and matrices plotted against MgO (wt.%). 48
Figure 23: Graph of Mg# (Mg/Mg + Fe) showing a variation in Mg# in the Diana's Pool orbicular core, shells and matrix from samples BM14780D, BM14780F and BM14780A, respectively. A core and matrix exhibiting high Mg#, and shells containing biotite with low Mg# characterize the Diana's Pool orbicules. The two sigma represent the minimum and maximum values, the box represents the interquartile range, x represents the mean, and the middle straight line represents the median.....49
Figure 24: Diana's Pool biotites plotted on compositional classification diagrams: (a) Fe/ (Fe +Mg) versus Si (apfu) after Makutu et al. (2004). (b) Fe/ (Fe+ Mg) versus Al^{IV} after Deer et al. (1992). (c) Chemical composition of biotite using the (FeO+ MnO) - 10 TiO_2-MgO ternary diagram after Natchit et al. (2005). (d) Plot of Diana's Pool biotites on Al_2O_3-FeO-MgO ternary biotite discrimination diagram after Abdel-Rahman (1994). 50
Figure 25: Initial $^{87}Sr/^{86}Sr$ isotopic compositions of plagioclase from the Diana's Pool orbicules relative to the model depleted mantle taken from Eglington (2006). 51
Figure 26: Graph showing the initial $^{87}Sr/^{86}Sr$ ratios in the Diana's Pool orbicular cores, shells and matrix plotted against the An content. There is a little variation in initial $^{87}Sr/^{86}Sr$ ratios in plagioclase from cores to shells to the matrix and a large variation is observed in the An content

in shells and cores of different samples. The highest An contents are exhibited by plagioclase in the matrix sample BM14780A.....52
Figure 27: Photomicrographs showing outcrops of the massive Koperberg Suite rocks associated with the orbicular outcrops in different orbicular localities: (a, b) Nababeep Gneisses in contact with orbicules from Orbicule Koppie containing mafic and pegmatitic veins (black arrows). (c) An outcrop showing contacts between the orbicular body and the surrounding Nababeep Gneisses. (d) The contact between the gneiss and the diorite grading from a non-orbicular diorite to an orbicule-hosting diorite. (e) Biotite- rich diorite (mica diorite) at the contact point between the Nababeep Gneisses and massive diorite. (d) A less biotite- rich rock away from the contact between diorite and gneiss grading to the orbicule host rock. (g) The Concordia Granite outcrop in contact with the Henderson South orbicular rocks comprising pegmatitic and mafic veins. (h) Quartz veins associated with a quartz diorite comprising copper staining (yellow arrow) in Henderson South. 55
Figure 28: The rhombic-shaped Orbicule Koppie orbicule outcrop and the surrounding country rocks. 56
Figure 29: Pictures of Orbicule Koppie orbicular outcrops showing: (a) Orbicules with no preferred orientation characterized by felsic cores and shells hosted in a coarse-grained and felsic matrix. Some of these orbicules do not have distinct cores and they resemble enclaves (red arrow). (b) Sulphide mineralization and copper staining hosted in a felsic matrix. (c) Epidote patches in the felsic matrix hosting closely packed orbicules that displace and deform each other. (d) Deformed (east-west trending, red-dotted lines) orbicule boulder near the Orbicule Koppie outcrop.....57
Figure 30: The Hoogkraal Lease orbicule outcrop and the surrounding diorite, anorthosite and Concordia Granite. 58
Figure 31: Boulders from the Hoogkraal Lease orbicule outcrop: (a) A boulder showing ~ 30% orbicules to 70% host matrix relative volumes. (b) A boulder showing more orbicules to matrix relative volume. (c) Radiating orthopyroxene texture (red arrow) restricted to the orbicular shells. (d) An outcrop showing different shapes of orbicules, both elongated (black arrow) and spherical. 59
Figure 32: Sketch map (not to scale) of the Henderson North orbicular body and the surrounding country rocks. 60

Figure 33: Boulders from the Henderson North orbicular outcrop: (a) A boulder showing spherical orbicules hosted in a coarse-grained pyroxene-bearing diorite. (b) A more coarse-grained pyroxene-bearing diorite characterized by aligned and coarse-grained plagioclase. (c) Orbicule showing alternating mafic and felsic shells lacking the radiating texture. (d) An orbicule hosted in a felsic matrix characterized by a felsic core and mafic shells. 61
Figure 34: Geological sketch map of the Henderson South orbicular body and surrounding regional rocks (not to scale).....62
Figure 35: Orbicules from the Henderson South orbicule outcrops: (a) Henderson South outcrop characterized by elongated orbicules. (b) Spherical orbicules in a boulder next to the Henderson South outcrop. (c) Orbicules showing radiating orthopyroxene in shells (black arrows). (d) Elongated orbicules characterized my felsic cores and matrix. Shells are more mafic and dominated by biotite and pyroxene. 63
Figure 36: Photomicrographs of samples from Orbicule Koppie and Hoogkraal Lease: (a, b) Photomicrographs of the Nababeep Gneiss showing microcline that exhibits exsolution texture and poikilitic inclusions of magnetite.(c, d) Photomicrographs of the Concordia Granite from Hoogkraal Lease showing subhedral grains of quartz occurring adjacent to biotite and microcline. Microcline contains poikilitic inclusions of biotite, opaque minerals and quartz. 65
Figure 37: Photomicrographs showing oxides in the Nababeep Gneiss and the Concordia Granite from the Koperberg Suite. (a) Anhedral to subhedral magnetite grains in the Nababeep Gneiss from Orbicule Koppie. (b) Smaller and disseminated magnetite grains in the Hoogkraal Lease Concordia Granite. 66
Figure 38:Photomicrographs of anorthosites in contact with the Koperberg Suite orbicules: (a, b) Anorthosite from Henderson South comprising grains of plagioclase that are altered to sericite and comprising poikilitic inclusions of biotite. Microcline and plagioclase are enclosed by interstitial quartz that contains very small inclusions of magnetite. (c, d) Anorthosite from Orbicule Koppie containing grains of microcline, chlorite and plagioclase surrounded by interstitial quartz. Microcline locally exhibits exsolution textures and contains inclusions of magnetite. (e, f) Anorthosite from Hoogkraal Lease comprising plagioclase that exhibits discontinuous twinning and locally altered to sericite. Chloritisation of biotite is observed. (g, h) Anorthosite from Henderson North comprising inclusions of rounded quartz grains in plagioclase. Locally, plagioclase is altered to clay. 67

Figure 39: Photomicrographs showing sulphides and oxides in the Koperberg Suite anorthosites: (a) disseminated magnetite grains in anorthosite from the Henderson South adjacent to each other in plagioclase. (b) Disseminated chalcopyrite occurring adjacent to smaller magnetite grains in Orbicule Koppie anorthosite. (c) Larger magnetite grains from Hoogkraal Lease anorthosite. (d) Magnetite grains adjacent to smaller (<< 0.1 mm) grains of disseminated magnetite in anorthosite from Henderson North. 68
Figure 40: Photomicrographs of diorites from Koperberg Suite illustrating quantitative textural analysis: (a, b) Diorite from Orbicule Koppie composed of large microcline grains that contain poikilitic inclusions of anhedral magnetite and elongated (0.1-0.4 mm) grains of biotite. Microcline displays exsolution textures and it is altered to white mica. (c, d) Diorite from Hoogkraal Lease comprising plagioclase, quartz and biotite grains that occur adjacent to each other. Plagioclase occurs as smaller grains that occur adjacent to quartz and exhibit discontinuous twinning. Locally, plagioclase is surrounded by interstitial biotite. (e, f) Diorite from Henderson North containing small and disseminated hypersthene grains adjacent to plagioclase. Plagioclase locally exhibits discontinuous twinning and occurs adjacent to small biotite grains. (g, h) Diorite from Henderson South containing both unaltered and altered grains of plagioclase (sericite) that contain poikilitic inclusions of quartz and magnetite. Quartz occurs as anhedral grains that occur adjacent to biotite and plagioclase. Locally, quartz occurs as inclusions in biotite. 70
Figure 41: Photomicrographs showing the sulphide mineralization and magnetite in diorites from the Koperberg Suite: (a) Disseminated and anhedral to subhedral grains of magnetite in Henderson South diorite. (b) Subhedral grains of magnetite in the Orbicule Koppie diorite adjacent to smaller and disseminated grains of chalcopyrite. Locally, magnetite replaces chalcopyrite. (c) Small and anhedral magnetite in Hoogkraal Lease diorite concentrated in plagioclase. (d) Large magnetite grains adjacent to small and locally concentrated chalcopyrite grains in the Henderson North diorite. 71
Figure 42: Element maps of Orbicule Koppie sample SD-10-6C: (a) A mosaic showing the mapped area in a white rectangle. (b) A composite of selected element showing elements detected via the normal map spectrum showing the distribution of Al (orange), Ca (light green), K (pink), Si (blue) and: Fe (purple) in the sample. (c) Individual element map showing a uniform distribution of Al throughout the sample. (d) Element map showing the highest distributions and intensities of Si in the cores and the matrix. (e) Element map showing the highest distribution and intensity of

Fe in shells, matrix and some parts of cores. (f) Individual element map showing the distribution of Ca in different parts of the orbicules. (g) Element map showing the highest distribution and intensities of K in the matrix and some parts of the cores. (h) Element map showing the distribution of Cu in different parts of the orbicules. Cu is highly concentrated and yields high intensities in the matrix.....72
Figure 43: Full thin section photomicrographs of Orbicule Koppie orbicule sample SD-10-6A and corresponding TIMA image: (a) Plane–polarized (left) and cross-polarized light (right) full thin section images of sample SD-10-6A.....73
Figure 44: Full thin section photomicrographs of Orbicule Koppie orbicular core and corresponding TIMA image: (a) Plane–polarized (left) and cross-polarized light (right) full thin section images of sample SD-10-6B. (b) TIMA image of sample SD-10-6B characterized by fine to medium-grained core predominated by plagioclase, quartz, microcline, chlorite and titanite..74
Figure 45: Photomicrographs showing mineral phases and textures in orbicular cores from Orbicule Koppie: (a, b) Altered plagioclase grains (sericite) containing small inclusions of anhedral biotite and muscovite. (c, d) Small subhedral quartz grains that occur as inclusions in sericite. Quartz also occurs adjacent to anhedral biotite and epidote inclusions. (e, f) Subhedral plagioclase grains containing magnetite inclusions enclosed in interstitial microcline. (g, h) Large microcline grain exhibiting exsolution textures and containing small inclusions of euhedral apatite and anhedral to subhedral grains of biotite.....75
Figure 46: Small and disseminated chalcopyrite grains in Orbicule Koppie orbicular cores 76
Figure 47: A photomicrograph of a zoomed-in image with the red dotted line showing a sharp contact between the highly altered core and a fine- to medium-grained shell. The blue dotted line marks the sharp contact between the medium-grained shells to a coarse-grained matrix. (a) and (b) show the location of image c in the full orbicule sample SD-10-6A. 77
Figure 48: Photomicrographs showing mineral phases and textures in the orbicular shells from Orbicule Koppie orbicules: (a, b) Plagioclase containing small and disseminated biotite and magnetite grains. Biotite occurs both adjacent to and as inclusions in plagioclase. The inclusions of biotite are associated with small muscovite, epidote and chlorite. (c, d) Poikilitic biotite inclusions in plagioclase that grows adjacent to wormy and vermicular small quartz forming myrmekite textures. (e, f) Altered shell comprising altered plagioclase (sericite) in contact with a coarse-grained matrix. The red dotted line shows the sharp contact from a fine-grained shell to a

more coarse-grained matrix. Epidote is common in contacts between the shells and the matrix. (g, h) Disseminated quartz grains adjacent to biotite, muscovite and magnetite. Quartz occurs as small and rounded inclusions in altered plagioclase. 78
Figure 49: Small and disseminated chalcopyrite grains in the orbicular shells from Orbicule Koppie. 79
Figure 50: Full thin section photomicrographs of Orbicule Koppie matrix and corresponding TIMA image: (a) Plane–polarized (left) and cross-polarized light (right) full thin section images of the matrix sample SD-10-6C. (b) TIMA image of sample SD-10-6C showing a coarse-grained matrix composed of plagioclase, microcline, quartz, biotite, chlorite, albite and titanite.....80
Figure 51: Photomicrographs showing mineral phases and textures in Orbicule Koppie matrix: (a, b) Large plagioclase grains containing inclusions of microcline lamellae that follows the orientation of the albite twinning (antiperthite). (c, d) Plagioclase altered to sericite occurring adjacent to microcline and orthoclase. Orthoclase contains small inclusions of apatite and it is altered to clay. Biotite occurs adjacent to epidote and they both occur as small inclusions in altered plagioclase. (e, f) Anhedral quartz grains occurring adjacent to plagioclase. Locally, quartz occurs as vermicular intergrowths in plagioclase (myrmekite texture). Small muscovite grains occur adjacent to quartz and the altered to plagioclase. (g, h) Anhedral to subhedral quartz grains containing biotite inclusions. Quartz grains occur next to biotite and altered plagioclase. Locally, biotite is altered to chlorite**.** 81
Figure 52: Photomicrographs showing sulphide mineralization and oxides in the matrix from the Orbicule Koppie orbicules: (a) Massive chalcopyrite grain replaced by magnetite occurring adjacent to smaller and disseminated chalcopyrite grains. (b) Massive chalcopyrite grain replaced by magnetite occurring adjacent to smaller and disseminated chalcopyrite grains. (b) Massive chalcopyrite grains adjacent to smaller and disseminated chalcopyrite grains. (c) Small and disseminated chalcopyrite grains occurring as poikilitic inclusions in magnetite. (d) Chalcopyrite replaced by magnetite and adjacent to massive magnetite. 82
Figure 53: Element maps of Hoogkraal Lease sample SD-22-11: (a) A mosaic showing the mapped area in a white rectangle. (b) A composite of selected element showing elements detected via the normal map spectrum showing the distribution of Al (green), Si (blue), Fe (pink), Ti (red) and Ca (green) in the sample. 83

Figure 54: Full thin section photomicrographs of Hoogkraal Lease orbicular rock sample and corresponding TIMA image:(a) Plane–polarized (left) and cross-polarized light (right) full thin84
Figure 55: Full thin section photomicrographs of the Hoogkraal Lease orbicular core sample and corresponding TIMA image: (a) Plane-polarized and cross-polarized light full thin section image of the Hoogkraal Lease orbicular core. (b) TIMA image of the orbicular texture showing a medium-grained core comprising plagioclase, hypersthene, quartz and biotite. Sharp contact (red-dotted line) marks the transition from the core to the shells. 85
Figure 56: Small chalcopyrite grains within radiating hypersthene grains in Hoogkraal Lease orbicule cores.....86
Figure 57: Photomicrographs of the orbicular cores from Hoogkraal Lease: (a, b) Large and highly fractured phenocrysts of hypersthene occurring as inclusions in microcline and plagioclase. Hypersthene contains inclusions of elongated biotite. (c, d) Large hypersthene grains with small inclusions of subhedral quartz and elongated biotite grains. (e, f) Plagioclase exhibiting discontinuous twinning containing small and subhedral hypersthene inclusions. Hypersthene grows into plagioclase and microcline as elongated and subhedral grains of different birefringence. (g, h) Small and subhedral equigranular grains of quartz adjacent to feldspars and occurring as small inclusions in interstitial biotite. Biotite occurs adjacent to and as inclusions in feldspars. .87
Figure 58: A zoomed image of sample SD-27-14 showing shells from Hoogkraal Lease. These are alternating biotite and intermediate (plagioclase with hypersthene and minor biotite) shells. They are also characterized by radiating hypersthene grains. The radiating texture (yellow arrows) is cut perpendicular by the concentric biotite shells. Insert a are full thin section photomicrographs of the Hoogkraal Lease orbicular sample SD-27-14 in plane–polarized (left) and cross-polarized light (right) light showing the location of image c. 88
Figure 59: Photomicrographs of orbicular shells from Hoogkraal Lease orbicules: (a, b) Plagioclase grains adjacent to the radiating hypersthene grains. Small-scale alteration of plagioclase is observed. Biotite occurs as continuous grains that crosscut the hypersthene grains. (c, d) Radiating hypersthene grains are cut perpendicular by the continuous biotite shells. (e, f) small quartz grains that occur as poikilitic inclusions in biotite and adjacent to hypersthene and plagioclase. 89
Figure 60: Disseminated, small and anhedral chalcopyrite adjacent to subhedral to euhedral magnetite. 90

Figure 61: Full thin section photomicrographs of the Hoogkraal Lease matrix and corresponding TIMA image: (a) Plane–polarized (left) and cross-polarized light (right) full thin section images of the matrix sample SD-22-11C. (b) TIMA image of sample SD-22-11C showing a medium- to coarse-grained matrix comprising feldspars, biotite, magnetite, quartz and accessory apatite and chlorite.....91
Figure 62: Photomicrographs of a matrix from the Hoogkraal Lease orbicules: (a, b) Plagioclase adjacent to smaller and subhedral quartz grains. Quartz also occurs adjacent to interstitial biotite surrounding microcline. (c, d) Large and anhedral biotite grains with quartz inclusions growing into microcline adjacent to plagioclase. Microcline contains inclusions of quartz and magnetite. (e, f) Large and touching grains of subhedral quartz inclusions in plagioclase. Quartz occurs adjacent to biotite containing smaller quartz inclusions. Plagioclase is altered to clay. (g, h) Large and elongated biotite crosscutting large quartz grains, creating reaction rims. Biotite also occurs as an interstitial phase enclosing smaller quartz grains.....92
Figure 63: Photomicrographs showing mineral phases and textures in the Hoogkraal Lease matrix: (a, b) Large and euhedral microcline grains adjacent to large and subhedral quartz grains. Microcline contains poikilitic inclusions of plagioclase following the same trend as the twinning creating perthite textures. (c, d) Small and subhedral grains of quartz adjacent to biotite and feldspars. Quartz occurs as inclusions enclosed in interstitial biotite that is adjacent to feldspar. (e, f) Plagioclase contains inclusions of subhedral hypersthene that contains inclusions of quartz...93
Figure 64: Small, anhedral and disseminated chalcopyrite grain in a matrix from the Hoogkraal Lease orbicules. 94
Figure 65: Element maps of the Henderson North sample SD-40-19: (a) A mosaic showing the mapped area in the white rectangle. (b) A composite of selected element showing elements detected via the normal map spectrum showing Al (green), Ca (pink), K (bright blue), Fe (orange) and Si (dark blue) . (c) Individual element map showing a uniform concentration of Al throughout the orbicule sample. (d) Individual element map showing the highest concentrations and intensities of Si in cores and the matrix. (e)Element map showing the highest concentrations and intensities of Fe in shells, matrix and some parts of the cores. (f) Element map showing the distribution and concentrations of K in different parts of the orbicules. (g) Individual element map showing uniform Ca concentrations in the orbicule sample. (h) Individual element map showing the distribution and

concentrations of Cu in different parts of the orbicules. Cu is highly concentrated in the matrix. 95
Figure 66: Full thin section photomicrographs of the Henderson North orbicule sample SD-10-36A and corresponding TIMA image: (a) Plane–polarized (left) and cross-polarized light (right) full thin section images of sample SD-10-36A. (b) TIMA image of sample SD-10-36A. (b) TIMA image of sample SD-10-36A showing a medium-grained core dominated by plagioclase, microcline, and magnetite. Sharp contact (red dotted line) marks the transition from the core to the shell. The shell is predominated by magnetite and plagioclase. The medium-grained matrix comprises plagioclase, microcline chlorite and biotite. 96
Figure 67: Full thin section photomicrographs of the Henderson North orbicule sample SD-36-18C and corresponding TIMA image: (a) Plane–polarized (left) and cross-polarized light (right) full thin section images of sample SD-36-18C. (b) TIMA image of sample SD-36-18C. (b) TIMA image of sample SD-36-18C showing a medium- to coarse-grained core composed of plagioclase, hypersthene, microcline and magnetite. The red-dotted line marks the gradational contact between the core and the shell. There is a visible increase in magnetite and a decrease in microcline modal abundance in the shell. 97
Figure 68: Photomicrographs showing mineral phases and textures in the orbicular cores from the Henderson North orbicules: (a, b) Large phenocrysts of hypersthene containing small and rounded inclusions of quartz. (c, d) Microcline adjacent to plagioclase that contains poikilitic inclusions of magnetite. (e, f) Larger hypersthene phenocrysts in plagioclase.....98
Figure 69: Full thin section photomicrographs of the Henderson North orbicule sample SD-40-19B and corresponding TIMA image: (a) Plane–polarized (left) and cross-polarized light (right) full thin section images of sample SD-40-19B. (b) TIMA image of the sample showing alternating felsic (predominated by plagioclase and minor biotite) and mafic (predominated by biotite and minor plagioclase) shells. Sharp contacts (red-dotted lines) are observed between the core, shells and matrix.....99
Figure 70: Locally clustered magnetite grains adjacent to smaller chalcopyrite grains in the Henderson North orbicular shells. 100
Figure 71: Photomicrographs showing mineral phases and textures in the Henderson North orbicular shells: (a, b) Microcline adjacent to plagioclase grains that contain poikilitic inclusions of magnetite. Adjacent to microcline is anhedral and interstitial biotite enveloping feldspars. (c, d)

Biotite is altered to chlorite and grows adjacent to plagioclase and magnetite. (e, f) Interstitial biotite surrounding euhedral grains of plagioclase. (g, h) Interstitial biotite surrounding plagioclase 101
Figure 72: Full thin section photomicrographs of the Henderson North orbicule matrix and corresponding TIMA image: (a) Plane–polarized (left) and cross-polarized light (right) full thin section images of sample SD-40-19D. (b) TIMA image of the sample showing the coarse-grained matrix comprising plagioclase, biotite, microcline, chlorite and magnetite as the predominant phases. 102
Figure 73: Photomicrographs showing mineral phases and textures in the Henderson North matrix: (a, b) Interstitial biotite surrounding plagioclase and quartz. Biotite also occurs as small grains adjacent to plagioclase. (c, d) Poikilitic inclusions of euhedral biotite and magnetite in plagioclase. (e, f) Biotite containing plagioclase inclusions that occur adjacent to plagioclase. (g, h) Microcline and plagioclase surrounded by interstitial biotite. Biotite also occur as inclusions in plagioclase 103
Figure 74: Massive chalcopyrite grain replaced by magnetite. The massive chalcopyrite grain occur adjacent to smaller (<0.1 mm) and disseminated chalcopyrite grains.....104
Figure 75: Element maps of Henderson South sample SD-55-24: (a) A mosaic showing the mapped area in a white rectangle. (b) A composite of selected element showing elements detected via the normal map spectrum showing Al (purple), Si (blue), Ca (pink), Fe (red) and K (light green). (c) Element map showing uniform distribution of Al throughout the orbicule sample. (d)Element map showing the highest distribution and intensities of Si in the cores and the matrix. (e) Element map showing the highest distribution and intensities of Fe in shells and matrix. Cores are less ferroan. (f)Element map showing the distribution and concentrations of K in different parts of the orbicules. (g) Uniform Ca distribution throughout the orbicule sample. However, the radiating grains are less sodic (h) Element map showing the distribution and of Cu in different parts of the orbicules. The shells and some parts of the matrix are rich in Cu, and Cu yields the highest intensities in the matrix. 105
Figure 76: Full thin section photomicrographs of the Henderson South orbicule sample SD-55-24B and the corresponding TIMA images: (a) Plane–polarized full thin section images of sample SD-55-24B. (b) TIMA image of the sample showing a medium-grained core that is composed of plagioclase, quartz and unclassified radiating grains (black). (c)TIMA image of the selected area

(red box in image b) showing that the radiating grains have high silica than the surrounding feldspars. (d) TIMA image of the selected area showing that the radiating grains have no calcium and the calcium content in the grains is lower than in the surrounding feldspars. (e, f) TIMA images of the selected area showing that the radiating grains are enriched in iron and magnesium relative to the surrounding calcic plagioclase. 106
Figure 77: Full thin section photomicrographs of the Henderson South orbicule core sample SD-55-24C and corresponding TIMA image: (a) Plane–polarized (left) and cross-polarized light (right) full thin section images of the sample. (b) TIMA image of the sample showing a medium-grained core composed of plagioclase, unclassified grains, quartz, biotite, chlorite and accessory magnetite. 107
Figure 78: Photomicrographs showing mineral phases and textures in the Henderson South orbicular cores: (a, b) Poikilitic inclusions of biotite and altered hypersthene in plagioclase. Plagioclase is highly fractured and grains of quartz intergrown with altered hypersthene fill in the fractures. (c, d) interstitial biotite occurring around plagioclase and containing elongated grains of muscovite. (e, f) Small plagioclase grains adjacent to quartz. Plagioclase is altered to sericite and contains inclusions of magnetite and smaller euhedral apatite.....108
Figure 79: Locally concentrated chalcopyrite grains adjacent to magnetite in radiating altered hypersthene grain. 109
Figure 80: Photomicrographs showing mineral phases and textures of Henderson South orbicular shells: (a, b) Radiating and elongated grains of altered hypersthene and quartz that are restricted to the shells. (c, d) Poikilitic inclusion of rounded and altered hypersthene and magnetite in plagioclase. Plagioclase is altered to clay, and it is highly fractured locally and altered hypersthene fills in these fractures. (e, f) Smaller and subhedral grains of quartz and plagioclase occurring adjacent to bigger plagioclase grains containing poikilitic inclusions of magnetite. (g, h) Biotite adjacent to plagioclase containing quartz inclusions. Plagioclase occurs adjacent to altered hypersthene that grows both as inclusions and as fractures in plagioclase. Locally, smaller plagioclase grains form granoblastic and equigranular textures, where smaller and equal grains grow adjacent to each other. 110
Figure 81: Full thin section photomicrographs of the Henderson South orbicule matrix sample SD-55-24D and corresponding TIMA image: (a) Plane–polarized (left) and cross-polarized light

(right) full thin section images of sample SD-55-24D. (b) TIMA image of the sample showing a medium-grained matrix predominated by plagioclase, quartz, chlorite, biotite and magnetite. .111
Figure 82: Photomicrographs of the Henderson South matrix: (a) Large chalcopyrite grains that are replaced by bornite. These are adjacent to smaller chalcopyrite and bornite grains. (b) Smaller chalcopyrite replaced by bornite. 112
Figure 83: Photomicrographs showing mineral phases and textures in the matrix from the Henderson South orbicules: (a, b) Altered biotite grains and chlorite adjacent to smaller and altered plagioclase grains. (c, d) Biotite containing inclusions of quartz adjacent to smaller plagioclase grains. (e, f) T-junctions (120 ^{o}) angles forming where quartz and plagioclase equigranular grains form polygonal textures (blue arrow). Biotite occurs as subhedral grains adjacent to quartz and plagioclase. Locally, plagioclase is altered to sericite. (g, h) Equigranular grains of plagioclase and quartz, where plagioclase contains inclusions of magnetite. 113
Figure 84: A classification of feldspars from the Koperberg Suite massive rocks and the orbicules on a ternary albite-anorthite-orthoclase diagram: (a) The Massive Koperberg Suite rocks plotted on the feldspar classification diagram. They range from andesine to labrodorite in composition. (b) Plagioclase in the Koperberg Suite orbicules plotted on the feldspar classification diagram. Similar to the massive Koperberg Suite rocks, plagioclase in the orbicules ranges between andesite and labradorite in composition. 116
Figure 85: The graph showing the An content in plagioclase from the Koperberg Suite orbicular cores, shells and matrices and the surrounding Namaqualand Metamorphic Complex (NMC) and the massive Koperberg Suite rocks. The massive Koperberg Suite and the NMC An content were adapted from Van Zwieten et al. (1996) and Brandriss and Cawthorn (1996). The graph shows little variation in An contents in the orbicules and the surrounding massive and non-orbicular Koperberg Suite rocks.The two sigma represent the minimum and maximum values, the box represents the interquartile range, x represents the mean, and the middle straight line represents the median.....117
Figure 86: The graph of Mg# (Mg/Mg + Fe) in biotite showing the variation in Mg# in the Koperberg Suite orbicules. The Henderson North orbicules are the most magnesian whilst the Henderson South orbicules are the least magnesian of the Koperberg Suite orbicules. However, there is no variation in Mg# within the different orbicular domains in individual orbicular

localities. The two sigma represent the minimum and maximum values, the box represents the interquartile range, x represents the mean, and the middle straight line represents the median. 118
Figure 87: Koperberg Suite biotite plotted on compositional classification diagrams: (a) Fe/ (Fe + Mg) versus Si (apfu) after Makutu et al. (2004). (b) Fe/ (Fe + Mg) versus Al^{IV} after Deer et al. (1992). (c) Chemical composition of biotite using the (FeO+ MnO) - 10TiO O_2-MgO ternary diagram after Natchit et al. (2005). (d) Plot of Diana's Pool biotite on Al_2O_3-FeO-MgO ternary biotite discrimination diagram after Abdel-Rahman (1994). 119
Figure 88: Chemical variation diagrams showing the variation of different oxides in plagioclase from Orbicular Koppie orbicular cores, shells, matrix, diorite, and anorthosite plotted against SiO_2 (wt.%). 120
Figure 89: The graph of An content showing a variation in An content in the Orbicule Koppie orbicular core, shells, matrix and the surrounding anorthosite and diorite. Plagioclase in the matrix are more calcic and thus high An contents than plagioclase in the core, shells, diorite and anorthosite. The two sigma represent the minimum and maximum values, the box represents the interquartile range, x represents the mean, and the middle straight line represents the median. 121
Figure 90: Chemical variation diagrams showing a variation of the different oxides in biotite from Orbicule Koppie orbicular core, shell and matrix plotted against SiO_2 (wt. %). 122
Figure 91: The graph of Mg# in biotite showing little to no variation in the Mg# in Orbicule Koppie orbicular core, shell and matrix samples. The two sigma represent the minimum and maximum values, the box represents the interquartile range, x represents the mean, and the middle straight line represents the median. 123
Figure 92: In-situ chemical variation diagrams showing the variation of different oxides in plagioclase from Hoogkraal Lease orbicular cores, shells, diorite, anorthosite and the matrix plotted against SiO2 (wt. %).....125
Figure 93: The graph of An content showing a variation in An content in the Hoogkraal Lease orbicular cores, shells, matrix and the surrounding anorthosite and diorite. The matrix comprises plagioclase that are more sodic and have low An contents than plagioclase in the cores, the shells, diorite and anorthosite. Sample SD-27-14 core comprises plagioclase with a high An content than plagioclase in the core sample SD-22-11C. The two sigma represent the minimum and maximum values, the box represents the interquartile range, x represents the mean, and the middle straight line represents the median. 126

Figure 94: In-situ chemical variation diagrams showing the variation of different oxides in biotite from Hoogkraal Lease orbicular cores, shells, and matrix plotted against MgO (wt. %).....127
Figure 95: The graph of Mg# in biotite showing homogeneous Mg# in Hoogkraal Lease orbicular domains. The two sigma represent the minimum and maximum values, the box represents the interquartile range, x represents the mean, and the middle straight line represents the median. 128
Figure 96: Chemical variation diagrams showing variation of different oxides in plagioclase from the Henderson North orbicular domains, diorite, and anorthosite plotted against SiO_2 (wt. %).129
Figure 97: The graph of An content showing a variation in the An content in plagioclase in the Henderson North orbicular domains and the surrounding anorthosite and diorite. The two sigma represent the minimum and maximum values, the box represents the interquartile range, x represents the mean, and the middle straight line represents the median. 131
Figure 98: Chemical variation diagrams showing variation of different oxides in biotite from Henderson North orbicular cores, shells, and matrix plotted against MgO (wt. %).....132
Figure 99: The graph of Mg# in biotite showing homogeneous Mg# in Henderson North orbicular domains. The two sigma represent the minimum and maximum values, the box represents the interquartile range, x represents the mean, and the middle straight line represents the median. 133
Figure 100: Chemical variation diagrams showing variation of different oxides in plagioclase from the Henderson South orbicular domains, anorthosite and diorite plotted against SiO_2 (wt. %).
.....134
Figure 101: The graph of An content showing a variation in An content in Henderson South orbicular domains and the surrounding anorthosite and diorite. The two sigma represent the minimum and maximum values, the box represents the interquartile range, x represents the mean, and the middle straight line represents the median.....135
Figure 102: Chemical variation diagrams showing variation of different oxides in biotite from Henderson South orbicular cores, shells, and matrix plotted against MgO (wt. %).....136
Figure 103: The graph of Mg# showing a variation in Mg# in Henderson South orbicular domains. The cores are more magnesian than the shells and matrix. The two sigma represent the minimum and maximum values, the box represents the interquartile range, x represents the mean, and the middle straight line represents the median. 137
Figure 104: Graph showing a variation in the initial $^{87}Sr/^{86}Sr$ ratios in plagioclase from the Koperberg Suite orbicules and the surrounding Koperberg Suite massive diorites and anorthosite,

and the Namaqualand basement rocks. The initial $^{87}Sr/^{86}Sr$ isotopic ratios in orbicules are within range with the initial $^{87}Sr/^{86}Sr$ ratios (adapted from Van Zwieten et al. (1996) of the massive Koperberg Suite and the Namaqualand basement rocks. The two sigma represent the minimum and maximum values, the box represents the interquartile range, x represents the mean, and the middle straight line represents the median. 138

Figure 105: Graphs of An content plotted against the initial $^{87}Sr/^{86}Sr$ ratios: (a) Graph of the An content plotted against initial $^{87}Sr/^{86}Sr$ of plagioclase from Orbicule Koppie showing homogeneous initial $^{87}Sr/^{86}Sr$ ratios in orbicules and the surrounding anorthosite and diorite. However, the An content varies and it is higher in the more calcic matrix than in the sodic cores and shells. (b) Graph of An content plotted against initial $^{87}Sr/^{86}Sr$ on plagioclase from Hoogkraal Lease showing more radiogenic and sodic matrices together with calcic and less radiogenic cores, shells, diorite and anorthosite. (c) Graph of An content plotted against initial $^{87}Sr/^{86}Sr$ on plagioclase from Henderson North showing a large variation in initial $^{87}Sr/^{86}Sr$ ratios in the more radiogenic orbicules and anorthosite and the less radiogenic diorite. A variation is observed in both An content and in initial $^{87}Sr/^{86}Sr$ ratios in plagioclase from different samples. (d) Graph of An content plotted against initial $^{87}Sr/^{86}Sr$ ratios on plagioclase from Henderson South showing homogeneous An content and homogeneous initial $^{87}Sr/^{86}Sr$ ratios in orbicules. Anorthosite, however, is less radiogenic and more sodic than orbicules. Diorite is less radiogenic than orbicules and anorthosite and the An content is within range with orbicules. Green and yellow Shaded circles, triangles, diamonds and hexagons represent diorite nd anorthosite, respectively. 140

Figure 106: Initial Sr isotope compositions of units from the Koperberg Suite orbicules, Namaqua-Natal (Eglington et al., 1989), Bushveld Complex (Hayes et al., 2018; Scoon et al., 2020; Bourdeau et al., 2022), Ritchersveld Subprovince (Reid, 1977; 1979; 1991; 1997) , and the Kaapvaal Craton (Donnelly et al., 2012) relative to the model depleted mantle Eglington, 2006). 141

Figure 107: Cathodoluminescence (CL) images of representative zircon grains from the Koperberg Suite and Diana's Pool orbicules. Red circles represent the spot analysed for U-Pb dating. (a, b, c) Zircon grains from the Orbicule Koppie matrix are characterized by light cores and dark mantles and rims surrounded by quartz (Qtz), plagioclase (Pl), biotite (Bi) and epidote (Ep). (d) Resorbed and sub-angular zircon from the Dina's Pool matrix characterized by sector zoning. 144

Figure 108: Representative U-Pb geochronology results of zircon (reported to 1σ): (a) Wetherill U-Pb concordia diagram for zircon from Orbicule Koppie matrix sample SD-10-6C. Rejected data are shown in white (outliers and >10% discordance). (b) Weighted mean diagram showing $^{207}Pb/^{206}Pb$ age of zircon from sample SD-10-6C (<10% discordance). 146
Figure 109: Photomicrographs of representative sulphide phases in the orbicules: (a, b) Photomicrographs in both transmitted and reflected light showing opaque phases occurring along or close to silicate grain boundaries. Smooth and rounded grain boundaries characterize oxides and feathered margins characterize the sulphides. (c) Independent and massive chalcopyrite grain in Orbicule Koppie matrix that is replaced by magnetite. (d) Interstitial bornite and chalcopyrite overgrowths surrounding altered plagioclase that contain small poikilitic inclusions of chalcopyrite. (e) Inclusion of chalcopyrite grains along cleavage planes in biotite surrounded by grains of chalcopyrite and bornite overgrowths. (f) Jubilee Pit sample characterized by bornite and chalcopyrite overgrowths. The grains grow adjacent to magnetite and locally grow along the grain boundaries of magnetite. Some of the photomicrographs (d and e) show the laser spots used for trace element analysis of sulphides. 148
Figure 110: Cu-Fe-S plots of weight percent composition of sulphides from Jubilee Pit, Henderson North, Henderson South and Orbicule Koppie orbicular matrices. 149
Figure 111: Trace element (ppm) variation diagrams of chalcopyrite (ccp) and bornite (bn) from the Koperberg Suite orbicules: (a) Bi vs Ag diagram showing bornite from different localities enriched in Bi relative to chalcopyrite. Chalcopyrite shows a large variation in Ag. (b) In vs Cd diagram showing that chalcopyrite in the Koperberg Suite is enriched in Cd and depleted in In relative to bornite. (c) Sn vs Se showing that the Koperberg Suite bornite is enriched in Se and depleted in Sn relative to chalcopyrite. (d) Mn vs Pb plot showing high concentrations of Pb and low concentrations of Mn (below detection limit) in the Koperberg Suite bornite. The highest Mn and lowest Pb concentrations are observed in chalcopyrite. (e) Ge vs Ga diagram showing the Koperberg Suite chalcopyrite enriched in Ge relative to bornite. Ga in bornite is below the detection limit (plotted at 0 ppm). (f) Ni in chalcopyrite is below detection limit (plotted at 0); however, the highest concentrations of Ni and lowest concentrations of Co (below the detection limit) are exhibited by the Jubilee Pit bornite. OK= Orbicule Koppie, HS=Henderson South, HN=Henderson North, HL=Hoogkraal Lease and Jp= Jubilee Pit. 152

Figure 112: Graph showing a variation in the initial $^{87}Sr/^{86}Sr$ ratios in plagioclase plotted against Sr (ppm) from the Koperberg Suite orbicules and the whole-rock data from the surrounding Koperberg Suite massive rocks, taken from Van Zwieten et al. (1996). The in-situ data from this study is within range with the whole-rock data from Van Zwieten et al. (1996). 166
Figure 113: An energy constrained MCS model simulating Fractional Crystallization (FC), Recharge-Fractional Crystallization (RFC), Assimilation-Fractional Crystallization (AFC) with both the Nababeep Gneiss and the Concordia Granite, and Recharge-Assimilation-Fractional Crystallization (RAFC) using depleted mantle-derived MORB composition taken from Salters and Stracke (2004) run at 1.5 kbars. WR = whole-rock and JP = Jubilee Pit. 167
Figure 114: An energy constrained MCS model simulating FC, RFC, AFC with both the Nababeep Gneiss and the Concordia Granite and RAFC using depleted mantle-derived Karoo Large Igneous 167
Figure 115: An energy constrained MCS model simulating FC at 1.5 kbar using the Cascade arc basalt magma composition. 169
Figure 116: An energy constrained MCS model simulating RFC at 1.5 kbar using the Cascade arc basalt magma composition. 169
Figure 117: An energy constrained MCS model simulating AFC using the Cascade arc basalt composition, the Nababeep Gneiss and the Concordia Granite wallrock at 1 kbar. 171
Figure 118: An energy constrained MCS model simulating AFC using the Cascade arc basalt composition, the Nababeep Gneiss and the Concordia Granite wallrock at 1.5 kbar. 171
Figure 119: An energy constrained MCS model simulating AFC using the Cascade arc basalt composition, the Nababeep Gneiss and the Concordia Granite wallrock at 2 kbar. 172
Figure 120: An energy constrained MCS model simulating AFC using the Cascade arc basalt composition, the Nababeep Gneiss and the Concordia Granite wallrock at 6 kbar. 173
Figure 121: An energy constrained MCS model simulating RAFC using the Cascade arc basalt composition, the Nababeep Gneiss and the Concordia Granite wallrock at 1.5 kbar. 174
Figure 122: A schematic hornblende-plagioclase binary phase diagram showing how disequilibrium crystallization (undercooling) can cause oscillatory banding in the orbicules adapted from Zhang and Lee (2021). 181

List of Tables

Table 1: Relation between intrusive, metamorphic and deformational events in the O'okiep Copper District after Raith and Harley (1998). Ages are given according to: [1] Clifford et al. (1995),[2]Reid et al. (1991),[3] Nicolaysen and Burger (1965), [4]Reid (1979),[5] Robb et al. 1997. 8

Table 2: Table of parameters used for Micro- XRF analyses. 23

Table 3: Table showing different samples that were analyzed for EPMA and in-situ Sr. "X" shows what was analyzed in each sample. 43

Table 4: Table showing the ranges of major elements (in wt. %) in plagioclase from cores, shells and matrices of differed Diana's Pool orbicular samples. 43

Table 5: Table showing the ranges of major elements (wt. %) in biotite from cores, shells and matrices of differed Diana's Pool orbicular samples. 47

Table 6: Table showing the ranges of initial $^{87}Sr/^{86}Sr$ in plagioclase from cores, shells and matrices of differed Diana's Pool orbicular samples. 52

Table 7: Table showing the ranges of the major elements (wt. %) in plagioclase from the core, the shells and the matrix samples of the orbicules from Orbicule Koppie. 120

Table 8: Table showing the ranges of the major elements (wt. %) in biotite from the core, the shells and the matrix of the Orbicule Koppie orbicular rocks. 122

Table 9: Table showing the ranges of the major elements (wt. %) in plagioclase from the cores, the shells and the matrix of the orbicules from Hoogkraal Lease. 124

Table 10: Table showing the range of the major elements (wt. %) in biotite from the cores, the shells and the matrix of the Hoogkraal Lease orbicular rocks. 127

Table 11: Table showing the ranges of the major elements (wt. %) in plagioclase from the cores, the shells and the matrix of the orbicules from Henderson North. 129

Table 12: Table showing the ranges of the major elements (wt. %) in biotite from the cores, the shells and the matrix of the Henderson North orbicular rocks. 132

Table 13: Table showing the ranges of the major elements (wt. %) in plagioclase from the cores, the shells and the matrix of the orbicules from Henderson South. 134

Table 14: Table showing the ranges of the major elements (wt. %) in biotite from the cores, the shells and the matrix of the orbicules from Henderson South. 136

Table 15: Results of U-Pb spots analyses of zircon from the Koperberg Suite orbicules. 145

Table 16: Table showing the ranges of Cu, Fe and S in wt. (%) in chalcopyrite from the Koperberg Suite orbicules.....150
Table 17: Table showing ranges of Cu, Fe and S in wt. (%) in bornite from Jubilee Pit and Henderson South orbicules.....150
Table 19: Parental Melt (PM), Recharge magma (RM) and Whole-Rock (WR) compositions used in the models taken from literature. 164
Table 20: Thermal and chemical parameters used in RAFC models for four MCS simulations. Temperature in in ^{o}C. 165
Table 21: Diana's Pool Plagioclase data 207
Table 22: Microprobe analysis of biotite in Diana's Pool orbicules. 211
Table 23: In-situ initial $^{87}Sr/^{86}Sr$ isotopic compositions of the Diana's Pool orbicules.....226
Table 24: Koperberg Suite country rocks plagioclase data. OK=Orbicule Koppie, HL=Hoogkraal Lease, HS=Henderson South and HN=Henderson North 230
Table 25: Orbicule Koppie plagioclase data.....235
Table 26: Microprobe analysis of biotites from the Orbicule Koppie orbicules. C= core, S= shells and M= matrix. 241
Table 27: Hoogkraal Lease EPMA plagioclase data.....255
Table 28: Microprobe analyses of biotite from Hoogkraal Lease. C= Core, S=Shell and M= Matrix. 261
Table 29: Henderson North plagioclase data.....275
Table 30: Microprobe analyses of biotites from the Henderson North Orbicules. C=core, S= Shells and M=matrix 283
Table 31: Henderson South plagioclase data.....297
Table 32: Microprobe analyses of biotite from Henderson South orbicules.....309
Table 33: In-situ initial $^{87}Sr/^{86}Sr$ isotopic compositions of the Koperberg Suite orbicules and surrounding rocks.OK=Orbicule Koppie, HS=Henderson South, HN=Henderson North and HL=Hoogkraal Lease 318
Table 34: Major and trace element results in bornite and chalcopyrite from the Koperberg Suite orbicules. CCP=Chalcopyrite, Bn= Bornite, OK=Orbicule Koppie, JP=Jubilee pit, HN=Henderson North and HS=Henderson South. Co As Se Pb Bi Ag Cd Sn Sb Te Mn and Zn are all trace elements in this table,.....333

1. Introduction

Orbicular rocks (Figure 1) have been recognized as rocks of geological curiosity since their earliest mention in 1802 (von Buch, 1802). To date, more than three hundred occurrences of orbicular rocks have been described with examples from every continent (Figure 2; Barbey, pers. comm., 2023) and hosted in rocks with variable compositions (Sederholm, 1928; Ray, 1952; Leveson, 1966; Palmer et al., 1967; Garvie, 1969; Barrière et al., 1971; Garvie, 1971; Couturié, 1973; Enz et al., 1979; Vernon, 1985; Symes et al., 1987; Ort et al., 1992; Monod et al., 1995; Smillie and Turnbull, 2013; McCarthy et al., 2016; McCarthy and Müntener, 2016; Barbey et al., 2021; Zhang and Lee, 2021). Orbicular rocks are rocks of typically magmatic, metamorphic and/or metasomatic origin characterized by shells of contrasting mineral abundances and textures about a central core (Leveson, 1966; Palmer et al., 1967; Leveson, 1973; Monod et al., 1995; Zhang and Lee, 2021).

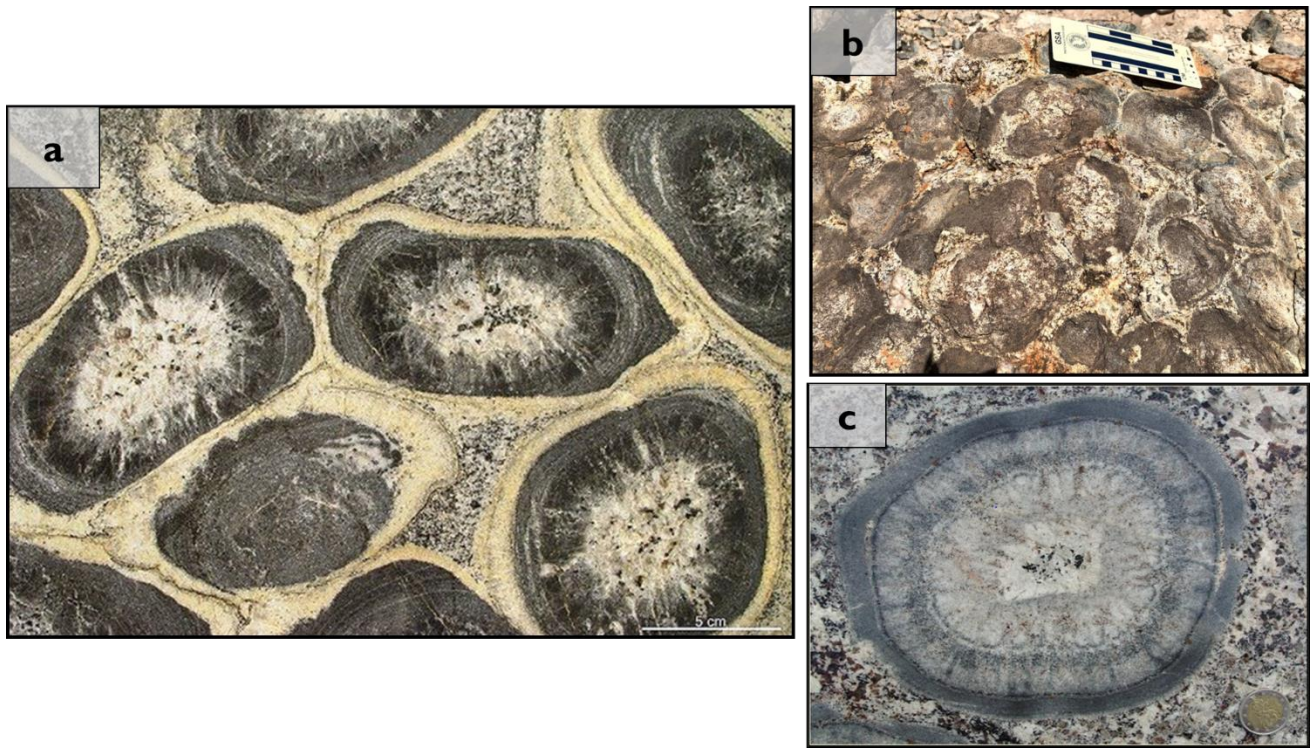


Figure 1: *Photographs showing different orbicular textures: (a) a heterogeneous orbicular sample from Finland (Lahti et al., 2005).(b) A sample showing orbicules characterized by multiple shells hosted in a granitic matrix taken from Orbicule Koppie, Koperberg Suite. (c) A sample showing combined radial and concentric orbicular textures (Lahti et al., 2005). In general, orbicules are spherical to ellipsoidal in shape; however, some orbicules are deformed, possibly resulting from indentation on interaction with other orbicules. In addition, the shapes observed in 2D with respect to the cores, are not erosional surfaces but they are observed on a variety of surfaces, suggesting that they are 3D as opposed to 2D.*

These rocks have a wide range of compositions and textures; however, they typical exhibit both chemical and mineralogical compositions of granites (Elliston, 1984). The diversity of geological settings (Figure 2) in which these rocks occur and the wide variety of mineralogical, textural, and chemical characteristics that they display compound their problematic petrogenesis (Leveson, 1966; Symes et al., 1987; Decitre et al., 2002; Smillie and Turnbull, 2013; Zhang and Lee, 2021).

Rocks showing typical characteristics and typical rhythmic banding features of the classical Finnish orbicular granites described by Sederholm (1928) outcrop at the Proterozoic Koperberg Suite (Northern Cape, South Africa) and the Archean Diana's Pool area (Matopo Hills, Zimbabwe).

The Koperberg Suite contains orbicules at ~63 known occurrences that were described by Enzman (1953). In his study, Enzman (1953) used field observations and petrography to investigate and describe the genesis of these orbicular textures in the Koperberg Suite. However, there is little data presented to support his conclusions on the genesis of these rocks.

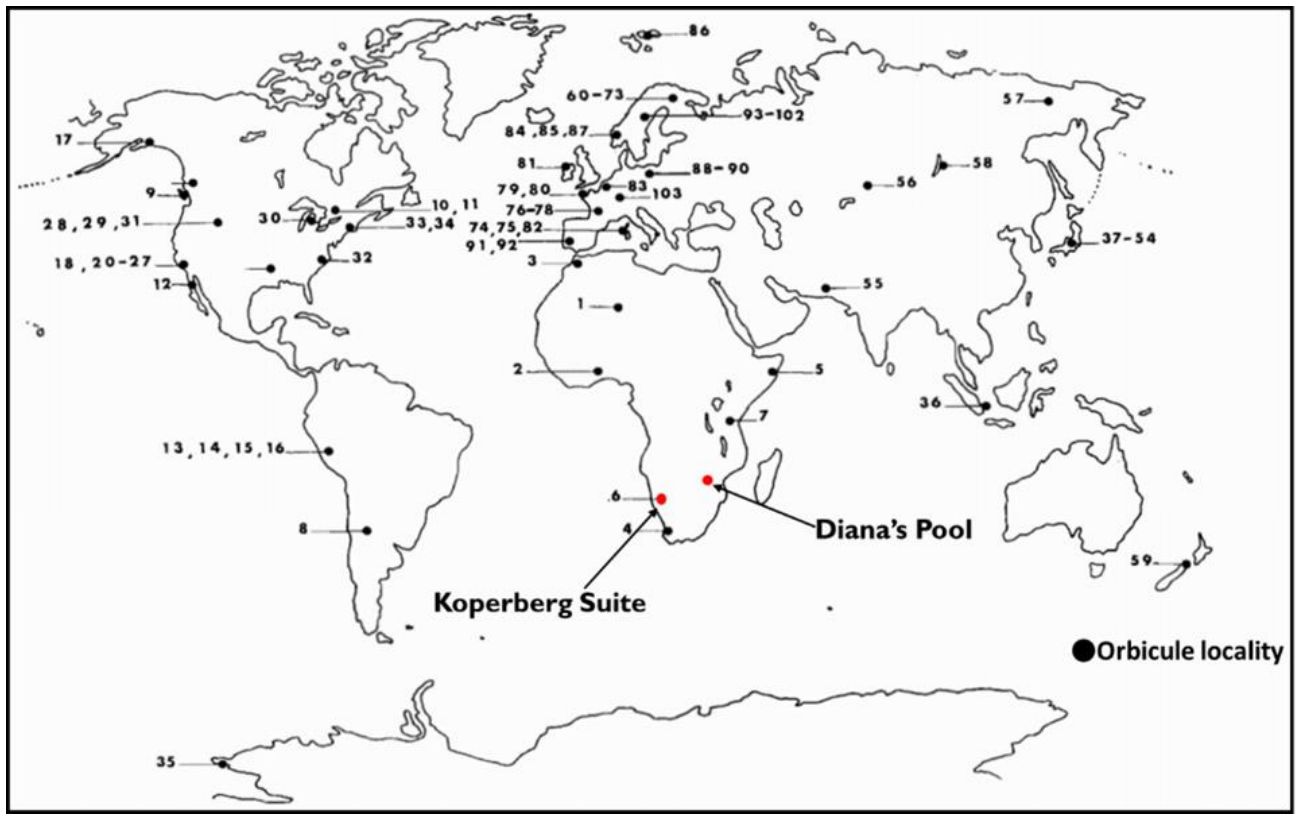


Figure 2: *World map showing some of the orbicule localities (black circles) and the studied Koperberg Site and Diana's Pool orbicules (red circles), after Leveson (1966).*

In addition, one unusual feature of some of the orbicule localities is that they contain sulphide mineralization (e.g., Orbicule Koppie and the Jubilee pit) and no link is made between the metallogenesis of the sulphides and the genesis of orbicular rocks.

The Archean Diana's Pool orbicular rocks were described by Garvie (1969, 1971), although not in detail. Garvie (1969, 1971) described these rocks as outcropping in the Matobo Hills area, within the Matopos granite, south of Bulawayo in Zimbabwe. Similar to Enzman, Garvie (1969, 1971) described the Diana's Pool orbicules and only limited petrological and geochemical work has been published as far as can be ascertained.

Previous work lacks detailed geochemical, mineral chemistry and isotope data to support their conclusions on the genesis of these rocks. Hence, the purpose of this study. This study documents a selection of orbicules from the Koperberg Suite and the Diana's Pool area, with the main aim of the contributing to the understanding of the genesis of the orbicules in both the Koperberg Suite and Diana's Pool area. This will enable the comparison of these rocks to assist in determining those processes which are similar and therefore fundamental to the genesis of orbicules and those that are

dissimilar and presumably subject to local geological controls. The project will also investigate the link between orbicule formation and sulphide mineralization in the Koperberg Suite orbicules.

1.1. Petrology of Orbicular rocks

Orbicular textures occur in ultramafic to silicic, and both undersaturated and oversaturated igneous and metamorphic rocks (Leveson, 1966). The compositions and mineralogy of the host rocks are typically different from the composition and mineralogy of the orbicules (Symes et al., 1987; Decitre et al., 2002; Zhang and Lee, 2021; Barbey et al., 2021). Orbicules vary in shape, size, and mineral assemblages and can be subdivided into core, mantle, shells and the host matrix, although not all of these features are always present (Figure 3; Leveson, 1966; Palmer et al., 1967; Barrière et al., 1971; Couturié, 1973; Leveson, 1973; Monod et al., 1995; McCarthy et al., 2016; McCarthy and Müntener, 2016; Zhang and Lee, 2021; Barbey et al., 2021).

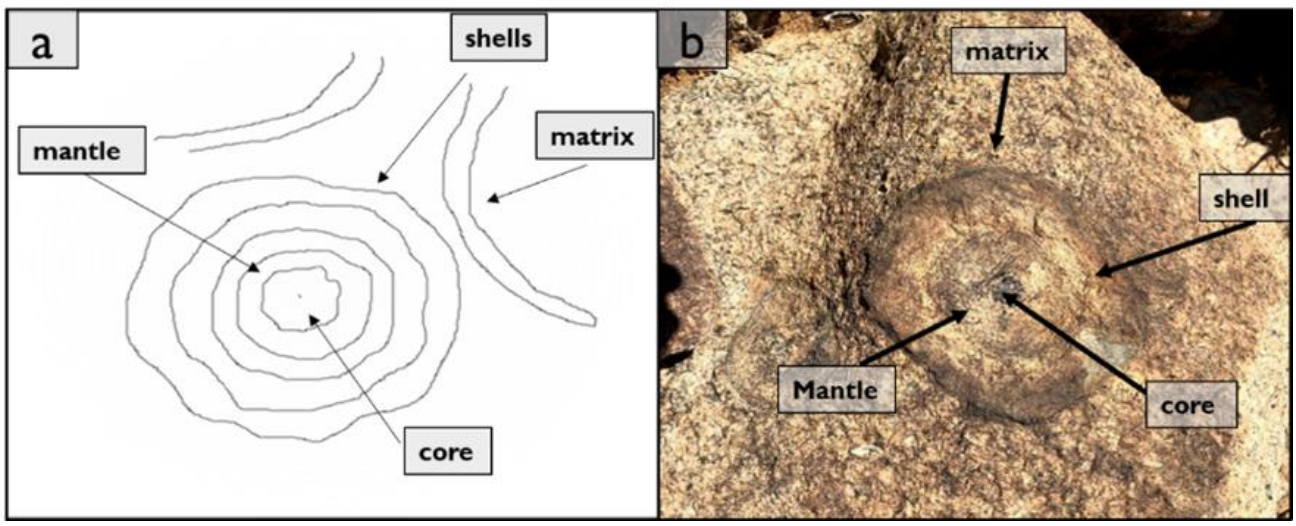


Figure 3: *Images showing a classification of the internal structure of orbicules: (a) schematic diagram showing the core, mantle, shell and matrix classification (Enzman, 1953). (b) Field photograph of an orbicule showing the different parts of an orbicule taken from the Henderson North outcrop, Namaqualand.*

Cores are generally igneous rocks (granites, diorites, and gabbros; metamorphic rocks (amphibolites), or crystals (feldspars, Figure 3). The orbicular mantle lies between the shell/s and core (Decitre et al., 2002). Common major minerals in the orbicular mantle include plagioclase, K-feldspar, quartz, amphiboles, pyroxenes, micas, olivine, sphene, epidote, sillimanite, cordierite, chromite, ilmenite, magnetite and tourmaline (Leveson, 1973; Ray, 1952). Orbicule cores and shells are characterized by radial, concentric and tangential textures.

Shells generally comprise K-feldspar or plagioclase, which are radially oriented and also contain quartz and biotite (Decitre et al., 2002). These textures can be attributed to aligned minerals (feldspars, amphiboles, micas, pyroxenes) or an aggregate of oriented minerals (Leveson, 1966). Cores, shells, matrices, and host rocks differ in both the nature and quantities of minerals present (Sederholm, 1928; Ray, 1952; Palmer et al., 1967; Enz et al., 1979). There is no consensus or one single hypothesis explaining how these rocks form (Leveson, 1973; Symes et al., 1987; Decitre et al., 2002; McCarthy et al., 2016; McCarthy and Müntener, 2016; Zhang and Lee, 2021; Barbey et al., 2021). Instead, different petrologists have put various models forward to explain their genesis and these include magmatic, metamorphic, metasomatic models, and/or combinations of these.

1.1.1. Magmatic models

Throughout the late 1900s into the 21st century, the growing consensus has emphasized the magmatic origin of orbicular rocks (Sederholm, 1928; Palmer et al., 1967; Enz et al., 1979; Vernon, 1985; Symes et al., 1987; Ray, 1952; Ort, 1992; Monod et al., 1995; Smillie and Turnbull, 2013; McCarthy et al., 2016; McCarthy and Müntener, 2016; Zhang and Lee, 2021; Barbey et al., 2021; Li et al., 2021). The magmatic models include assimilation or incorporation of new material in a magma, liquid immiscibility, superheating and subsequent undercooling, incomplete mixing and mingling between magmas of different compositions, oscillatory crystallization processes through rhythmic supersaturation of excessive crystallization of feldspar and mafic components, fluctuations of melt about a eutectic due to temperature and pressure variations, magma reactions with xenoliths, movements of the nucleus through parts of the magma with different compositions and emplacement in melt extraction zones associated with decompression of mafic melts in sub-volcanic conduits or sub-vertical dykes (Leveson, 1966; Leveson, 1973). In recent years and in addition to liquid immiscibility and devitrification models, two main magmatic models were proposed: (1) a model of outward crystallization from a core within dykes (McCarthy and Mutineer, 2016 and Barbey et al., 2021), but following to some extent previous researchers such as Vernon (1985) among others; and (2) a model of magma interaction proposed by Zhang and Lee (2021), which considers slow quenching of hot dioritic blobs incorporated into a cooler granitic magma.

Several occurrences of orbicules occur at pluton margins and this, together with alternating layers of contrasting mineralogy, and radiating textures or comb layering have been put forward as evidence that undercooling near pluton margins, followed by rise in temperatures from latent heat of crystallization causes orbicule formation (Leveson, 1973; Moore and Lockwood, 1973). Radial growth is also presented as evidence for a magmatic origin because it occurs mainly near contacts due to upward migration of aqueous fluids along magma and wall rock contacts (Moore and Lockwood, 1973). Alternating compositional layers are also attributed to, and used as evidence for rhythmic supersaturation during crystallization of a magma saturated with more than one mineral (Symes et al., 1987). Orbicules typically exhibit alternating shells and this alternation is attributed to syn-magmatic processes involving late aqueous fluids in which the periodicity of shell formation results from fluctuations in P_{H_2O} (Leveson, 1966). Some orbicular rocks exhibit shells that are characterized by sharp outer boundaries and these shells are indicative of changes in the physico-chemical environment in the magma (Symes et al., 1987).

There may be a connection between spheroidal inclusions and orbicules in mineral assemblages, textures and alteration (Nockolds, 1931). Spheroids result from crystallization of a magma around a nucleus that is not necessarily a rock fragment or an alteration product. If remnants of spheroidal inclusions are contained in orbicules, then the orbicules may have been derived from the material similar to that of spheroidal inclusions. If the inclusions and the orbicules exhibit similar feature (shape and size), then it seems reasonable that the spheroidal inclusions may have been transformed into orbicules (Nockolds, 1931). This is only possible if there is a reaction between xenoliths and the magma; hence, it is presented as evidence for this mechanism of orbicular formation. However, this model is not adequate as a general explanation but is valid in some instances (Leveson, 1966).

Leveson (1966) claimed that orbicules are not restricted to limited or particular magma-rock compositions, suggesting that liquid immiscibility is unlikely to be significant in their formation. However, Lapin and Vartiainen (1983) attribute differences in matrix and core composition together with orbicular and non-orbicular rocks having the same compositions to segregation of the initial melt and that the differences in viscosity of the melts and limited solubility promotes fractionation. They present this as evidence in support of liquid immiscibility being the mechanism behind the formation of orbicules in orbicular and spherulitic carbonatites from Solki and Vuorijarvi.

Morse (1980), Grove et al. (1992), McCarthy and Müntener (2016) and Barbey et al. (2021) stated that variations in pressure during decompression of magma pulses in dykes play a significant role on the stability of minerals. This would account for the change in the nature of ferromagnesian phases from the cores to the shells observed in orbicules worldwide. In addition to this, some crystals in the ferromagnesian shells are fine, branched, and comb-layered (radiating-textures), indicating disequilibrium conditions during orbicule crystallisation and rapid growth in a fluid-rich environment (e.g., Lofgren and Donaldson, 1975). Smillie and Turnbull (2013), Barbey et al. (2021), Li et al. (2021) and Zhang and Lee (2021) claimed that this indicates a fast and unimpeded crystal growth in a highly undercooled magma under non-equilibrium conditions. A sudden and important temperature variation is not conceivable in a plutonic environment; hence, the most likely process for rapid supersaturation is volatile exsolution on decompression, displacing liquidus temperature (McCarthy and Müntener, 2016; Barbey et al., (2021), which is consistent with a magmatic origin.

1.1.2. Metamorphic and metasomatic models

Metamorphic and metasomatic origins of orbicular rocks have also been emphasized (Eskola, 1938; Leveson, 1966; Leveson, 1973; Moore and Lockwood, 1973; Thompson and Giles, 1974). Two metamorphic models have been put forward to explain orbicular formation and these include: (a) origin by active diffusion and granitisation and, (b) the influx of Na^{1+} ions and outward diffusion of Ca^{2+}, Mg^{2+}, and Fe^{2+} ions during sodium metasomatism of mafic rocks, which creates conditions under which orbicules may form. Evidence put forward for these models includes (Leveson, 1996; Decitre et al., 2002):

1.1.2.1. Origin by active diffusion and granitization

Evidence of granitization includes: orbicules hosted in granitic rocks, orbicules showing progressive growth of feldspars and deformation of orbicules. Petrologists in support of the active diffusion model present the recrystallization and alteration of the primary mineral assemblages as evidence and attribute this to fluctuations in P_{H_2O}. Leveson (1973) considered it equally valid to use radial growth or comb layering (Moore and Lockwood, 1973) as evidence for orbicules forming by active diffusion. This is because radial growth develops through metamorphic recrystallization/replacement and that it also results sequential to magmatic activity (due to a static metasomatic process). The static metasomatic processes are common under conditions of active diffusion in water-rich and high temperature metamorphic environments. Changes like a decrease in An content of plagioclase from the core outwards and an increase in Na_2O in feldspathic parts of the orbicule from the core outwards

is used as evidence of albitization and active diffusion. However, granitization is now an outdated and largely discounted process (McBirney, 1963).

1.1.2.2. Influx of Na^{+1} ions and outward diffusion of Ca^{2+}, Mg^{2+}, and Fe^{2+}

This model proposes that the feldspathic parts of orbicules are consistent with diffusion fronts resulting from Ca^{2+} ions migrating from orbicule centers. This occurs simultaneously with Na and Si^{4+} ions migrating to the center, and this implies active feldspar growth. The feldsphathic nature of the cores is evidence that Mg^{2+}, and Fe^{2+} are diffusing out from the orbicules. However, these two metamorphic models are only valid in certain cases but lack or do not provide a general explanation of orbicular formation (Leveson, 1966).

Late magmatic aqueous fluids (metamorphic and metasomatic processes; e.g., Eskola, 1938; Leveson, 1966; Leveson, 1973; Moore and Lockwood, 1973; Thompson and Giles, 1974) certainly have an important effect on the final orbicular rock. Even Garvie (1969, 1971) and Enzman (1953), who studied the Diana's Pool and the Koperberg Suite rocks, respectively, attribute orbicular formation to metasomatic and metamorphic processes. However, recent work (e.g., McCarthy et al., 2016; McCarthy and Müntener, 2016; Zhang and Lee, 2021; Barbey et al., 2021; Li et al., 2021) have shown that magmatic processes are essential for the production of characteristics observed in orbicules. The data presented in this work will also show that metamorphic processes play little to no role in the formation of orbicular rocks and magmatic processes are behind orbicular rock formation.

1.2. Aims (s)

To constrain the genesis of orbicular granitoids and to demonstrate whether there is a genetic link between orbicular formation and ore genesis, This study focuses on two localities in southern Africa where orbicules are found in rocks of different ages and tectonomagmatic associations with the main aim of contributing to the understanding of the genesis of the rocks and investigate if there is any possible link with the metallogenesis of the mineralization, in the case of the Koperberg Suite.

1.3. Key research questions

In order to indicate lines of thoughts which the author imagines to be the most significant to understanding the mode of occurrence, genesis, destruction of orbicular textured rocks in Diana's Pool and the Koperberg Suite and the metallogenesis of the sulphide mineralization in the Koperberg Suite, the reader is introduced to the subject by the following research questions. If these questions can be answered, parameters will have been fixed, which will establish all the broader geological principles relating to orbicules in the Koperberg Suite and the Diana's Pool area. The objective of this thesis will be to answer the following six key research questions, and to elaborate them with some further detail.

(1) Are Diana's Pool and Koperberg Suite orbicules different from other global orbicular occurrences?

Do Diana's Pool and Koperberg Suite orbicules differ from other global occurrences? Are the two localities also distinct from each other? The author proposes that these orbicules are similar to other global occurrences.

(2) Are Diana's Pool and Koperberg Suite orbicules similar or different? What are the implications?

Comparing these localities will enable the comparison of these rocks to assist in determining those processes which are similar and therefore fundamental to the genesis of orbicules and those that are dissimilar and presumably subject to local geological controls. The author proposes that these rocks formed by similar processes.

(3) Are the orbicules in both localities of magmatic or metamorphic/metamorphic origin?

Although Garvie (1969) and Enzman (1953) proposed a metasomatic origin, the magmatic origin is seldom question recently and this work will provide lines of evidence, which either will agree with or disproved the work of these authors. The author here proposes a magmatic origin of the Diana's Pool and the Koperberg Suite orbicules.

(4) How do orbicules commence to form and how are they destroyed? Physical orbicular forming processes

How may the shape of orbicular bodies be explained? Is there any reason for variation in types and sizes within one body? Is there any variation in mineral chemistry and isotopic data? The author proposes that the formation of orbicular bodies is not dependent on the magma composition, is dependent of physical processes.

(5) What is the origin of the sulphide mineralization? Is the bornite-chalcopyrite-magnetite assemblage primary or secondary?

The bornite problem? Why is the sulphides assemblage (bornite +chalcopyrite + magnetite) controversial? Why is the mineralization only prevalent in the mafic bodies and only in the matrices? The author proposes that the sulphides are not primary but secondary mineralization.

(6) Is there any link between orbicular rock genesis and sulphides metallogenesis in the Koperberg Suite?

Are the physical processes that formed the orbicules in the Koperberg Suite behind the metallogenesis of the sulphides? The author proposes that there is no link between sulphides metallogenesis and orbicular genesis.

1.4. Objectives

The objectives of the project are:

- Documenting and understanding the occurrences and variability of orbicules and sulphide mineralization.to understand the spatial relationship between orbicular rocks, sulphide mineralization, structures and the surrounding rocks in both the Koperberg Suite. A detailed field mapping and sample collections of orbicules from the Koperberg Suite will achieve this. Please note detailed field mapping was achieved only for Koperberg Suite orbicular bodies, not for Diana's Pool because of restrictions in accessing Zimbabwe and cost reasons.
- Using petrographic techniques to classify compare different orbicule types and sulphide occurrences/ assemblages. This will be done by using a full section microscope in the

Wits Petrology Lab to scan the thin sections at high-resolution, ahead of detailed textural analysis using a Tescan Integrated Mineral Analyzer (TIMA) to analyze the mineral assemblages and textures in the cores, matrices, shells, and mantle of the orbicules from both the Koperberg Suite and Diana's Pool area. *In-situ* major element analyses by Electron Probe Microanalysis (EPMA) at Wits University will reveal the identity of mineral phases within the orbicules and may help in the understanding of the magma processes operating during orbicule formation. The *in-situ* mineral data from the cores, shells and the matrices will help reveal how the major elements vary from the cores to the matrices, especially for elements like Ca, Mg and Fe. In this way, different hypotheses will be tested.

- Analysis of *in-situ* Sr isotopes using MC-ICP-MS at the University of Johannesburg, to be used as a geochemical tracer to test and trace the processes that occurred to form these rocks e.g., assimilation and magma mixing.

- Analysis of *in-situ* trace element compositions of various textural divisions of the orbicule structures (e.g. cores, shells, and the matrices) using a LA-ICP-MS at Stellenbosch University, to characterize the trace element constituents of the sulphides. Trace element analyses will be useful to trace the source of sulphides by tracking processes such as liquid immiscibility to see if they are behind the formation of sulphides. They will also be useful in testing fluid alteration or fluid mobility and in addition mixing, assimilation, liquid immiscibility and metamorphism. Trace elements to test for fluid alteration or fluid mobility.

- Investigating the age relationship between orbicular rocks and the surrounding host rocks in both Diana's Pool area and the Koperberg Suite using the LA-ICP-MS U-Pb zircon, methods at the University of Johannesburg.

2. Geological Setting(s)

2.1. Regional Namaqualand Metamorphic Complex

The 1100 to 1000 Ma Namaqua Metamorphic Complex (NMC; Figure 4) forms the western part of the Namaqua-Natal orogenic belt, which is exposed in South Africa's Northern Cape and KwaZulu-Natal provinces, forming a continuous arcuate orogenic belt that extends beneath the Karoo Supergroup (Geringer, 1988; Cornell et al., 2006; Sithole, 2018). It comprises metamorphic and igneous rocks that are believed to have formed and been metamorphosed at approximately 1300-1000 Ma during the Namaqua Orogeny (Geringer et al., 1986; Geringer, 1988; Macey et al., 2018).

The rocks of Namaqualand formed during the amalgamation of Rodinia, which was assembled at 1200 to 1000 Ma (Sithole, 2018; Cornell et al., 2006). It extends from an area north-west of Vanrhynsdorp to the Orange River and eastwards to Prieska and Upington (McCarthy, 1976) and contains a well-exposed zone of low-pressure granulite-facies rocks that are a product of the Namaqua tectonothermal event (Cornell et al., 2006; Thomas et al., 1996).

The NMC contains SW-directed stacks of thin, laterally extensive, thrust-bounded sheets, which form tectonostratigraphic domains that are distinguished based on their lithostratigraphy, tectonic and metamorphic history (Macey et al., 2018). These domains are (Figure 4a; Macey et al., 2018):

- The low- to medium-grade Ritchersveld Subprovince (Paleoproterozoic), which contains the oldest crustal material (1900 Ma) in the Namaqua sector.
- The Bushmanland Subprovince (BSP), which forms the southernmost domain of the Namaqua sector. It is composed of ~1850 Ma gneisses and migmatites in the northwestern part while pre- and post-tectonic Mesoproterozoic granites dominate the rest. Mafic rocks are minor components of the intrusions in the western BSP, represented by pre-tectonic amphibolites, granulites and noritic bodies of the post-tectonic Koperberg Suite.
- The Areachap Domain, which comprises 1300-1220 Ma arc-generated amphibolite facies grade supracrustal rock intruded by granitoids (1220-1100 Ma).

  The Kakamas Domain that tectonically overlies the Ritchersveld Subprovince. It comprises rafts of granulite facies meta-sedimentary rocks (~ 1220-1200 Ma) that are intruded by igneous rocks (1210-1080 Ma).
- The granulite Aus Domain located NW of the Kakamas Domain. It contains granitoid gneisses and granites (1120-1085 Ma) and subordinate migmatitic supracrustal gneisses.

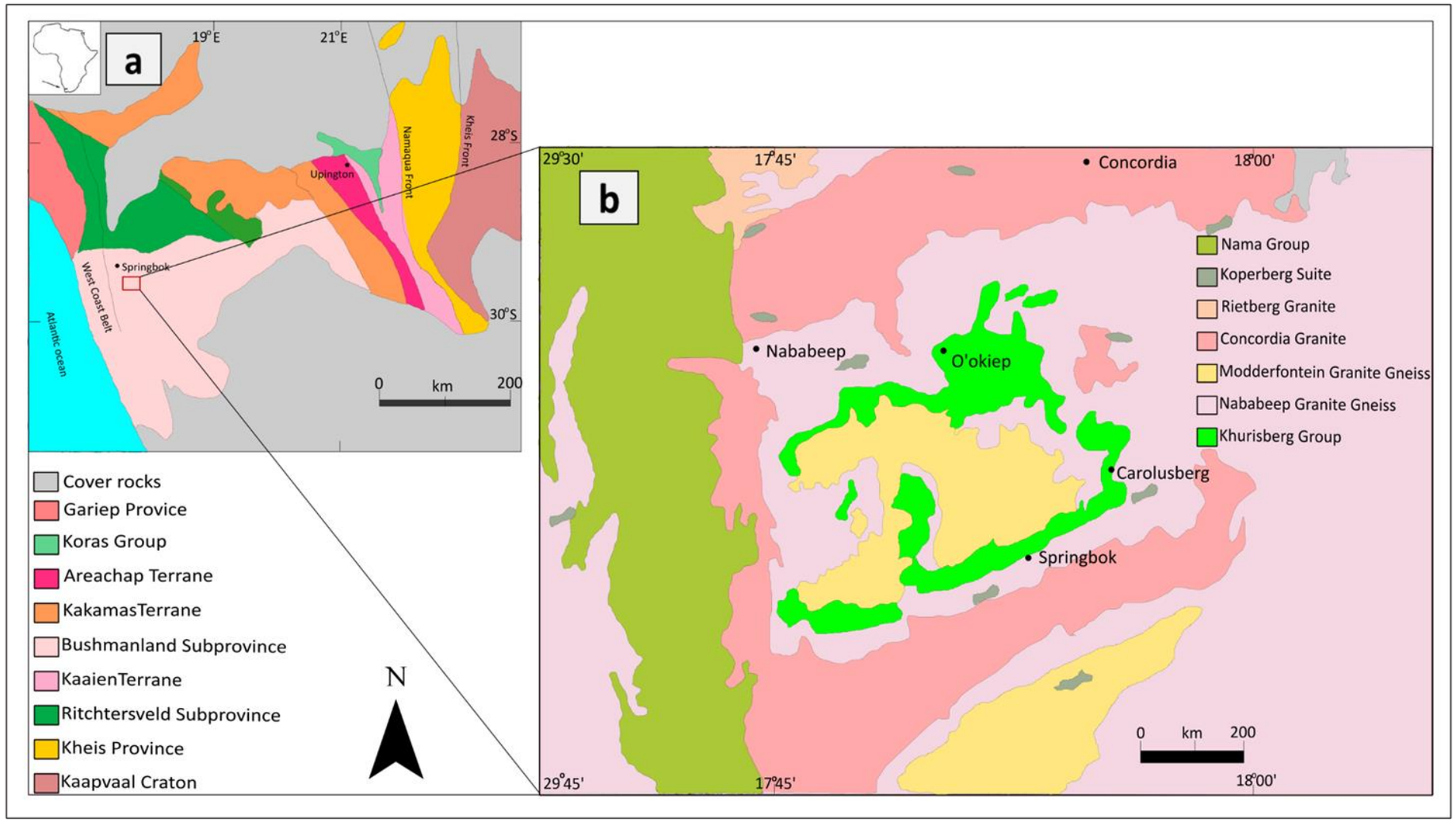


Figure 4: *Simplified geological map showing the regional tectonic setting of the Namaqua-Natal Province: (a) A map of Namaqualand showing different domains, sub provinces and the study area (red rectangle) modified after Cornell et al. (2006). (b) Geological map of the O'okiep Copper District modified after Lombaard et al. (1986).*

- The Kaaien Domain, which forms a tectonic transition zone between the Kaapvaal Craton and Kheis Province and the Namaqua sector. It comprises ~ 870 Ma metaquartzites, ~ 1370 and 870 Ma bimodal volcano-sedimentary rocks and 1100 Ma granitic Intrusions.

- The Kheis Province, which forms the eastern most tectonic domain of the Namaqua sector. It represents a Mesoproterozoic thin-skinned fold and thrust belt deformed during the early stage of the Namaquan orogeny.

2.1.1. Structure

A sequence of deformation events has been established in the NMC (Table 1): D_1 (Pre-Kibaran), D_2 and D_3 (Syn-Kibaran) and D_4 (Late Kibaran).

Table 1: *Relation between intrusive, metamorphic and deformational events in the O'okiep Copper District after Raith and Harley (1998). Ages are given according to: [1] Clifford et al. (1995),[2]Reid et al. (1991),[3] Nicolaysen and Burger (1965), [4]Reid (1979),[5] Robb et al. 1997.*

Age	**Deformation**	Metamorphism	Intrusions / Mineralization
c. 500-550 [1]		M_4 High-grade	Low-T alteration Remobilization of Cu-deposits
78 ± 7 [2] 950-1000 [3]			Mafic dykes Pegmatites, syenite dykes
1029 ± 10 [1] (U-Pb Zircon) 1022 ± 42 (Sm-Nd)	D_3 Steep Structures (Syn-Kibaran)	M_3 High-grade cooling	**Koperberg Suite** -Cu deposits **Spektakel Suite** -Kweekfontein Granite -Rietberg Granite -Concordia Granite
1064 ± 31 [5] (U-Pb Zircon)	D_{2b} (Syn-Kibaran)	M_{2b}	W-Mo Deposits
1223 ± 48 (Rb-Sr) [1] 1997 ± 15 (U-Pb zircon)	D_{2a} (Syb-Kibaran)	M_{2a}	**Little Namaqualand** -Modderfontein Granite Gneiss -Nababeep Granite Gneiss
c. 800-2000 [4] 1822 ± 365 [5] (U-Pb Zircon)	D_1 (Pre-Kibaran)	M_1	**Gladkop Suite** -Noeomaasberg Granite Gneiss -Brandewysbang Granite Gneiss

Joubert (1986) stated that in the Bushmanland Subprovince, D_1 is described as the earliest deformation event and is recorded as tight intrafolial folds (F_1) in older gneissic units. The second deformation phase (D_2) of Clifford et al. (2004) and D_1 of Cornell et al. (2006) is described as the main and major deformation event in the Namaqua sector (Kisters et al., 1996; Raith and Harley, 1998) and normally occurs as a penetrative sub-horizontal foliation of metamorphic layering combined with the formation of isoclinal to recumbent F_2 folds. Kisters et al. (1996) suggested that this was due to large-scale southwards thrusting. The D_2 event in Bushmanland Subprovince has been subdivided by Macey et al. (2018) into three stages. These include the ~1200 Ma D_{2a} event characterized by syn-deformation magmatism and metamorphism in all the Namaqua sector domains, the D_{2b} event characterized by sediment deposition and extension prevalent in most parts of the Namaqua sector; and the D2c event characterized by reshuffling and thrusting of the crust, producing the E-W striking S_2 (subhorizontal gneissosity) at ~1110 Ma. The D_2 event produced the pervasive subhorizontal gneissosity (well

observed in the Nababeep and Modderfontein Granite Gneisses and the Concordia Granite). D_3 is the third deformation phase and it refolded D_2 structures. This resulted in the formation of open upright F_3 folds and sub-vertical, E-W trending steep structures that are major control of the Cu-mineralization in the Koperberg Suite (Kisters et al., 1996). The emplacement of the Koperberg Suite occurred during this localized ductile deformation event that formed the steep structures in the host granite-gneisses (Benedict et al.1964). Many of the Koperberg Suite intrusions were emplaced along the flanks of the steep structures (Benedict et al., 1964; Lombaard et al., 1986). Kisters et al. (1994; 1996) stated that the D_3 event also resulted in the reactivation of the Skelmfontein thrust and this even resulted in regional open folds (Springbok Dome and Springbok synform). Minor N to NW orientated sub-vertical shear zones (Kisters et al., 1996; Kisters et al., 2003) represent the D_4 structures. The granite-gneiss terrane in the O'okiep Copper District is characterized by a granulite facies metamorphism (Kisters et al., 1996).

2.1.2. Metamorphism

The Bushmanland Domain has undergone at least two major cycles of metamorphism (M_2 and M_3) after the M_1 event related to the D_1 event (Cornel et al., 2006). Raith and Harley (1998) and Clifford and Barton (2012) have interpreted the metamorphic events in two ways. This is because the Bushmanland domain is characterized by asymmetric metamorphic zonation (upper granulite facies zone in the central parts of the domain and amphibolite zone in the northern and southern parts of the domain; Waters, 1986) leading to the proposition of anticlockwise and clockwise pressure-temperature paths. Raith and Harley (1998) described the clockwise path as a syn-D_2 granulite facies metamorphism (750-870^{o} C, 5-6 kbar) related to magmatism (~1200 Ma), followed by subsequent upper amphibolite facies metamorphism (580-660 ^{o}C, 5.8 kbar). The Koperberg Suite was then emplaced during this event (~1030 Ma) into hot mid-crustal rocks at upper amphibolite or granulite facies temperatures (Clifford et al., 2004; Clifford and Barton, 2012).

2.2. Koperberg Suite

The lithostratigraphy of the 3000 km^2 O'okiep Copper District (Figure 4b) within the NMC (Bushmanland Subprovince) has been divided into two broad subdivisions (Van Zwieten et al., 1996). These are meta-volcano-sedimentary sequences known as Khurisberg Subgroup and Lammershoek Subgroup, and several phases of intrusive granites; Gladkop, Little Namaqualand, Spektakel Suites and the Koperberg Suite (Figure 4b) that intrude the NMC granites and gneisses. Located in the O'okiep Copper District (Bushmanland Subprovince, NMC) are numerous, predominantly E-W trending and < 1 km in strike length dyke-, diapir- and sill-like bodies of the Koperberg Suite. These dykes, diapirs and sills intruded the Namaqua-aged granitic gneisses and granites under amphibolite or granulite facies conditions (Figure 4b; Cawthorn and Meyer, 1993; Mclver et al., 1983; Gadd-Claxton, 1981; Kisters et al., 1996; Raith and Harley, 1998; Mouri et al., 2003). The Koperberg Suite also cut other country rock units including the Rietberg Granite (External examiner 1, pers. comm., 2023). The Koperberg Suite has been dated at 1040 to 1020 Ma by Duschene et al. (2007) and at 1100 Ma from the U-Pb zircon geochronology (Stumpfl et al., 1976). Zircon U-Pb geochronology by (Clifford et al., 1995, 2004; Bailie et al., 2019) indicates that the Koperberg Suite was emplaced

between 1057 ± 8 to 1029 ± 10 Ma. These rocks are collectively referred to as 'basic' bodies (Lombaard and Schreuder, 1978) or noritoids (Benedict et al., 1964).

2.2.1. Petrography and mineral compositions

The Koperberg Suite dykes, diapirs and sills are dominantly anorthosite and diorite, but also include syenite, quartz anorthosite, quartz diorite, biotite diorite, hypersthene diorite, and glimmerite (Gadd-Claxton, 1981; Conradie and Schoch, 1988). The early intrusions are felsic anorthosites through mica-diorite, with pyroxene leucodiorite and pyroxene diorite characterizing the last magmatic pulses (Cawthorn and Meyer, 1993). The main silicate phases include orthopyroxene (En_{58-68}), plagioclase, and biotite, with accessory chalcopyrite, bornite, apatite, and subordinate iron-titanium oxides (Clifford et al., 1981; Schoch and Conradie, 1990). Plagioclase is predominantly andesitic in composition (An_{31-39}) ranging up to labradorite (An_{52}) (Clifford and Barton, 2012). Apatite is abundant and occurs as rounded and tabular grains in the mafic rocks (Conradie and Schoch, 1988). Clinopyroxene, zircon and hornblende are rare and monazite occurs as a common accessory phase (Stumpfl et al., 1976).

2.2.2. Sulphide mineralization

The Koperberg Suite contains copper mineralization that has been exploited since before the Dutch colonists arrived in Southern Africa in 1652 (Marais et al., 2001). The sulphide mineralization is more common in ultramafic to mafic rocks of the Koperberg Suite, forming Ni-Cu ± PGE deposits (Clifford and Barton, 2012). In addition, rare orbicular-bearing intrusions of the Koperberg Suite (e.g., Orbicule Koppie and the Jubilee pit) contain sulphide mineralization, which is unusual since the more mafic members of the Koperberg Suite (pyroxenite and leucodiorite) are commonly the host rocks to economic Cu mineralization. Studies noted that the mineralization style ranges from fine disseminations, vein-like aggregates and massive concentrations (Gibson et al., 1996).

Sulphides occur as interstitial phases around silicates, in association with oxide phases, along planes of biotite cleavage or replacing oxides (Cawthorn and Meyer, 1993). The principal sulphide ore parageneses include bornite and chalcopyrite, together with chalcocite as an alteration product of bornite (Stumpfl et al., 1976; Clifford and Barton, 2012). Magnetite is pervasive and in some places contains exsolution lamellae of ilmenite (Conradie and Schoch, 1988). Hematite, rutile and ilmenite form as alteration products of magnetite (Stumpfl et al., 1976). Pyrrhotite and pentlandite are less common assemblages and they are restricted to Narrap, Wheal Heath and the East O'okiep mines. Pyrite is a minor phase and galena and sphalerite have been documented in the suite, with no economic significance (Stumplf et al., 1976). Valleriite, native copper, sylvanite, niccolite and molybdenite are other common phases in the suite (Lombaard et al., 1986). Cawthorn and Meyer (1993), based on the main sulphide assemblages at specific mines and localities in the O'okiep Copper District, subdivided the Koperberg Suite ore into the following three groups:

(1) The Narrap-type (chalcopyrite + pyrrhotite ± pentlandite) ore exhibiting low Cu/S (036-0.97), low S/Se ratios (13899-21000) and high $\delta^{34}S$ values compared to the Carolusberg type.
(2) The Carolusberg-type ore (bornite-magnetite ± chalcopyrite) characterized by low S/Se ratios, high Cu/S (1.68-3.93) and low $\delta^{34}S$ values (-1.5 to 4.1‰; Cawthorn and Meyer, 1993; Boer et

al., 1994). The Carolusberg-type ore exhibit values of Cu/S and S/Se ratios and $\delta^{34}S$ values atypical of mantle-derived rocks. Hence the ore is interpreted to be a product of oxidation and sulphur devolitization of the primary Narrap-type ore during granulite facies metamorphism (Cawthorn and Meyer, 1993).

(3) Intermediate Hoist-type ore characterized by a bornite + chalcopyrite assemblage (Clifford et al., 1975).

Granular textures between sulphides and pyroxenes with polyhedral angles between them have been observed in the Koperberg Suite (Cawthorn and Meyer, 1993). This has been described as uncharacteristic of sulphides formed from the segregation of an immiscible sulphide liquid (Cawthorn and Meyer, 1993). Hence, different mechanisms for the genesis of the Koperberg Suite magmas and the metallogenesis of the related sulphide mechanism have been put forward. According to the primary magmatic model, sulphides in the Koperberg Suite crystallized from a sulphide melt that segregated from a basaltic magma upon intrusion and emplacement along the steep structures (Mclver et al., 1983; Boer et al., 1994; Van Zwieten et al., 1996). Upon intrusion, the sulphide melt was subjected to contamination by a granitic partial melt derived from the country rocks (Van Zwieten et al., 1996). The metal content would have been derived from the mafic magma and the different Koperberg Suite lithologies would have resulted from gravitational segregation of the mafic phases and various degrees of contamination (Maier, 2000). However, it is impossible to crystallize bornite from the model sulphide magma by a primary magmatic process (Maier and Barnes, 1999). Bornite formation would only be possibly if the parental silicate melt was unusually enriched in Cu (~ 400 ppm) and in this case the segregating melt would have a higher Cu content (~40 wt.%), potentially forming primary bornite. However, such high contents of Cu has never been reported from basaltic magmas (Maier and Barnes, 1999). In addition, this model fails to explain the unusual bornite + magnetite assemblage (e.g., Cawthorn and Meyer, 1993; Maier and Barnes, 1999; Maier, 2000; Maier et al., 2012) and the textures between the silicates and the sulphides (Cawthorn and Meyer, 1993). In addition, the Cu/Ni ratios in sulphides that crystallized in a basaltic magma are ~3 with few magmatic deposits having higher ratios (>3, e.g., Norwegian stormyrplutten ores with Cu/Ni = 8; Maier and Barnes, 1999). The Cu/Ni ratios in the Koperberg orbicules are relatively high and are not regarded as primary magmatic (Maier and Barnes, 1999).

A hydrothermal model has also been put forward to explain the unusual assemblage in the Koperberg Suite rocks. According to Maier et al. (2012), an *in-situ* hydrothermal or metamorphic remobilization could well explain the high Cu/Ni ratios in the sulphides, since the primary magmatic model cannot, and can well explain the high modal abundances of mica and saussurisation of plagioclase observed in the Koperberg Suite rocks. Cu is relatively mobile in hydrothermal fluids and because bornite requires higher Cu/Fe ratios, it is usually found in hydrothermal deposits (e.g., porphyry copper deposits; Maier and Barnes, 1999). Sulphide mineralization in the Koperberg Suite is exclusively hosted in the more mafic rocks (orthopyroxenites and norites) within a high temperature granulite facies environment (Waters, 1986; Waters, 1989; Clifford et al., 1995). This may be because percolating fluids precipitated copper on pre-existing magmatic sulphides hosted in the mineralized rocks due to localized processes and changes in the intensive parameters (e.g., Maier and Barnes, 1999). However, the Koperberg Suite country rocks are generally anhydrous (Maier and Barnes, 1999), suggesting a primary magmatic

feature for the hydration of the Cu-bearing rocks rather than hydrothermal alteration. Maier et al. (2012) stated that this model is considered unlikely, and it is discredited as a possible mechanism in the formation of sulphides in the Koperberg Suite.

Crustal assimilation of a Cu-rich contaminant at depth has also been proposed as a possible mechanism to explain the metallogenesis of the sulphides in Koperberg Suite. In general, most authors discredit the *in-situ* hydrothermal introduction of metals as the Cu-mineralization in the Koperberg Suite is only hosted in mafic rocks (Maier, 2000). Instead, according to Maier (2000), as a result of partial assimilation of deep-seated Cu-bearing country rocks (e.g., porphyry copper deposits in the nearby Eburnian-aged basement rocks north of the O'okiep Copper District, Minnitt, 1986) the ascending Koperberg Suite magma may have become enriched in Cu. The radiogenic $^{87}Sr/^{86}Sr$ isotope signatures that are exhibited by the Koperberg Suite rocks are consistent with significant crustal contamination (Van Zwieten et al., 1996). However, this model cannot be directly constrained (Maier et al., 2012).

Maier (2000) proposed that the Carolusberg orthopyroxenite containing bornite, chalcopyrite and magnetite in the Koperberg Suite is a restite of a lower-crustal protolith intruded as pyroxenitic crystal slurry, enriched in Cu-sulphides and magnetite. Read (1951), Mclver et al. (1983), and Clifford et al. (1975) have previously considered a residual origin for the Koperberg Suite pyroxenites. They propose a model whereby the Koperberg Suite underwent anatexis post-emplacement into the present setting. However, these authors did not attempt to explain the refractory behavior of the granitic-gneisses during the melting event (Maier, 2000). The restitic model for the Koperberg Suite is consistent with the high-grade metamorphic setting of the O'okiep ores, including the desulphidization model. Petrographic descriptions of the Koperberg Suite include references to the abundance of apatite, where it is occasionally described as a major-rock forming mineral (Mclver, 1983). The resistic model provides a solution to the problem of crystallizing a pyroxenite from a highly differentiated magma with apatite and zircon on the liquidus (Maier, 2000; Maier et al., 2012). Apatite refractivity depends on the silica activity and the water content of the magma (Harrison and Watson, 1984; Maier, 2000). Crustal anatexis of a gabbroic to dioritic protolith typically produces dry melts and those melts generally do not dissolve much P_2O_5, Zr or Fe^{3+} (Maier, 2000). During segregation, these residual phases, upon ascent and intrusion, may yield atypical ultramafic assemblages (orthopyroxene, magnetite and apatite) observed in the O'okiep District (Maier, 2000). A resistic origin of the pyroxenites of the Koperberg Suite would address many of the observed compositional features of the ores (bornite, magnetite and chalcopyrite assemblage) and their high-grade metamorphic setting (Maier et al., 2000). However, this model would demand ascent and emplacement of a pyroxene crystal mush enriched in apatite, magnetite and Cu-sulphides - whether this is geologically realistic is questionable and remains to be modelled quantitatively (Maier, 2000).

An Iron-Oxide-Copper-Gold (IOCG) model is another possibility that has been proposed to explain the sulphide assemblages in the Koperberg Suite (e.g., Maier et al., 2012). Andreoli et al. (2006) and Maier et al. (2012) stated that in a global extent, the O'okiep, Phalaborwa and the Curaçá Valley Cu deposits may be rare magmatic end-members of the IOCG class of deposits. This array of unusual and distinctive deposits suggest that the SCLM (Sub-Continental Lithospheric Mantle) under southern Africa was anomalously fertile and raises the possibility of magmatic IOCG deposits in the terranes of

Africa (Maier et al., 2012). Maier et al. (2012) observed that the O'okiep deposits exhibit high Au/PGE ratios, similar to those of the subcontinental lithospheric mantle (SCLM). Similar to the Caraiba and Phalaborwa deposits, O'okiep rocks exhibit high REE, U and Th contents leading to the proposed melting of a fertile metasomatised mantle and production of alkaline and volatile-rich melts for these deposits. Although they are not hydrothermal, these deposits exhibit characteristics of IOCG deposits. These characteristics include the occurrence of Cu and/or Au as major economic minerals, along with enrichment in LREE, Th, U, P, and abundance of Fe-Ti oxides. Therefore, the O'okiep deposits have been proposed to be magmatic end-members of IOCG deposits.

In the context of the IOCG model, the magmas in the Koperberg Suite would have been triggered by crustal extension (e.g., in response to orogenic collapse caused by extreme radiogenic heating at mid- to lower crustal depth; Mouri et al., 2003). This resulted in the SCLM producing magmas enriched in volatiles, CO_2, Cu, LILE, HFS and MgO (Maier et al., 2012) typical of the Koperberg Suite magma. Due to high volatile content, the magmas would ascend rapidly into the crust and sulphur would have been stable as a sulphate in the oxygenated magma (Mungall et al., 2006), preventing early sulphide saturation and allowing Cu to be concentrated in the magma until the advanced stages of differentiation (Campbell et al., 1998). An addition of external S as a contaminant would then trigger sulphide saturation and the magmas would ascend rapidly into the crust through trans-lithospheric structures, delaying sulphide saturation until the advanced stages of differentiation, causing advanced enrichment in copper (Maier et al., 2012).

The Koperberg Suite occurs in a high grade metamorphic terrane (Clifford et al., 1975; Thomas et al.,, 1994) similar to other Cu-rich deposits hosted by orthopyroxenites, norites and diorites like Serrote de Laje Complex in Brazil and the Angmagssalike area in east Greenland (Maier and Barnes, 1999). The occurrence of these rocks in metamorphic terranes suggest a metamorphic control on the origin of these ores (e.g., Cawthorn and Meyer, 1993; Maier and Barnes, 1999; Maier, 2000; Maier et al., 2012). Hence, the metamorphic model has been proposed to explain the unusual Koperberg Suite ores. Cawthorn and Meyer (1993) invoked a metamorphic oxidation and desulphidization model to explain the unusual bornite dominated ores of the Koperberg Suite. They proposed a metamorphic oxidation and desulphidization of a primary magmatic ore (pyrrhotite, chalcopyrite and pentlandite) to an assemblage consisting of chalcopyrite, bornite and pure magnetite (Equation 1; Cawthorn and Meyer, 1993, Maier and Barnes, 1996).

> **Equation 1:** $5CuFeS_2$ (chalcopyrite) + $5FeS$ (pyrrhotite) + $6H_2O$ +$8O_2$ = $CuFeS_4$ (bornite) + 3 Fe_3O_4 (magnetite) +6 H_2S + $5SO_2$

Maier and Barnes (1999) explained this unusual assemblage by the relationship of phases in the Cu-Fe-S system. Cu-poor *mss* is the first phase to crystallize in a Cu-Fe-S melt and as a result, the fractionating melt will be enriched in Cu, however, the Cu enrichment will end with the *iss* appearance on the liquidus (Cu content ~30 wt. %; Maier and Barnes, 1999). This also supported by Ballhaus et al. (2001), who states that a S-rich sulphide melt will crystallize in the *iss* stability field, producing chalcopyrite and pyrrhotite. However, if such a sulphide melt is oxidized, oxidation will result in a S-poor melt with metal/S >1, resulting in fractionation past the *iss* stability field (owing to liquidus and solidus temperatures).

Ballhaus et al. (2001) stated that the oxidation of a sulphide melt would result in an increase in both Cu and Ni contents of the melt and subsequent crystallization of bornite-digenite-*iss* assemblage or a bornite-digenite assemblage with no *iss.* Cawthorn and Meyer (1993) and Boer et al. (1994) proposed that the dehydration of country rocks during prograde metamorphism would have provided the chemically bound oxygen for the oxidation of the primary ores and the relatively high S/Se and the abundance of magnetite in Koperberg Suite sulphides substantiate this. Magnetite constitutes approximately 50 % of the opaque phases; however, typical Cu-Ni sulphide deposits contain 2 and 15% oxides (Maier and Barnes, 1999). In addition, the annealed polygonal textures of magnetite and the sulphide observed petrographically in the Koperberg Suite rocks suggest that oxidation occurred during high-temperature metamorphism (Cawthorn and Meyer, 1993). One of the main arguments put forward by Cawthorn and Meyer (1993) in support of the metamorphic oxidation and desulphidization model was the relatively high S/Se ratios of the ores and S/Se ratios are generally utilized to evaluate S-loss of magmatic sulphides (Maier, 2000).

Howard III (1977) stated that Se is a chalcophile element and is relatively immobile during low-temperature alteration and insoluble in oxidizing high-T fluids. Hence, S/Se ratios of sulphide ores would increase in the event of metamorphic S-loss (Peck and Keays, 1990). The high modal abundances of magnetite in the orbicules also preclude the magmatic origin. Magnetite may have formed by oxidation of pyrrhotite (Cawthorn and Meyer, 1993). Cawthorn and Meyer (1993) also noted a variation in Cu/S ratios in different samples and suggested that the variation is not magmatic, but it is attributed to oxidation, where S and not Se is lost during the process. They interpreted the sulphides with the highest Cu/S ratios as the most oxidized and those having the lowest Cu/S ratios as less oxidized. They attribute this overall trend through the entire source to variable volatilization of S. The origin and the timing of the fluid that oxidized the Koperberg Suite ores is difficult to constrain (Cawthorn and Meyer, 1993). However, based on the textures of bornite, magnetite and pyroxene (textures suggest that they equilibrated under high-grade metamorphism) it mostly likely originated at greater depths during this event and were highly oxidizing. Cawthorn and Meyer (1993) attribute variations in the degree of oxidation of the different ore bodies to metamorphic fluids focused in steep structures. However, Maier and Barnes (1996), Maier and Barnes (1999), Maier (2000) and Maier et al. (2012) stated that the model of desulphidization provides no explanation for low Ni concentrations and the high Cu/Ni ratios (up to 80) in the Koperberg Suite sulphides.

2.2.3. Isotope studies

Limited work has been done on both radiogenic and stable isotopes in the Koperberg Suite silicates and sulphides. The most recent work was by Boer et al. (1994) and Brandriss and Cawthorn (1996). Silicate phases are enriched in ^{18}O ($\delta\,^{18}O_{plagioclae.}$ = 6.2-9.6 ‰, $\delta\,^{18}O_{orhopyroxene}$ = 6.2-7.4 ‰ and $\delta\,^{18}O_{rock}$= 5.9 - 8.3 ‰) relative to the mantle-derived basic rocks ($\delta\,^{18}O$ values of 5.7 ± 0.3 ‰; Boer et al., 1994). This enrichment is because Koperberg Suite magmas from the mantle were subjected to contamination by the granite-gneiss country rocks ($\delta\,^{18}O$ values of 7.8-8.7 ‰) and low temperature alteration of sulphides (Boer et al., 1994). Sulphur isotope studies have also been carried out on diorite- and norite-hosted sulphides, providing ranges of $\delta\,^{34}S_{chalcopyrite}$ 1.5 to 3.8 ‰, and $\delta\,^{34}S_{bornite}$ 1.9 to 4 ‰. The bulk ore samples are characterized by a systematic decrease in $\delta^{34}S$ values with increasing Cu/S ratios (Boer

et al., 1994). These ratios are light relative to mantle values and the co-genetic mineral pairs show a lack of temperature concordancy. Boer et al. (1994) described this as being diagnostic of an oxidation process and degassing of SO_2-rich vapor phase because of granulite facies metamorphism that was followed by an alteration event. Fractional crystallization processes and assimilation modified the original magma that formed the Koperberg Suite and later modification occurred at the level of emplacement through differentiation and metamorphism (Boer et al., 1994). Cawthorn and Meyer (1993) described high initial $^{87}Sr/^{86}Sr$ ratios in the basic bodies and a decrease in the initial Sr ratio with an increase in En content in pyroxene and An content in plagioclase from the oldest to the youngest intrusions. Hence, these intrusions have been described as separate intrusive pulses and cannot be from the differentiation of one single pulse (Cawthorn and Meyer, 1993). The origin of the enriched O-isotope values, high levels of incompatible trace elements and high initial $^{87}Sr/^{86}Sr$ ratio is attributed to crustal contamination.

2.2.4. The genesis of the Koperberg Suite

Different petrologists have described the Koperberg Suite as unique because of the following:

(1) Sulphide-silicate textures are atypical of magmatic deposits (i.e., granular textures; Gibson et al., 1996).
(2) The An and En compositions of coexisting plagioclase and orthopyroxene are different from other magmatic deposits (Van Zwieten et al., 1996).
(3) Unusual occurrences of Cu mineralization in the felsic anorthosite bearing complexes (Conradie and Schoch, 1988).
(4) High U, Th, K, P and REE concentrations atypical of mafic rocks (Andreoli et al., 2006).
(5) Atypical sulphide assemblage (chalcopyrite and bornite; Cawthorn and Meyer, 1993).
(6) Atypical geochemical characteristics of sulphides (high Cu/Ni ratios, high Fe_2O_3 and TiO_2 ratios and low S/Se ratios; Cawthorn and Meyer, 1993)

The above-mentioned are some of the inconsistencies that have sparked debates and contrasting views on the Koperberg Suite petrogenesis (source of magmas) and the related sulphide mineralization. Hence, different models have been put forward:

2.2.4.1. Field relationships and emplacement models

Based on distribution and field relationships, the early intrusions in the Koperberg Suite are felsic anorthosites through mica-diorite, with pyroxene leucodiorite and pyroxene diorite as the last phase (Conradie and Schoch, 1988; Cawthorn and Meyer, 1993; Van Zwieten et al., 1996). Sharp contacts with no discernible chilled margins, consistent with intrusion at granulite facies metamorphic conditions are generally observed in the Koperberg Suite (Lombaard and Schreuder, 1978). -Pre-existing anisotropies in the granite-gneiss country rocks (e.g., stratigraphic contacts and S_2 and S_3 gneissosity) and cusp-like folds were the major controls during the emplacement of the Koperberg Suite magmas (Kisters et al., 1994; 1996). Each of the geometries (sill, dyke- and diapir- like) are related to emplacement at specific stratigraphic levels in the country rocks (Kisters et al., 1994). The sill-like bodies were the first to be emplaced earlier in the deformation history. This is based on the development of sills mainly along stratigraphic contacts and along subhorizontal gneissosity in the

gneisses (Kisters et al., 1994). The mafic dykes exploited the subvertical S_3 foliation, which crosscuts the stratigraphic contacts (Kisters et al., 1994). Felsic phases (e.g., anorthosites) occur as diapir-like bodies that have been emplaced at higher stratigraphic levels indicating higher viscosity relative to country rocks (Kisters et al., 1994).

2.2.4.2. Petrogenic models of the Koperberg Suite

Different petrologists have put forward various contrasting views on the Koperberg Suite's genesis. The petrogenic models that have been put forward include differentiation (e.g., Latsky, 1942; Boer et al., 1994; Lombaard et al., 1986), crustal melting (Clifford et al., 1981), an Iron Oxide Copper Gold occurrence (IOCG, e.g., Maier et al., 2012), and contamination (e.g., Schoch and Conradie, 1990; Boer et al., 1994; Brandriss and Cawthorn, 1996; Geringer, 1988) models.

- **Differentiation models**

Differentiation is one of the earliest proposed models of the Koperberg Suite by Lombaard et al. (1986). The Koperberg Suite bodies lack post-intrusive differentiation. In addition, the felsic members were emplaced first and were later followed by the more mafic phases, and this is indicative of extensive differentiation in a deep-seated magma chamber prior to emplacement (Latsky, 1942; Lombaard et al., 1986).

The intrusive nature of the noritoids was recognized by Van Zyl (1967), who attributed the formation of the Koperberg Suite to magmatic differentiation in a deep-seated magma chamber, where the magma emplacement took places in successive pulses of different compositions. Hence, the Koperberg Suite has been described as being emplaced by tapping off the top of a differentiated magma reservoir and sequential emplacement of progressively more basic fractions. The contamination model is also one of the differentiation models that were proposed to explain the Koperberg Suite.

- ***Contamination model***

The contamination model proposes the crustal contamination of basaltic mantle-derived magmas in the mid- to lower crust at upper amphibolite to granulite facies conditions (e.g., Schoch and Conradie, 1990; Boer et al., 1994; Brandriss and Cawthorn, 1996; Geringer, 1988). They propose the following as evidence for contamination:

(1) The discordance of orthopyroxene (En_{60}) and plagioclase (An_{40}) which are normally more similar in mafic intrusions. This is interpreted as a result of assimilation of granitic contaminant (possibly the Nababeep Granite Gneiss), which lowered the Ca/Na ratios, which then lowered the An content of plagioclase, while En values in orthopyroxene remained unaffected (Van Zwieten et al., 1996).
(2) Presence of granite-gneiss country rock xenoliths in the Koperberg Suite (Lombaard and Schreuder, 1978).
(3) The presence of abundant orthopyroxene, which is common in anorthosite complexes produced from the mantle below thickened crust that has been subjected to contamination (Cawthorn and Meyer, 1993).
(4) Enriched $\delta^{18}O$ (5.9-9.6‰) ratios relative to mantle derived ratios (5.3-6.0‰; Boer et al., 1994).

(5) High initial $^{87}Sr/^{86}Sr$ ratios in the basic bodies and a decrease in initial Sr ratio with an increase in En content in pyroxene and An content in plagioclase from the oldest (felsic) to the youngest (mafic) intrusions (Cawthorn and Meyer, 1993). Brandriss and Cawthorn (1996) proposed that this implies hybridization of two genetically distinct components, a radiogenic (initial $^{87}Sr/8^{6}Sr$ ratios of 0.722-0.727) and LILE-rich felsic component from granitic crust and a less radiogenic (initial $^{87}Sr/^{86}Sr$ ratios less or equal to 0.710) and dioritic mafic component derived from the mantle.

(6) The sulphide minerals are characterized by low $\delta^{34}S$ (1.5 to 4.1‰) relative to mantle-derived rocks (~0‰). Boer et al. (1994) attributed this to crustal assimilation, sulphur devolitization and an increase in oxygen.

- **Crustal melting**

This model proposes a gabbronoritic lower crustal mafic granulite as the source of the Koperberg Suite magmas (Duchesne et al., 2007). Radiogenic isotope work on country rocks and the Koperberg Suite has been done previously and yielded ε_{Nd} values of -7 for the Concordia Granite, high initial strontium ratios (0.7061) and μ ratios of 910.1, with low ε_{Nd} values (-9) for the Koperberg Suite at 1030 Ma. Hence, the presence of an ancient lower crustal source at 1030 Ma in the lithosphere of the Bushmanland Domain has been proposed (Clifford et al., 1995; Clifford et al., 2004).

Conradie and Schoch (1986, 1988) and Schoch and Conradie (1990) emphasized the similarities between the Koperberg Suite noritoids and massif-type anorthosite complexes and suggest that the Koperberg Suite represents the deeper levels of such anorthosite complexes. This was supported by experimental work done by Duchesne et al. (2007) on jotunites of the Koperberg Suite. The experiment showed that parental melts of jotunites are produced by melting of plagioclase + two pyroxene rocks at granulite conditions. Hence, Duchesne et al. (2007) proposed that the jotunites of the Koperberg Suite are likely to be parental magmas to anorthosites; hence, the suite is classified as a massif-type anorthosite complex.

Based on the negative ε_{Nd} (-5 to -11), the variation in Rb/Sr ratios and the $^{87}Sr/^{86}Sr$ ratios at 1030 Ma observed in the Koperberg Suite, Duchesne et al. (2007) proposed the following sequence of events leading to the formation of the Koperberg Suite:

(1) Magma extraction from the mantle (~1900 Ma) followed by the formation of LRRE-enriched oceanic crust.
(2) Hydrothermal alteration of the oceanic crust, yielding variations in Rb/Sr, followed by formation of Trans-Atlantic-Geotraverse (TAG) hydrothermal mound-type massive Cu-Fe sulphide deposits.
(3) Subduction and incorporation of the oceanic crust into the lower crust, and granulite facies metamorphism yielding mafic granulite.
(4) Melting in a post-collisional setting (during the O'okiepian episode) causing the emplacement of voluminous granitic material.

(5) Melting of the lower crustal mafic granulite triggering the emplacement of the Koperberg Suite, accompanied by remobilization of Cu-Fe sulphide mineralization forming the Koperberg deposits.

- **Iron Oxide Copper-Gold (IOCG) deposit model**

The IOCG model was proposed by Maier et al. (2012) based on his study on the copper-rich O'okiep deposits (e.g., Eezelsfontein and Hondekloof). Maier et al. (2012) stated that the O'okiep Cu deposits share certain similarities with the Brazilian Caraiba copper deposits. These include high Cu/Ni and Se/S ratios, dominantly magnetite and bornite in the main ore assemblages and high apatite and phlogophite contents. The O'okiep, the Caraiba and the Phalaborwa Cu deposits may be unusual magmatic end-members of IOCG deposits.

Maier et al. (2012) states that the O'okiep deposits exhibit high Au/PGE ratios, similar to those of the subcontinental lithospheric mantle (SCLM). Similar to Caraiba and Phalaborwa deposits, O'okiep rocks also exhibit high REE, U and Th contents and because of this, Maier et al. (2012) proposed melting of a fertile metasomatised mantle to have led to the production of alkaline and volatile-rich source melts for these deposits. Although they are not hydrothermal, these deposits exhibit characteristics of IOCG deposits.

These characteristics include the occurrence of Cu and /or Au as major economic minerals, enrichment in LREE. Th, U, P, and an abundance of Fe-Ti oxides. From this, the O'okiep deposits have been proposed to be magmatic end-members of IOCG deposits.

In support of the IOCG model, Maier et al. (2012) proposed the following:

(1) Crustal extension in response to orogenic collapse because of extreme radiogenic heating of mid- to lower crustal depth.
(2) Subsequent small-degree partial melting of the SCLM producing magmas enriched in volatiles, CO_2, LILE, HFS, Au, Cu, P, Low PGE contents, and other compatible elements.
(3) Rapid magma ascent to crust because of high volatile content. In the oxygenated magma, S (sulphate) was stable, preventing early saturation of sulphide and allowing concentration of Cu and Au in the magma with advanced stages of differentiation.
(4) Addition of external S and contamination triggered sulphide saturation resulting in low ε_{Nd} and $\delta^{34}S$ values.
(5) Continental magma ascent resulted in extensive sulphide fractionation in dynamic magma conduits (favored by oxidation).
(6) Deposition of relatively Ni-rich ores (e.g., Hondekloof) and progressively more Cu-rich ores with decreasing emplacement depth.
(7) The relatively high Au/PGE ratios of the ores mirror those of the SCLM

2.2.5. Orbicular Rocks in the Koperberg Suite

Enzman (1953) carried out a study on understanding the genesis of orbicular textures in the Koperberg Suite. He described about 63 orbicular bodies in the Koperberg Suite and seven of them in detail. He

observed that orbicular bodies in the Koperberg Suite are all emplaced in steep-structures (Figure 5), described as discordant anticlines.

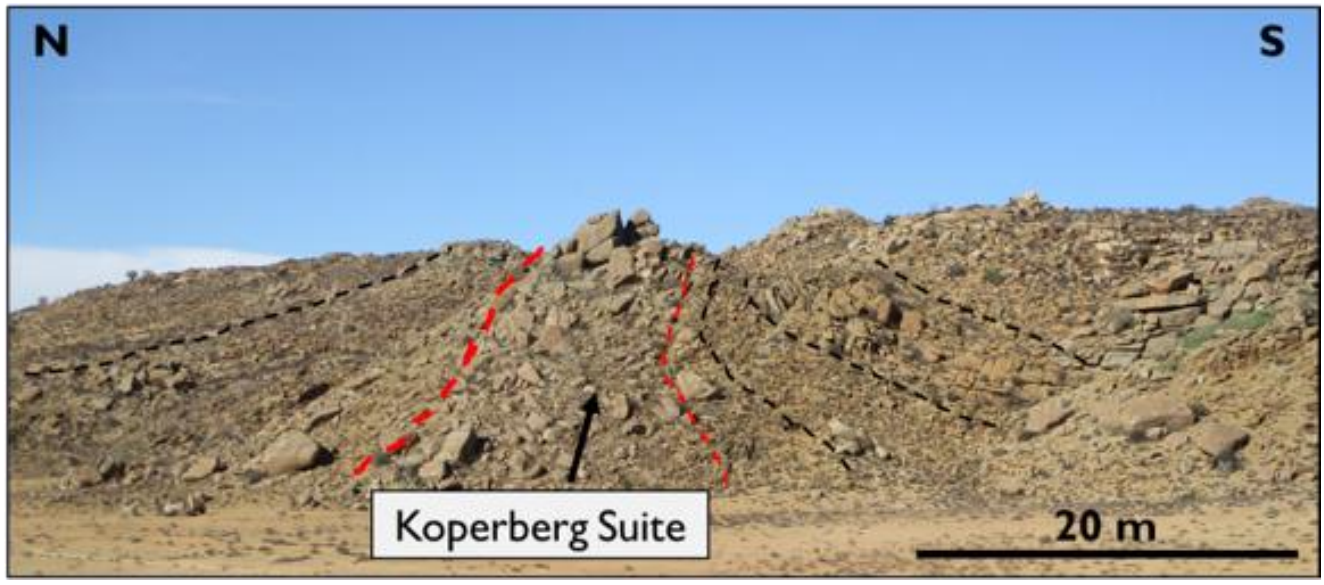


Figure 5: *An example of a steep structure from the Klondike east area showing a Koperberg Suite dyke (red dotted line) intruded in the central part of the steep structure (black dotted line) from Marima (2021).*

Initial fieldwork was able to locate some of the orbicule localities described by Enzman and some that Enzman did not describe in detail (Figure 6). He concluded that the orbicule textures in the Koperberg Suite resulted from structural control of migrating (metasomatic) ions and ionic complexes fluxed in an aqueous medium. He also concluded that the orbicules commence forming in a mafic nucleus. Enzman described the shape of the orbicular bodies as rhombic or "modified rhombic" and attribute the shape as a direct result of their formation on the flanks or above discordant anticlines.

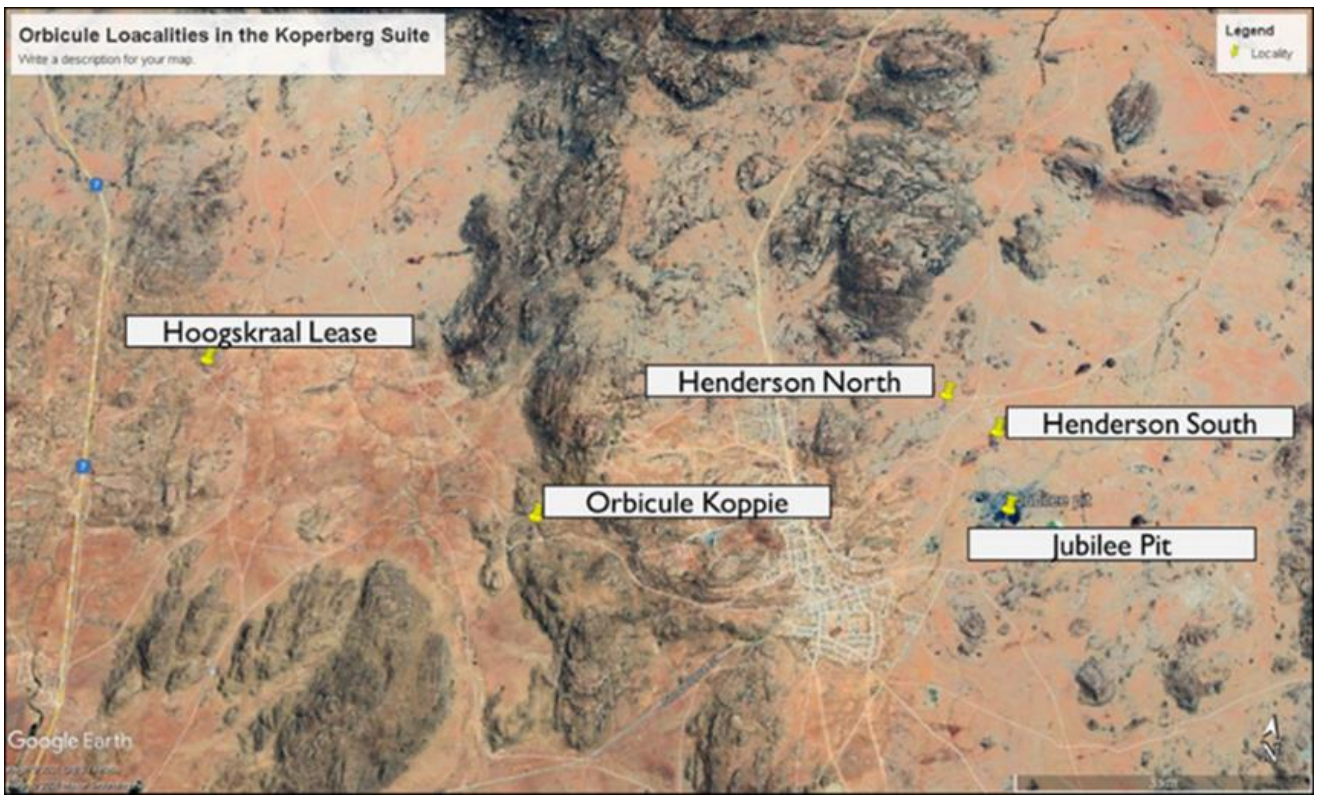


Figure 6: *A Google Earth image showing the location of some of the orbicular localities mapped by Enzman (1953).*

2.3. Matopos granite and the Diana's Pool area

The Diana's Pool orbicular granite (Figure 7) described by Garvie (1969, 1971) occur within the Matobo Hills World Heritage site in Zimbabwe. The Matobo Hills area lies at ~ 30 km south of Bulawayo and covers an area of about 3100 km^2, of which 424 km^2 is a national park (Garson, 1995). The geology at the Matopos area is mainly the Matopos granite batholith, which is composed of the Matopos granite. The Matopos granite batholith represents part of the ~2600 Ma Chilimanzi Granite Suite (Smith and Fripp, 1973; Broderick and Hubbard, 2016).The batholith is bound by the Bulawayo Greenstone Belt (in the north), the Gwanda and Antelope Belts (in the south) and the Filabusi Belt (in the east) (Smith and Fripp, 1973). Broderick and Hubbard (2016) stated that the Chilimanzi Granite Suite intrudes into the older Archean granite greenstone terrane making up the Zimbabwean Craton. The Matopos granite batholith (2.65 Ga) is an irregular oval body (100 km east-west dimension and 30 km north-south dimension), and very little work has been done on its geology. The first scientific work done was by Mennell (1902) who described the Matopos batholith as a microcline-biotite granite and he remarked upon its gneissic margin near Bulawayo and attributed the foliation to movement before consolidation. Mennell (1904) later described the batholith in detail and referred to it as featuring the incorporation of basic material from the schists and mentions that hornblende is the dominant mafic mineral (Smith and Fripp, 1973). Amm (1940), who mapped the Bulawayo Greenstone Belt, briefly described the Matopos granite batholith and described it as intrusive to the basement schists and into the older gneissic granite. Macgregor (1951) described the Matopos granite batholith as being intrusive into the older gneisses in his synthesis of published information on Rhodesian granites. According to Macgregor (1951), the Matopos granite batholith "seems to be a reconstruction of older rocks with some addition of potash and other constituents".

2.3.1. Petrography and mineral compositions of the Matopos granite Porphyry

The Matopos granite is typically grey-pink and contains megacrysts of microcline and oligoclase in a fine to medium-grained groundmass of biotite, feldspars and quartz with accessory epidote, apatite, magnetite and zircon (Garson, 1995). The Matopos granite batholith is massive, and its porphyritic character is evident in thin section (Smith and Fripp, 1973). It is granitic in composition, with K_2O/Na_2O values of 1.0-1.5 with an average of 1.43 calculated from known localities within the batholith (Garson, 1995). Using Harpum's (1963) classification of granites based on alkali ratios, a study by Smith and Fripp (1973), shows that it is highly heterogeneous. Based on Harpum's classification, the composition falls within the adamellite range. However, all the chemical analyses available to date now shows a wide compositional variation of the Matopos granite porphyry (Smith and Fripp, 1973). The samples range from true granites to tonalities to granodiorites, and this suggests that the Matopos granite batholith cannot be regarded as homogeneous.

An interesting variation within the Matopos granite is orbicule development outcropping at Diana's Pool area (Figure 7b) in the western Matopos National Park (Garvie, 1967; Garson, 1995; Smith and Fripp, 1973). Smith and Fripp (1973) and Smith (1986) described the nature of contact between the Matopos granite and the Bulawayo greenstone belt.

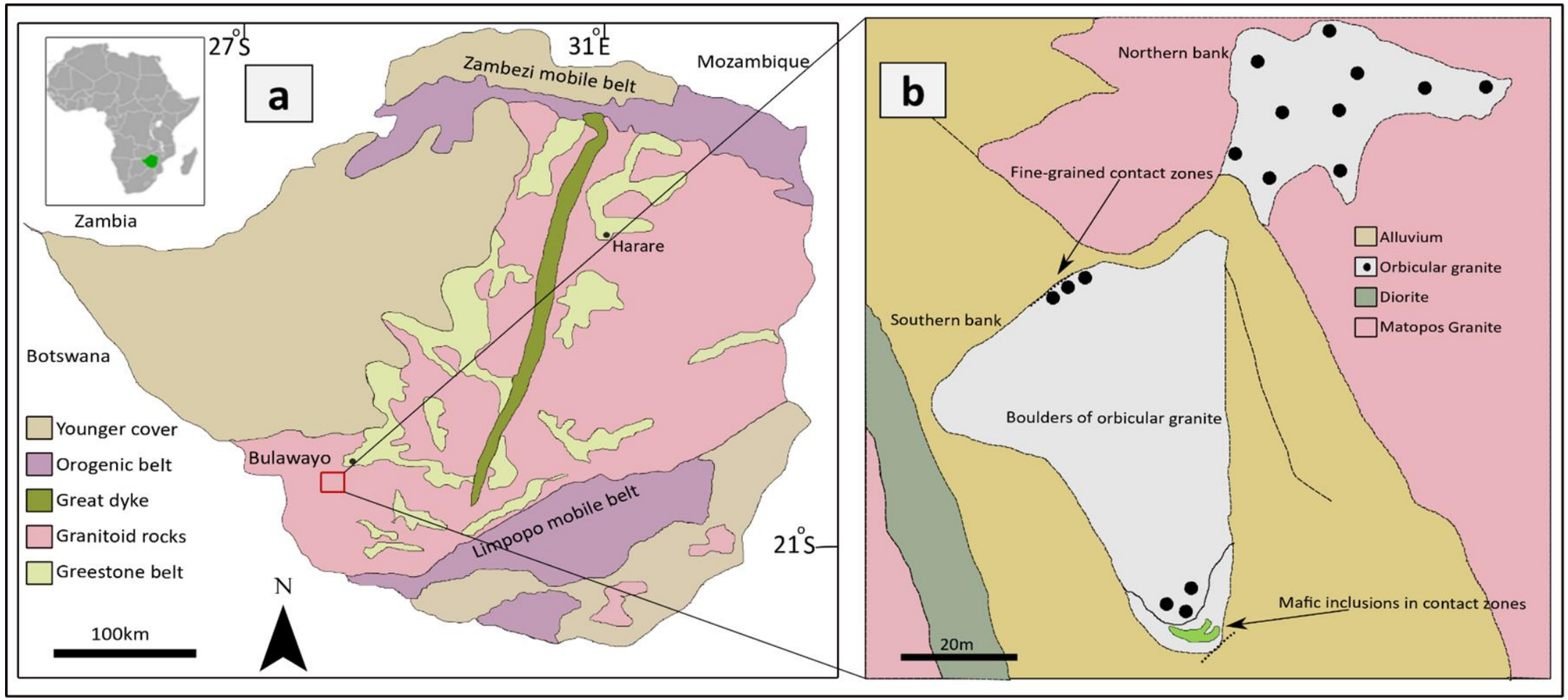


Figure 7: *Geological map of Zimbabwe and Diana's Pool area: (a) Geological map of Zimbabwe modified after Broderick and Hubbard (2016) and the red square shows where Diana's Pool is located. (b) Simplified geological sketch map of the orbicular granite outcropping 400 m downstream of Diana's Pool modified after Garson (1995). The Matopos granite porphyry to the north, east and south and a 13 m wide NW trending dolerite dyke to the west surround the orbicular granite.*

The interaction of the granite and the greenstone belt produced a contact facies zone of rocks (Figure 7b), which are regarded as older gneisses (Smith and Fripp, 1973). Associated with these contact facies, are orbicular granites (Figure 7b) known from two orbicular localities: one near Diana's Pool (8 km from the greenstone contact) and the other 5 km SSE of the Mpopoma dam (25 km from the greenstone contact; Smith and Fripp, 1973). Diana's Pool orbicules outcrop at the Diana's Pool area, which is about 58 km SE of Bulawayo in Zimbabwe (Garvie, 1969). The orbicular outcrop is located approximately 366 m downstream from Diana's Pool waterfall (Garvie, 1969). The orbicules occur within the Matopos Porphyritic Granite (Garvie, 1969). Limited work has been done on these orbicules and only basic petrological and geochemical work has been published as far as can be ascertained. Garvie (1969, 1971) has done most of the basic work on them and he describes the Diana's Pool outcrop as being small (~ 46 m long and ~ 30 m wide) and characterized by more orbicules (60-70 %) to the rock volume or matrix. He describes the outcrop as characterized by orbicules that differ in size, ranging from 5-20 cm. He describes the orbicules as not having a preferred shape and ranging from spherical to ellipsoidal in shape. The orbicules are closely packed and surrounded by a matrix that is granitic in composition and exhibiting a pegmatitic character locally (Garvie, 1969).

Felsic cores comprising hornblende and biotite forming radial textures characterize these orbicules (Garvie, 1969). The cores are dominated by subhedral andesine (70 %) and anhedral microcline (10 %). Garvie describes a late-stage crystallization of strained quartz as being present between feldspars. Magnetite and biotite occur as large irregular masses that are concentrated in the cores and they decrease in grain-size outwards (towards the rims) and forming radial textures towards the shell's outer layers (Garson, 1995). Shells consisting of mafic and felsic layers of plagioclase, magnetite, microcline, quartz, and accessory chlorite characterize these orbicules (Garvie, 1969). Plagioclase shows minor compositional changes throughout the layers of various shells (Garvie, 1969; Garson, 1995). The matrix is described as typically granitic in composition and comprising fine to medium-grained Matopos granite with slightly more abundant biotite than the typical Matopos granite (Garvie, 1969; Garvie, 1971; Garson, 1995). Garvie (1969) carried out chemical analysis on some parts (cores, shells, and matrices) of the orbicular granites. Garvie's analyses show that the whole rock has a tonalitic composition, and the matrix has a composition of an alkali-feldspar granite. He considered that Diana's Pool orbicules originated by granitisation of mafic inclusions. This involved passive rearrangement of ferromagnesian minerals in the diffusion front by Si, Ca, and Na ions towards the centre of orbicules to produce felsic cores and outwards migration of Mg and Fe ions to form the mafic shells (Garvie, 1969, 1971). Diana's Pools orbicule samples (samples number: BM14780a, b, c) were collected by an unknown person in the last century and were deposited at the School of Geoscience's Bleloch Museum, at the University of the Witwatersrand. As the locality is within the Matopos Hills World Heritage Site (Broderick & Hubbard, 2016) samples used in this study are from the historical collections housed in the Bleloch Museum collection of the School of Geosciences at the University of the Witwatersrand.

3. Methodology

3.1.1. Sample collection and preparation

Detailed field mapping in the Koperberg Suite was undertaken for a period of two weeks in March 2019. Several samples were collected from the Concordia, O'okiep and Nababeep towns and they were brought to Wits for detailed analyses. Prof. Paul Nex provided samples from the Diana's Pool area, since no fieldwork was carried out in this area. The samples were then prepared for petrographic and chemical analyses.

3.1.2. Micro- XRF

Two hand samples from the Diana's Pool area and one hand sample from each of the Koperberg Suite orbicule localities were taken to MinTek in Johannesburg, South Africa for Micro-XRF analyses to produce element maps. This was done to investigate the elemental distribution in the samples and allow for the identification of specific phases and areas of interest by providing complimentary information at a larger scale of observation and the following parameters were used (Table 2).

Table 2: *Table of parameters used for Micro- XRF analyses.*

Sample Name						
Mapping Parameters	BM14780B	BM14780A	SD-22-11	SD-55-24	SD-40-19	SD-10-6
Width	170 mm	79 mm	171	186 mm	150 mm	14 mm
Height	106 mm	64 mm	125 mm	82 mm	55 mm	110 mm
Pixel Size	100 µm	100 µm	100 µm	100 µm	100 µm	100 µm
Total number of pixel	1809226	505600	2137500	1525200	825000	1540000
Acquisition parameters						
Pixel time	10 ms/pixel	10 ms/pixel	10 ms/pixel	10 ms/pixel	10 ms/pixel	10 ms/pixel
Tube parameter						
High voltage	50 kV	50 kV	50 kV	50 kV	50 kV	50 kV
Anode current	599 µA	599 µA	599 µA	599 µA	599 µA	599 µA
Filter	Empty	Empty	Empty	Empty	Empty	Empty
Optic	Lens	Lens	Lens	Lens	Lens	Lens
Spot Size	20 µm	20 µm	20 µm	20 µm	20 µm	20 µm
Chamber at	Air 2 mbar	Air 2 mbar	Air 2 mbar	Air 2 mbar	Air 2 mbar	Air 2 mbar
Anode current	Rh	Rh	Rh	Rh	Rh	Rh

3.1.3. Petrographic analyses

Samples were cut into polished thin sections for petrographic analyses. The thin sections were first examined using optical microscopy at the School of Geosciences (University of the Witwatersrand). Both transmitted and reflected light were used to identify and describe silicate, carbonate, sulphate, oxide, and sulphide minerals present in the samples. Petrography was undertaken to classify, compare different orbicule types and sulphide occurrences/ assemblages. The thin sections were then scanned at high resolution using a full thin section microscope ahead of detailed textural analysis using the

TIMA. The high-resolution images were then used for point counting to obtain modal abundances for each rock type, and the point counting was done using tracing paper. A grid was constructed on a tracing paper with points that were 1 cm apart. The modal percentage was then obtained by dividing the total number of minerals observed by the sum of the points on the tracing paper. After petrography was completed, the thin sections were then carbon coated at the Wits TIMA lab for detailed textural analyses.

3.1.4. Tescan Integrated Mineral Analyzer (TIMA) Analyses

Twenty representative orbicular thin section from the five-orbicular localities were analyzed for detailed textural analyses using the TIMA. Phase and element maps of minerals were semi-quantified by energy-dispersive X-ray spectroscopy (EDS) using the VEGA3 SEM instrument and VEGA3 X64 TESCAN TIMA 1.7.0 software. The beam conditions during quantitative analyses on the VEGA3 X64 TESCAN SEM were 25 kV accelerating voltage, 43 µA emission current, with a working distance of 21.33 mm, a specimen beam current of 17.68 nA and a spot size of 590.00 nm with an absorption current of <1pA. The scanning mode was set at resolution mode, the heating at 47%, the filament live time was at 431 hours and the gun pressure was at $1.6x10^{-3}$ Pa while the column pressure was at 5.5 $x10^{-3}$ Pa. The system is also designed to perform high-resolution mapping (liberation and modal analysis), concurrently with imaging with a resolution of up to 2 µm per pixel with a working distance of 15 mm. Modal abundances were obtained and were later compared to the modal abundances that were obtained manually. Preparations for Zr geochronology were also done using the TIMA and BSE and CL images.

3.1.5. Electron Probe Micro Analyses (EPMA)

EPMA analysis was conducted using a CAMECA SX-5 FE electron probe equipped with five WDS spectrometers at the University of the Witwatersrand. The chemical compositions of plagioclase and biotite were determined. The analytical conditions for both analyses were relatively similar with an accelerating potential of 15 keV and a beam current of 20 nA. These analytical measurements were accompanied by standards for each analysis type, which produced accepted values. Recorded counting times were 10 seconds on peak and 5 seconds on the background. The data was collected using CAMECA software and an automated XPHI matrix algorithm was used for matrix effect correction.

3.1.6. Sr isotope Analyses

In-situ $^{87}Sr/^{86}Sr$ isotope analyses were conducted using a laser ablation system connected to a Nu Plasma II multicollector (MC)-ICP-MS system at the University of Johannesburg, South Africa. $^{87}Sr/^{86}Sr$ isotopes in plagioclase were measured on representative thin sections using a spot ablation method and a spot size of 100 µm for 60 seconds. Laser energy was set at 6 mJ with a frequency of 10 Hz and an attenuator value of 50 %, resulting in an on-sample fluence of approximately 3.5 J cm^2. Detector set-up was as follow: H5 = ^{88}Sr (+ $^{176}Yb^{2+}$); H3 = ^{87}Sr + ^{87}Rb (+ $^{174}Yb^{2+}$); H1 = ^{86}Sr (+ $^{172}Yb^{2+}$); L1 = ^{85}Rb (+ $^{170}Er^{2+}$ + $^{170}Yb^{2+}$); L3 = ^{84}Sr + ^{84}Kr (+ $^{168}Er^{2+}$ + $^{168}Yb^{2+}$) and IC1 = ^{82}Kr (+ $^{164}Er^{2+}$). The background was subtracted from the ablation signal. Krypton was monitored on mass 83, but no corrections were necessary for its interference on the masses of interest other than the initial background subtraction. The Nu Plasma NICE data processing program was used to do background

subtraction and all other computations. This tool also estimates 1 SE for reported values, taking into account the individual points and the integration period. The approved $^{86}Sr/^{88}Sr$ ratio of 01194 was used in the calculations for the Sr mass bias adjustment. The ^{87}Rb contribution was calculated from the ^{85}Rb signal using the standard $^{87}Rb/^{85}Rb$ ratio of 0.3858.The secondary standard used to evaluate accuracy was an in-house plagioclase glass standard; reference glass BHVO2G (Elburg et al., 2005) and a calcite reference material WC-1 ($^{206}Pb/^{238}U$ age: 254.64 ± 6.4 Ma; Roberts et al., 2017; Rasbury et al., 2021). The Sr mass bias correction factor was adjusted through analysis of the BHVO2G reference glass to effectively correct for Rb mass bias to obtain the accepted $^{87}Sr/^{86}Sr$ value of 0.70347.

3.1.7. Geochronology

Micro-XRF element maps were first utilized to target areas with high zirconium concentrations in hand samples prior to cutting thin sections. Sixteen representative orbicule samples from the five-orbicule localities were analyzed for detailed textural analyses using the Wits TIMA. The TIMA was then used to look for zircons, which were imaged using cathodoluminescence (CL) and back scattered electrons (BSE) to characterize the internal features of zircons such as growth zones and inclusions and to provide a base map for recording laser spot locations. The U-Pb analyses were conducted using a Nu Plasma II Multi Collector-Inductively Coupled Plasma-Mass Spectrometry (MC-ICP-MS) at the University of Johannesburg employing an Australian Scientific Instruments (ASI) Resolution 193 nm ArF excimer system. The U-Th-Pb data were acquired by single spot analysis (30 μm), using a laser repetition rate of 2 Hz and a fluence of 1.2 Jcm-2.

Total signal acquisition time was 40 seconds, comprising 15 seconds of pre- and post-ablation (gas blank) and 30 seconds of ablation measurements. The following gas flows were applied: coolant (13.0 L/min), auxiliary (0.80 L/min), Nebulizer (0.9 L/min) and He (0.31 L/min). Zircon standard CDQGNG ($^{206}Pb/^{238}U$ age: 1842.0±3.1 Ma ; Black et al., 2003) was used to evaluate accuracy, and OGC1 ($^{207}Pb/^{206}Pb$ age: 3465.4 ± 0.6 Ma ; Stern et al., 2009), 91500 ($^{207}Pb/^{206}Pb$ age: 1065.4 ± 0.3 Ma; Wiedenbeck et al., 1995), GJ1 (ca. 609 Ma; Jackson et al., 2004) and A382 ($^{207}Pb/^{206}Pb$ age: 1882.4 ± 3 Ma ; Huhma, 2012) zircon primary standards were used to correct for instrumental mass bias and elemental fractionation. Data from the primary calibration standards were obtained at the beginning and end of a sequence, and approximately ten analyses of unknowns were followed by analyses of the secondary standards for quality control purposes. The following masses were measured (six samples per peak): ^{204}(Pb + Hg), ^{206}Pb, ^{207}Pb, ^{208}Pb, ^{232}Th and $^{23}8U$ and the NuAge2 program (Andersen et al., 2009; Andersen et al., 2018) was used to calculate corrected ratios and ages.

3.1.8. Trace Element analyses in sulphides

The selected orbicule localities are felsic in composition; hence, there is a low concentration of sulphides in them. Because of this, thin sections from the more mafic Jubilee pit orbicules, which are 579 m southwest of Henderson North and 5.5 km east of Orbicule Koppie (Figure 6), were collected from Miss B.A Jogee (pers.comm., unpublished Honors project) and analyzed to understand the sulphide metallogeneses in the Koperberg Suite orbicules. Prior to trace element analysis, nine representative thin sections (2 thin sections from the mafic Jubilee pit orbicules and 7 thin sections from the felsic orbicules) were first examined by optical microscopy. The thin sections were analyzed

in reflected light and were used to identify the sulphide minerals present in the samples. EPMA analysis was then conducted on bornite and chalcopyrite using the CAMECA SX-100 probe (equipped with four spectrometers) at the University of Johannesburg. The analytical conditions for both chalcopyrite and bornite spot analyses (1 μm) were relatively similar with an accelerating potential of 20 kV and a beam current of 40 nA. These analytical measurements were accompanied by the analysis of pyrite and copper metal standards for each analysis type for quality control.

The samples were then taken to Stellenbosch University, and they were analyzed using by Laser Ablation Inductively Coupled Mass Spectrometry (LA-ICP-MS). A Resolution 193 nm Excimer laser from Applied Spectra connected to an Agilent 8800 QQQ ICP-MS was used in the analysis of trace elements in sulfide grains. Ablation took place in a helium (He) filled sample cell, the ablated material is then mixed with argon and a small amount of nitrogen before being transported to the ICP-MS. Initially laser gas flow and ICP-MS settings were optimized for best sensitivity and low oxide ratios (< 0.4 %) while ablating on NIST612. A method using oxygen as reactive cell gas, at a flow of 0.68 ml/min, was then used to measure all the analytes, either on mass or mass-shifted (analyte mass + 16), depending on the sensitivity or possible interferences to be removed.

The helium ablation gas was set at a flow rate of 0.5 L/min, argon at 1 L/min and nitrogen at 0.004 L/min. The internal standard element (ISTD used was ^{57}Fe. Since sulfide material ablates completely different from the NIST silicate glasses typically used for LA-ICP-MS quantification, a matrix-matched standard MASS-1 - produced by the US Geological Survey, was used. After deciding the appropriate spot size, determined to be 20 and 30μm, matrix optimised ablation parameters such as laser energy and frequency were optimized during spot ablation of MASS-1. Parameters were set at 3 J/cm^2 energy and 6 Hz frequency to produce a stable signal with good sensitivity and introducing minimal laser-induced element fractionation. Data processing was done using the LA-ICP-MS data reduction software package LADR from Norris Scientific (Norris and Danyushevsky, 2018). In order to correct for variations in ablation yield between standards and samples, an internal standard element (^{57}Fe) is used (Longerich et al., 1996).

Final concentrations were calculated from normalizing the total element components to 100%, with this summed signal proportional to the material ablated (Leach and Hieftje, 2000). Reference values for MASS-1 sulphide from the GEOREM data base (Jochum et al., 2005; Jochum et al., 2016). Detection limit (LOD) for each element is calculated using the equation from (Longerich et al., 1996).

3.1.9. Modelling using the Magma Chamber Simulator (MCS)

The Koperberg Suite's isotopic compositions have been shown to be affected by contamination by several researchers, although they do not identify the specific contaminant; instead, they assume it the Nababeep Gneiss (e.g., Van Zwieten et al., 1996). In order to demonstrate that the variable isotopic compositions of the Koperberg Suite magmas and orbicules can be simulated with reasonable assimilation of either the Concordia Granite or the Nababeep Gneiss, A develop a Recharge-Assimilation-Fractional Crystallization (RAFC; Bohrson et al., 2020; Heinonen et al., 2022) model utilizing the Magma Chamber Simulator (MCS) is developed here.

What is the Magma Chamber Simulator (MCS)? The MCS is an open system thermodynamic model that simulates how a magma body evolves as it thermally and reactively interacts with the surrounding country rock through the assimilation of partial melts of wallrock, stoping of wallrock, and/or magma mixing by recharge during cooling and concurrent fractional crystallization (Bohrson et al., 2020). The resident magma, wallrock, and various (0 to 30) recharge magma reservoirs or stopped block compositions are only a few of the various sub-systems that make up the composite system. Bohrson et al. (2020) and Heinonen et al. (2022) described the MCS as a forward modelling tool that may be used in several ways to clarify how magmatic systems evolve. Forward modelling allows better understanding of how changes in the values of particular parameters (such as pressure, parental magma composition, the initial temperature of the wallrock, and the quantity and mass of recharge episodes) affect the evolution of magmatic systems (Bohrsonn et al., 2020). With the help of this method, one can develop an intuitive grasp of open system magmatic processes as well as a foundation for determining which factors have the biggest impact in magmatic evolution.

Forward modelling is helpful when trying to simulate a certain natural system. In this situation, input parameters can be changed to best replicate petrological and geochemical data from a specific collection of igneous rocks (Bohrson et al., 2020). In order to achieve a variety of objectives in the study of igneous rocks, MCS is used to both develop intuition and model data from specific volcanic or plutonic systems (Bohrson et al., 2020). Among the questions that can be addressed by MCS, are how does the balance of mantle and crust change over time in a specific magmatic system? Are there systematic differences in mantle versus crustal input in different tectonic settings? What factors affect where magma storage zones form (shallow, middle, or deep crust)? What conditions favor large versus small magma bodies? And what processes and/or conditions modelled by MCS influence magma bodies to erupt? The MCS tracks and reports phase equilibria and major element, trace element, and isotope concentrations within all sub-systems using one of four MELTS phase equilibria engines coupled to a user-defined executive (IGOR) based on equilibrium thermodynamics (Bohrson et al., 2020).

Bohrson et al. (2020) and Heinonen et al., (2022) stated that many options are provided by the adaptable user interface and can be customized to simulate certain natural systems or model analogs. A diabatic and semi-permeable boundary in the MCS couples the resident Magma subsystem (M), which is originally a finite mass of melt in a clearly defined thermodynamic state, to its host Wallrock (WR) (Bohrson et al., 2020). AFC processes cause wallrock to heat up and maybe partially melt as sensible (melt cooling) and latent heat (creation of cumulates by fractional crystallization, FC) flow over the M-WR boundary (Bohrson et al., 2020). In the event that partial melt forms and the wallrock melt fraction rises above a rheologically established, user-specified critical threshold (f_m^0 or fmZero), this anatectic melt thoroughly combines and equilibrates with melt in the M subsystem (referred to as M melt for simplicity). Crystals that form in response to AFC join a reservoir of cumulate that is chemically isolated from, but thermally connected to M melt. Key variables related to the surrounding geological conditions and initial bulk compositions control how much matter transfers between WR and M (Bohrson et al., 2020; Heinonen et al., 2022). In addition to partial wallrock melt contamination of M melt, stoping (S) can also cause contamination (Bohrson et al., 2020; Heinonen et al., 2022). The

contaminated system achieves a new equilibrium state at a new thermodynamically controlled temperature in MCS when stooped wallrock is added in large quantities to M melt (Bohrson et al., 2020; Heinonen et al., 2022).

The stoping event may result in the precipitation of crystallized solids or a fluid, and naturally, the contaminated M melt changes in bulk composition (Bohrson et al., 2020; Heinonen et al., 2022). Magma mixing by recharge (R) is the final process taken into account by MCS. The new mixture reaches chemical potential equilibrium when a finite mass of thermodynamically stable, internally equilibrated recharge magma is introduced to the M melt during R (Bohrson et al., 2020; Heinonen et al., 2022). The stoping operation and this operation are computationally identical. A specified M melt temperature or a temperature decrease from the most recent S or R event is the user-defined condition that sets off an R or S event. The maximum number of different S or R events allowed by the present version of MCS is 30 (Bohrson et al., 2020).

There are two steps involved in the MCS calculations: (1) MCS- PhaseEQ: the computation of the major element and phase equilibria for the evolution of the RASFC; and (2) MCS-Traces: the trace element and isotopic (Sr, Nd, Hf, Pb, Os, and O) consequences for the RASFC scenario derived from the output of MCS-PhaseEQ (Bohrson et al., 2020). This bipartite structure takes into account that reliable calculations of trace elements and isotopes must be based on major element solutions that precisely quantify phase abundances, compositions, and temperatures (Bohrson et al., 2020; Heinonen et al., 2022). Prior to exerting effort into trace element and isotopic modelling, a researcher may iterate in step 1 by comparing observables with projected outcomes.

In contrast, a researcher can use the same part (1) RASFC solution to perform multiple trace element and isotopic ratio calculations using, for instance, various initial trace element compositions and/or mineral-melt, mineral-fluid partition coefficients for M, WR, S, and R (Bohrson et al., 2020; Heinonen et al., 2022). Since major phase stability is typically not trace element sensitive, feedback to MCS-PhaseEQ for various trace element concentrations and isotopic ratios is not necessary (Bohrson et al., 2020; Heinonen et al., 2022). The bipartite technique aids in comprehending the sensitivity of a whole solution (phase equilibria, trace elements, and isotopes) to the beginning conditions and parameters while maintaining the greatest amount of flexibility in the quest of a "best-fit" model (Bohrson et al., 2020; Heinonen et al., 2022). MCS-PhaseEQ is the result of the merger of an executive brain and a computational thermodynamic engine (Bohrson et al., 2020).

The Visual Basic programming language from Microsoft is used to create the executive brain. The brain is in charge of carrying out the specific RnASnFC scenario that the user has specified by (1) sending instructions to the selected rhyolite- or pMELTS engine, (2) performing additional internal calculations based on values returned from rhyolite- or pMELTS, (3) making the necessary conditional and complex sequential executive decisions, and (4) producing a variety of real-time and archived graphical and numerical data (Bohrson et al., 2020; Heinonen et al., 2022). One of the existing rhyolite or pMELTS codes is the thermodynamic engine used in the MCS- PhaseEQ (Bohrson et al., 2020). Ghiorso and Sack (1995), Asimow and Ghiorso (1998), Ghiorso et al. (2002), Gualda et al. (2012), and Ghiorso and Gualda (2015) stated that these are designated as pMELTS and rhyolite-MELTS versions 1.0.2, 1.1.0, or 1.2.0.

A key component of rhyolite- or pMELTS is a thermodynamic model for the relationship between the Gibbs free energy of silicate liquids and melt composition, temperature (about 1000–2000 K), and pressure (approximately 0–3 GPa). The thermodynamic rules followed in rhyolite- and pMELTS are insufficient for numerical computations and must be coupled with the thermodynamic characteristics of the materials making up the composite system (Bohrson et al., 2020).

In the studied orbicules, strontium analyses was carried out *in-situ* in plagioclase and during the analyses, the strontium concentrations (ppm) were not measured since the (MC)-ICP-MS is a poor quantitative method. However, these were recalculated by comparing the ^{88}Sr signal of the orbicules to the ^{88}Sr for the reference material (BHVO2G and WC-1). The Sr concentration of the BHVO2G (Elburg et al., 2005) and WC-1 (Rasbury et al., 2021) are 396 and 1500 ppm, respectively. A calibration using the ^{88}Sr signal against the standards was created and ultimately, the Sr (ppm) in the orbicules was qualitatively determined.

4. Diana's Pool Orbicules

4.1. Hand sample descriptions

The orbicular samples used in this study are characterized by closely packed orbicules (70%) in a granitic inter-matrix (30% rock volume; Figure 8a, c). The orbicules range from spherical to ellipsoidal in shape, however, some orbicules appear to have been abraded, where the cores seem to be intact but large parts of the shells have been removed (Figure 8c, d). Some orbicules have been deformed where layers in the shells are bent (Figure 8e), possibly resulting from indentation on interaction with other orbicules. Shells that incorporate and surround matrix material, which has moved into one segment of the shell, creating a thickening or pocket. The orbicules range in size from 6 to 14 cm in diameter and from 5 to 3 cm in width (Figure 8a). Different types of orbicules characterize the hand samples: orbicules characterized by felsic cores with dark ferromagnesian shells (Figure 8a); orbicules characterized by felsic cores with dark and felsic shells (Figure 8b); more complex orbicules characterized by cores with abundant coarse-grained hornblende and biotite (Figure 8e).

Felsic and medium- to coarse-grained cores contain locally concentrated and irregular biotite and hornblende, which characterizes the orbicules (Figure 8a; c); however, the modal abundances of biotite and hornblende vary from one orbicule to another. Cores comprise subhedral and plagioclase (60%), K-feldspars (10%), quartz (10%) and (20%) mafic biotite and hornblende (Figure 8a), however, irregular masses of hornblende are not present in all orbicular cores (Figure 8).

Sharp contacts mark the transitions from cores to shells (Figure 8a, b). Alternating mafic and felsic shells characterize the orbicules (Figure 8a, b). Mafic shells are predominantly biotite and minor quartz, magnetite, and feldspar, while the felsic cores are comprised principally of feldspar and magnetite with minor quartz and biotite. Sharp contacts are observed between shells and the medium- to coarse- grained matrix (Figure 8b).

The matrix composition is comparable to the cores, and it composed of quartz, plagioclase, K-feldspars, biotite, and hornblende (Figure 8d, c). In places, the matrix is pegmatitic (Figure 8b). Some orbicules appear to have been "shaved" or truncated along one or more margins where the matrix granite occurs between the shells (Figure 8a). Orbicule shells also incorporate and build up over remobilized matrix material which has moved into one segment of the shell, creating a thickening or pocket (yellow arrow; Figure 8e). Locally, the samples are characterized by joining of the core, shell, and the matrix (Figure 8d).

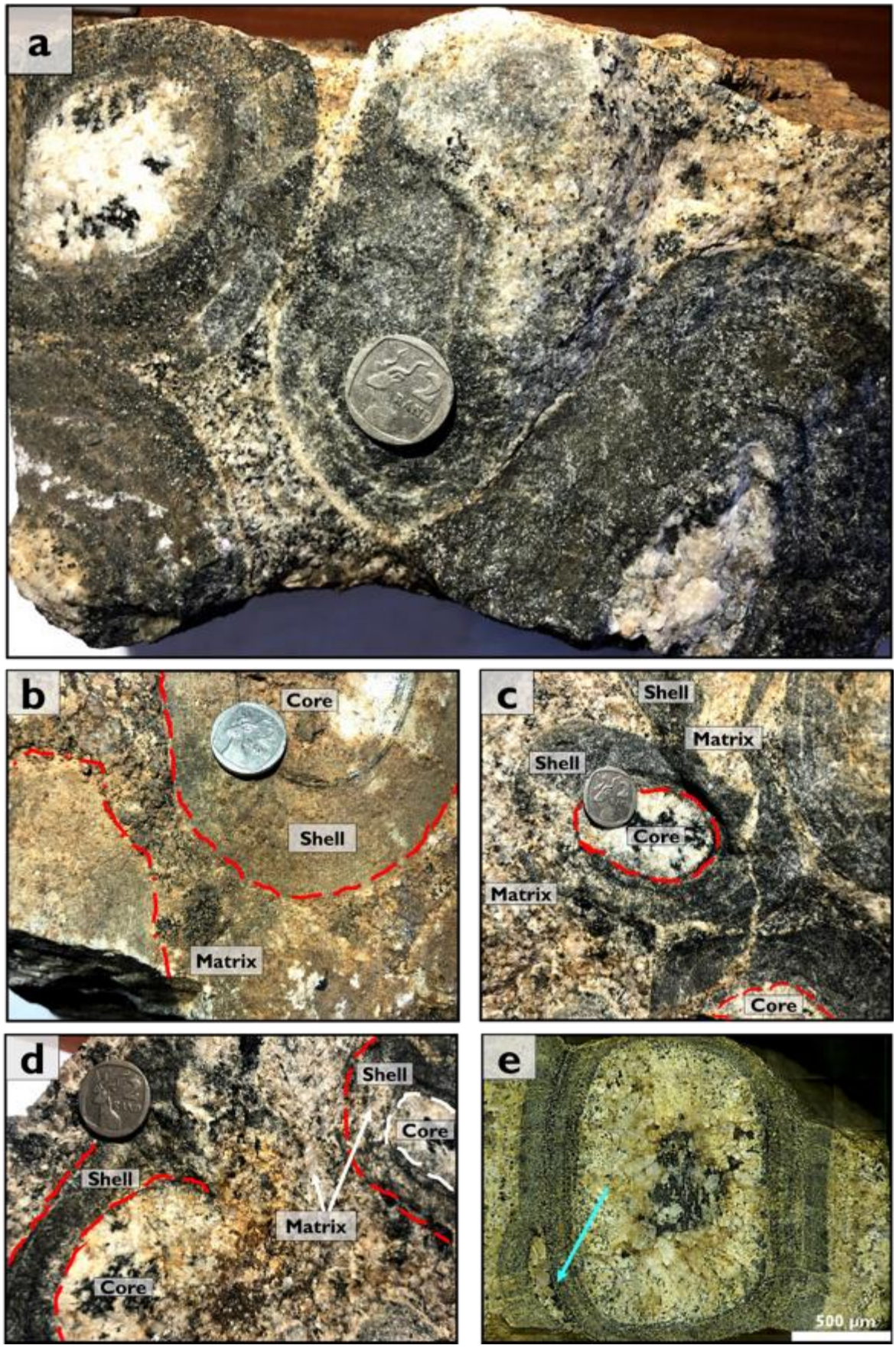


Figure 8: *Orbicular granite samples from the Diana's Pool area: (a) A sample showing the general appearance of Diana's Pool orbicules. These spherical to ellipsoidal orbicules make up approximately 70% of the rock volume and are characterized by felsic and medium-grained cores dominated by feldspars and patches of dark hornblende surrounded by alternating mafic and felsic shells in a pegmatitic and granitic host matrix. (b) Closely packed orbicules surrounded by a pegmatitic matrix. The red dotted lines show the sharp contacts between orbicules and the host matrix. (c, d) Pegmatitic matrix crosscutting the mafic orbicular shells and the felsic cores. (e) Inclusions of the granitic host matrix material (blue arrow) in mafic shells creating a "saddle reef". The coin is 23 mm in diameter.*

4.2. Petrography

Petrographic techniques combined with micro-XRF were used to classify, compare, and contrast different orbicule types and sulphide occurrences in Diana's Pool orbicules.

Samples BM14780B (Figure 9) and BM14780A (Figure 10) were scanned at high resolution using qualitative micro-XRF to produce element maps showing elemental distribution in cores, shells and matrices of the orbicules. The matrix and cores are more calcic and exhibit higher Ca concentrations than the shells (Figure 9h). The presence of hornblende in some of the cores and in the matrix is indicated by lower Si and Al and increased Ca than the rest of the orbicules (Figure 9h; Figure 10h). Si is present in all minerals and so shows high abundances in cores, core to shell boundaries and in the host matrix (Figure 9d; Figure 10d). Conversely, the shells are less siliceous due to proportionally less quartz (Figure 10d; Figure 9d)

Potassium is abundant in the matrix, the granitic material that is incorporated in shells, and the darker mafic shells as well as some places in the cores (Figure 9g; Figure 10g). Low K concentrations are observed in the felsic shells (Figure 10g). However, the mafic and the intermediate shells (Figure 9g) have a slightly higher K concentration and the highest K intensities are observed in core to shells contacts (Figure 9g; Figure 10g). Iron (Fe) is highly concentrated in shells and yields the highest intensities in mafic shells, the matrices and in the dark patches of hornblende in the cores (Figure 9e; Figure 10e). The granitic matrix material between shells and cores exhibits no Fe (Figure 9e; Figure 10).The element maps show high concentrations of Zr in the matrix and in core to shells boundaries (Figure 9f; Figure 10f). However, some cores have very low or no Zr (Figure 9f; Figure 10f).

This variation in element concentrations in the orbicules reflects the mineralogical variation in the core, shells, and matrix of the orbicules and the relative proportions of the different minerals.

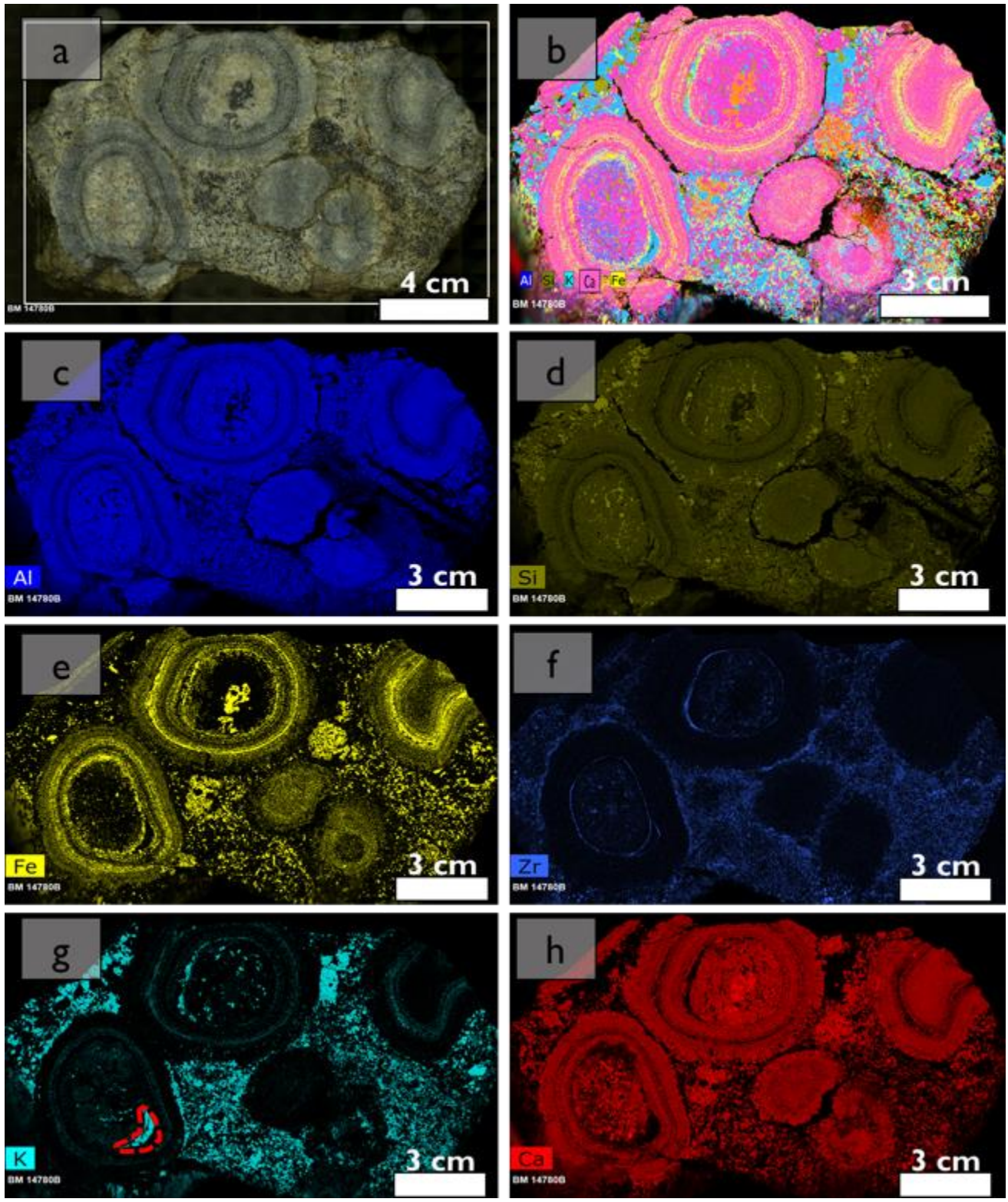


Figure 9: *Element maps of the Diana's Pool sample BM 14780B: (a) A mosaic showing the mapped area in white rectangle. (b) A composite of selected elements (Al-dark blue, Si-green, Ca-pink, Fe-yellow and K-light blue) and their distribution shown in a full orbicule sample. (c) Element map showing uniform distribution of Al throughout the sample. However, the dark patches in central cores and some places in shells and matrices do not contain Al. (d) Element map showing uniform distribution of Si in cores and the matrix however, high intensities of Si are observed in the pegmatitic matrix. (e) Element map showing high distribution and intensities of Fe in shells, matrix and some parts of the cores. (f) Element map showing the distribution and concentrations of Zr in different parts of the orbicules. (g) Element map showing the highest concentrations and intensities of K in the matrix, the granitic matrix between the shells (red-dotted area), and some parts of the cores. (h) Element map showing the distribution and concentrations of Ca in different parts of the orbicules.*

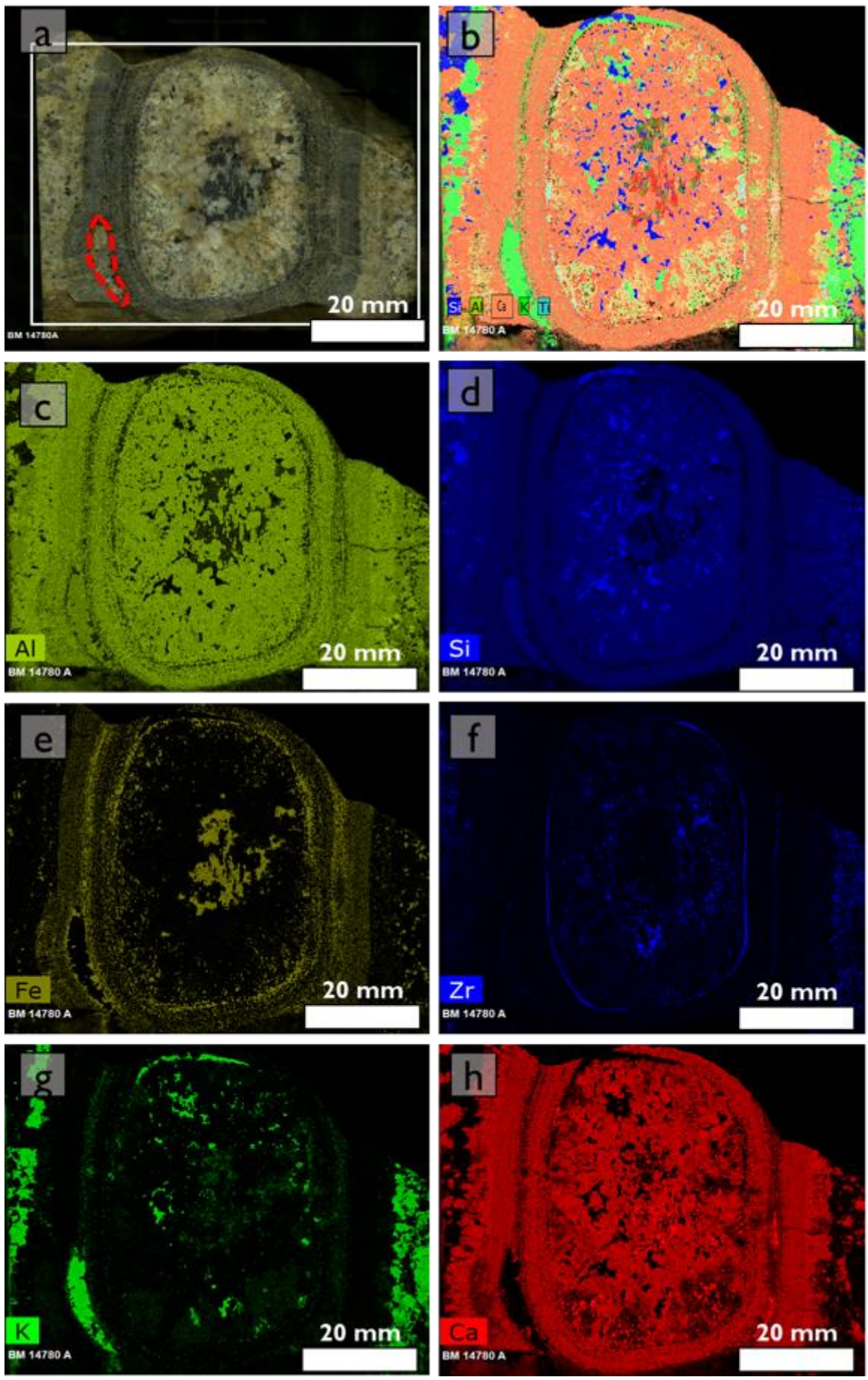


Figure 10: *Element maps of the Diana's Pool sample BM 14780A: (a) A mosaic showing the mapped area in white rectangle. (b) A composite of selected elements (Al-green, Si-dark blue, Ca-orange, Ti-light blue, and K-neon) and their distribution shown in a full orbicule sample. (c) Element map showing uniform distribution of Al in sample with dark patches containing no Al. (d) Element map showing the highest distribution and intensities of Si in the core and the matrix. (e) Element map showing the distribution and high intensities of Fe in shells, matrix and in the dark patches in the core.*

Figure 10 Continued: *(f) Element map showing the distribution and concentrations of Zr in different parts of the orbicules. The highest intensities of Zr are observed in the core and matrix. (g) Element map showing the distribution and intensities of K in the matrix, the granitic matrix material between shells, and some parts of the core. (h) Element map showing the distribution and concentrations of Ca in different parts of the orbicules.*

Medium- to coarse-grained cores comprising plagioclase, quartz, biotite, hornblende, magnetite, orthoclase, microcline, and other accessory phases (Figure 11) characterize Diana's Pool orbicules. Cores to shells and shells to matrix boundaries are marked by sharp contacts (Figure 11).In addition to this, there is an abrupt change in grain size and distribution of mineral phases between shells on one hand (fined-grained, homogeneous distribution), and cores and matrix on the other (coarse-grained, heterogeneous distribution; Figure 11).

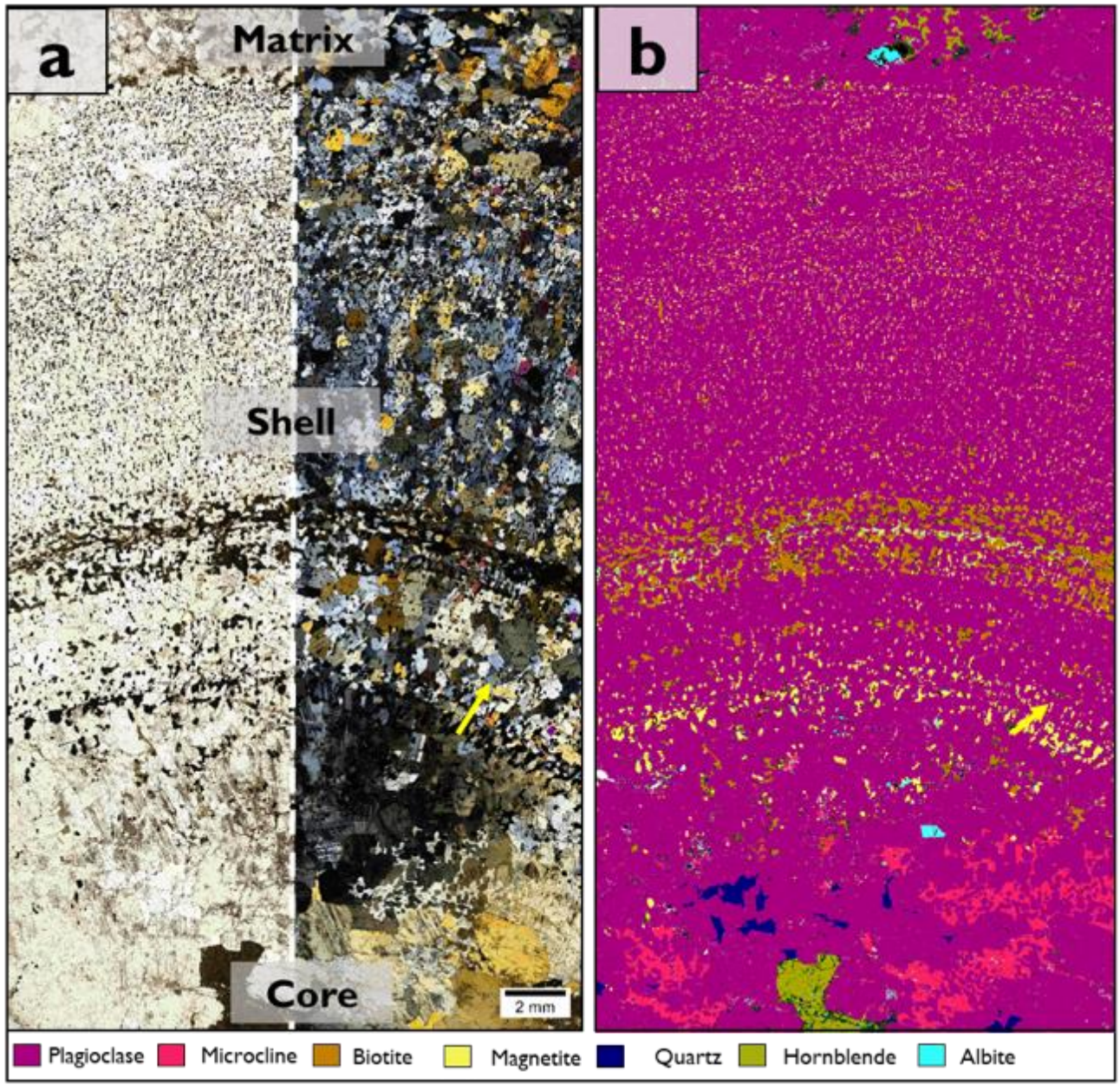


Figure 11: *Full thin section photomicrographs of the orbicule samples and corresponding TIMA image: (a) Plane–polarized (left) and cross-polarized light (right) full thin section images of sample BM14780F. (b) TIMA image of orbicule sample BM14780F showing a medium-grained core predominated by feldspars, quartz and hornblende; fine-grained and alternating mafic and felsic shells predominated by feldspars, biotite, magnetite, and a pegmatitic matrix predominated by feldspars and hornblende.*

- **Cores**

Cores are typically composed of plagioclase (75%), quartz (10%), microcline (~5%), hornblende (5%), biotite (~3%), chlorite (~3%), magnetite (3%) and other accessory phases (Figure 12).

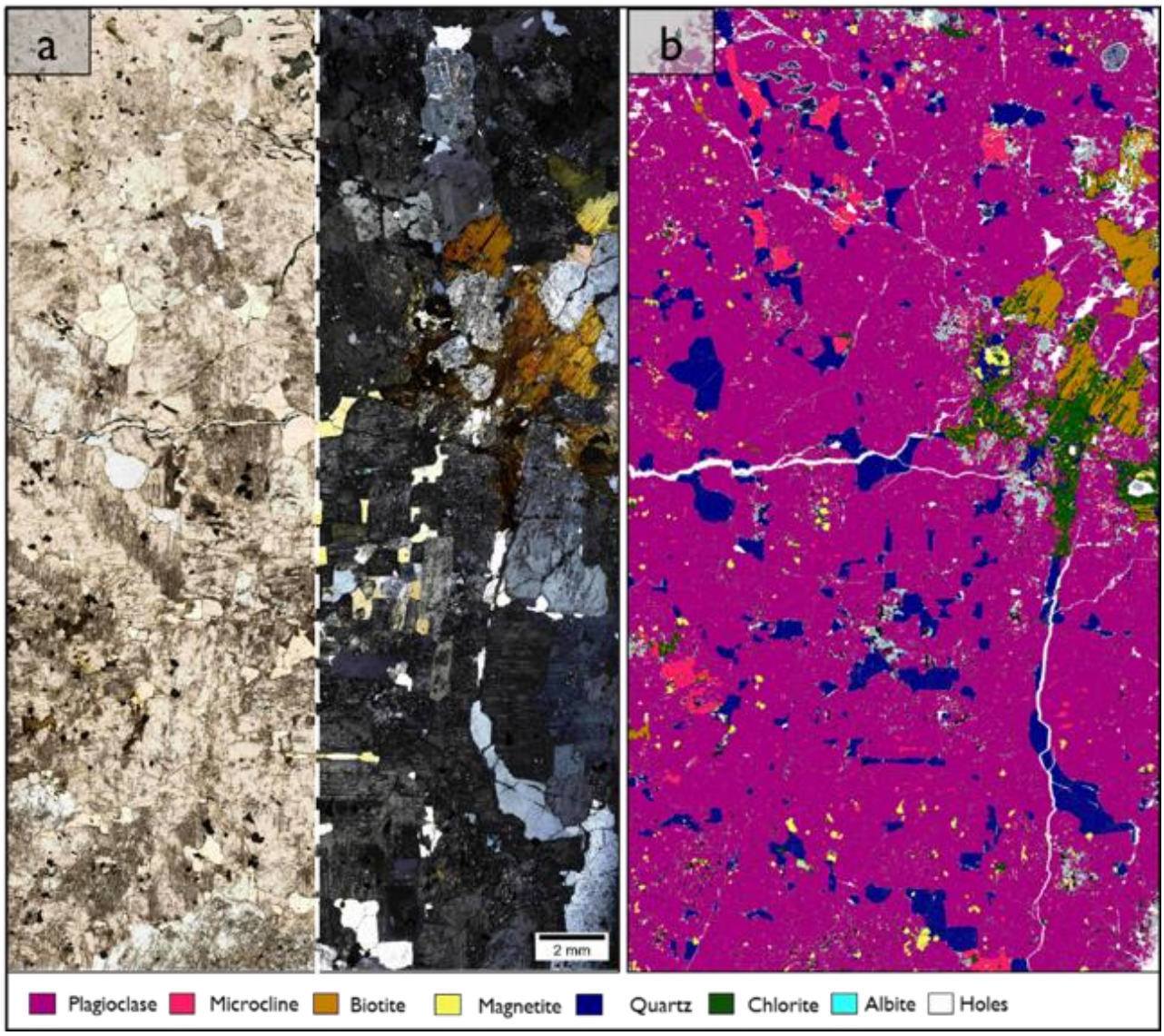


Figure 12: *Full thin section photomicrographs and TIMA image of the Diana's Pool orbicular core: (a) Plane–polarized (left) and cross-polarized light (right) full thin section images of sample BM14780D. (b) TIMA image of orbicule sample BM14780D showing a medium-grained core comprising feldspars, quartz, biotite and chlorite.*

Plagioclase occurs as the predominant mineral in cores occurring as subhedral (0.1-1 cm) grains adjacent to quartz, microcline, and biotite (Figure 12). Locally, plagioclase contains poikilitic inclusions of quartz, microcline, and magnetite (Figure 13d, f). Small-scale alteration of plagioclase to sericite is observed in some of the plagioclase grains locally (Figure 13c). Surrounding large plagioclase grains is interstitial microcline (Figure 13e, f). Microcline contains inclusions of unaltered plagioclase, quartz, biotite, and magnetite. Granophyric textures are observed where microcline and quartz are intergrown. Microcline also occurs as small and subhedral (0.1-0.2 mm) grains that are inclusions in plagioclase. Quartz occurs as small to medium grains (0.1-1 mm) that are adjacent to feldspars. Locally, it occurs as poikilitic inclusions in plagioclase and microcline (Figure 13d). Quartz is also in an interstitial position in cores (Figure 13c, d, e). Biotite occurs as large and anhedral to subhedral (0.1- 6 mm) grains that grow into plagioclase and microcline (Figure 13a, b).

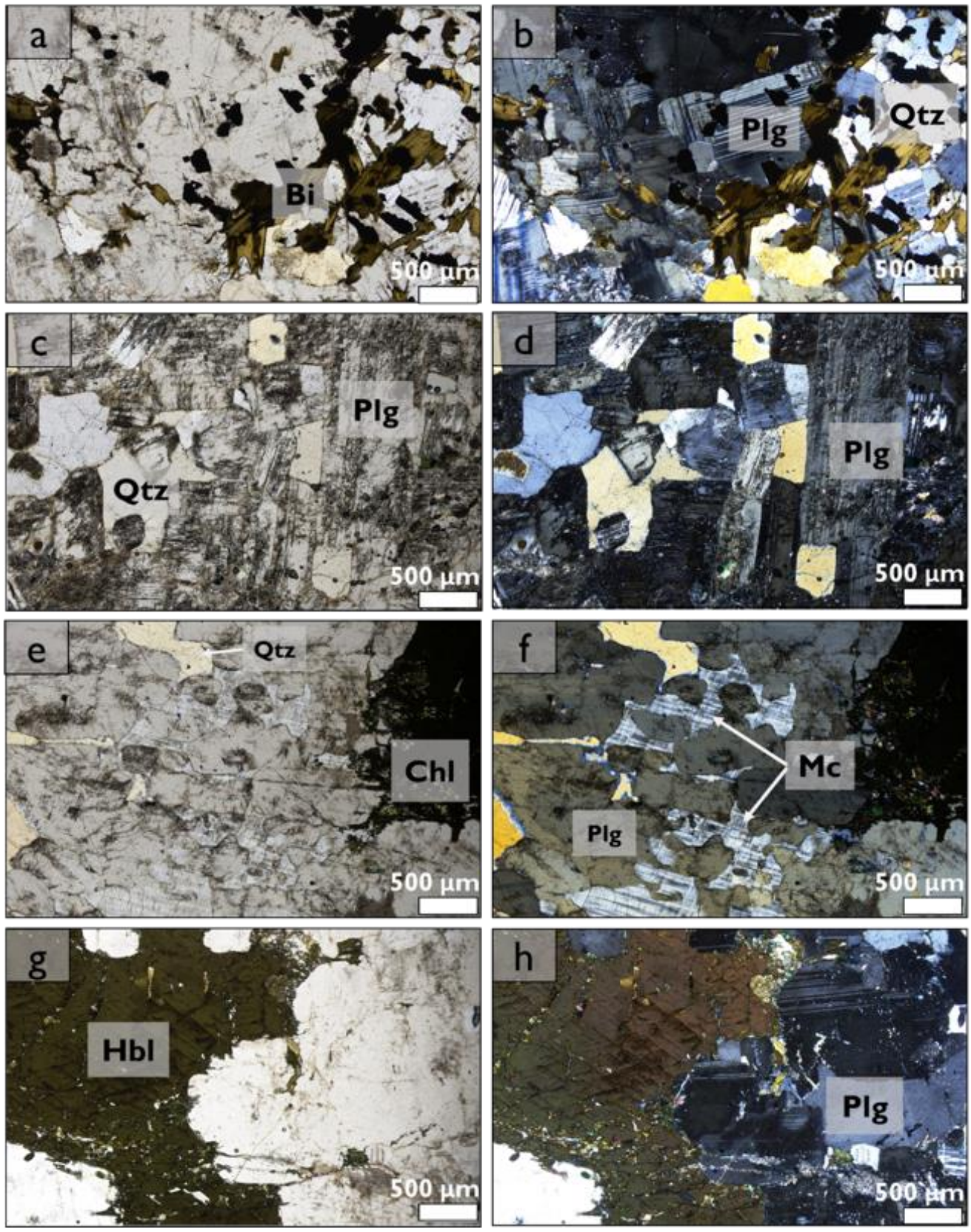


Figure 13: *Photomicrographs showing mineral phases and textures in orbicular cores taken from Diana's Pool orbicules: (a, b) Subhedral plagioclase grains occurring adjacent to quartz and biotite. (c, d) Subhedral plagioclase grains occurring adjacent to quartz. Plagioclase is altered to sericite. (e, f) Interstitial microcline enveloping large plagioclase grains that occur adjacent to hornblende. (g, h) Large hornblende grains adjacent to plagioclase and quartz.*

Locally, biotite grows as an interstitial phase around large plagioclase grains and as poikilitic inclusions in plagioclase and microcline (Figure 13a, b). Hornblende occurs as a minor mineral in the orbicules. It occurs as large (0.1-6 mm) grains that grow adjacent to plagioclase (Figure 13g, h) and microcline. Locally, it contains smaller inclusions of magnetite and biotite.

- **Shells**

Gradational contacts between cores and shells (Figure 11) characterize Diana's Pool orbicules, although some orbicules are characterized by sharp contacts. Transitions from cores to shells are also characterized by changes in mineral assemblages and textures (Figure 14). Alternating felsic and intermediate shells characterize these orbicules.

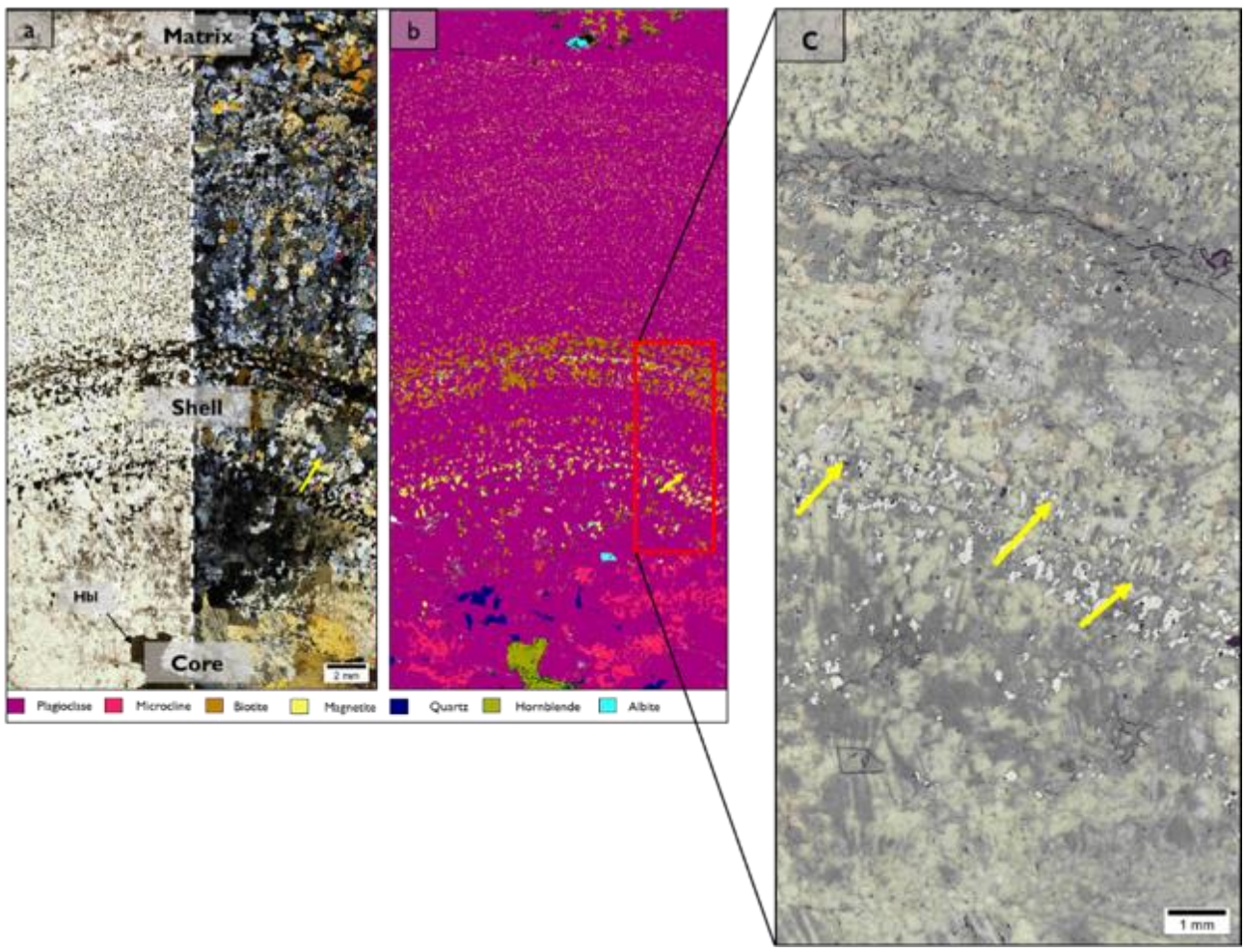


Figure 14: *Reflected light image showing radiating grains of magnetite (yellow arrows) within a shell of sample BM1478F. (a) and (b) are the full thin section photomicrographs of the orbicule sample and corresponding TIMA image of sample BM14780F showing the location of the reflected light image.*

Unlike the coarse-grained cores characterized by phaneritic textures, shells are more fine-grained and characterized by polygonal textures and by an increase in magnetite and biotite modal abundances (Figure 14).The orbicules are characterized by alternating felsic and intermediate shells that contain grains of roughly the same size, forming polygonal textures (Figure 14). Contacts between mafic and felsic shells are gradational (Figure 14), however, sharp contacts are observed in some of the samples. Mafic shells are dominantly biotite (40%), plagioclase (30%), quartz (10%) and magnetite (20%). Biotite occurs as subhedral (0.1-0.5 mm) laths that are adjacent to plagioclase and quartz (Figure 16c, d).

Locally, biotite occurs as an interstitial phase where it surrounds feldspars and quartz. Biotite also occurs as poikilitic inclusions in plagioclase (Figure 16g, h). Some mafic shells comprise more than 90% biotite and this is where shells are made entirely of concentric biotite with small inclusions of magnetite and quartz (Figure 14, Figure 15). Plagioclase (45%), quartz (15%), magnetite (30%), biotite (10%) and accessory microcline predominate in the felsic shells. The plagioclase is subhedral (0.1-0.5 mm), with smaller plagioclase and quartz grains closely packed and forming granoblastic polygonal

textures (red arrow; Figure 16h). Magnetite occurring as poikilitic inclusions in both plagioclase and quartz also predominates within the felsic shells. Magnetite also grows as large irregular masses concentrated in shells, which decrease in grain-size outwards (towards the rims) and form radial textures towards the shells outer layers (yellow arrows, Figure 14; Figure 15b). These radial grains of magnetite are restricted to shells. An additional interesting point is visible in Figure 16, where magnetite grains show a homogeneous distribution. These radial grains of magnetite are restricted to shells.

Granitic material that has the same composition as the host matrix crosscuts some of the shells (Figure 15). This differs in composition to the shells, and it is more coarse-grained (Figure 15). The contact where this matrix material intrudes the shells is sharp and the transition from the shells to this material is marked by changes in mineral assemblages and textures (Figure 15).

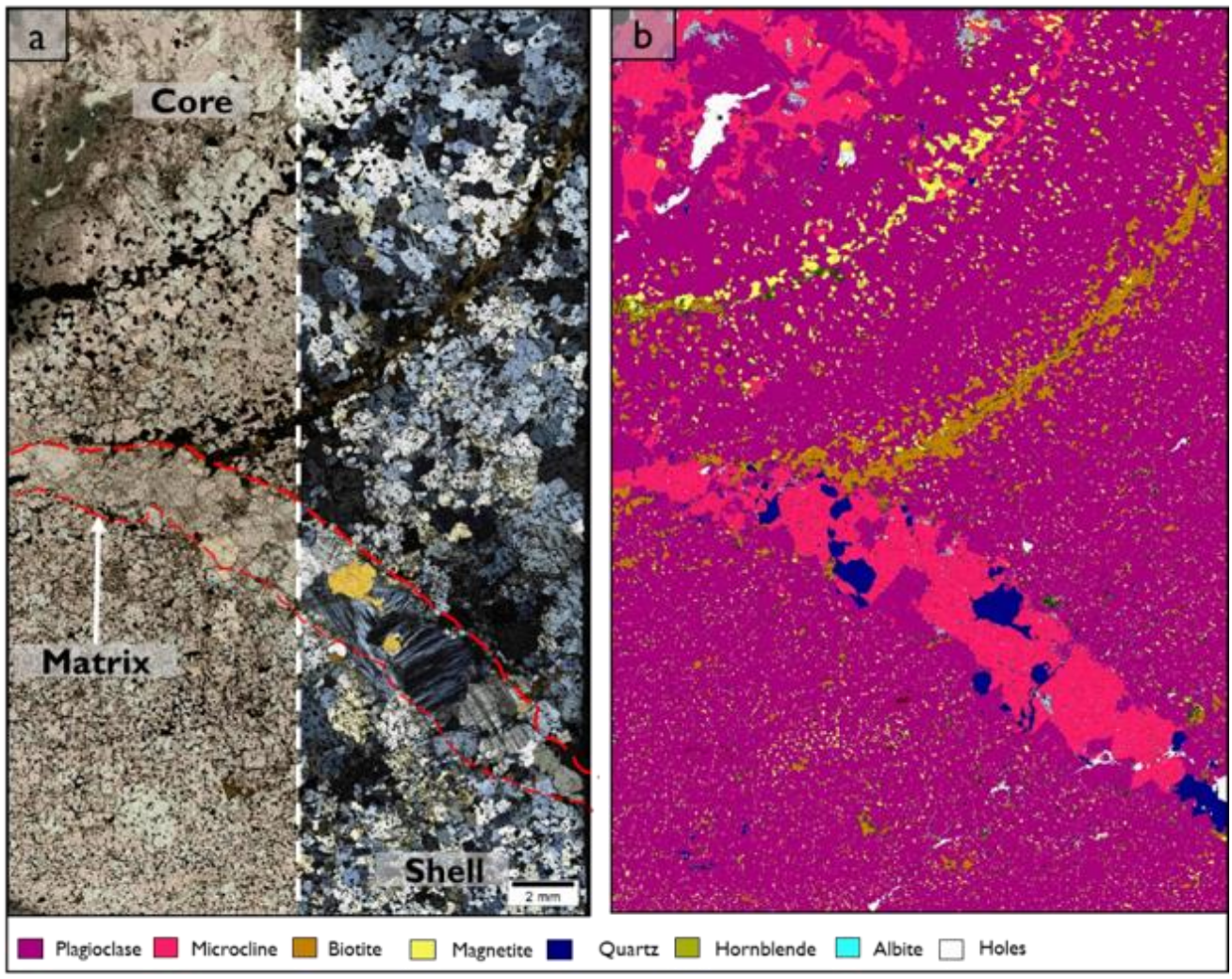


Figure 15: *Full thin section photomicrographs of Diana's Pool orbicule sample BM14780H: (a) Plane–polarized (left) and cross-polarized light (right) full thin section images of sample BM14780H. (b) TIMA image of orbicule sample BM14780H showing fine-grained shells crosscut by a pegmatitic and granitic matrix.*

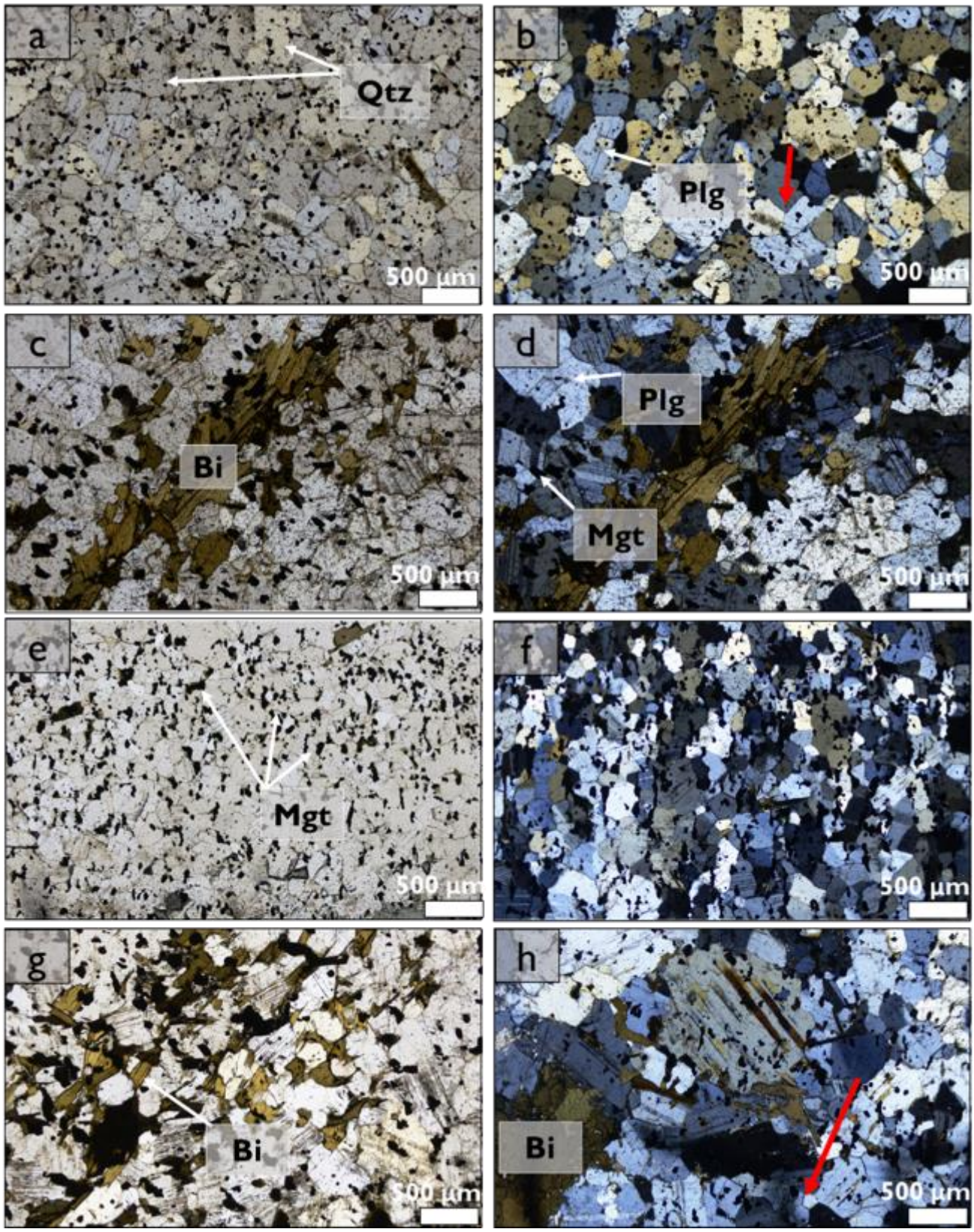


Figure 16: *Photomicrographs showing mineral phases and textures in Diana's Pool orbicular shells: (a, b) Equigranular grains of feldspars, quartz and magnetite occurring close to each other and forming granoblastic textures. (c, d) Mafic shells comprising biotite containing poikilitic inclusions of quartz and magnetite adjacent to smaller plagioclase and quartz grains. (e, f) Felsic shells characterized by less biotite and more quartz and feldspars with poikilitic inclusions of magnetite. (g, h) Equigranular grains of plagioclase and quartz forming T- junctions (120 ^{o}; red arrow). Plagioclase contains poikilitic inclusions of magnetite and elongate biotite.*

- **Matrix characteristics**

The contacts from shells to the matrix are sharp. The matrix compositions are comparable to the core compositions. However, the slight differences are in modal abundances and the degree of mineral alteration. The matrix is distinctly richer in K-feldspar than the cores and contains microcline (30%), plagioclase (20%), quartz (30%), orthoclase (5%), biotite (5%), chlorite (5%) and other accessory phases (Figure 17).

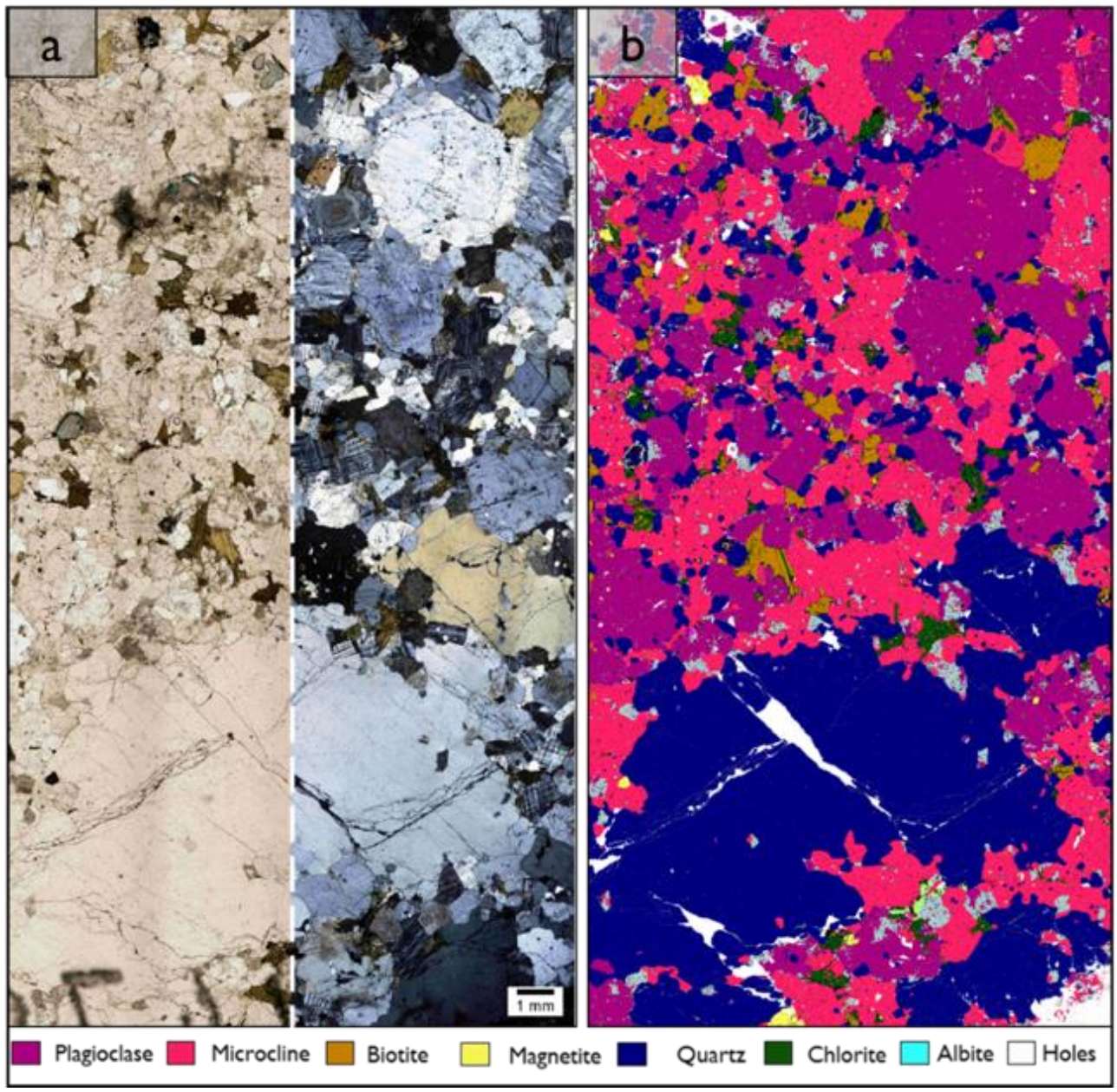


Figure 17: *Full thin section photomicrographs of the Diana's Pool matrix: (a) Plane–polarized (left) and cross-polarized light (right) full thin section images of sample BM14780A. (b) TIMA image of the Diana's Pool orbicule sample BM14780A showing a coarse-grained to pegmatitic and granitic matrix comprising feldspars, quartz, biotite and chlorite as predominant phases.*

The transition from the shells to the matrix is marked by a decrease in magnetite concentration and changes in textures (Figure 14; Figure 11). Similar to cores, the matrix is coarse-grained and more felsic than the fine-grained and intermediate to mafic shells. Microcline occurs as a dominant phase in the matrix, and it occurs as subhedral (0.1-2 mm) grains that are adjacent to quartz, biotite and plagioclase (Figure 18b, f, e). Locally, microcline contains small poikilitic inclusions of quartz and magnetite (Figure 18f). Growing adjacent to microcline are sub-rounded and sub-angular (0.1-1 mm) grains of quartz. The quartz grains also grow as poikilitic inclusions in plagioclase and microcline

(Figure 18e, f). Granophyric textures (Figure 18b) are observed where microcline and quartz grow together. Plagioclase occurs as large and subhedral (0.1-2 mm) grains that grow adjacent to quartz, microcline, and biotite (Figure 18e, f). It contains small quartz inclusions (Figure 18f) and locally, it is altered to sericite. Biotite occurs as anhedral to subhedral (0.1-0.5 mm) grains that grow adjacent to microcline, quartz, and plagioclase (Figure 18e). Locally, biotite contains small poikilitic inclusions of quartz and magnetite. Orthoclase (Figure 18d) occurs as the least abundant phase in the matrix. It occurs as subhedral grains that grow adjacent to microcline and plagioclase. Biotite, microcline, plagioclase, quartz, and orthoclase also occur as cumulus crystals locally, where they are surrounded by interstitial hornblende (Figure 18d). Hornblende also occurs as large (0.2-2 mm) grains that grow adjacent to feldspars, quartz, and biotite (Figure 18a).

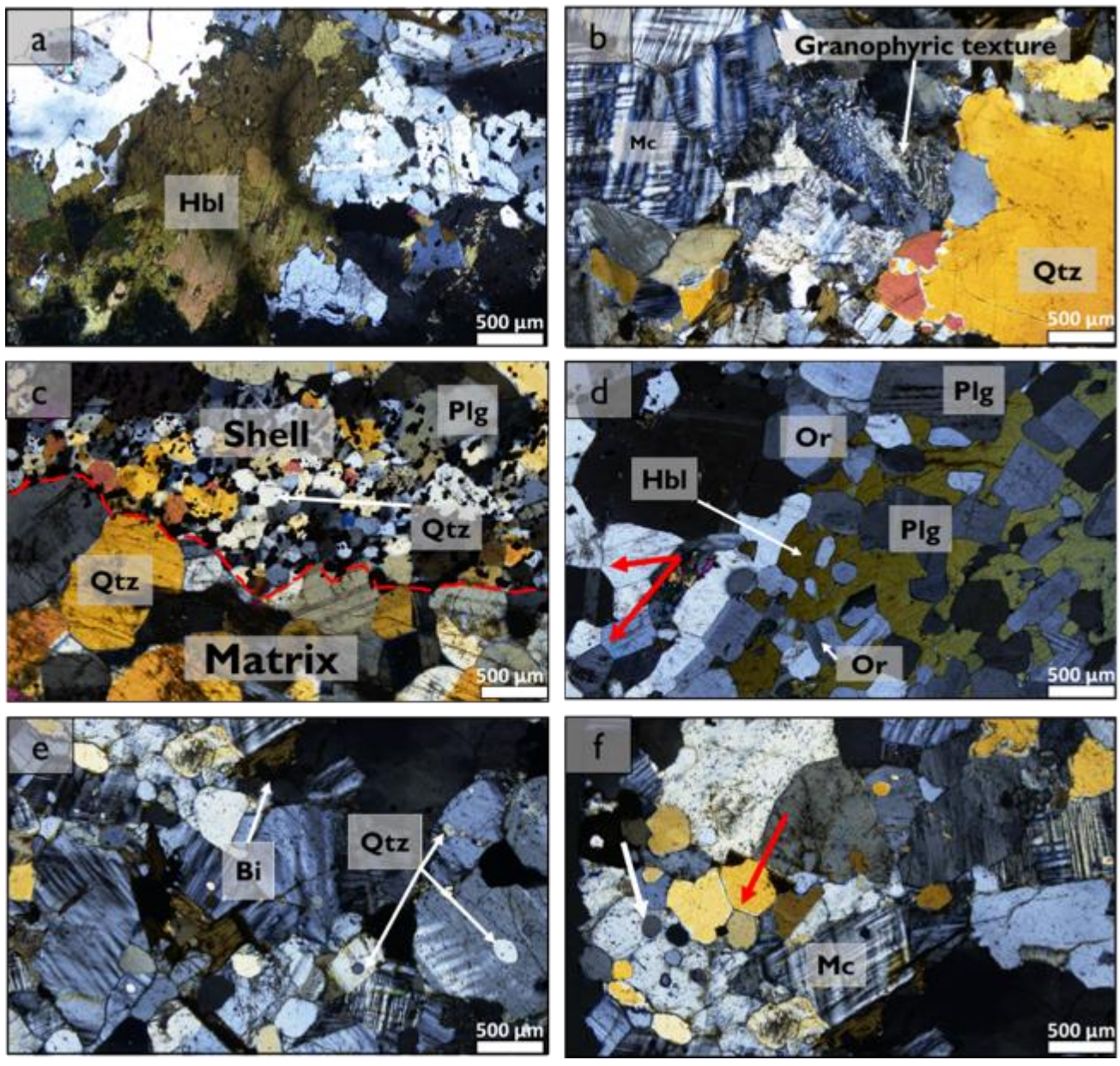


Figure 18: *Photomicrographs showing mineral phases and textures in the Diana's Pool matrix: (a) large grain of anhedral hornblende that grows into feldspars and quartz. Hornblende contains small poikilitic inclusions of quartz and grows adjacent to biotite (b) Microcline and quartz grains adjacent to each other. Granophyric textures are observed where microcline and quartz grow together. (c) Sharp contact between a coarse-grained matrix and a medium to fine- grained shell. (d) Interstitial hornblende enveloping touching grains of feldspars. (e) Poikilitic inclusions of quartz in feldspars. (f) Granoblastic textures where touching quartz grains form T-junctions (white arrows).*

4.3. Geochemistry

4.3.1. *In-situ* compositions of mineral phases

Plagioclase and biotite mineral compositions together with *in-situ* $^{87}Sr/^{86}Sr$ were determined in the Diana's Pool orbicular cores, shells and matrix with an aim of understanding the evolution of the magma (s) and the processes that were operating in the magma (s) during crystallization. The analyzed samples are shown in Table 3, showing what minerals in what orbicular structure were analyzed in each sample.

Table 3: *Table showing different samples that were analyzed for EPMA and in-situ Sr. "X" shows what was analyzed in each sample.*

Sample	**BM14780A**	**BM14780D**	**BM14780E**	**BM14780F**	**BM14780G**
Core		X		X	
Shells			X	X	X
Matrix	X			X	
Plagioclase	X	X	X	X	X
Biotite	X	X		X	
$^{87}Sr/^{86}Sr$	X	X	X	X	

4.3.1.1. Plagioclase

Unaltered plagioclase grains were analyzed for major elements in cores, shells and matrices of different orbicule samples (Table 4).

Table 4: *Table showing the ranges of major elements (in wt. %)-in plagioclase from cores, shells and matrices of differed Diana's Pool orbicular samples.*

Structure	**Cores**		**Shells**			**Matrices**	
Sample#	**BM14780D**	**BM14780F**	**BM14780E**	**BM14780G**	**BM14780F**	**BM14780F**	**BM14780A**
CaO	4.91-5.80	4.90-5.73	5.68-5.97	5.16-5.35	5.00-5.52	4.61-6.00	2.78-7.50
Na_2O	8.70-9.36	7.43-9.08	6.76-9.43	8.53-8.89	8.28-9.27	7.66-9.08	7.75-9.95
K_2O	0.10-0.24	0.09-0.35	0.16-0.35	0.52-0.36	0.11-0.29	0.12-1.15	0.07-0.46
Al_2O_3	24.05-24.68	26.78-27.79	22.72-24.33	26.45-27.45	36.34-27.34	26.48-27.90	21.05-29.24
SiO_2	59.46-61.18	56.78-58.12	60.05-61.67	57.27-58.05	57.04-57.95	56.37-59.08	53.84-64.08

The ranges of SiO_2, CaO, K_2O, Al_2O_3 and Na_2O in (wt. %) in cores, shells and matrices of different samples are shown in Table 4 and the rest of the major elements in (Table 20; Appendix A).

The data were plotted on major element variation diagrams (Figure 19) which show the variation of selected oxides between different orbicule samples plotted against SiO_2.From the variation diagrams, it is clear that there are two groups or clusters of cores, shells and matrices (Figure 19; Table 4) characterized by varying major element compositions. Owing to data dispersion there is no interpretable differences in Na_2O (Figure 19c) and K_2O (Figure 19d) contents between the samples. Samples BM14780F and BM1478080G form a specific cluster (core, shell and matrix) with silica around 57 % (Figure 19), rather high alumina (~27 %; Figure 19a) and low CaO (~5 %; Figure 19b). Samples BM1478080E and 80D show higher silica contents (around 60-62 %; Figure 19) and low alumina content (~24 %; Figure 19a). Sample BM1478080A show two groups of matrix plagioclase, one with low silica (around 55 %) and high alumina (around 28 %; Figure 19a), and the other with high silica (~ 61 % and low alumina (around 24 % ; Figure 19a) close to compositions of samples BM1478080E and BM1478080D.

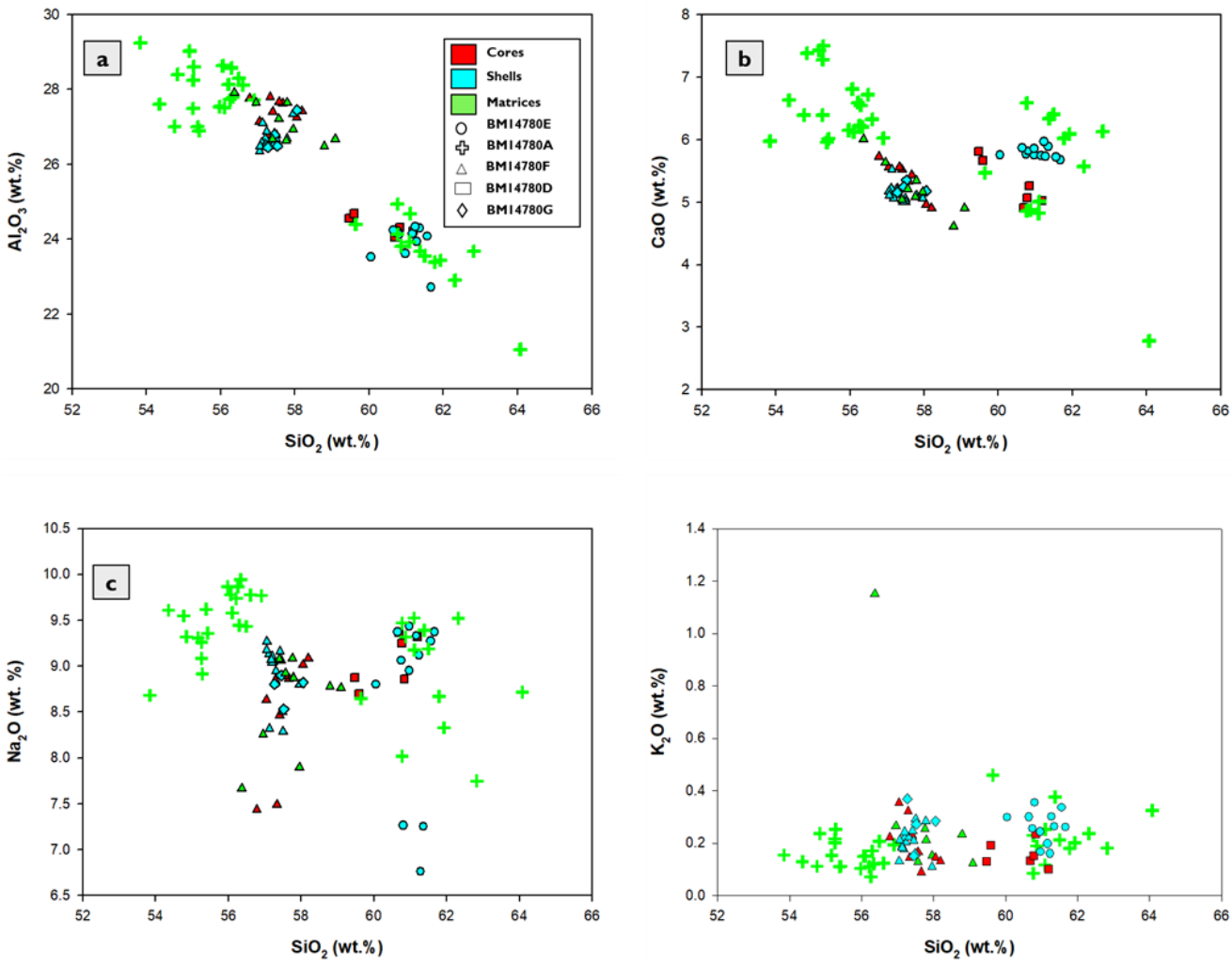


Figure 19: *Chemical variation diagrams showing the variation of different oxides in plagioclase from the Diana's Pool orbicular cores, shells and matrices plotted against SiO2 (wt.%).*

A similar variation is seen in CaO, where plagioclase from sample BM14780F is slightly more calcic than plagioclase from sample BM14780D (Figure 19b; Table 4). Similarly, there is minor variation in Na_2O between the two samples (Figure 19c; Table 4). Conversely, little variation is observed in K_2O between these samples (Figure 19d; Table 4). Sample BM14780D cores are slightly more sodic than BM14780F cores (Figure 19c; Table 4).

Plagioclase from three shells samples were analyzed (BM14780F, BM14780E and BM14780G) and there is variation in the composition of plagioclase between them (Figure 19d; Table 4). Samples BM14780F and Sample BM14780G shells contain plagioclase with the slightly similar compositions and there is little to no variation in the plagioclase compositions between them. However, plagioclase in samples BM14780F and BM14780G shells are more aluminous (Figure 19a), more calcic (Figure 19b), less sodic (Figure 19c) and less siliceous (Figure 19) than in sample BM147E. Similar to the cores and shells, a variation in plagioclase in the matrices of different samples is observed (Figure 19). However, this variation is not only between plagioclase of different samples, but also observed in plagioclase grains of the same samples Figure 19). Plagioclase in the two matrix samples (BM14780A and BM14780F) was analyzed and there is a distinct compositional variation between them (Figure 19). Sample BM14780A comprises plagioclase with varying compositions (Figure 19). Some of the plagioclase grains in sample BM14780A are more aluminous and some are less aluminous than plagioclase in sample BM14780F matrix (Figure 19a). Some plagioclase grains in sample BM14780A matrix grains are also more calcic Figure 19) and less sodic (Figure 19c) than plagioclase in sample BM1470F. Similar to plagioclase in cores and shells, there little variation in K_2O in plagioclase grain from the matrices of the same or different samples (Figure 19d).

Plagioclase from the Diana's Pool orbicules are sodic (An_{20-31}; Figure 20) and all plagioclase analyzed in the cores, the shells, and the matrices plot in the oligoclase field on the feldspar ternary classification diagram (Figure 20).

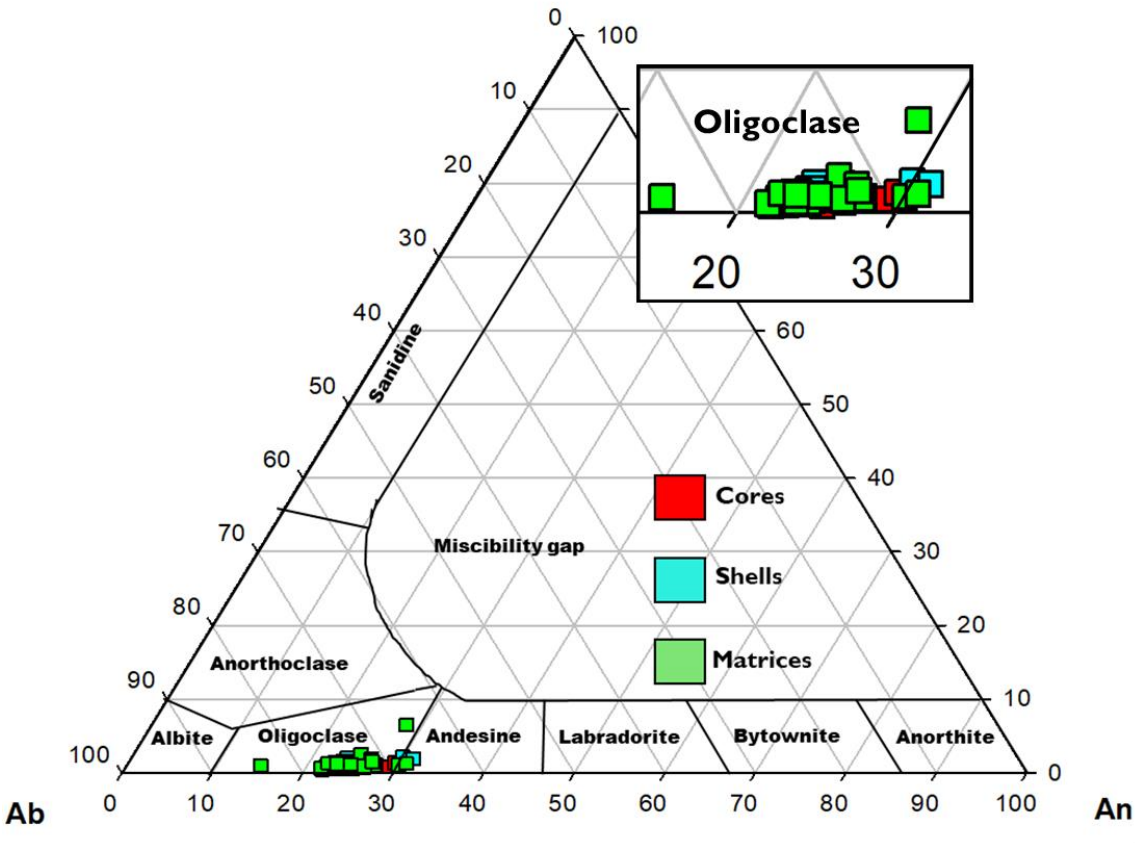


Figure 20: *A classification of feldspars from Diana's Pool orbicules on a ternary albite-anorthite-orthoclase diagram.*

Samples BM14780F (An_{23-27}) and BM14780G (An_{24-25}) shells are composed of plagioclase that are less calcic than in sample BM14789E shells (An_{24-31}) shells. Sample BM14780F (An_{23-29}) cores

contain plagioclase that are more calcic than in sample BM14780D core (An_{22-26}). Sample BM14780F matrix (An_{22-28}) comprise plagioclase that are slightly more sodic than in sample BM14780A matrix (An_{22-30}). In summary, there is little variation observed in cores, shells and matrix plagioclase compositions from different orbicule samples. In sample BM14780F which shows a full orbicule, plagioclase shows a decrease in the An content from the core to shells and an increase from shells to the matrix (Figure 21). The core ($\overline{x} = An_{26}$) and the matrix ($\overline{x} = An_{25}$) have slightly overlapping compositions, showing little variation in the An content (Figure 21). However, the shells are slightly sodic and evolved ($\overline{x} = An_{24}$; Figure 19; Figure 21). The An content in the inner ($\overline{x} = An_{24}$) to middle ($\overline{x} = An_{24}$) to outer ($\overline{x} = An_{24}$) shells homogeneous and shows little to no variation.

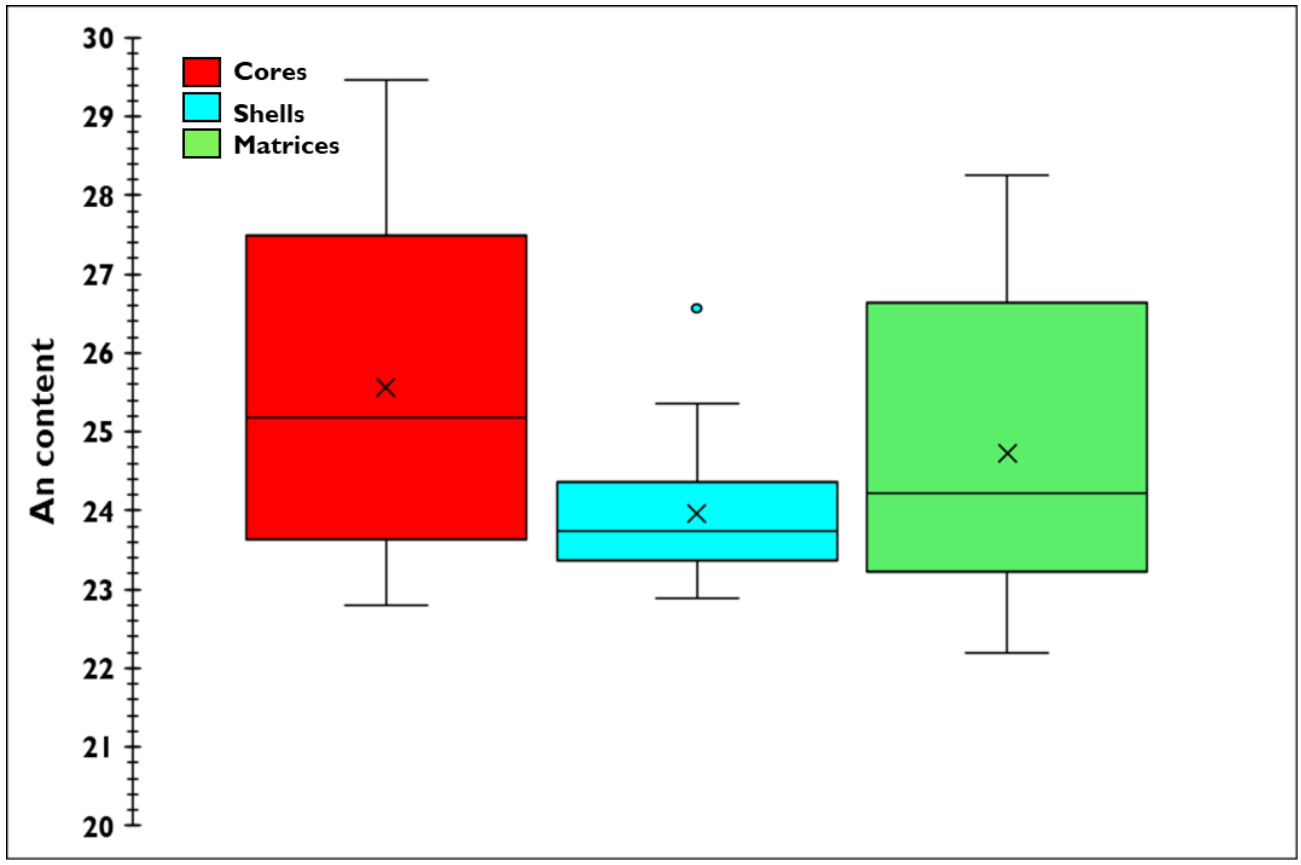


Figure 21: *The graph showing the An content in plagioclase from Diana's Pool orbicular core, shells and matrix from orbicule sample BM14780F (representative of a full orbicule with a core, shells and a matrix). The graph shows little variation in the An contents in the core and matrix, however, the shells have slightly low An contents. The two sigma represent the minimum and maximum values, the box represents the interquartile range, x represents the mean, and the middle straight line represents the median.*

4.3.1.2. Biotite

Chemical compositions of unaltered biotite in cores, shells, and matrices were analyzed. The analyzed samples include samples BM14780F, BM14780G, BM14780A, and BM14780D (Table 3) and (Table 5).

Table 5: *Table showing the ranges of major elements (wt. %) in biotite from cores, shells and matrices of differed Diana's Pool orbicular samples.*

Structure	**Core**	**Shells**		**Matrix**
Sample#	**BM14780D**	**BM14780G**	**BM14780F**	**BM14780A**
TiO_2	2.11-2.83	2.04-4.04	1.62-3.68	1.78-4.00
MgO	4.36-5.72	2.67-3.56	1.79-3.89	4.11-5.86
FeO	21.48-25.00	4.60-27.31	23.70-27.15	22.38-32.19
SiO_2	36.84-43.93	36.99-38.72	36.01-42.89	36.54-43.97
Al_2O_3	13.62-18.03	14.83-15.48	14.89-16.18	12.87-18.26

The ranges between the major elements MgO, Al_2O_3, SiO_2 and TiO_2 are shown in Table 4 and the rest of the elements are shown in Tables 8, 9, and 10 (Table 21; Appendix A).

Unlike plagioclase, unaltered biotite in these samples is scarce, hence only a few samples were analyzed. Similar to plagioclase, biotite analyzed in shell samples BM14780F and BM15780G exhibit similar compositions and show little to no variation (Figure 22). The core and the shells contain biotite that is more aluminous than in the matrix (Figure 22a), although some biotite in the core is less aluminous. The biotites are more magnesian in the core and matrix and biotite in the shells are less magnesian and rich in FeO_2 (Table 5; Figure 22b).The core and matrix contain biotite that are slightly more siliceous than the shells, although there is a large variation in SiO_2 in the core (Table 5; Figure 22c). The TiO_2 content shows little variation in the core, shells and the matrix (Figure 22d). However, it is slightly higher in some biotite from the shells and matrix.

Using the MgO-FeO-Al_2O_3 ternary diagram after Abdel-Rahman (1994) and Nachit et al. (2005), biotite in Diana's Pool orbicular core, shells and matrix plot in the peraluminous (S-type) granite suite (Figure 24d) and they are all considered primary magmatic compositions (Figure 24c). Unaltered biotite compositions were plotted in biotite classification diagrams and following the nomenclature after Makutu et al. (2004) and Deer et al. (1992), the Diana's Pool cores, shells and matrices all plot in the annite field (Figure 24a, b).

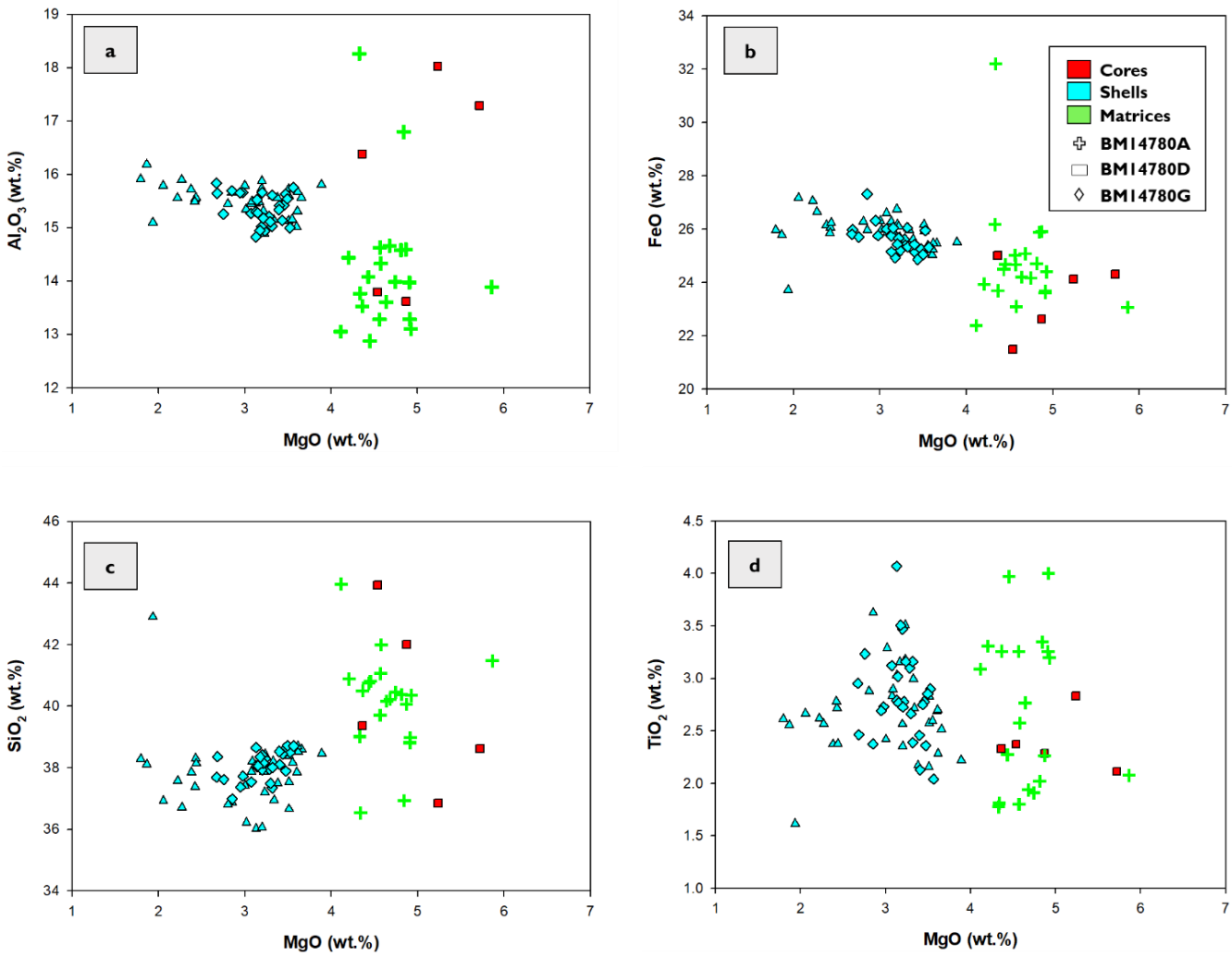


Figure 22: *Chemical variation diagrams showing variation of different oxides in biotite from the Diana's Pool orbicular cores, shells and matrices plotted against MgO (wt.%).*

Biotite shows a systematic variation in Mg# from cores to shells to the matrix (Figure 23). Biotite in the orbicule core sample (Mg# = 27) and the matrix sample (Mg# = 25) are more magnesian and have higher Mg# than in the ferroan shells (Figure 23). Compared to the variation in plagioclase compositions, biotite seems to be homogeneous in shells of different samples, showing little variation in Mg#. The average Mg#s are 17 and 28 in shell samples BM14780F and BM14780G, respectively.

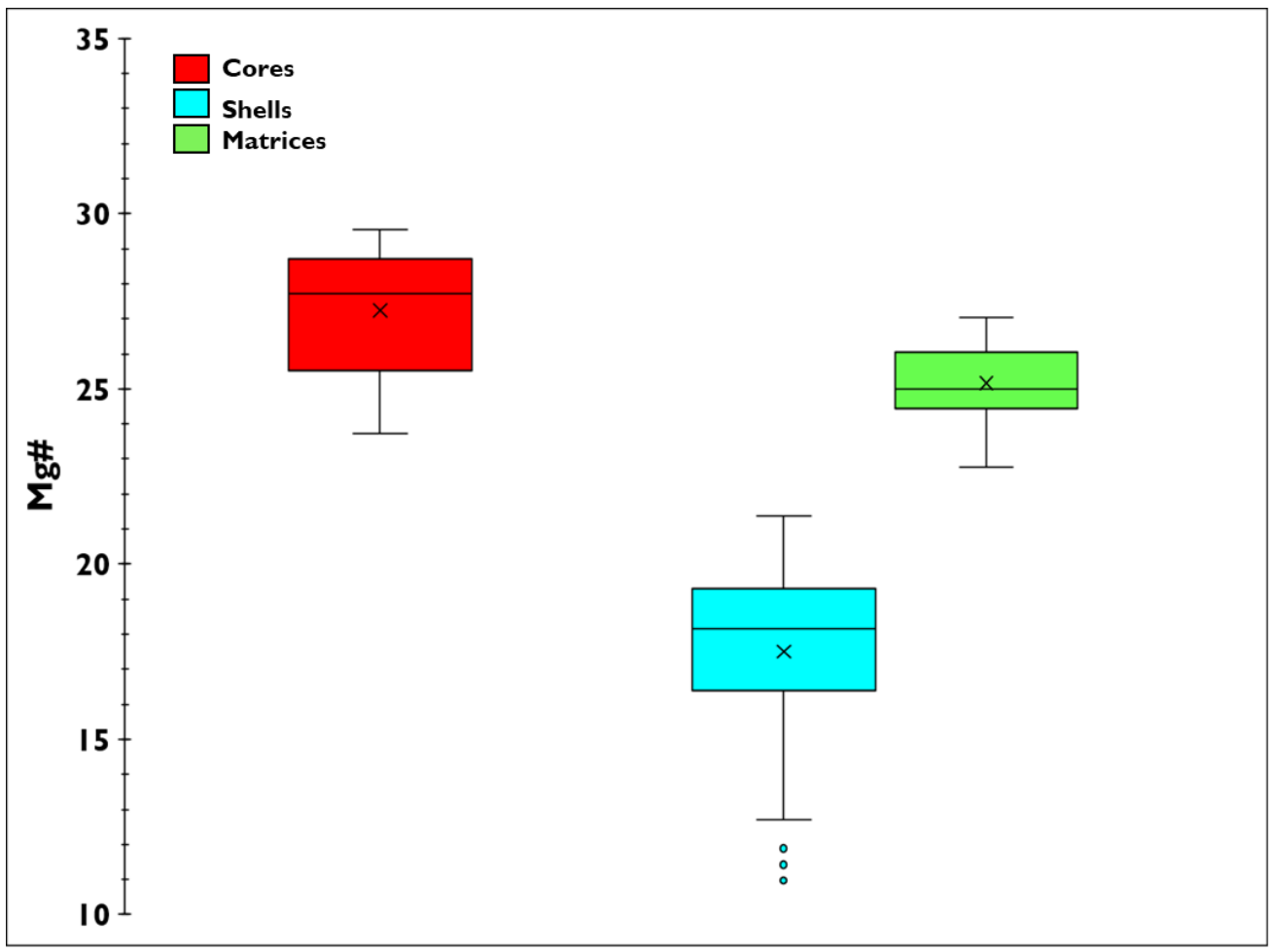


Figure 23: *Graph of Mg# (Mg/Mg + Fe) showing a variation in Mg# in the Diana's Pool orbicular core, shells and matrix from samples BM14780D, BM14780F and BM14780A, respectively. A core and matrix exhibiting high Mg#, and shells containing biotite with low Mg# characterize the Diana's Pool orbicules. The two sigma represent the minimum and maximum values, the box represents the interquartile range, x represents the mean, and the middle straight line represents the median.*

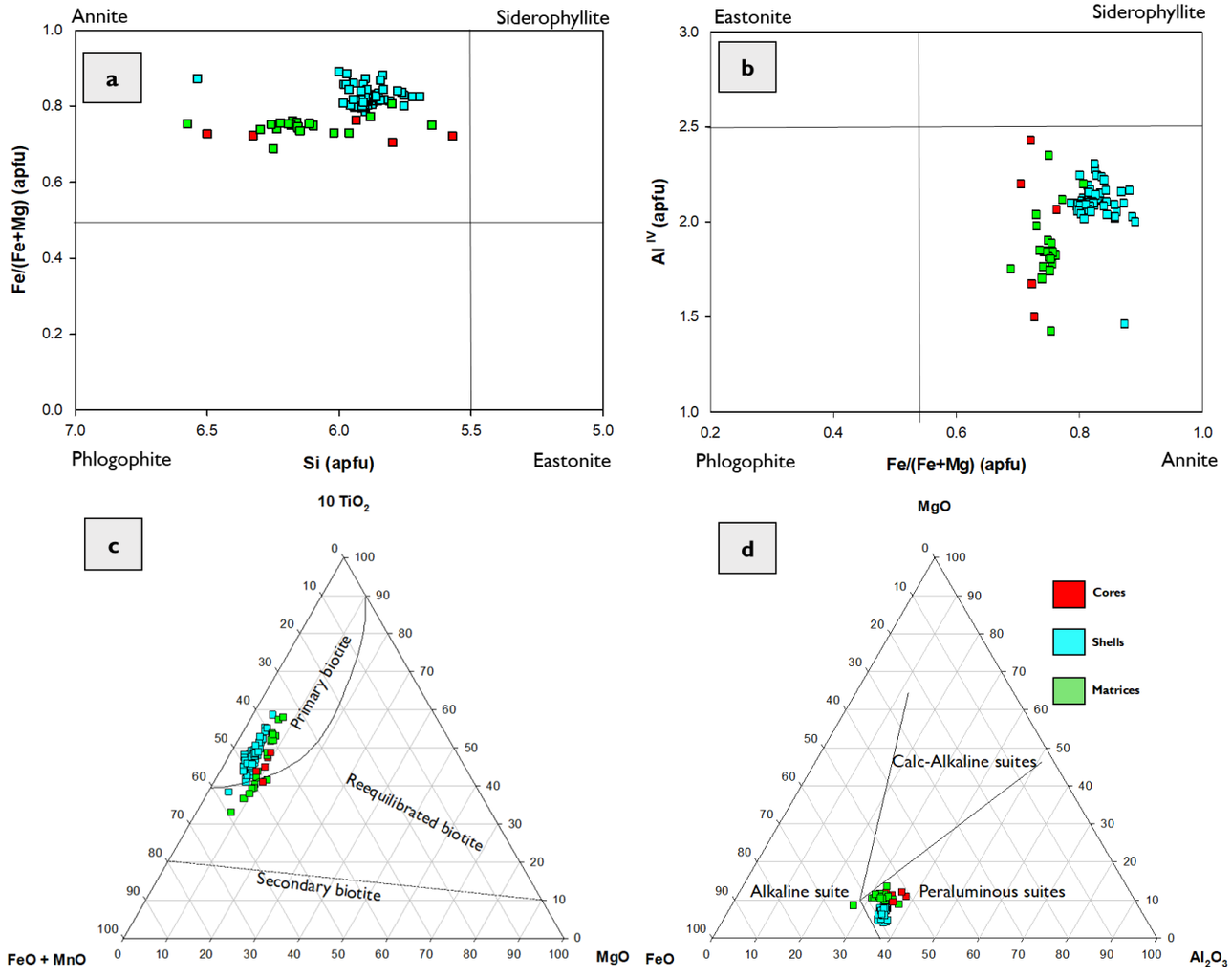


Figure 24: *Diana's Pool biotites plotted on compositional classification diagrams: (a) Fe/ (Fe +Mg) versus Si (apfu) after Makutu et al. (2004). (b) Fe/ (Fe+ Mg) versus* Al^{IV} *after Deer et al. (1992). (c) Chemical composition of biotite using the (FeO+ MnO) - 10* TiO_2*-MgO ternary diagram after Natchit et al. (2005). (d) Plot of Diana's Pool biotites on* Al_2O_3*-FeO-MgO ternary biotite discrimination diagram after Abdel-Rahman (1994).*

4.3.2. Initial $^{87}Sr/^{86}$ Sr isotopes ratios in plagioclase

Initial $^{87}Sr/^{86}Sr$ isotopic compositions were determined in plagioclase from the cores, shells and matrix of different Diana's Pool samples and the ranges are shown in Table 6. Strontium isotopes were analyzed as geochemical tracers to trace and test the processes behind orbicular formation (e.g., assimilation). The initial $^{87}Sr/^{86}Sr$ ratios (Table 22; Appendix A) were calculated using the model age of 2650 Ma of the Matopos granite (Broderick and Hubbard, 2016) . In general, there is little variation in the initial $^{87}Sr/^{86}Sr$ ratios in cores, shells and matrices (Table 6) and the Diana's Pool orbicules comprise plagioclase that exhibit radiogenic $^{87}Sr/^{86}Sr$ isotopic compositions that plot away from the depleted mantle (Figure 25).

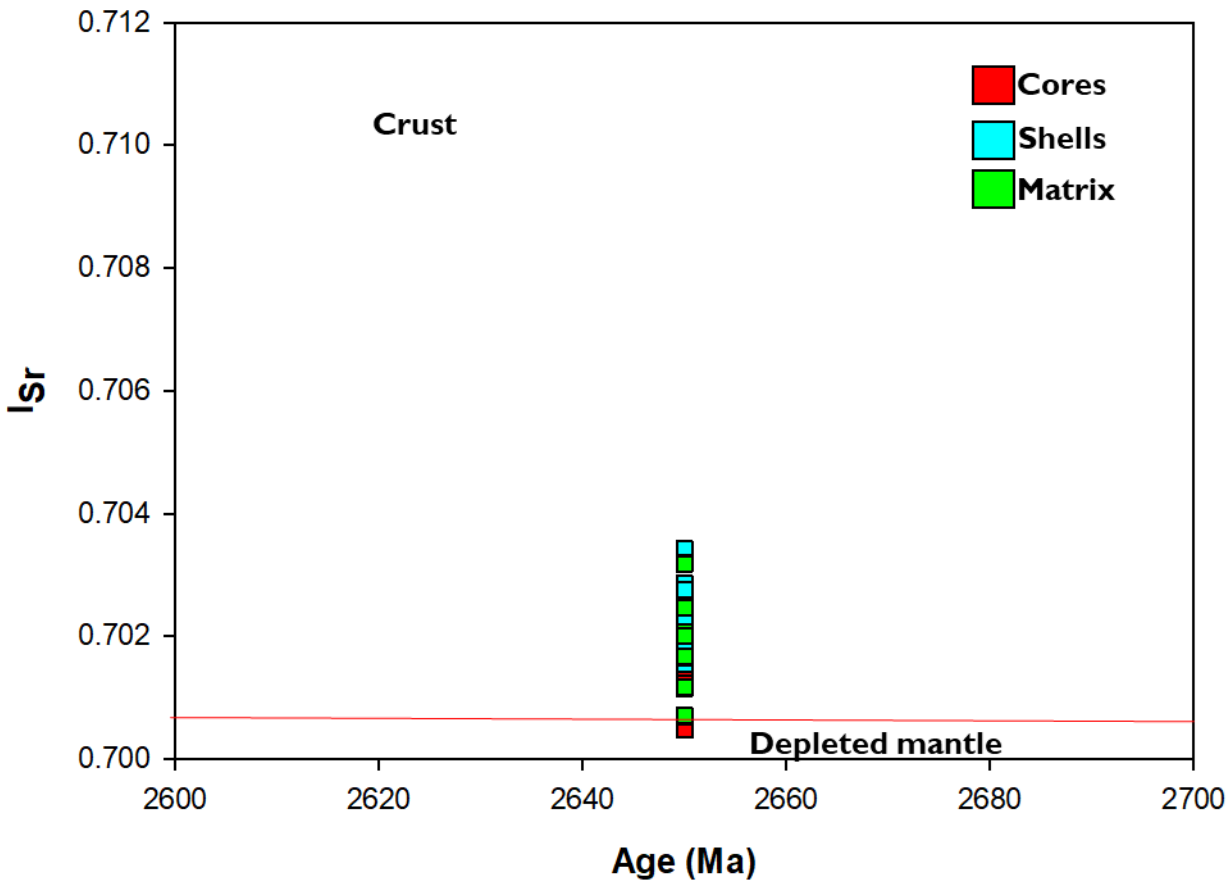


Figure 25: *Initial $^{87}Sr/^{86}Sr$ isotopic compositions of plagioclase from the Diana's Pool orbicules relative to the model depleted mantle taken from Eglington (2006).*

Plagioclase in the cores and the shells samples have slightly more radiogenic initial $^{87}Sr/^{86}Sr$ ratios than the less radiogenic ratios in plagioclase in the matrix (Figure 26; Table 6). Similar to the major elements in plagioclase and biotite, a variation in $^{87}Sr/^{86}Sr$ is observed in cores and shells of different samples (Table 6: Figure 26). Plagioclase in the core sample BM14780F are more radiogenic than in core sample BM14780D (Table 6). Plagioclase in shell sample BM14780E are less radiogenic than in shell sample BM14780F (Table 6).

A comparison of the An content and initial $^{87}Sr/^{86}Sr$ ratios in plagioclase shows little variation in $^{87}Sr/^{86}Sr$ ratios and a variation in An content in the core, the shells and the matrix (Figure 26). There is very little variation in $^{87}Sr/^{86}Sr$ ratios in cores of different samples (Figure 26), and the calcic sample BM14780F comprise plagioclase that are more radiogenic than the less radiogenic and sodic plagioclase in sample BM14780D core (Table 6; Figure 26).

Table 6: *Table showing the ranges of initial $^{87}Sr/^{86}Sr$ in plagioclase from cores, shells and matrices of differed Diana's Pool orbicular samples.*

Structure	**Cores**		**Shells**		**Matrix**
Sample#	**BM14780D**	**BM14780F**	**BM14780E**	**BM14780F**	**BM14780A**
Initial $^{87}Sr/^{86}Sr$	0.700477 ± 0.000198 to 0.702407 ± 0.000163	0.701229 ± 0.000163 to 0.705350 ± 0.000169	0.701547 ± 0.000184 to 0.702758 ± 0.000182	0.7001642 ± 0.000013 to 0.703423 ± 0.000171	0.700701 ± 0.000231 to 0.703188 ± 0.000274

The calcic plagioclase in shell sample BM14780E are slightly less radiogenic than the slightly more radiogenic and sodic plagioclase in sample BM14780F (Figure 26).

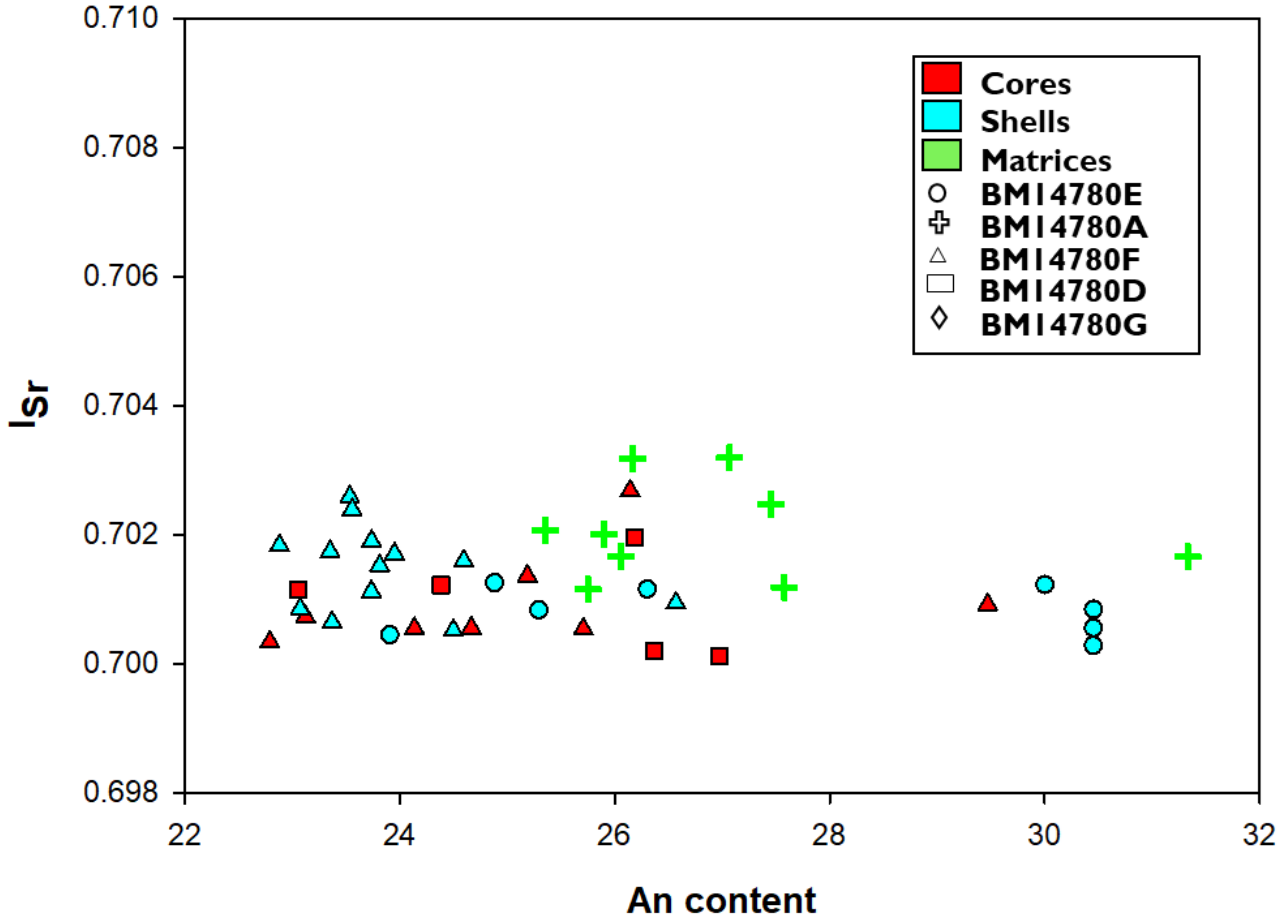


Figure 26: *Graph showing the initial $^{87}Sr/^{86}Sr$ ratios in the Diana's Pool orbicular cores, shells and matrix plotted against the An content. There is a little variation in initial $^{87}Sr/^{86}Sr$ ratios in plagioclase from cores to shells to the matrix and a large variation is observed in the An content in shells and cores of different samples. The highest An contents are exhibited by plagioclase in the matrix sample BM14780A.*

Summary of Diana's Pool orbicules

The studied orbicular samples are characterized by closely packed orbicules in a granitic matrix. They have felsic and coarse-grained cores, fine-grained and alternating mafic and felsic shells, and a coarse-grained to pegmatitic inter-matrix. These orbicules range from spherical to ellipsoidal in shape and they range from 6 to 14 cm in diameter and 5 to 13 cm in width. Some orbicules appear to have been deformed where the granitic matrix occurs between the shells, crosscutting some shells and cores. At microscale, medium- to coarse- grained cores are composed of plagioclase, quartz, biotite, hornblende, magnetite, orthoclase, and microcline.

Transitions from the central cores to the inner shells are marked by sharp contacts. The modal abundance of felsic minerals, the grain size and the degree of plagioclase alteration all decrease from the cores towards the inner shells. Alternating fine-grained ferromagnesian and feldspathic shells characterize the Diana's Pool orbicules. The mafic shells are predominated by biotite and magnetite with minor feldspar and quartz. Conversely, feldspar, quartz and minor biotite and magnetite predominate the felsic shells. Polygonal, radiating and granoblastic textures characterize shells. The boundaries between the outer shells and the matrix are sharp. An increase in grain size, as well as an increase in feldspar and quartz modal abundances, and a decrease in magnetite concentration mark this transition from the outer shell to the coarse-grained to pegmatitic matrix. The matrix composition and grain-size are comparable to that of the cores.

Plagioclase from the Diana's Pool orbicules are sodic (An_{20-30}) and all plagioclase analyzed in cores, shells, and the matrix are oligoclase. The core, the shells, and the matrix have overlapping compositions, showing little variation in An content. The An content from the inner to middle to outer shells is homogeneous and shows no variation. All biotite in cores, shells and matrix is primary and plots in the annite field on the biotite classification diagrams. Biotite from the cores and the matrix are more magnesian than the ferroan shells. There is little variation observed in the initial $^{87}Sr/^{86}Sr$ ratios in the cores, the shells, and the matrix. However, $^{87}Sr/^{86}Sr$ ratios values from plagioclase in the shells and the matrix are slightly more radiogenic than in the cores.

5. The Koperberg Suite orbicules

5.1. Field Observations

Initial fieldwork was undertaken in the Northern Cape Province (Concordia, O'okiep and Nababeep) for a period of one week, where spatial relationships between country rocks, sulphide mineralization, and orbicular rocks were investigated (Figure 6). During this period, basic mapping was carried out to produce basic sketch maps of some of the orbicule localities. Samples of the country rocks and orbicules from different localities were collected. However, sampling was not undertaken from in-situ outcrop in Orbicule Koppie, as it is a National Monument. Boulders found around the orbicule outcrop were used as samples for this project, as well as material from the School of Geosciences historical collections. Granites and gneisses in contact with anorthosite lenses, diorites and orbicules generally dominate the part of the Koperberg Suite where this study was carried out. This section describes the spatial relationships between orbicules and the surrounding regional rocks in the Koperberg Suite.

5.1.1. Country Rock: Nababeep Gneiss and the Concordia Granite

Orbicule Koppie orbicules are different from the other three Koperberg Suite orbicule localities. They are the only orbicules in contact with the Nababeep Gneiss and not the Concordia Granite. The Nababeep Gneiss outcrop in this region is medium-grained and characterized by a prominent foliation (Figure 27a, b) with a general strike of 290^{o} and dip of 4^{o} in the NE direction. The gneiss also contains 2.5-5 cm mafic veins that trend in the NW-SE direction which displace the foliation (Figure 27a). The melanocratic mafic veins comprise mostly biotite with minor plagioclase and quartz (Figure 27b). The gneiss also comprises 7-12 cm pegmatitic veins (Figure 27b) striking at 198^{o} and dipping at 2^{o} east. The veins contain plagioclase, quartz, K-feldspars, and biotite (Figure 27b). Henderson South, Henderson North, and the Hoogkraal Lease orbicules are in contact with the Concordia Granite. The Concordia Granite outcropping in Henderson South is not well exposed. However, it is coarse-grained and contains pegmatitic and mafic veins (Figure 27g). It is in contact with diorite comprising sub-horizontal and vertical (1 m) thick quartz veins (Figure 27h). The Concordia Granite outcrops in contact with Hoogkraal Lease and Henderson North orbicules share similar characteristics. They are typical coarse-grained granites comprising K-feldspars, quartz, plagioclase, mica, and accessory magnetite.

5.1.2. Koperberg Suite host rocks to orbicular granites: Anorthosite and Diorite

Anorthosite in contact with the Hoogkraal Lease orbicules is light green to grey and comprises altered plagioclase, quartz and biotite. The anorthosite is also in contact with diorite, which has proto-orbicules (less developed orbicules). The diorite is composed of medium-grained plagioclase, biotite and accessory magnetite. Similar to Hoogkraal Lease, diorite from Orbicule Koppie is composed of very prominent biotite (Figure 27e) and grades into a less-biotite rich diorite that hosts proto- orbicules (Figure 27f). South of the orbicular rocks-hosting Koppie is an anorthosite Koppie (Figure 28) in contact with the Nababeep Gneiss. The anorthosite does not contain orbicules and it is in contact with both diorite and the Nababeep Gneiss.

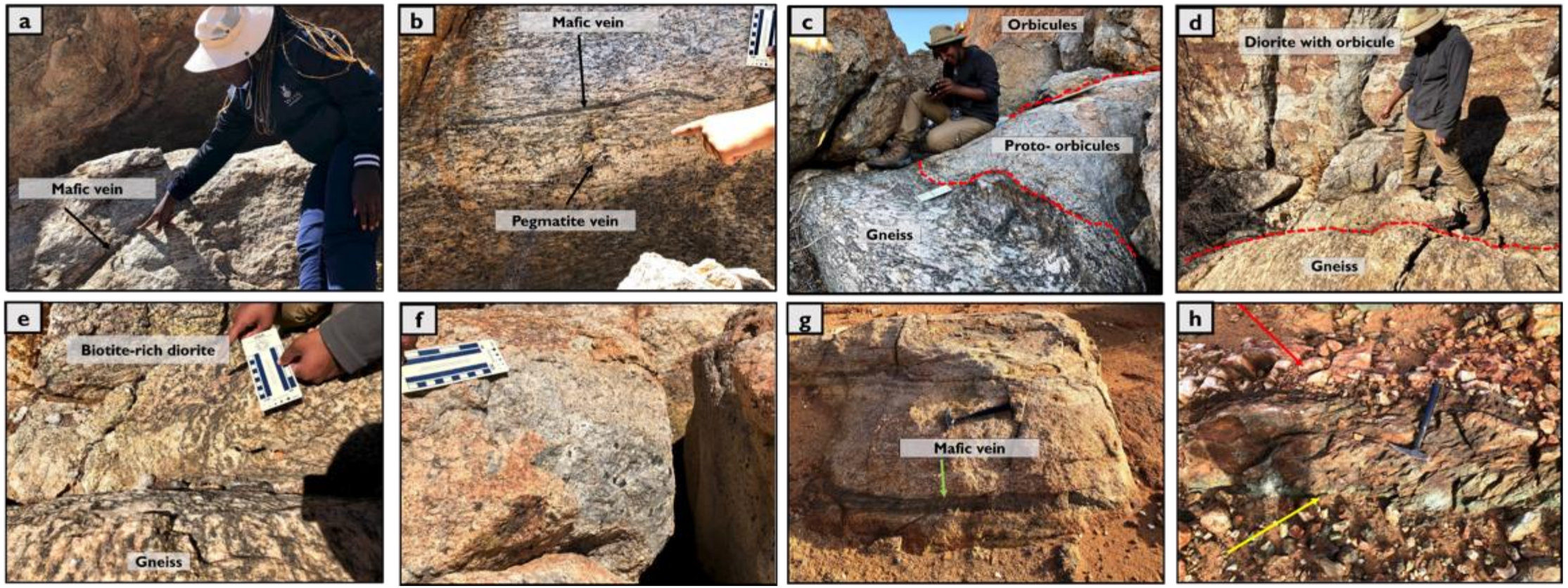


Figure 27*: Photomicrographs showing outcrops of the massive Koperberg Suite rocks associated with the orbicular outcrops in different orbicular localities: (a, b) Nababeep Gneisses in contact with orbicules from Orbicule Koppie containing mafic and pegmatitic veins (black arrows). (c) An outcrop showing contacts between the orbicular body and the surrounding Nababeep Gneisses. (d) The contact between the gneiss and the diorite grading from a non-orbicular diorite to an orbicule-hosting diorite. (e) Biotite- rich diorite (mica diorite) at the contact point between the Nababeep Gneisses and massive diorite. (d) A less biotite- rich rock away from the contact between diorite and gneiss grading to the orbicule host rock. (g) The Concordia Granite outcrop in contact with the Henderson South orbicular rocks comprising pegmatitic and mafic veins. (h) Quartz veins associated with a quartz diorite comprising copper staining (yellow arrow) in Henderson South.*

The contact between anorthosite and diorite is not easily observed but it grades into the less biotite-rich diorite (Figure 27d) which grades into an orbicule-hosting rock (Figure 27c). Diorite from Henderson South differs from the other three localities as it comprises orthopyroxene (<5%). It is medium-grained and comprises plagioclase (0.1-2 mm), biotite (0.1-0.2 mm) and orthopyroxene (0.1- 0.2 mm). Anorthosite in Henderson North occurs as lenses in diorite and is dominated by medium-grained plagioclase (0.1-0.2 mm), biotite (0.1-0.2 mm), magnetite, and accessory orthopyroxene (0.1-0.3 mm).

5.1.3. Orbicules in the Koperberg Suite

The studied orbicules are hosted in rocks ranging between felsic to the more mafic and orthopyroxene-bearing diorites (more evidence from the geochemistry data in section 5.3). Hence, they cannot be easily classified using modal abundances on the Streckeisen diagram. In addition, all the geochemical analyses in the orbicules were *in-situ* and the data could not be used to classify the host rocks in other classification diagrams (e.g., Q'ANOR diagrams).

5.1.3.1. The Orbicule Koppie orbicules

The Orbicule Koppie orbicular outcrop is an approximately 50 m wide and 35 m long rhombic body of orbicules that is intrusive to the Nababeep Gneiss (Figure 28). The orbicules are hosted in quartz diorite and rest directly above the steepening foliation in the Nababeep Gneisses (Figure 28).

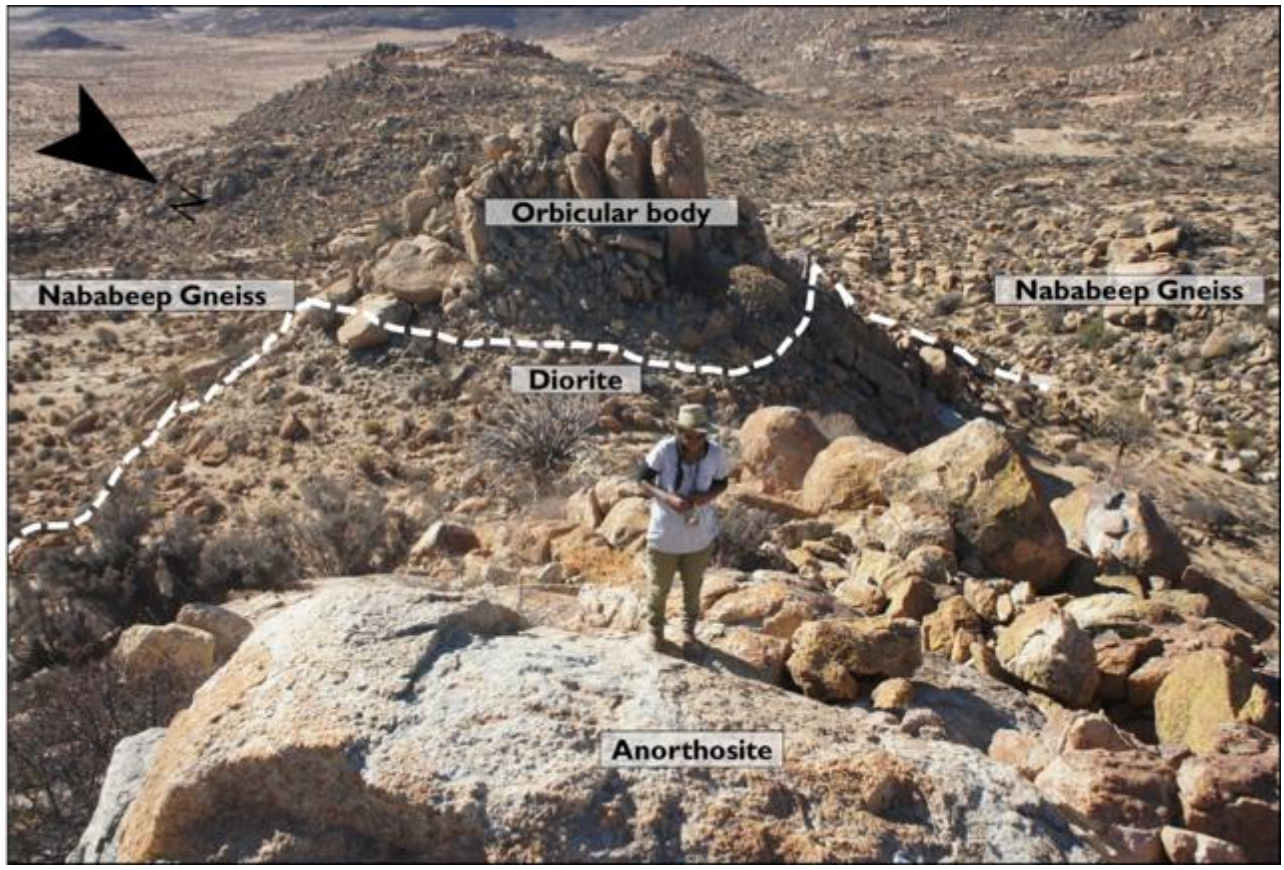


Figure 28: *The rhombic-shaped Orbicule Koppie orbicule outcrop and the surrounding country rocks.*

The orbicule outcrop is ~90% orbicules to 10% host matrix or rock volume and the orbicules do not exhibit a general trend but are elongated randomly (Figure 29a, c) and are all similar in size and shape. The cores are leucocratic and are composed of plagioclase, K-feldspar, quartz and minor biotite and magnetite. Some of these orbicules do not have distinct cores but they resemble enclaves (red arrow; Figure 29a). The contact between cores and the shells is sharp macroscopically (Figure 29a). The

orbicules are single-shelled (Figure 29a, c) and the shells are melanocratic and composed of quartz, plagioclase and minor biotite. The boundaries between the shells and matrix are sharp (Figure 29a, c).

The matrix is comparable in composition to the cores, but it is more coarse-grained and pegmatitic in places (Figure 29a). The matrix is leucocratic and has roughly equal amounts of plagioclase, K-feldspar, quartz, biotite, and small-disseminated accessory epidote (Figure 29a, c). Some boulders next to the outcrop comprise weathered and deformed orbicules (Figure 29d). These are closely packed and have a preferred east-west orientation (Figure 29d). In places, the matrix appears to deform some parts of the shells (white arrows; Figure 29a). There is also evidence of sulphide mineralization (Figure 29b), which is mainly bornite and chalcopyrite hosted in the coarse-grained inter-orbicular host matrix and only associated with the mafic mineral phases (Figure 29b). Copper staining is observed in the matrix associated with chalcopyrite and bornite (Figure 29b).

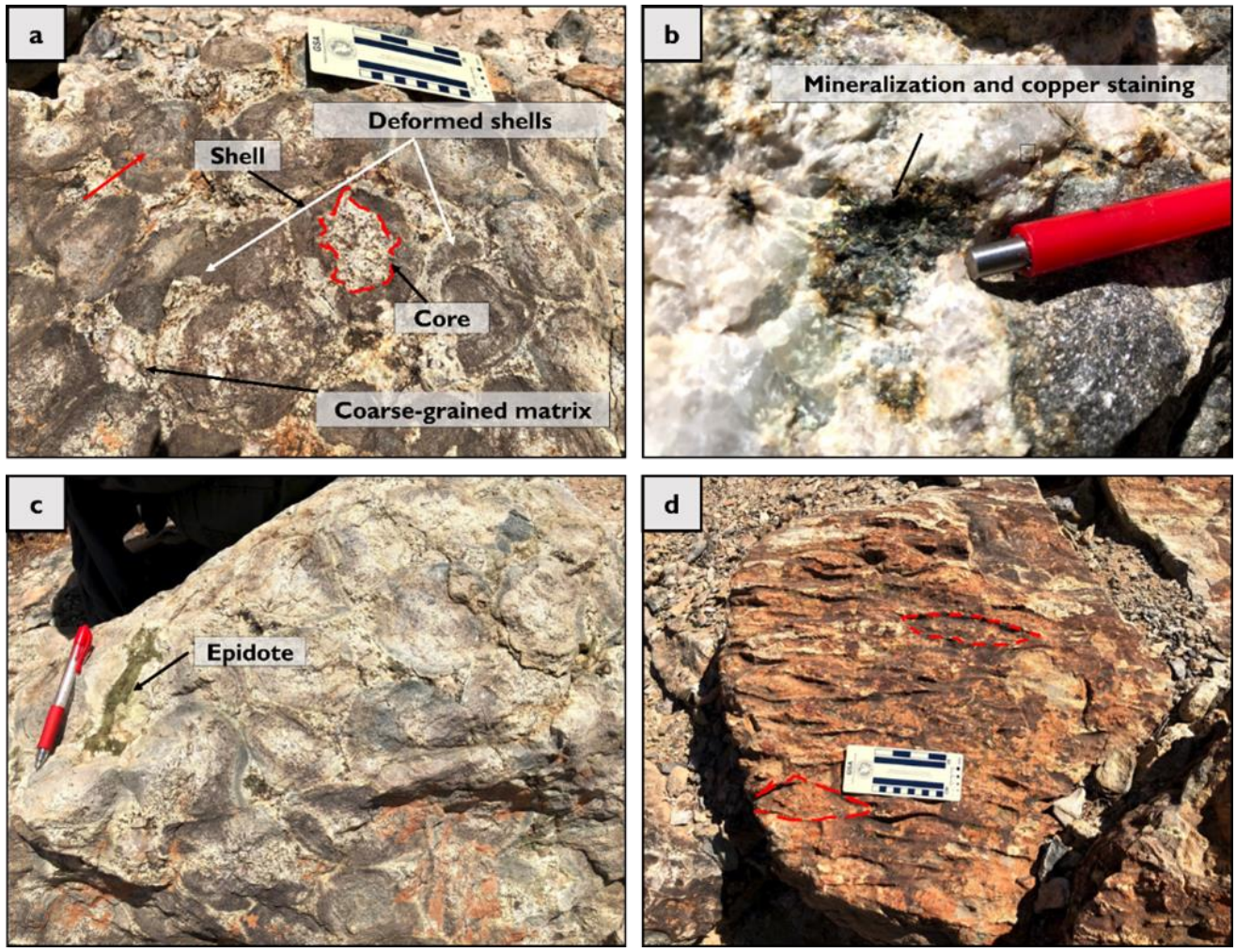


Figure 29: *Pictures of Orbicule Koppie orbicular outcrops showing: (a) Orbicules with no preferred orientation characterized by felsic cores and shells hosted in a coarse-grained and felsic matrix. Some of these orbicules do not have distinct cores and they resemble enclaves (red arrow). (b) Sulphide mineralization and copper staining hosted in a felsic matrix. (c) Epidote patches in the felsic matrix hosting closely packed orbicules that displace and deform each other. (d) Deformed (east-west trending, red-dotted lines) orbicule boulder near the Orbicule Koppie outcrop.*

5.1.3.2. The Hoogkraal Lease orbicules

The Hoogkraal Lease orbicule outcrop is an approximately 5 m high and 30 m diameter body of orbicules (Figure 30) that is approximately 4 km NW of Orbicule Koppie. Hoogkraal Lease orbicules occur in a pyroxene-bearing diorite. Unlike Orbicule Koppie orbicules, Hoogkraal Lease orbicules intrude the Concordia Granite (Figure 30).

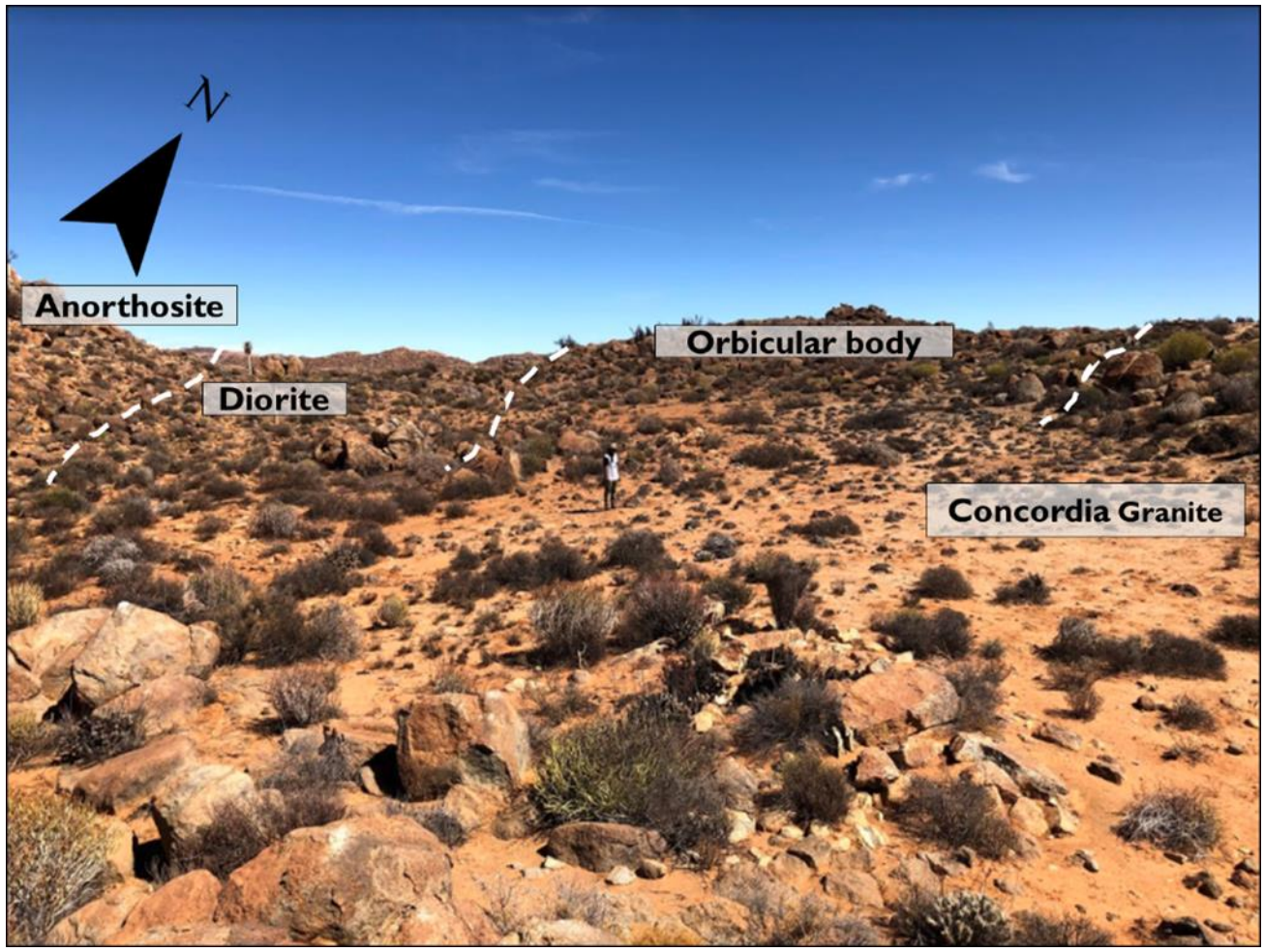


Figure 30: *The Hoogkraal Lease orbicule outcrop and the surrounding diorite, anorthosite and Concordia Granite.*

Relative volumes of 30% orbicules to 70% host matrix characterize the orbicular outcrop (Figure 31a). However, some boulders around the outcrop are (80%) orbicules to (20%) matrix (Figure 31b). The orbicules have no preferred orientation and are randomly oriented. They are mostly spherical and elongate in some places in the outcrop and surrounding boulders (Figure 31b, d). They differ in size, ranging from 1-7 cm in diameter. Like the Orbicule Koppie orbicules, cores comparable in composition to the matrix characterize the Hoogkraal Lease orbicules (Figure 31a).

Hoogkraal Lease orbicular cores and matrix are composed of plagioclase, orthopyroxene, biotite, quartz and accessory magnetite. The core to shell boundaries are sharp (Figure 31a), and unlike Orbicule Koppie orbicules, Hoogkraal Lease orbicules are multi-shelled and are composed of alternating mafic and intermediate shells (Figure 31a, b). The intermediate shells are dominated by orthopyroxene, biotite and minor plagioclase and quartz. The intermediate shells are composed mainly of plagioclase with minor biotite, orthopyroxene, and magnetite.

The continuous growth of orthopyroxene and plagioclase forms a radiating texture (comb-layering; Moore and Lockwood, 1973) that is only restricted to shells (red arrows, Figure 31c). At the macroscale, there is no evidence of sulphide mineralization in the Hoogkraal Lease orbicules.

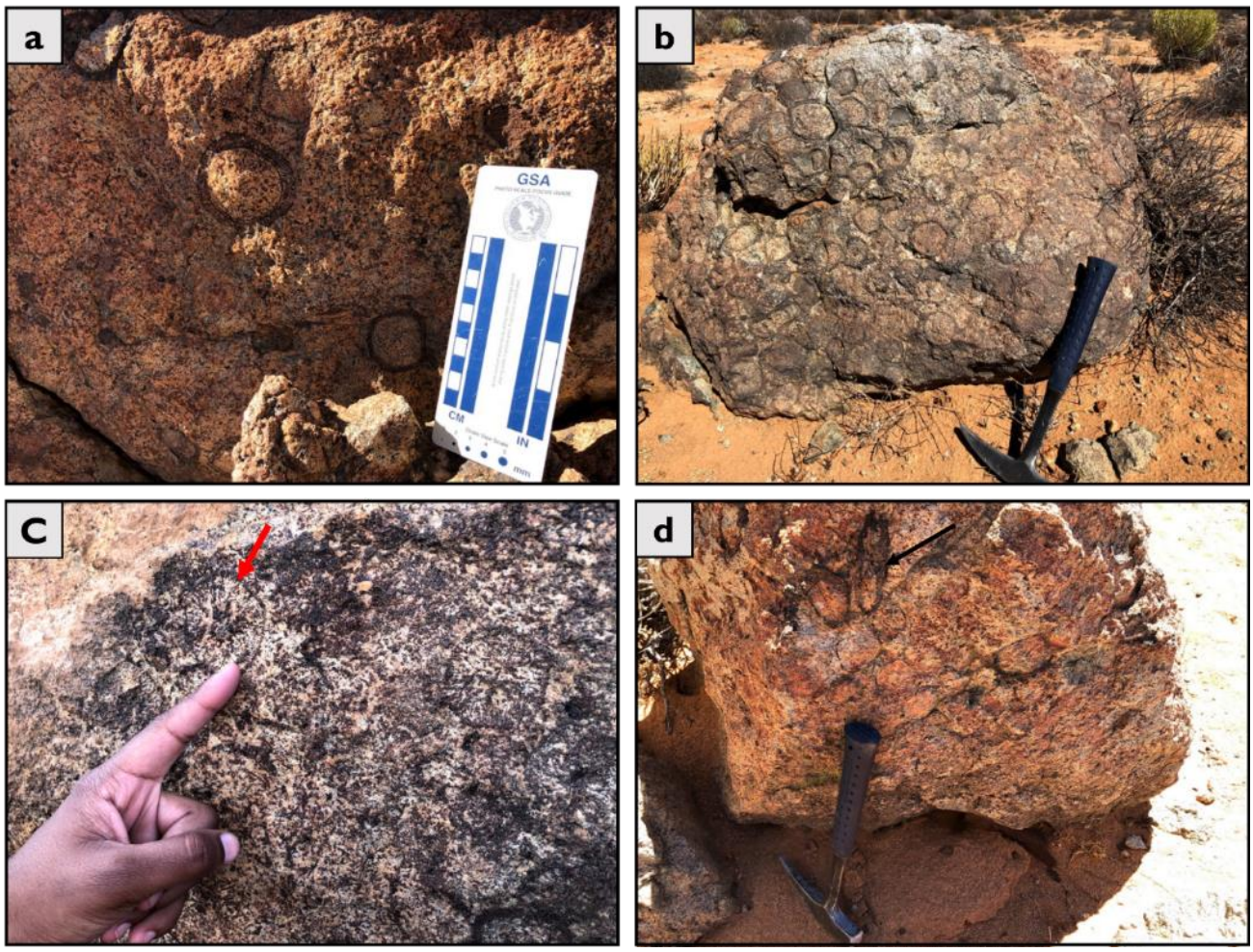


Figure 31: *Boulders from the Hoogkraal Lease orbicule outcrop: (a) A boulder showing ~ 30% orbicules to 70% host matrix relative volumes. (b) A boulder showing more orbicules to matrix relative volume. (c) Radiating orthopyroxene texture (red arrow) restricted to the orbicular shells. (d) An outcrop showing different shapes of orbicules, both elongated (black arrow) and spherical.*

5.1.3.3. The Henderson North orbicules

The Henderson North orbicular body is located approximately 5 km NE of Orbicule Koppie. It is the largest of the Koperberg Suite orbicular bodies, and it is approximately 1 km in diameter and 6 m high (Figure 32) and it intrudes the Concordia Granite.

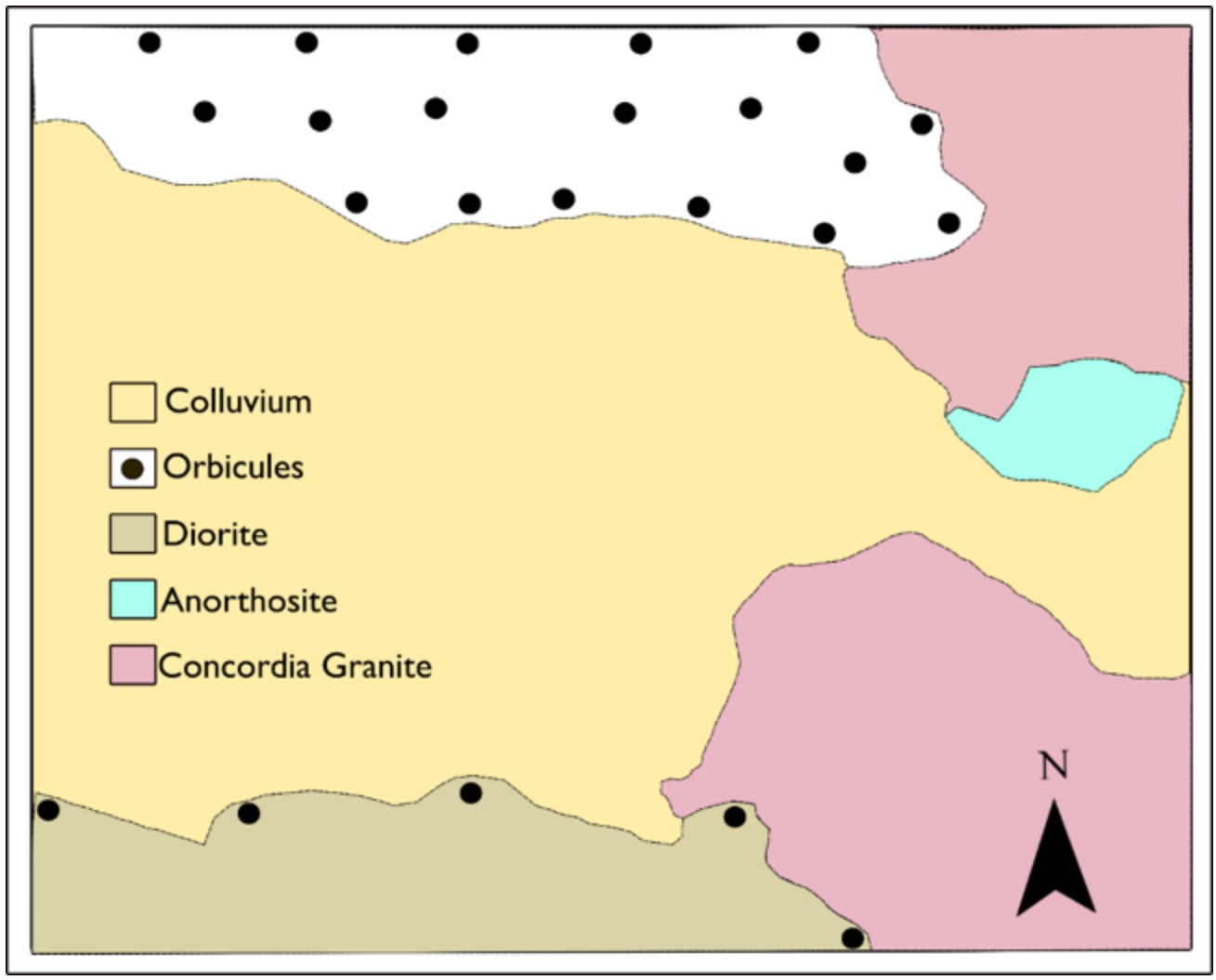


Figure 32*: Sketch map (not to scale) of the Henderson North orbicular body and the surrounding country rocks.*

Orbicules in this locality are hosted in a felsic to mafic host rock that comprises plagioclase and is pyroxene bearing. The host rock is coarse-grained (Figure 33a) and contains plagioclase grains that have a preferred E-W orientation (Figure 33b). The outcrop is 10% orbicules to 90% host matrix and the orbicules differ in shape. Some are elongated and they are trending E-W, some are spherical (Figure 33c), and they do not have a preferred orientation but are randomly oriented (Figure 33a, b).

They also differ in size ranging from 1-15 cm (Figure 33b, c). The leucocratic cores contain plagioclase, quartz, K-feldspars, orthopyroxene, magnetite, and biotite. Sharp contacts mark the transitions from core to shells. The shells are characterized by alternating mafic (dominated by biotite and magnetite with minor plagioclase and quartz) and felsic shells (dominated by plagioclase and quartz with minor mafic minerals; Figure 33c). Sharp contacts mark the transitions from shells to the matrix. The matrix and the core compositions are comparable, and the matrix is composed of plagioclase, biotite, quartz, K-feldspars, minor orthopyroxene, opaque minerals and (Figure 33c, d).

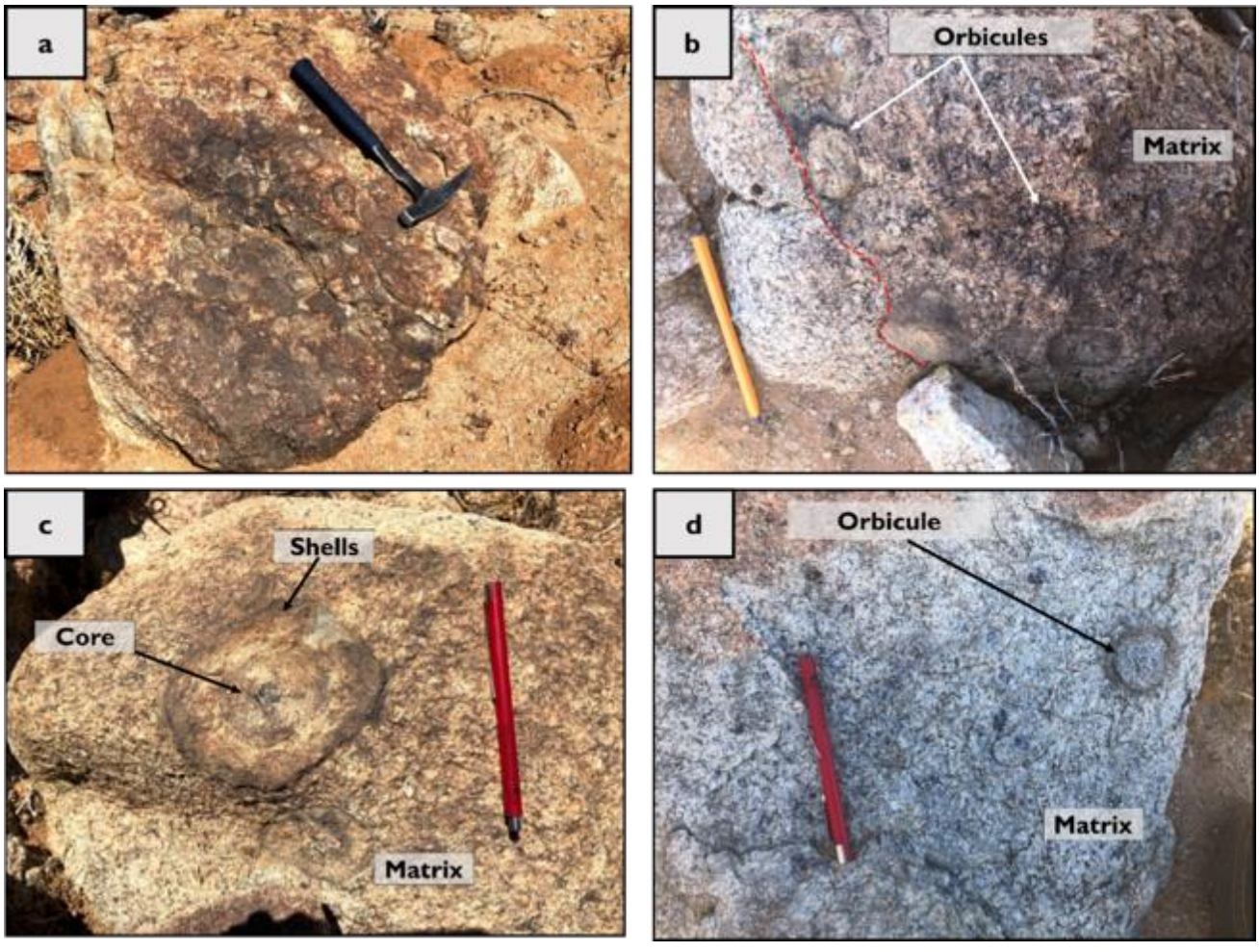


Figure 33: *Boulders from the Henderson North orbicular outcrop: (a) A boulder showing spherical orbicules hosted in a coarse-grained pyroxene-bearing diorite. (b) A more coarse-grained pyroxene-bearing diorite characterized by aligned and coarse-grained plagioclase. (c) Orbicule showing alternating mafic and felsic shells lacking the radiating texture. (d) An orbicule hosted in a felsic matrix characterized by a felsic core and mafic shells.*

5.1.3.4. The Henderson South orbicules

The Henderson South orbicular body is an approximately 150 m diameter and 5 m high body of orbicules that is approximately 4 km NE of Orbicule Koppie that intrudes the Concordia Granite (Figure 34).

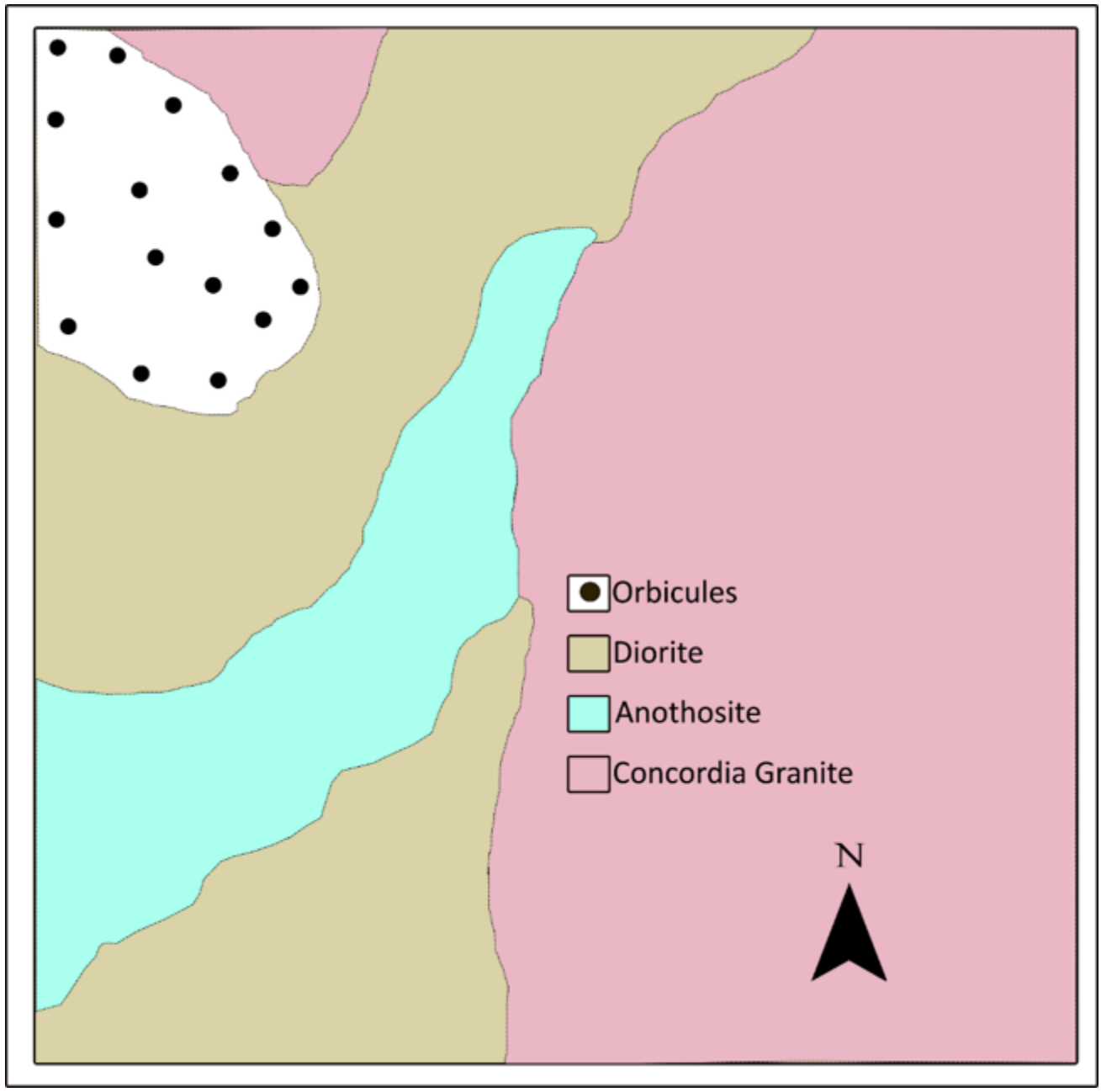


Figure 34: *Geological sketch map of the Henderson South orbicular body and surrounding regional rocks (not to scale).*

The Henderson South orbicules occur in a diorite dominated by pyroxene and the outcrop is characterized by 80% orbicules to 20% matrix or rock volume. Similar to the other orbicule localities, the Henderson South orbicules differ in shape, some are elongated (Figure 35a) and some are spherical.

Cores composed of plagioclase, quartz, biotite, minor orthopyroxene pyroxene and accessory magnetite characterize the orbicules (Figure 35d). Alternating mafic (dominated by biotite, orthopyroxene, plagioclase, and magnetite) and felsic shells (dominated by plagioclase, biotite and quartz) characterize them (Figure 35d). A radiating texture is observed in shells (black arrow; Figure 35c) where orthopyroxene grows as elongated grains from the core to shell contacts. This texture is only restricted to the shells. The matrix is comparable in composition to the cores and is composed of

plagioclase, quartz, biotite, orthopyroxene and accessory magnetite. There is no macroscopic evidence of sulphide mineralization observed in these orbicules.

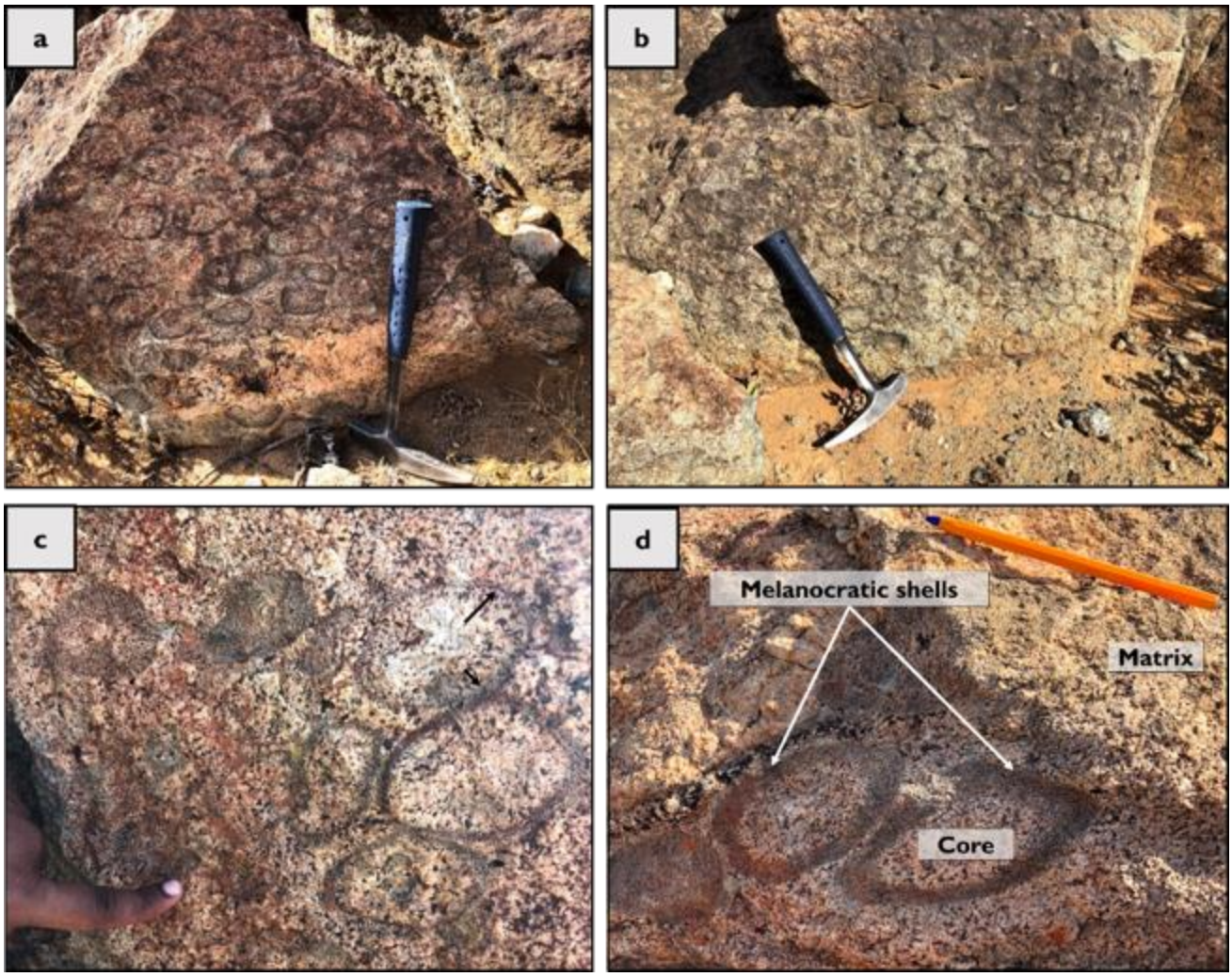


Figure 35: *Orbicules from the Henderson South orbicule outcrops: (a) Henderson South outcrop characterized by elongated orbicules. (b) Spherical orbicules in a boulder next to the Henderson South outcrop. (c) Orbicules showing radiating orthopyroxene in shells (black arrows). (d) Elongated orbicules characterized my felsic cores and matrix. Shells are more mafic and dominated by biotite and pyroxene.*

5.1.4. Summary of Field observations

The rocks that host the orbicules differ in composition from one locality to another in the Koperberg Suite orbicules. The different Koperberg Suite orbicular bodies are all in contact with anorthosites and diorites. However, the Orbicule Koppie orbicules are intrusive to the Nababeep Gneiss, whilst the Henderson North, the Henderson South, and the Hoogkraal lease orbicule outcrops intrude the Concordia Granite.

The main common feature in the Koperberg Suite orbicules is similar mineral assemblages or compositions in both the matrices and the cores. However, the matrices in the Orbicule Koppie and the Henderson North orbicules are more coarse-grained than cores. This is not the case in both the Henderson South and Hoogkraal Lease orbicules, which are characterized by medium-grained cores and matrices.

The main difference in the four different orbicule localities is in the orbicule to matrix relative volumes, more orbicules to matrix ratios characterize Orbicule Koppie and the Henderson South orbicules, and this is not the case in Hoogkraal Lease and Henderson North orbicules. Orbicules varying in size and shape characterize different orbicules from different localities.

At hand specimen scale, sharp cores to shells and shells to matrices boundaries or contacts characterize the Henderson North, Hoogkraal Lease, Orbicule Koppie and the Henderson South orbicules. However, this is not always the case in core-to-shell boundaries, e.g., the core shell boundaries are also gradational in Orbicule Koppie orbicules.

Orbicule Koppie orbicules do not exhibit alternating mafic and felsic shells, this makes them different from the other orbicule localities that exhibit alternating mafic and felsic shells. The radiating texture is observed only in the Hoogkraal Lease and the Henderson South orbicular shells. Deformed orbicules and macroscopic sulphide mineralization are only observed in Orbicule Koppie orbicules and may be observed at microscale in other localities at a later stage in the project.

5.2. Petrographic Observations

Similar to Dina's Pool orbicules, petrographic techniques together with micro-XRF were utilized in order to try to classify, compare and contrast different orbicule types and sulphide occurrences in the Koperberg Suite orbicules and the surrounding rocks. The data is presented in this section.

5.2.1. Country Rock: Nababeep Gneiss and the Concordia Granite

The Nababeep Gneiss in contact with Orbicule Koppie orbicules is composed of microcline (48%), biotite (10%), plagioclase (30%), quartz (10%), white mica (2%) and accessory magnetite. Microcline occurs as subhedral (0.3-6 mm) grains adjacent to quartz, biotite, and plagioclase (Figure 36a, b). Biotite occurs as subhedral and elongated (0.1-0.5 mm) grains adjacent to microcline and white mica, and as poikilitic inclusions in larger grains of microcline.

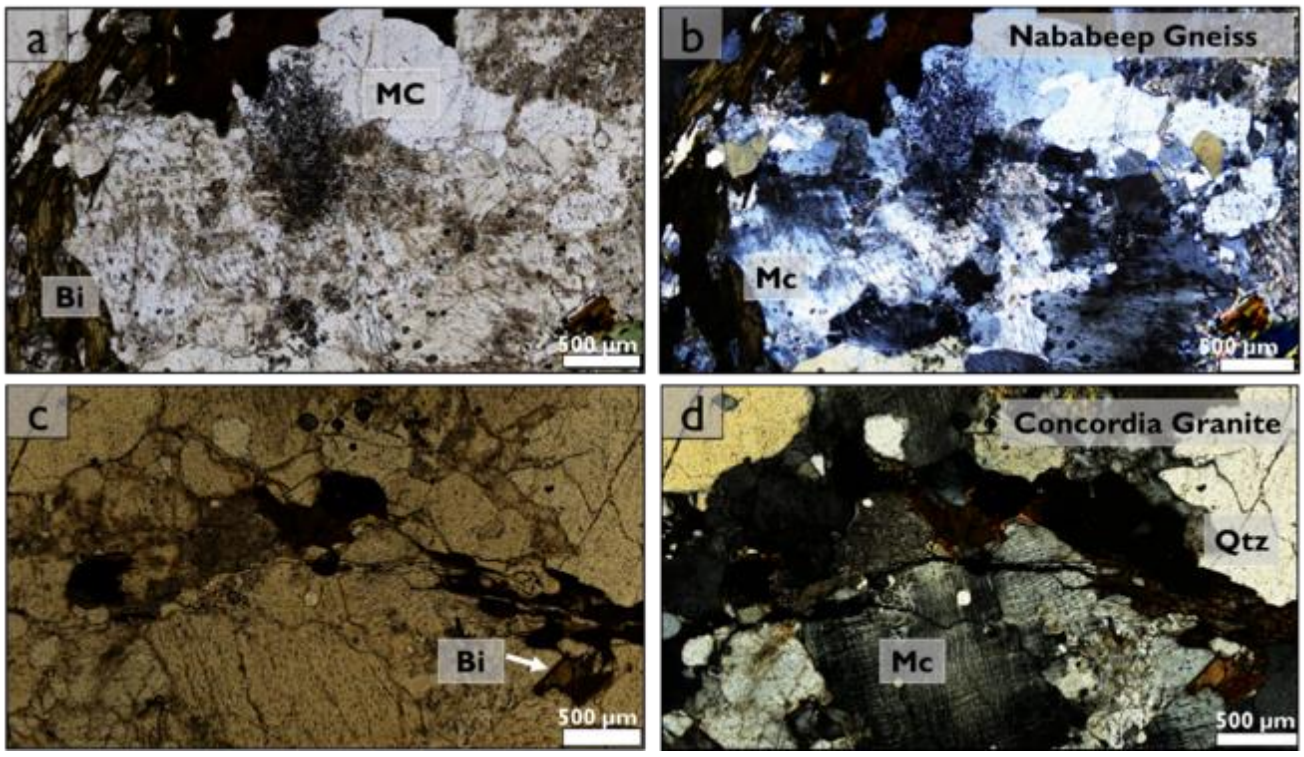


Figure 36: *Photomicrographs of samples from Orbicule Koppie and Hoogkraal Lease: (a, b) Photomicrographs of the Nababeep Gneiss showing microcline that exhibits exsolution texture and poikilitic inclusions of magnetite. (c, d) Photomicrographs of the Concordia Granite from Hoogkraal Lease showing subhedral grains of quartz occurring adjacent to biotite and microcline. Microcline contains poikilitic inclusions of biotite, opaque minerals and quartz.*

Quartz occurs as subhedral (0.1- 2 mm) grains adjacent to microcline, biotite, and plagioclase. Locally, quartz contains inclusions of biotite and magnetite. Plagioclase occurs as subhedral grains (0.3-1 mm) that are altered to sericite. Locally, plagioclase contains small poikilitic inclusions of biotite and quartz.

The Concordia Granite in contact with the Hoogkraal Lease, Henderson North and Henderson South orbicules comprises quartz, microcline, plagioclase, and biotite. Quartz (60%) occurs as rounded and subhedral grains (0.1-0.5 mm). Microcline (0.2-1 cm) is the most predominant K-feldspar in the granite. Some of the large microcline grains contain poikilitic inclusions of quartz (Figure 36c, d). Biotite occurs as randomly distributed anhedral grains (0.1- 0.3 mm) that are adjacent to microcline and quartz. Plagioclase is the least common phase and occurs as subhedral grains (0.1-0.5 mm) that are adjacent to microcline and quartz. Plagioclase also occurs as inclusions in microcline. Accessory

minerals include magnetite and white mica. There is no evidence of sulphide mineralization in either the Nababeep Gneiss or the Concordia Granite. Both the gneiss and the granite contain disseminated magnetite grains. In the Concordia Granite (Figure 37b), magnetite occurs as disseminated (0.1-2 mm) grains in feldspars. In the Nababeep Gneiss, magnetite occurs as anhedral (0.1-0.5 mm) grains in feldspars (Figure 37a).

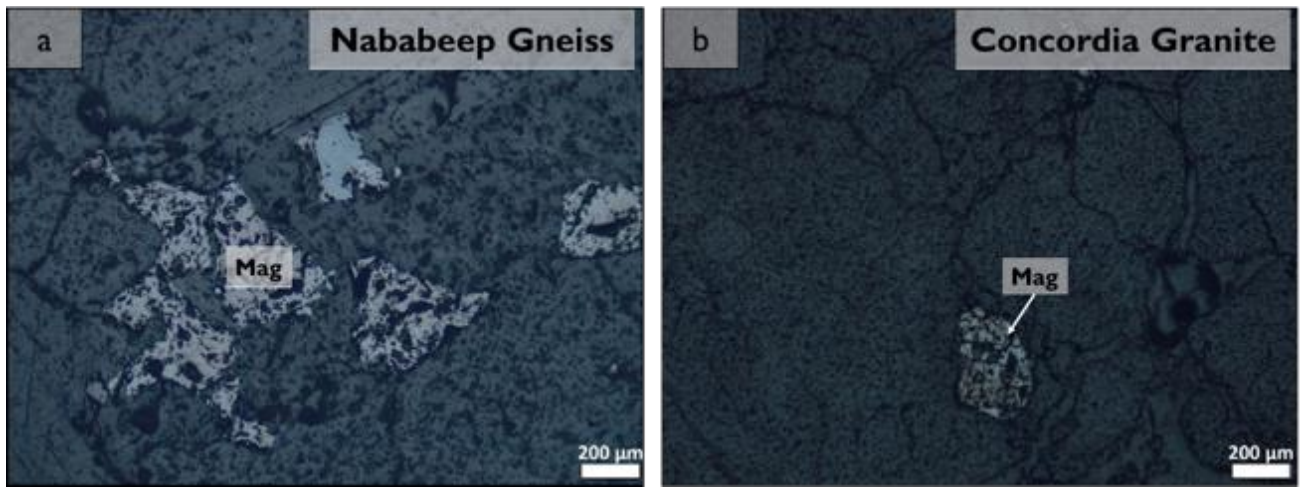


Figure 37*: Photomicrographs showing oxides in the Nababeep Gneiss and the Concordia Granite from the Koperberg Suite. (a) Anhedral to subhedral magnetite grains in the Nababeep Gneiss from Orbicule Koppie. (b) Smaller and disseminated magnetite grains in the Hoogkraal Lease Concordia Granite.*

5.2.2. The Koperberg Suite anorthosite

Anorthosite in Hoogkraal Lease is highly altered and contains plagioclase and hypersthene (5%) as the predominant phases (Figure 38e, f). Plagioclase occurs as subhedral (1-6 mm) grains that are altered to sericite locally (Figure 38e). Locally, some plagioclase grains exhibit discontinuous twinning. Hypersthene occurs as subhedral (0.1-2 mm) grains that occur as small poikilitic inclusions in plagioclase. Quartz, biotite and microcline occur as accessory phases. Similar to the Hoogkraal Lease anorthosite, anorthosite from Henderson North is composed of plagioclase (90%) with minor apatite, quartz, biotite and chlorite as accessory phases. Plagioclase occurs as (0.1-6 mm) grains that exhibit discontinuous twinning and contain poikilitic inclusions of quartz, apatite, and magnetite (Figure 38g, h). Plagioclase is highly altered to sericite, and locally it contains smaller muscovite and plagioclase inclusions. Anorthosite from Henderson South is composed of plagioclase (90%) and biotite (5%) as the predominant phases. Plagioclase occurs as anhedral to subhedral grains (0.1-8 mm) that locally host poikilitic inclusions of biotite and magnetite. Accessory phases include epidote (Figure 38a), chlorite and muscovite. The plagioclase grains are altered to sericite (Figure 38a, b) and locally, they are highly fractured and the fractures are filled in by biotite, epidote and minor chlorite (Figure 38a, b). Biotite occurs as randomly distributed elongate and needle-shaped and anhedral grains (0.1-0.5 mm) which are locally altered to chlorite. Quartz, muscovite (Figure 38a, b) and microcline occur as accessory phases. Similar to other localities, anorthosite from Orbicule Koppie comprises mainly plagioclase, biotite, accessory quartz and microcline (Figure 38c, d). Plagioclase occurs as subhedral and elongated (0.1- 7mm) grains adjacent to biotite and quartz.

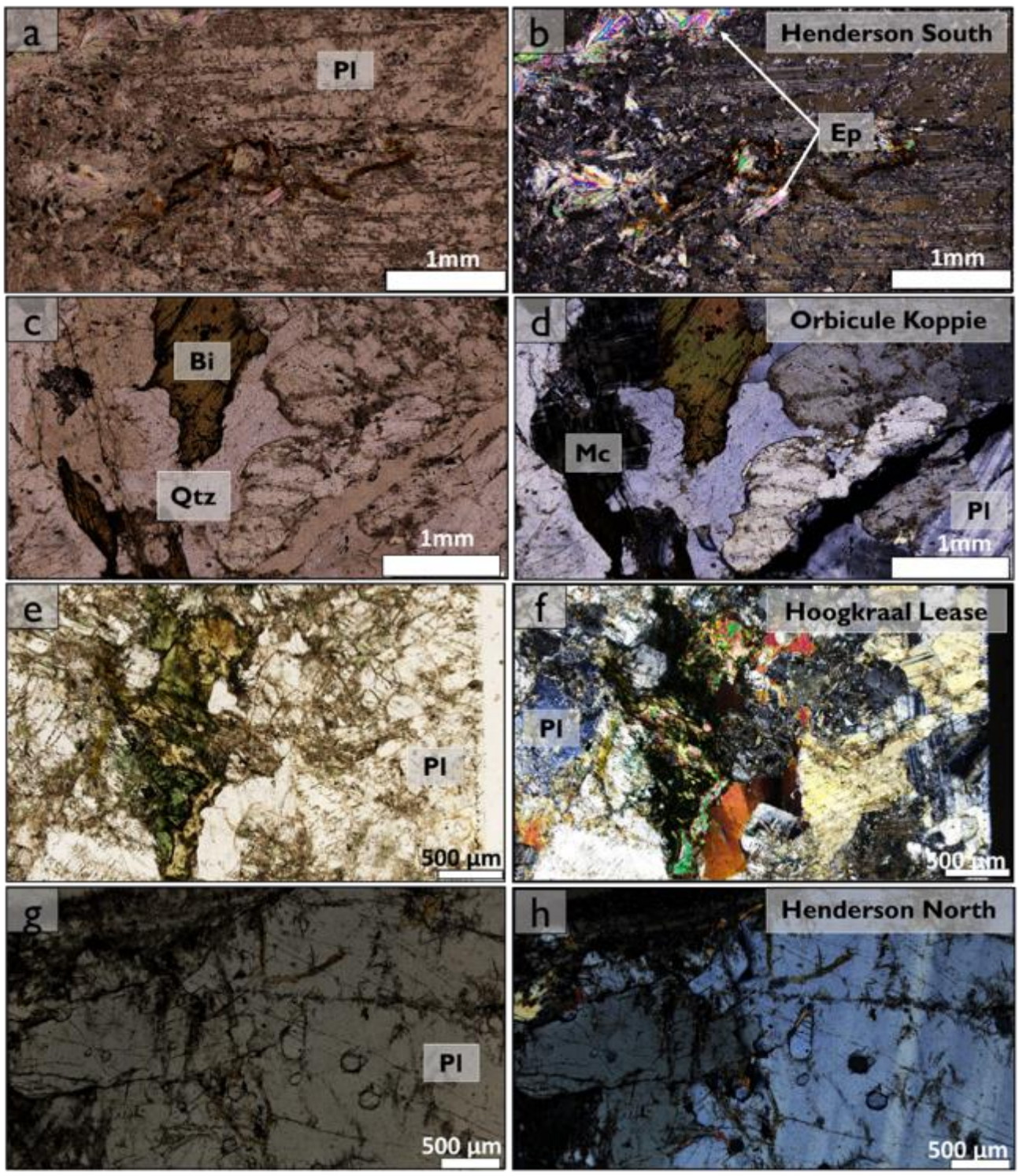


Figure 38:*Photomicrographs of anorthosites in contact with the Koperberg Suite orbicules: (a, b) Anorthosite from Henderson South comprising grains of plagioclase that are altered to sericite and comprising poikilitic inclusions of biotite. Microcline and plagioclase are enclosed by interstitial quartz that contains very small inclusions of magnetite. (c, d) Anorthosite from Orbicule Koppie containing grains of microcline, chlorite and plagioclase surrounded by interstitial quartz. Microcline locally exhibits exsolution textures and contains inclusions of magnetite. (e, f) Anorthosite from Hoogkraal Lease comprising plagioclase that exhibits discontinuous twinning and locally altered to sericite. Chloritisation of biotite is observed. (g, h) Anorthosite from Henderson North comprising inclusions of rounded quartz grains in plagioclase. Locally, plagioclase is altered to clay.*

Locally, plagioclase is characterized by discontinuous deformation twinning. Biotite and minor muscovite occur as inclusions in some of the plagioclase grains. Locally, plagioclase is altered to sericite, which also contains poikilitic biotite inclusions. Biotite occurs as disseminated anhedral to subhedral elongate (0.1-0.2 mm) grains that occur adjacent to plagioclase, accessory muscovite, and

accessory quartz. Locally, biotite is altered to chlorite and has small (0.2-0.5 mm) quartz inclusions. Accessory minerals include magnetite, quartz, and muscovite. The anorthosite lenses contain sulphide mineralization (<2%) associated mostly with the mafic minerals. The mineralization varies in modal abundances from one locality to another. No sulphide mineralization is observed in the anorthosite in contact with Henderson South (Figure 39a) and Hoogkraal Lease (Figure 39c) orbicule outcrops, except for the disseminated and randomly distributed magnetite. Conversely, small concentrations of chalcopyrite and magnetite are observed in anorthosite in contact with Orbicule Koppie (Figure 39b) and Henderson North orbicules (Figure 39d).

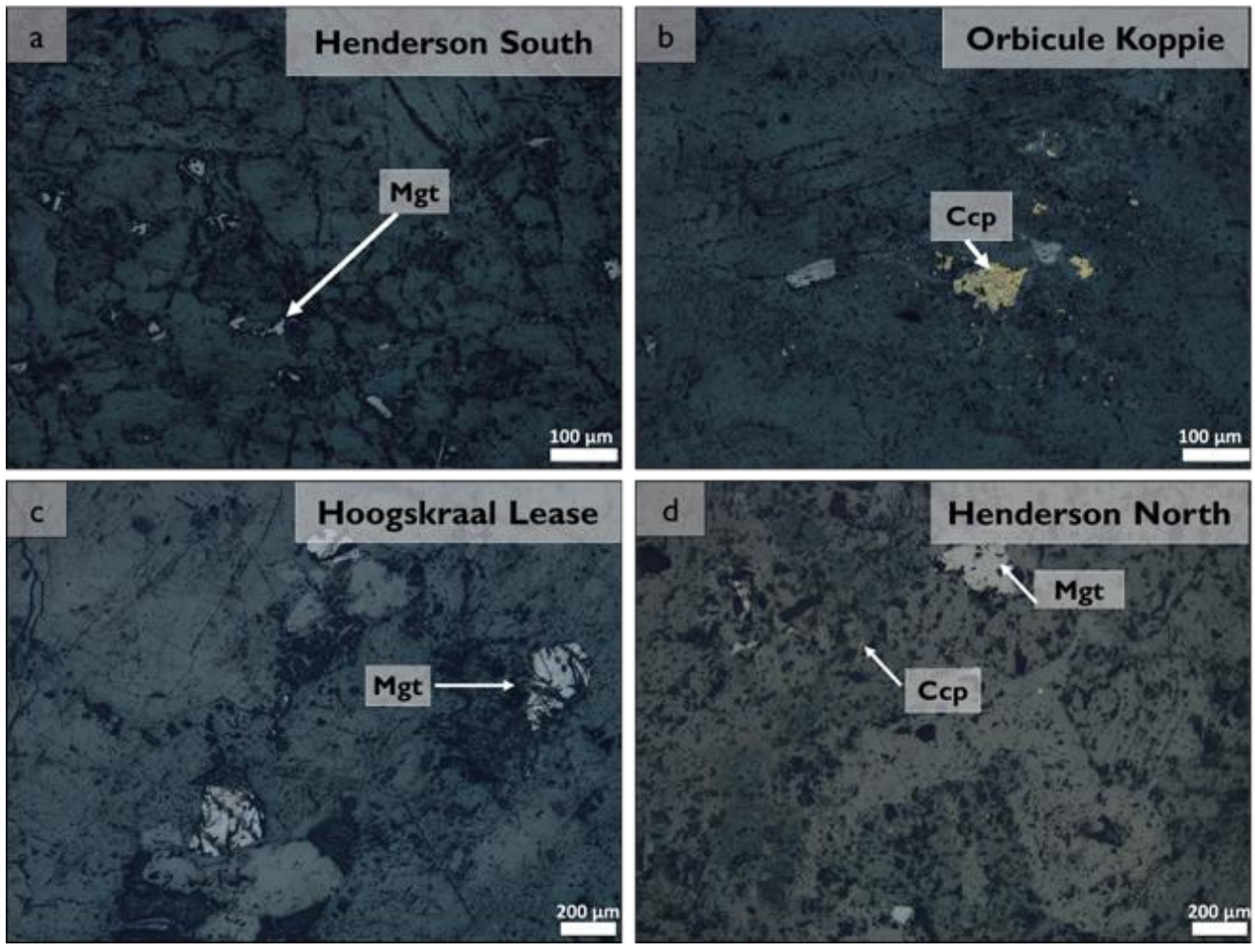


Figure 39: *Photomicrographs showing sulphides and oxides in the Koperberg Suite anorthosites: (a) disseminated magnetite grains in anorthosite from the Henderson South adjacent to each other in plagioclase. (b) Disseminated chalcopyrite occurring adjacent to smaller magnetite grains in Orbicule Koppie anorthosite. (c) Larger magnetite grains from Hoogkraal Lease anorthosite. (d) Magnetite grains adjacent to smaller (<< 0.1 mm) grains of disseminated magnetite in anorthosite from Henderson North.*

In Henderson North, chalcopyrite occurs as small (< 0.1 mm) grains that are locally clustered and adjacent to magnetite (Figure 39d). Magnetite (0.1-0.2 mm) occur as disseminated and subhedral grains next to chalcopyrite (Figure 39d). Similar to the Henderson North anorthosite, the Orbicule Koppie anorthosite comprises chalcopyrite and magnetite. Chalcopyrite occurs as very small (0.1-0.4 mm) grains that are disseminated in plagioclase (Figure 39b). Magnetite occurs as disseminated (0.1-0.4 mm) grains. Locally, magnetite replaces chalcopyrite (Figure 39b).

5.2.3. The Koperberg Suite diorite

Diorite in Hoogkraal Lease is composed mainly of plagioclase (70%) and equal amounts of biotite (10%) and hypersthene (10%), with accessory quartz and magnetite. Plagioclase occurs as anhedral to subhedral grains (1-5 mm). Some plagioclase grains (Figure 40d) comprise discontinuous deformation twins. Locally, plagioclase is altered to sericite.

Biotite is the second predominant mineral phase and occurs as anhedral to subhedral elongate grains, which locally occurs as inclusions in plagioclase. It also occurs as an interstitial phase surrounding plagioclase (Figure 40c, d). Hypersthene in plagioclase occurs as subhedral (0.5-1 mm) poikilitic inclusion with no well-defined cleavage. Quartz occurs as subhedral and rounded grains (0.1-1 mm) that are adjacent to plagioclase and biotite. Locally, quartz occurs as small, rounded inclusions in plagioclase. Accessories include magnetite, which mainly occurs as inclusions in plagioclase.

Diorite in Orbicule Koppie contains plagioclase (70%), biotite (10%), magnetite (5%) and quartz (5%). Plagioclase occurs as anhedral to subhedral grains (0.1 mm -1 cm) that are altered to sericite in places. Locally, it contains inclusions of biotite and other smaller plagioclase grains (Figure 40a). Some plagioclase grains exhibit exsolution textures (Figure 41b). These grains also contain biotite inclusions (Figure 40). Biotite occurs as elongate grains (0.1-1mm) adjacent to plagioclase and as inclusions in plagioclase. Accessory minerals include microcline.

Diorite from Henderson North contains plagioclase (70%), hypersthene (10%; Figure 40e, f), biotite (10%), magnetite (3%) and other accessory phases. Plagioclase is anhedral (0.1-2 mm) and contains magnetite and quartz inclusions. Locally, plagioclase is altered to sericite. Hypersthene occurs as randomly distributed anhedral gains (0.1-1 mm) adjacent to plagioclase (Figure 40e, f). Accessory minerals include microcline and quartz.

Similar to the Hoogkraal Lease diorite, diorite in Henderson South comprises mainly plagioclase (85%) and biotite (10%) with minor quartz (5%) and magnetite (< 1%). Unaltered plagioclase occurs as anhedral to subhedral grains (0.1-2 mm) with some grains containing biotite and magnetite inclusions. In places, plagioclase is altered to sericite. Adjacent to plagioclase is biotite that occurs as randomly distributed anhedral grains (0.1-0.5 mm). In places, biotite is altered to chlorite (Figure 40g, h). Accessory minerals include hypersthene and magnetite.

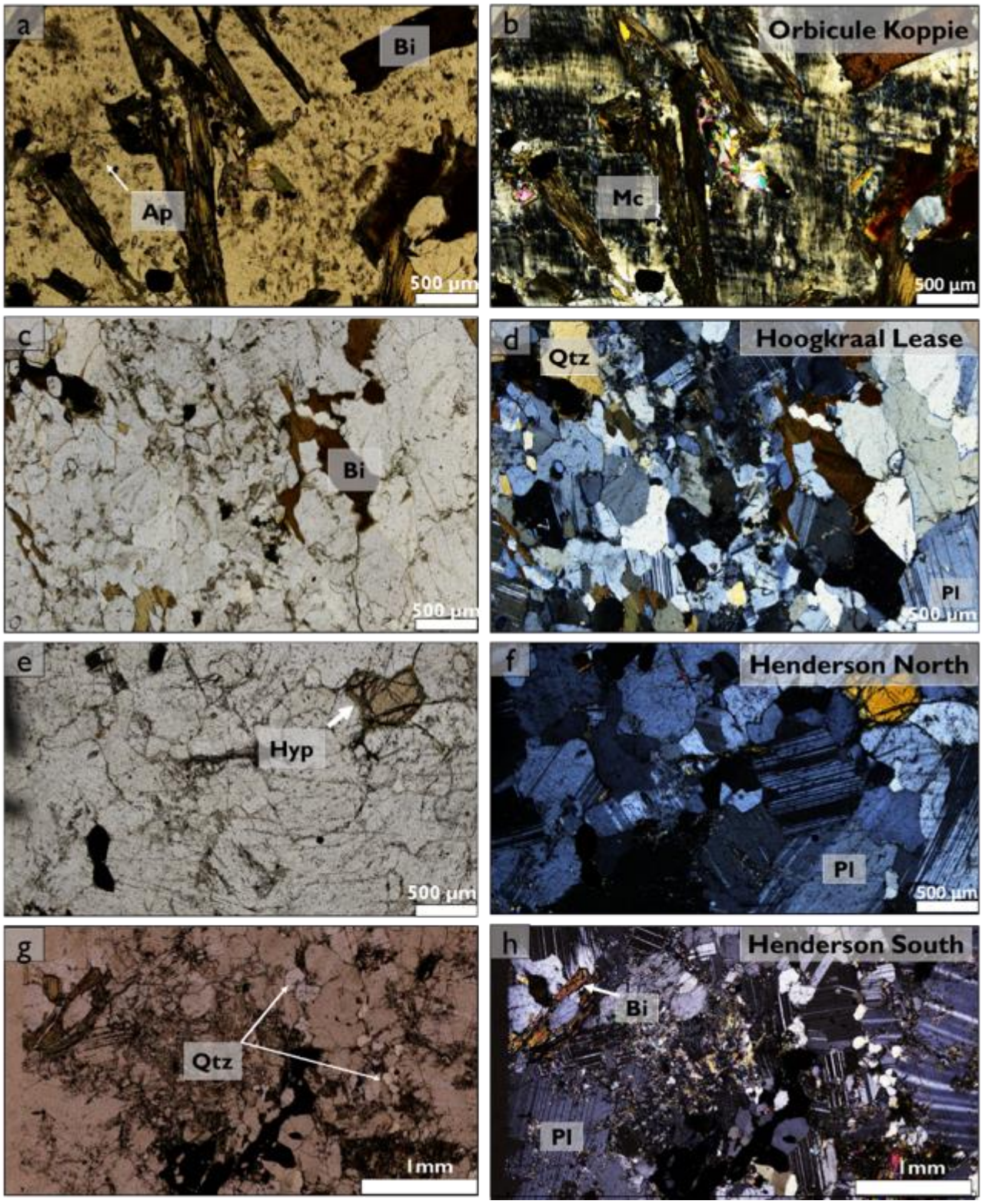


Figure 40:*Photomicrographs of diorites from Koperberg Suite illustrating quantitative textural analysis: (a, b) Diorite from Orbicule Koppie composed of large microcline grains that contain poikilitic inclusions of anhedral magnetite and elongated (0.1-0.4 mm) grains of biotite. Microcline displays exsolution textures and it is altered to white mica. (c, d) Diorite from Hoogkraal Lease comprising plagioclase, quartz and biotite grains that occur adjacent to each other. Plagioclase occurs as smaller grains that occur adjacent to quartz and exhibit discontinuous twinning. Locally, plagioclase is surrounded by interstitial biotite. (e, f) Diorite from Henderson North containing small and disseminated hypersthene grains adjacent to plagioclase. Plagioclase locally exhibits discontinuous twinning and occurs adjacent to small biotite grains. (g, h) Diorite from Henderson South containing both unaltered and altered grains of plagioclase (sericite) that contain poikilitic inclusions of quartz and magnetite. Quartz occurs as anhedral grains that occur adjacent to biotite and plagioclase. Locally, quartz occurs as inclusions in biotite.*

Associated with both the mafic and felsic mineral phases are chalcopyrite (<<<1%) and magnetite which vary in modal abundance from one locality to another. The Henderson South diorite contains small (<< 0.1 mm) and disseminated grains of chalcopyrite that occur adjacent to small (0.1-0.5 mm) grains of disseminated magnetite (Figure 41a). Diorite from Orbicule Koppie is similar to diorite rom Henderson South and contains small (<< 0.01 mm) grains of chalcopyrite that are disseminated and anhedral (Figure 41b). Chalcopyrite occurs adjacent to randomly distributed magnetite grains (0.1-0.5 mm; Figure 41b).

Diorites from Henderson North and Hoogkraal Lease both contain chalcopyrite and magnetite. Diorite from Hoogkraal Lease contains very small (<< 0.1 mm) grains of chalcopyrite that occur as disseminated and anhedral grains that occur adjacent to magnetite. Magnetite occurs as randomly distributed (0.1-0.5 mm) grains (Figure 41c).

Similar to Hoogkraal Lease, diorite from Henderson North contains small (0.1-0.2 mm) and disseminated grains of chalcopyrite in plagioclase. These occur adjacent to the disseminated magnetite grains (0.1-0.4 mm; Figure 41d).

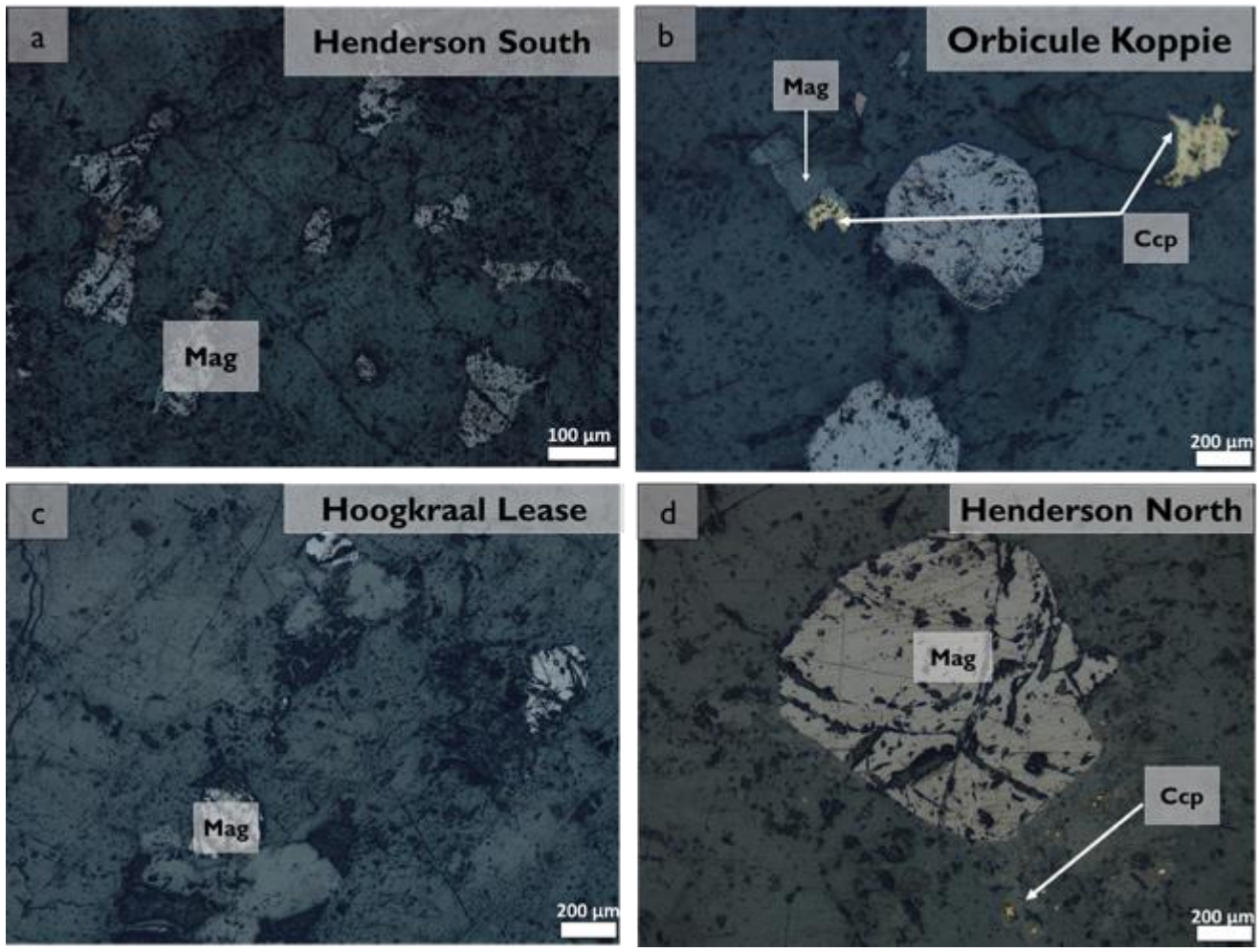


Figure 41: *Photomicrographs showing the sulphide mineralization and magnetite in diorites from the Koperberg Suite: (a) Disseminated and anhedral to subhedral grains of magnetite in Henderson South diorite. (b) Subhedral grains of magnetite in the Orbicule Koppie diorite adjacent to smaller and disseminated grains of chalcopyrite. Locally, magnetite replaces chalcopyrite. (c) Small and anhedral magnetite in Hoogkraal Lease diorite concentrated in plagioclase. (d) Large magnetite grains adjacent to small and locally concentrated chalcopyrite grains in the Henderson North diorite.*

5.2.4. Orbicules

5.2.4.1. Orbicule Koppie

A cut slab from sample SD-10-6A (Figure 42) from Orbicule Koppie was scanned at high resolution using Micro-XRF to produce element maps showing element distributions.

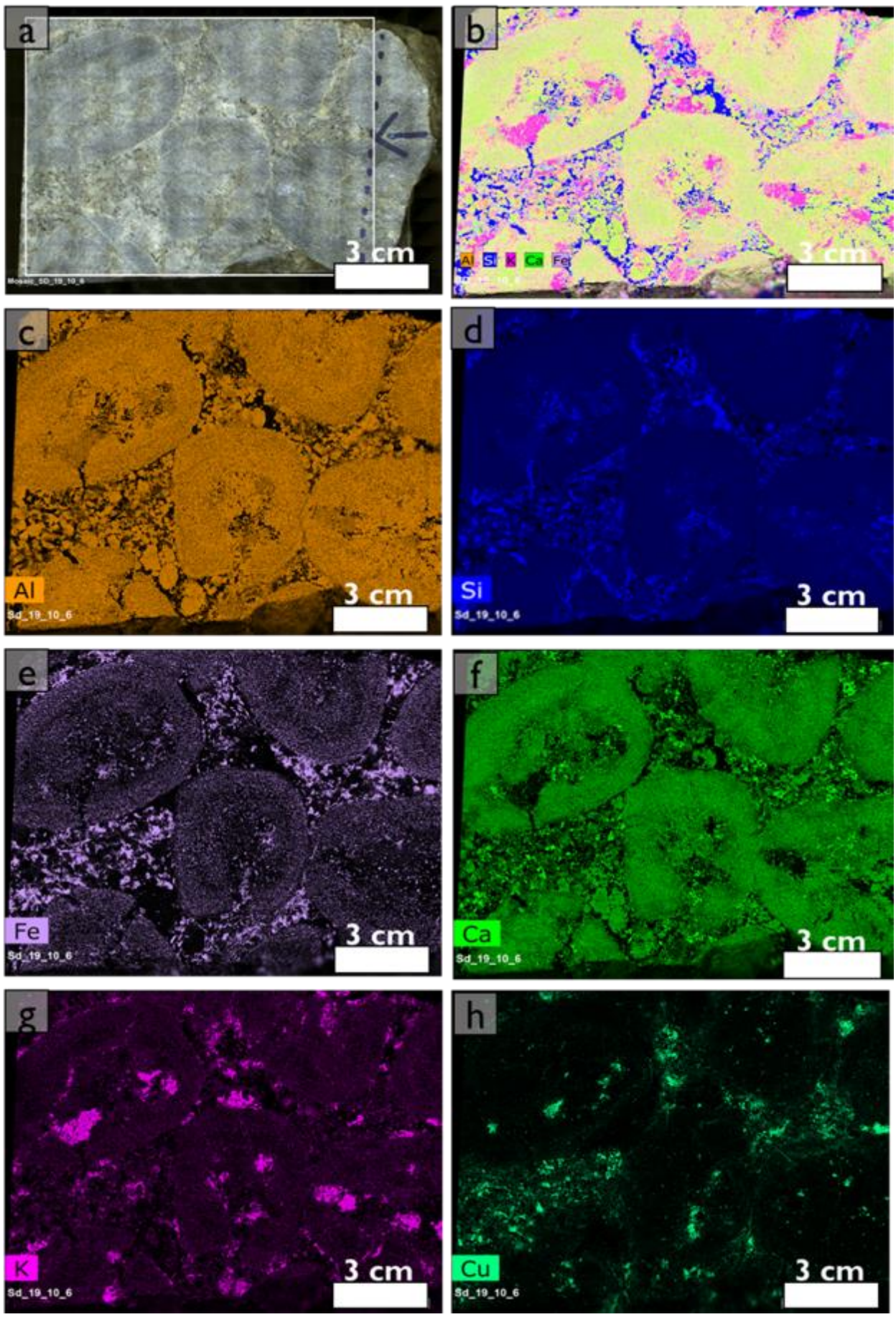


Figure 42: *Element maps of Orbicule Koppie sample SD-10-6C: (a) A mosaic showing the mapped area in a white rectangle. (b) A composite of selected element showing elements detected via the normal map spectrum showing the distribution of Al (orange), Ca (light green), K (pink), Si (blue) and*

Figure 42 continued*: Fe (purple) in the sample. (c) Individual element map showing a uniform distribution of Al throughout the sample. (d) Element map showing the highest distributions and intensities of Si in the cores and the matrix. (e) Element map showing the highest distribution and intensity of Fe in shells, matrix and some parts of cores. (f) Individual element map showing the distribution of Ca in different parts of the orbicules. (g) Element map showing the highest distribution and intensities of K in the matrix and some parts of the cores. (h) Element map showing the distribution of Cu in different parts of the orbicules. Cu is highly concentrated and yields high intensities in the matrix.*

Element maps show a uniform distribution of Al and Ca in the shells and cores (Figure 42c, f). However, these elements are less concentrated in some places in the matrix. In some parts of the matrix, Ca has high intensities (Figure 42f). Silicon yields high intensities (corresponding to high modal abundances of quartz), and it is distributed throughout the cores and the matrix (Figure 42d). Conversely, the shells are less siliceous (Figure 42d). Similar to Si, K yields high intensities and concentrations in the cores and the matrix, indicating the presence of microcline (Figure 42g). Felsic shells lack K (Figure 42g). The matrix has high Fe (corresponding to high modal abundances of biotite) than the shells and the cores (Figure 42g). The distribution of Cu is low in the cores and the shells, and the highest intensities and distributions are observed in the matrix (Figure 42h).

At the microscale, fine-grained cores containing by microcline, plagioclase, quartz, biotite, chlorite and magnetite (Figure 43) characterize the Orbicule Koppie orbicules.

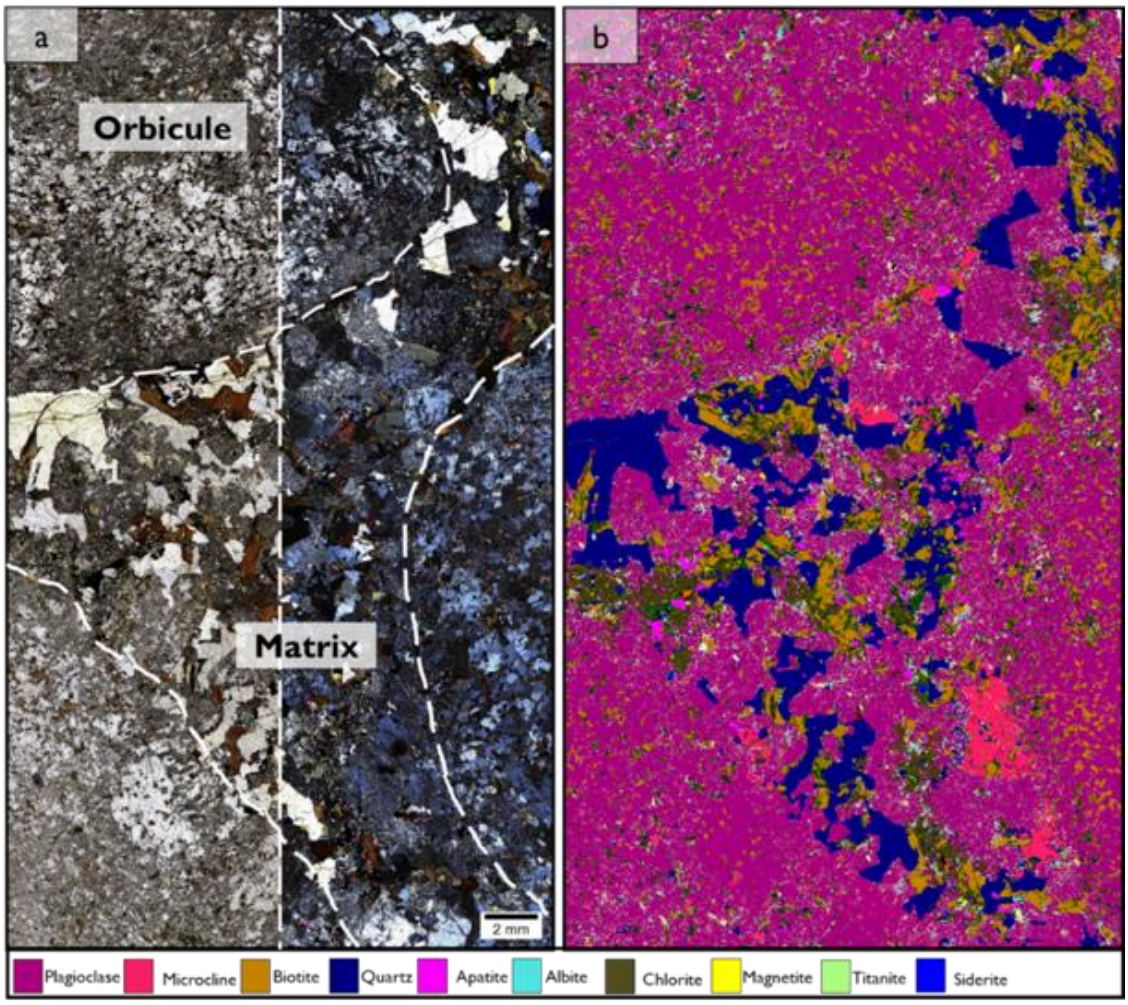


Figure 43: *Full thin section photomicrographs of Orbicule Koppie orbicule sample SD-10-6A and corresponding TIMA image: (a) Plane–polarized (left) and cross-polarized light (right) full thin section images of sample SD-10-6A.*

Figure 43 continued: *(b) TIMA image of sample SD-10-6A showing medium-grained cores comprising plagioclase, K-feldspars, quartz, chlorite and albite; fine-grained felsic shells composed of plagioclases, biotite and chlorite and the pegmatitic matrix dominated by plagioclase, microcline, biotite, apatite and quartz.*

The orbicules do not exhibit distinct shells. The core-to-shell boundaries are gradational and sharp contacts are observed between cores and the matrix (Figure 43).

- **Cores**

Fine- to coarse-grained and highly altered cores (Figure 44) characterize the Orbicule Koppie orbicules. The cores are composed of plagioclase (56%), microcline (20%), quartz (12%) muscovite (3%), biotite (3%), and other accessory phases (Figure 44).

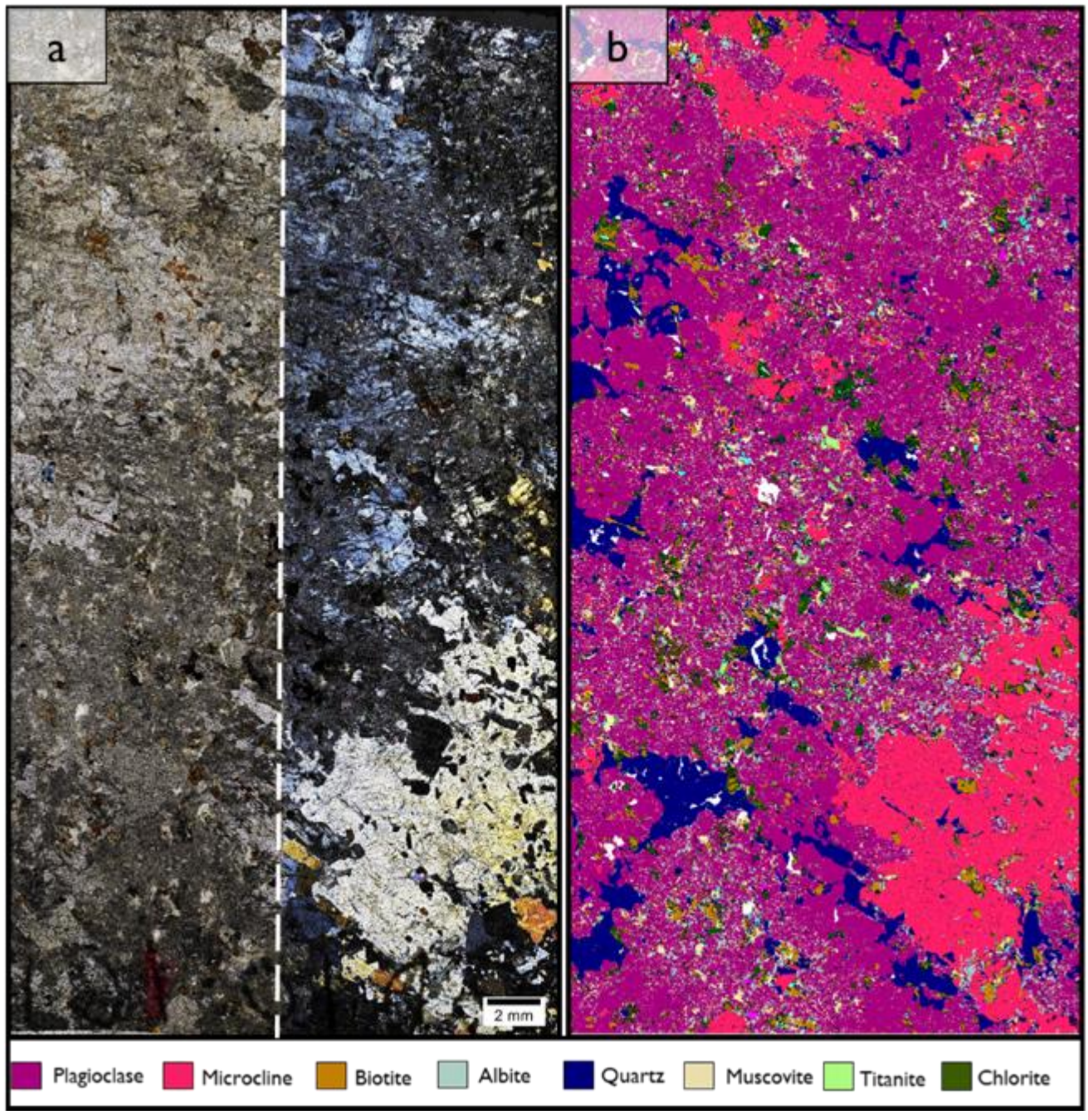


Figure 44: *Full thin section photomicrographs of Orbicule Koppie orbicular core and corresponding TIMA image: (a) Plane–polarized (left) and cross-polarized light (right) full thin section images of sample SD-10-6B. (b) TIMA image of sample SD-10-6B characterized by fine to medium-grained core predominated by plagioclase, quartz, microcline, chlorite and titanite.*

Plagioclase occurs as large (0.1-7 mm) grains adjacent to quartz, microcline, and orthoclase (Figure 45a, b). It is altered to sericite and contains inclusions of smaller biotite and apatite grains (Figure 45c, d). Adjacent to plagioclase, are large microcline grains exhibiting exsolution textures (Figure 45g, h) and containing poikilitic inclusions of biotite, magnetite, apatite, and smaller plagioclase grains.

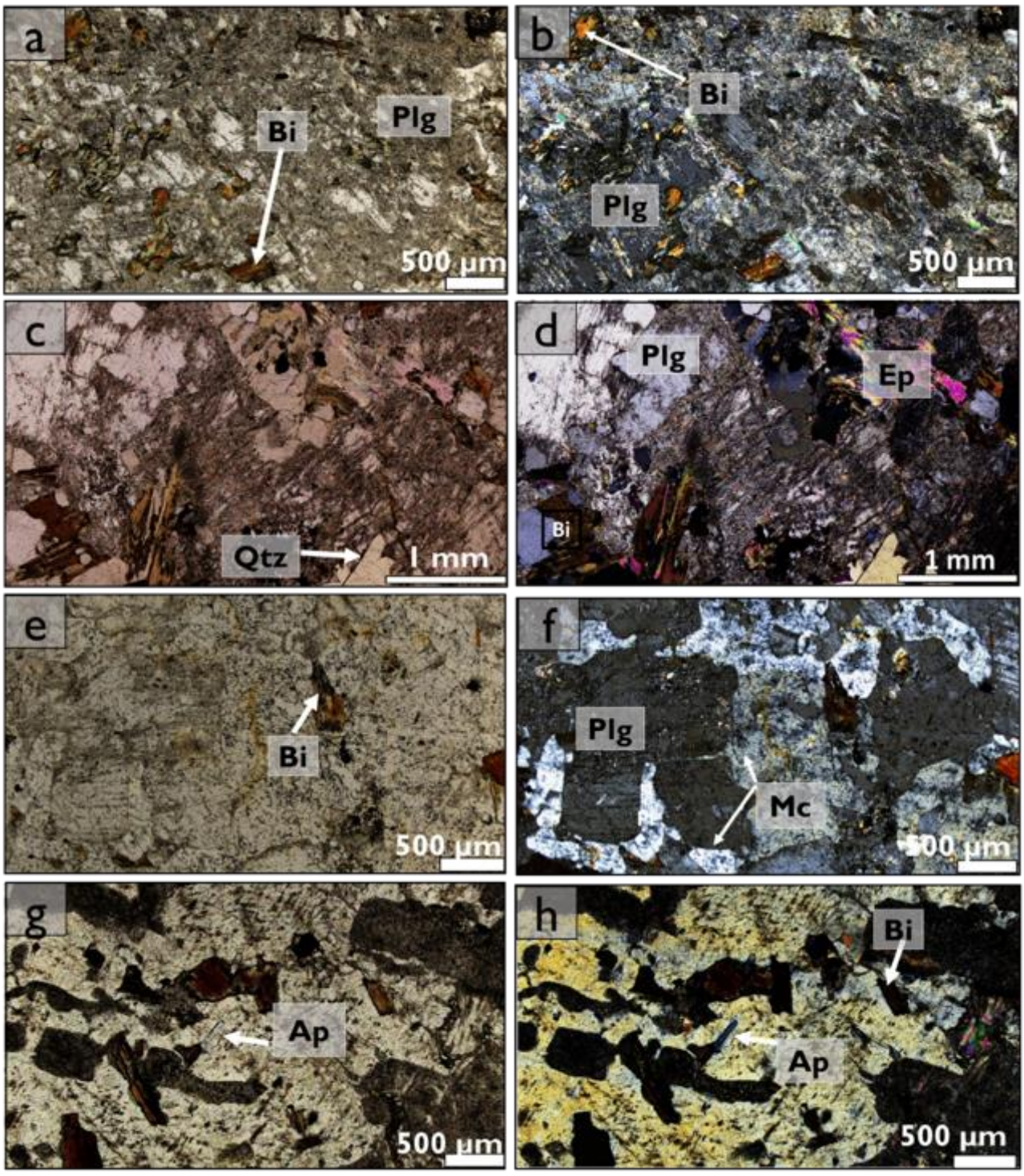


Figure 45: *Photomicrographs showing mineral phases and textures in orbicular cores from Orbicule Koppie: (a, b) Altered plagioclase grains (sericite) containing small inclusions of anhedral biotite and muscovite. (c, d) Small subhedral quartz grains that occur as inclusions in sericite. Quartz also occurs adjacent to anhedral biotite and epidote inclusions. (e, f) Subhedral plagioclase grains containing magnetite inclusions enclosed in interstitial microcline. (g, h) Large microcline grain exhibiting exsolution textures and containing small inclusions of euhedral apatite and anhedral to subhedral grains of biotite.*

Biotite occurs as disseminated grains that occur mostly as poikilitic inclusions in altered plagioclase and microcline (Figure 45g, h). In places, biotite occurs as anhedral (0.1-0.2 mm) grains adjacent to

muscovite, epidote and apatite (Figure 45g, h). Quartz occurs as intergrowths in plagioclase (forming a myrmekitic texture). It also occurs as small and subhedral (0.1 mm) inclusions in microcline and plagioclase. Locally, quartz occurs adjacent to smaller biotite and muscovite grains (Figure 45c, d). Associated with the small, needle-shaped muscovite grains is epidote (Figure 45c, d) occurring as smaller (< 0.1 mm) grains adjacent to muscovite and biotite (Figure 45d). Locally, it occurs as small inclusions in altered microcline. Orthoclase and microcline (Figure 45, h) are the predominant K-feldspars in the cores.

Orthoclase occurs as elongated (0.1 mm) grains that exhibit simple twinning. Locally, orthoclase contains small inclusions of anhedral biotite. Alteration of microcline and orthoclase to clay is observed in places. Microcline exhibit exsolution textures (Figure 45g, h) where plagioclase grows as lamellae (perthite) and contains inclusions of biotite, epidote and apatite (Figure 45g, h). Locally, microcline occurs as an interstitial phase, where it surrounds larger and euhedral grains of plagioclase (Figure 45f).

Apatite occurs as one of the least predominant phases in the orbicular cores. It mostly occurs as elongated and subhedral (< 0.1 mm) inclusions in microcline and plagioclase (Figure 45g, h). It also occurs in close association with biotite and muscovite. Muscovite occurs as an accessory phase. It occurs as needle-shaped grains that occur in close association with biotite and as inclusions in plagioclase and microcline. There is evidence of small (<< 0.1%) and disseminated subhedral chalcopyrite grains (Figure 46). They occur mostly in biotite and plagioclase grains as small grains that are adjacent to smaller and disseminated magnetite.

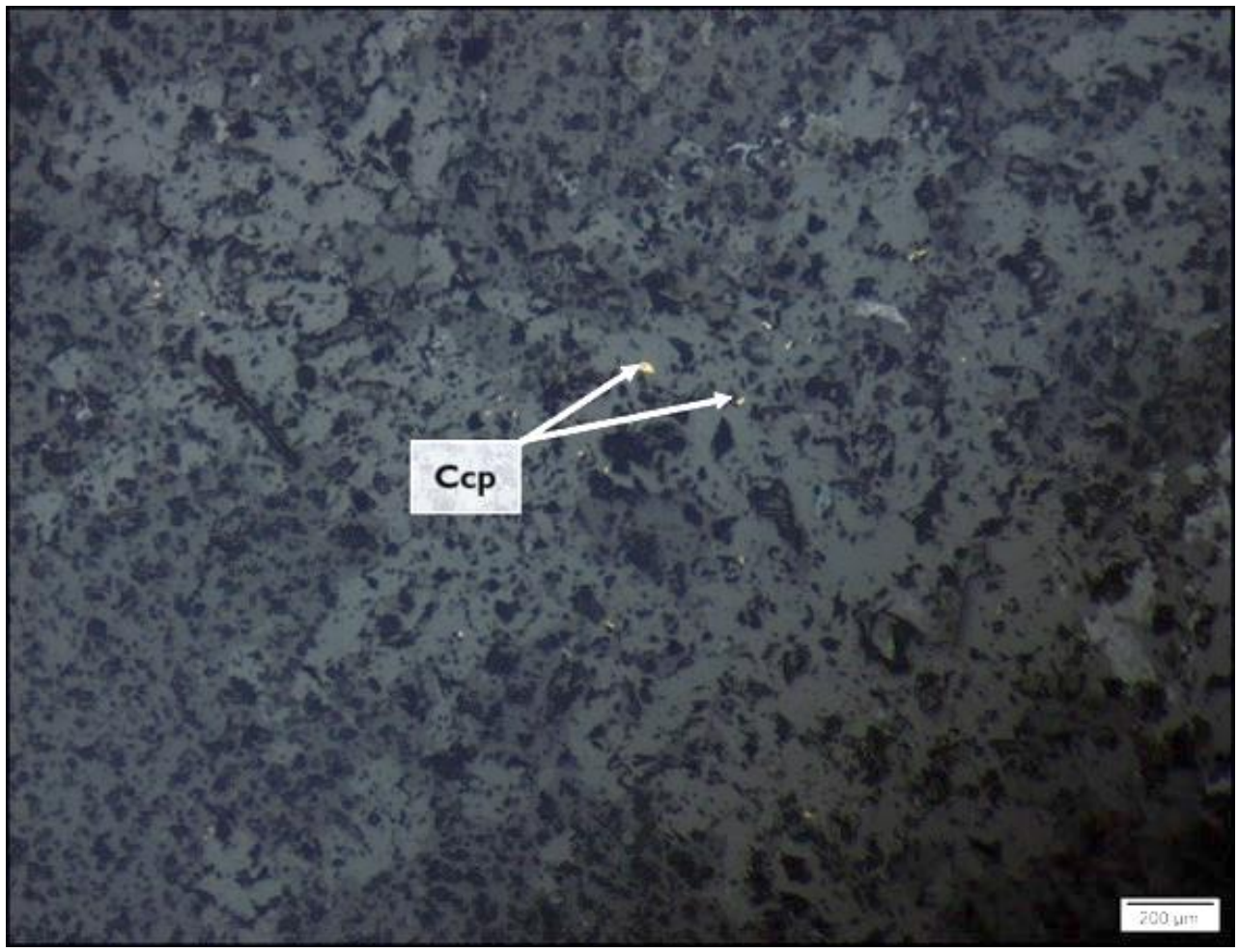


Figure 46: *Small and disseminated chalcopyrite grains in Orbicule Koppie orbicular cores*

- **Shells**

Sharp contacts between cores and shells characterize Orbicule Koppie orbicules (Figure 47), hence, the shells are not distinct and the orbicules resemble enclaves. However, under high magnification, transitions from the cores to the shells are observed and are characterized by changes in modal abundances and the degree of mineral alteration (Figure 47c). The shell composition is comparable to the core composition, but small changes in textures are observed from the core to the shells (Figure 47).

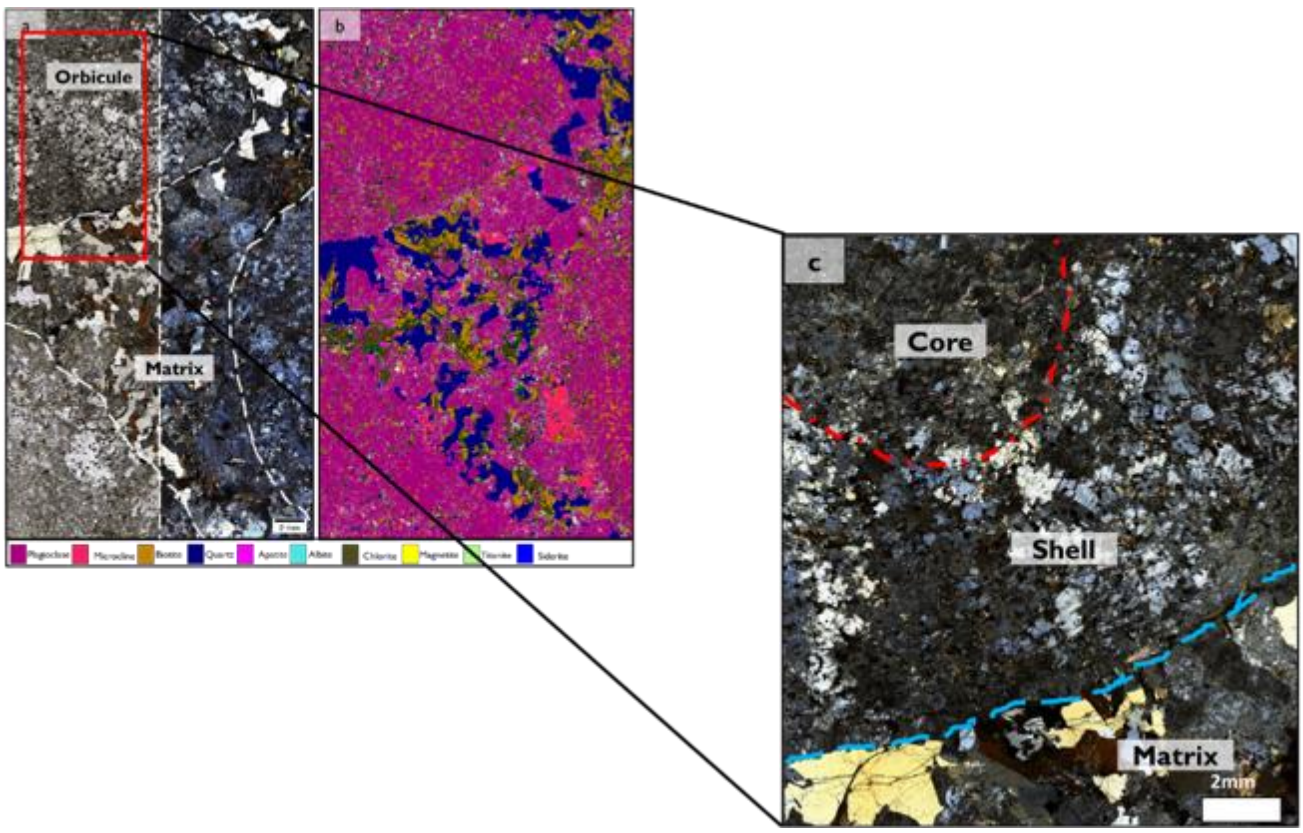


Figure 47: *A photomicrograph of a zoomed-in image with the red dotted line showing a sharp contact between the highly altered core and a fine- to medium-grained shell. The blue dotted line marks the sharp contact between the medium-grained shells to a coarse-grained matrix. (a) and (b) show the location of image c in the full orbicule sample SD-10-6A.*

The shells contain of plagioclase (40%) and biotite (40%), with quartz, microcline, chlorite, muscovite and magnetite making up the remaining 20% (Figure 47). Plagioclase dominates the shells and occurs as large (0.1-4 mm) closely packed and touching grains. They contain poikilitic inclusions of biotite, magnetite, and quartz (Figure 48c, d). Locally, plagioclase is altered to sericite that contains small inclusions of epidote, muscovite, chlorite, and biotite (Figure 48e; f). Biotite occurs as a second most abundant phase in the shells (Figure 48a, b). It occurs as anhedral to subhedral (0.1-0.5 mm) grains that are adjacent to plagioclase (Figure 48c, d) and as inclusions in plagioclase (Figure 48a, b) and in places, it is altered to chlorite.

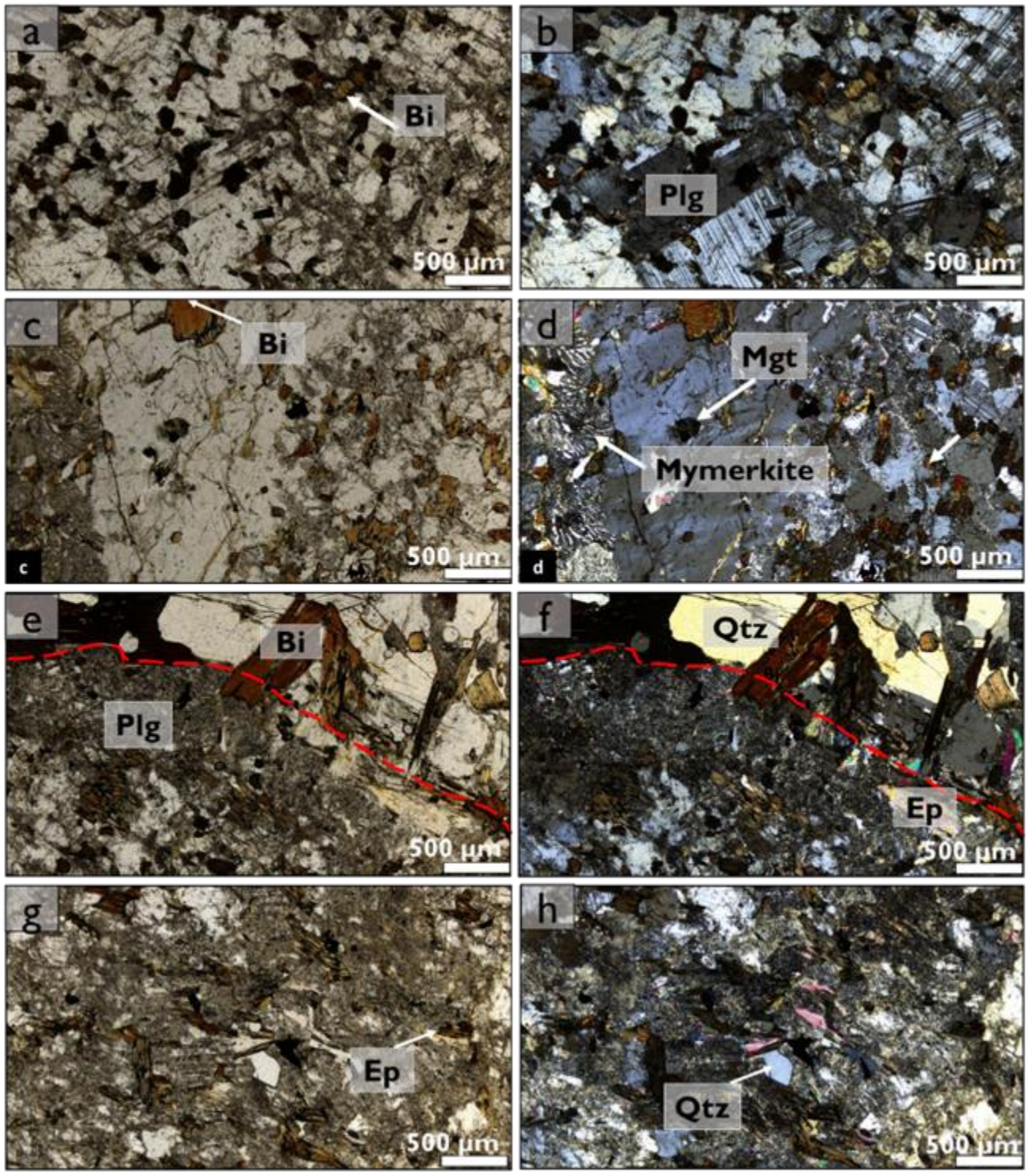


Figure 48: *Photomicrographs showing mineral phases and textures in the orbicular shells from Orbicule Koppie orbicules: (a, b) Plagioclase containing small and disseminated biotite and magnetite grains. Biotite occurs both adjacent to and as inclusions in plagioclase. The inclusions of biotite are associated with small muscovite, epidote and chlorite. (c, d) Poikilitic biotite inclusions in plagioclase that grows adjacent to wormy and vermicular small quartz forming myrmekite textures. (e, f) Altered shell comprising altered plagioclase (sericite) in contact with a coarse-grained matrix. The red dotted line shows the sharp contact from a fine-grained shell to a more coarse-grained matrix. Epidote is common in contacts between the shells and the matrix. (g, h) Disseminated quartz grains adjacent to biotite, muscovite, and magnetite. Quartz occurs as small and rounded inclusions in altered plagioclase.*

Associated with biotite and muscovite are small epidote grains that occur as anhedral laths mostly in contacts between the shells and the matrix (Figure 48e, f). Epidote also occurs adjacent to biotite and chlorite and as very small inclusions in biotite. Quartz occurs as small (0.1 mm) grains adjacent to chlorite, biotite, and muscovite (Figure 48g, h). Locally, quartz occurs as inclusions in altered plagioclase (Figure 48g, h). The shells-to-host matrix transition is characterized by sharp contacts and the occurrence of wormy and vermicular quartz intergrowth forming myrmekitic textures (white arrow, Figure 48c, d) with plagioclase (myrmekite texture). K-feldspars (orthoclase) are the least abundant minerals and occur as accessory phases and as small poikilitic inclusions in plagioclase.

Similar to cores, the shells comprise small (< 1%) chalcopyrite grains. There is not much change in the modal abundance of chalcopyrite observed from the cores to the shells. Chalcopyrite occurs as small (<0.1 mm) subhedral and disseminated grains associated with small magnetite grains (Figure 49).

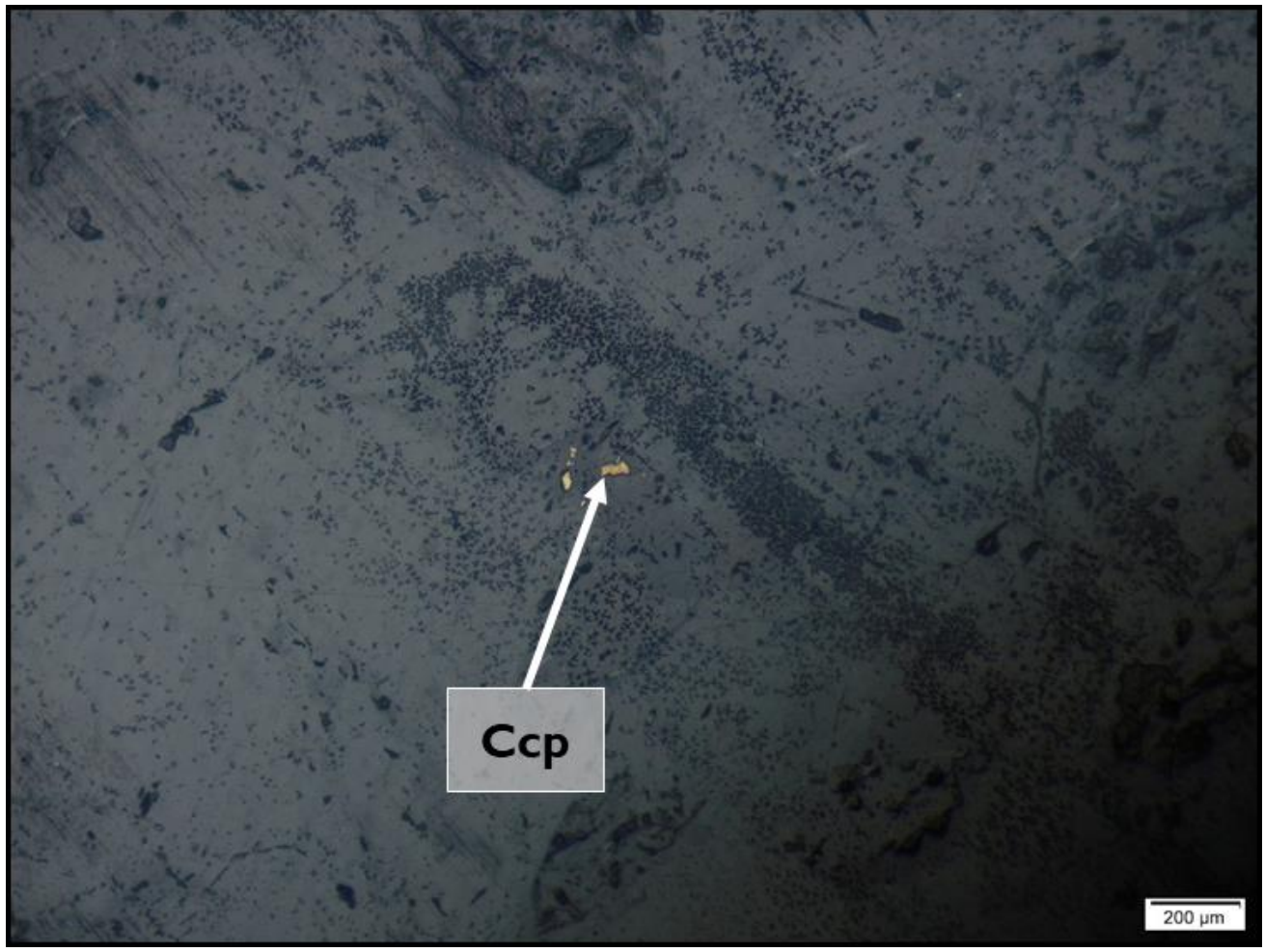


Figure 49: *Small and disseminated chalcopyrite grains in the orbicular shells from Orbicule Koppie.*

- **Matrix characteristics**

The shells to matrix boundaries are marked by sharp contacts (Figure 42). The matrix composition is comparable to the cores compositions, however, the matrix is slightly more coarse-grained and less altered (Figure 44; Figure 50). Similar to the cores, the matrix comprises plagioclase, biotite, K-feldspars, quartz and other accessory phases (Figure 50).

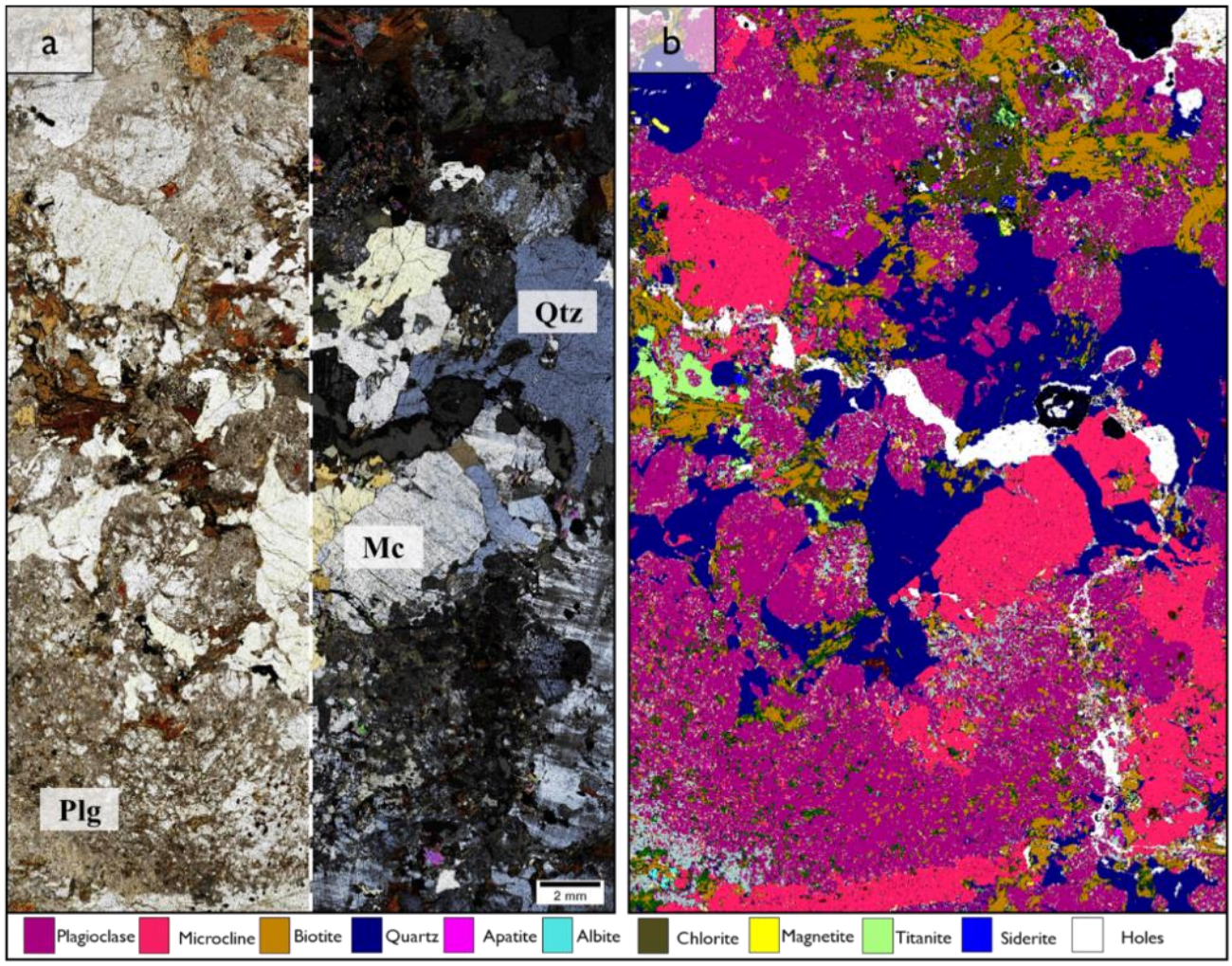


Figure 50: *Full thin section photomicrographs of Orbicule Koppie matrix and corresponding TIMA image: (a) Plane–polarized (left) and cross-polarized light (right) full thin section images of the matrix sample SD-10-6C. (b) TIMA image of sample SD-10-6C showing a coarse-grained matrix composed of plagioclase, microcline, quartz, biotite, chlorite, albite and titanite.*

The matrix comprises plagioclase (34%), quartz (20%), biotite (10%), microcline (15%), chlorite (5%), titanite (3%) and other accessory phases (Figure 50). Plagioclase occurs as (0.1-7 mm) subhedral grains adjacent to K-feldspars, biotite and quartz. It contains inclusions of biotite (Figure 51g, h), chlorite, muscovite, quartz and microcline (Figure 51a, b). Small poikilitic grains of microcline occur along and follow the orientation of the albite twinning in plagioclase (antiperthite; Figure 51a, b). Plagioclase is altered to sericite in places.

Occurring in association with plagioclase is quartz that occurs as large (0.1-6 mm) subhedral grains adjacent to K-feldspars and plagioclase. Quartz contains poikilitic inclusions of biotite, magnetite (Figure 51g, h) and small euhedral laths of plagioclase. In places, quartz occurs as subhedral and rounded grains that occur as inclusions in the altered plagioclase (Figure 51g, h).

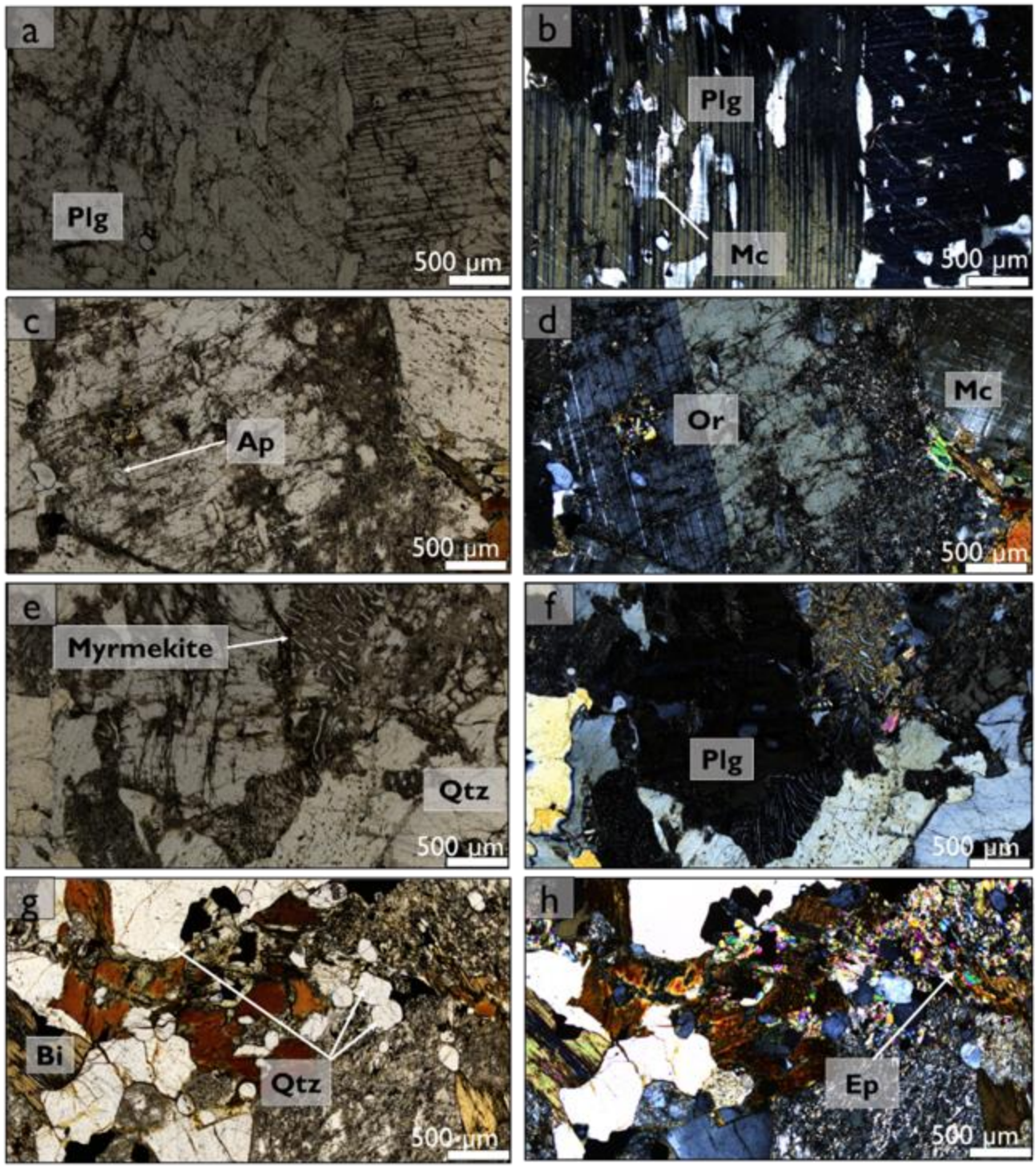


Figure 51: *Photomicrographs showing mineral phases and textures in Orbicule Koppie matrix: (a, b) Large plagioclase grains containing inclusions of microcline lamellae that follows the orientation of the albite twinning (antiperthite). (c, d) Plagioclase altered to sericite occurring adjacent to microcline and orthoclase. Orthoclase contains small inclusions of apatite, and it is altered to clay. Biotite occurs adjacent to epidote and they both occur as small inclusions in altered plagioclase. (e, f) Anhedral quartz grains occurring adjacent to plagioclase. Locally, quartz occurs as vermicular intergrowths in plagioclase (myrmekite texture). Small muscovite grains occur adjacent to quartz and the altered to plagioclase. (g, h) Anhedral to subhedral quartz grains containing biotite inclusions. Quartz grains occur next to biotite and altered plagioclase. Locally, biotite is altered to chlorite***.***

Quartz grows as elongate, vermicular, and wormy grains (Figure 51e, f) with plagioclase, forming myrmekitic textures. Orthoclase (Figure 51c, d) occurs as subhedral (2mm) grains that exhibit simple twinning. These grains contain small (< 0.1 mm) inclusions of apatite (Figure 51c, d) and (< 0.1 mm) grains of quartz (Figure 51c, d). In places, orthoclase is altered to clay (Figure 51c, d). Microcline occurs as subhedral (0.1- 2 mm) grains (Figure 51c, d) and in places, it contains lamellae of plagioclase

forming perthite textures. Microcline also occurs as small inclusions in quartz. Muscovite occurs as small and needle-shaped laths and as small poikilitic inclusions in altered plagioclase (Figure 51e, f). Occurring in closed proximity to chlorite and muscovite is biotite, occurring as flaky grains that occur as inclusions in altered plagioclase (Figure 51c, d).

These (0.1-2 mm) grains of biotite contain inclusions of quartz, magnetite, and apatite (Figure 51g, h). Epidote (Figure 51c, d) and chlorite (Figure 51g, h) occur as accessory phases in close association with biotite and muscovite. In places, they occur as small needle-shaped inclusions in altered feldspars and quartz. Hosted in biotite and plagioclase in the matrix are chalcopyrite and magnetite. Unlike in the cores and the shells, a drastic increase in chalcopyrite and magnetite modal abundances is observed in the matrix (Figure 52b). The grain size of chalcopyrite also drastically increases in the matrix (Figure 52). Chalcopyrite (2%) occurs as massive and disseminated grains (0.2-0.7 mm) in plagioclase and biotite (Figure 52). Chalcopyrite is altered to magnetite (Figure 52a, c, d). Locally, the massive chalcopyrite grains occur adjacent to smaller and disseminated chalcopyrite grains (Figure 52a).

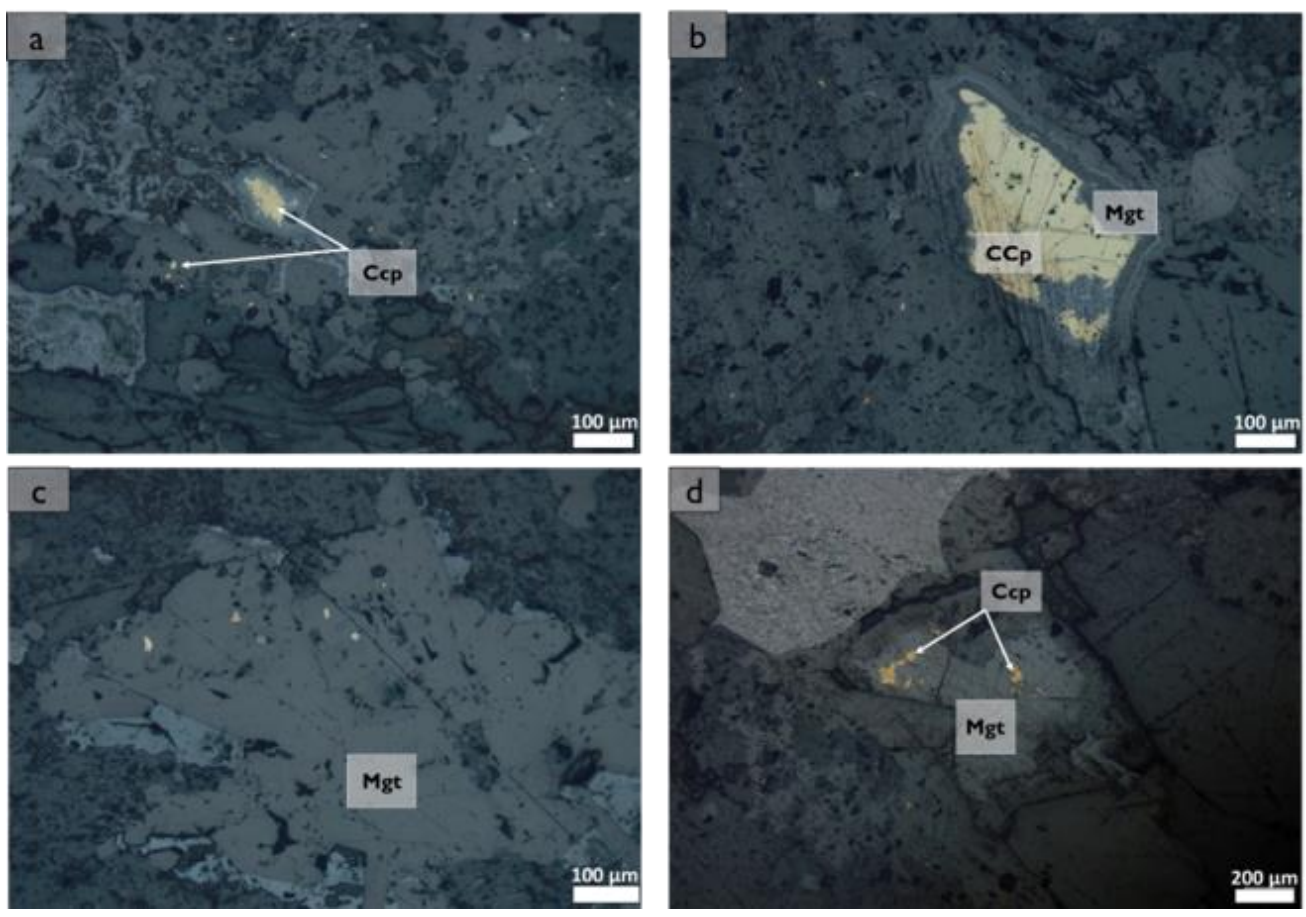


Figure 52: *Photomicrographs showing sulphide mineralization and oxides in the matrix from the Orbicule Koppie orbicules: (a) Massive chalcopyrite grain replaced by magnetite occurring adjacent to smaller and disseminated chalcopyrite grains. (b) Massive chalcopyrite grain replaced by magnetite occurring adjacent to smaller and disseminated chalcopyrite grains. (b) Massive chalcopyrite grains adjacent to smaller and disseminated chalcopyrite grains. (c) Small and disseminated chalcopyrite grains occurring as poikilitic inclusions in magnetite. (d) Chalcopyrite replaced by magnetite and adjacent to massive magnetite.*

5.2.4.2. Hoogkraal Lease

A cut slab from sample SD-22-11 (Figure 53) from Hoogkraal Lease was scanned at high resolution using Micro-XRF to produce element maps showing element distributions.

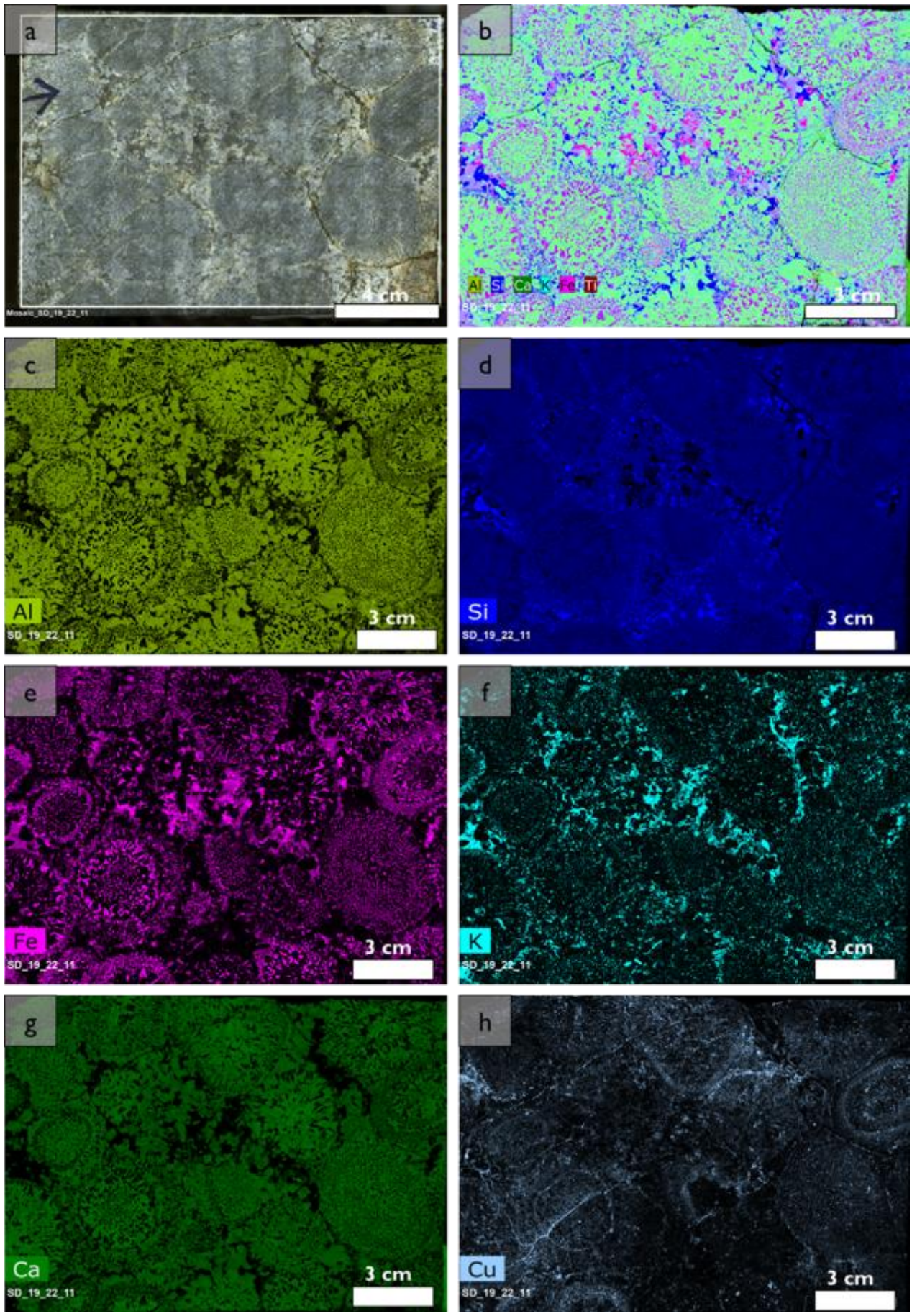


Figure 53: *Element maps of Hoogkraal Lease sample SD-22-11: (a) A mosaic showing the mapped area in a white rectangle. (b) A composite of selected element showing elements detected via the normal map spectrum showing the distribution of Al (green), Si (blue), Fe (pink), Ti (red) and Ca (green) in the sample.*

Figure 53 continued: *(c) Element map showing a uniform distribution of Al throughout the sample, however, the radiating hypersthene grains are less aluminous. (d) Element map showing the highest distribution and intensities of Si in the matrix. (e) Element map showing the highest distributions and intensities of Fe in shells, matrix, and some parts of the cores. (f) Element map showing the distribution of K in different parts of the orbicules. K is highly concentrated in the matrix. (g) Element map showing the distribution of Ca in cores, shells, and matrix. However, Ca is less concentrated in radiating hypersthene grains. (h) Individual element map showing the distribution and concentrations of Cu in different parts of the orbicules. Cu yields high intensities in the host matrix.*

Visual inspection of micro-XRF element maps of the orbicule sample SD-22-11 from Hoogkraal Lease (Figure 53c, g) shows high abundances of Al and Ca (corresponding to the presence of feldspar) in the cores and the felsic shells. However, these elements show low intensities in the radiating hypersthene grains and some parts of the host matrix (Figure 53c, g). Silica and K are less distributed in the cores and in the shells; however, the distribution and amount of these elements increase in the matrix (Figure 53d, f). The shells, the matrix and the radiating hypersthene grains have high Fe (corresponding with an increase in hypersthene and biotite modal abundances) than the cores (Figure 53e). The outer shells and the matrix contain Cu (Figure 53h) and the highest Cu intensities are observed in fractures that cross-cut the orbicules and in shell-matrix contacts or boundaries (Figure 53h). At the microscale, cores surrounded by distinct alternating mafic biotite and intermediate (plagioclase and hypersthene) shells characterize the Hoogkraal Lease orbicules (Figure 54). The orbicules are characterized by sharp contacts between the cores, the shells and the matrix (Figure 54).

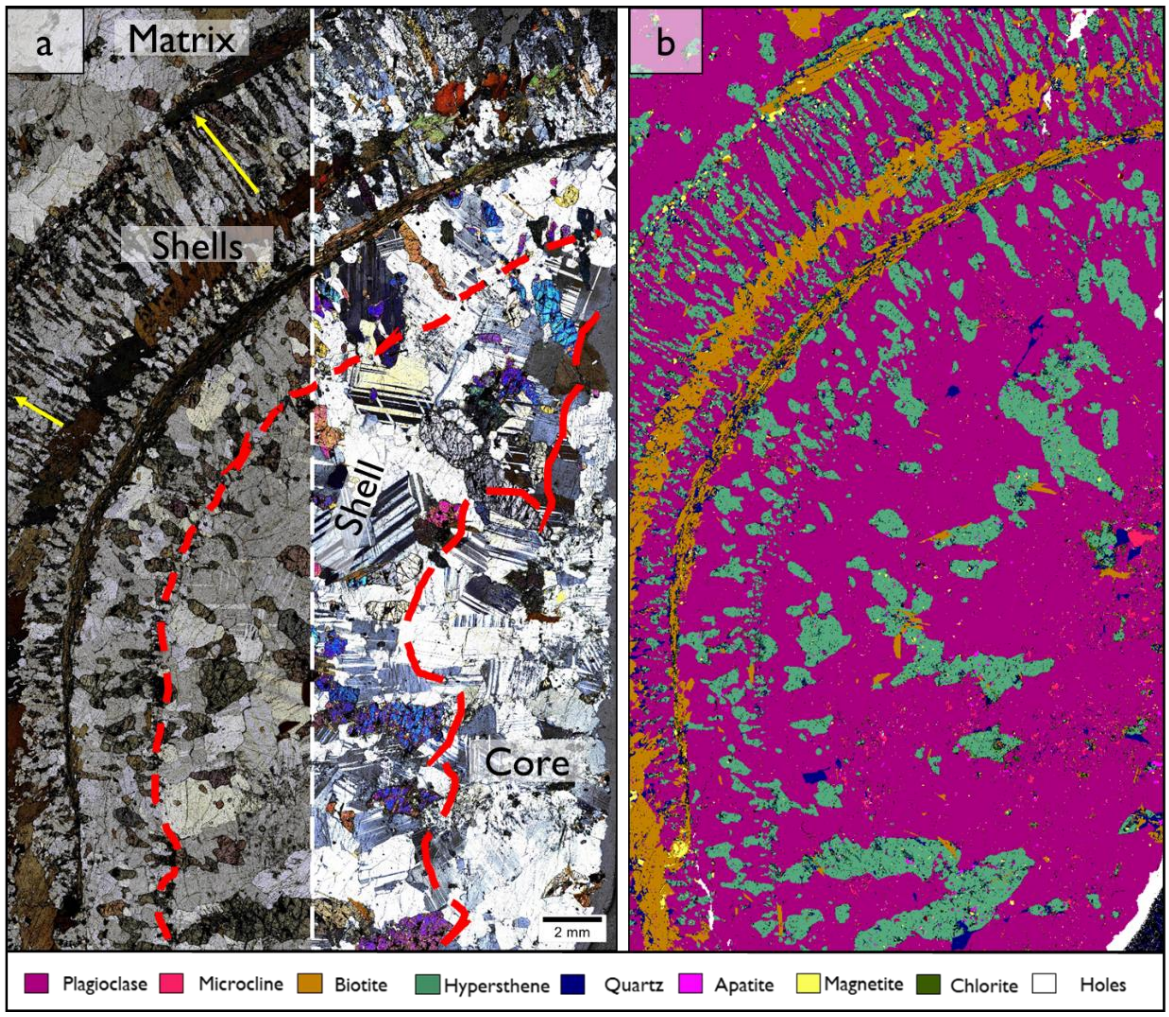


Figure 54: *Full thin section photomicrographs of Hoogkraal Lease orbicular rock sample and corresponding TIMA image:(a) Plane–polarized (left) and cross-polarized light (right) full thin*

Figure 54 continued: *section images of sample SD-27-14. (b) TIMA image of sample SD-27-14 showing a coarse-grained core comprising feldspars, quartz, and hypersthene. Sharp contacts (red arrow) mark the transition from the core to the shells.*

- **Cores**

The cores are medium- to coarse-grained and are composed of plagioclase, hypersthene, biotite, quartz, and other accessory phases (Figure 55).

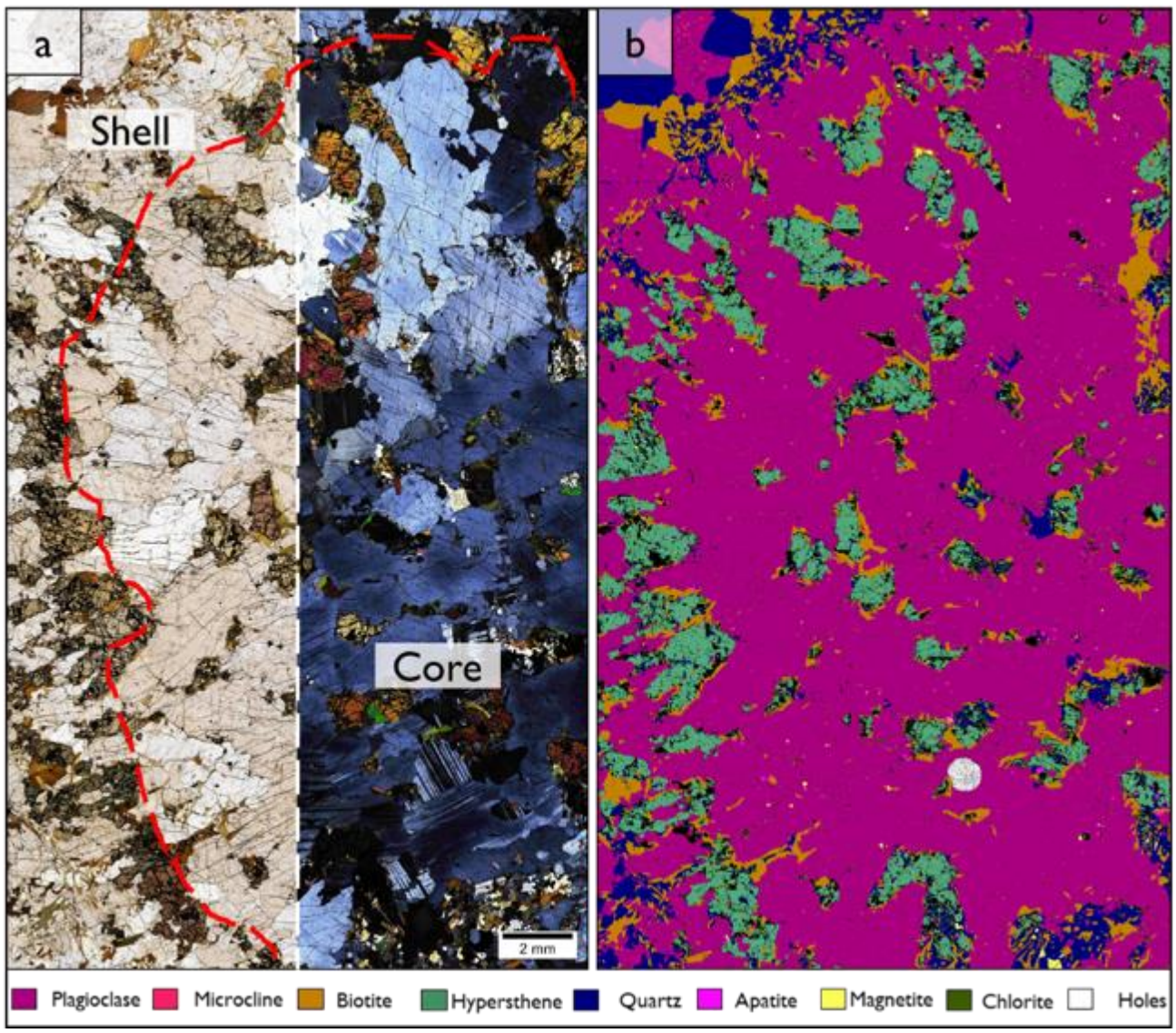


Figure 55: *Full thin section photomicrographs of the Hoogkraal Lease orbicular core sample and corresponding TIMA image: (a) Plane-polarized and cross-polarized light full thin section image of the Hoogkraal Lease orbicular core. (b) TIMA image of the orbicular texture showing a medium-grained core comprising plagioclase, hypersthene, quartz and biotite. Sharp contact (red-dotted line) marks the transition from the core to the shells.*

The cores are composed of unaltered mineral assemblages (Figure 55) and plagioclase (70%), hypersthene (15%) and biotite (10%) are the major minerals. Plagioclase occurs as unaltered, large and subhedral (0.5-8 mm) grains and in places, it grows into microcline, forming poikilitic textures. These large plagioclase grains contain inclusions of smaller plagioclase grains, hypersthene (Figure 57e, f) quartz, magnetite, and subhedral to anhedral biotite and chlorite grains. In places, plagioclase exhibits discontinuous twinning (Figure 57e, f). Hypersthene occurs as the second predominant phase, as large phenocrysts (0.5-3 mm) in plagioclase and microcline (Figure 57a, b, c, d, e, and f). Hypersthene is highly fractured and contains small quartz, biotite, and plagioclase inclusions (Figure

57). Locally, the hypersthene phenocrysts occur in microcline and plagioclase as inclusions (Figure 57e, f). Associated with the hypersthene grains, are locally concentrated, small (<1%; < 0.1 mm) and anhedral grains of chalcopyrite adjacent to the anhedral grains of magnetite (Figure 56).

Biotite occurs as small (0.1-0.3 mm) grains adjacent to quartz, chlorite, plagioclase, and hypersthene (Figure 57g, h). It occurs as inclusions in plagioclase and hypersthene (Figure 57c, d). Quartz occurs as very small (< 0.1 mm) grains that occur as inclusions in hypersthene (Figure 57c, d). Quartz also occurs as small and subhedral equigranular grains adjacent to feldspars and as inclusions in interstitial biotite (Figure 57g, h). Microcline occurs as large and subhedral grains (0.1-3 mm) grains that contain phenocrysts of hypersthene and subhedral to euhedral laths of biotite.

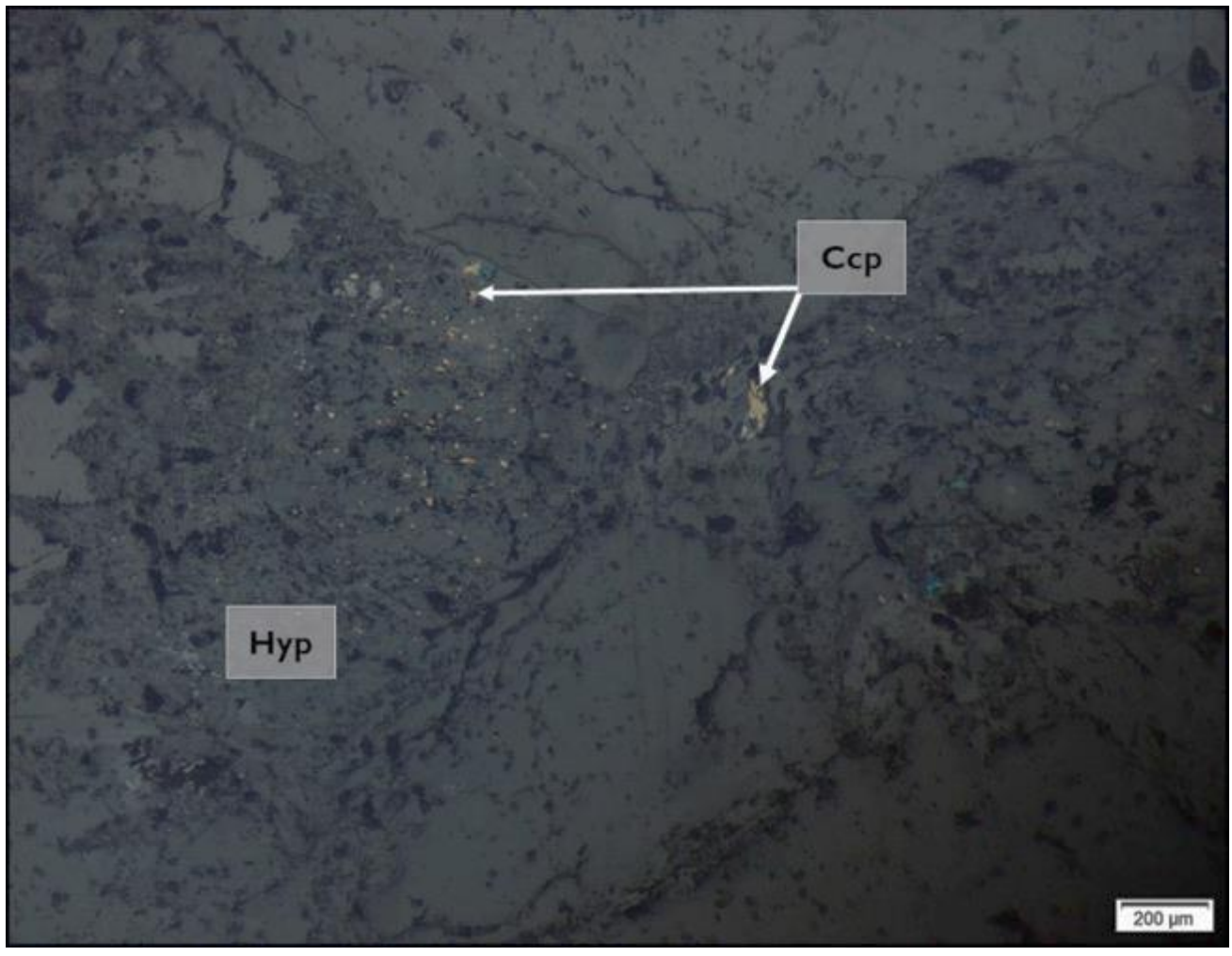


Figure 56: *Small chalcopyrite grains within radiating hypersthene grains in Hoogkraal Lease orbicule cores.*

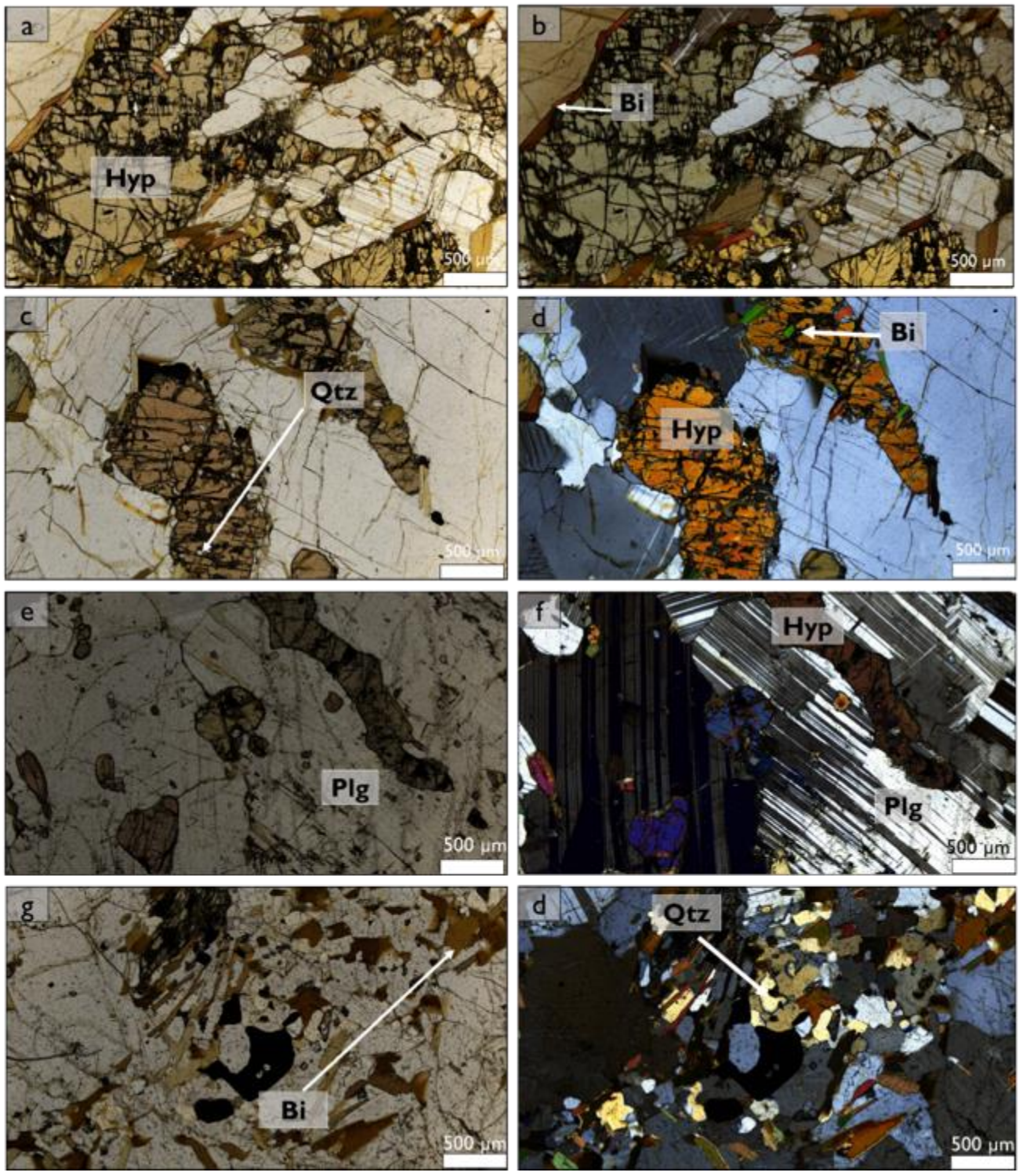


Figure 57*: Photomicrographs of the orbicular cores from Hoogkraal Lease: (a, b) Large and highly fractured phenocrysts of hypersthene occurring as inclusions in microcline and plagioclase. Hypersthene contains inclusions of elongated biotite. (c, d) Large hypersthene grains with small inclusions of subhedral quartz and elongated biotite grains. (e, f) Plagioclase exhibiting discontinuous twinning containing small and subhedral hypersthene inclusions. Hypersthene grows into plagioclase and microcline as elongated and subhedral grains of different birefringence. (g, h) Small and subhedral equigranular grains of quartz adjacent to feldspars and occurring as small inclusions in interstitial biotite. Biotite occurs adjacent to and as inclusions in feldspars.*

- **Shells**

Sharp contacts are observed between the cores and the shells (Figure 58) in the Hoogkraal Lease orbicules. The orbicules are characterized by alternating mafic biotite and intermediate (dominated by plagioclase and hypersthene with minor biotite and quartz) shells (Figure 58). Sharp contacts mark the boundaries between shells of different compositions (Figure 58).

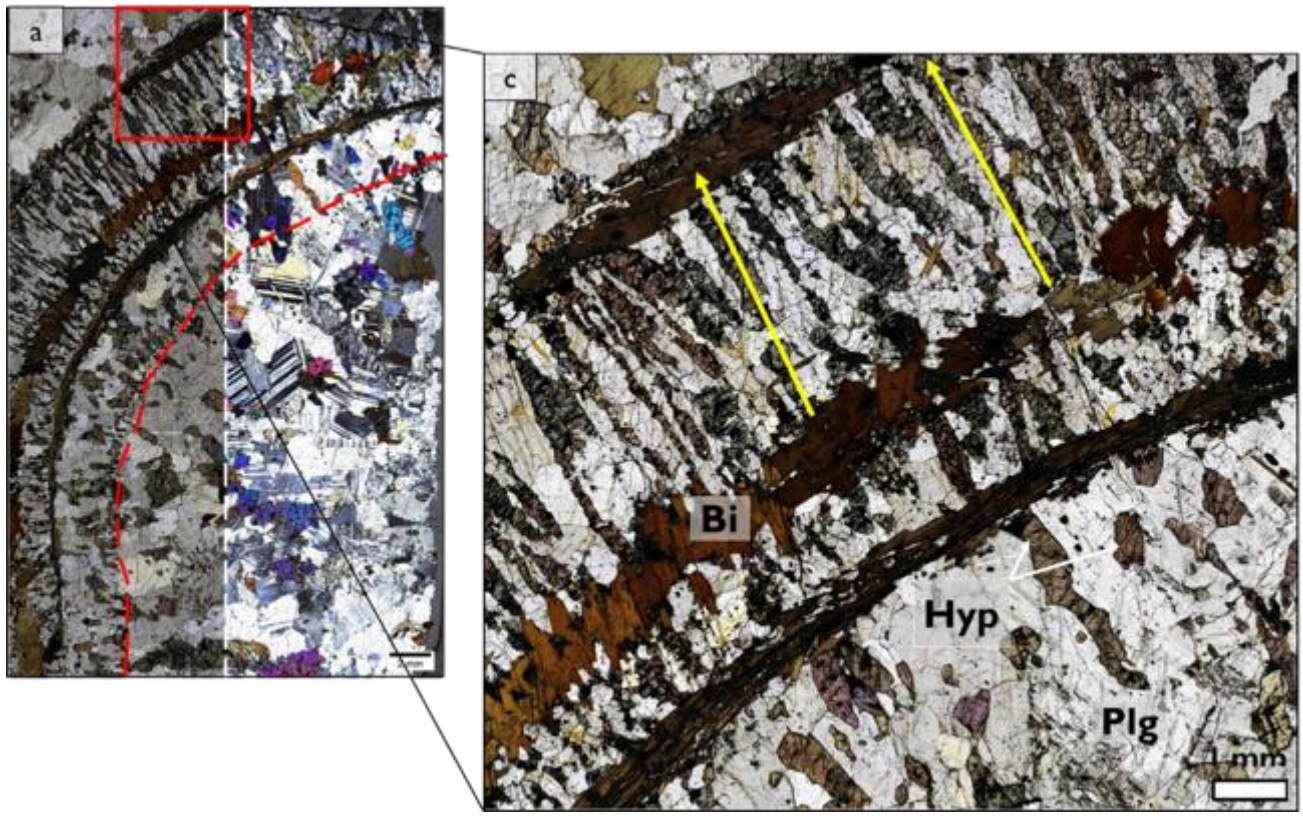


Figure 58: *A zoomed image of sample SD-27-14 showing shells from Hoogkraal Lease. These are alternating biotite and intermediate (plagioclase with hypersthene and minor biotite) shells. They are also characterized by radiating hypersthene grains. The radiating texture (yellow arrows) is cut perpendicular by the concentric biotite shells. Insert a are full thin section photomicrographs of the Hoogkraal Lease orbicular sample SD-27-14 in plane–polarized (left) and cross-polarized light (right) light showing the location of image c.*

The fine- to medium-grained shells occur as alternating mafic and intermediate shells (Figure 58). The mafic shells are made entirely of biotite (>95%; Figure 58). These concentric biotite layers also comprise inclusions of small magnetite, quartz, chlorite, and apatite grains (Figure 59a, b). The intermediate shells, however, comprise mainly and radiating or comb-layered (Moore and Lockwood, 1973) hypersthene and plagioclase (Figure 59e, f). Hypersthene (30%) radiates from the edge of the core towards the outer shell rim and extends extends on a distance corresponding to one shell (Figure 59). Hypersthene contains inclusions of quartz, magnetite, and biotite (Figure 59e, f). Plagioclase (50%) crystals fill the gaps between hypersthene (Figure 59d) and occur as large and plumose laths containing small quartz (5%), biotite and microcline (5%) inclusions. It is also important to note that biotite is also radiating and also occur as shells that crosscut the comb-layered hypersthene and plagioclase grains perpendicularly (Figure 59a, b) and some of the biotite shells are discontinuous (Figure 58).

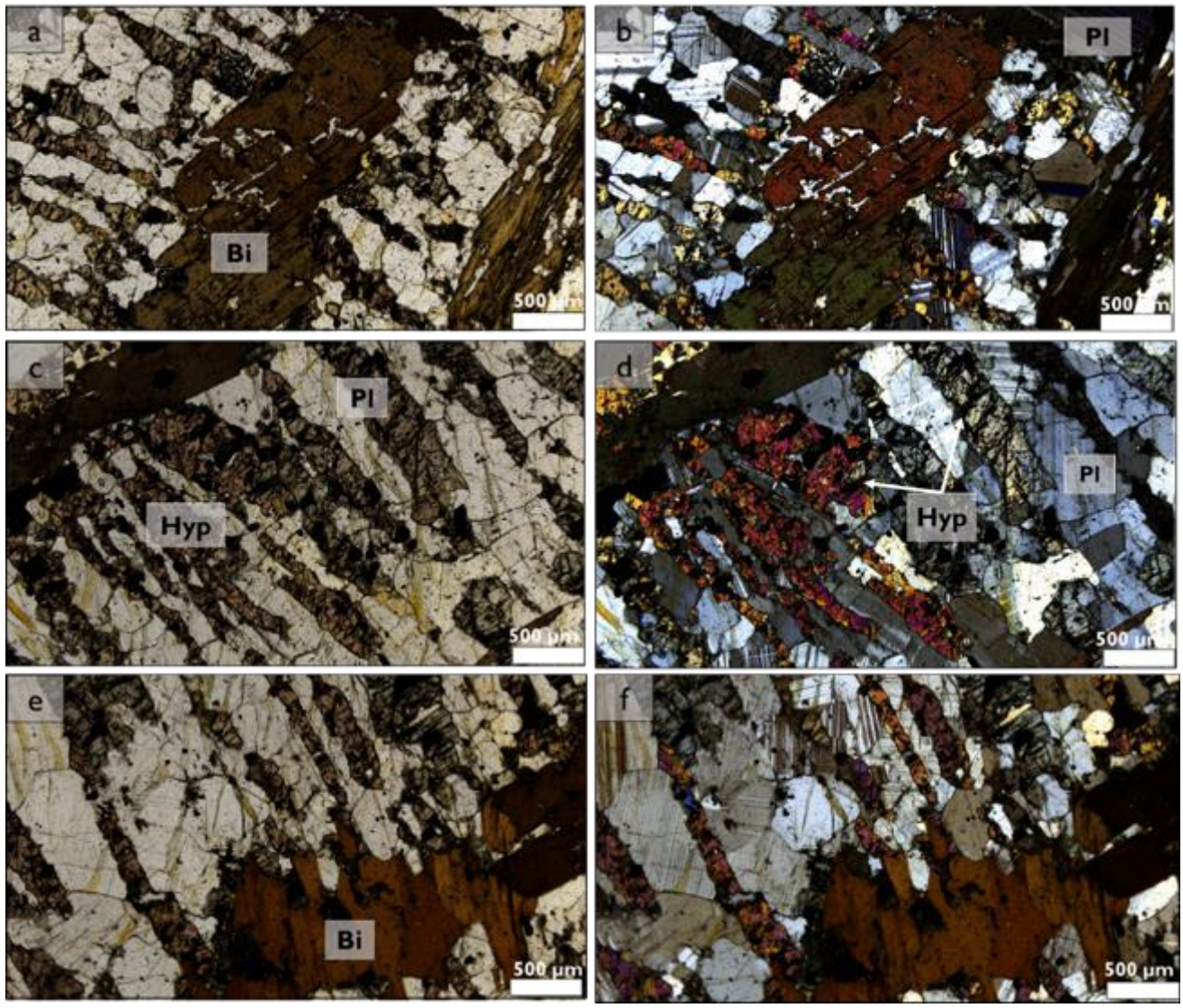


Figure 59: *Photomicrographs of orbicular shells from Hoogkraal Lease orbicules: (a, b) Plagioclase grains adjacent to the radiating hypersthene grains. Small-scale alteration of plagioclase is observed. Biotite occurs as continuous grains that crosscut the hypersthene grains. (c, d) Radiating hypersthene grains are cut perpendicular by the continuous biotite shells. (e, f) small quartz grains that occur as poikilitic inclusions in biotite and adjacent to hypersthene and plagioclase.*

The modal abundance of magnetite from the cores to the shells increases, while chalcopyrite remains the same. Magnetite occurs in hypersthene as disseminated, anhedral and equigranular grains adjacent to each other (Figure 60). These grains occur adjacent to smaller, anhedral, and disseminated (<< 0.1%) chalcopyrite grains. Chalcopyrite is closely associated with hypersthene, mostly as poikilitic inclusions in hypersthene (Figure 60).

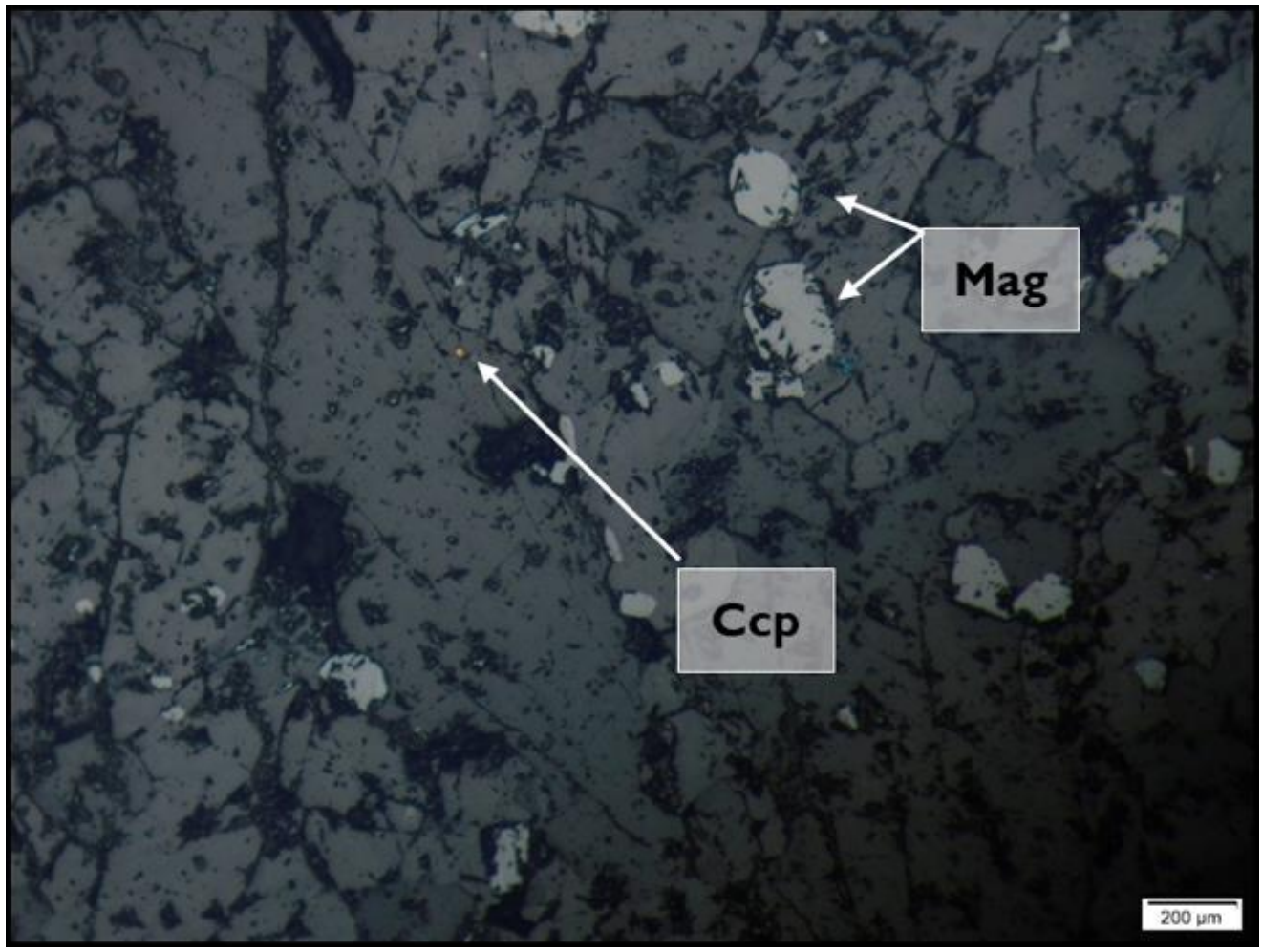


Figure 60: *Disseminated, small and anhedral chalcopyrite adjacent to subhedral to euhedral magnetite.*

- **Matrix characteristics**

The transition from the outer mafic biotite shells to the matrix is characterized by sharp contacts (Figure 54), a decrease in hypersthene modal abundance and an increase in the abundance of biotite, quartz and magnetite (Figure 61).

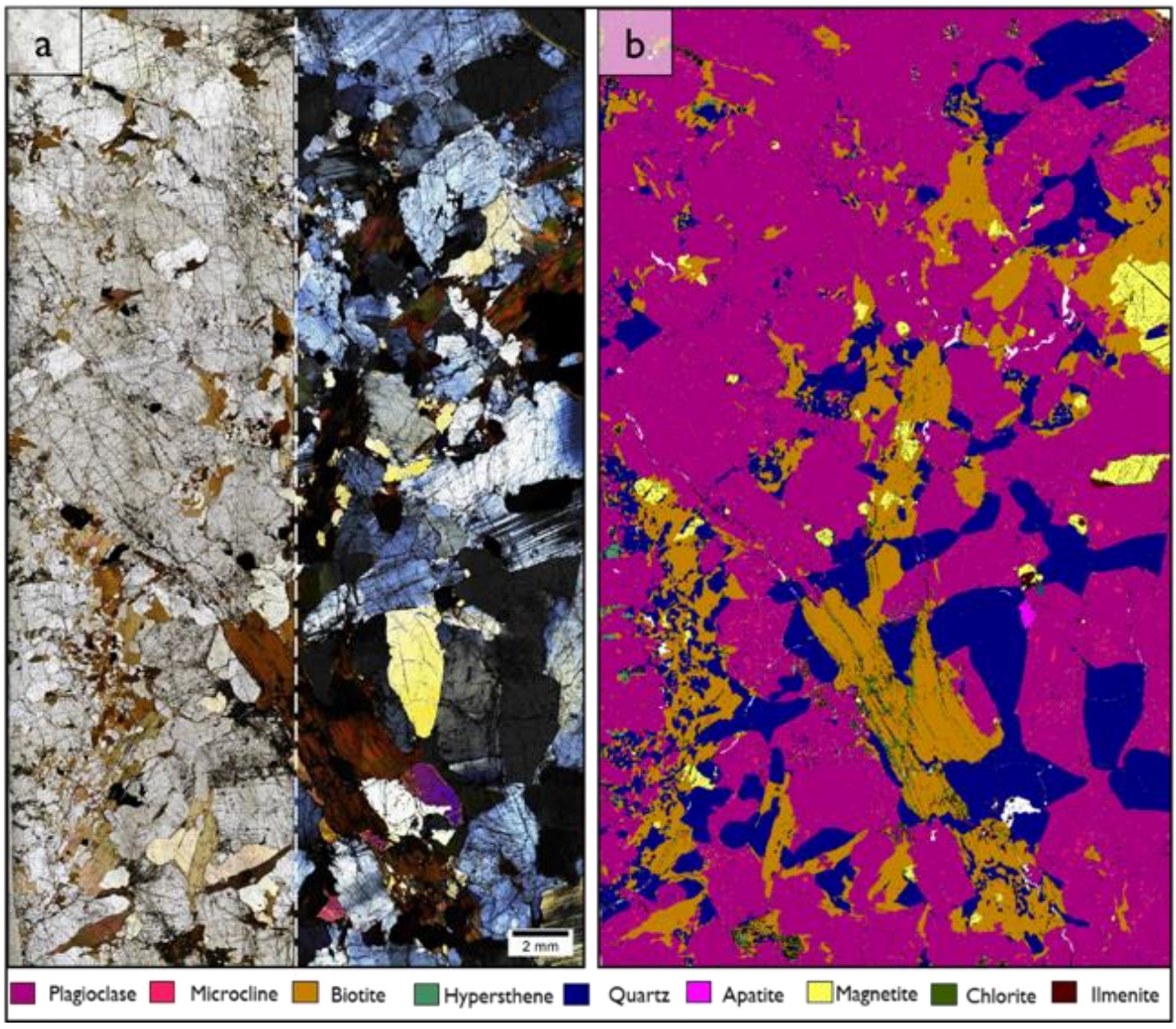


Figure 61: *Full thin section photomicrographs of the Hoogkraal Lease matrix and corresponding TIMA image: (a) Plane–polarized (left) and cross-polarized light (right) full thin section images of the matrix sample SD-22-11C. (b) TIMA image of sample SD-22-11C showing a medium- to coarse-grained matrix comprising feldspars, biotite, magnetite, quartz and accessory apatite and chlorite.*

The matrix is composed of plagioclase (60%), biotite (17%), quartz (15%), magnetite (3%) and other accessory phases (Figure 61). Plagioclase occurs as large (0.2-3 mm) grains adjacent to biotite and microcline (Figure 62g, h). Plagioclase occurs as less altered grains that comprise poikilitic inclusions of small and rounded grains of quartz, biotite and minor chlorite. Locally, plagioclase exhibits discontinuous twinning (Figure 63e, f) and grows into adjacent plagioclase grains. Locally, small inclusions of plagioclase occur in microcline, and they are in the same trend as the twinning forming a perthite texture (Figure 63a, b). Biotite occurs as subhedral and elongated (0.1-2 mm) grains next to plagioclase, microcline and quartz. In places, it contains inclusions of anhedral quartz that grows as a network of grains that forms polygonal textures (Figure 63c, d).

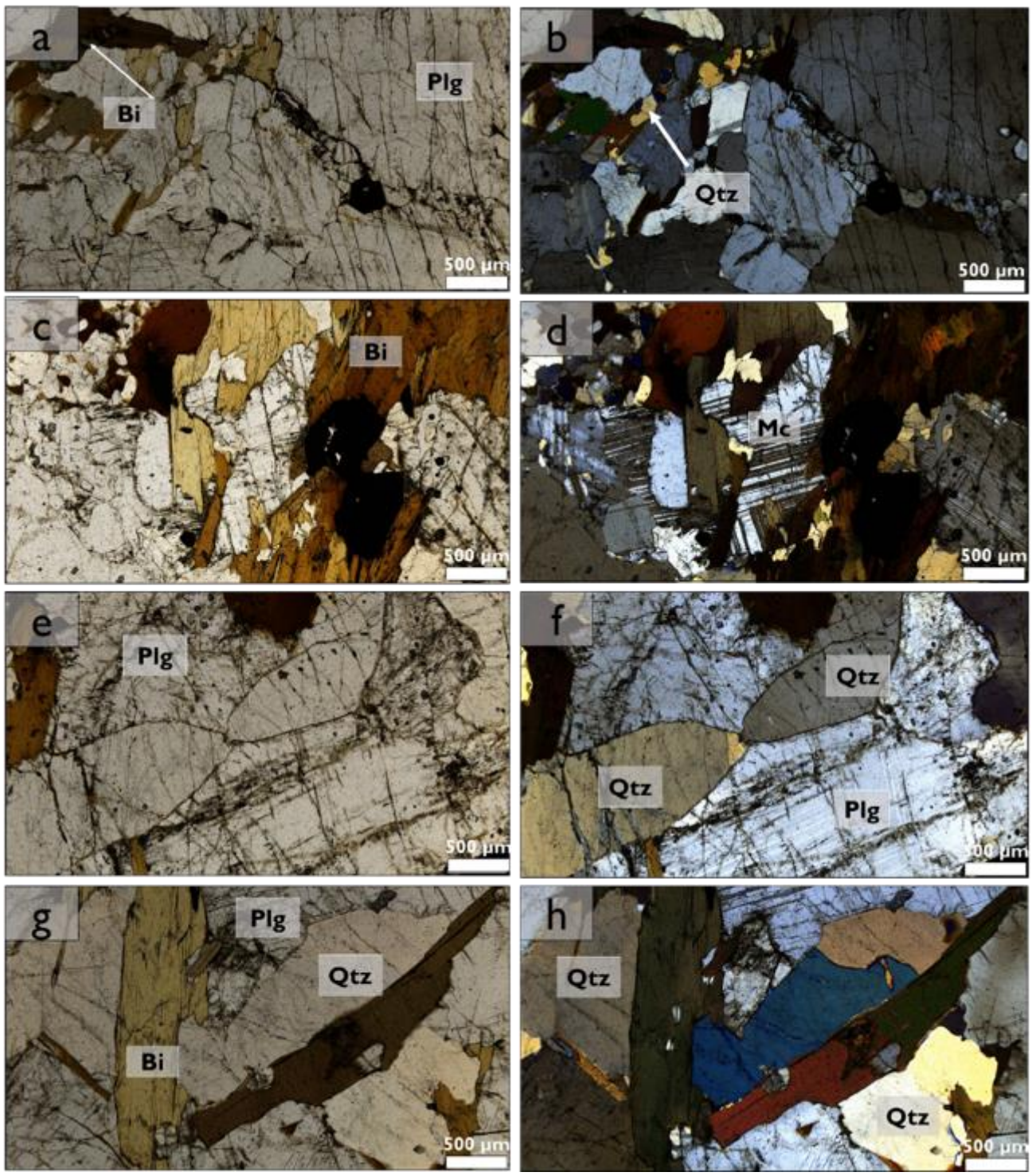


Figure 62: *Photomicrographs of a matrix from the Hoogkraal Lease orbicules: (a, b) Plagioclase adjacent to smaller and subhedral quartz grains. Quartz also occurs adjacent to interstitial biotite surrounding microcline. (c, d) Large and anhedral biotite grains with quartz inclusions growing into microcline adjacent to plagioclase. Microcline contains inclusions of quartz and magnetite. (e, f) Large and touching grains of subhedral quartz inclusions in plagioclase. Quartz occurs adjacent to biotite containing smaller quartz inclusions. Plagioclase is altered to clay. (g, h) Large and elongated biotite crosscutting large quartz grains, creating reaction rims. Biotite also occurs as an interstitial phase enclosing smaller quartz grains.*

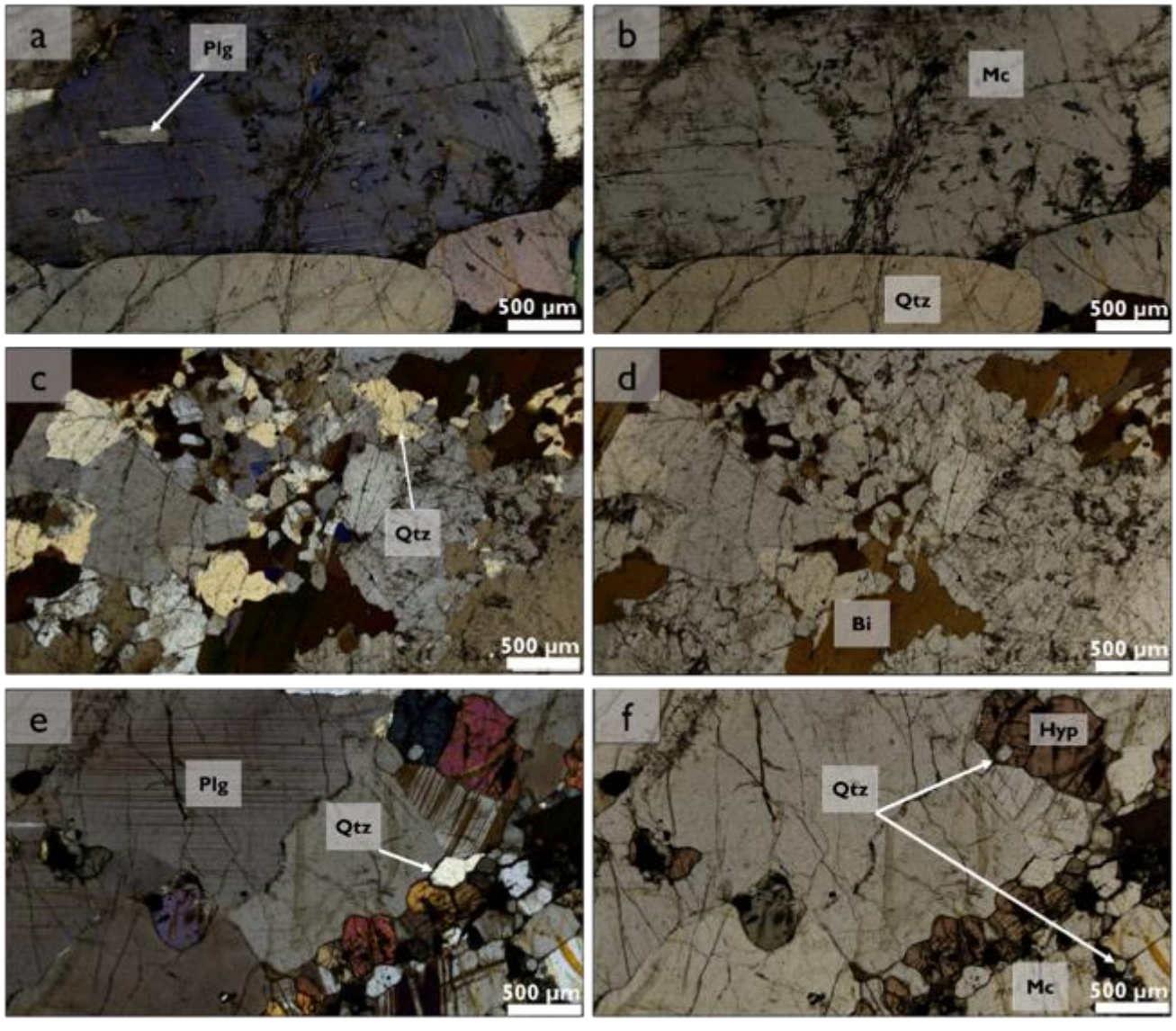


Figure 63: *Photomicrographs showing mineral phases and textures in the Hoogkraal Lease matrix: (a, b) Large and euhedral microcline grains adjacent to large and subhedral quartz grains. Microcline contains poikilitic inclusions of plagioclase following the same trend as the twinning creating perthite textures. (c, d) Small and subhedral grains of quartz adjacent to biotite and feldspars. Quartz occurs as inclusions enclosed in interstitial biotite that is adjacent to feldspar. (e, f) Plagioclase contains inclusions of subhedral hypersthene that contains inclusions of quartz.*

Reaction rims are common where biotite grows adjacent to quartz and plagioclase (Figure 62g, h). In places, biotite grows as a network of continuous and elongated grains that contain quartz and grows into larger plagioclase and quartz grains (Figure 62g, h).

Quartz occurs as small and rounded (0.1 mm) grains next to microcline and plagioclase (Figure 62f, Figure 63b). It occurs as inclusions in biotite, microcline, and plagioclase, and as equigranular grains locally forming polygonal textures in biotite (Figure 63d). The modal abundance of hypersthene decreases in the matrix compared to the shells and the cores. Hypersthene occurs as small (<5%) subhedral inclusions in plagioclase (Figure 63e, f) and in places, it contains smaller inclusions of quartz (Figure 63e, f).

Similar to the cores and the shells, the Hoogkraal Lease matrix contains chalcopyrite and magnetite, and the modal abundance of chalcopyrite decreases from shells to the matrix. Very small (<<1%), disseminated and anhedral chalcopyrite grains are observed (Figure 64) and they occur next to subhedral and disseminated grains of magnetite.

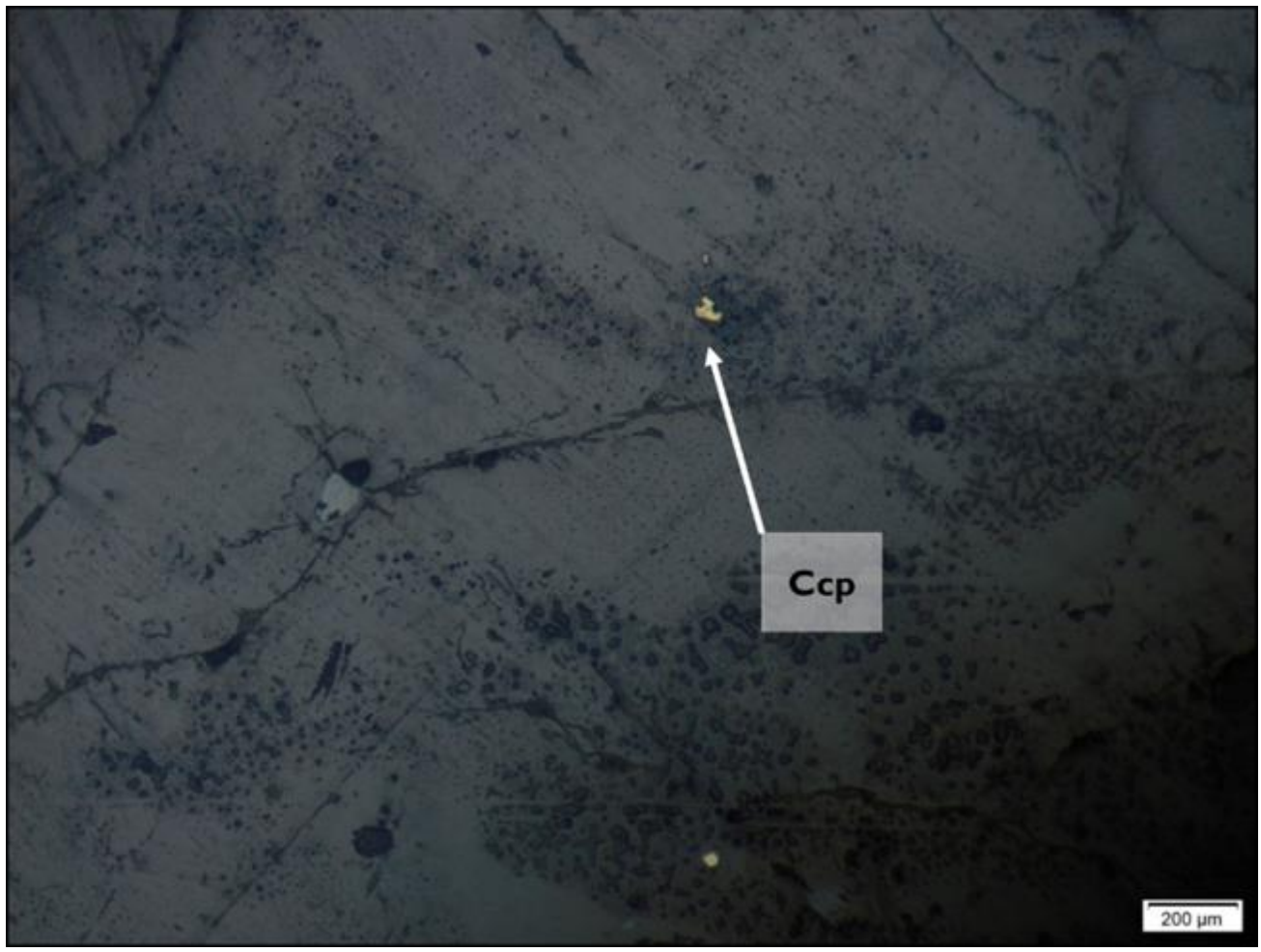


Figure 64: *Small, anhedral and disseminated chalcopyrite grain in a matrix from the Hoogkraal Lease orbicules.*

5.2.4.3. Henderson North

Element maps of a cut slab from the Henderson North orbicular sample show a uniform distribution of Al, Si and Ca in the cores and the matrix, although there is a slight decrease in the concentration of these elements in the shells (Figure 65b, c, d, g). The matrix and the shells are potassic and yield high K intensities (Figure 65f). The outer shells and the matrix contain high Fe, the cores; however, have low Fe (Figure 65e). The sample shows areas in the matrix and shells with high Cu concentrations as indicated by the high Cu intensities (Figure 65h).

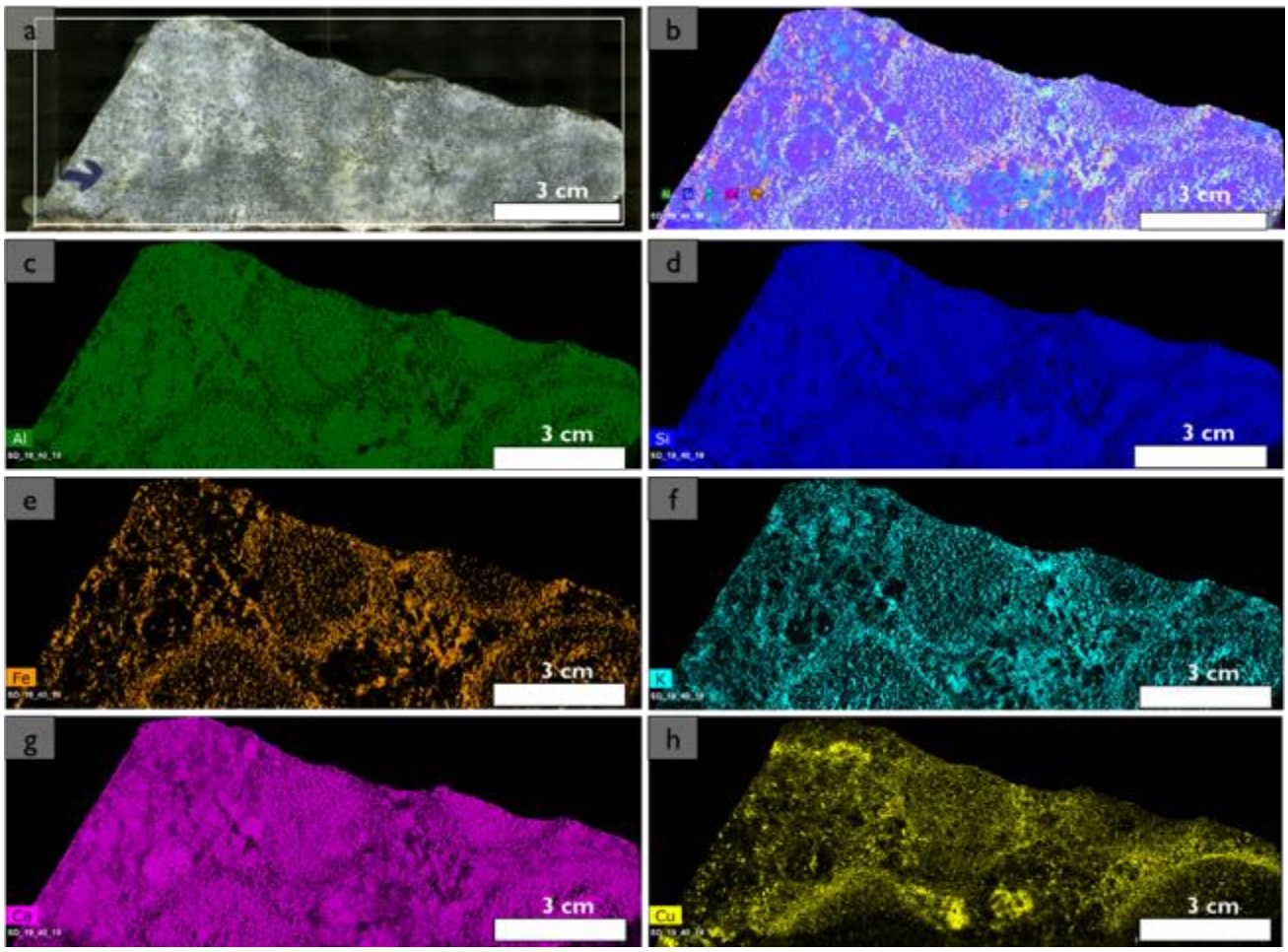


Figure 65: *Element maps of the Henderson North sample SD-40-19: (a) A mosaic showing the mapped area in the white rectangle. (b) A composite of selected element showing elements detected via the normal map spectrum showing Al (green), Ca (pink), K (bright blue), Fe (orange) and Si (dark blue) . (c) Individual element map showing a uniform concentration of Al throughout the orbicule sample. (d) Individual element map showing the highest concentrations and intensities of Si in cores and the matrix. (e)Element map showing the highest concentrations and intensities of Fe in shells, matrix and some parts of the cores. (f) Element map showing the distribution and concentrations of K in different parts of the orbicules. (g) Individual element map showing uniform Ca concentrations in the orbicule sample. (h) Individual element map showing the distribution and concentrations of Cu in different parts of the orbicules. Cu is highly concentrated in the matrix.*

At the microscale, medium-grained cores, distinct shells, and a medium- to coarse-grained matrix (Figure 66) characterize the Henderson North orbicules. The core to shells and the shells to matrix boundaries are marked by sharp contacts (Figure 66). Mineralogically, the matrix composition is comparable the core composition. However, modal abundances of different mineral assemblages vary (Figure 66).

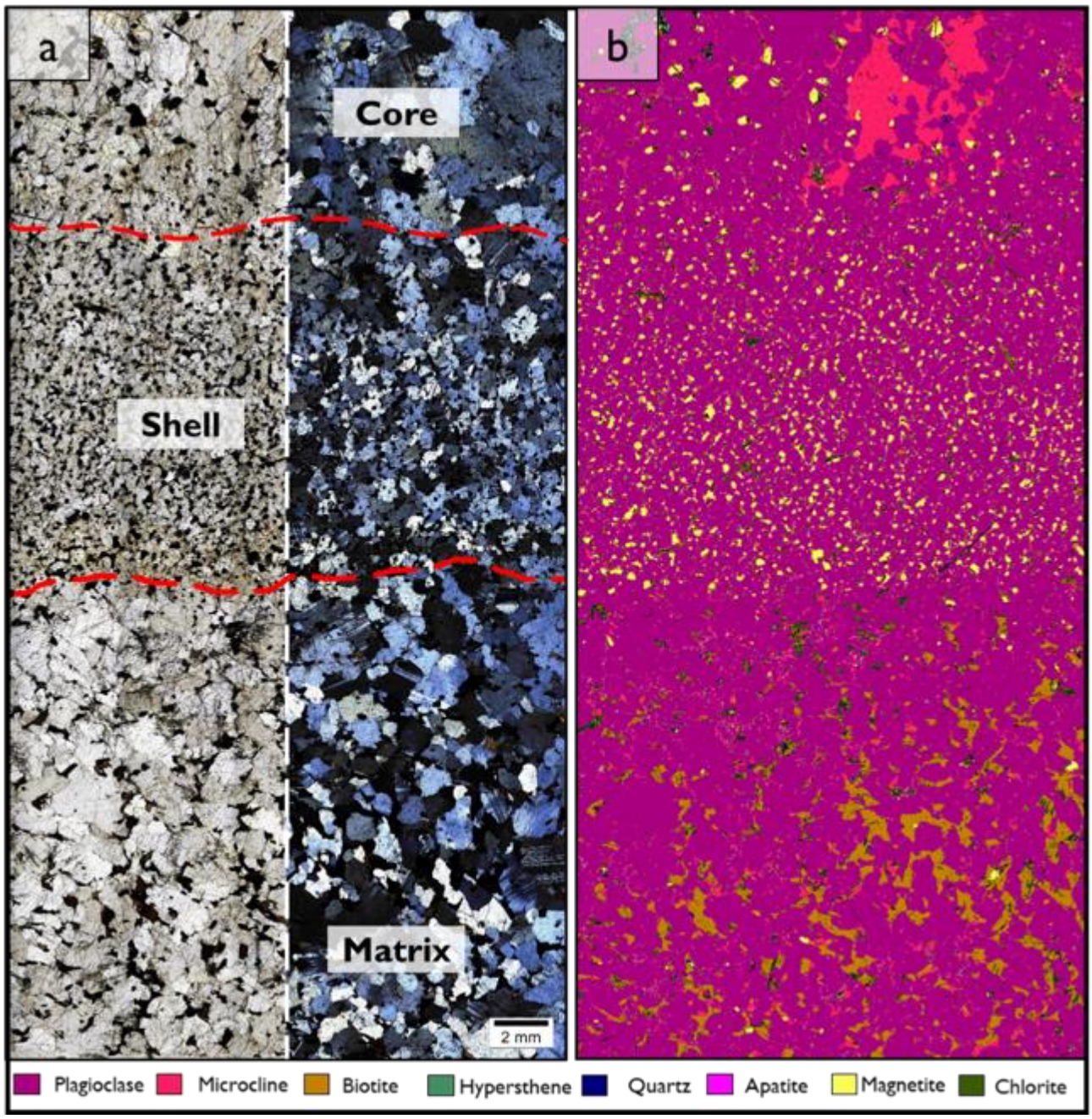


Figure 66: *Full thin section photomicrographs of the Henderson North orbicule sample SD-10-36A and corresponding TIMA image: (a) Plane–polarized (left) and cross-polarized light (right) full thin section images of sample SD-10-36A. (b) TIMA image of sample SD-10-36A. (b) TIMA image of sample SD-10-36A showing a medium-grained core dominated by plagioclase, microcline, and magnetite. Sharp contact (red dotted line) marks the transition from the core to the shell. The shell is predominated by magnetite and plagioclase. The medium-grained matrix comprises plagioclase, microcline chlorite and biotite.*

- **Cores**

The cores are medium- to coarse-grained and are composed of plagioclase, hypersthene, biotite, microcline magnetite and other accessory phases (Figure 67).

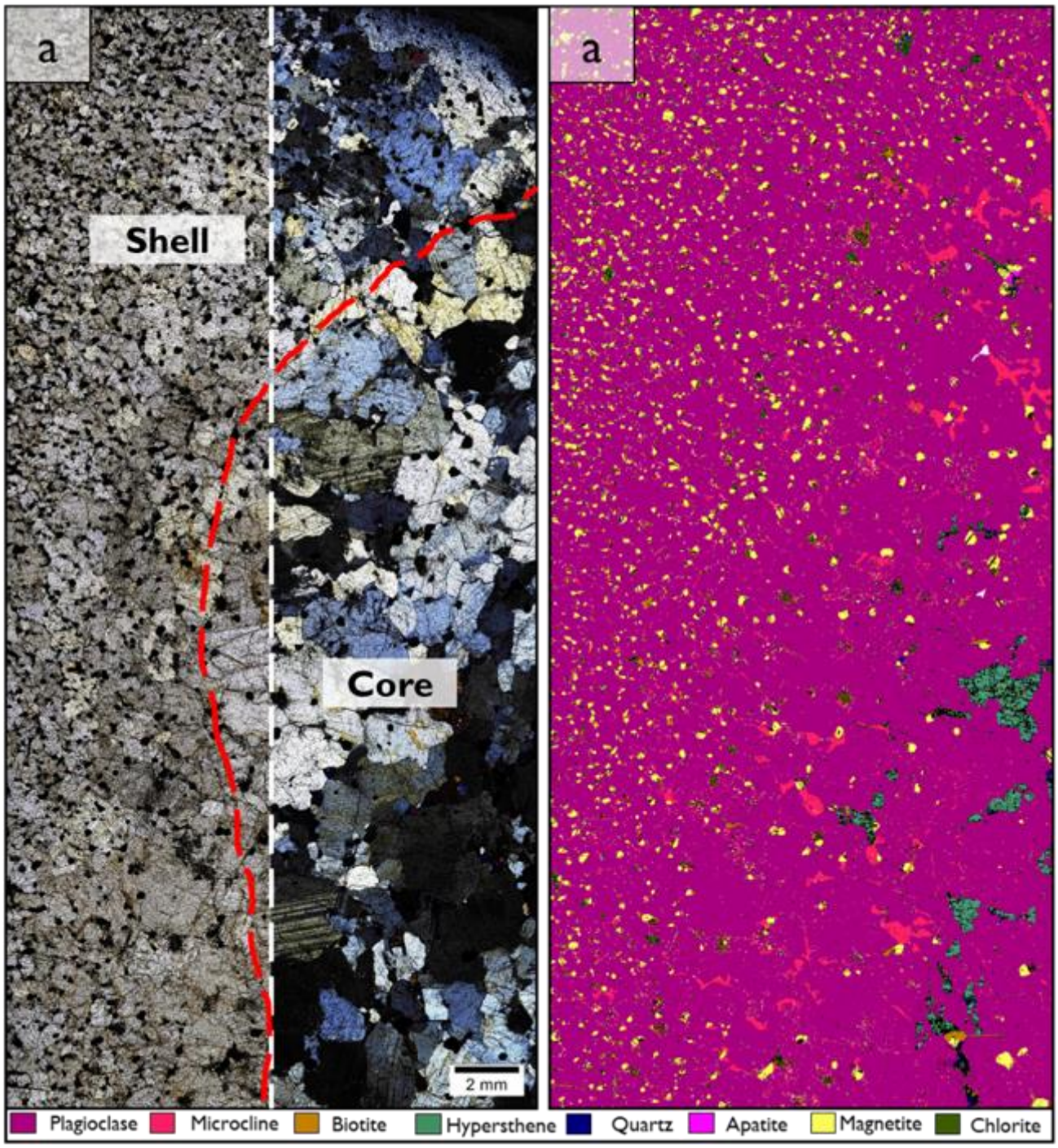


Figure 67: *Full thin section photomicrographs of the Henderson North orbicule sample SD-36-18C and corresponding TIMA image: (a) Plane–polarized (left) and cross-polarized light (right) full thin section images of sample SD-36-18C. (b) TIMA image of sample SD-36-18C. (b) TIMA image of sample SD-36-18C showing a medium- to coarse-grained core composed of plagioclase, hypersthene, microcline and magnetite. The red-dotted line marks the gradational contact between the core and the shell. There is a visible increase in magnetite and a decrease in microcline modal abundance in the shell.*

Cores comprise plagioclase (76%), magnetite (3%), biotite (2%), microcline (10%), hypersthene (2%) and other accessory phases (Figure 67). Plagioclase occurs as large (0.1-6 mm) grains containing inclusions of rounded (0.1 mm) grains of magnetite and small and elongated (< 0.1 mm) grains of biotite (Figure 68c, e, f). It also occurs adjacent to large grains of hypersthene. Hypersthene also occurs

as large phenocrysts in plagioclase (Figure 68a, e). In places, hypersthene grows on plagioclase, crosscutting it (Figure 68a, b). Adjacent to hypersthene and plagioclase are subhedral (0.1- 0.2 mm) grains of quartz that occur as inclusions in plagioclase. Biotite occurs as subhedral (0.1-0.2 mm) grains next to plagioclase and hypersthene. Locally, biotite occurs as inclusions in plagioclase (Figure 68f). There is evidence of small (<0.1 mm) grains of disseminated chalcopyrite adjacent to bigger (0.1-0.2 mm) grains of subhedral magnetite. These are associated with plagioclase and hypersthene.

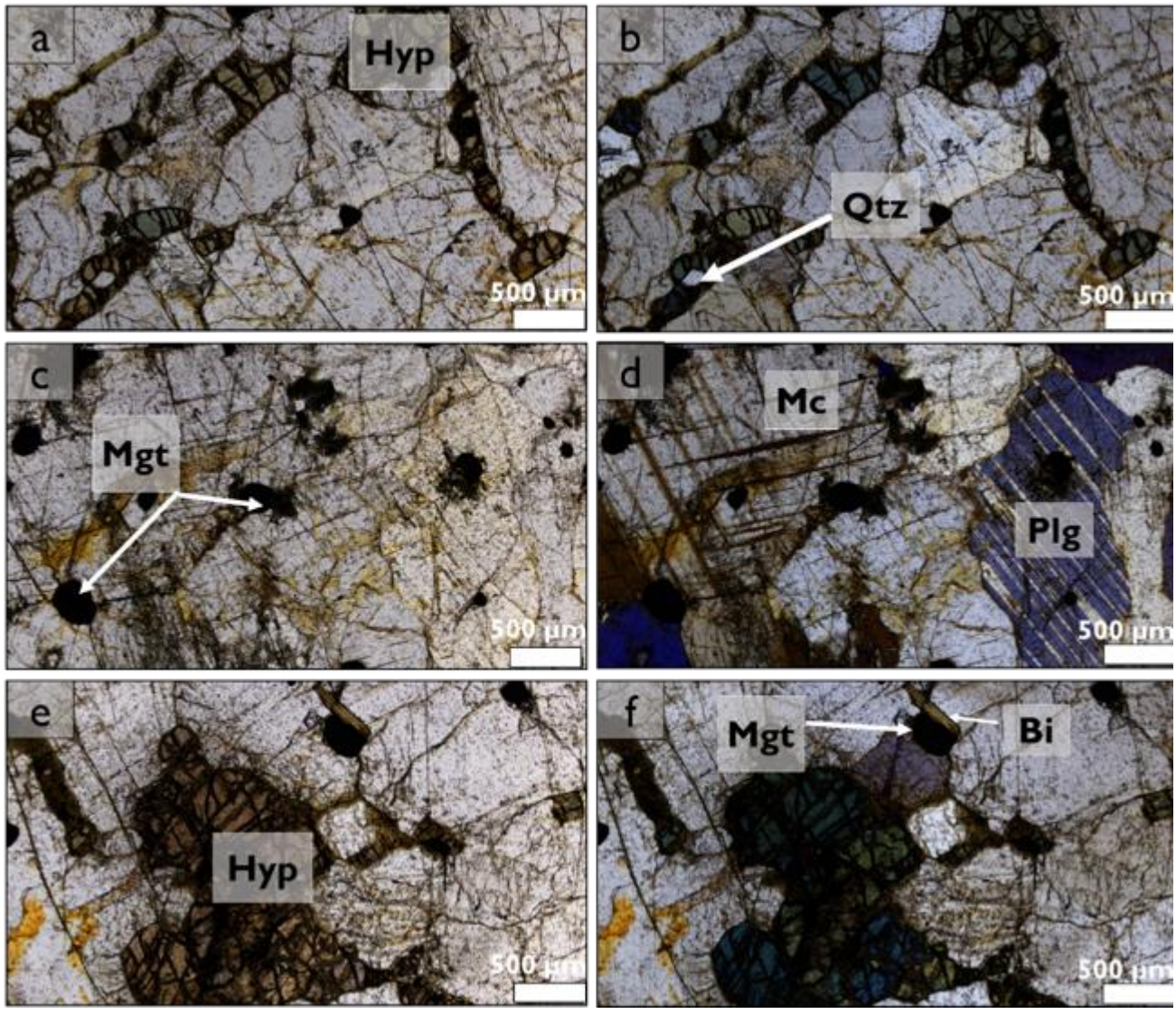


Figure 68: *Photomicrographs showing mineral phases and textures in the orbicular cores from the Henderson North orbicules: (a, b) Large phenocrysts of hypersthene containing small and rounded inclusions of quartz. (c, d) Microcline adjacent to plagioclase that contains poikilitic inclusions of magnetite. (e, f) Larger hypersthene phenocrysts in plagioclase.*

- **Shells**

Sharp contacts between cores and shells characterized by changes in mineral assemblages, textures and modal abundances (Figure 69) are features of these orbicules.

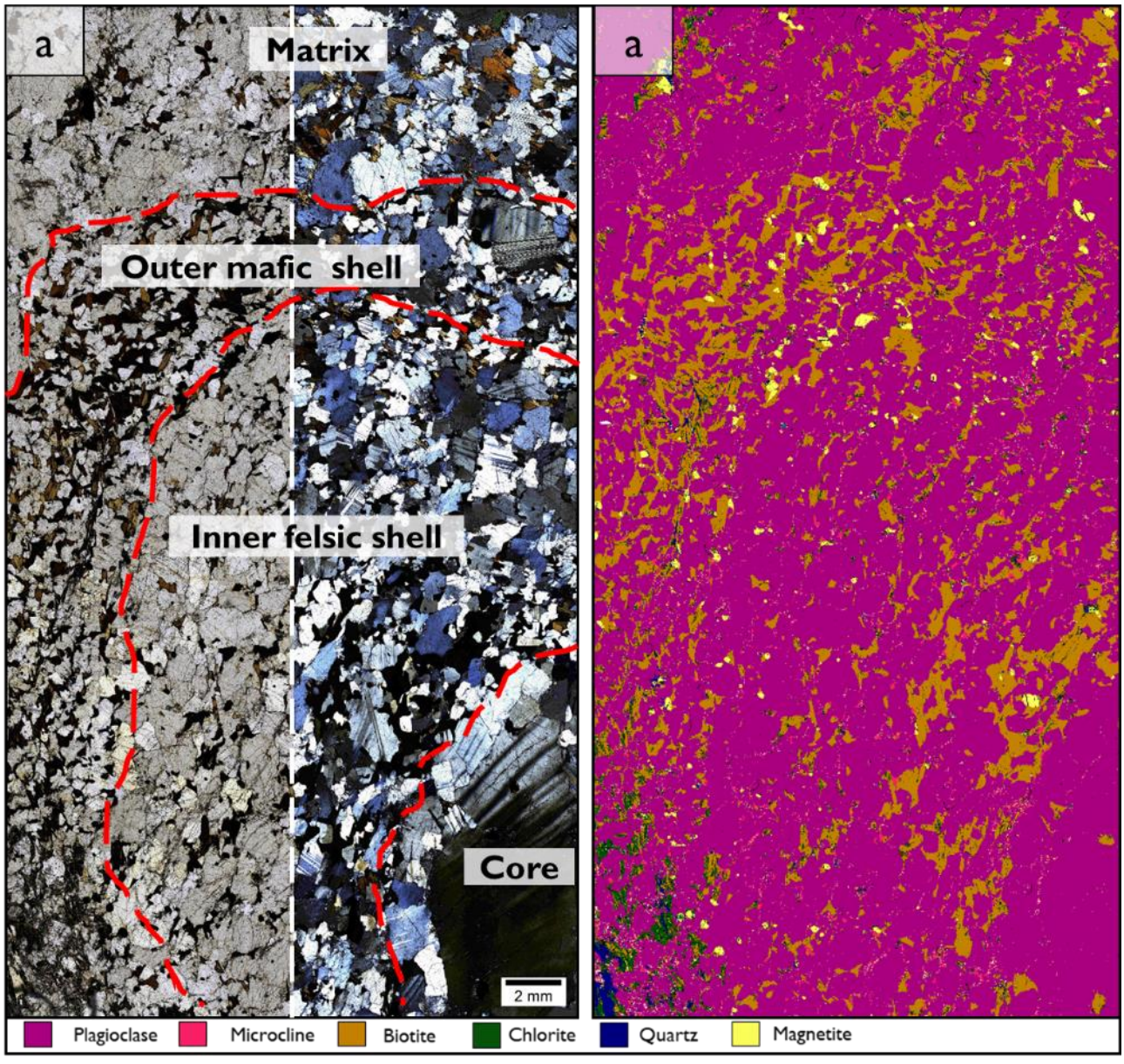


Figure 69: *Full thin section photomicrographs of the Henderson North orbicule sample SD-40-19B and corresponding TIMA image: (a) Plane–polarized (left) and cross-polarized light (right) full thin section images of sample SD-40-19B. (b) TIMA image of the sample showing alternating felsic (predominated by plagioclase and minor biotite) and mafic (predominated by biotite and minor plagioclase) shells. Sharp contacts (red-dotted lines) are observed between the core, shells and matrix.*

The Henderson North orbicules are characterized by alternating felsic inner (70% plagioclase, 20% biotite and accessory K-feldspar and quartz; Figure 69) and an intermediate outer (plagioclase (40%) and biotite (55%) and magnetite (4%), with accessory quartz and K-feldspars; Figure 69) shells. In the felsic inner shells, plagioclase occurs as the predominant phase. It occurs as subhedral (0.1-0.5 mm) grains that exhibit discontinuous twinning and contain inclusions of subhedral (0.1 mm) grains of magnetite and biotite.

Biotite also occurs as an interstitial phase surrounding smaller plagioclase grains (Figure 71e; f) and as poikilitic, inclusions in both plagioclase and microcline (Figure 71e). The transition from the felsic inner to intermediate outer shells is marked by sharp contacts and an increase in biotite and quartz modal abundances (Figure 71g, h). In the intermediate shells, plagioclase (40%) occurs as subhedral

(0.1-0.3 mm) grains that contain inclusions of subhedral and rounded to elongated (0.1 mm) grains of biotite and magnetite. Biotite grains occur as inclusions in plagioclase and microcline. In places, biotite occurs as an interstitial phase, where it surrounds larger plagioclase grains (Figure 71h). Microcline occurs as euhedral (0.1-0.2 mm) grains that contain inclusions of biotite. Quartz occurs as smaller and rounded (< 0.1 mm) accessory grains adjacent to feldspars and biotite. Locally, microcline, plagioclase and biotite are altered to clay and chlorite respectively (Figure 71c, d).

Similar to the cores, shells contain chalcopyrite and magnetite (Figure 70). The modal abundance of chalcopyrite and magnetite increases from cores to shells. Magnetite occurs as locally concentrated equigranular and subhedral (0.1 mm) grains that are adjacent to smaller and locally concentrated chalcopyrite grains (Figure 70).

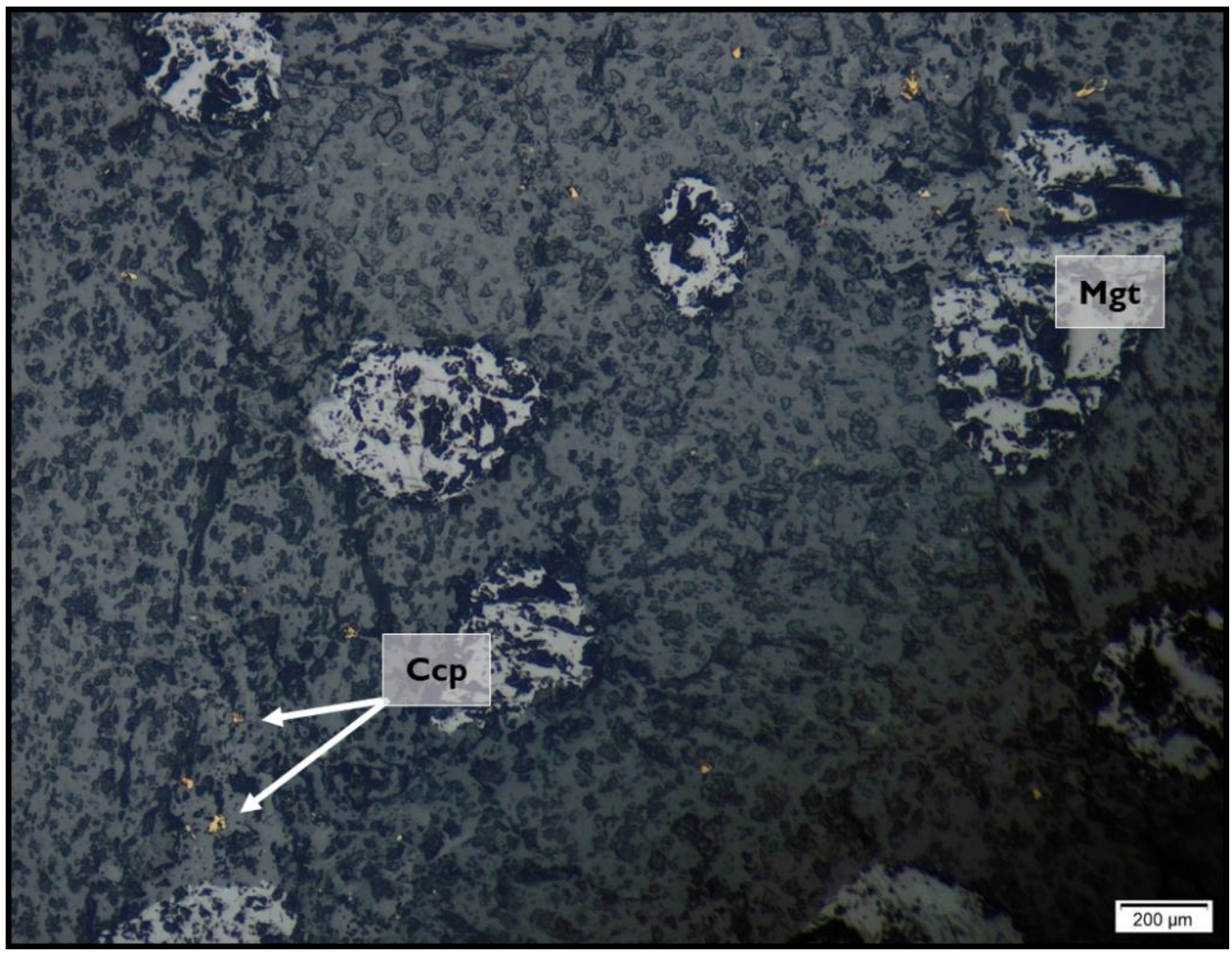


Figure 70: *Locally clustered magnetite grains adjacent to smaller chalcopyrite grains in the Henderson North orbicular shells.*

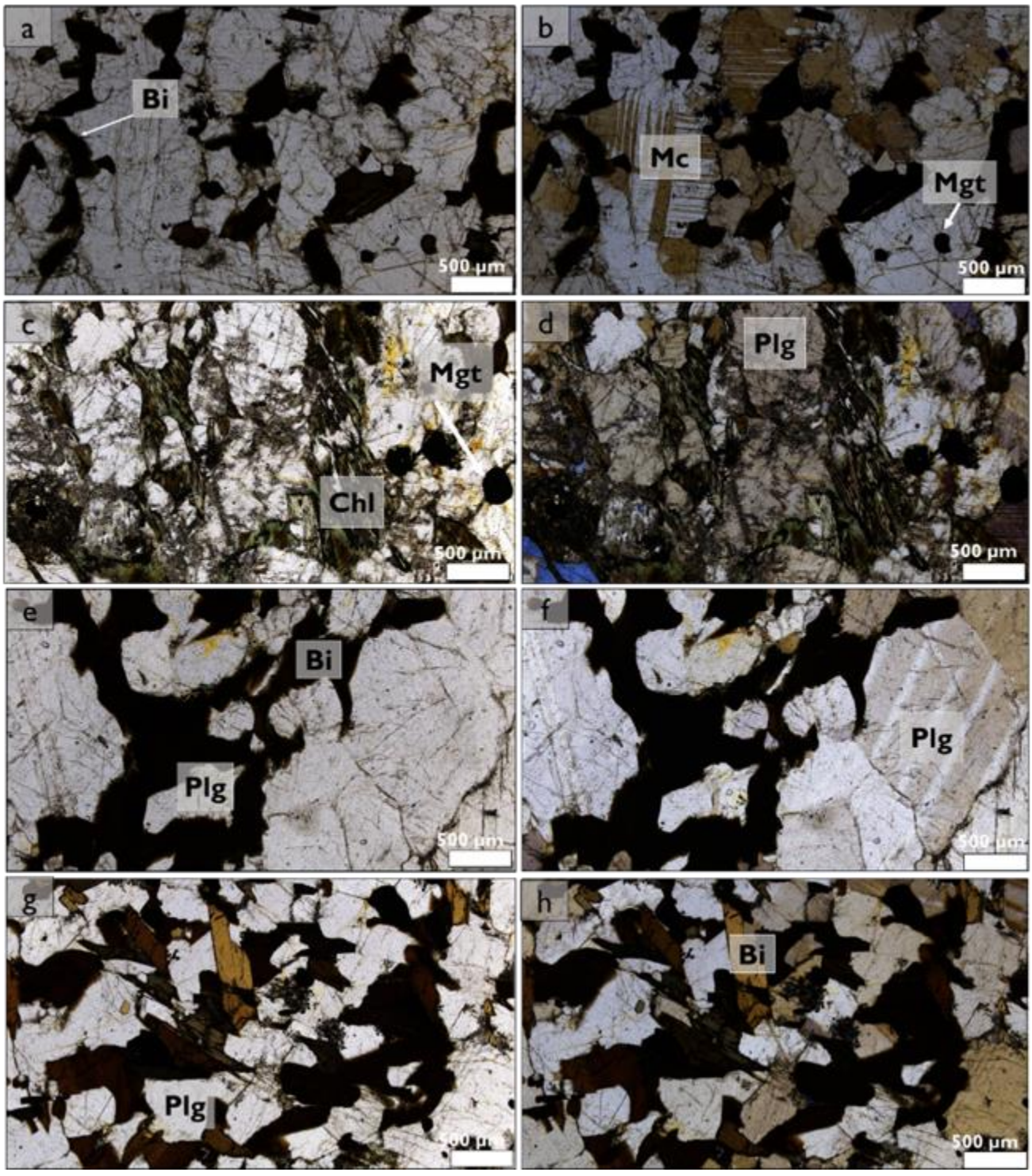


Figure 71: *Photomicrographs showing mineral phases and textures in the Henderson North orbicular shells: (a, b) Microcline adjacent to plagioclase grains that contain poikilitic inclusions of magnetite. Adjacent to microcline is anhedral and interstitial biotite enveloping feldspars. (c, d) Biotite is altered to chlorite and grows adjacent to plagioclase and magnetite. (e, f) Interstitial biotite surrounding euhedral grains of plagioclase. (g, h) Interstitial biotite surrounding plagioclase.*

- **Matrix characteristics**

The contacts between shells and the matrix are sharp in different samples of the Henderson North orbicules. The matrix compositions are similar to cores, and the matrix comprises (76%) plagioclase, biotite (10%), muscovite (3%), magnetite (3%), microcline (5%) and other accessory phases (Figure 72).

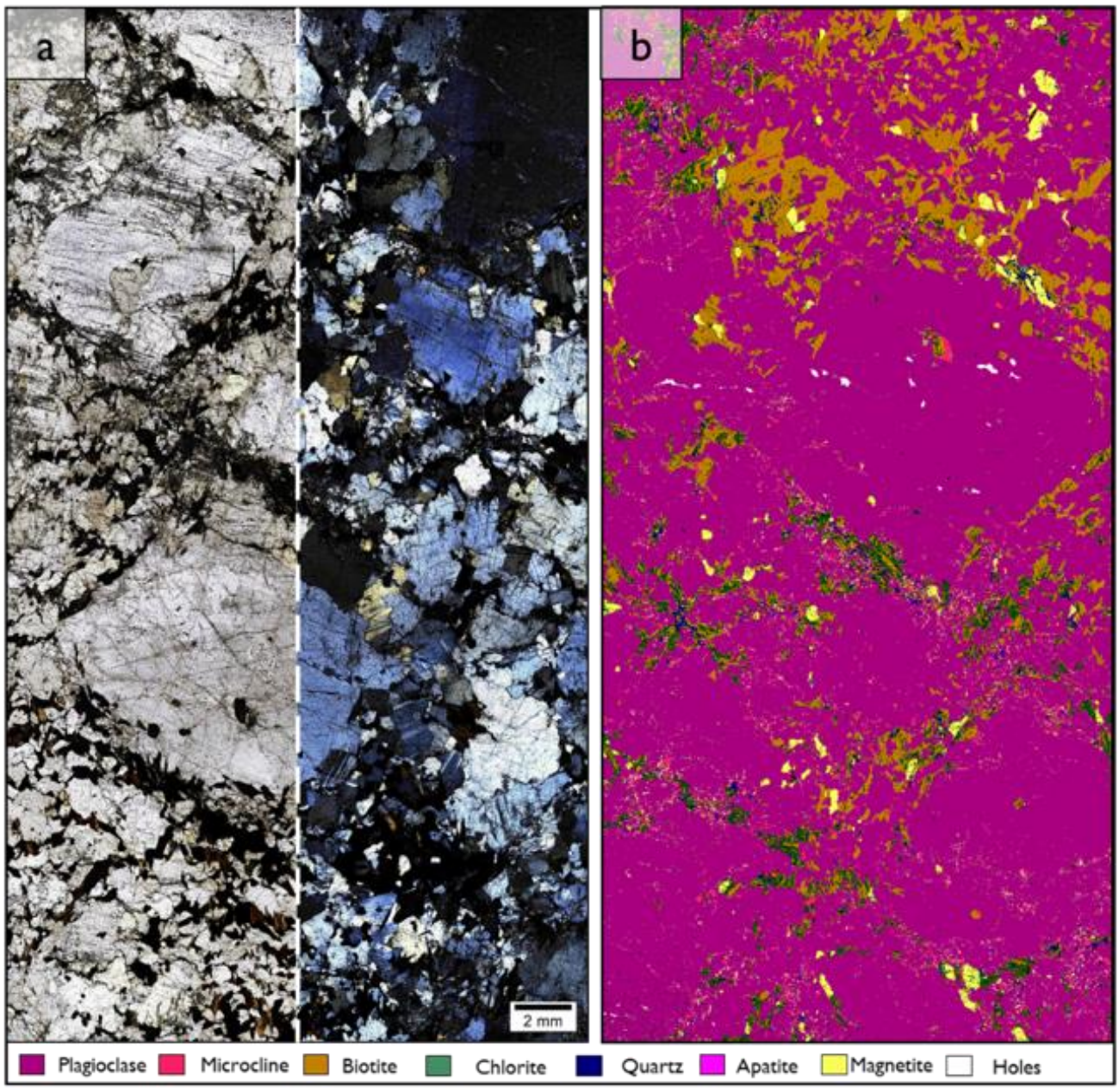


Figure 72: *Full thin section photomicrographs of the Henderson North orbicule matrix and corresponding TIMA image: (a) Plane–polarized (left) and cross-polarized light (right) full thin section images of sample SD-40-19D. (b) TIMA image of the sample showing the coarse-grained matrix comprising plagioclase, biotite, microcline, chlorite and magnetite as the predominant phases.*

Plagioclase occurs as subhedral (0.1-6 mm) grains that exhibit discontinuous twinning and contain inclusions of other smaller plagioclase grains, biotite and magnetite (Figure 73c, d). In places, plagioclase is altered to sericite. Biotite occurs as a second predominant phase and as subhedral to elongate (0.1-0.2 mm) grains. It occurs as inclusions in plagioclase and microcline in places (Figure 73g, h). Biotite occurs as an interstitial phase enveloping feldspars and grows into larger plagioclase grains (Figure 73a, b). It is locally altered to chlorite.

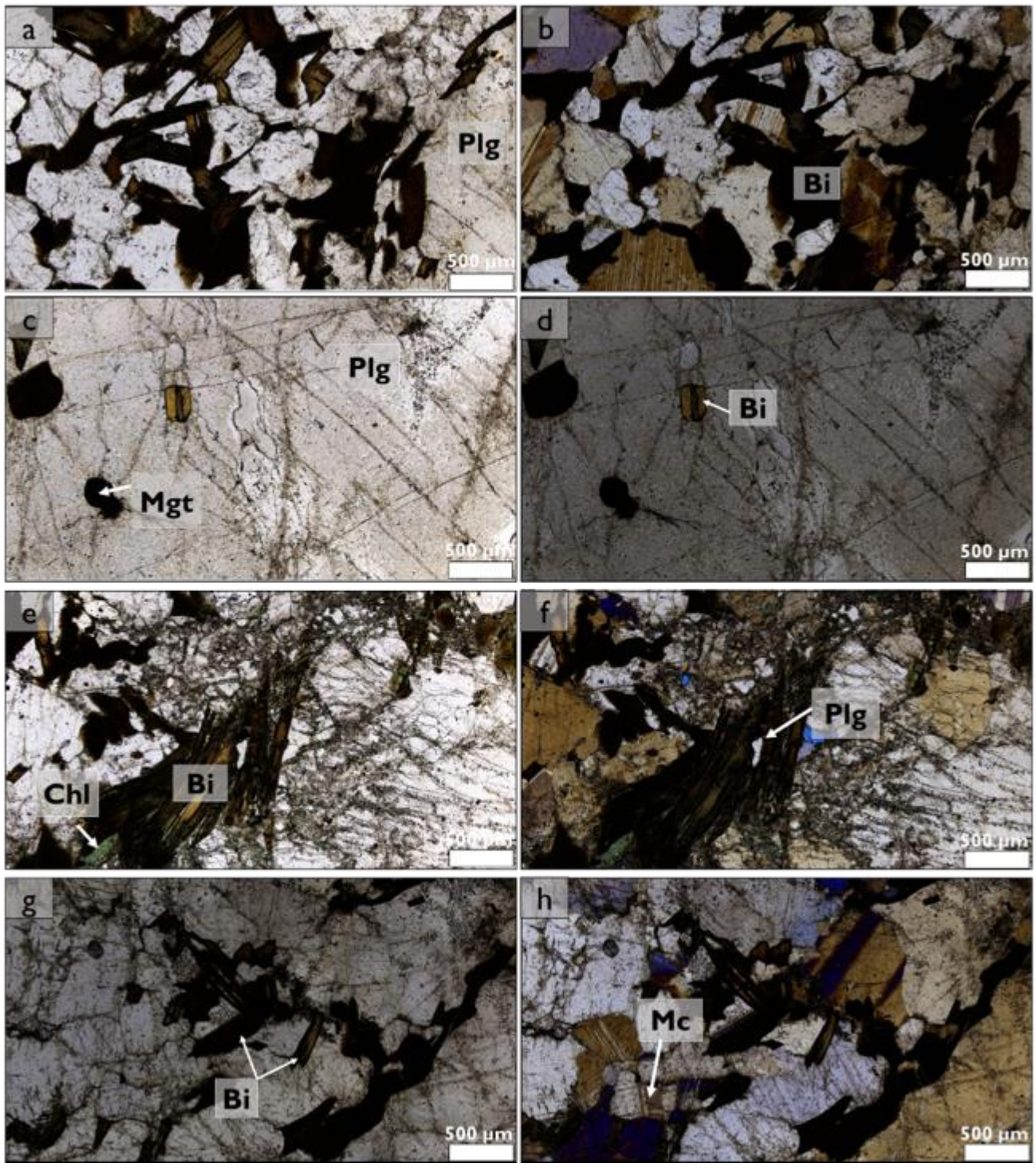


Figure 73: *Photomicrographs showing mineral phases and textures in the Henderson North matrix: (a, b) Interstitial biotite surrounding plagioclase and quartz. Biotite also occurs as small grains adjacent to plagioclase. (c, d) Poikilitic inclusions of euhedral biotite and magnetite in plagioclase. (e, f) Biotite containing plagioclase inclusions that occur adjacent to plagioclase. (g, h) Microcline and plagioclase surrounded by interstitial biotite. Biotite also occur as inclusions in plagioclase*

Chalcopyrite modal abundance increase from the shells to the matrix (Figure 74). Very small and disseminated (<< 0.5%) chalcopyrite grains and magnetite are observed in the matrix. Locally, massive chalcopyrite grains are replaced by magnetite (Figure 74) and they occur adjacent to the disseminated and smaller chalcopyrite grains (Figure 74).

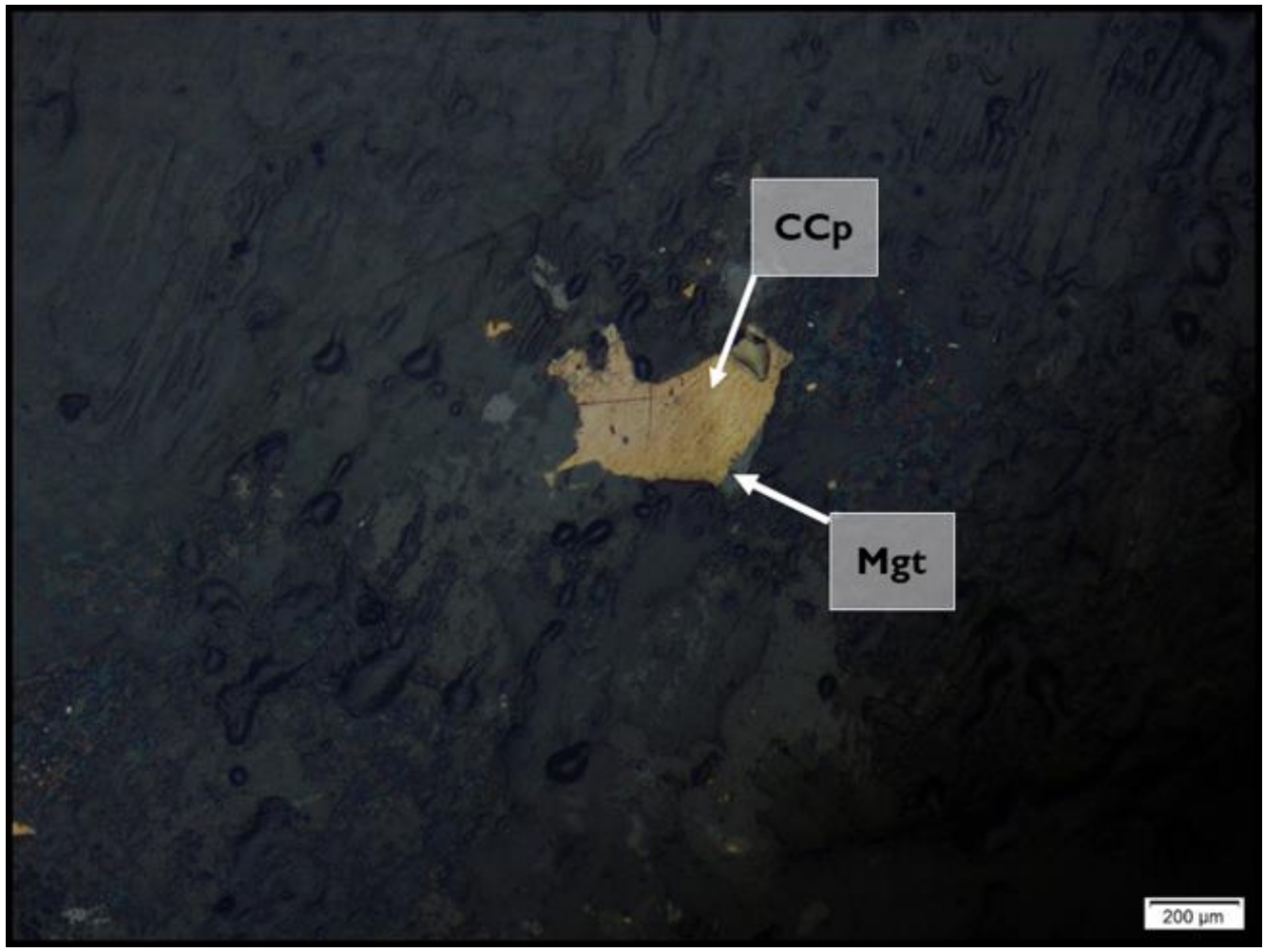


Figure 74: *Massive chalcopyrite grain replaced by magnetite. The massive chalcopyrite grain occur adjacent to smaller (<0.1 mm) and disseminated chalcopyrite grains.*

5.2.4.4. Henderson South

Based on the element maps of a cut slab from the Henderson South orbicular sample SD-55-24, Al and Si in the Henderson South orbicules are uniform in the cores and the matrix (Figure 75c, d, g). Zones yielding high Ca and Si intensities are observed as small and randomly distributed patches in the matrix and the radiating grains (Figure 75g, d). The shells, the matrix and the cores have high K, however, some places in the cores and the shells are less potassic (Figure 75f). The shells and the matrix are more enriched in Cu than the cores and in places, Cu yields high intensities in some parts of the matrix (Figure 75h).

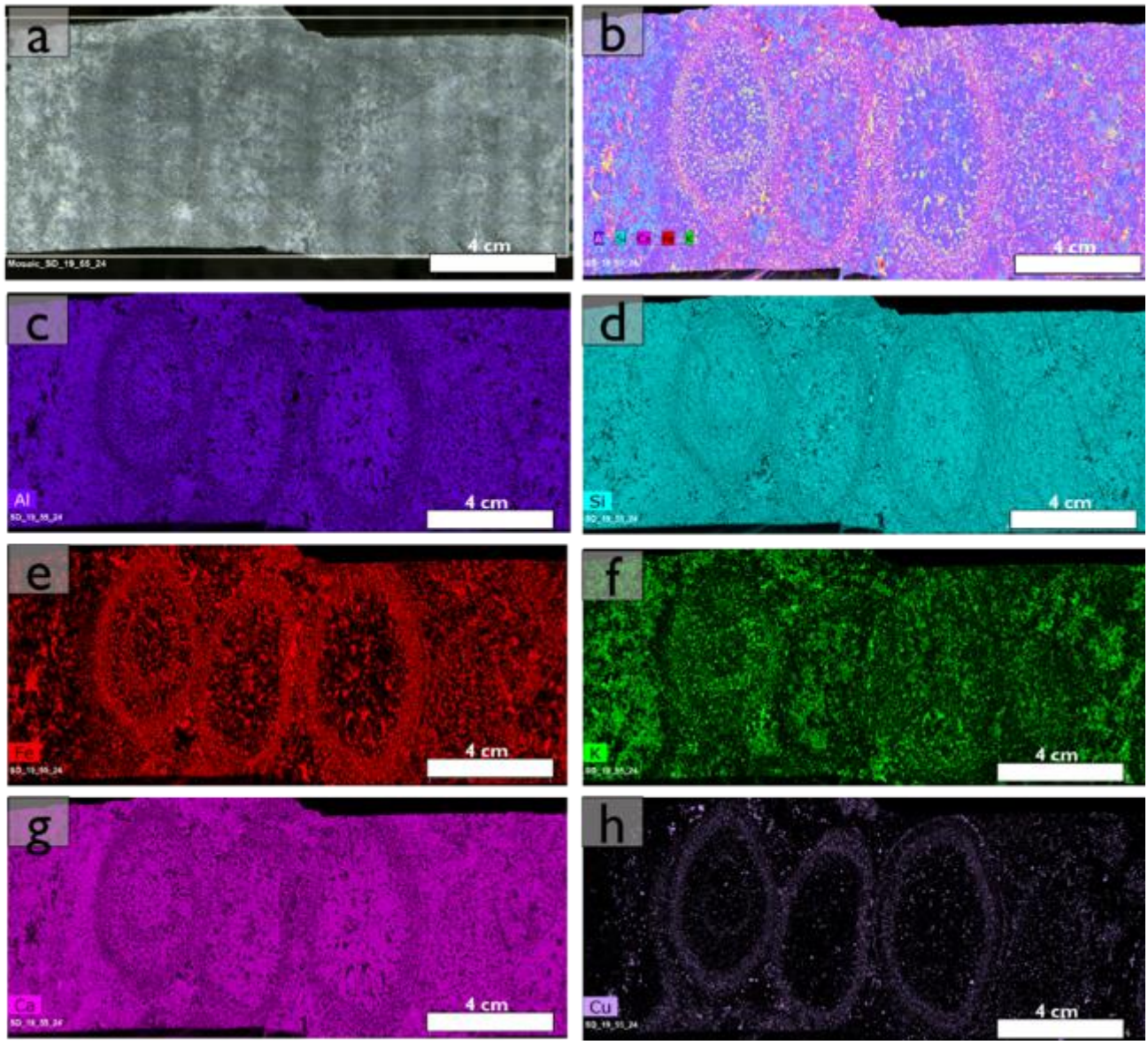


Figure 75: *Element maps of Henderson South sample SD-55-24: (a) A mosaic showing the mapped area in a white rectangle. (b) A composite of selected element showing elements detected via the normal map spectrum showing Al (purple), Si (blue), Ca (pink), Fe (red) and K (light green). (c) Element map showing uniform distribution of Al throughout the orbicule sample. (d)Element map showing the highest distribution and intensities of Si in the cores and the matrix. (e) Element map showing the highest distribution and intensities of Fe in shells and matrix. Cores are less ferroan. (f)Element map showing the distribution and concentrations of K in different parts of the orbicules. (g) Uniform Ca distribution throughout the orbicule sample. However, the radiating grains are less sodic (h) Element map showing the distribution and of Cu in different parts of the orbicules. The shells and some parts of the matrix are rich in Cu, and Cu yields the highest intensities in the matrix.*

Distinct shells, cores and matrix (Figure 76) characterize the Henderson South orbicules. The cores to shells and the shells to matrix boundaries are marked by gradational and sharp contacts (Figure 76), and the matrix composition is mineralogically similar to core compositions.

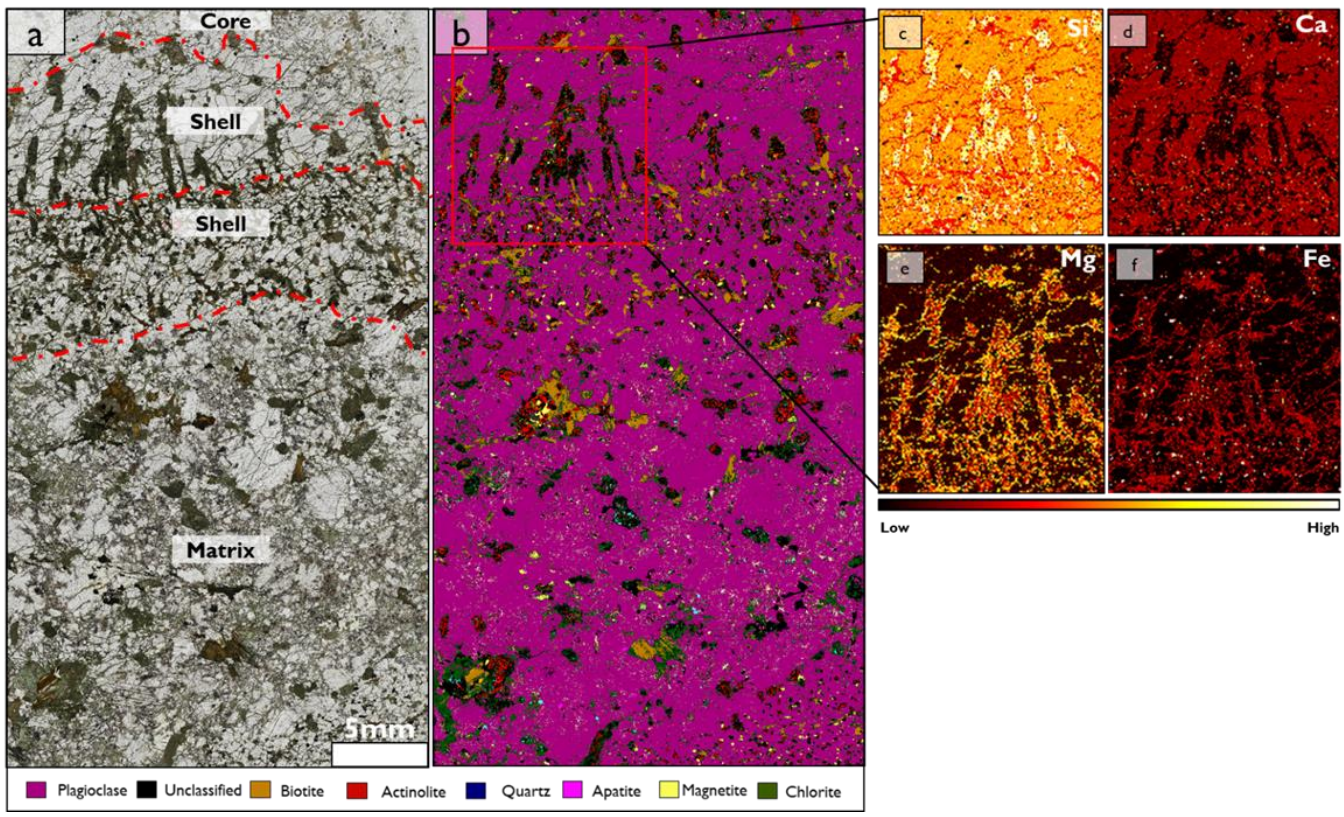


Figure 76: *Full thin section photomicrographs of the Henderson South orbicule sample SD-55-24B and the corresponding TIMA images: (a) Plane–polarized full thin section images of sample SD-55-24B. (b) TIMA image of the sample showing a medium-grained core that is composed of plagioclase, quartz and unclassified radiating grains (black). (c)TIMA image of the selected area (red box in image b) showing that the radiating grains have high silica than the surrounding feldspars. (d) TIMA image of the selected area showing that the radiating grains have no calcium and the calcium content in the grains is lower than in the surrounding feldspars. (e, f) TIMA images of the selected area showing that the radiating grains are enriched in iron and magnesium relative to the surrounding calcic plagioclase.*

- **Cores**

The cores comprise plagioclase (66%), chlorite (8%), quartz (5%), biotite (3%), an unclassified phase (10%) and other accessory phases (Figure 77).

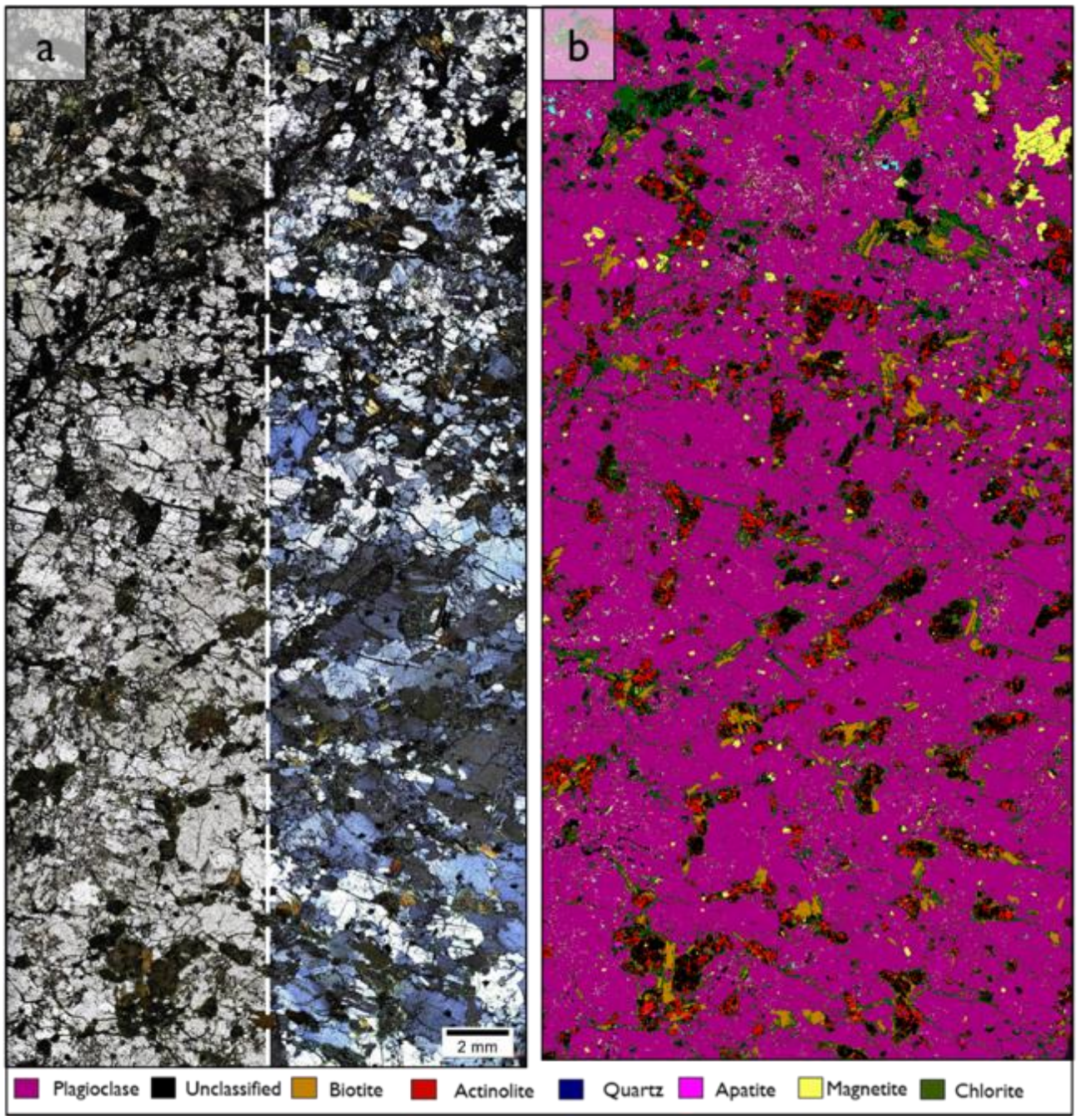


Figure 77*: Full thin section photomicrographs of the Henderson South orbicule core sample SD-55-24C and corresponding TIMA image: (a) Plane–polarized (left) and cross-polarized light (right) full thin section images of the sample. (b) TIMA image of the sample showing a medium-grained core composed of plagioclase, unclassified grains, quartz, biotite, chlorite and accessory magnetite.*

Plagioclase occurs as anhedral to subhedral (0.1-2 mm) grains that contain small inclusions of anhedral biotite (Figure 78a, b), muscovite, apatite, and magnetite (Figure 78a, b). Locally, plagioclase is fractured, and the fractures are filled in by the green chlorite, and quartz (Figure 78a). The second most abundant phase are the elongated and rounded grains of a highly altered mineral phase rich in silica, magnesium, and iron (Figure 76). It is not easily classified in TIMA, however, based on the micro-XRF element maps and element maps from TIMA (Figure 76), it is most likely hypersthene that has been altered to actinolite (Figure 77; Figure 78a, b) and from now on, the unclassified grains will be referred to as hypersthene. Quartz occurs as (0.1-0.3 mm) grains that are poikilitic inclusions in elongated grains of altered hypersthene. The more rounded grains of quartz and altered hypersthene

occur as inclusions in plagioclase (Figure 78a) and they are adjacent to quartz and microcline. Biotite occurs as anhedral (0.1- 0.2 mm) grains that are altered to chlorite. In places, biotite occurs as poikilitic inclusions in plagioclase and as an interstitial phase surrounding muscovite, quartz and plagioclase (Figure 78c, d). In places, biotite contains inclusions of epidote (Figure 78c, d). Microcline occurs as the least dominating phase. It occurs with quartz and plagioclase as small subhedral (0.2 mm) grains containing inclusions of magnetite.

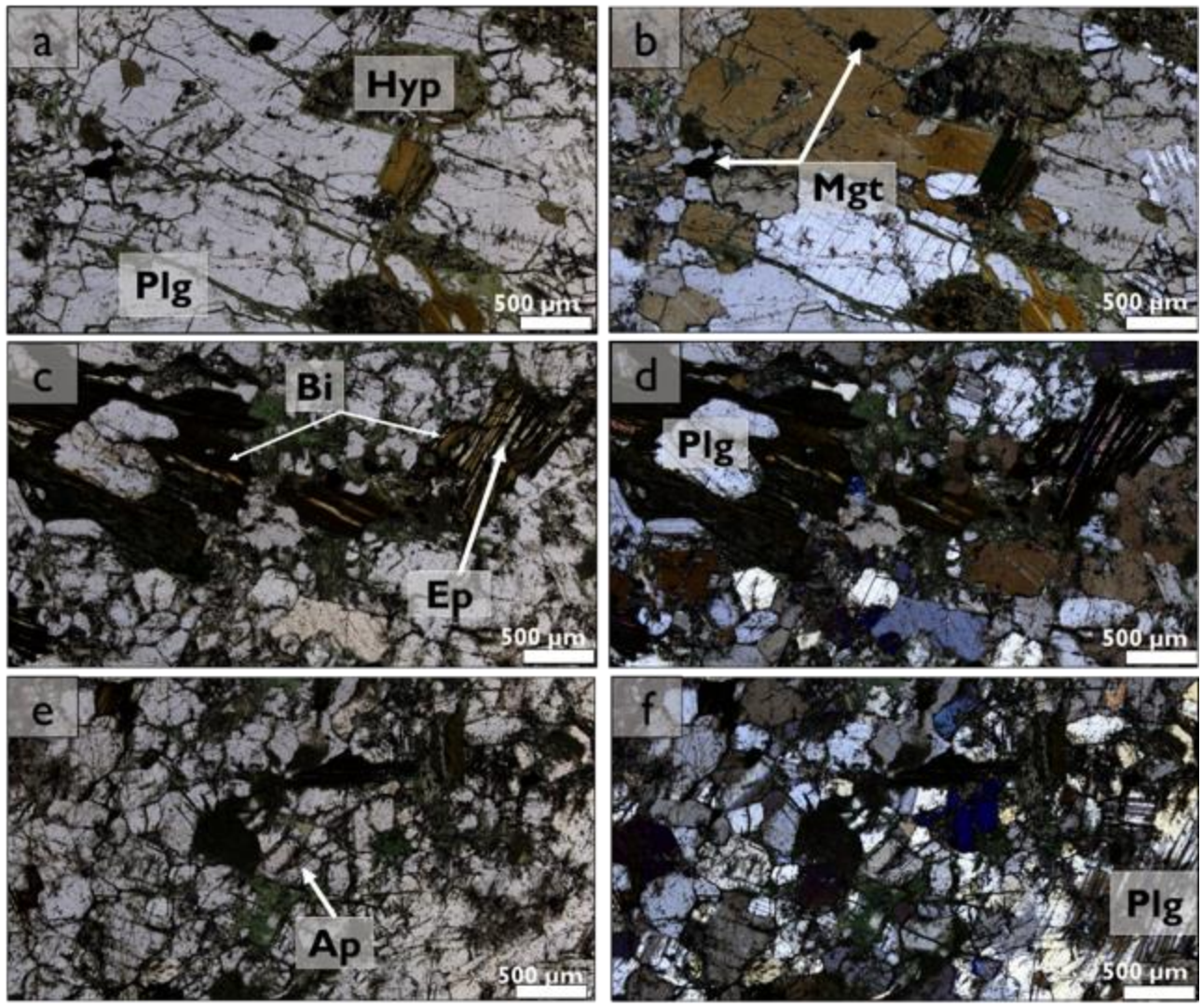


Figure 78: *Photomicrographs showing mineral phases and textures in the Henderson South orbicular cores: (a, b) Poikilitic inclusions of biotite and altered hypersthene in plagioclase. Plagioclase is highly fractured and grains of quartz intergrown with altered hypersthene fill in the fractures. (c, d) interstitial biotite occurring around plagioclase and containing elongated grains of muscovite. (e, f) Small plagioclase grains adjacent to quartz. Plagioclase is altered to sericite and contains inclusions of magnetite and smaller euhedral apatite.*

The cores contain chalcopyrite and magnetite that are hosted in the radiating grains of the altered hypersthene, biotite, and minor plagioclase. Chalcopyrite occurs as smaller (< 0.1 mm; <1%) and disseminated grains that are adjacent to the slightly bigger (0.1- 0.2 mm) grains of subhedral magnetite (Figure 79).

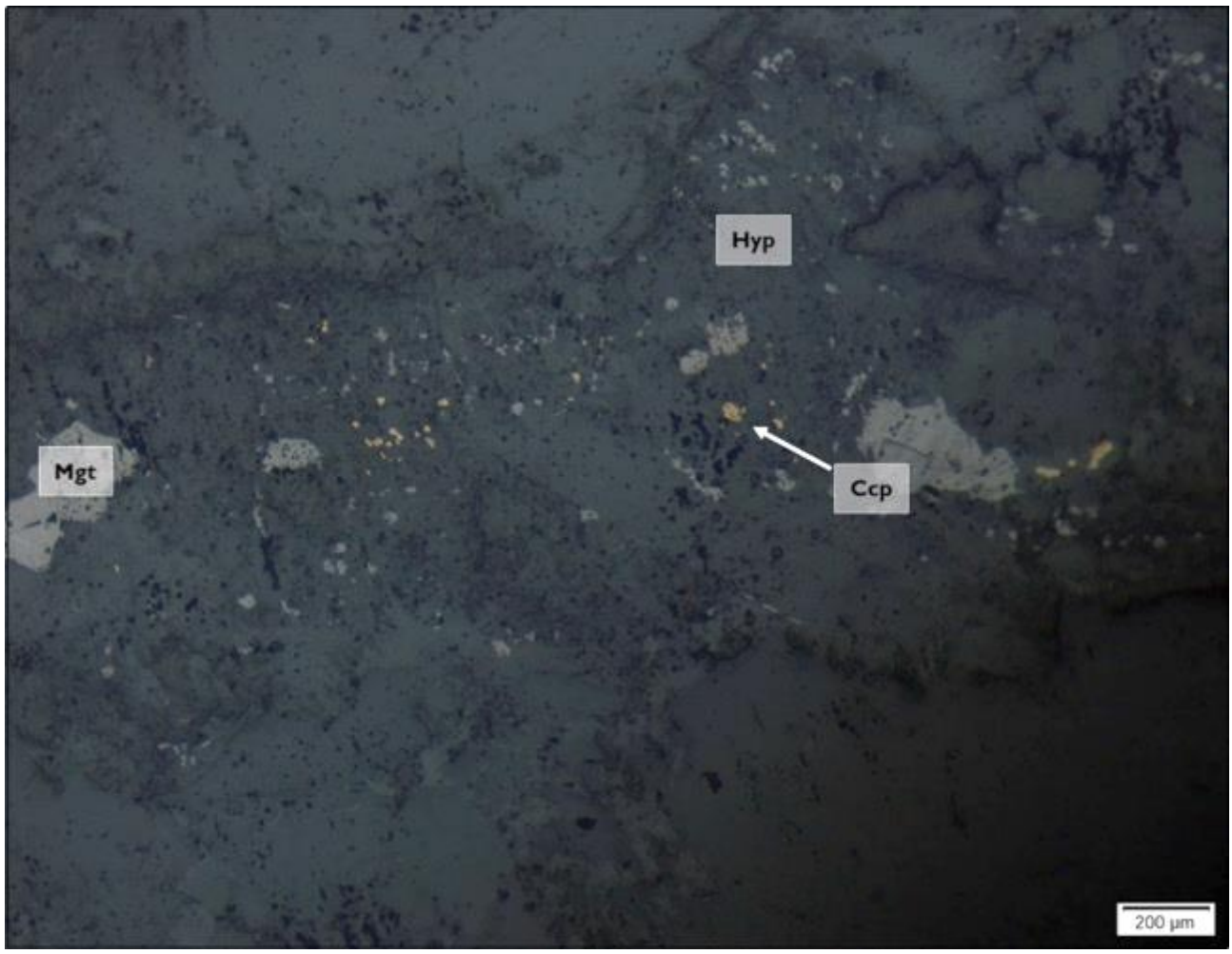


Figure 79: *Locally concentrated chalcopyrite grains adjacent to magnetite in radiating altered hypersthene grain.*

- **Shells**

The Henderson South orbicules are characterized by alternating intermediate shells comprising plagioclase (60%), hypersthene (20%), quartz (10%), and biotite (5%) with accessory microcline and magnetite (Figure 76). Plagioclase and quartz occur as the predominant phases (Figure 76). They occur as equigranular (0.1-0.2 mm) grains that form polygonal textures (Figure 80g, h). These equigranular grains occur adjacent to microcline and biotite. Locally, plagioclase contains inclusions of magnetite, quartz and altered hypersthene (Figure 80c, d), and it is locally altered to sericite. Adjacent to the equigranular quartz and plagioclase is biotite, which occurs as anhedral to subhedral (0.1 mm) grains that locally contain inclusions of quartz (Figure 80g, h).

Crosscutting the felsic shells are elongate and subhedral grains of quartz and altered hypersthene (Figure 80a, b). The altered hypersthene grains (0.1-0.2 mm) occur as radiating grains that form a radiating texture that grows into plagioclase and other adjacent phases (Figure 80a, b). Similar to Hoogkraal Lease orbicules, the radiating texture is only restricted to the shells (Figure 80a, b). These radiating grains contain inclusions of biotite, ilmenite, apatite, albite and magnetite (Figure 80b). Accessory microcline occurs as small (0.1 mm) grains adjacent to the equigranular and polygonal plagioclase and quartz grains. The shells contain chalcopyrite and magnetite hosted in the radiating

altered hypersthene, biotite and plagioclase. Chalcopyrite concentration remains relatively the same in cores and shells.

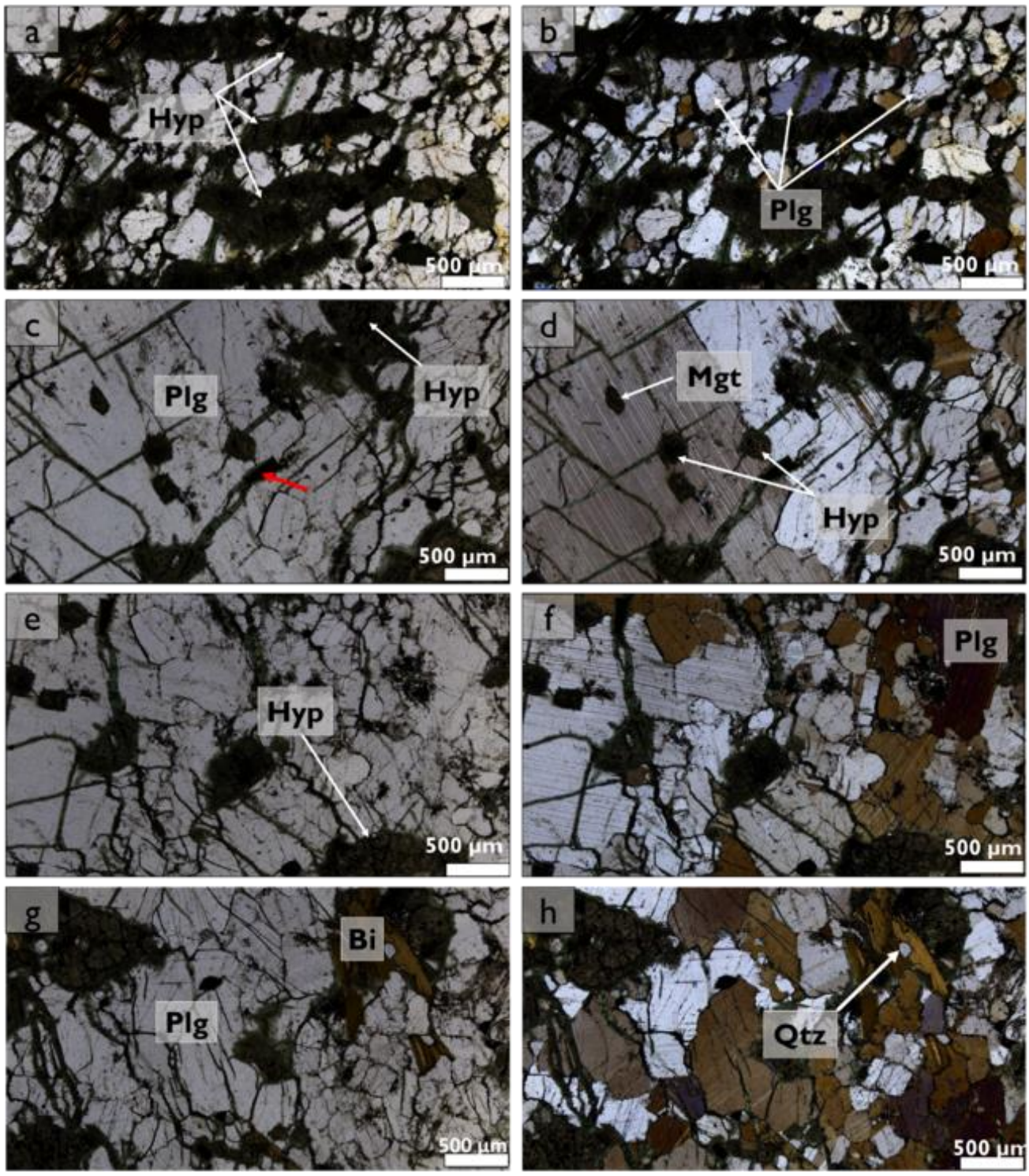


Figure 80: *Photomicrographs showing mineral phases and textures of Henderson South orbicular shells: (a, b) Radiating and elongated grains of altered hypersthene and quartz that are restricted to the shells. (c, d) Poikilitic inclusion of rounded and altered hypersthene and magnetite in plagioclase. Plagioclase is altered to clay, and it is highly fractured locally and altered hypersthene fills in these fractures. (e, f) Smaller and subhedral grains of quartz and plagioclase occurring adjacent to bigger plagioclase grains containing poikilitic inclusions of magnetite. (g, h) Biotite adjacent to plagioclase containing quartz inclusions. Plagioclase occurs adjacent to altered hypersthene that grows both as inclusions and as fractures in plagioclase. Locally, smaller plagioclase grains form granoblastic and equigranular textures, where smaller and equal grains grow adjacent to each other.*

- **Matrix characteristics**

Sharp contacts mark the transitions from the shells to the matrix. The matrix compositions are similar to the core compositions (Figure 81). It is composed of plagioclase (67%), chlorite (9%), quartz (6%), biotite (3%), altered hypersthene (2%) and other accessory phases (Figure 81).

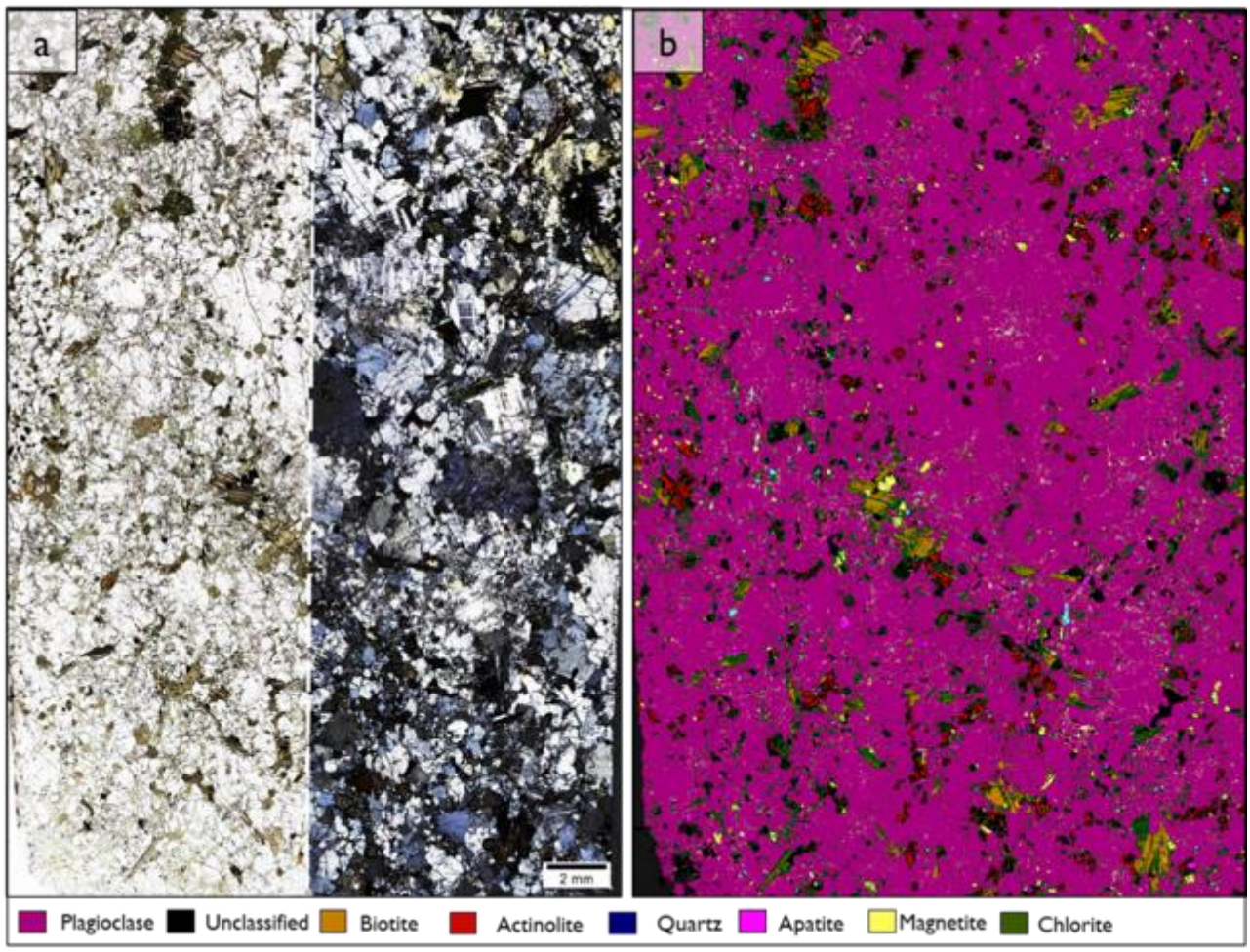


Figure 81: *Full thin section photomicrographs of the Henderson South orbicule matrix sample SD-55-24D and corresponding TIMA image: (a) Plane–polarized (left) and cross-polarized light (right) full thin section images of sample SD-55-24D. (b) TIMA image of the sample showing a medium-grained matrix predominated by plagioclase, quartz, chlorite, biotite and magnetite.*

Plagioclase occurs as subhedral to euhedral (0.1-0.3 mm) grains adjacent to quartz and biotite (Figure 83e, f). In places, plagioclase is altered to sericite and contains inclusions of rounded and altered hypersthene, smaller muscovite, quartz, magnetite, and apatite. Adjacent to the polygonal plagioclase grains is quartz Figure 83g, h) that occurs adjacent to microcline and altered hypersthene grains that grow into plagioclase. T-Junctions (120 ^{o}) angles are formed where equigranular plagioclase and quartz grains occur adjacent to each other forming polygonal textures (blue arrow; Figure 83e, f). Biotite occurs as anhedral to subhedral (0.1-0.2 mm) grains that occur both as inclusions and adjacent to plagioclase. It contains inclusions of magnetite, quartz (Figure 83c, d) and muscovite. Locally, biotite is altered to chlorite. It also occurs adjacent to altered hypersthene and quartz, and as poikilitic inclusions in altered hypersthene. Altered hypersthene occurs as rounded and elongated (0.1-0.2 mm) grains that grow into plagioclase and quartz. These occur as disseminated grains in the matrix. Locally, hypersthene contains inclusions of quartz and rounded (0.1-0.2 mm) grains of magnetite. The sulphide mineralization (1%) in the matrix differs from the cores and shells. The matrix contains massive chalcopyrite grains that are replaced by bornite (Figure 82). Bornite appears to occur as inclusions in

chalcopyrite where it replaces chalcopyrite (Figure 82a, b). Adjacent to the massive bornite and chalcopyrite grains are small and locally clustered chalcopyrite and bornite grains (Figure 82a, b).

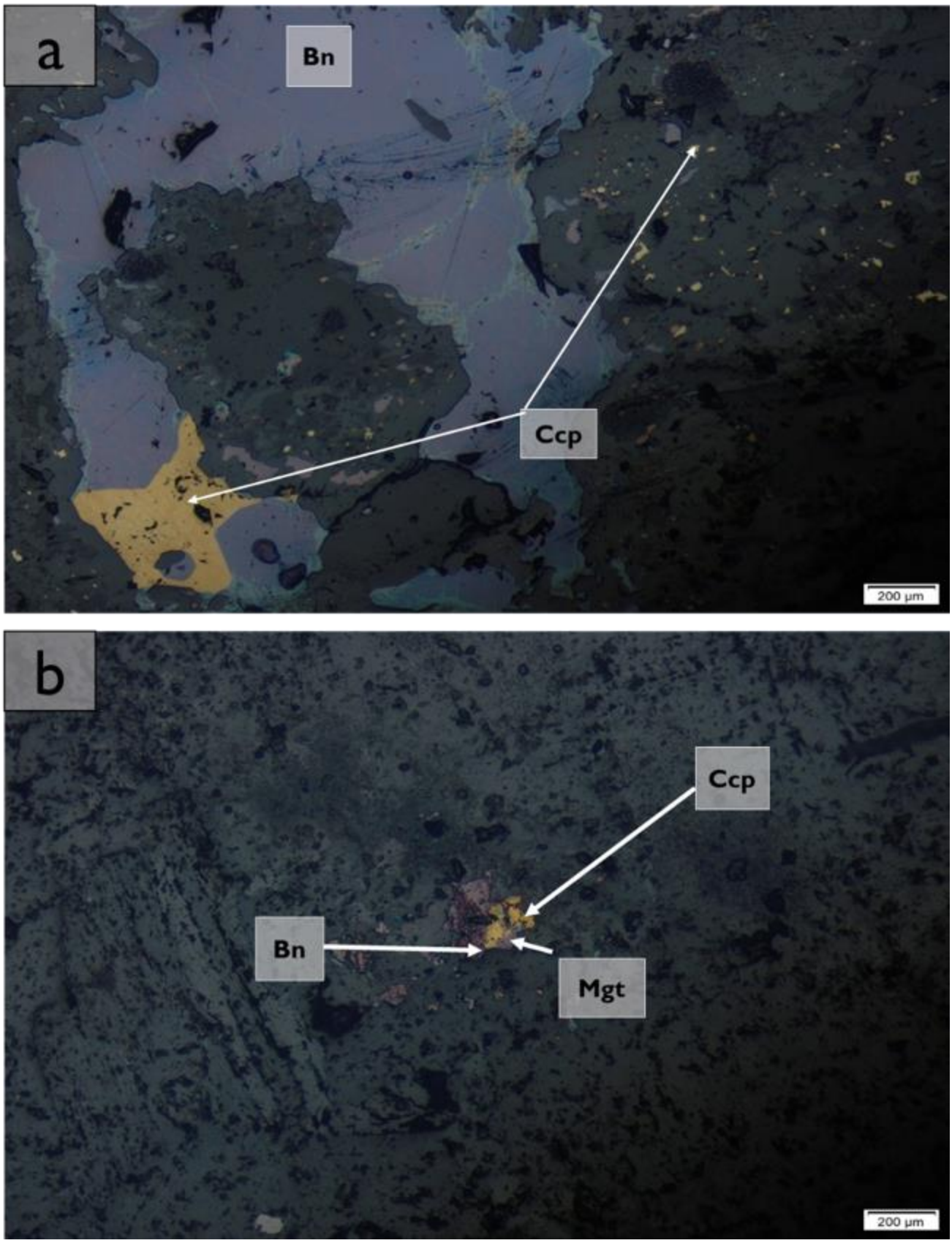


Figure 82*: Photomicrographs of the Henderson South matrix: (a) Large chalcopyrite grains that are replaced by bornite. These are adjacent to smaller chalcopyrite and bornite grains. (b) Smaller chalcopyrite replaced by bornite.*

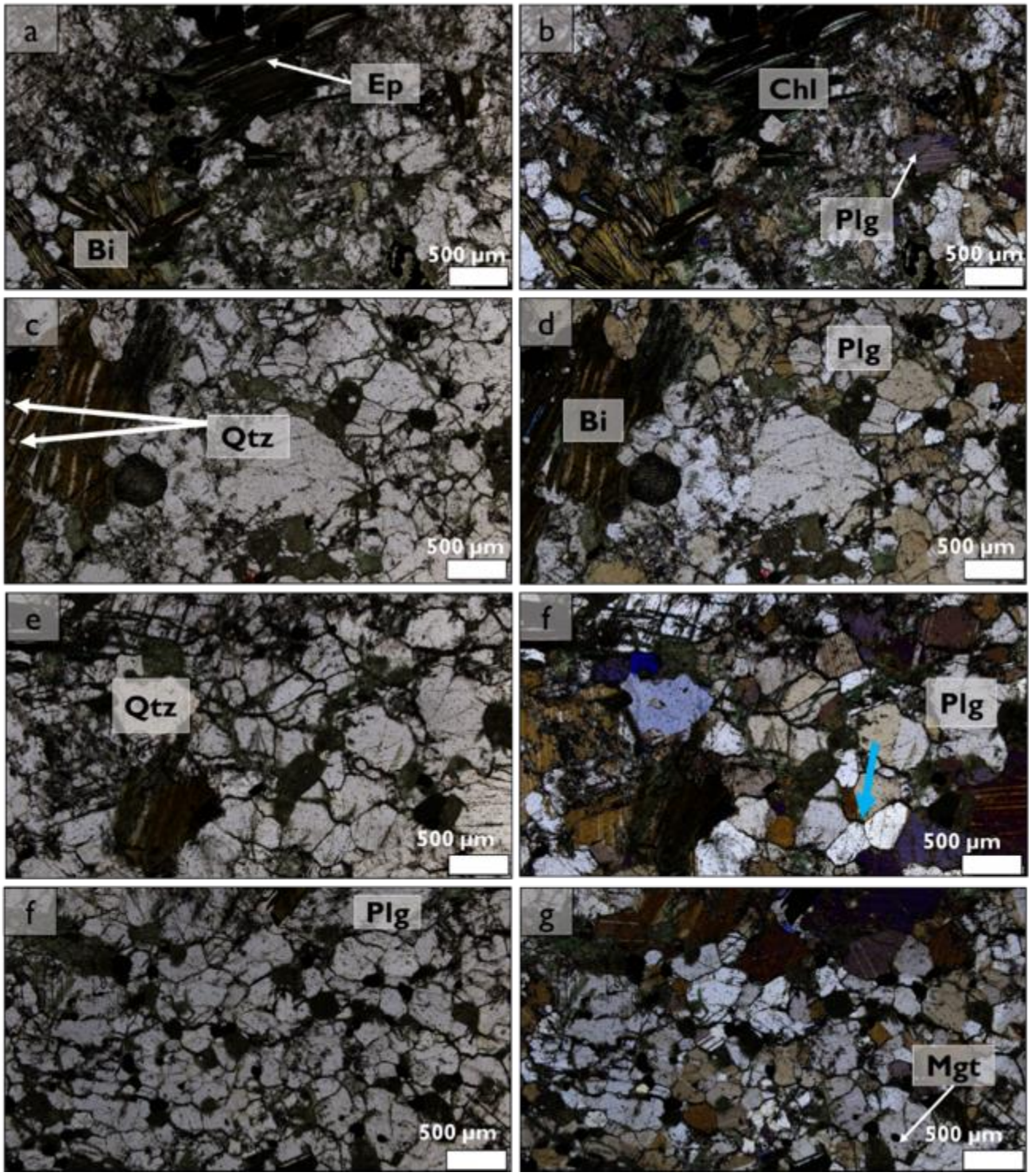


Figure 83: *Photomicrographs showing mineral phases and textures in the matrix from the Henderson South orbicules: (a, b) Altered biotite grains and chlorite adjacent to smaller and altered plagioclase grains. (c, d) Biotite containing inclusions of quartz adjacent to smaller plagioclase grains. (e, f) T-junctions (120 °) angles forming where quartz and plagioclase equigranular grains form polygonal textures (blue arrow). Biotite occurs as subhedral grains adjacent to quartz and plagioclase. Locally, plagioclase is altered to sericite. (g, h) Equigranular grains of plagioclase and quartz, where plagioclase contains inclusions of magnetite.*

5.2.5. Summary of the petrographic observations

The Koperberg Suite orbicules share some similarities, but they are also different. All the Koperberg Suite orbicules are hosted in different lithologies ranging from felsic to mafic in composition. The orbicules are characterized by felsic matrices dominated by plagioclase, biotite, hypersthene, and K-feldspar.

The cores are generally medium-grained with abundant plagioclase with minor biotite, alkali-feldspars, magnetite and accessory chlorite and epidote. However, the Henderson North, Hoogkraal Lease and Henderson South orbicular cores also contain hypersthene, which is not the case in the Orbicule Koppie orbicules. Disseminated chalcopyrite and magnetite grains that occur as poikilitic inclusions in hypersthene, biotite and plagioclase are abundant in the cores. The modal abundances of chalcopyrite and magnetite generally decrease from cores to shells. Chalcopyrite is replaced by magnetite in the cores.

The different orbicule localities are characterized by alternating intermediate (roughly equal amounts of plagioclase, alkali-feldspar and minor mafic minerals) and felsic (dominated by feldspars with minor mafic minerals) shells. This is not the case in Orbicule Koppie orbicules, which are characterized by single shells.

The Henderson South and the Hoogkraal Lease orbicule shells contain hypersthene, which forms the radiating textures, restricted only to the shells. However, the Hoogkraal Lease orbicules are unique, as mafic shells comprising (> 90%) biotite appear to be in continuity with the radiating hypersthene grains. Hypersthene grains appears to be cut by the concentric and radiating grains of biotite. Sharp contacts mark the transitions from the shells to the matrices and the grain size and textures generally change from the shells to the matrices.

The matrices are comparable in composition to the cores. The matrices are medium-grained, but this is not the case in Orbicule Koppie orbicules, which are characterized by a coarse-grained to pegmatitic matrix. The modal abundance of chalcopyrite and magnetite generally increases from the shells to matrices.

The matrices from all the localities contain chalcopyrite and magnetite in higher modal abundances than in the shells and the cores. However, chalcopyrite occurs as massive and disseminated grains in the matrices compared to the fine-grained and disseminated chalcopyrite in the cores and shells. In addition, the Henderson South orbicules contain chalcopyrite that is replaced by bornite and magnetite.

.

5.3. Geochemistry

5.3.1. Regional *in-situ* compositions of mineral phases

In this section, *in*-situ major element compositions of plagioclase and biotite in the massive (anorthosite and diorite) and the different orbicular structures (cores, shells, and matrices) of the orbicular rocks from the Koperberg Suite were analyzed to understand the evolution of the magma(s) and the processes that were operating in the magma during the crystallization and formation of orbicular rocks. The data are presented in this section.

Mean ($\overline{x}$) magnesium numbers of biotite (molecular ratio Mg# = MgO/ (MgO +FeO) *100), together with mean plagioclase An contents (molecular ratio An = Ca/ ($Ca+Na_2O+K_2O$)*100) are used to compare the orbicules and the surrounding massive Koperberg Suite rocks. The plagioclase grains that were analyzed in the different orbicular structures in both the massive Koperberg Suite rocks and in orbicules were plotted on the ternary orthoclase-albite-anorthite diagram (Figure 84) of Deer et al. (1992).

The Koperberg Suite orbicules contain plagioclase that are andesine to labradorite in composition (Figure 84b) and characterized by An_{30-70} (Figure 84b). The plagioclase compositions in the orbicules are within range with plagioclase analyzed in anorthosites and diorites in contact with orbicules (Figure 84a). The Orbicule Koppie orbicules, diorite and anorthosite in contact with the orbicules are more calcic than the Nababeep Gneiss ($\overline{x} = An_{14}$; McCarthy, 1976) in the vicinity of the orbicule outcrop (Figure 85).

Although slightly calcic ($\overline{x} = An_{48}$), the Orbicule Koppie orbicules are within range of the mica diorite (An_{43}), the pyroxene diorite (An_{48}) and the pyroxene leucodiorite (An_{46}) that were analyzed by Van Zwieten et al. (1996) and diorite and anorthosite that we analyzed in this study (Figure 85). The Concordia Granite ($\overline{x} = An_{26}$; McCarthy, 1976) in contact with the Hoogkraal lease, the Henderson North and the Henderson South orbicules contain more sodic plagioclase than the more calcic plagioclase in the orbicules from these localities (Figure 85).

Similar to the Orbicule Koppie orbicules, Hoogkraal Lease, Henderson North and Henderson South orbicules contain plagioclase that is within range and slightly more calcic than the pyroxene diorite, the mica diorite and the pyroxene leucodiorite analyzed by Van Zwieten et al. (1996). Intra-locality variation in An contents is documented in the following section.

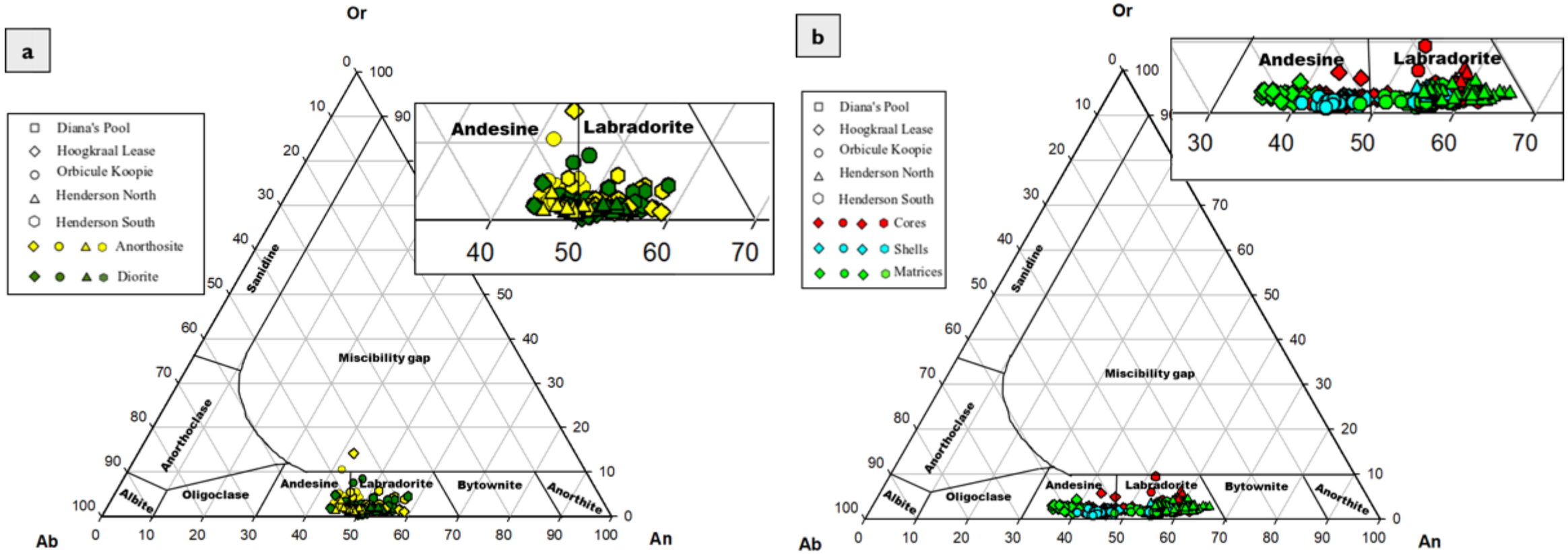


Figure 84: *A classification of feldspars from the Koperberg Suite massive rocks and the orbicules on a ternary albite-anorthite-orthoclase diagram: (a) The Massive Koperberg Suite rocks plotted on the feldspar classification diagram. They range from andesine to labrodorite in composition. (b) Plagioclase in the Koperberg Suite orbicules plotted on the feldspar classification diagram. Similar to the massive Koperberg Suite rocks, plagioclase in the orbicules ranges between andesite and labradorite in composition.*

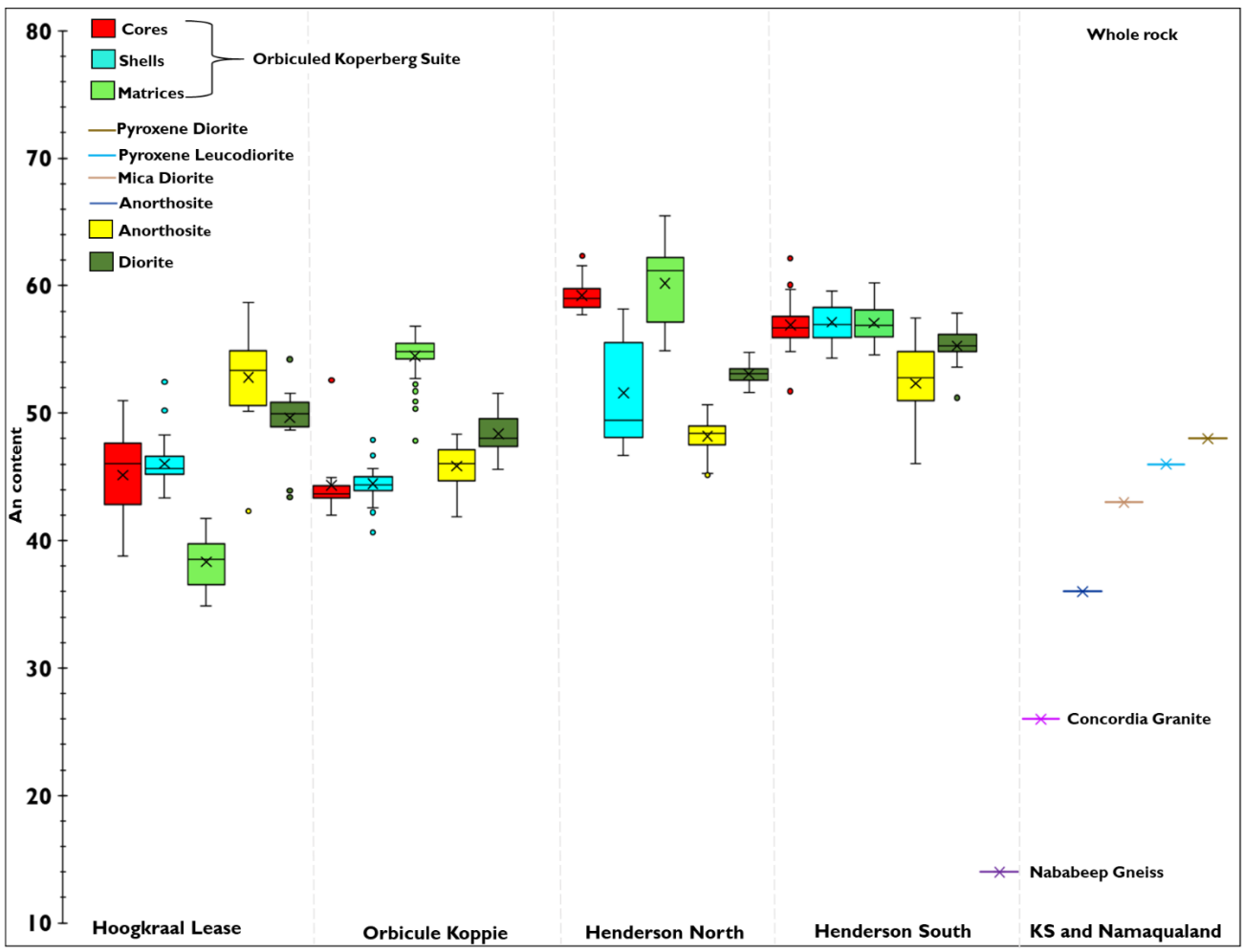


Figure 85: *The graph showing the An content in plagioclase from the Koperberg Suite orbicular cores, shells and matrices and the surrounding Namaqualand Metamorphic Complex (NMC) and the massive Koperberg Suite rocks. The massive Koperberg Suite and the NMC An content were adapted from Van Zwieten et al. (1996) and Brandriss and Cawthorn (1996). The graph shows little variation in An contents in the orbicules and the surrounding massive and non-orbicular Koperberg Suite rocks. The two sigma represent the minimum and maximum values, the box represents the interquartile range, x represents the mean, and the middle straight line represents the median.*

Biotite in different orbicule structures in the Koperberg Suite orbicules was analyzed for the following major elements: SiO_2, Al_2O_3, TiO_2, FeO, MnO, MgO, CaO, Na_2O, K_2O, Cr_3O_2, BaO, SrO, NiO, ZnO, F, CuO and Cl.

Biotite in diorites and anorthosites in contact with the orbicules were not analyzed because they were highly altered or not present at all in the samples. The Mg# in biotite is not homogeneous throughout the Koperberg Suite orbicules and shows a variation between different localities (Figure 86). However, there is little to no variation in Mg# between the different orbicular domains (core, shells, and matrices) in the individual orbicule localities (Figure 86).

In general, the Koperberg Suite orbicules comprise biotite with high Mg# (between 50 and 80; Figure 86). Similar to the An content, a variation in Mg# is observed in the Koperberg Suite orbicules (Figure 86), and based on Mg#, the Henderson North orbicules exhibit the highest Mg# and the Hoogkraal Lease orbicules exhibit the lowest Mg#. In addition to this, there is no variation in Mg# between the different domains in individual orbicular localities (Figure 86).

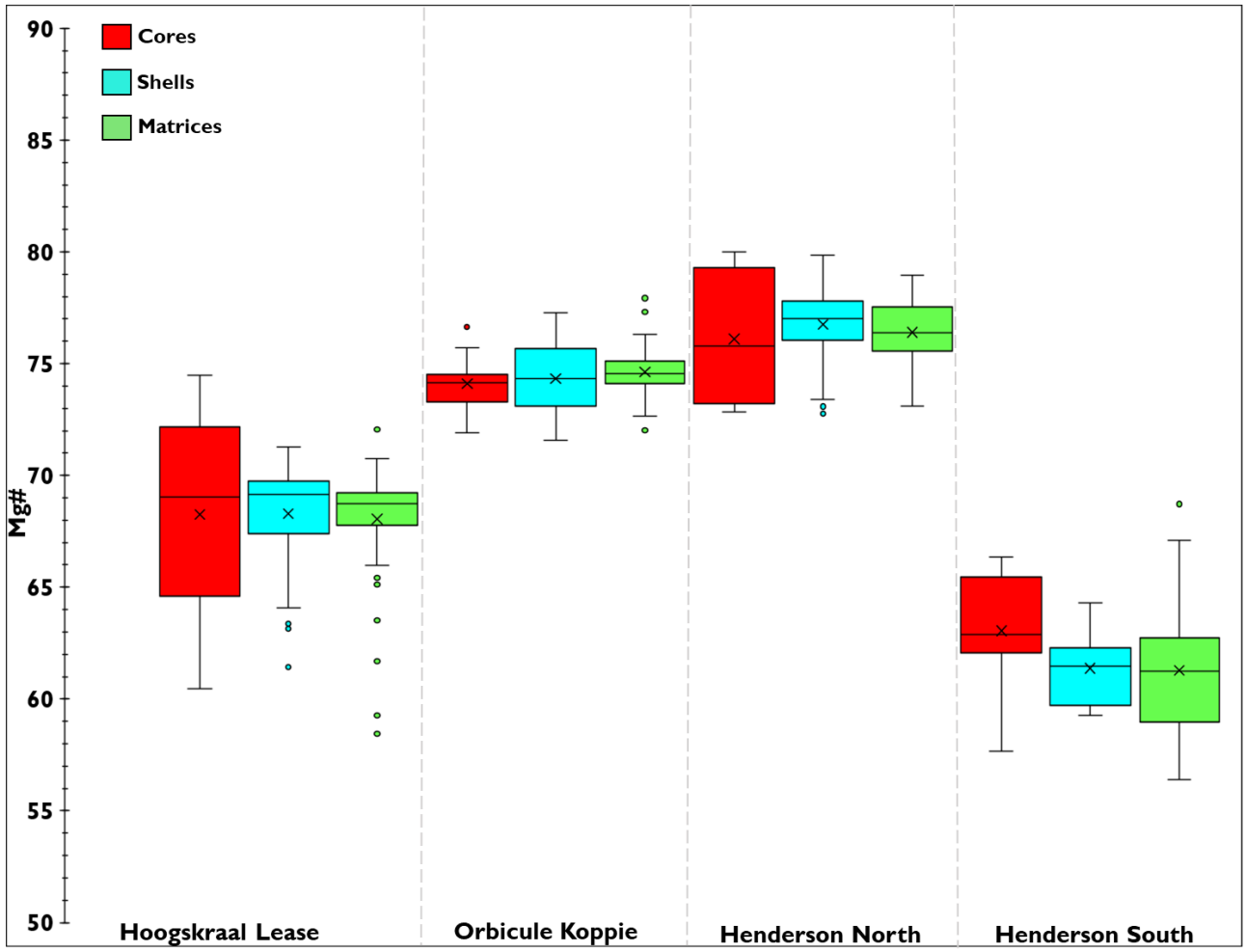


Figure 86*: The graph of Mg# (Mg/Mg + Fe) in biotite showing the variation in Mg# in the Koperberg Suite orbicules. The Henderson North orbicules are the most magnesian whilst the Henderson South orbicules are the least magnesian of the Koperberg Suite orbicules. However, there is no variation in Mg# within the different orbicular domains in individual orbicular localities. The two sigma represent the minimum and maximum values, the box represents the interquartile range, x represents the mean, and the middle straight line represents the median.*

Following the nomenclatures of Makutu et al. (2004) and Deer et al. (1992), the Koperberg Suite biotites plot in the eastonite field (Figure 87a, b). Using the MgO-FeO-Al_2O_3 ternary diagram after Abdel-Rahman (1994), the Koperberg Suite orbicules all plot in the calc-alkaline orogenic suite (Figure 87d). Titanium is present in minor amounts within the orbicules (0.14-0.52 apfu) and according to the 10* TiO_2 - FeO + MnO - MgO diagram after Nachit et al. (2005), biotite in Koperberg Suite orbicules are positioned in the reequilibrated biotite field (Figure 87c).

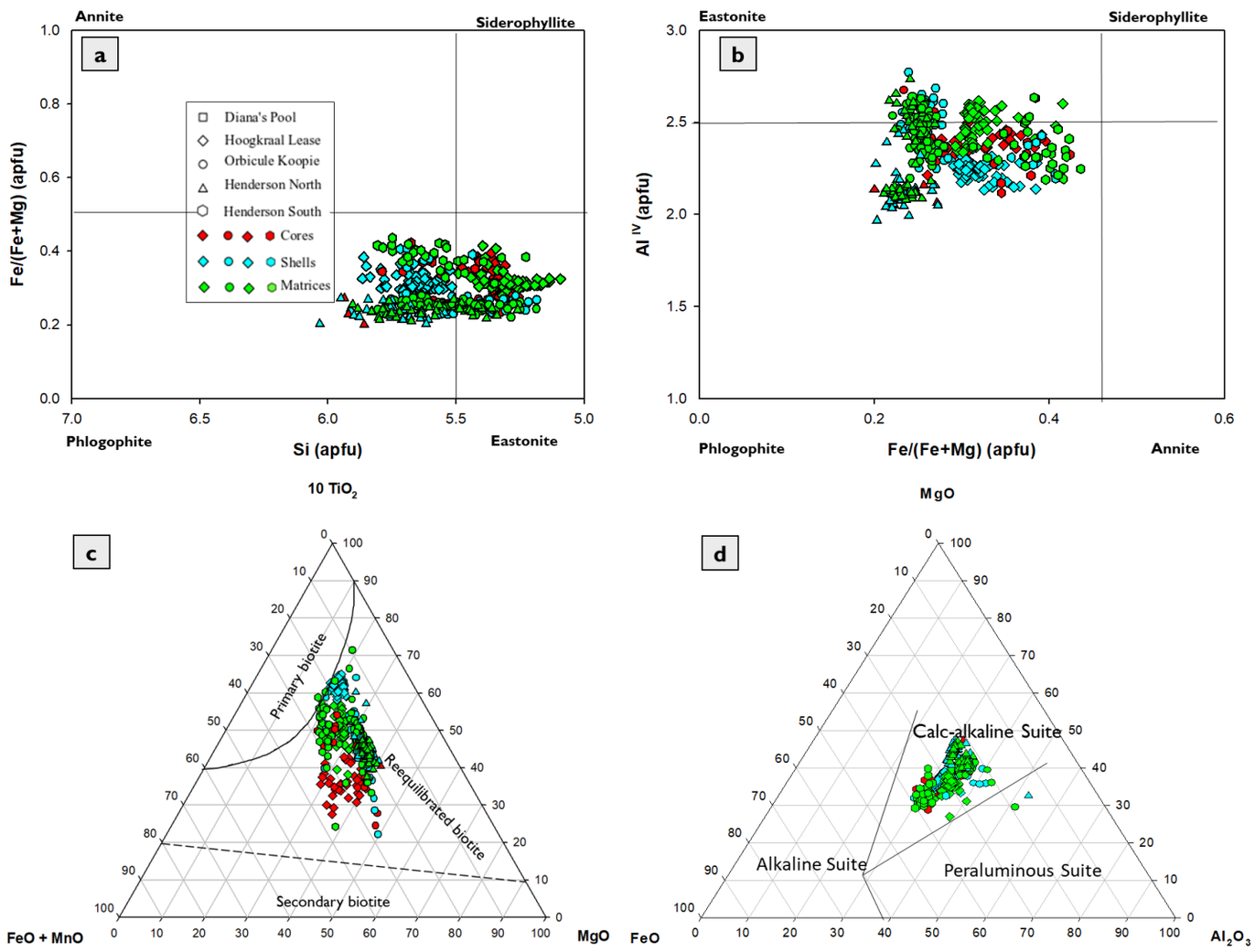


Figure 87: *Koperberg Suite biotite plotted on compositional classification diagrams: (a) Fe/ (Fe + Mg) versus Si (apfu) after Makutu et al. (2004). (b) Fe/ (Fe + Mg) versus Al^{IV} after Deer et al. (1992). (c) Chemical composition of biotite using the (FeO+ MnO) - 10TiO O_2-MgO ternary diagram after Natchit et al. (2005). (d) Plot of Diana's Pool biotite on Al_2O_3-FeO-MgO ternary biotite discrimination diagram after Abdel-Rahman (1994).*

5.3.2. Intra-locality *in-situ* major element mineral chemistry

5.3.2.1. Orbicule Koppie

Unaltered plagioclase (Table 24; Appendix B) and biotite in samples SD-10-6A (full orbicule sample), SD-10-6B (core sample), SD-10-6C (matrix sample), diorite and anorthosite (Table 23; Appendix B) were analyzed by EPMA to establish their chemical compositions. Plagioclase compositions of the shells were analyzed in sample SD-10-6A. The summarized major element compositions of plagioclase are presented in Table 7 and the rest of the oxides are in Table 24 (Appendix B)

Table 7: *Table showing the ranges of the major elements (wt. %) in plagioclase from the core, the shells and the matrix samples of the orbicules from Orbicule Koppie.*

Oxide	Core	Shells	Matrix	Diorite	Anorthosite
Na_2O	5.05-6.05	5.55-6.21	4.46-5.05	5.18-6.32	4.81-6.08
K_2O	0.17-1.26	0.11-0.38	0.12-0.38	0.35-1.60	0.29-1.44
CaO	7.94-13.00	7.88-9.75	8.64-11.32	8.35-10.29	8.47-11.62
SiO_2	52.00-57.18	55.32-57.74	52.56-56.96	52.21-55.84	50.33-5696
Al_2O_3	24.99-28.60	27.92-29.00	27.73-31.43	26.87-29.93	26.21-29.39

Plagioclase is composed of Al_2O_3 that shows little variation and that is homogeneous in the shell, the core, in the surrounding anorthosite and diorite (Figure 88a). However, plagioclase in the matrix is slightly more aluminous (Table 7; Figure 88a).

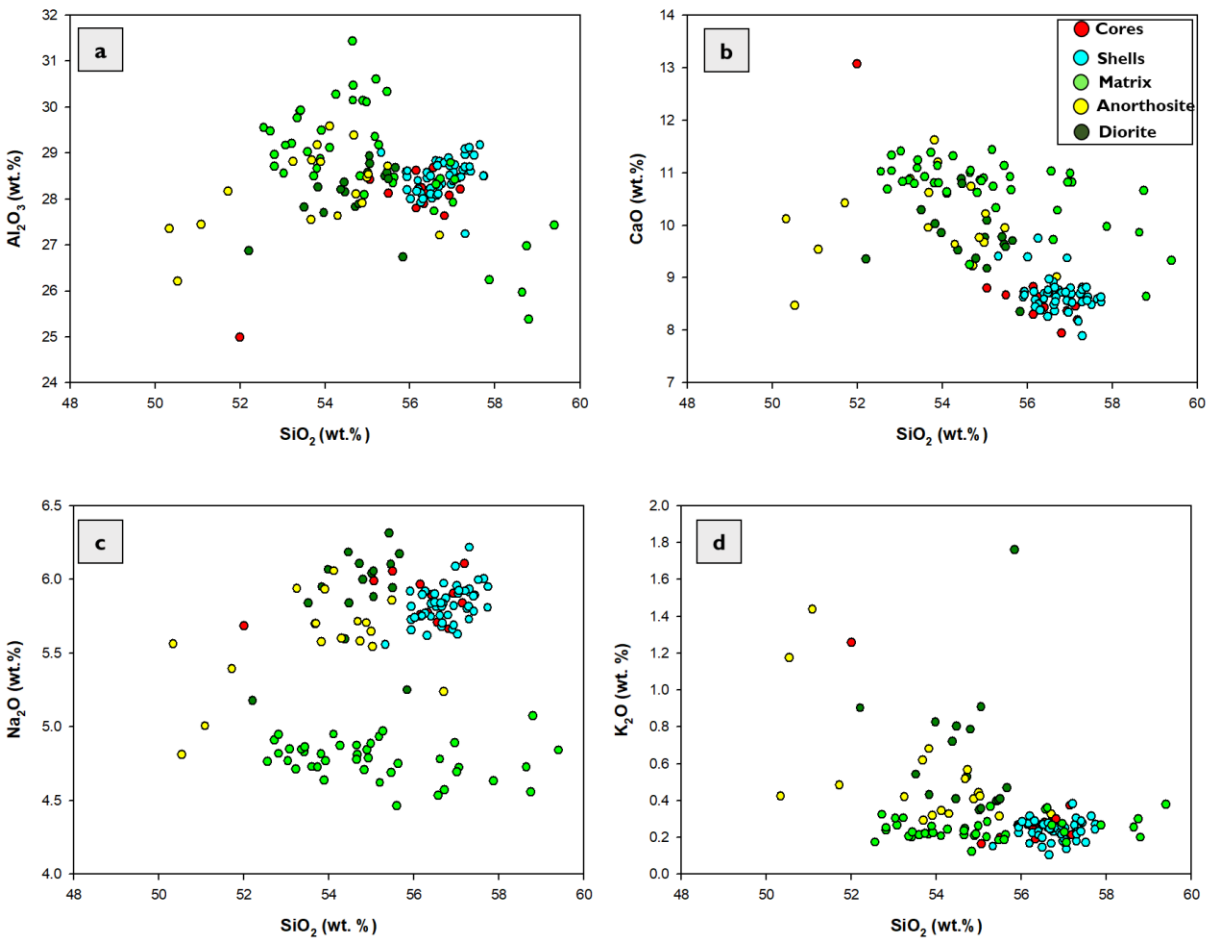


Figure 88: *Chemical variation diagrams showing the variation of different oxides in plagioclase from Orbicular Koppie orbicular cores, shells, matrix, diorite, and anorthosite plotted against SiO_2 (wt.%).*

Plagioclase in the matrix is more calcic (Figure 88c) than the less calcic and more sodic plagioclase in the core and shells. Plagioclase grains in diorite and anorthosite (Figure 88c) are more calcic than plagioclase in the core and the shells of the samples and they exhibit CaO contents that are within range with plagioclase in the matrix (Figure 88c). Plagioclase in the shells and the core are more siliceous than those in the matrix, diorite and anorthosite (Figure 88; Table 7). K_2O shows little to no variation in plagioclase in the core, the shells and the matrix (Figure 88; Table 7). Conversely, there is a large variation in the K_2O content in the slightly potassic plagioclase in diorite and anorthosite (Figure 88d).

A variation in the An content is observed in plagioclase in the core, the shells and the matrix (Figure 89). Plagioclase in the matrix is more calcic (An_{54-56}) than in the shells (An_{42-47}) and the core (An_{42-44}). Diorite (An_{42-48}) and anorthosite (An_{46-52}) comprise plagioclase with An content that are within range with the core and the shells (Figure 89) and more sodic than plagioclase in the matrix.

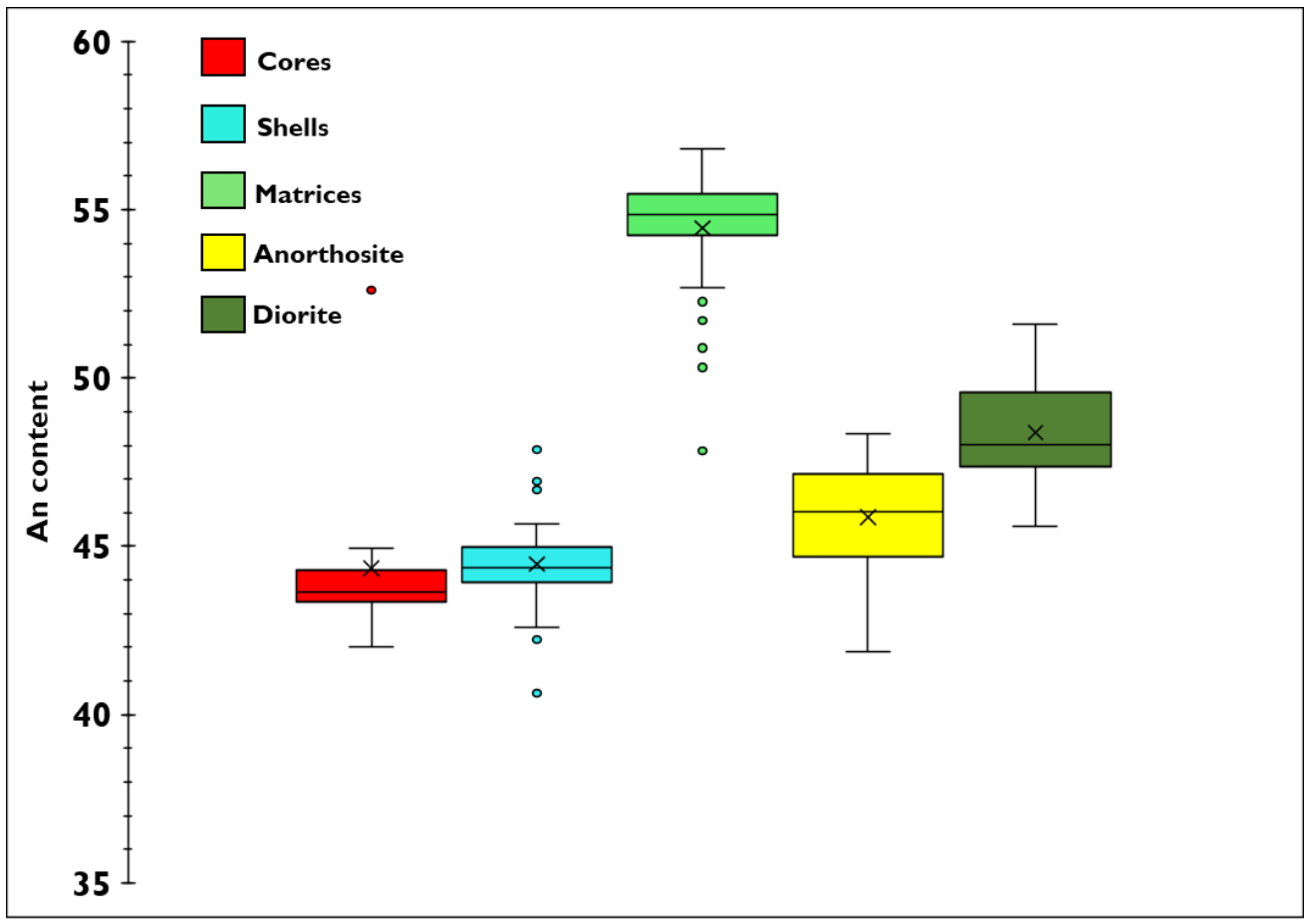


Figure 89: *The graph of An content showing a variation in An content in the Orbicule Koppie orbicular core, shells, matrix and the surrounding anorthosite and diorite. Plagioclase in the matrix are more calcic and thus high An contents than plagioclase in the core, shells, diorite and anorthosite. The two sigma represent the minimum and maximum values, the box represents the interquartile range, x represents the mean, and the middle straight line represents the median.*

Similar to plagioclase, biotite was analyzed in the orbicular core, shells and matrix samples (Table 25; Appendix B). Biotite in samples SD-10-6A (full orbicule sample), SD-10-6B (core sample), SD-10-6C (matrix sample) were analyzed to establish their chemical compositions and the summarized major element compositions are presented in Table 8. Biotite in the surrounding diorite and anorthosite was either not present or much altered to be analyzed.

Contrary to plagioclase, biotite compositions are homogeneous throughout the orbicule samples (Figure 90). The TiO_2, MgO, SiO_2 and FeO contents show little variation from the core to the shells and the matrix (Table 8; Figure 90).

Table 8: *Table showing the ranges of the major elements (wt. %) in biotite from the core, the shells and the matrix of the Orbicule Koppie orbicular rocks.*

Oxide	Core	Shells	Matrix
TiO_2	1.03-3.14	0.87-4.18	1.47-5.55
MgO	15.02-20.04	14.81-19.39	10.79-17.99
FeO	9.61-12.94	8.03-12.10	7.43-11.14
K_2O	6.39-13.71	6.38-13.82	7.26-1.04
Al_2O_3	13.99-17.49	14.08-18.37	13.22-18.81
SiO_2	36.67-39.25	35.01-42.86	34.99-41.41

Owing to data scattering, there is no significant differences in composition of biotite between core, shell and matrix, with the exception of K_2O (Figure 90).

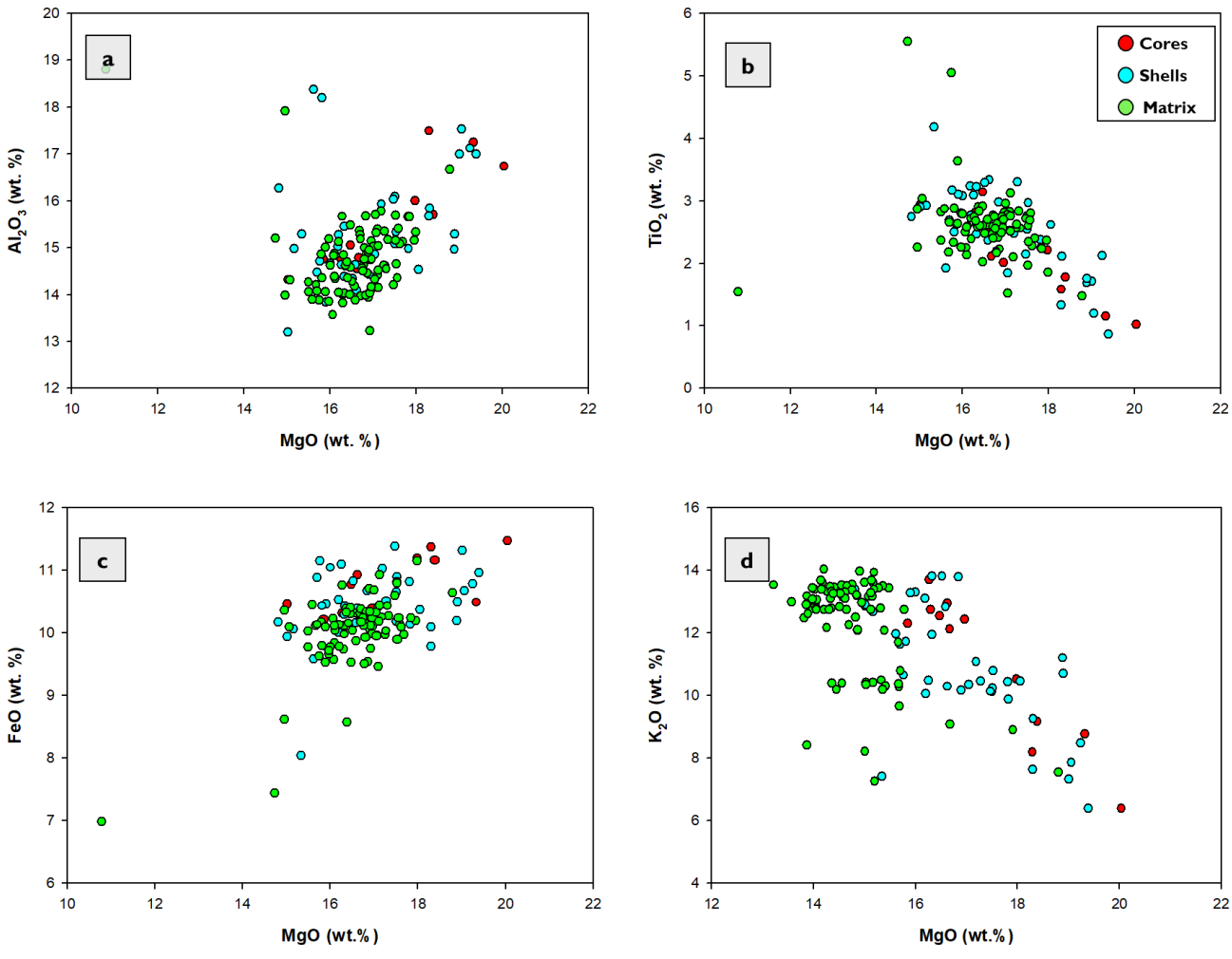


Figure 90: *Chemical variation diagrams showing a variation of the different oxides in biotite from Orbicule Koppie orbicular core, shell and matrix plotted against SiO_2 (wt. %).*

Al_2O_3 is homogeneous in these orbicules (Figure 90a). However, biotite in the core and the shells are slightly more aluminous than in the matrix (Figure 90a; Table 8). TiO_2 shows little variation between the different orbicular domains (Figure 90b). However, the TiO_2 content is slightly higher in biotite in the matrix than in the shells and the core, respectively (Table 8, Figure 90b).
Similar to the other elements, FeO shows little variation in biotite in the core, the shells, and the matrix samples (Figure 90c). Similar to FeO, MgO shows little variation (Figure 90) in biotite from the cores, the shell, and the matrix. Contrary to the trends of the other oxides, K_2O shows a different trend, and it varies between biotite of the same samples. Some biotite in the core, the shell and the matrix are more potassic than the other less potassic groups of plagioclase grains (Figure 90d).

Unlike plagioclase, biotite shows little to no variation in Mg# in biotites from the core, the shells, and the matrix samples (Figure 91). The average Mg# is homogeneous in the cores, the shells and the matrix.

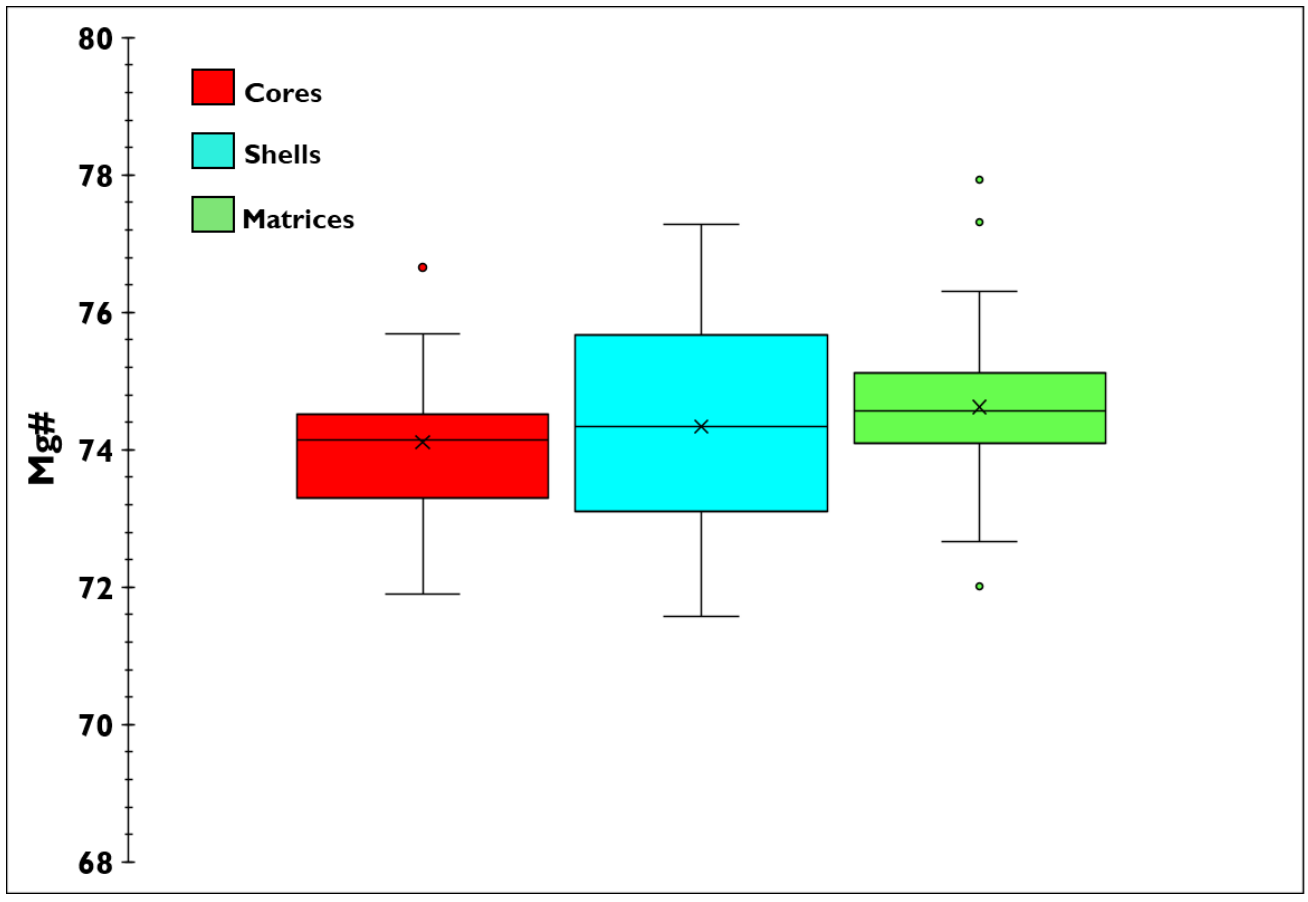


Figure 91*: The graph of Mg# in biotite showing little to no variation in the Mg# in Orbicule Koppie orbicular core, shell and matrix samples. The two sigma represent the minimum and maximum values, the box represents the interquartile range, x represents the mean, and the middle straight line represents the median.*

5.3.2.2. Hoogkraal Lease

Plagioclase (Table 26; Appendix B) in samples SD-27-14 (full orbicule sample), SD-22-11C (core sample), SD-22-11D (matrix sample) and the surrounding diorite and anorthosite (Table 23; Appendix B) were analyzed to establish their chemical compositions. Plagioclase in the cores were analyzed in samples SD-27-14 and SD-22-11C. Plagioclase in the shells and the matrix were analyzed in samples SD-27-14 and SD-22-11D, respectively. The summarized major element compositions are presented in Table 9.

Table 9: *Table showing the ranges of the major elements (wt. %) in plagioclase from the cores, the shells and the matrix of the orbicules from Hoogkraal Lease.*

Structure	**Cores**		**Shells**	**Matrix**	**Diorite**	**Anorthosite**
Sample#	**SD-22-11C**	**SD-27-14**	**SD-27-14**	**SD-22-11D**	**SD-19-9**	**SD-20-10**
Na_2O	5.49-6.93	5.70-7.05	5.08-6.86	6.47-7.42	5.34-5.54	5.83-6.70
K_2O	0.21-0.93	0.26-1.05	0.28-0.48	0.25-0.79	0.21-2.66	0.08-0.85
CaO	10.02-11.50	8.43-10.38	9.83-11.40	7.37-8.97	9.40-14.27	9.90-12.83
SiO_2	54.70-56.15	51.83-55.50	53.27-56.55	54.18-59.45	49.75-53.29	48.92-52.43
Al_2O_3	26.87-27.99	27.84-31.63	26.55-28.12	26.85-30.11	27.15-30.57	28.71-30.39

Based on the variation diagrams, there are two groups of cores with different compositions in the Hoogkraal Lease orbicules (Figure 92). In general, plagioclase in the Hoogkraal Lease orbicules are more siliceous than plagioclase in diorite and the anorthosite in contact with the orbicular body (Figure 92). However, there is a variation in SiO_2 between the cores, the shells and the matrix. The matrix sample SD-22-11D comprises plagioclase that are more siliceous than plagioclase in the shells and in the cores (Figure 92).

In addition, this variation in SiO_2 is also observed in cores of different samples (Figure 92).The core sample SD-27-14 comprises plagioclase that are more siliceous than plagioclase in sample SD-22-11C (Figure 92). Similar to SiO_2, a variation in Al_2O_3 is also observed between the orbicules and the surrounding diorite and anorthosite (Figure 92a). Plagioclase in the orbicules are less aluminous than in diorite and anorthosite (Figure 92a). The matrix sample comprises plagioclase that are more aluminous than plagioclase in the shells and in sample SD-27-14 core.

However, the core sample SD-27-14 comprises plagioclase that are more aluminous and within range with plagioclase in diorite and anorthosite (Figure 92a). The highest CaO content are exhibited by plagioclase in diorite and anorthosite (Figure 92b) and the orbicules are more sodic (Figure 92b). In addition, a variation in CaO is observed between the cores, the shells, and the matrix.

Plagioclase in the matrix are more sodic (Figure 92c) and have low CaO contents than the more calcic shells (Figure 92b). The core sample SD-27-14 comprises plagioclase that are more calcic than plagioclase in the core sample SD-22-11C (Figure 92b; Table 9).

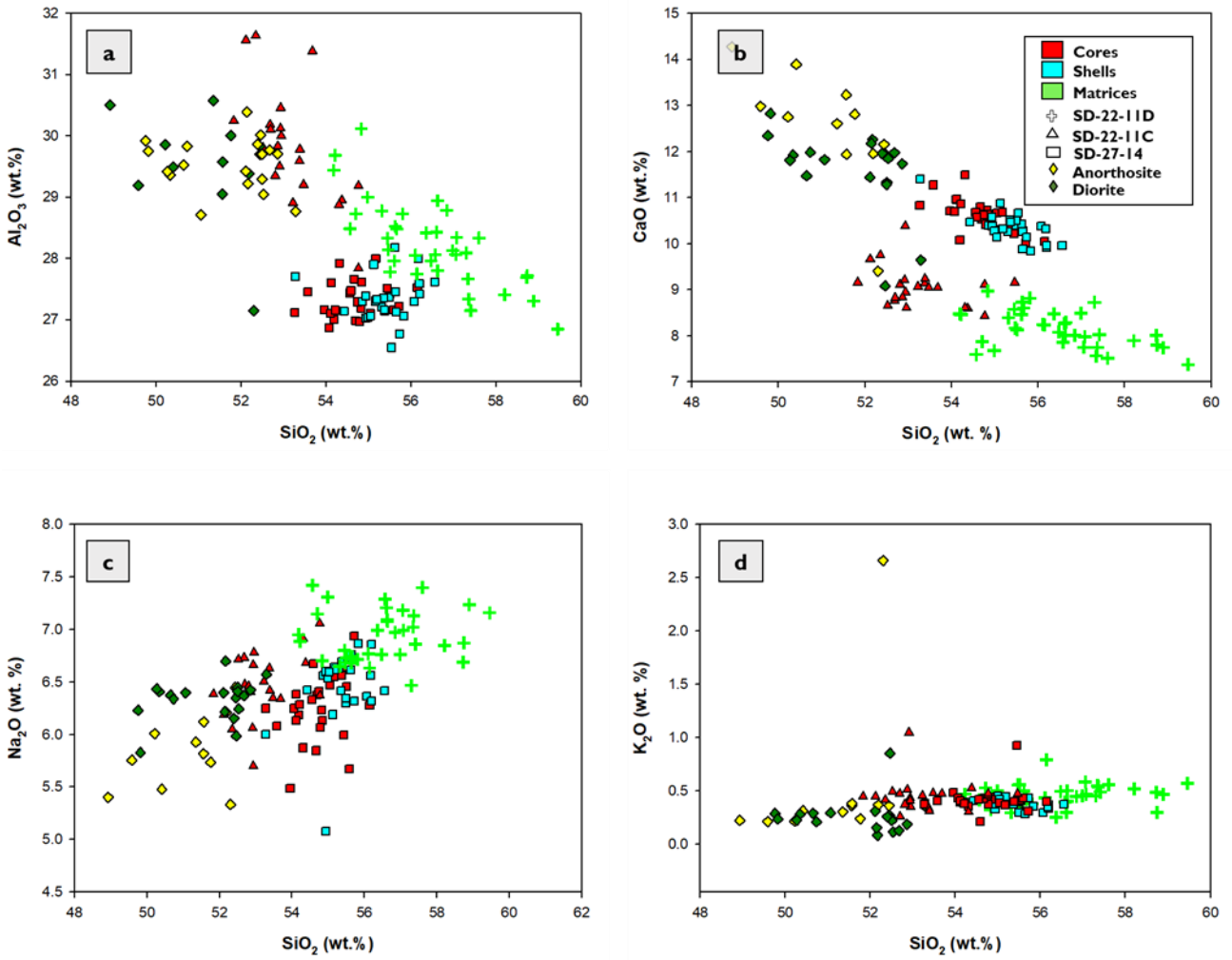


Figure 92*: In-situ chemical variation diagrams showing the variation of different oxides in plagioclase from Hoogkraal Lease orbicular cores, shells, diorite, anorthosite and the matrix plotted against SiO2 (wt. %).*

Compared to the other oxides, there is little variation in K_2O in the orbicules (Figure 92d) and K_2O is slightly higher in the matrix than in plagioclase in the cores and shells (Table 9; Figure 92d). There is also little to no variation in K_2O in plagioclase from different core samples (Figure 92d). Compared to diorite and anorthosite, the orbicules comprise plagioclase that are slightly more potassic (Figure 92d).

The An content is not homogeneous in the cores, the shells and the matrix (Figure 93). Plagioclase in the matrix is more sodic (An_{35-42}) than the more calcic plagioclase in the shells (An_{43-52}) and the cores (An_{39-51}; Figure 93). A variation in the An content is also observed in the cores of different samples (Figure 93). Sample SD-27-14 core comprises calcic plagioclase (An_{44-51}) than plagioclase in sample SD-22-11C (An_{39-49}). Similar to the cores, a variation in the An content is observed in the shells of orbicule sample SD-27-14. Plagioclase in the inner shell are more calcic ($\overline{x} = An_{46}$) than plagioclase in the more sodic outer shell ($\overline{x} = An_{44}$). The surrounding diorite (An_{43-52}) and anorthosite (An_{42-59}) comprise plagioclase with An content that are slightly more calcic than plagioclase in orbicules (Figure 93).

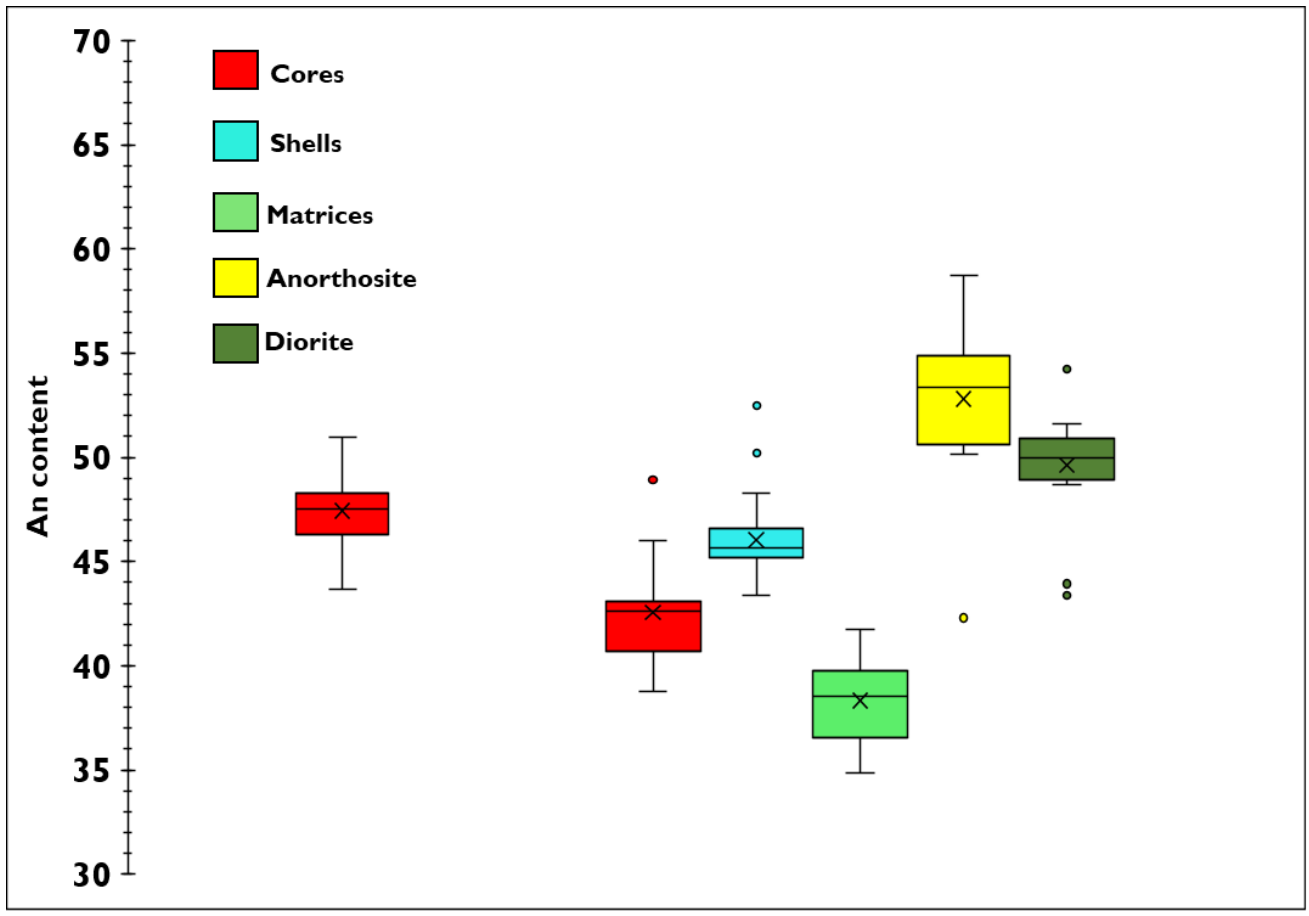


Figure 93: *The graph of An content showing a variation in An content in the Hoogkraal Lease orbicular cores, shells, matrix and the surrounding anorthosite and diorite. The matrix comprises plagioclase that are more sodic and have low An contents than plagioclase in the cores, the shells, diorite and anorthosite. Sample SD-27-14 core comprises plagioclase with a high An content than plagioclase in the core sample SD-22-11C. The two sigma represent the minimum and maximum values, the box represents the interquartile range, x represents the mean, and the middle straight line represents the median.*

Biotite was analyzed in the different orbicular domains (Table 27; Appendix B). Biotite in the core, the shells and the matrix were analyzed in samples SD-22-11C, SD-27-14, and SD-22-11D, respectively. The summarized major element compositions are presented in Table 10.

Biotite in the core and the matrix samples are more aluminous and exhibit higher Al_2O_3 contents than biotite in the shells (Figure 94a; Table 10). The highest TiO_2 contents are exhibited by biotite in the shells and the matrix, respectively (Table 10; Figure 94b). Biotite in the core sample, however, are depleted in TiO_2 relative to biotite in the shells and the matrix (Figure 94b).

Table 10: *Table showing the range of the major elements (wt. %) in biotite from the cores, the shells and the matrix of the Hoogkraal Lease orbicular rocks.*

Oxide	**Core**	**Shells**	**Matrix**
Sample#	**SD-22-11C**	**SD-27-14**	**SD-22-11D**
TiO_2	1.14-2.24	3.79-5.12	1.78-3.68
MgO	13.94-18.33	13.35-16.37	12.02-16.59
FeO	10.87-16.53	11.59-15.14	11.46-15.71
K_2O	9.35-11.09	8.95-10.76	7.26-1.04
Al_2O_3	13.47-15.03	12.28-15.26	13.87-17.63
SiO_2	36.37-38.42	37.09-40.65	35.86-38.54

Biotite from the core are slightly more magnesian than biotite in the shells and the matrix, respectively (Figure 94; Table 10). Biotite in the cores are more potassic than in the shells, and the matrix (Figure 94d). FeO contents (Figure 94c) are higher in the core than in shells and the matrix, respectively (Table 10; Figure 94c).

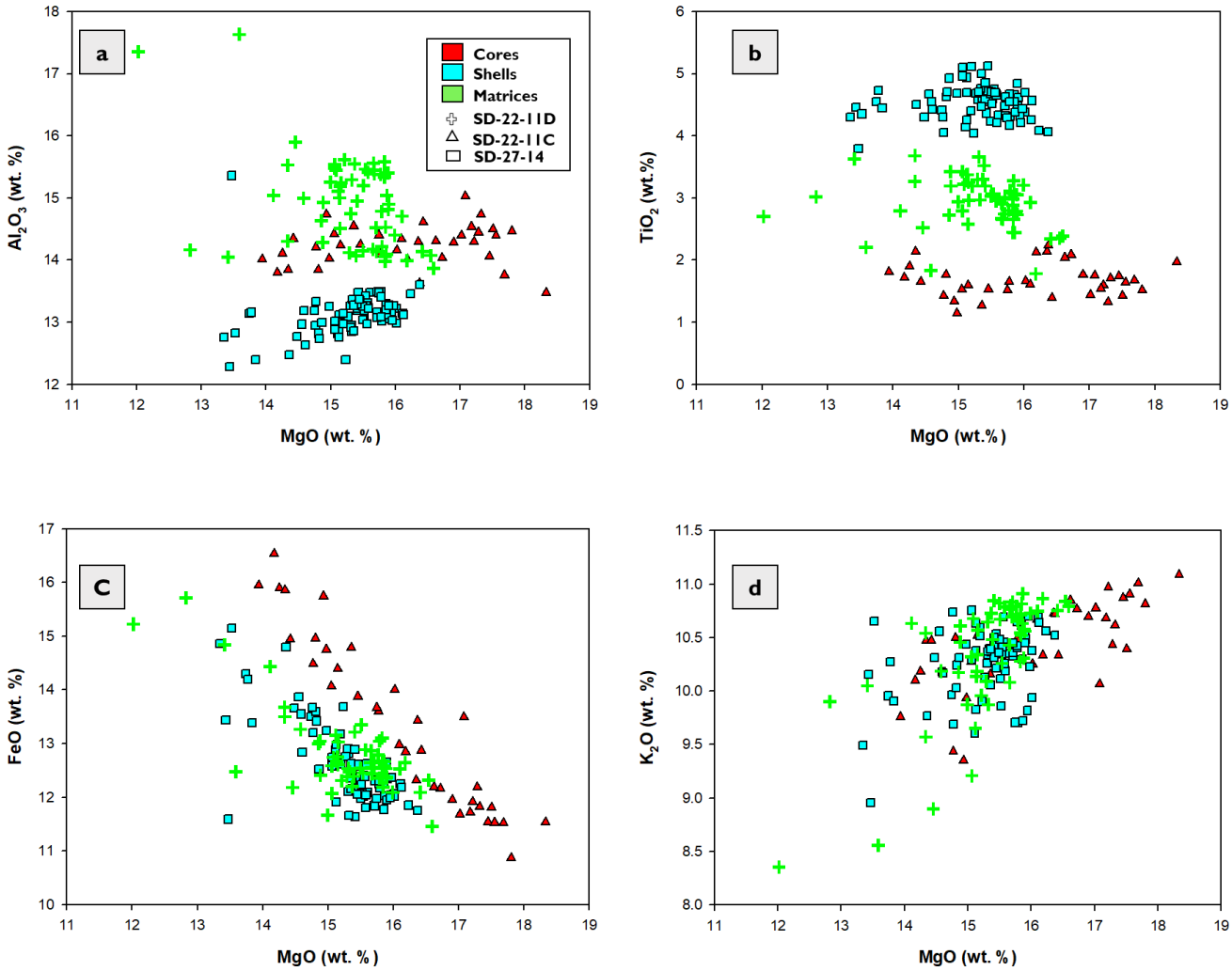


Figure 94: *In-situ chemical variation diagrams showing the variation of different oxides in biotite from Hoogkraal Lease orbicular cores, shells, and matrix plotted against MgO (wt. %).*

Similar to Orbicule Koppie, biotite in Hoogkraal Lease orbicules shows little to no variation in Mg# in the core, the shells and the matrix samples (Figure 95). However, there is a slight variation and a progressive decrease in Mg# from the inner to the outer shells of the shells sample SD-27-14 (Figure 54). The inner intermediate shell comprises magnesian biotite ($\overline{x}$ = Mg# 68.1), while biotite making up the first concentric biotite shells is slightly more primitive ($\overline{x}$ = Mg# 69.0). The outer intermediate and the second biotite shells comprise biotite with $\overline{x}$ = Mg# 66 and $\overline{x}$ = Mg# 69, respectively.

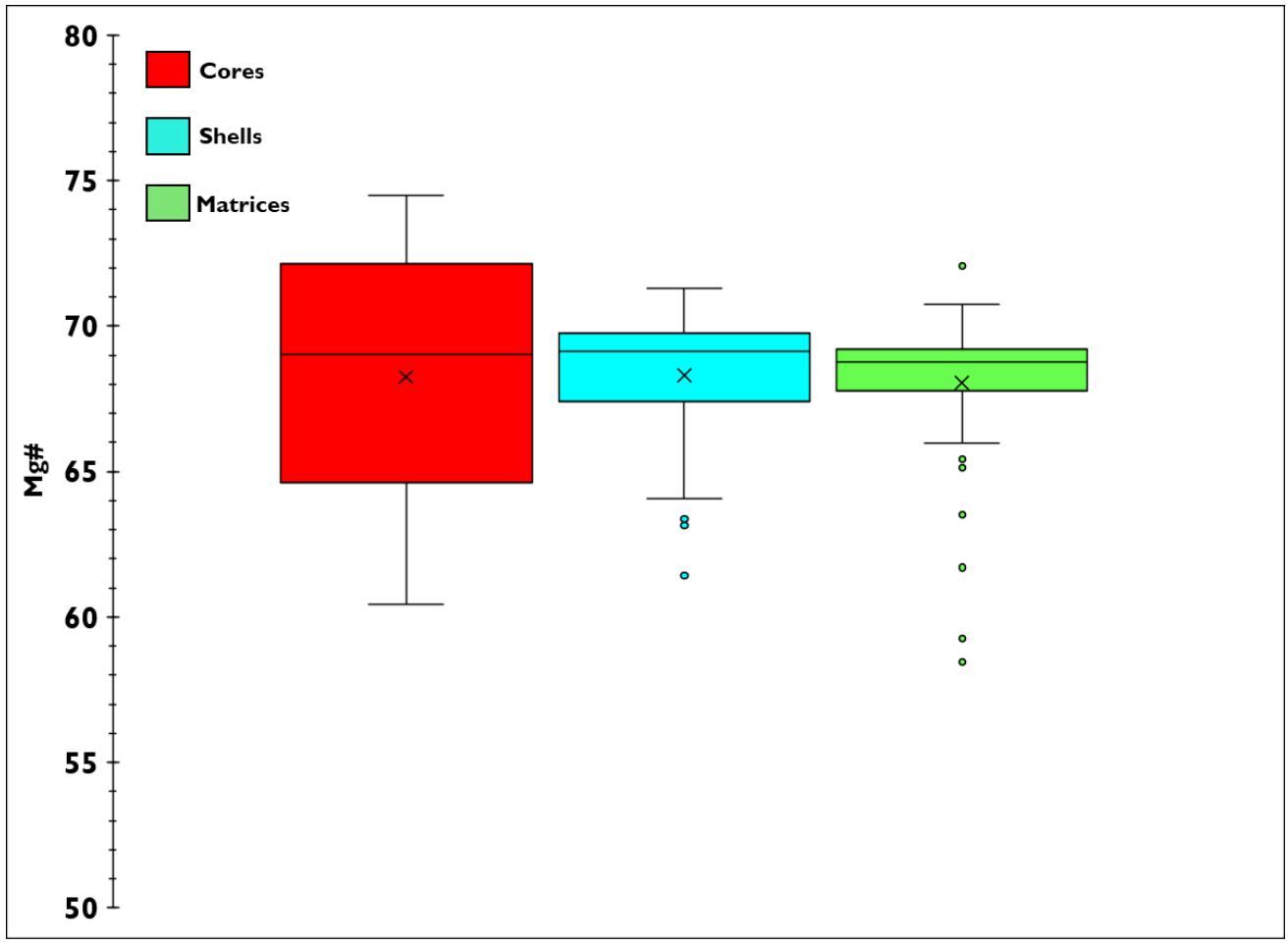


Figure 95: *The graph of Mg# in biotite showing homogeneous Mg# in Hoogkraal Lease orbicular domains. The two sigma represent the minimum and maximum values, the box represents the interquartile range, x represents the mean, and the middle straight line represents the median.*

5.3.2.3. Henderson North

Plagioclase (Table 28; Appendix B) and biotite (Table 29; Appendix B) in samples SD-10-36A (full orbicule sample), SD-36-18C (core sample), SD-40-19B (shell sample), SD-40-19D (matrix sample) and the surrounding diorite and anorthosite (Table 23; Appendix B) were analyzed to establish their chemical compositions. The summarized data is presented in Table 11.

Table 11: *Table showing the ranges of the major elements (wt. %) in plagioclase from the cores, the shells and the matrix of the orbicules from Henderson North.*

Structure	**Cores**	**Shells**		**Matrices**		**Anorthosite**	**Diorite**
Sample#	**SD-36-18C**	**SD-10-36A**	**SD40-19B**	**SD-10-36A**	**SD-40-19D**	**SD-20-10**	**SD-19-9**
Na_2O	3.72-4.33	3.71-4.13	6.61-7.28	3.67-3.99	3.55-4.27	6.24-6.80	5.38-6.32
K_2O	0.29-1.07	0.33-0.52	0.23-0.42	0.24-0.53	0.29-0.76	0.16-0.65	0.19-0.35
CaO	11.28-12.21	8.79-10.18	11.30-12.89	9.23-10.24	10.99-13.92	10.33-12.16	11.57-13.02
SiO_2	53.12-57.97	52.78-58.55	51.51-53.89	54.43-57.94	52.50-57.36	51.89-53.81	49.49-52.54
Al_2O_3	26.45-29.13	27.37-31.33	26.41-28.97	27.98-31.04	27.16-30.78	28.50-30.51	28.60-31.77

Based on the variation diagrams (Figure 96) and the major elements data (Table 11), there are two groupings of shells and matrices with different compositions in the Henderson North orbicules (Figure 96).

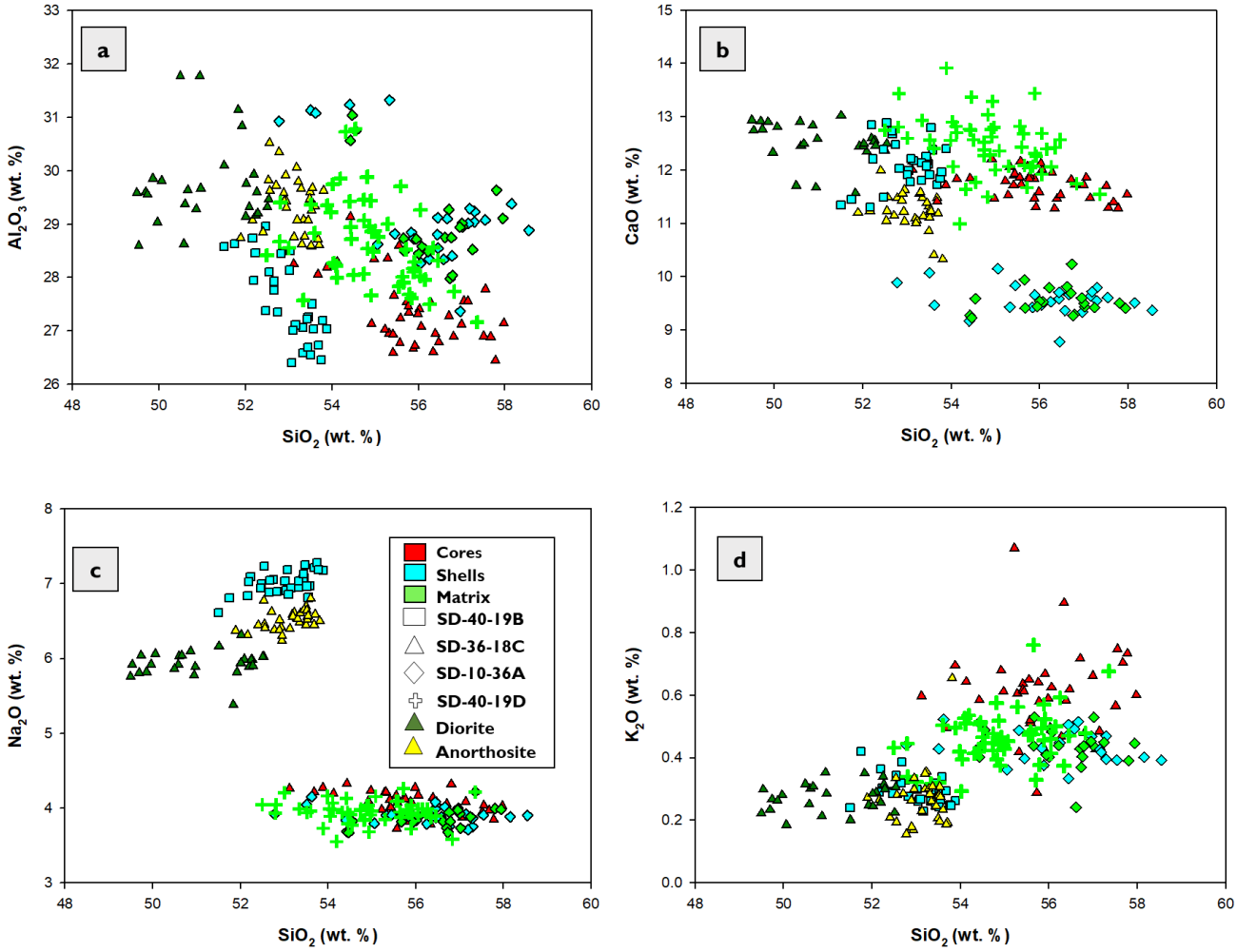


Figure 96: *Chemical variation diagrams showing variation of different oxides in plagioclase from the Henderson North orbicular domains, diorite, and anorthosite plotted against SiO_2 (wt. %).*

The diorite and anorthosite in contact with the Henderson North orbicules are composed of plagioclase that is more aluminous than plagioclase in the orbicules (Figure 96a). However, similar to Orbicule Koppie and Hoogkraal Lease orbicules, there is a variation in Al_2O_3 in plagioclase from the core sample, the shells and the matrices. In addition, the variation in Al_2O_3 is observed in the plagioclase in shells and matrices of different samples (Figure 96a). Sample SD-10-36A shells comprise plagioclase that are more aluminous than plagioclase in shells sample SD-409B (Figure 96a). The matrix sample SD-10-36A comprises plagioclase that are more aluminous than those in sample SD-40-19D (Figure 96a)

The highest CaO contents are exhibited by plagioclase in the diorite sample, the matrix sample SD-40-19D, the shells sample SD-40-19B, and in the core sample (Figure 96b). Plagioclase in the matrix sample SD-10-36A are more sodic than in sample SD-40-19D (Figure 96c). The shell sample SD-40-19B comprises plagioclase that are more calcic than the more sodic plagioclase in shells sample SD-10-36A (Figure 96c).

Plagioclase in diorite and anorthosite are less siliceous than in the orbicules (Figure 96). Plagioclase in sample SD-10-36A matrix are more siliceous than in the sample SD-40-19D (Figure 96). Plagioclase in the core sample comprise a SiO_2 content that is within range with the SiO_2 content in the shell samples SD-10-36A and SD-40-19B (Figure 96).

The highest Na_2O contents are exhibited by plagioclase in sample SD-40-19B shells, anorthosite and diorite (Figure 96c). The Na_2O content shows a little variation (Figure 96c) in plagioclase in the core sample, the matrix sample SD-10-36A, the matrix sample SD-40-19 and the shell sample SD-10-36A (Figure 96c).

Plagioclase in diorite and anorthosite are less potassic than plagioclase in the orbicules (Figure 96d). In the orbicules, the core sample comprises plagioclase that is more potassic than in the shells and the matrix (Figure 96d). Plagioclase in the shells sample SD-10-36A are more potassic than in the shell sample SD-40-19B. The matrix sample SD-40-19 plagioclase are more potassic than in the matrix sample SD-10-36A (Figure 96d).

Similar to other orbicular localities, there is a variation in the An content in the cores, the shells and the matrix in the Henderson North orbicules (Figure 97). In general, plagioclase in the matrix and the cores are more calcic than plagioclase in the shells, diorite and anorthosite (Figure 97). The analyzed core sample comprises calcic plagioclase (An_{57-62}; An_{59}). However, there is a large variation in the An content in the shells and the matrices of different samples (Figure 97).

Plagioclase in sample SD-10-36A shells are more calcic (An_{56-58}) than plagioclase in sample SD-40-19B (An_{47-50}) shells. The matrix sample SD-40-19D comprises calcic plagioclase (An_{58-65}) than plagioclase in sample SD-10-36A matrix (An_{55-59}; Figure 97).The surrounding diorite (An_{452-55}) and anorthosite (An_{45-51}) comprise plagioclase with An contents that are slightly more sodic than the more calcic plagioclase in the orbicules (Figure 97).

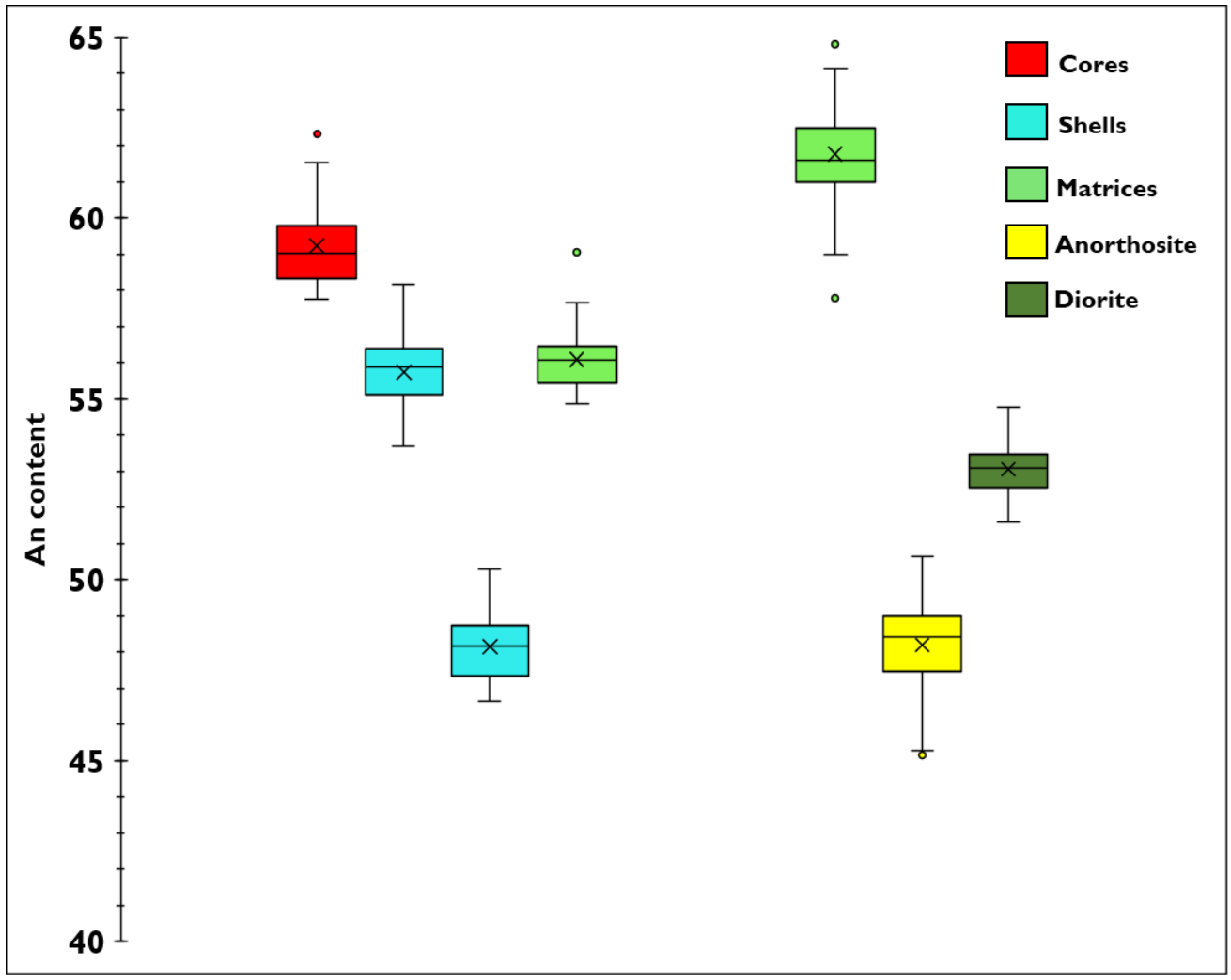


Figure 97: *The graph of An content showing a variation in the An content in plagioclase in the Henderson North orbicular domains and the surrounding anorthosite and diorite. The two sigma represent the minimum and maximum values, the box represents the interquartile range, x represents the mean, and the middle straight line represents the median.*

Biotite was different orbicular domains in samples SD-36-18C, SD-40-19B, SD-10-36A, and SD-40-19D, respectively. The summarized major element compositions are presented in Table 12.

Table 12: *Table showing the ranges of the major elements (wt. %) in biotite from the cores, the shells and the matrix of the Henderson North orbicular rocks.*

Oxide	**Core**	**Shells**	**Matrix**	
Sample#	**SD-36-18C**	**SD-40-19B**	**SD-10-36A**	**SD-40-19D**
TiO_2	1.88-2.43	1.85-3.63	1.79-2.44	1.75-2.50
MgO	15.99-19.10	12.24-19.83	16.41-10.81	16.49-19.38
FeO	8.51-9.83	5.55-10.85	9.28-10.81	16.49-19.38
K_2O	12.04-12.99	7.53-13.23	9.61-13.21	8.97-13.19
Al_2O_3	12.85-12.68	11.31-19.78	14.22-15.73	12.00-13.22
SiO_2	39.95-41.00	37.18-42.44	35-60-41.00	37.72-1.00

Based on the major elements, there are two groups of matrices characterized by biotites that varies in compositions in the Henderson North orbicules (Figure 98; Table 12).

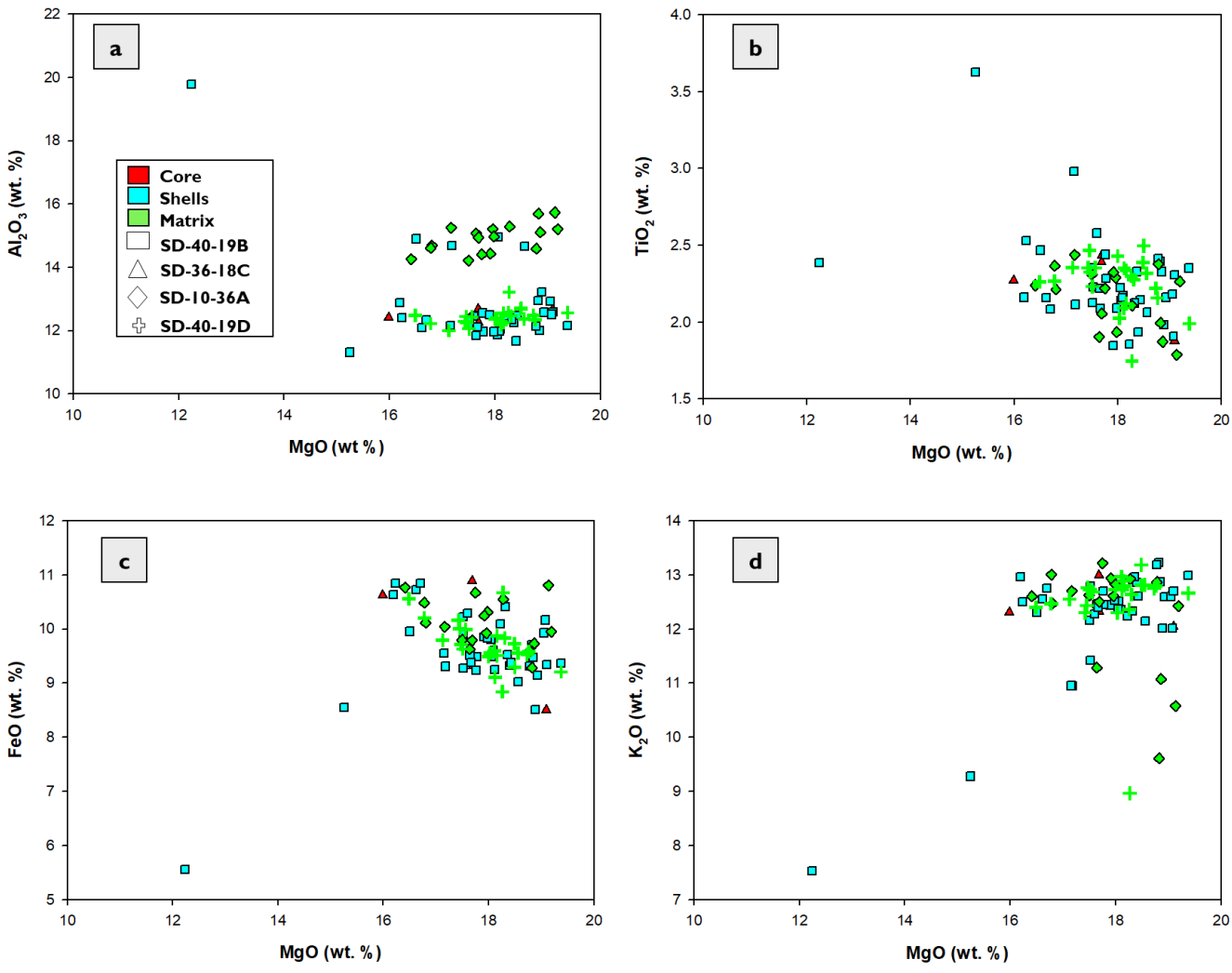


Figure 98: *Chemical variation diagrams showing variation of different oxides in biotite from Henderson North orbicular cores, shells, and matrix plotted against MgO (wt. %).*

The matrix sample SD-10-36A comprises biotite that are more aluminous than biotite in the matrix sample SD-40-19D, the core sample, and the shells (Figure 98a). TiO_2, MgO, FeO show little to variation in the core, the shells and the matrix (Table 12; Figure 98b, c, d). However, MgO is slightly higher in Sample SD-40-19D matrix than in sample SD-10-36A (Table 12; Figure 98).

Biotite compositions in the Henderson North orbicular cores are highly heterogeneous and slightly less magnesian than in the more magnesian shells and matrix samples (Figure 99). In addition, a variation in matrices is observed and the Mg# is higher in the matrix sample SD-40-19D than in sample SD-10-36A (Table 12; Figure 99).

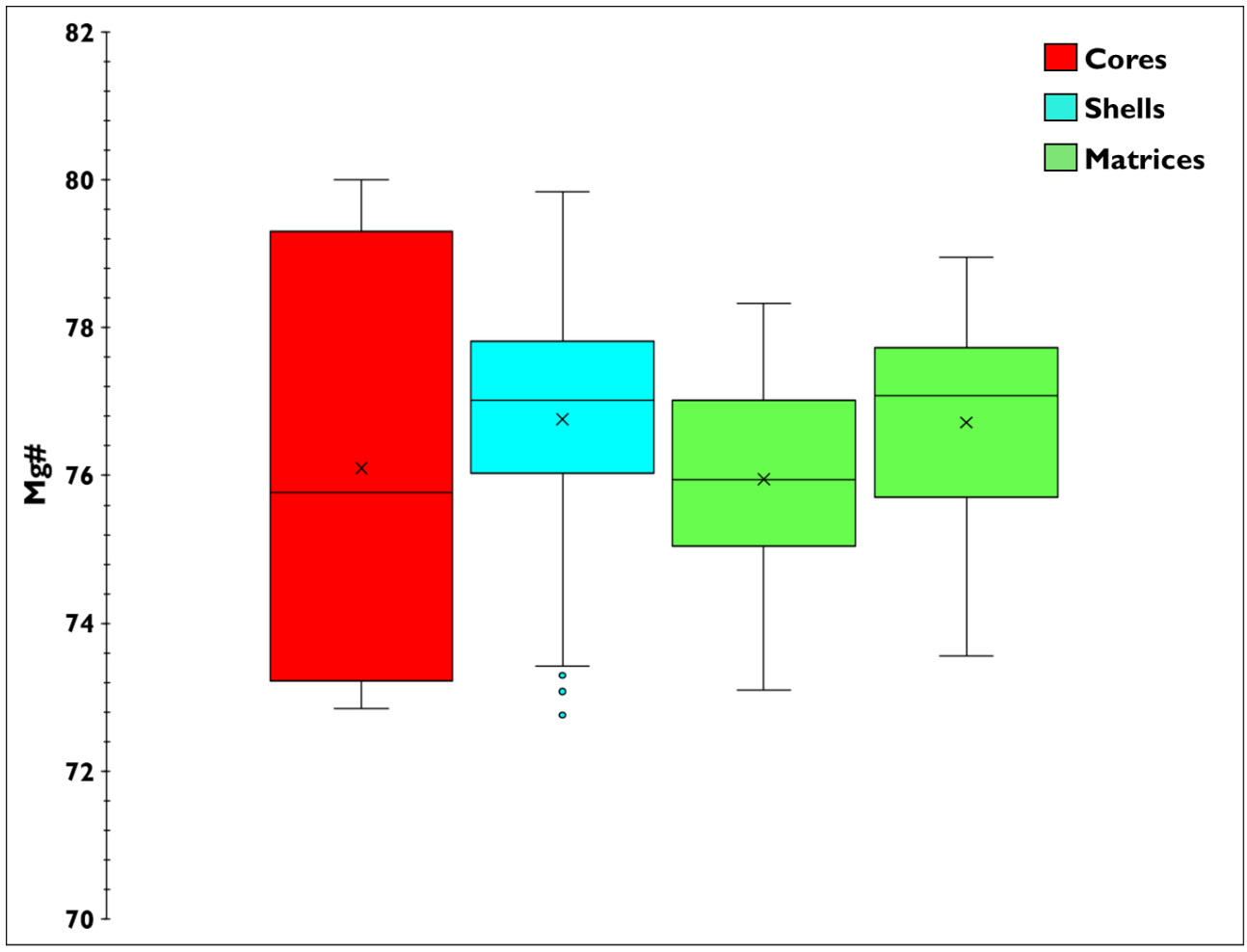


Figure 99: *The graph of Mg# in biotite showing homogeneous Mg# in Henderson North orbicular domains. The two sigma represent the minimum and maximum values, the box represents the interquartile range, x represents the mean, and the middle straight line represents the median.*

5.3.2.4. Henderson South

Plagioclase (Table 30; Appendix B) in samples SD-55-24C (full orbicule sample), SD-55-24B (full orbicule sample), SD-55-24A (full orbicule sample), SD-55-24D (matrix sample), and the surrounding diorite and anorthosite (Table 21) were analyzed to establish their chemical compositions and the summarized major elements data is presented in Table 13.

Table 13*: Table showing the ranges of the major elements (wt. %) in plagioclase from the cores, the shells, and the matrix of the orbicules from Henderson South.*

Oxide	Cores	Shells	Matrices	Diorite	Anorthosite
Na_2O	3.89-4.6	3.90-4.61	3.84-4.57	4.58-5.44	3.92-5.53
K_2O	0.21-1.51	0.26-0.54	0.34-0.64	0.24-1.06	0.24-0.79
CaO	9.72-12.43	10.06-11.46	10.11-11.59	9.21-13.51	9.17-12.38
SiO_2	53.54-55.99	54.97-55.52	52.37-57.43	50.37-54.49	47.40-53.26
Al_2O_3	28.05-30.93	28.09-30.45	27.87-32.05	28.26-30.92	27.07-30.36

Plagioclase in the Henderson South orbicules is homogeneous and shows little to no variation in different oxides in the core, shells and matrix (Table 13; Figure 100). In addition, there is no variation in the major elements in plagioclase of different samples and plagioclase will not be described according to different samples.

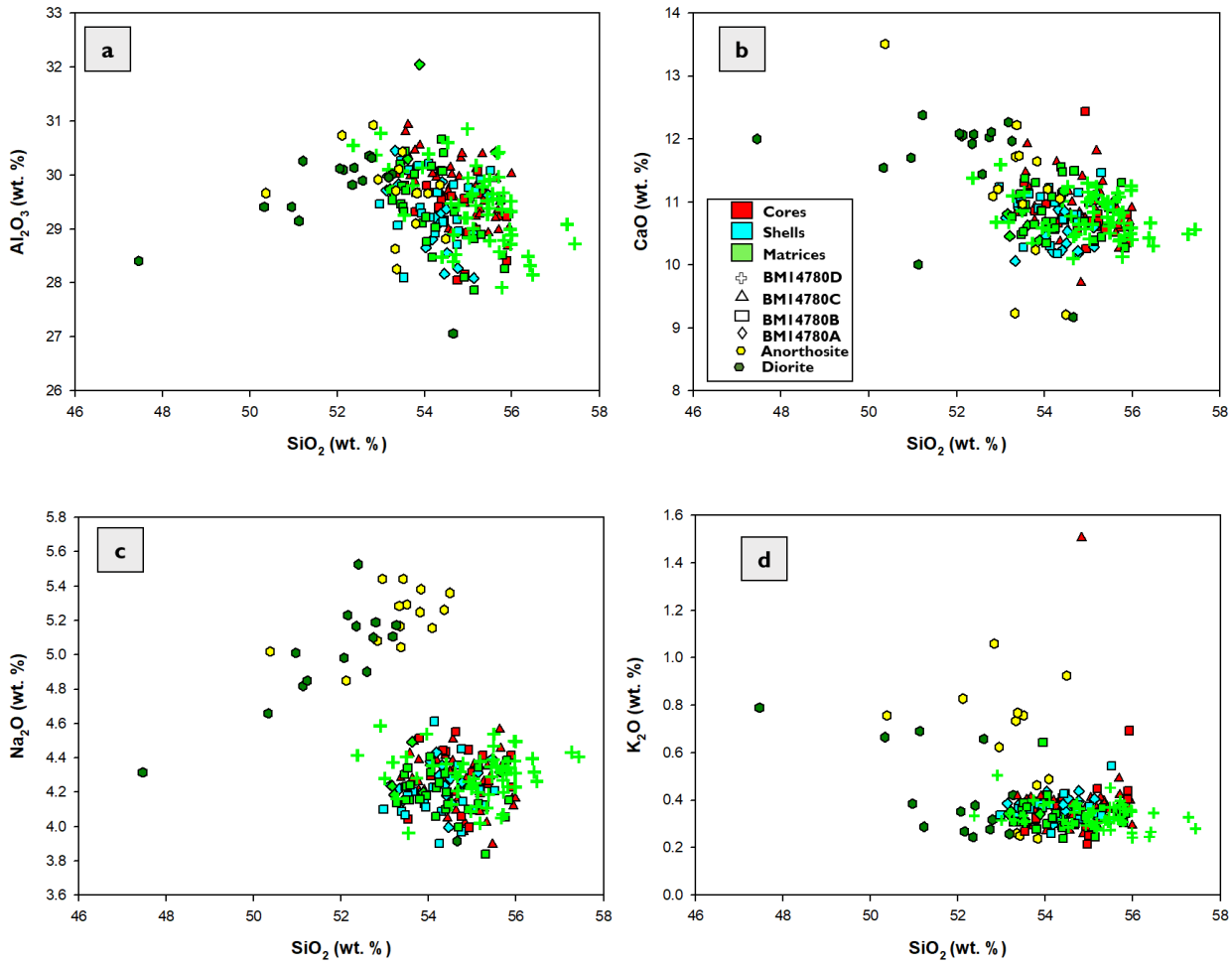


Figure 100: *Chemical variation diagrams showing variation of different oxides in plagioclase from the Henderson South orbicular domains, anorthosite and diorite plotted against SiO_2 (wt. %).*

However, there is a variation in the oxides between orbicules and the surrounding diorite and anorthosite (Figure 100). There is small variation in Al_2O_3 in plagioclase from the cores, the shells, the matrix, and the surrounding anorthosite and diorite (Figure 100a). Plagioclase in diorite and anorthosite are more sodic than in the orbicules (Figure 100a). However, Na_2O shows little variation in the cores, the shells, and the matrix (Figure 100c).

Similar to the other oxides, orbicules are composed of plagioclase with K_2O content that is homogeneous in the cores, the shells, and the matrix (Table 13; Figure 100d). However, K_2O is high in plagioclase in the surrounding diorite and anorthosite (Figure 100d). SiO_2 is also homogeneous in the orbicules, however, plagioclase in orbicules have a slightly higher SiO_2 content than in diorite and anorthosite (Figure 100d). CaO is high in anorthosite and diorite, but slightly lower and homogeneous in the orbicules (Figure 100b).

Unlike in the other orbicular localities, there is no variation in the An content in the cores, the shells and the matrices of the Henderson South orbicules (Figure 101). In general, plagioclase in the orbicules are more calcic than in the surrounding diorite and anorthosite (Figure 101). The An content is homogeneous in the cores (An_{52-62}), the shells (An_{54-60}) and the matrix (An_{55-60}). Plagioclase in anorthosite (An_{47-57}) and in diorite (An_{51-58}) are more sodic than plagioclase in the orbicules.

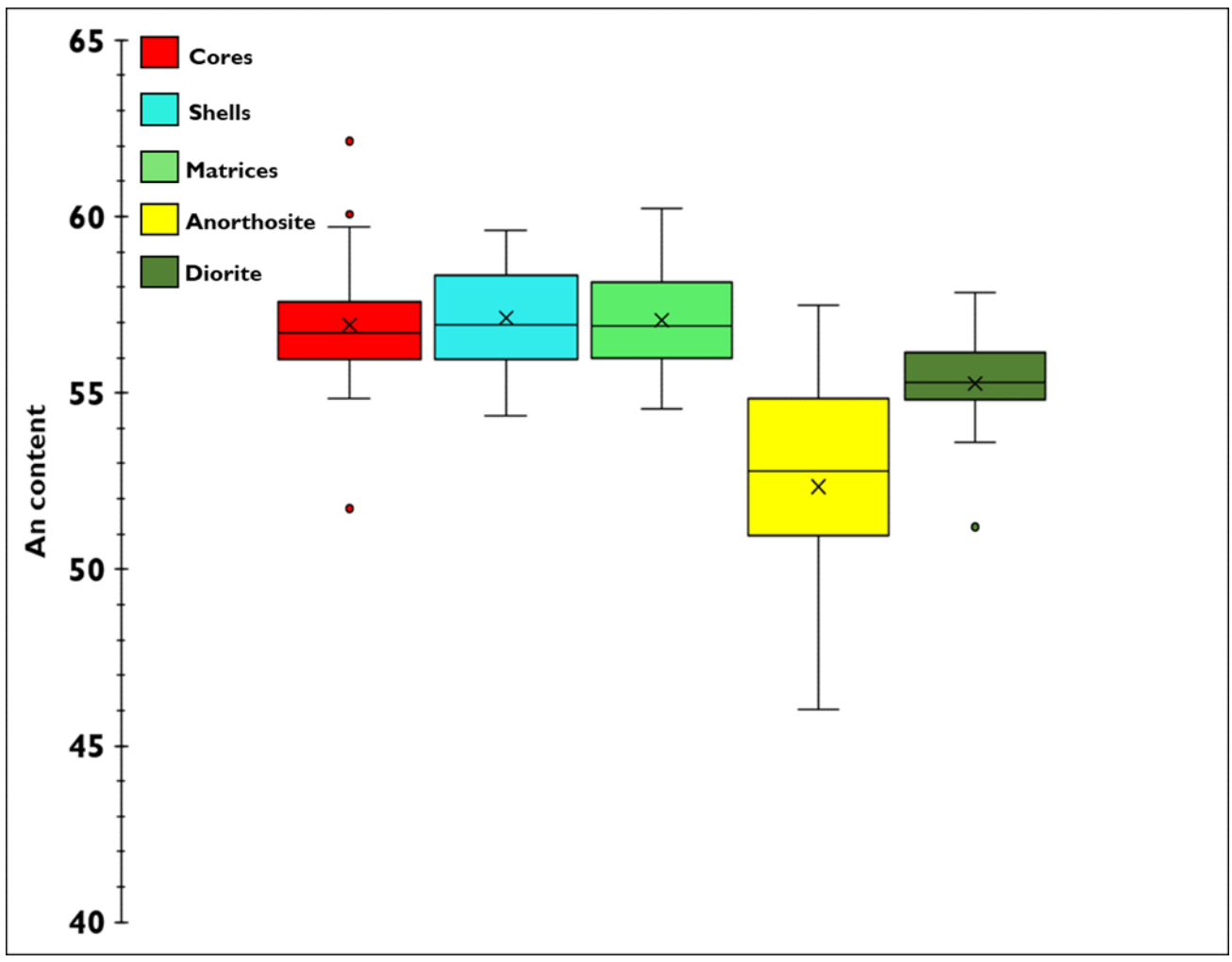


Figure 101: *The graph of An content showing a variation in An content in Henderson South orbicular domains and the surrounding anorthosite and diorite. The two sigma represent the minimum and maximum values, the box represents the interquartile range, x represents the mean, and the middle straight line represents the median.*

Biotite was analyzed in different orbicular domains (Table 31; Appendix B) in samples were SD-55-24A, B, C and D. Summarized major element compositions are presented in Table 14.

Table 14: *Table showing the ranges of the major elements (wt. %) in biotite from the cores, the shells and the matrix of the orbicules from Henderson South.*

Oxide	**Cores**	**Shells**	**Matrices**
TiO_2	2.59-3.63	2.13-4.37	1.08-5.64
MgO	12.81-16.71	13.61-15.05	12.32-19.71
FeO	14.43-16.78	14.29-16.93	14.28-17.60
K_2O	7.26-9.52	7.14-9.76	6.02-9.75
Al_2O_3	12.21-14.80	12.36-15.68	12.65-15.33
SiO_2	37.26-39.08	37.29-39.63	35.82-39.69

Similar to plagioclase, biotite compositions are homogeneous throughout the orbicules (Figure 102; Table x). TiO_2, MgO, K_2O and FeO show little variation in plagioclase from cores, shells and matrices of the same sample or of different samples (Table 14). Although the variation is not high, the cores are slightly more magnesian than the shells and the matrix, respectively Figure 102).

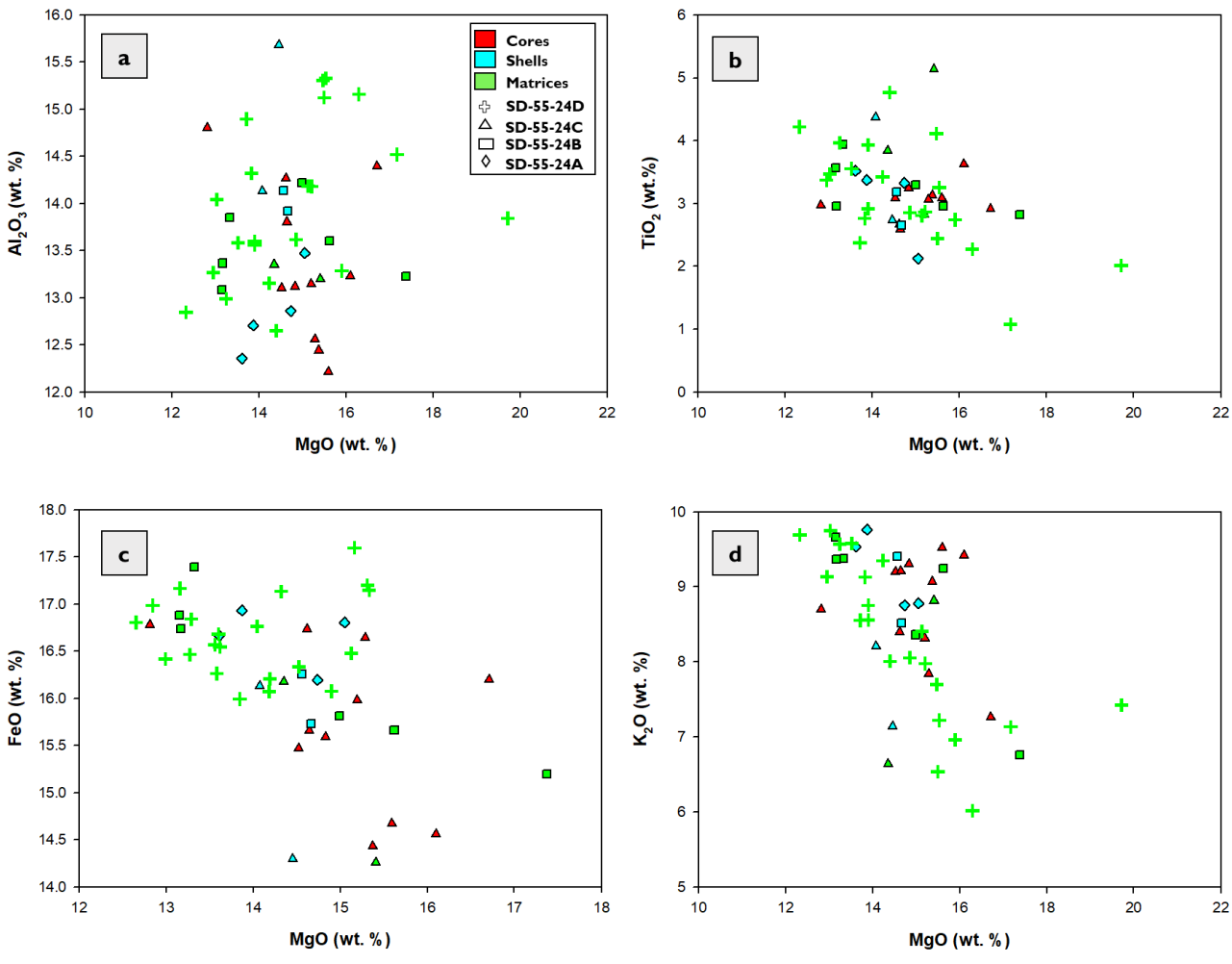


Figure 102*: Chemical variation diagrams showing variation of different oxides in biotite from Henderson South orbicular cores, shells, and matrix plotted against MgO (wt. %).*

Unlike in other orbicular localities, Henderson South orbicules comprise biotite that shows a variation in Mg# in the cores, the shells, and the matrix (Figure 103). The cores are slightly more magnesian than the shells and the matrix.

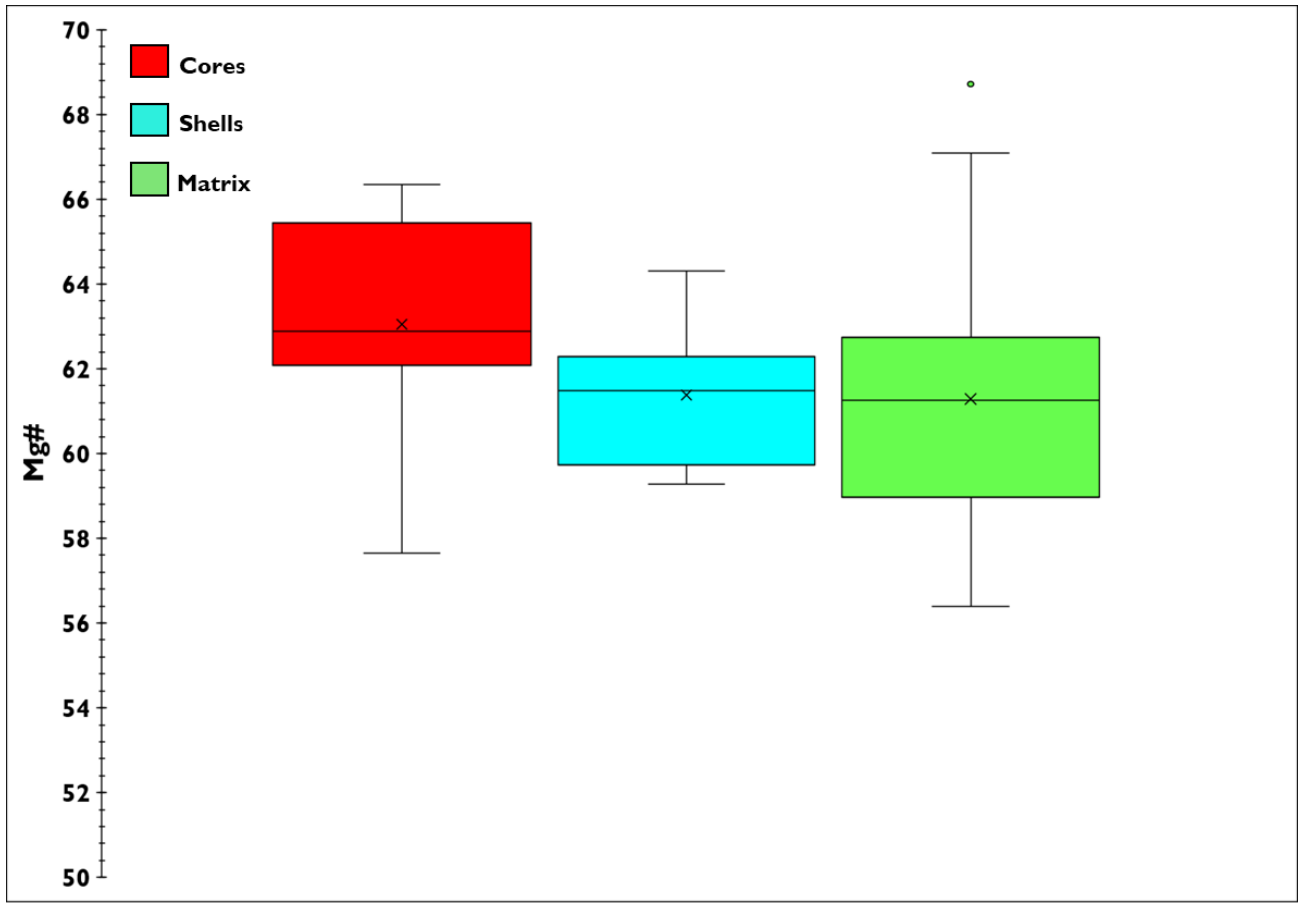


Figure 103: *The graph of Mg# showing a variation in Mg# in Henderson South orbicular domains. The cores are more magnesian than the shells and matrix. The two sigma represent the minimum and maximum values, the box represents the interquartile range, x represents the mean, and the middle straight line represents the median.*

5.3.3. *In-situ* $^{87}Sr/^{86}$ Sr ratios

Initial $^{87}Sr/^{86}Sr$ isotopic determinations in plagioclase from the four Koperberg Suite orbicular localities and the surrounding diorite and anorthosite were determined to test and trace the processes involved in orbicular rock formation (e.g., assimilation, recharge and magma mixing). The initial $^{87}Sr/^{86}Sr$ ratios (Table 32; Appendix B) were calculated assuming the crystallization age of 1030 Ma (Clifford et al., 1995). Strontium isotopic compositions on plagioclase complement the data by Clifford et al. (1975); Geringer et al. (1986); Van Zwieten et al. (1996); and Brandriss and Cawthorn (1996). However, the initial $^{87}Sr/^{86}Sr$ ratios are not homogeneous in all orbicule localities. In addition, initial $^{87}Sr/^{86}Sr$ ratios vary between different orbicular domains in the individual orbicule localities (Figure 104).

Orbicule Koppie orbicules are less radiogenic and have the lowest initial $^{87}Sr/^{86}Sr$ ratios than the other Koperberg Suite orbicule localities (Figure 104). In addition, Orbicule Koppie orbicules are characterized by homogeneous and overlapping initial $^{87}Sr/^{86}Sr$ isotopic compositions (Figure 104; Figure 105a), showing no significant differences. The initial $^{87}Sr/^{86}Sr$ ratios in both anorthosite and diorite in contact with the Orbicule Koppie orbicules are within range with orbicules (Figure 104; Figure 105a). The Nababeep Gneiss has an initial $^{87}Sr/^{86}Sr$ isotopic value of 0.737 (reported to 3

significant figures) at 1030 Ma, which is more radiogenic and not within range with the Orbicule Koppie orbicules, which intrude into it (Figure 104; McCarthy, 1976)). Instead, the initial isotopic compositions of Orbicule Koppie orbicules are within range with the Concordia Granite (Figure 104).

The Koperberg Suite orbicules in the Henderson South region are the second least radiogenic (Figure 104). Similar to Orbicule Koppie, there is little variation in the initial $^{87}Sr/^{86}Sr$ ratios in the Henderson South orbicules (Figure 104; Figure 105d). The initial $^{87}Sr/^{86}Sr$ ratios from plagioclase in anorthosite in contact with the Henderson South orbicules are more radiogenic than in the orbicules (Figure 104; Figure 105d). Conversely, plagioclase in diorite has low initial $^{87}Sr/^{86}Sr$ ratios than plagioclase in anorthosite and the orbicules (Figure 105d).

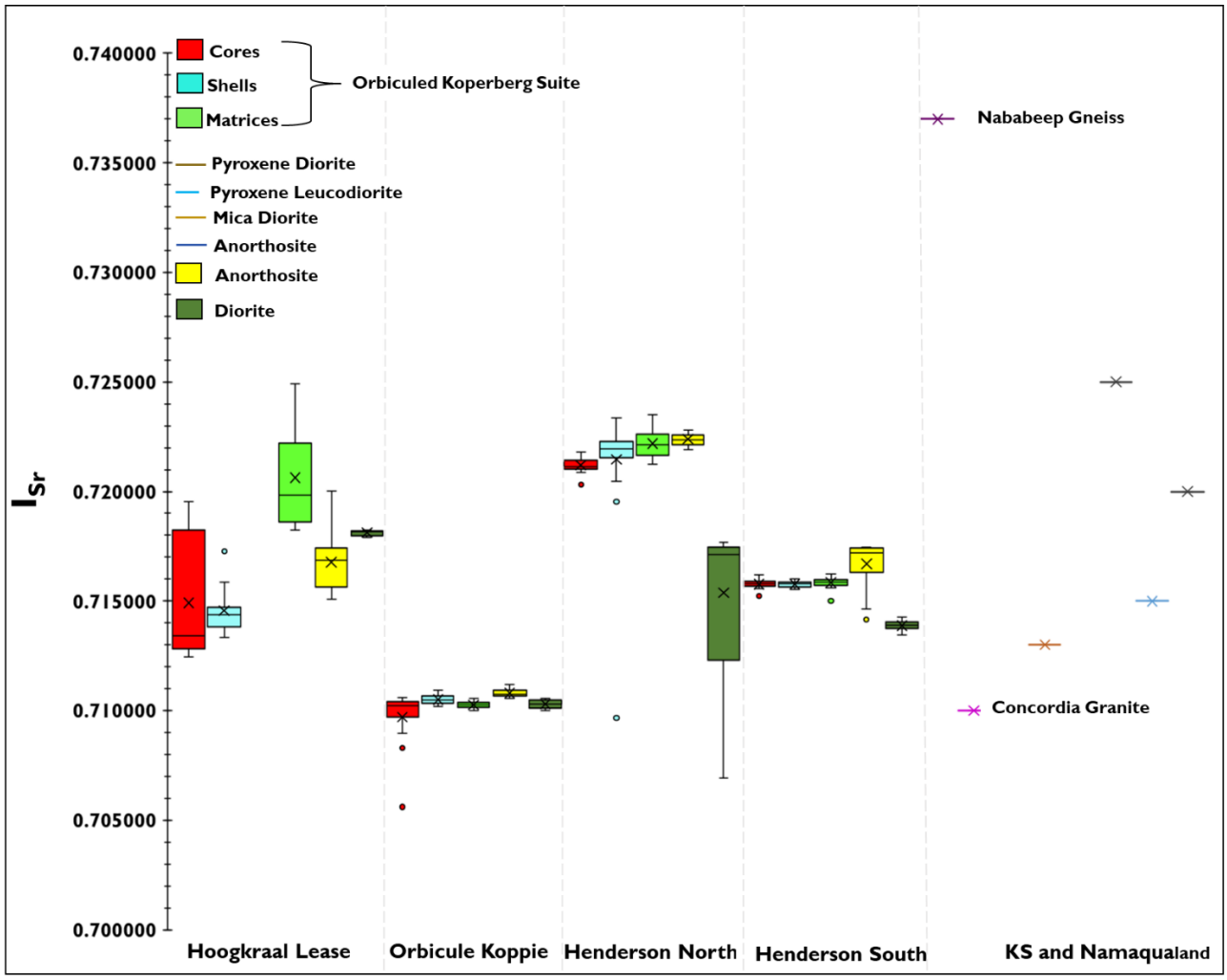


Figure 104*: Graph showing a variation in the initial $^{87}Sr/^{86}Sr$ ratios in plagioclase from the Koperberg Suite orbicules and the surrounding Koperberg Suite massive diorites and anorthosite, and the Namaqualand basement rocks. The initial $^{87}Sr/^{86}Sr$ isotopic ratios in orbicules are within range with the initial $^{87}Sr/^{86}Sr$ ratios (adapted from Van Zwieten et al. (1996) of the massive Koperberg Suite and the Namaqualand basement rocks. The two sigma represent the minimum and maximum values, the box represents the interquartile range, x represents the mean, and the middle straight line represents the median.*

In Hoogkraal Lease, the orbicules comprise plagioclase with more radiogenic initial $^{87}Sr/^{86}Sr$ isotopic compositions than Orbicule Koppie and the Henderson South orbicules (Figure 104). The Hoogkraal Lease matrix comprises plagioclase that has more radiogenic initial $^{87}Sr/^{86}Sr$ ratios than in the shells and the cores (Figure 104; Figure 105b). Similar to the other orbicular localities, initial $^{87}Sr/^{86}Sr$ ratios in diorite and anorthosite are within range with orbicules (Figure 104; Figure 105b).

The Henderson North orbicules are composed of plagioclase with the most radiogenic initial $^{87}Sr/8^{6}Sr$ ratios relative to other Koperberg Suite orbicules (Figure 104). Similar to the other localities, a variation in initial $^{87}Sr/^{86}Sr$ ratios is observed in the cores, the shells and the matrix of the Henderson North orbicules (Figure 104; Figure 105c). Similar to the An content, there is a variation in the initial $^{87}Sr/^{86}Sr$ ratios in shells of different samples (Figure 104; Figure 105c) and sample SD-10-36A plagioclase are more radiogenic than in plagioclase from sample SD-40-19B shells. Similar to shells, there is a slight variation in the initial $^{87}Sr/8^{6}Sr$ ratios in plagioclase in matrices of different samples (Figure 105c). Sample SD-10-36A matrix comprises more radiogenic plagioclase than plagioclase in the matrix sample SD-40-19D (Figure 105c). The surrounding Henderson North diorite is less radiogenic than the orbicules and the anorthosite is within range with the orbicules (Figure 104; Figure 105c).

The comparison of the An content in plagioclase with the initial $^{87}Sr/^{86}Sr$ ratios (Figure 105) shows that there is a distinct relationship between the An content and *in-situ* initial $^{87}Sr/^{86}Sr$ isotopic compositions of plagioclase. In Orbicule Koppie, the initial $^{87}Sr/^{86}Sr$ ratios are homogeneous in orbicules and in surrounding diorite and anorthosite (Figure 105a). Plagioclase in the matrix, however, has a higher An content and are more calcic than in the cores and the shells (Figure 105a). The An content in the surrounding diorite and anorthosite are within range with An content in the cores and the shells, which are slightly less calcic and more sodic than the matrix (Figure 105a).

A similar trend is observed in the Henderson South orbicules, where the initial $^{87}Sr/^{86}Sr$ ratios and the An content are homogeneous in orbicules (Figure 105d). However, plagioclase in the surrounding anorthosite has more radiogenic and elevated initial $^{87}Sr/^{86}Sr$ ratios than the orbicules and diorite, respectively (Figure 105d). In addition, plagioclase in anorthosite is more sodic and has lower An content than plagioclase in diorite and orbicules (Figure 105d).

In Hoogkraal Lease, diorite and anorthosite comprise plagioclase that has a higher An content than plagioclase in the orbicules. However, the initial $^{87}Sr/^{86}Sr$ ratios are homogeneous in both diorite and anorthosite (Figure 105b). In the orbicules, the shells and the cores are less radiogenic and have a higher An content than the more radiogenic and sodic plagioclase in the matrix (Figure 105b). In general, plagioclase in Henderson North orbicules are more radiogenic than plagioclase in diorite (Figure 105c). However, the An content varies between the different orbicule samples.

Sample SD-10-36A shells have high An content and slightly low initial $^{87}Sr/^{86}Sr$ isotopic compositions than the more radiogenic and sodic sample SD-40-19B shells (Figure 105c). A similar trend is observed in matrices, where calcic plagioclase in sample SD-40-19D is less radiogenic than the more sodic and more radiogenic plagioclase from sample SD-10-36A (Figure 105c). In general, in the orbicules, diorite and anorthosite, plagioclase with high An content has low initial $^{87}Sr/^{86}Sr$ isotopic ratios. This is broadly consistent with studies conducted by Van Zwieten et al. (1996) in the Jubilee Pit (Koperberg Suite).

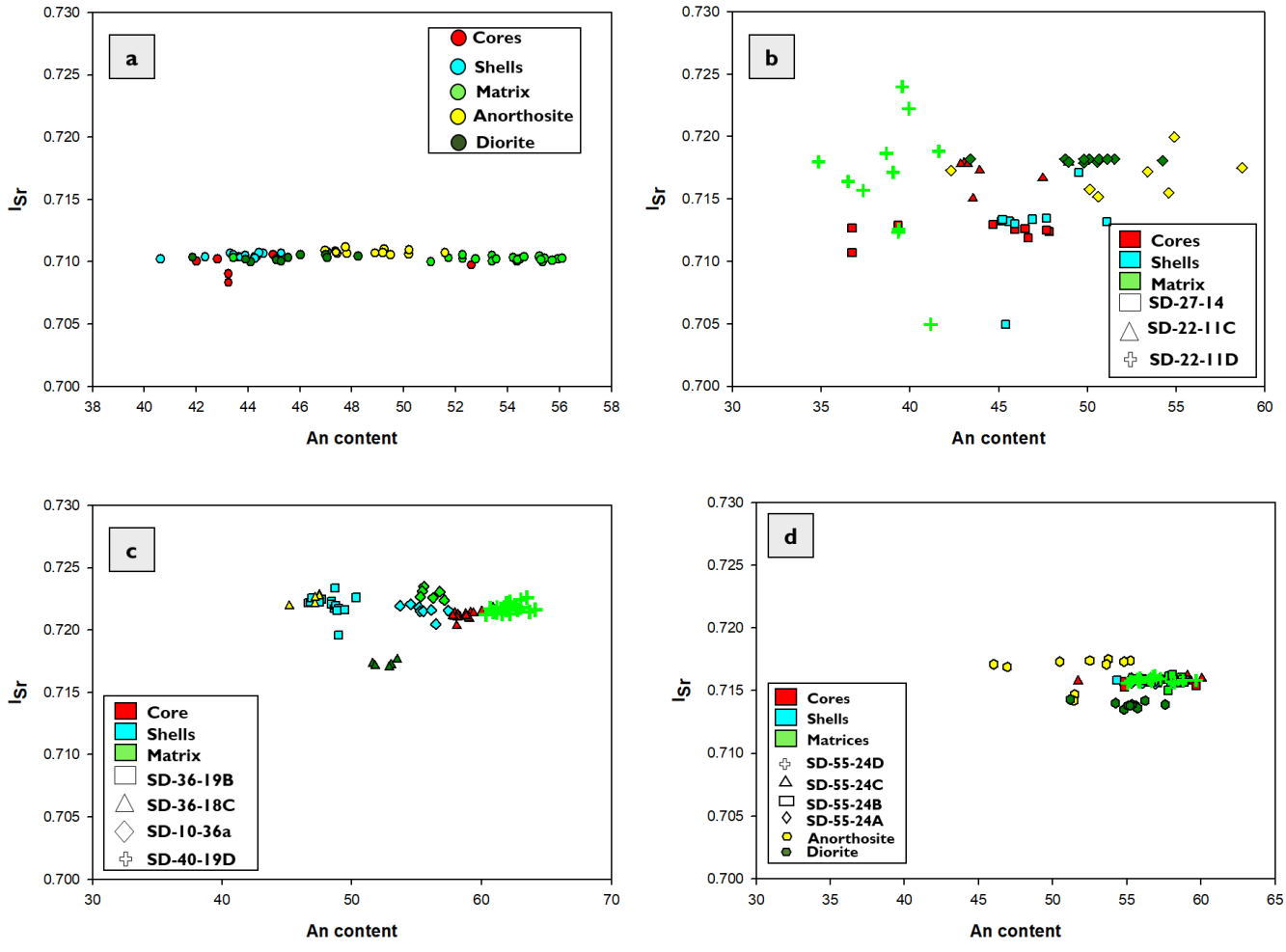


Figure 105: *Graphs of An content plotted against the initial $^{87}Sr/^{86}Sr$ ratios: (a) Graph of the An content plotted against initial $^{87}Sr/^{86}Sr$ of plagioclase from Orbicule Koppie showing homogeneous initial $^{87}Sr/^{86}Sr$ ratios in orbicules and the surrounding anorthosite and diorite. However, the An content varies and it is higher in the more calcic matrix than in the sodic cores and shells. (b) Graph of An content plotted against initial $^{87}Sr/^{86}Sr$ on plagioclase from Hoogkraal Lease showing more radiogenic and sodic matrices together with calcic and less radiogenic cores, shells, diorite and anorthosite. (c) Graph of An content plotted against initial $^{87}Sr/^{86}Sr$ on plagioclase from Henderson North showing a large variation in initial $^{87}Sr/^{86}Sr$ ratios in the more radiogenic orbicules and anorthosite and the less radiogenic diorite. A variation is observed in both An content and in initial $^{87}Sr/^{86}Sr$ ratios in plagioclase from different samples. (d) Graph of An content plotted against initial $^{87}Sr/^{86}Sr$ ratios on plagioclase from Henderson South showing homogeneous An content and homogeneous initial $^{87}Sr/^{86}Sr$ ratios in orbicules. Anorthosite, however, is less radiogenic and more sodic than orbicules. Diorite is less radiogenic than orbicules and anorthosite and the An content is within range with orbicules. Green and yellow Shaded circles, triangles, diamonds and hexagons represent diorite nd anorthosite, respectively.*

Plotted on the depleted mantle curve, the Koperberg Suite orbicules show large variations in the initial $^{87}Sr/^{86}Sr$ ratios ranging between 0.710 and 0.725. The orbicules plot far from the depleted mantle curve and they are more radiogenic than the Concordia Granite and less radiogenic than the Nababeep Gneiss (Figure 106). Isotopic compositions of various lithologies from the southern portion of the Natal sector of the Namaqua-Natal Belt were studied by Eglington (2006). These rocks show a variation in $^{87}Sr/^{86}Sr$ ratios with time, and they are less radiogenic than the orbicules from the Namaqua-sector (Figure 106). Initial $^{87}Sr/^{86}Sr$ ratios from studies carried out on different zones and limbs of the Bushveld Complex (e.g., Hayes et al., 2018; Scoon et al., 2020; Bourdeau et al., 2022) were plotted on the depleted mantle curve for comparison.

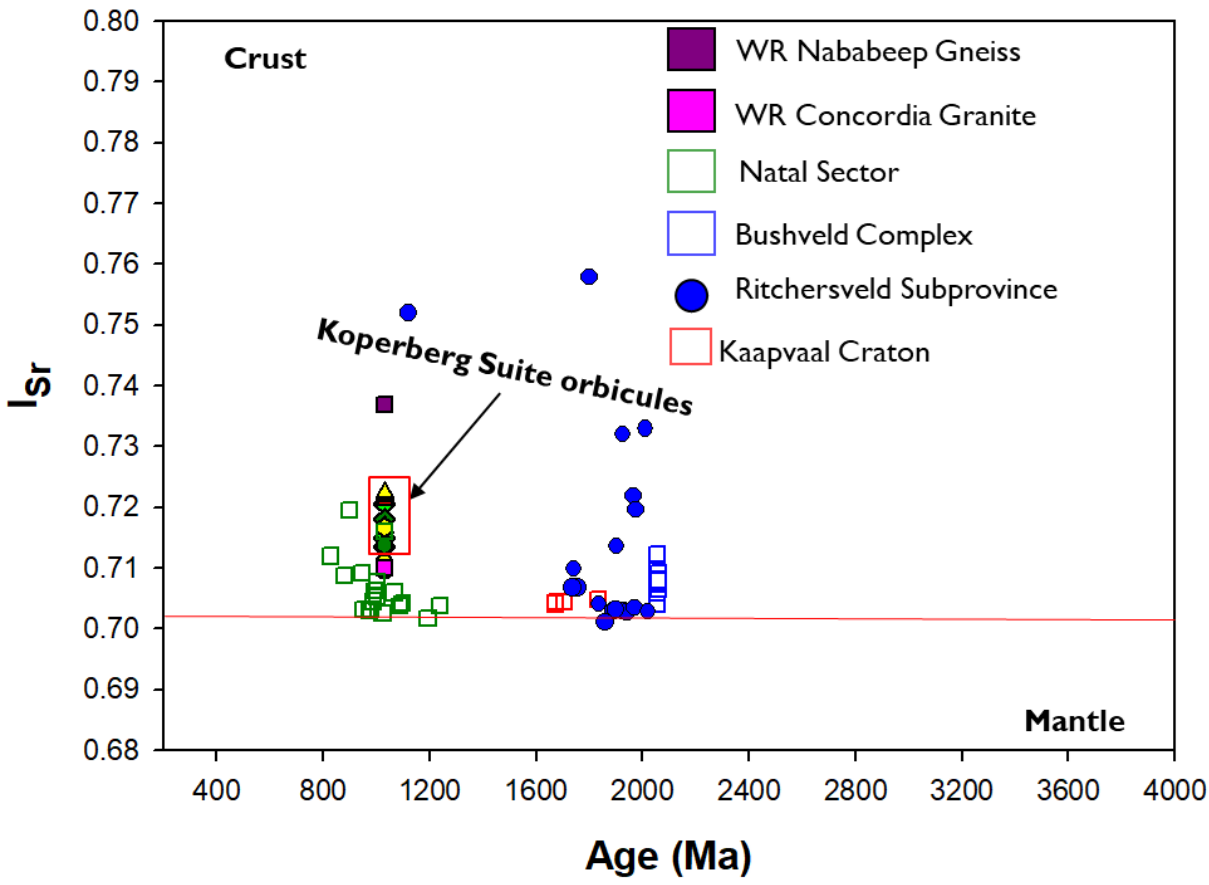


Figure 106: *Initial Sr isotope compositions of units from the Koperberg Suite orbicules, Namaqua-Natal (Eglington et al., 1989), Bushveld Complex (Hayes et al., 2018; Scoon et al., 2020; Bourdeau et al., 2022), Ritchersveld Subprovince (Reid, 1977; 1979; 1991; 1997) , and the Kaapvaal Craton (Donnelly et al., 2012) relative to the model depleted mantle Eglington, 2006).*

Comparing the initial $^{87}Sr/^{86}Sr$ compositions of the Koperberg Suite orbicules to the Bushveld Complex (at 2060 Ma) compositions, the Koperberg Suite orbicules are more radiogenic and plot far from the depleted mantle curve relative to the Bushveld Complex, which plots closer to the depleted mantle (Figure 106). The initial $^{87}Sr/^{86}Sr$ ratios of the Richtersveld Subprovince (Haib volcanic Supergroup and Vioolsdrift suite; Reid, 1977; 1979; 1991; 1997) vary with time, approaching model depleted mantle with increasing age (Figure 106). The Koperberg Suite orbicules are within range with some of the Richtersveld Subprovince rocks (Haib volcanic Supergroup) with initial $^{87}Sr/^{86}Sr$ ratios ranging between 0.70 and 0.728 (Figure 106).

5.3.4. Mineral chemistry summary

Unaltered plagioclase and biotite in orbicule samples and the surrounding diorite and anorthosite in different Koperberg localities were analyzed to establish their chemical compositions. The Koperberg Suite orbicules comprise plagioclase that are andesine to labradorite in composition and characterized by An_{30-70}. Plagioclase composition in orbicules is within range with plagioclase analyzed in host anorthosites and diorites in contact with orbicules. Plagioclase in the Henderson North and Henderson South orbicules are more calcic than plagioclase in Hoogkraal Lease and Orbicule Koppie orbicules. The orbicules comprise plagioclase that is within range and slightly more calcic than the pyroxene diorite, mica diorite and the pyroxene leucodiorite in the Jubilee Pit that were analyzed by Van Zwieten et al. (1996).

In general, the Koperberg Suite orbicules comprises magnesian biotite. Similar to the An content, a variation in Mg# is observed in the Koperberg Suite orbicules and based on Mg#s, the Henderson North orbicules are the most magnesian and the Hoogkraal Lease orbicules are the least magnesian of the Koperberg suite orbicules. Biotite in the Henderson North and Orbicule Koppie orbicules are more magnesian than biotite in the Henderson South and Hoogkraal Lease orbicules. Unlike in plagioclase, there is little to no variation in Mg# within cores, shells and matrices in individual orbicule localities. Although the cores are slightly more magnesian, the Henderson South orbicules comprise biotite that shows little variation in Mg# in the cores, the shells, and the matrix. A similar trend is observed in Henderson North, Orbicule Koppie and Hoogkraal Lease orbicules, which comprise biotite that shows little to no variation in Mg# in the different orbicular domains.

Strontium isotopic compositions in plagioclase in the orbicules complement and augment the data reported in Clifford et al. (1975); Geringer et al. (1986); Van Zwieten et al. (1996); and Brandriss and Cawthorn (1996). However, the initial $^{87}Sr/^{86}Sr$ ratios are not homogeneous in all orbicule localities. In addition, initial $^{87}Sr/^{86}Sr$ ratios vary from cores, shells and matrices in individual orbicule localities. Plagioclase in the Henderson North orbicules is characterized by elevated and radiogenic initial $^{87}Sr/^{86}Sr$ ratios than plagioclase in the other orbicule localities.

6. Geochronology

U-Pb zircon geochronology was carried out to investigate the age relationships between the orbicular structures (core, shells, and matrices) and the surrounding rocks in both the Koperberg Suite and Diana's Pool. The analytical data are presented in this section.

Zircons are present in both the Koperberg Suite and Diana's Pool orbicules. Samples from both localities were selected for U-Pb zircon analysis. Zircons in all thin sections were examined in transmitted light and imaged using backscattered-electrons (BSE) to identify inclusions, textures and areas of replacement by other phases. Cathodoluminescence (CL) was also used to identify growth domains. Zircons occur in a variety of shapes and sizes, ranging from anhedral to euhedral in shape, and from μm to cm in size (Figure 107). In general, the Koperberg Suite and Diana's Pool orbicules contain zircons with cores that display a range of bright-dark intensities and are often characterized by oscillatory zoning and sector zoning (Figure 107). Mantles generally surround the cores, and they are dark in CL and often characterized by sector zoning. The rims are narrow, have an irregular thickness and are generally dark in CL (Figure 107).

There are a few zircons in the Koperberg Suite orbicular cores, and they are all generally less than 50 μm in size. The Hoogkraal Lease, Henderson South, Henderson North and Orbicule Koppie orbicular cores contain zircons that are generally rounded to sub-prismatic, lack any type of zoning and are featureless. Conversely, Diana's Pool orbicular cores contain zircons that are slightly larger than those in the Koperberg Suite (>100 μm) orbicules. They are generally sub-rounded to rounded and others are prismatic (Figure 107h), highly irregular and exhibit oscillatory zoning (Figure 107h) with fractured cores and rims. Some of the grains show multiple stages of resorption and regrowth (Figure 107d). Similar to the cores, the shells generally contain a few zircons, most of them are generally less than 50 μm in size, and they are too small for U-Pb dating. This is generally observed in samples from Orbicule Koppie, Diana's Pool and Henderson South orbicular shells. However, a few datable grains are present in Hoogkraal Lease and Henderson North orbicular shells. Zircons in Hoogkraal Lease orbicule shells are generally prismatic and characterized by sector zoning and fracturing. Henderson North shells, however, are characterized by more rounded zircons, with a few fractured grains and some grains exhibiting oscillatory zoning. Unlike in the cores and shells, large zircons (>100 μm) are hosted in the matrices in both the Koperberg Suite and the Diana's Pool orbicules. These zircons display multiple growth domains in CL, referred to as cores, mantle and rims (Figure 107). Hoogkraal Lease, Diana's Pool and Orbicule Koppie orbicular matrices contain larger and datable zircons than in the other localities. Hoogkraal Lease zircons are generally sub-rounded to sub-prismatic, and they are characterized by xenocrystic cores, growth or oscillatory zoning and fractured rims, hosted in plagioclase (Figure 107f). The Orbicule Koppie matrix contains euhedral to anhedral, rectangular (Figure 107a) to rounded (Figure 107b,c) zircon grains that exhibit light cores, dark mantles and rims surrounded by plagioclase, epidote and quartz.

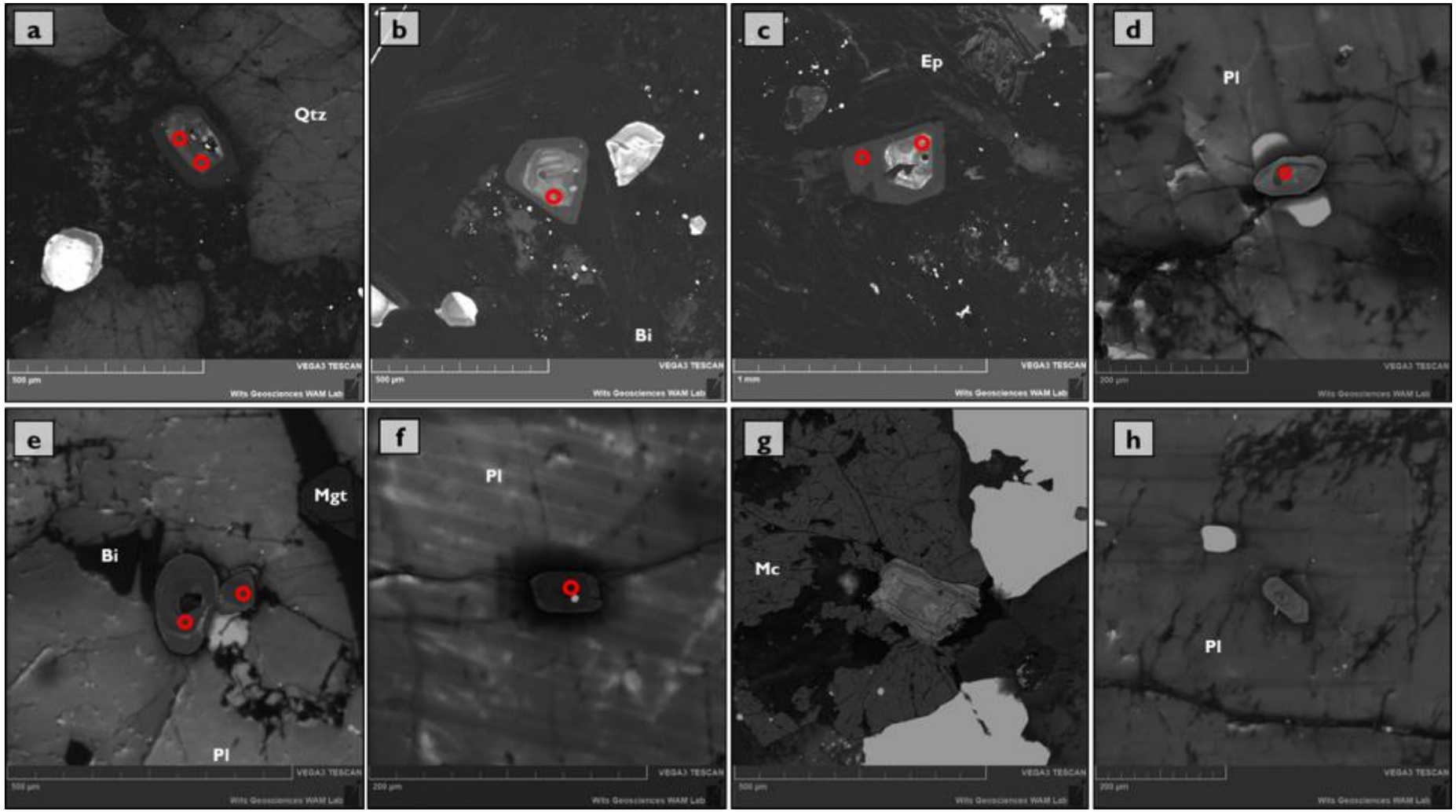


Figure 107: *Cathodoluminescence (CL) images of representative zircon grains from the Koperberg Suite and Diana's Pool orbicules. Red circles represent the spot analysed for U-Pb dating. (a, b, c) Zircon grains from the Orbicule Koppie matrix are characterized by light cores and dark mantles and rims surrounded by quartz (Qtz), plagioclase (Pl), biotite (Bi) and epidote (Ep). (d) Resorbed and sub-angular zircon from the Dina's Pool matrix characterized by sector zoning.*

Figure 107 continued: *(e) Sub-rounded to rounded zircons from the Henderson North matrix characterized by dark cores and rim, with light mantles hosted in plagioclase and surrounded by magnetite (Mgt) and biotite. (f) Euhedral zircon from Hoogkraal Lease matrix characterized by a dark core and light and fractured rim. (g) Anhedral and fractured zircon from Diana's Pool matrix. (h) Elongate and prismatic zircon from Diana's orbicular core exhibiting oscillatory zoning and hosted in plagioclase.*

Diana's Pool matrix contains anhedral and fractured zircons characterized by oscillatory zoning (Figure 107g) and surrounded by feldspars and quartz. Some grains are characterized by sector zoning that has been truncated or overgrown. The zircons were dated *in-situ* using the LA-ICP-ICPMS (Table 15). However, most of the grains were too small and had high common lead (PbC, >0.2%) and they were not suitable. However, the matrix sample SD-10-6C from Orbicule Koppie contains a few datable and usable zircons with PbC less than 0.2% and discordance less than 10%. The online IsoplotR software (Vermeesch, 2018) was used to present the U-Pb data on a Wetherill Concordia diagram and a $^{207}Pb/^{206}Pb$ weighed mean age distribution chart for the data (<10% discordant; Figure 108;Table 15). The weighted mean of $^{207}Pb/^{206}Pb$ age of Orbicule Koppie zircon (<10% discordant) is 1036.10 ± 5.94 Ma (MSWD=1.7, *n*= 4) (Figure 108b). Zircon data for $^{206}Pb/^{238}U$ and $^{207}Pb/^{235}U$ (<10% discordance) plotted on the Wetherill concordia diagram yielded an age of 1036.03 ± 5.92 Ma (Figure 108a) and this age is within the uncertainty of the $^{207}Pb/^{206}Pb$ weighted mean age (Figure 108). The Koperberg Suite has been dated at 1050 Ma (1042 ± 40 Ma) with a Rb-Sr whole-rock age (Nicolysen and Burger, 1965) and at 1100 Ma from a U-Pb Zircon age (Stumpfl et al., 1976) and zircons from Orbicule Koppie matrix sample yielded an age within this published age range.

Table 15: *Results of U-Pb spots analyses of zircon from the Koperberg Suite orbicules.*

Sample	Locality	$^{238}U/^{206}Pb$	SE	$^{207}Pb/^{206}Pb$	SE	Rho*
SD-10-6C (1)-Zr2	Orbicule Koppie	0.17344	0.00164	0.07229	0.00025	0.940
SD-10-6C (1)-Zr7	Orbicule Koppie	0.17284	0.00138	0.07223	0.00028	0.903
SD-10-6C (2)-Zr7	Orbicule Koppie	0.19435	0.00298	0.07216	0.00034	0.956
SD-10-6C (2)-Zr3	Orbicule Koppie	0.17466	0.00178	0.07179	0.00039	0.883
SD-10-6C (2)-Zr5	Orbicule Koppie	0.17640	0.00255	0.07006	0.00031	0.957
SD-10-6C (1)-Zr5	Orbicule Koppie	0.17565	0.00127	0.07158	0.00049	0.726
SD-22-11c-Zr1	Hoogkraal Lease	0.16890	0.00219	0.07392	0.00027	0.962
SD-10-36A-Zr4	Henderson North	0.18350	0.00250	0.07213	0.00024	0.970
SD-40-19B-Zr2	Henderson North	0.11463	0.00286	0.05762	0.00194	0.596
SD-40-19D-Zr2	Henderson North	0.19384	0.00431	0.07344	0.00027	0.987
SD-40-19D-Zr3	Henderson North	0.20464	0.00558	0.07177	0.00026	0.991
SD-40-19D-Zr7	Henderson North	0.14143	0.00324	0.06830	0.00026	0.986
SD-40-19D-Zr9	Henderson North	0.17034	0.00242	0.07284	0.00032	0.956
SD-40-19D-Zr8	Henderson North	0.14916	0.00300	0.06875	0.00027	0.982
SD-36-18C-Zr3	Henderson North	0.15362	0.00196	0.07052	0.00055	0.851
SD-10-6B-Zr3	Orbicule Koppie	0.16765	0.00159	0.07291	0.00062	0.743

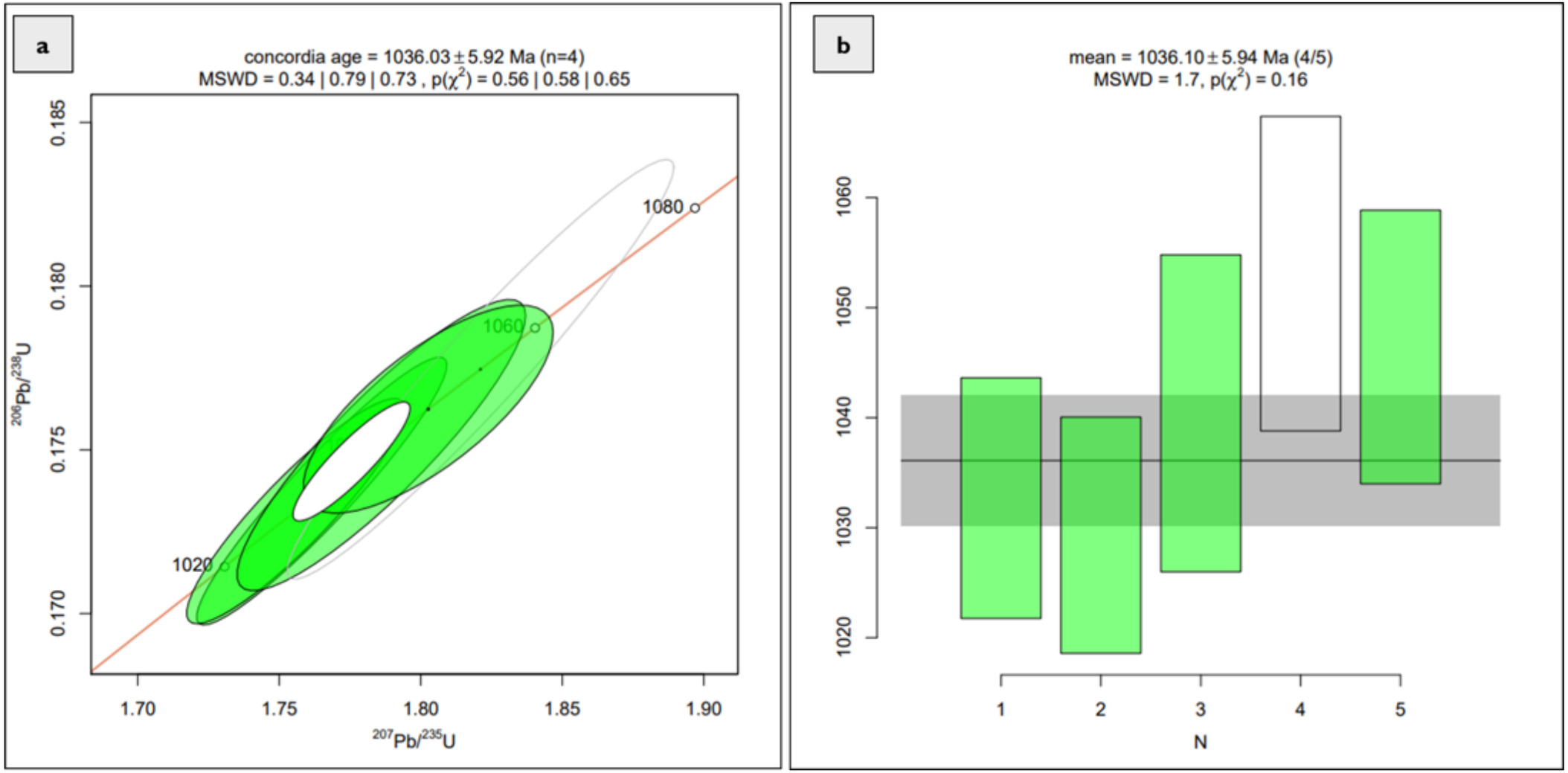


Figure 108: *Representative U-Pb geochronology results of zircon (reported to 1σ): (a) Wetherill U-Pb concordia diagram for zircon from Orbicule Koppie matrix sample SD-10-6C. Rejected data are shown in white (outliers and >10% discordance). (b) Weighted mean diagram showing $^{207}Pb/^{206}Pb$ age of zircon from sample SD-10-6C (<10% discordance).*

7. Sulphide Mineralization

In a previous section (Section 5.2), it was stated that the Koperberg Suite orbicules are associated with sulphide mineralization. Conversely, there is no evidence of such mineralization in the Diana's Pool orbicules. Samples studied for this project are from the more felsic Koperberg Suite orbicules and the mineralization is less common in these rocks. The mineralization in the Koperberg Suite is seldom hosted in felsic rocks (e.g., granites, tonalites, diorites), but it is prevalent in the more mafic members (e.g., pyroxene bearing diorites, norites and leucodiorites; Cawthorn and Meyer, 1993). A similar study on orbicules and sulphide mineralization on the more mafic Jubilee Pit orbicules (~660 m from Henderson South; Figure 6) was carried out by Jogee (2019, honors project). Sulphide mineralization is prevalent in the mafic Jubilee Pit orbicules and some of the samples from Jubilee Pit (Jogee, 2019) in combination with some of the samples from this project were used to study and understand the metallogenesis of the sulphides in the Koperberg Suite orbicules. This section describes estimated modal abundances, textural relationships, and chemical characteristics of sulphides in the Koperberg Suite orbicules to try to understand their metallogenesis in order to test if there is any link between orbicule petrogenesis and sulphide metallogenesis.

7.1. Microscopic descriptions

The oxide and sulphide phases constitute ~5 % of the modal composition in felsic orbicules and ~7% modal composition in the mafic Jubilee Pit orbicules. Approximately 80 % of the sulphides are hosted as inclusions in hypersthene, biotite and plagioclase and the rest are interstitial to the silicate minerals. The oxides (mainly magnetite) constitute ~4% of the modal composition in the felsic orbicules and ~ 5 % in the mafic Jubilee pit orbicules. The oxides have a distinct poikilitic textural relationship with the silicates. They occur as disseminated poikilitic grains within the silicates (Figure 109a). Magnetite, which is the predominant oxide, frequently displays a polygonal shape and exhibits smooth and rounded grain boundaries (Figure 109a, b). Magnetite also exhibits a wide range of habits and sizes, from anhedral to sub-rounded, and from 0.1-1 mm in size (Figure 109). Granular textures are observed between sulphides, oxides, and the silicate phases (Figure 109a).

The sulphides are highly irregular, ranging from fine disseminations (Figure 109b) to coarse grains (Figure 109c, d, e, f) and in places, massive concentrations are observed. They are characterized by feathered margins (Figure 109 c, d, e, and f) and the dominant sulphide assemblages in the mafic Jubilee Pit and the felsic (Orbicule Koppie, Henderson North, Hoogkraal Lease and Henderson South) orbicules are chalcopyrite and bornite (Figure 109). Chalcopyrite is the most widespread sulphide, but it is a minor constituent in the bornite-bearing parageneses. The sulphides occur mainly in the matrices in both the felsic and mafic orbicules and occur as poikilitic inclusions in silicates (Figure 109c), along grain boundaries, along biotite cleavage planes (Figure 109e), and as independent grains. They also occur as chalcopyrite-bornite-magnetite intergrowths (Figure 109e, f). In places, sulphides are interstitial to the silicate phases (Figure 109d) with polygonal and straight grain boundaries against oxides and silicates (Figure 109f). In places, chalcopyrite is replaced by bornite and locally, both bornite and chalcopyrite are replaced by magnetite. Country rocks and the massive Koperberg Suite rocks (diorite and anorthosite) surrounding orbicules seldom contain sulphides. The opaque phase is

mainly magnetite; however, small concentrations of chalcopyrite (<<0.1 mm) are observed in anorthosite in contact with Orbicule Koppie and Henderson North orbicules.

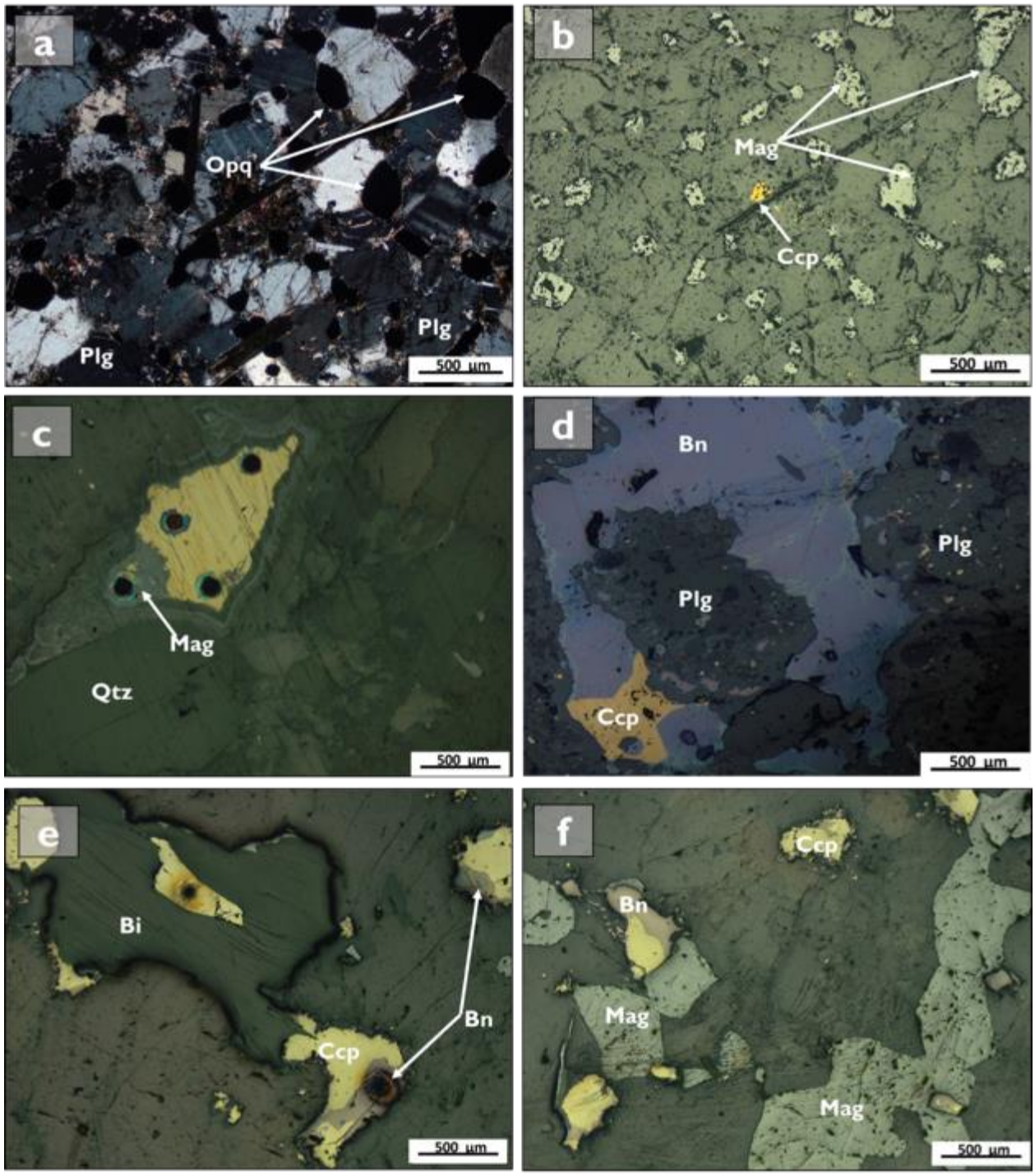


Figure 109: *Photomicrographs of representative sulphide phases in the orbicules: (a, b) Photomicrographs in both transmitted and reflected light showing opaque phases occurring along or close to silicate grain boundaries. Smooth and rounded grain boundaries characterize oxides and feathered margins characterize the sulphides. (c) Independent and massive chalcopyrite grain in Orbicule Koppie matrix that is replaced by magnetite. (d) Interstitial bornite and chalcopyrite overgrowths surrounding altered plagioclase that contain small poikilitic inclusions of chalcopyrite. (e) Inclusion of chalcopyrite grains along cleavage planes in biotite surrounded by grains of chalcopyrite and bornite overgrowths. (f) Jubilee Pit sample characterized by bornite and chalcopyrite overgrowths. The grains grow adjacent to magnetite and locally grow along the grain boundaries of magnetite. Some of the photomicrographs (d and e) show the laser spots used for trace element analysis of sulphides.*

7.2. Chemistry

7.2.1. EPMA analyses

Prior to trace element analysis by LA-ICP-MS, major element compositions of the sulphide phases were determined using EPMA techniques to confirm the identity of the main phases and to provide necessary wt. % Fe values as an internal standard for quantitative LA-ICP-MS analysis. The analytical results from EPMA are presented in (Table 33; Appendix C). Oxide phases were not analyzed, and the analyses have been grouped according to localities. Only chalcopyrite from Jubilee Pit, Henderson North, Henderson South and Orbicule Koppie orbicules were analyzed. Bornite was analyzed from the Jubilee Pit and the Henderson South orbicules. Only two grains of chalcopyrite and two grains of bornite were analyzed in the Henderson South orbicules (Table 4).

Chalcopyrite and bornite were analyzed for the following elements: S, Fe, Co, Ni, Cu, As, Se, Nb, Bi, Ag, Cd, Sn, Sb, Te, Mn and Zn (Table 33; Appendix C). Only Ag, Bi, Se, Pb, and Cd were noted alongside the major elements at concentrations that are comparable with those measured by LA-ICP-MS. Irrespective of host rock or orbicule locality, bornite and chalcopyrite from the analyzed orbicules from different localities are compositionally similar (Figure 110).

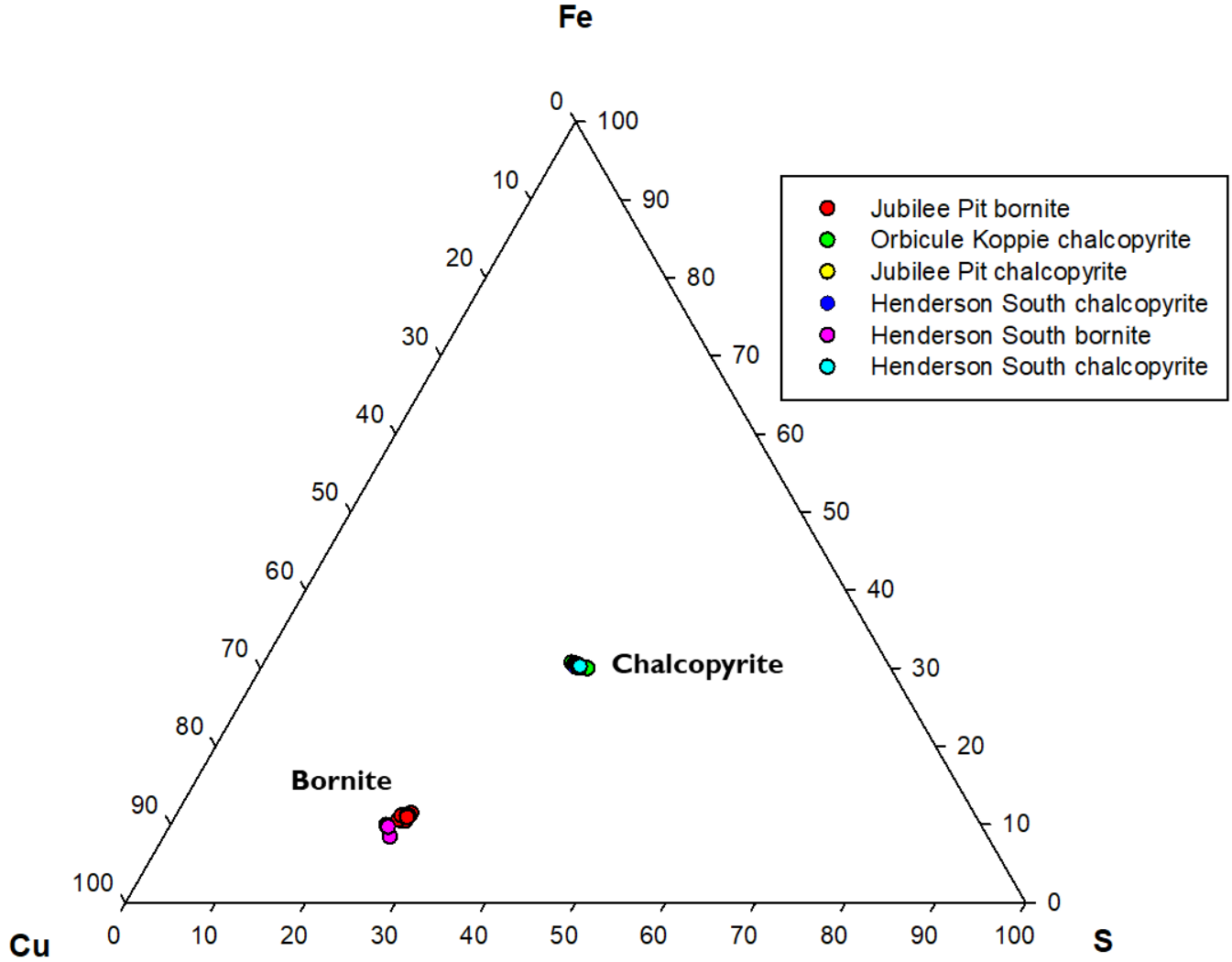


Figure 110: *Cu-Fe-S plots of weight percent composition of sulphides from Jubilee Pit, Henderson North, Henderson South and Orbicule Koppie orbicular matrices.*

7.2.1.1. Chalcopyrite

Chalcopyrite ($CuFeS_2$) was analyzed from Orbicule Koppie, the Henderson South, the Henderson North and the Jubilee Pit orbicules and the ranges of the major elements are shown in Table 16.

Table 16: *Table showing the ranges of Cu, Fe and S in wt. (%) in chalcopyrite from the Koperberg Suite orbicules.*

Locality	Cu	Fe	S	Average Cu/S ratio
Orbicule Koppie	31.9-34.4	28.4-29.9	33.3-35.1	1.0
Henderson North	34.9-34.2	29.7-29.9	34.5-35.0	1.0
Henderson South	34.0-34.4	29.5-29.4	34.0-34.4	1.0
Jubilee Pit	33.9-34.4	29.6-29.8	34.0-34.8	1.0

Chalcopyrite analyzed in samples from different orbicule localities are similar in composition and show little variation in Cu, Fe, and S (Table 16; Figure 110). Hence, there is no variation in the Cu/S ratios (Table 16). Elements including Co, Ni, As, Se, Nb, Bi, Ag, Cd, Sn, Sb, Te, Mn and Zn are all <1 wt. % or below the detection limit (Table 33; Appendix C).

7.2.1.2. Bornite

Bornite (Cu_5FeS_4) is only present in the Jubilee Pit and the Henderson South orbicules. In addition, only two bornite grains were analyzed in the Henderson South orbicules. The ranges of the major elements (Cu, Fe and S) are shown in Table 17 and the rest of the elements in (Table 33; Appendix C).

Table 17: *Table showing ranges of Cu, Fe and S in wt. (%) in bornite from Jubilee Pit and Henderson South orbicules.*

Locality	Cu	Fe	S	Average Cu/S ratio
Jubilee Pit	61.1-67.1	10.0-11.1	24.5-25.8	2.5
Henderson South	65.6-66.4	8.3-9.7	24.6-24.9	2.7

Bornite was only analyzed in the mafic Jubilee Pit orbicules and in the Henderson South orbicules, and all bornite are compositionally similar (Figure 110; Table 17). However, the Cu/S ratios are higher in the Henderson South bornite than in the Jubilee Pit bornite (Table 17). Similar to chalcopyrite, elements including Co, Ni, As, Se, Nb, Bi, Ag, Cd, Sn, Sb, Te, Mn and Zn are all <1 wt. % or below the detection limit (Table 33; Appendix C).

7.2.2. LA-ICP-MS Trace Element analyses

The geological process and the environment in which the trace elements occur, as well as their partition coefficients in a sulphide liquid and the sulphide structure (George et al., 2018) determine the trace element concentration of magmatic sulphides. Because trace element systematics are utilized to understand how sulphide liquid fractionates and how trace elements are distributed among sulphide liquids, they have a considerably wider range of applications in the formation of ore (Helmy et al., 2010), hence, they were analyzed in the Koperberg Suite sulphides. Quantitative trace element analyses were carried out on bornite (Henderson South and Jubilee Pit) and chalcopyrite (Henderson North, Orbicule Koppie, Henderson South and Jubilee Pit) from the Koperberg Suite orbicules (Table5) by LA-ICP-MS. Bornite and chalcopyrite were analyzed for the following elements: Mn, Co, Ni, Cu, Ga, Ge, As, Se, Nb, Mo, Ag., Cd, In, Sn, Sb, W, Tl, Pb and Bi (Table5).

Bornite contains appreciable Bi, Pb, Se, and variable Ni and lacks In, Sn, Ga and Co (Figure 111). Cobalt, Sn, Ge, and In are present in the Jubilee Pit chalcopyrite in variable quantities (Figure 111f, c, e, b), which typically lacks Cd, Bi, Ni and Ga (Figure 111b, a, f, e). Conversely, Orbicule Koppie chalcopyrite lacks In (Figure 111 b) and contains appreciable amounts of Cd, Se, Mn and Ge (Figure 111b, c, d, e). Bismuth, Ni and Se in these sulphides appear to partition into bornite while Ag, In, Cd, Sn, Mn, Ge and Co partition into chalcopyrite (Figure 111).

The only LA-ICP-MS study that has been carried out on bornite that enables comparison of the trace elements in bornite is the study by Cook et al. (2011). Their study provides a set of baseline data on minor and trace element contents in hypogene bornite and accompanying Cu-sulphides from ores from 12 deposits, with emphasis on syn-metamorphic Cu-vein systems in Norway, and skarn, porphyry and epithermal systems in SE Europe.

The main aim of the Cook et al. (2011) study was to identify the more common trace elements in these minerals and to establish common trends in the data. Similar to this study, bornite and chalcocite analyzed by Cook et al. (2011) are poor in Co and Ni, Ga and Ge. In line with the behavior of Ni and Co in other common sulphides, they assume that there must be a degree of substitution of the two elements into the Fe site within bornite and chalcocite. Compared to the Koperberg Suite bornite (where Ag ranges between 15.42 and 111.82; Bi ranges between 90.69 and 128.42; Figure 111b), the Cretaceous skarn, epithermal and porphyry deposits exhibit higher Ag (121 to 1698 ppm) and Bi (134 to 7666 ppm) contents. Bi (618-3045) and Ag (282 to 8078 ppm) contents are even higher in the late Proterozoic metamorphosed veins.

Based on the high concentrations of Ag and Bi in bornite, Cook et al. (2011) concluded that these chalcophile elements are clearly in solid solution and that bornite is an excellent host for both these trace elements and they state that when high-temperature bornite cools, Bi is preferentially partitioned into bornite.

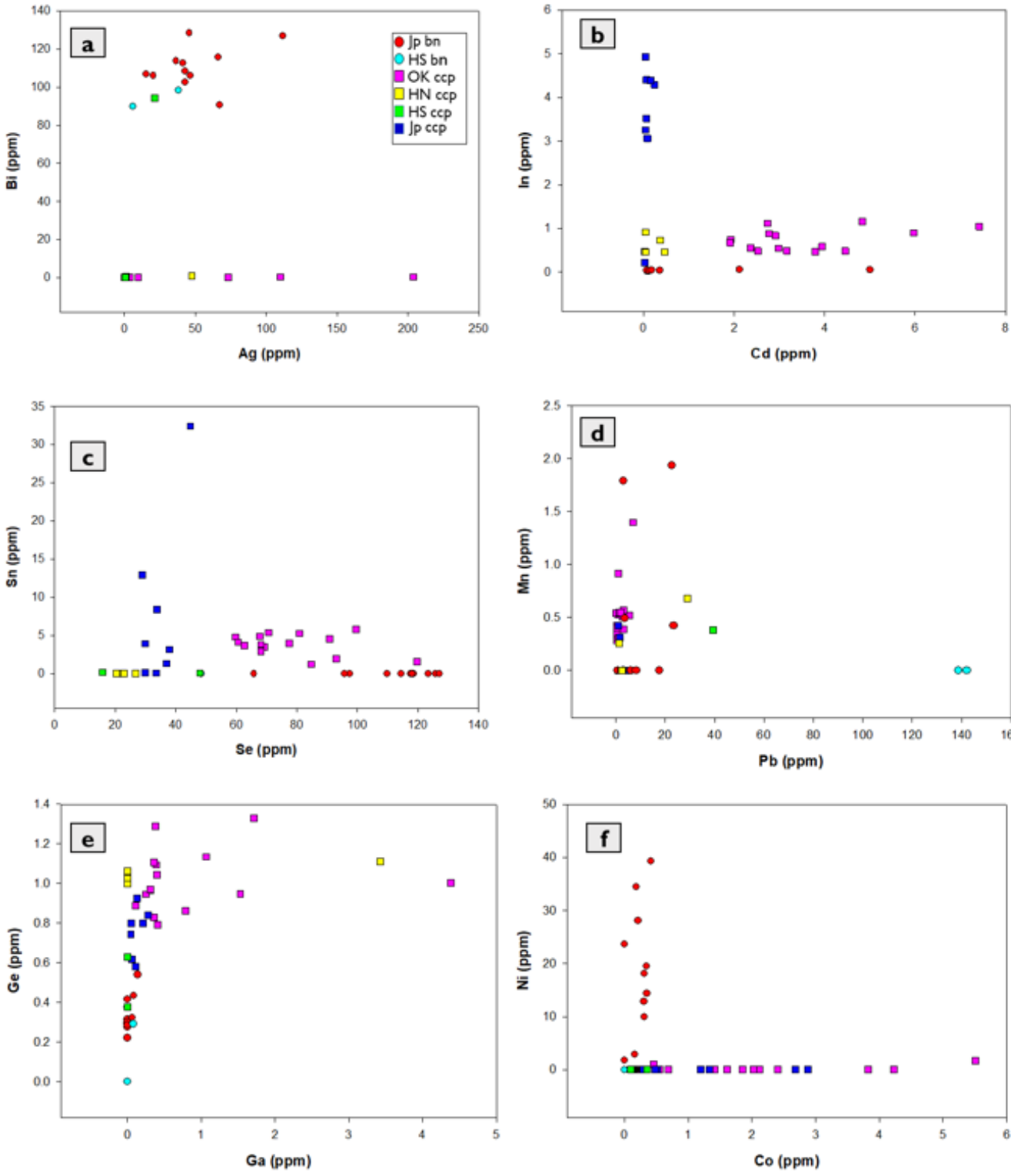


Figure 111: *Trace element (ppm) variation diagrams of chalcopyrite (ccp) and bornite (bn) from the Koperberg Suite orbicules: (a) Bi vs Ag diagram showing bornite from different localities enriched in Bi relative to chalcopyrite. Chalcopyrite shows a large variation in Ag. (b) In vs Cd diagram showing that chalcopyrite in the Koperberg Suite is enriched in Cd and depleted in In relative to bornite. (c) Sn vs Se showing that the Koperberg Suite bornite is enriched in Se and depleted in Sn relative to chalcopyrite. (d) Mn vs Pb plot showing high concentrations of Pb and low concentrations of Mn (below detection limit) in the Koperberg Suite bornite. The highest Mn and lowest Pb concentrations are observed in chalcopyrite. (e) Ge vs Ga diagram showing the Koperberg Suite chalcopyrite enriched in Ge relative to bornite. Ga in bornite is below the detection limit (plotted at 0 ppm). (f) Ni in chalcopyrite is below detection limit (plotted at 0); however, the highest concentrations of Ni and lowest concentrations of Co (below the detection limit) are exhibited by the Jubilee Pit bornite. OK= Orbicule Koppie, HS=Henderson South, HN=Henderson North, HL=Hoogkraal Lease and Jp= Jubilee Pit.*

Table5: *Trace elements concentrations of bornite and chalcopyrite (ppm) in the Koperberg Suite Orbicules. "-"= Below detection limit.*

Locality	Structure	Mn	Co	Ni	Cu	Ga	Ge	As	Se	Nb	Mo	Ag	Cd	In	Sn	Sb	W	Tl	Pb	Bi
OK_CCP	Core	0.50	0.45	0.96	355384.25	4.39	1.00	-	119.78	0.00	2.13	386.15	7.42	1.05	1.58	-	-	-	2.74	-
OK_CCP	Core	0.34	0.19	-	350485.63	0.36	0.83	-	84.85	0.00	0.57	36.25	1.92	0.74	1.21	-	0.01	-	0.47	-
OK_CCP	Matrix	1.40	5.51	1.67	338544.70	1.06	1.14	-	80.96	-	2.37	109.91	4.83	1.16	5.28	-	-	0.32	6.96	0.38
OK_CCP	Matrix	0.53	3.82	-	323208.29	0.38	1.29	0.95	67.73	0.01	-	0.37	2.77	0.88	4.89	-	-	-	0.97	0.11
OK_CCP	Matrix	0.91	4.23	-	344210.20	0.40	1.04	-	59.81	-	0.01	0.50	5.97	0.90	4.78	-	-	-	0.91	0.14
OK_CCP	Matrix	0.52	1.85	-	396915.26	1.53	0.95	-	93.05	-	6.97	203.89	3.94	0.58	1.98	-	-	0.05	5.32	0.46
OK_CCP	Matrix	0.39	1.61	-	320906.02	0.39	1.09	-	69.20	-	0.09	3.93	2.99	0.54	3.46	-	-	0.06	3.06	0.26
OK_CCP	Matrix	0.28	0.68	-	344284.66	0.41	0.79	-	68.12	-	-	0.40	2.36	0.55	2.91	-	-	-	0.36	0.04
OK_CCP	Matrix	0.42	0.69	-	346617.15	0.32	0.97	-	68.13	-	-	0.31	1.91	0.67	3.81	-	-	-	0.34	-
OK_CCP	Matrix	0.30	2.11	-	333490.95	0.25	0.95	0.33	77.46	-	0.01	0.34	2.74	1.12	3.95	-	-	-	1.05	0.15
OK_CCP	Matrix	0.54	0.52	-	346340.99	0.11	0.89	-	62.76	-	-	0.23	2.52	0.48	3.67	-	-	-	0.19	-
OK_CCP	Matrix	0.55	2.02	-	380860.31	1.71	1.33	0.69	90.86	0.00	0.63	73.39	2.91	0.84	4.55	-	-	0.03	1.27	0.07
OK_CCP	Matrix	0.57	0.54	-	328135.40	0.36	1.11	-	60.58	-	0.04	9.83	3.16	0.49	4.10	0.06	0.04	0.05	3.13	0.10
OK_CCP	Matrix	0.55	1.41	-	334896.02	0.31	0.97	0.65	70.70	0.01	-	0.45	3.79	0.47	5.37	-	0.03	-	1.83	0.18
OK_CCP	Matrix	0.40	2.41	-	360901.24	0.79	0.86	-	99.64	-	7.30	226.98	4.46	0.48	5.79	-	-	-	0.40	-
JP_CCP	Matrix	-	1.33	-	341595.92	0.21	0.80	-	44.86	0.00	-	0.39	0.06	4.41	32.41	-	-	-	1.23	0.03
JP_CCP	Matrix	-	0.49	-	340352.32	0.28	0.84	-	29.83	0.00	-	0.30	0.08	3.07	0.12	-	-	-	1.61	0.20
JP_CCP	Matrix	-	0.28	-	311577.57	0.13	0.92	0.29	30.14	-	0.02	1.12	0.02	0.47	-	-	0.00	0.02	5.16	0.53
JP_CCP	Matrix	-	0.51	-	342744.22	-	0.73	0.24	33.56	-	-	1.44	0.06	3.52	0.07	0.01	0.01	-	2.60	0.27
JP_CCP	Matrix	0.31	2.88	-	324857.40	0.05	0.74	-	33.74	-	-	0.32	0.16	4.39	8.42	-	0.01	-	1.45	0.04
JP_CCP	Matrix	-	0.15	-	320662.41	0.06	0.62	-	36.92	-	-	0.54	0.04	3.25	1.33	-	-	-	1.44	0.06

JP= Jubilee pit, OK=Orbicule Koppie, HN=Henderson North and HS= Henderson South

Table 5 (continued)

Locality	Structure	Mn	Co	Ni	Cu	Ga	Ge	As	Se	Nb	Mo	Ag	Cd	In	Sn	Sb	W	Tl	Pb	Bi
JP_CCP	Matrix	-	2.68	-	314458.79	0.11	0.58	-	28.88	0.00	-	0.23	0.24	4.29	12.89	-	0.01	-	1.22	0.07
JP_CCP	Matrix	0.42	0.48	-	333059.77	-	0.74	0.33	29.93	-	-	0.40	0.02	0.22	3.93	-	0.05	-	0.96	0.03
JP_Bn	Matrix	1.79	0.18	34.44	599653.56	-	0.37	-	125.97	0.00	0.00	41.32	5.01	0.05	-	-	-	0.02	2.91	112.49
JP_Bn	Matrix	-	-	1.74	608784.92	-	0.31	-	65.83	-	0.04	20.33	0.14	0.04	-	0.03	-	-	0.68	106.13
JP_Bn	Matrix	-	0.41	39.23	599840.21	-	0.42	-	109.84	-	-	45.72	0.08	0.02	-	-	-	-	2.92	128.42
JP_Bn	Matrix	-	0.21	28.08	610548.00	-	0.29	-	114.41	-	-	46.35	0.10	0.03	0.05	-	-	-	5.90	106.06
JP_Bn	Matrix	0.42	0.16	2.90	605498.68	-	0.28	-	118.52	0.00	-	66.34	2.12	0.06	-	-	-	-	23.32	115.87
JP_Bn	Matrix	-	0.31	18.09	605556.21	-	0.30	-	97.53	-	-	67.41	0.09	0.01	-	-	-	0.03	8.12	90.69
JP_Bn	Matrix	0.49	0.35	14.36	624574.55	0.07	0.32	0.41	123.47	0.01	-	42.82	0.36	0.04	-	-	0.03	0.05	3.49	108.26
JP_Bn	Matrix	-	0.35	19.51	652866.66	0.08	0.43	-	127.19	0.01	-	36.38	0.07	0.04	-	-	0.01	-	17.57	113.77
JP_Bn	Matrix	1.94	0.31	12.81	654610.72	0.14	0.54	-	117.73	0.02	-	111.82	0.12	0.03	0.11	-	0.03	-	22.60	126.73
JP_Bn	Matrix	-	0.31	9.92	591633.94	-	0.22	-	118.06	0.00	-	42.90	0.17	0.05	-	-	-	-	2.71	102.61
JP_Bn	Matrix	0.75	-	23.63	622120.18	-	0.29	-	95.90	0.00	-	15.42	0.09	-	-	0.04	0.00	-	0.77	106.96
HS_Bn	Matrix	-	-	-	623282.01	0.08	0.29	-	21.20	0.00	-	6.20	-	-	-	-	-	0.54	142.04	89.91
HS_Bn	Matrix	-	-	-	627130.81	-	-	-	48.45	0.00	-	38.44	-	0.01	-	-	-	-	138.52	98.38
HS_CCP	Matrix	-	0.36	-	329966.30	-	0.63	-	15.79	0.00	-	0.51	0.21	0.02	0.15	-	-	-	2.23	0.14
HS_CCP	Matrix	0.38	0.10	-	631337.89	-	0.38	-	47.97	0.00	0.04	21.49	-	-	0.07	-	-	-	39.35	94.37
HN_CCP	Matrix	0.26	0.19	-	340417.81	-	1.00	-	21.86	-	-	0.89	0.47	0.47	-	-	-	-	1.40	0.06
HN_CCP	Matrix	-	0.06	-	321532.43	-	1.06	-	22.93	-	-	0.08	0.04	0.46	-	-	-	0.03	2.90	0.24
HN_CCP	Matrix	0.68	-	-	341272.39	3.42	1.11	-	20.40	-	91.57	47.48	0.37	0.73	-	0.04	0.01	0.09	28.98	0.89
HN_CCP	Matrix	-	-	-	325177.39	-	1.03	-	26.68	-	-	0.19	0.03	0.91	-	0.03	-	-	2.41	0.17

8. Discussion

8.1. Comparing Koperberg Suite and Diana's Pool orbicules with global occurrences

Are the orbicules found in the Koperberg Suite and Diana's Pool different from orbicules elsewhere? Almost one-third of the world's known orbicular outcrops are found in Finland and have been discussed and described in detail by different authors including Eskola (1938), Edelman (1983), Pertunnen (1983) and Laitakari et al. (1996) amongst the others. Other examples are from France, the United Kingdom, Ireland, the United States of America, Norway, Antarctica, Australia, Pakistan, Mexico, Japan and Canada, among others. Typical orbicular rocks are plutonic rocks with K-feldspar and plagioclase, quartz and dark minerals (hornblende and biotite).

These orbicules are round bodies, which show a wide variation in size and composition. Some are spherical and some are elongated due to deformation. All orbicules contain a core in the middle that is surrounded by radially grown crystals and the outer parts show concentric shells. Some contain one single shell but most of them contain multiple shells. The shells are composed of different layers of crystals. Some layers are radially grown crystals (often plagioclase), some are tangential, and others are composed of small grains without any orientation. The size of orbicules is related to the chemistry of the rock (Lahti, 2005). The larger orbicules (diameters more than 10 cm to 40 cm) are found in silicic rocks with high amounts of feldspars and quartz. Mafic rocks show smaller orbicules and the smallest in ultramafic, peridotitic or carbonatic rocks (Lahti, 2005). The cores and shells are always separated by a matrix. The studied orbicular rocks in the Koperberg Suite and the Diana's Pool area are no different and they show similar features as remarkable examples of typical orbicular textures described globally. Similar to most orbicular rocks, the Koperberg Suite orbicules are located at the margins of an intrusive complex, where the mafic rock domain and magma-host rock interaction is more prevalent. No fieldwork was carried out in the Diana's Pool area, however a map from Smith and Fripp (1973) suggests that these orbicules also outcrop at margins of an intrusive plutonic complex. Similar to the orbicules elsewhere, both the Koperberg Suite and Diana's Pool orbicules are characterized by shells of contrasting mineral assemblages about the central cores. They contain central cores, shells, and a host matrix. In addition, the shells exhibit radial textures (e.g., Diana's Pool, Hoogkraal Lease and Henderson South). As there is no consensus on the genesis of orbicular rocks globally, it is also important to emphasize that all orbicular rocks almost certainly do not form in the same manner and the Diana's Pool and the Koperberg Suite orbicules are no different. In addition, the main question to address is whether these rocks in the Koperberg Suite and Diana's Pool have a magmatic, metamorphic or metasomatic origin - this is discussed in the following section.

8.2. A magmatic vs a metasomatic origin?

Are orbicules in Diana's Pool and the Koperberg Suite of metasomatic, metamorphic, or magmatic origin? Enzman (1953) and Garvie (1969, 1971) have previously attributed the formation of these orbicules both in the Koperberg Suite and in Diana's Pool to metasomatic processes. Enzman (1953) stated that the Koperberg Suite orbicular rocks outcrop on the flanks or above the steep structures and he concluded that they form from structurally controlled migrating (metasomatic) matter-ions and ionic complexes fluxed in an aqueous medium. Similar to the Koperberg Suite orbicules, Garvie (1969)

proposed a metasomatic origin for Diana's Pool orbicules. He described Diana's Pool orbicules as characterized by shells which are equally spaced and attributed them to rhythmic diffusion processes involving migration of Ca^{2+}, Na^{+1} and Si^{4+} ions inwards towards the orbicule centers and simultaneous migration of Mg^{2+} and Fe^{2+} ions away from the centers of crystallization. However, the metamorphic origin postulated by Enzman (1953) and Garvie (1969; 1971) is disputed here, and the magmatic origin is supported by the petrographic, field observations and geochemical data presented.

Orbicular cores and shells that have comparable mineralogical compositions to the interstitial matrix, although differing only in modal proportions, characterize both the Koperberg Suite and Diana's Pool orbicules. The matrices comprise plagioclase that has striking textural similarities to that of the central cores, and this speaks against any possible reactions between them. A diffusion-reaction involving material from the center of the orbicule is unlikely if the cores and the matrix compositions are not divergent (Elliston, 1984). The uniformity of mineral assemblages from cores to matrices suggests a close relationship between these structures and argues for an common magmatic origin in which the crystalline phase is controlled by the magma (e.g., Enz et al., 1979). The ductile deformation features of Diana's Pool and Orbicule Koppie (Koperberg Suite) orbicules are an interesting argument in favour of the magmatic origin and they provide clues to their origin as the strongest evidence of the environment in which orbicular rocks are formed is given by the deformation structures (e.g., Ray, 1952; Barbey et al., 2021).

From the sample descriptions, Diana's Pool and Orbicule Koppie orbicules exhibit features indicative of transport from a deeper source as they are commonly fractured and/or deformed (Figure 8; Figure 29a, d) Although we did not carry out any fieldwork in Diana's Pool and we lack an understanding of the appearance and arrangement of the orbicular body, the appearance of orbicular samples (large, small and fragmented orbicules crosscut by granitic veins) suggest that the present form of the orbicular body is the result of sequential emplacement process involving different magma sources and magma injections containing orbicules (e.g., Barbey et al., 2021). Based on the deformation features, it is plausible to suggest that the Diana's Pool and Orbicule Koppie orbicules formed in deeper areas of the crust and were later emplaced in their present setting. They were most likely dragged by the inter-orbicular magma during a repeated sequential process. However, at the microscopic scale there is no evidence of deformation of mineral phases in both the Diana's Pool and the Koperberg Suite orbicules. This is an important argument to supporting the presence of a small amount of a melt phase (thus magmatic state), further indicating that the orbicules were not fully crystallized when they were emplaced.

Although it is believed that metamorphic and metasomatic processes can form orbicular rocks (Leveson, 1963; Thompson and Giles, 1974), it is difficult to explain the presence of fractured and deformed orbicules, other than proposing a magmatic origin for initial orbicule formation (Ray, 1952; Symes et al., 1987). Other orbicular localities (e.g., Hoogkraal Lease, Diana's Pool and Henderson South) are characterized by radial textures or comb-layering, and according to Lofgren and Donaldson (1975), these textures occur near the margins of intrusive bodies, which are most prone to supercooling. According to Diaz-Alvarado et al. (2017), orbicular granitoids often exhibit radial textures that are unique forms of magmatic crystallization controlled by varying conditions of temperature, pressure, and/or H_2O content. Although Moore and Lockwood (1973) attributed comb-layering to crystallization

from a low-density, low-viscosity aqueous fluid that is immiscible with the silicate magma of the parent intrusion, comb-layers would be unlikely to survive in an aqueous fluid, hence, a silicate magma is preferable and accounts better for evidence supporting a magmatic origin for comb-layering (Vernon, 1985). An experiment by Lofgren and Donaldson (1975) has also shown that an aqueous fluid is unnecessary in the formation of comb-layers since they can be produced by magmatic crystallization. Sharp boundaries between the matrices, the cores and the shells are observed in both the Koperberg Suite and Diana's Pool orbicules, and they are attributed to magmatic processes, where there are abrupt changes in the physico-chemical environment or conditions of crystallization (e.g., Enz et al., 1979; Sylvester, 2011). These boundaries cannot be due to an *in-situ* change in the conditions of crystallization (Vernon, 1985), and this disproves the diffusion and metasomatic origin suggested by Enzman (1953) and Garvie (1969). Both the Koperberg Suite (Figure 104) and Diana's Pool (Figure 25) orbicules exhibit initial $^{87}Sr/^{86}Sr$ ratios that are more radiogenic than the depleted mantle. Although elevated Sr ratios can be attributed to hydrothermal alteration, which may not be magmatic (Reid, pers. comm., 2023), Cawthorn and Meyer (1993) attribute these high isotopic ratios in the Koperberg Suite to crustal contamination, a differentiation process consistent with a magmatic origin. An addition of a crustal contaminant into a magmatic system that is evolving effects the whole-rock isotopic compositions of the whole-rock and minerals (Cawthorn and Meyer, 1993; Bybee, 2014), consistent with a magmatic origin.

Mg# in pyroxene and An content in plagioclase are normally similar in mafic igneous intrusions (Van Zwieten et al., 1996). However, there is a discordance between Mg# in biotite and An content in plagioclase in the Koperberg Suite orbicules, where the differences between the values are in order of 20 units (e.g., $\overline{x}$ = Mg# 77 biotite and $\overline{x}$= An_{57} in Henderson North orbicules). This is interpreted as indicative of assimilation and mixing with a granitic contaminant, where the contaminant lowers the Ca/Na ratios, hence, lowering the An content of plagioclase, whereas the Mg#s remain unaffected as there is so little Mg and Fe in the granitic component (e.g., Van Zwieten et al., 1996; Brandriss and Cawthorn, 1996). It is important to mention that Van Zwieten et al. (1996) and Brandriss and Cawthorn (1996) observed this discordance in plagioclase and orthopyroxene (not biotite) and here, biotite was analyzed. However, similar relationship is observed, therefore, plausible assumptions that need further work are made here.

From core to matrix in Diana's Pool orbicules, we see high Mg# (~27) in cores, low Mg# in shells (~17) an intermediate Mg# in the matrix (~25) (Figure 23), and this is consistent with progressive crystallization and changes in temperature regimes within the orbicule-forming magma channel (e.g., Lindh and Näsström, 2006). The An content in plagioclase is homogenous in cores, shells and matrix (Figure 21) and this indicates a close genetic relationship between these orbicule structures (i.e., they crystallized from the same magma). In addition, if there was a migration of Ca^{2+}, Na^{+1} and Si^{4+} ions inwards towards the orbicule centres and simultaneous migration of Mg^{2+} and Fe^{2+} ions away from the centres of crystallization in the Diana's Pool orbicules as Garvie (1969) proposed, then one would expect An contents to be higher in central cores and lower in the matrix and that is not the case. In addition, unlike in the Koperberg Suite orbicules, texturally and mineralogically, biotite is primary magmatic (Figure 24c) in Diana's Pool orbicules and shows no evidence of re-equilibration and metamorphism. These chemical similarities between orbicules and the magmatic matrices, as well as

a variety of syn-magmatic textures, rule out the metasomatic origin in both the Koperberg Suite and Diana's Pool orbicules. This work therefore supports a magmatic origin for these southern African orbicule occurrences.

8.3. Diana's Pool vs the Koperberg Suite orbicules: Similarities, differences and implications

The Koperberg Suite orbicules are younger (Proterozoic; 1020-1050 Ma) than the Diana's Pool orbicules (Archean; 2650 Ma) and the orbicules themselves are hosted in rocks of different compositions. The Diana's Pool orbicules are hosted in more granitic rocks compared to the Koperberg Suite orbicular rocks, which occur anorhosites and pyroxenite. However, despite the differences in age, composition and tectonic setting, we still find orbicular rocks occurring in both the Koperberg Suite and the Diana's Pool area. This implies that the formation of these rocks is not dependent on the magma composition that forms the orbicules, however, it is process related. Compared to other orbicules globally, Diana's Pool orbicules are typical granitic orbicules, with many similarities with orbicules from other global localities.

Although the Diana's Pool orbicules are older than the Koperberg Suite orbicules and they share some similarities, the Koperberg Suite orbicules are unique and different. They exhibit large heterogeneity and variation in petrography, field observation and geochemistry between orbicules of different bodies. Although there are other sole example of mineralized orbicules containing metallic elements (chromite orbicules found in ophiolites from the Maqsad area, Oman, Ceuleneer and Nicolas, 1985; orbicules containing molybdenite and chalcopyrite in Galway, Ireland, Feely et al., 2001; Leake, 200), the Koperberg Suite orbicules are the only example of orbicules containing controversial sulphides mineralization, as far it the author can ascertain.What is more intriguing and of interest is the occurrence of these sulphides and the high and more radiogenic $^{87}Sr/^{86}$ Sr ratios that observed in the Koperberg Suite orbicules than in other orbicules elsewhere. This makes the Koperberg Suite orbicules unique and fundamentally distinctive from the Diana's Pool orbicules. The only studies where strontium isotopes were analyzed in orbicules and there is published data are by Barbey et al. (2021) on the 335 Ma Lafaye orbicular granite in France and by Li et al. (2021) on the 1961 Ma Huangling orbicular granodiorite in China. The $^{87}Sr/^{86}Sr$ ratios range from 0.7110 to 0.71471 and from 0.705 to 0.708 in these orbicules, respectively. The $^{87}Sr/^{86}Sr$ ratios in Diana's Pool orbicules are within range with the Huangling granodiorite and slightly less radiogenic than the Lafaye orbicular granite. The Koperberg Suite orbicules however, record even higher and more radiogenic ratios, making them unique. The next section strictly focuses on the differences between the different Koperberg Suite orbicular localities, their petrogenesis, and the conditions that produce the unique Koperberg Suite orbicular rocks.

8.4. Petrogenesis of the Koperberg Suite orbicules

There are interesting variations in textures, mineral compositions and geochemistry between orbicules of different Koperberg Suite orbicular bodies. These differences include:

- **Field and textural differences**

All the Koperberg Suite orbicules are hosted in different lithologies ranging from quartz diorite (Orbicule Koppie) to pyroxene-bearing diorites (Hoogkraal Lease; Henderson North and Henderson South) in composition. The cores are generally medium-grained and dominated by plagioclase with minor biotite, alkali-feldspars, magnetite and accessory chlorite and epidote. However, the Henderson North, Hoogkraal Lease and Henderson South orbicular cores also contain hypersthene, which is not the case in Orbicule Koppie orbicules. The different orbicule localities are characterized by alternating intermediate (roughly equal amounts of plagioclase, alkali-feldspar and minor mafic minerals) and felsic (dominated by feldspars with minor mafic minerals) shells. This is not the case in Orbicule Koppie orbicules, which are characterized by single shells. The Henderson South and the Hoogkraal Lease orbicule shells contain hypersthene, which forms the radiating textures restricted to shells. However, the Hoogkraal Lease orbicules are unique as mafic shells comprising (> 90%) biotite cut by radiating hypersthene grains at 90^{o} angles. Sharp contacts mark the transitions from the shells to the matrices and the grain size and textures generally change from the shells to the matrices. The matrices are similar in composition to the cores. However, the modal abundances differ slightly from one locality to another. The matrices are medium- to coarse-grained, but in Orbicule Koppie orbicules, the matrix is coarse-grained to pegmatitic. There is also evidence of deformation in Orbicule Koppie orbicules - something that is not observed in the other localities. The matrices from all the localities contain chalcopyrite and magnetite in higher modal abundances than in the shells and the cores. However, chalcopyrite occurs as massive and disseminated grains in the matrices compared to the fine-grained and disseminated chalcopyrite in the cores and shells. In addition, the unusual bornite + magnetite + chalcopyrite assemblage is only prevalent in the matrices of the more mafic orbicular rocks and chalcopyrite is replaced by bornite and magnetite.

- **Geochemical differences**

Plagioclase in the Henderson North and Henderson South orbicules is more calcic than plagioclase in the Hoogkraal Lease and Orbicule Koppie orbicules. The orbicules comprise plagioclase that is within range and slightly more calcic than plagioclase from the host pyroxene diorite, mica diorite and the pyroxene leucodiorite in the Jubilee Pit that were analyzed by Van Zwieten et al. (1996). Similar to the An content, a variation in Mg# is observed in the Koperberg Suite orbicules. The Henderson North orbicules contain the most primitive biotite and the Hoogkraal Lease orbicules contain the most evolved biotites. Biotite in the Henderson North and Orbicule Koppie orbicules are more magnesian and primitive than biotite in the Henderson South and Hoogkraal Lease orbicules. Unlike in plagioclase, there is little to no variation in biotite Mg# within cores, shells and matrices in individual orbicule localities. Although the cores contain biotite that are slightly more primitive, the Henderson South orbicules comprise biotite that shows little variation in Mg# in the cores, the shells, and the matrix. A similar trend is observed in Henderson North, Orbicule Koppie and Hoogkraal Lease

orbicules, which contain biotite that shows little to no variation in Mg# in the cores, the shells, and the matrix. Sr isotopic compositions from plagioclase in the orbicules complement the data by Clifford et al. (1975), Geringer et al. (1986), Van Zwieten et al. (1996) and Brandriss and Cawthorn (1996). However, the initial $^{87}Sr/^{86}Sr$ ratios are not homogeneous in all orbicule localities. In addition, initial $^{87}Sr/^{86}Sr$ ratios vary from cores, shells and matrices in individual orbicule localities. Plagioclase in the Henderson North orbicules is characterized by elevated and radiogenic initial $^{87}Sr/^{86}Sr$ ratios compared with plagioclase in Henderson South, Hoogkraal Lease and in Orbicule Koppie, respectively. Although the formation of these rocks cannot be constraint by geochemical data, the variations and heterogeneity in petrography, mineral chemistry and initial $^{87}Sr/^{86}Sr$ ratios from one orbicule locality to another, imply that there are spatially localized processes at play in the Koperberg Suite, possibly providing suitable, but variable conditions for orbicular rocks formation.

8.4.1. Localized processes and the magma source (s) of the Koperberg Suite orbicules

Much of the Koperberg Suite's history has been debated for more than a century (Clifford and Barton, 2012). There is considerable disagreement, in particular, regarding the origin of the magma. Was the necessary volume of magma produced by the anatexis of the lower crust, or did melting of the mantle, whether depleted or enriched provide it? This is crucial because debates pertaining to the origin of the orbicules cannot be had without a knowledge of the origin of the Koperberg Suite magmas. Zircon textural characteristics are provided (see Section 6) and most of the zircons are hosted in the matrices, with minor occurrences in the cores and the shells. According to work presented in this thesis, the zircon grains in the matrix are believed to have originated from a "matrix melt," whilst the zircons in the alternating shells and in the cores are believed to have originated from an "orbicular melt" (e.g., Li et al., 2021). Only zircons in the Orbicule Koppie matrix were analyzed since the zircons in the shells and cores were too small and common Pb contaminated. It is feasible to interpret the age determined by zircons in the Orbicule Koppie matrix as a new magma input age. Based on the geochronology and dating of zircons in the Orbicule Koppie matrix (weighted mean of $^{207}Pb/^{206}Pb$ age of 1036.10 ± 5.94; Figure 108), the emplacement of the orbicular magmas, at least the Orbicule Koppie magma was coeval with the intrusion and emplacement of the Koperberg Suite (1020-1040 Ma; Duschene et al., 2007) during the late Proterozoic. Hence, the mechanisms behind the formation of the contentious Koperberg Suite rocks are most likely the sources of the orbicule-forming magmas, are behind the formation of orbicular rocks in this area and can account for the differences between the four distinct Koperberg Suite orbicular localities.

Based on the initial $^{87}Sr/^{86}Sr$ ratios (0.71-0.725), a study by Clifford et al. (1995) proposed that the Koperberg Suite forming magmas were derived totally from the lower crust. Clifford et al. (1995) envisaged a two-stage process whereby the Concordia Granite is the representative of a mid-Proterozoic crustal partial melt that was followed by melting of andesitic to basaltic material in the lower crust. This melting of the lower crust then produced the Koperberg Suite at 1022-1029 Ma, which is 70 Ma later (at the end of the M_2 metamorphism). However, this model poses several problems. Although Clifford et al. (1995) do not state the age of the andesitic-basaltic crust, it is assumed that it was generated at the same time as the major crust-forming event in the Mid-Proterozoic, Van Zwieten et al. (1996) consider it implausible and unlikely that the initial $^{87}Sr/^{86}Sr$

ratios could increase to ~0.725 by 1030 Ma to produce the trends exhibited by the Koperberg Suite rocks. In addition, because of large temperature ranges between solidus and liquidus, and because the highest degrees of melting would be expected during the peak metamorphism and not during the waning stages of metamorphism, near complete melting of mafic and crustal rocks at the end of prolonged metamorphism is considered implausible and unlikely (Van Zwieten et al., 1996). Morse (1991), who states that lower crustal melt to produce basaltic melts is thermodynamically impossible, further supports this. In addition, clinopyroxene and hornblende are absent from all the Koperberg Suite rocks and the orbicules, making the Koperberg Suite very distinctive. This is atypical in rocks derived by the melting of an andesitic-tholeiitic parent rock (Van Zwieten et al., 1996), further disproving Clifford's (1995) model.

A study by Brandriss and Cawthorn (1996), on the Hoogkraal Lease intrusion of the Koperberg Suite, proposed that Hoogkraal Lease can be divided into two groups: an early group of anorthosites and leucotonalites with high initial $^{87}Sr/^{86}Sr$ ratios (0.722-0.772) and a later group of diorites, leuconorites and monzodiorites with low initial $^{87}Sr/^{86}Sr$ ratios (0.706-0.720) that intrude the felsic anorthosites and leucotonalites. Brandriss and Cawthorn (1996) stated the range and variation of the initial $^{87}Sr/^{86}Sr$ ratios, similar to what is observed in Hoogkraal Lease, Henderson North and Henderson South orbicules (Figure 105b) reflect mixing of two genetically distinct components. These components include a relatively mafic and less radiogenic component derived from the mantle and a more felsic component derived from the granitoid crust. This hybridization between these two components possibly took place during ascent as the mantle-derived magma underwent differentiation and contamination. This mixing is observed in the graph of An vs initial $^{87}Sr/^{86}Sr$ ratios of plagioclase from Henderson South, Hoogkraal Lease and Henderson North orbicules and surrounding rocks (Figure 105d, b, c). Here orbicules display hybrid compositions between the felsic anorthosite and the more mafic diorite. In the Henderson North orbicules, there are two chemically distinct shells and matrices, one group with high An contents and low $^{87}Sr/^{86}Sr$ ratios and the other with low An contents and high $^{87}Sr/^{86}Sr$ ratios (Figure 97; Figure 105c). In addition, Hoogkraal Lease shows two chemically distinct cores (Figure 93; Figure 105b), which provides further evidence of mixing. According to Brandriss and Cawthorn (1996), this chemical relationship between the felsic anorthosites and the mafic diorites cannot be attributed to the simple fractionation of a single parental magma. The fractionation of one single pulse cannot account for the contrasting $^{87}Sr/^{86}Sr$ ratios of the two main groups of rocks. In addition, the fractionation of a single pulse of magma could not have produced early-formed anorthositic cumulates with high $^{87}Sr/^{86}Sr$ ratios and left a more mafic residue with low $^{87}Sr/^{86}Sr$ content, which would have been required to form the more radiogenic anorthosites and the less radiogenic diorites (e.g., Brandriss and Cawthorn, 1996; Van Zwieten et al., 1996). The mineralogical and isotopic differences observed in Hoogkraal Lease, Henderson North and Henderson South orbicules require the presence of at least two genetically distinct magma components. Hence, the author here proposes that magma mixing could have played a role in the formation of these Koperberg Suite orbicules as proposed by Brandriss and Cawthorn (1996) in the case of the Koperberg Suite rocks.

The variations in initial $^{87}Sr/^{86}Sr$ ratios and An content between the different orbicule localities and within cores, shells and matrices of individual orbicular bodies could also be attributed to crustal

contamination during magmatic differentiation. Schoch and Conradie (1990), Boer et al. (1994) and Brandriss and Cawthorn (1996) proposed that basaltic magmas that formed the Koperberg Suite were subjected to crustal contamination in the mid-to lower crust at upper amphibolite to granulite facies. This is supported by the high $^{87}Sr/^{86}Sr$ ratios of the Koperberg Suite in general, and the studied orbicules. The mafic (Mg# and En) and the anorthite (An) contents of co-existing mafic phases (e.g., biotite and orthopyroxene) and plagioclase are normally similar in mafic intrusions (Brandriss and Cawthorn, 1996; Van Zwieten et al., 1996). However, this is not the case in the Koperberg Suite orbicules as there is a discordance between Mg# in biotite and An content in plagioclase. This is interpreted as indicative of assimilation and mixing with a granitic contaminant (probably the Nababeep Gneiss or the Concordia Granite; Figure 106). In addition, the abundance of orthopyroxene (hypersthene in the Henderson North and Henderson South orbicules) is a common phenomenon in anorthosite complexes produced by basaltic melts derived from the mantle below a thickened crust that has been subjected to crustal contamination (Van Zwieten et al., 1996). The Koperberg Suite orbicules are also characterized by the absence of clinopyroxene and hornblende, and this is atypical of rocks derived by melting of an andesitic-tholeiitic parent rock (Van Zwieten et al., 1996). However, the assimilation of a peraluminous melt is limited when it comes to Henderson North and Henderson South orbicules because high alumina content will lead to growth of more aluminous mineral phases than orthopyroxene (e.g., cordierite and garnet; Barbey, pers.comm, 2023).These textural and geochemical constraints, along with isotopic data, indicate that these differentiation processes were localized and possibly took place during magma ascent and emplacement, possibly triggering the ideal conditions for orbicule and sulphide formation.

It is proposed in this study that the initial stage of the Koperberg Suite orbicular rocks formation began with the partial melting of a mantle source that produced the basaltic magma from which the Koperberg Suite intrusive phases were derived (e.g., Mclver et al., 1983). Possibly, at the mid-crustal level, there was mixing as evidenced by the large variation in and the high initial $^{87}Sr/^{86}Sr$ isotopic ratios. In addition, the discordance of En and Mg# of the mafic phases, together with the An content of plagioclase in the orbicules proves unequivocally that all the Koperberg Suite intrusions experienced some hybridization. However, quantitative modelling of the mixing process is difficult to constrain, as the composition of neither of the end members is known with certainty (e.g., Van Zwieten et al., 1996). Mixing probably occurred between an older and more contaminated felsic end-member composition, and a younger, less contaminated mafic end-member composition (e.g., Cawthorn and Meyer 1993; Brandriss and Cawthorn, 1996).

The magmas were then emplaced or injected along the east-west trending steep structures and were contaminated by a granitic component. Was it the Concordia Granite or the Nababeep Gneiss that contaminated the Koperberg Suite magmas? Cawthorn and Meyer (1993), Brandriss and Cawthorn (1996) and Van Zwieten et al. (1996) proposed that the Concordia Granite cannot be considered a suitable contaminant because of its low and less radiogenic initial $^{87}Sr/^{86}Sr$ ratio (0.709 at 1030 Ma). Hence, they propose the contamination to have been *in-situ* at depth by the Nababeep Gneiss of Little Namaqualand (Benedict et al., 1964). However, this remains to be tested and modelled. As there are complications and no trends in different orbicular bodies of the same suite, sophisticated modelling of

the hybridization (recharge) and contamination (the possible contaminant) is required utilizing the Magma Chamber Simulator (MCS) to model these different and localized processes that were at play when the Koperberg Suite orbicules were forming.

8.4.2. Modelling Recharge-Assimilation-Fractional Crystallization (RAFC)

The introduction of a crustal contamination into an emerging magmatic system affects not only the mineral compositions but also the whole-rock isotopic composition (Bybee, 2014). If minerals form in a gradually contaminated magma, this may lead to isotopic disequilibrium and the age and nature of the crust that the magma passes through affect the isotopic signature of the magma (Bybee, 2014). In this section, it is re-emphasized that the dramatic effect that crustal contamination has on the *in-situ* isotopic composition of the Koperberg Suite rocks and the orbicules as several workers have demonstrated in the past (e.g., Van Zwieten et al., 1996; Cawthorn and Meyer, 1993). It is this influence of crustal contamination that obscures the original isotopic signals of the magma and fuels debate around the source of the Koperberg Suite. According to the aforementioned findings and analysis, crustal contamination was crucial in developing the geochemical signatures of the Koperberg Suite in general and the studied orbicules. The Koperberg Suite's isotopic compositions have been shown to be affected by contamination by several researchers, although they do not identify the specific contaminant; instead, they assume it the Nababeep Gneiss (e.g., Van Zwieten et al., 1996). In order to demonstrate that the variable isotopic compositions of the Koperberg Suite orbicules can be simulated with reasonable assimilation of either the Concordia Granite or the Nababeep Gneiss, a Recharge-Assimilation-Fractional Crystallization (RAFC; Bohrson et al., 2020; Heinonen et al., 2022) model utilizing the Magma Chamber Simulator (MCS) described in detail in chapter 3 is developed. The objective of this energy constrained modelling is to reproduce the initial $^{87}Sr/^{86}Sr$ compositions seen in the orbicules, thereby providing a more quantitative model of their petrogenesis.

For more than two decades, AFC (Assimilation and Fractional Crystallization) mathematical models only have dealt with the exchange of mass between melt and wall rock (Bybee, 2014). Yet, in practice, any model that deals with assimilation and fractional crystallization must adhere to the fundamental limitations of thermal energy conservation and mass balance between a cooling magma and a warming, melting wall rock (Bybee, 2014). Spera and Bohrson (2001) have created models that are more intricate in recent years that simulate the geochemical path a magma takes as thermal equilibrium between the wall rock and magma is approached during fractional crystallization, assimilation, and recharge. These models are based on coupled non-linear ordinary differential equations (Spera and Bohrson, 2001; Bohrson and Spera, 2001). Much of assimilation modelling has been based on binary mixing and assimilation fractional crystallization (AFC) equations that only use trace element and isotopic data (e.g., DePaolo, 1981). However, the modeller is not informed about the associated changes in phase equilibrium or if the conclusions are reasonable in terms of energy conservation by these methods, which may be valuable for providing speculative information. However, from earlier studies that concentrated on mass balance (e.g., Taylor, 1980; DePaolo, 1981) to those that included mass and energy balance in the context of open system evolution (e.g., Spera and Bohrson, 2001; Bohrson and Spera, 2001), trace element and isotopic models of open system magma processes have evolved (Bohrson et al., 2020; Heinonen et al., 2022). Thermodynamic modelling has additionally advanced

significantly, and modern models such as the family of rhyolite-MELTS models (Ghiorso and Sack, 1995; Asimow and Ghiorso, 1998; Gualda et al., 2012), pMELTS (Ghiorso et al., 2002), and THERMOCALC (e.g., Powell and Holland, 1988; Powell and Holland, 1994, 1994; Powell et al., 1998) provide tools for identifying the mineral-melt-fluid phase equilibria in magmatic systems. Here we utilize the MCS (Bohrson et al., 2014) as a versatile computational tool for modelling recharge, assimilation and fractional crystallization. In this section, the utility of forward modelling is highlighted by providing a comparison of cases that illustrate the petrologic and geochemical consequences of recharge, assimilation, fractional crystallization (RAFC) scenarios for the genesis of the Koperberg Suite. The results of these models provide perspective on how melt + crystals + fluid in a crustal magma system may evolve in response to different combinations of open-system processes. These models (recharge, assimilation, and fractional crystallization models) require the specification of thermal (as well as chemical) parameters for the magma and crust due to the conservation of energy and mass. The starting parental melt, recharge magma and wall rock compositions specific to the Koperberg Suite scenario are listed in Table 18.

Table 18*: Parental Melt (PM), Recharge magma (RM) and Whole-Rock (WR) compositions used in the models taken from literature.*

	PM (resident) and RM	**Whole-Rock (WR)**	
	Cacscade Arc Basalt	Concordia Granite	Nababeep Gneiss
SiO_2	51.38	70.86	72.68
TiO_2	0.99	0.40	0.37
Al_2O_3	16.19	14.95	14.11
Fe_2O_3	3.82	1.30	0.81
FeO	3.84	1.76	1.20
MnO	0.10	0.37	0.03
MgO	6.99	0.36	0.45
CaO	8.26	0.44	1.80
Na_2O	3.58	2.15	2.47
K_2O	1.17	7.46	5.59
P_2O_5	0.40	0.08	0.10
H_2O	3.87	0.22	
CO_2	0.02	-	-
Sr (ppm)	1347	82	368
$^{87}Sr/^{86}Sr$	0.702254	0.709	0.737

PM and RM major element, $^{87}Sr/^{86}Sr$(re-calculated to 1030 Ma) and Sr (ppm) and compositions taken from Bacon et al. (1997).

Concordia Granite and Nababeep Gneiss compositions were taken from McCarthy (1976) and Clifford et al. (1975) and were normalized to 100 %.

Sr (ppm) and $^{87}Sr/^{86}Sr$ compositions of the contaminants were taken from Clifford et al. (1975) McCarthy (1976), Van Zwieten et al. (1996) and Andreoli et al. (2006).

Four MCS-PhaseEQ and MCS-Traces simulations that compare the melt composition and phase equilibria evolution of a magma body undergoing fractional crystallization (FC), recharge (one event), fractional crystallization (RFC), assimilation–fractional crystallization (AFC), and recharge (one event–assimilation–fractional crystallization (RAFC) are presented here. Models complying with predetermined thermal and chemical characteristics are employed generally. Models with optimized constraints are run if these parameters do not accurately reproduce the observed geochemistry for as long as the parameter modifications are justifiable. Table 19 below defines and details the thermal and chemical characteristics for the various scenarios that were looked at for this thesis.

Table 19: *Thermal and chemical parameters used in RAFC models for four MCS simulations. Temperature in in ^{o}C.*

	FC	RFC	AFC		RAFC	
			NG	CG	NG	CG
Magma liquidus temperature	1145	1141	1195	1195	1195	1195
Temperature decrement	5	5	5	5	5	5
Magma initial mass (m.u)	100	100	100	100	100	100
Hard stop temperature	900	900	800	800	800	800
Wallrock find solidus start temperature	-	-	880	850	850	880
Wallrock find solidus end temperature	-	-	700	700	700	700
Wallrock find solidus temperature decrement	-	-	5	5	5	5
Wall rock initial temperature	-	-	700	700	700	700
Wall rock initial mass (m.u)	-		200	200	200	200
Recharge event mass (m.u)	-	75	-	-	75	75
Recharge/stope event temperature of recharge when recharge occurs	-	1130	-	-	1130	1130
Recharge temperature of magma when recharge occurs	-	1050	-	-	1050	1050

Energy constrained MCS modelling is presented in the following sections and the models are discussed and compared in detail below. It is also important to mention that this modelling is not precise but quantitative. The Sr (ppm) of the orbicules was then plotted against $^{87}Sr/^{86}Sr$ (I_{Sr}; Figure 112) and compared to the whole-rock data from Van Zwieten et al. (1996). The *in-situ* data from this study is

within range with the whole-rock data from Van Zwiten et al. (1996) study on the Koperberg Suite rocks in the Jubilee Pit (Figure 112).

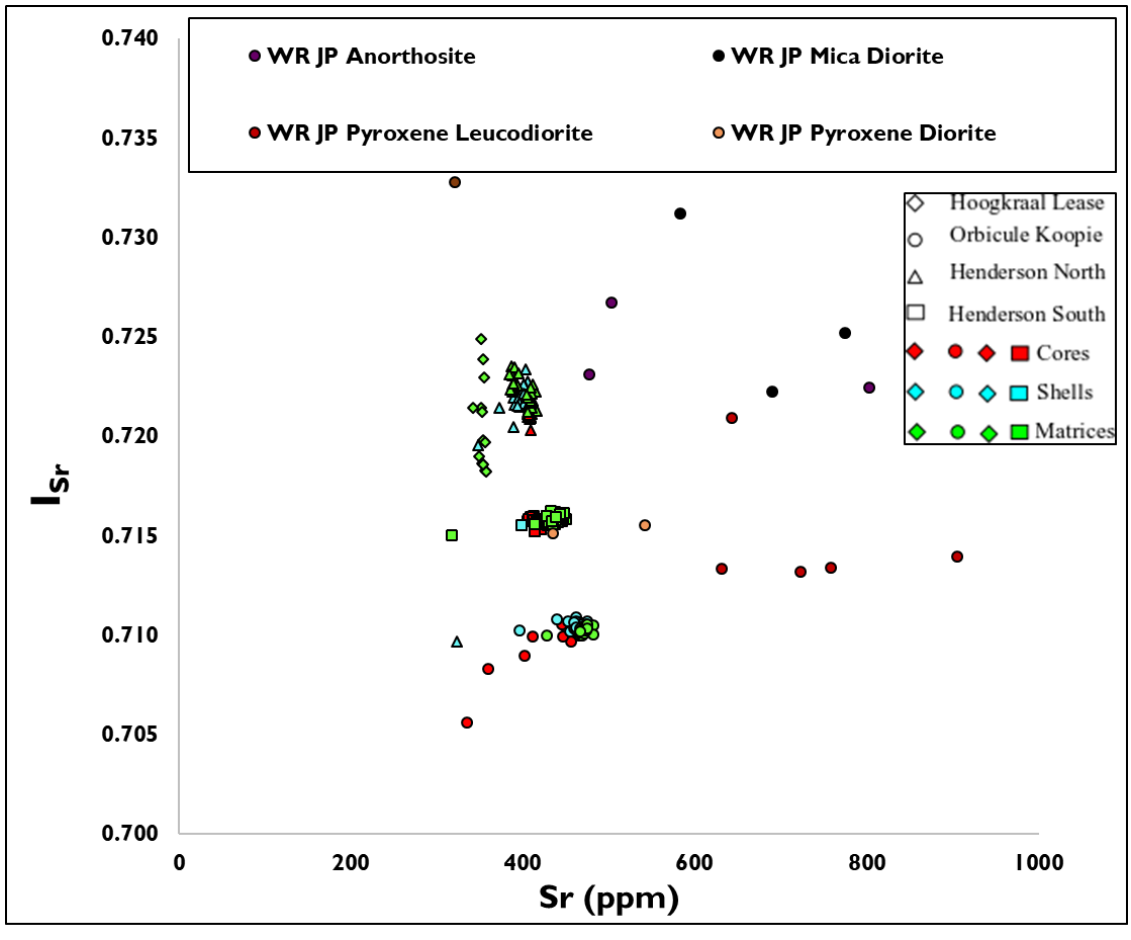


Figure 112: *Graph showing a variation in the initial $^{87}Sr/^{86}Sr$ ratios in plagioclase plotted against Sr (ppm) from the Koperberg Suite orbicules and the whole-rock data from the surrounding Koperberg Suite massive rocks, taken from Van Zwieten et al. (1996). The in-situ data from this study is within range with the whole-rock data from Van Zwieten et al. (1996).*

Prior to finding the "best fit" model or the model that can best reproduce the array or the isotopic signatures in plagioclase from the Koperberg Suite orbicules (Figure 112), different melt compositions had to be tested. Firstly, a depleted mantle (DM)-derived Mid-Ocean-Ridge-Basalt (MORB) major element compositions and the $^{87}Sr/^{86}Sr$ isotopic ratio from Salters and Stracke (2004) was modelled and failed to reproduce a model that can account for the isotopic signatures in the orbicules and/or the Koperberg Suite (Figure 113). Temperature, pressure (between 1 and 6 kbars) and the water content (wt. %) were modified, however, the isotopic signatures could not be reproduced (Figure 113). In this thesis, only the model run at 1.5 kbars is shown (Figure 113). When the MORB melt composition did not reproduce these isotopic signatures, a different melt composition had to be tested. The next parental magma that was then tested is depleted mantle-derived continental tholeiite from the Karoo Large Igneous Province (KLIP; ~180 Ma; Figure 114) (Luttinen and Furnes, 2000; Bohrson et al., 2020). Similar to the MORB composition, the KLIP plume composition (run at pressures between 1 and 6 kbars) did not produce these isotopic compositions. The model shown here was run at 1.5 kbars (Figure 114). Failing to produce these isotopic signatures using a tholeiitic composition further supports Van Zwieten et al.'s (1996) conclusions that these isotopic signatures are atypical of rocks derived by the melting of an andesitic-tholeiitic parent rock, further disproving Clifford's (1995) mid-Proterozoic crust partial melting, followed by melting of andesitic to tholeiitic material in the crust model.

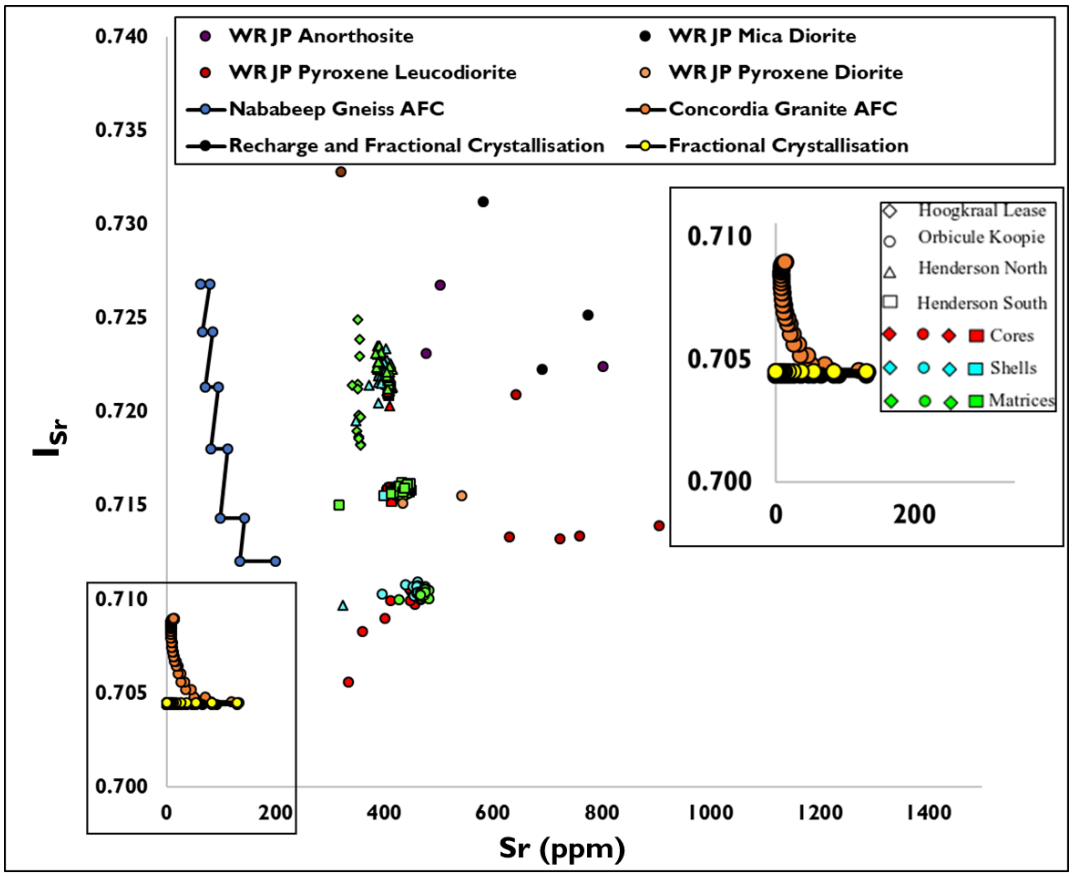


Figure 113: *An energy constrained MCS model simulating Fractional Crystallization (FC), Recharge-Fractional Crystallization (RFC), Assimilation-Fractional Crystallization (AFC) with both the Nababeep Gneiss and the Concordia Granite, and Recharge-Assimilation-Fractional Crystallization (RAFC) using depleted mantle-derived MORB composition taken from Salters and Stracke (2004) run at 1.5 kbars. WR = whole-rock and JP = Jubilee Pit.*

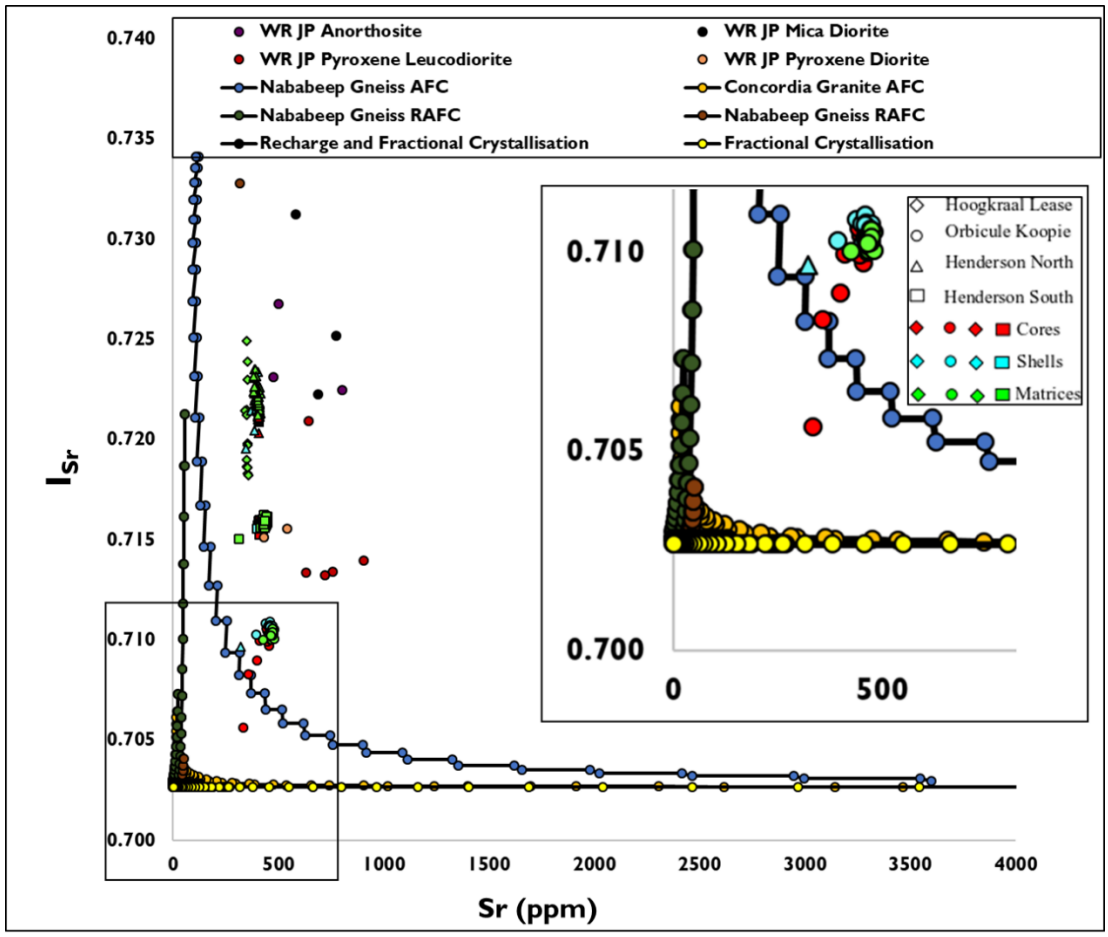


Figure 114: *An energy constrained MCS model simulating FC, RFC, AFC with both the Nababeep Gneiss and the Concordia Granite and RAFC using depleted mantle-derived Karoo Large Igneous*

Figure 114 continued: *Province composition taken from Bohrson et al. (2020) run at 1.5 kbars. WR = whole-rock and JP = Jubilee Pit.*

The isotopic signatures in the Koperberg Suite orbicules could only be reproduced from an arc basalt composition (Table 18). This is expected since Waters (1986) and Macey et al. (2022) proposed that the tectonic evolution of Namaqualand and its ore deposits suggest the development of a magmatic arc, with related and subsequent volcanic and sedimentary deposits in an extensional back-arc setting during the period 1300 to 100 Ma ago (Reid, pers. comm., 2023). The following sections present four MCS-PhaseEQ and MCS-Traces simulations that compare the arc basalt composition (from the Crater Lake, Cascade Arc; sample 80C354; Bacon et al., 1997; Table 18) and phase equilibria evolution of an arc basalt undergoing FC, RFC, AFC, and RAFC.

Case 1: Fractional crystallization (FC)

The FC case assumes that the mantle-derived parental magma (Table 19) intrudes the crust and undergoes fractional crystallization without involvement of any crustal. Thus, the entire compositional signal derives from the mantle mediated by low-pressure crystal fractionation (Bohrson et al., 2014).

However, given the realities of moving low-viscosity materials through significant areas of crust with contrasting compositions, as well as the episodic nature of magma intrusion, magmas that have only undergone fractional crystallization without interaction with crust and/or without magma mixing are probably rare (Bohrson et al., 2014).

This is no different in the case of magmas that formed the O'okiep Copper District and the Koperberg Suite. Simple fractional crystallization of an arc basalt magma composition with a liquidus temperature of 1145 ^{o}C at pressures between 1 and 6 kbars, stoping at a chosen temperature of 900 ^{o}C (Table 19) could not have produced the isotopic signatures exhibited by the Koperberg Suite orbicules and host rocks. In this thesis, I only show a FC modelling simulation run at 1.5 kbars (Figure 115). The FC modelling of an arc basalt magma produces a trend that does not account for both the range of strontium concentrations and the isotopic signatures exhibited by the Koperberg Suite orbicules.

This further supports Brandriss and Cawthorn (1996), who stated that fractionation of one single magmatic pulse cannot account for the contrasting $^{87}Sr/^{86}Sr$ ratios of the Koperberg Suite rocks and the orbicules in this study (Figure 115) .

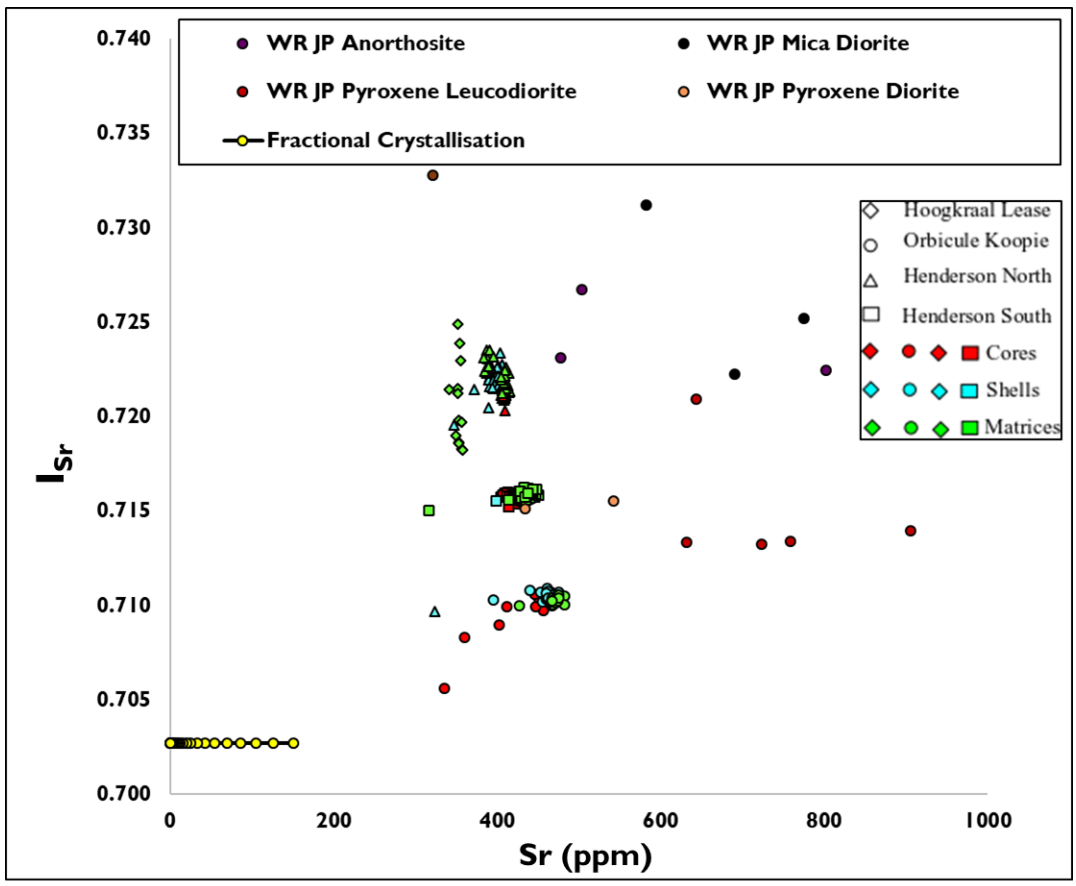


Figure 115*: An energy constrained MCS model simulating FC at 1.5 kbar using the Cascade arc basalt magma composition.*

Case 2: Recharge and Fractional Crystallization (RFC)

Based on this more robust MSC modelling, there is no significant component of recharge or mixing reflected by the $^{87}Sr^{86}Sr$ isotopic ratios of the orbicules (Figure 116).

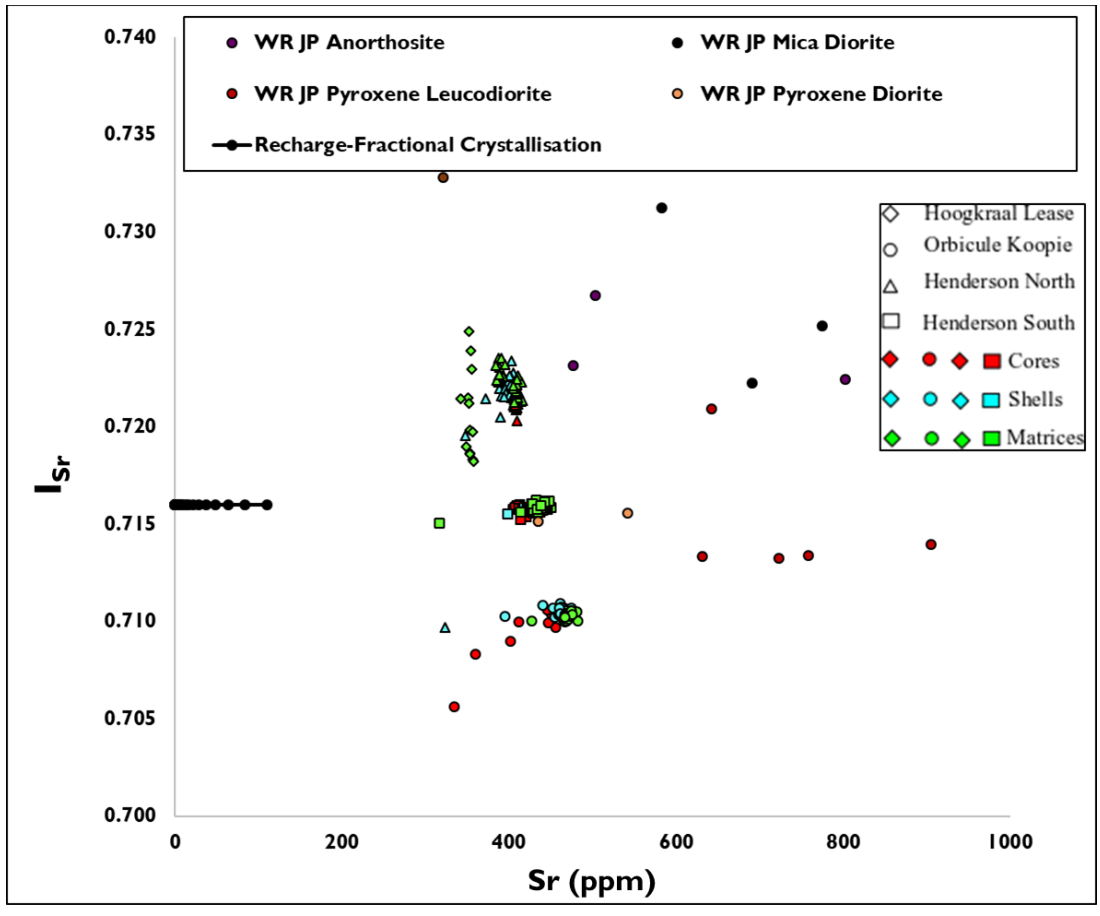


Figure 116: *An energy constrained MCS model simulating RFC at 1.5 kbar using the Cascade arc basalt magma composition.*

The recharge event simulates an intrusion of an arc basalt magma whose composition is comparable to that of the resident magma. The recharge event involves a recharge magma with an initial mass ratio of 0.75 (i.e., 75 mass units (m.u.) of recharge magma is added to an initial parent melt mass of 100 m.u.). This recharge magma at 1130 ^{o}C intrudes and mixes with the resident melt at 1086 ^{o}C. The isotopic compositions increase when more magma of the same composition is added, however, it is impossible to duplicate the isotopic compositions and Sr concentrations shown by the Koperberg Suite orbicules (Figure 116). During the modeling step, temperature, and pressure (between 1 and 6 kbars) were optimized; nevertheless, altering these factors still did not produce the "best fit" model (Figure 116).

Brandriss and Cawthorn (1996) attributed the range and variation of the initial $^{87}Sr/^{86}Sr$ ratios in the Koperberg Suite and the orbicules to mixing of two genetically distinct mafic and felsic components. This hybridization can account for some of the textural differences observed in orbicules of different localities (pyroxene-dominated and pyroxene-less dominated orbicules and mineralization) and the range and variation in the $^{87}Sr^{86}Sr$ isotopic ratios between orbicules of different localities. However, RFC cannot account for these high and more radiogenic $^{87}Sr^{86}Sr$ isotopic ratios in the Koperberg Suite orbicules (Figure 116). Hence, Brandiss and Cawthorn (1996) conclusions, that the hybridization between the two components possibly took place at depth during ascent as the magma underwent differentiation and contamination are supported in this study.

Case 3: Assimilation of wallrock anatectic melts - Fractional Crystallization (AFC) with the Concordia Granite and the Nababeep Gneiss.

The objective of this more realistic MCS AFC modelling is to demonstrate that the range of isotopic compositions exhibited by the orbicules of the Koperberg Suite may be produced by assimilation of crustal lithological units (the Nababeep Gneiss and/or the Concordia Granite), most likely during ascent and emplacement of the Koperberg-forming magma mushes. Additionally, and most importantly, I also want to demonstrate that an arc basalt magma involving crustal anataxis is capable of producing the geochemical signals observed. The AFC simulations presented here reflect assimilation of the Concordia Granite and the Nababeep Gneiss crust by a typical arc basalt magma evolving at different pressures (between 1 and 6 kbars).

Using the thermal and chemical parameters (Table 18; Table 19), the model involving the assimilation of Concordia Granite wallrock that has an initial temperature of 700 ^{o}C with an arc basalt magma could not successfully reproduce the observed isotopic compositions at pressures ranging between 1 kbar (Figure 117), 1.5 kbar (Figure 118), 2 kbars (Figure 118) and 5 kbar. Other parameters, including the water content (wt. %) were modified, but still did not accurately reproduce the observed geochemistry of the orbicular rocks. The Concordia Granite is an appropriately aged terrane for assimilation with Koperberg magmas; however, in any kind of assimilation scenario, this assimilant cannot reproduce the array and isotopic signatures exhibited by the Koperberg Suite orbicules (Figure 117; Figure 118).

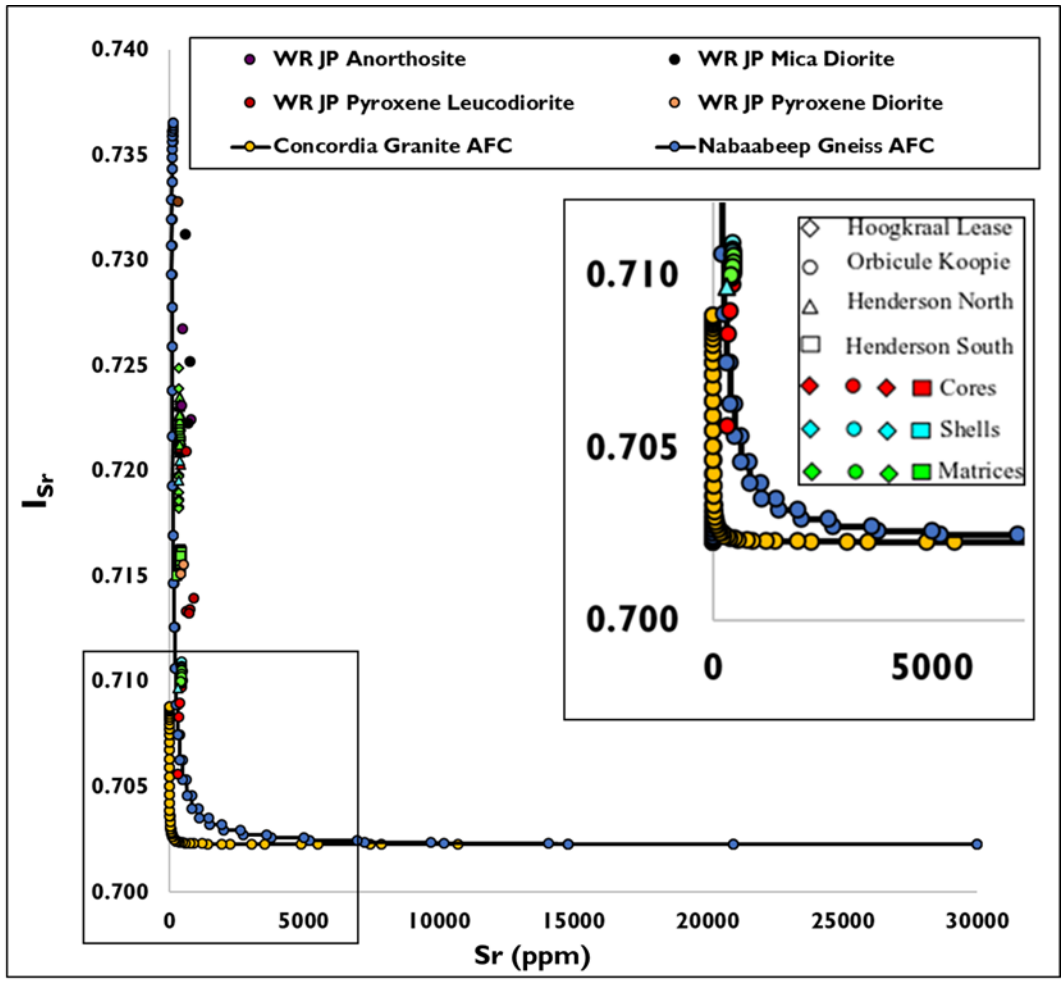


Figure 117: *An energy constrained MCS model simulating AFC using the Cascade arc basalt composition, the Nababeep Gneiss and the Concordia Granite wallrock at 1 kbar.*

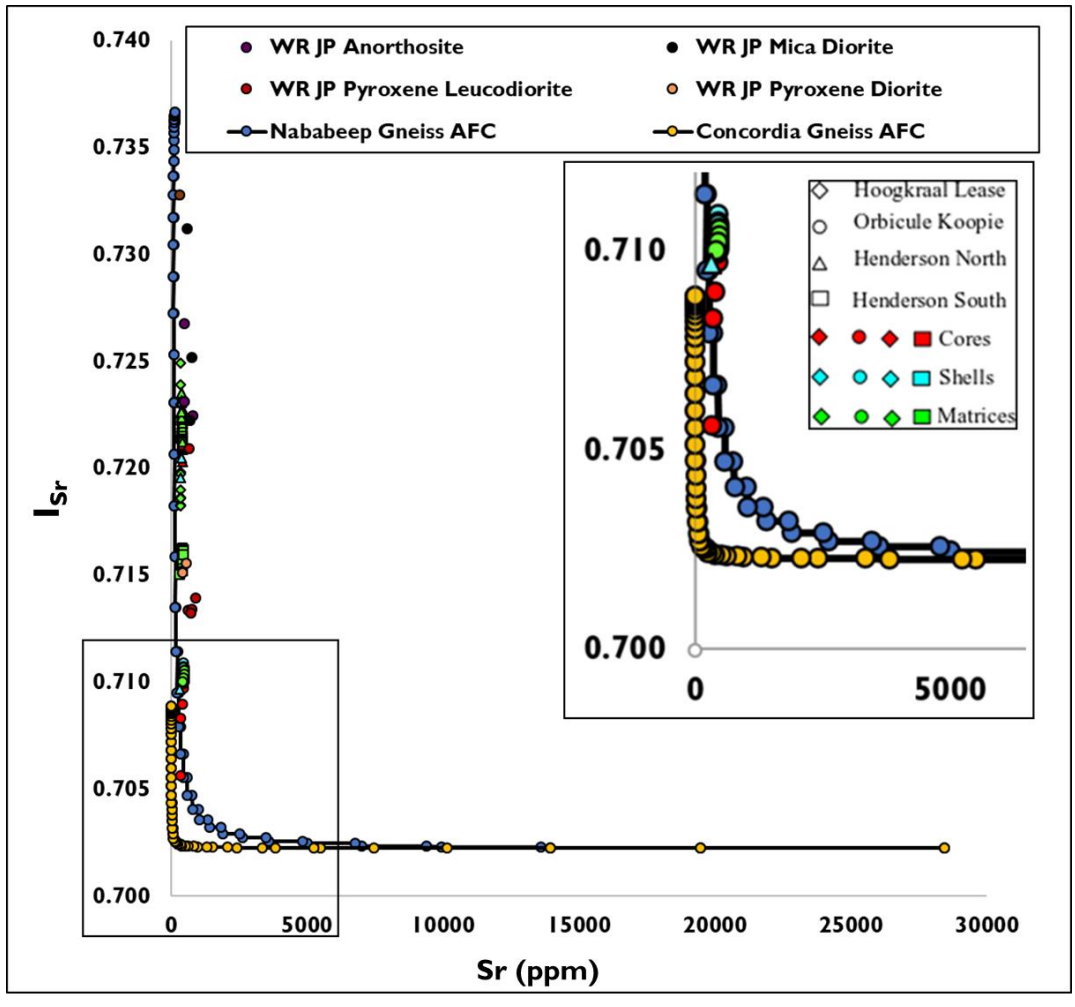


Figure 118: *An energy constrained MCS model simulating AFC using the Cascade arc basalt composition, the Nababeep Gneiss and the Concordia Granite wallrock at 1.5 kbar.*

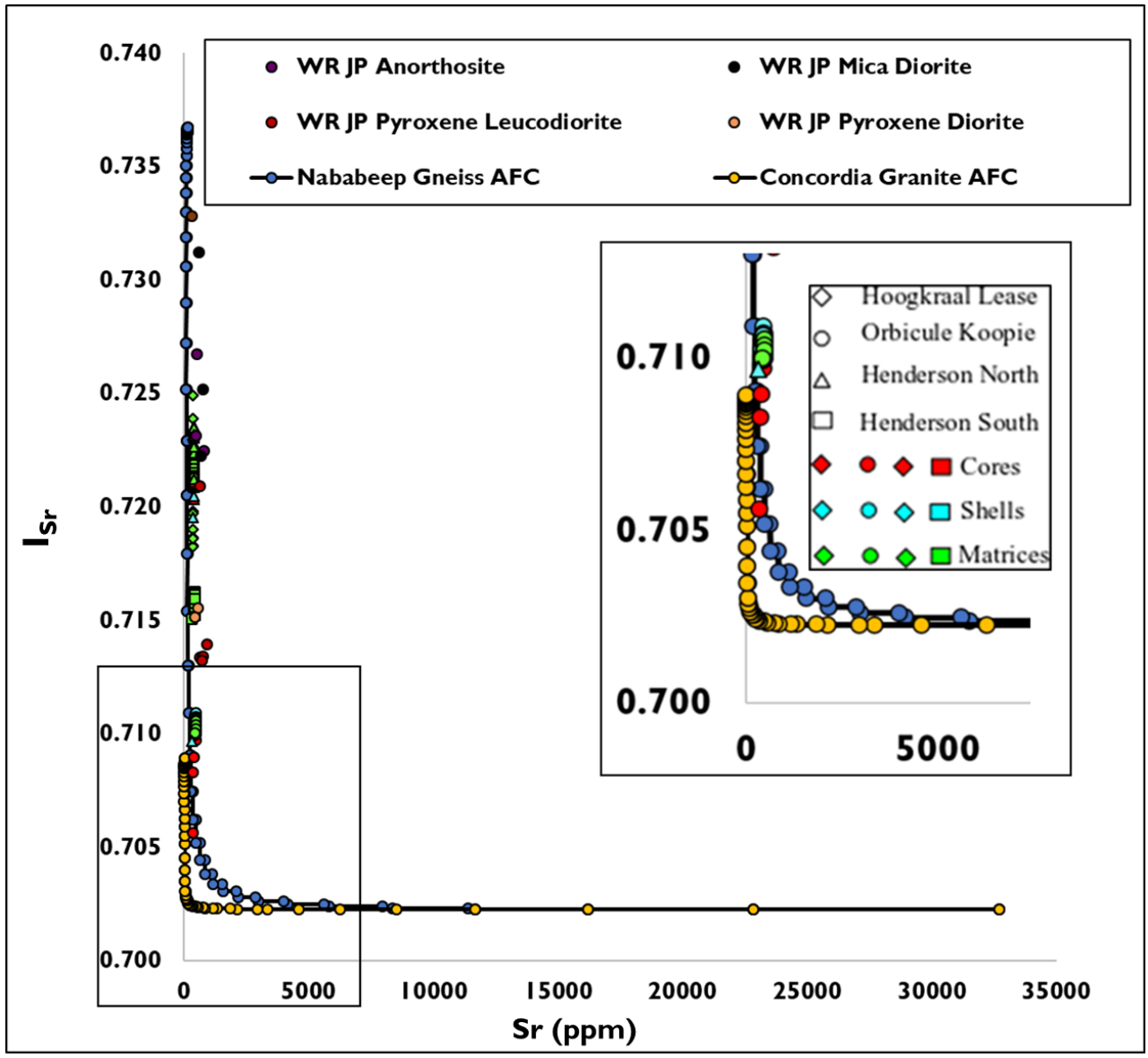


Figure 119: *An energy constrained MCS model simulating AFC using the Cascade arc basalt composition, the Nababeep Gneiss and the Concordia Granite wallrock at 2 kbar.*

Assimilation with the Concordia Granite reproduces a trend that accounts for the range of strontium concentrations not the isotopic signatures (Figure 117; Figure 118; Figure 119).

After the AFC simulation assimilating the Concordia Granite, the AFC model was simulated using the Nababeep Gneiss as a contaminant. Using the thermal and chemical parameters (Table 18; Table 19), the model involving the assimilation of Nababeep Gneiss wallrock that has an initial temperature of 700 ^{o}C with an arc basalt magma composition is mostly likely the model that can adequately explain and account for the observed isotopic compositions and strontium concentrations at pressures ranging between 1.5 kbar (~5 km depth; Figure 118) and 5 kbars (~ 16 km depth; Figure 117; Figure 118).

The "best fit" model and isotopic compositions are reproduced at 1.5 kbar pressure (~ 5 km depth), when hybridizing an arc basalt magma that has an initial temperature of 1195 ^{o}C with the Nababeep Gneiss (at equilibrium), the levels of assimilation were up to 32%. Although hotter wall rock would facilitate more assimilation as proposed by Van Zwieten et al. (1996), who by using a simple and less robust mixing model, implied up to 80 % assimilation in the case of the anorthositic rocks in the Jubilee Pit, the non-dimensional values (r) of 0.6 to 0.8 for the ratio of mass assimilated vs. mass crystallized are considered to be extremely implausible by Taylor (1980) and DePaolo (1981). When Orbicule Koppie cores started crystallizing, the degree of assimilation was 10 %, and by the temperature at

which the matrix had crystallized, the level and degree of assimilation was at 13 %. The Henderson South orbicules record crystallization when the degree of assimilation was at ~ 14 %. The Henderson North and Hoogkraal Lease later crystallized when the degree of contamination and hybridization with the Nababeep Gneiss was between 15 and 17 % (Figure 118). It is important to point out that the model considered as the "best fit" model is still not the "best" model and this may be because of the way the Sr (ppm) of the orbicules was recalculated. This suggests that further detailed *in-situ* trace element and isotopic analyses would be beneficial.

At pressures more than 5 kbar (e.g., 6 kbar; Figure 120), the AFC model assimilating the Nababeep Gneiss starts failing to reproduce the observed isotopic compositions and array exhibited by the orbicules. This means that the orbicules crystallized at depth less than 21 km, most likely between 5-16 km.

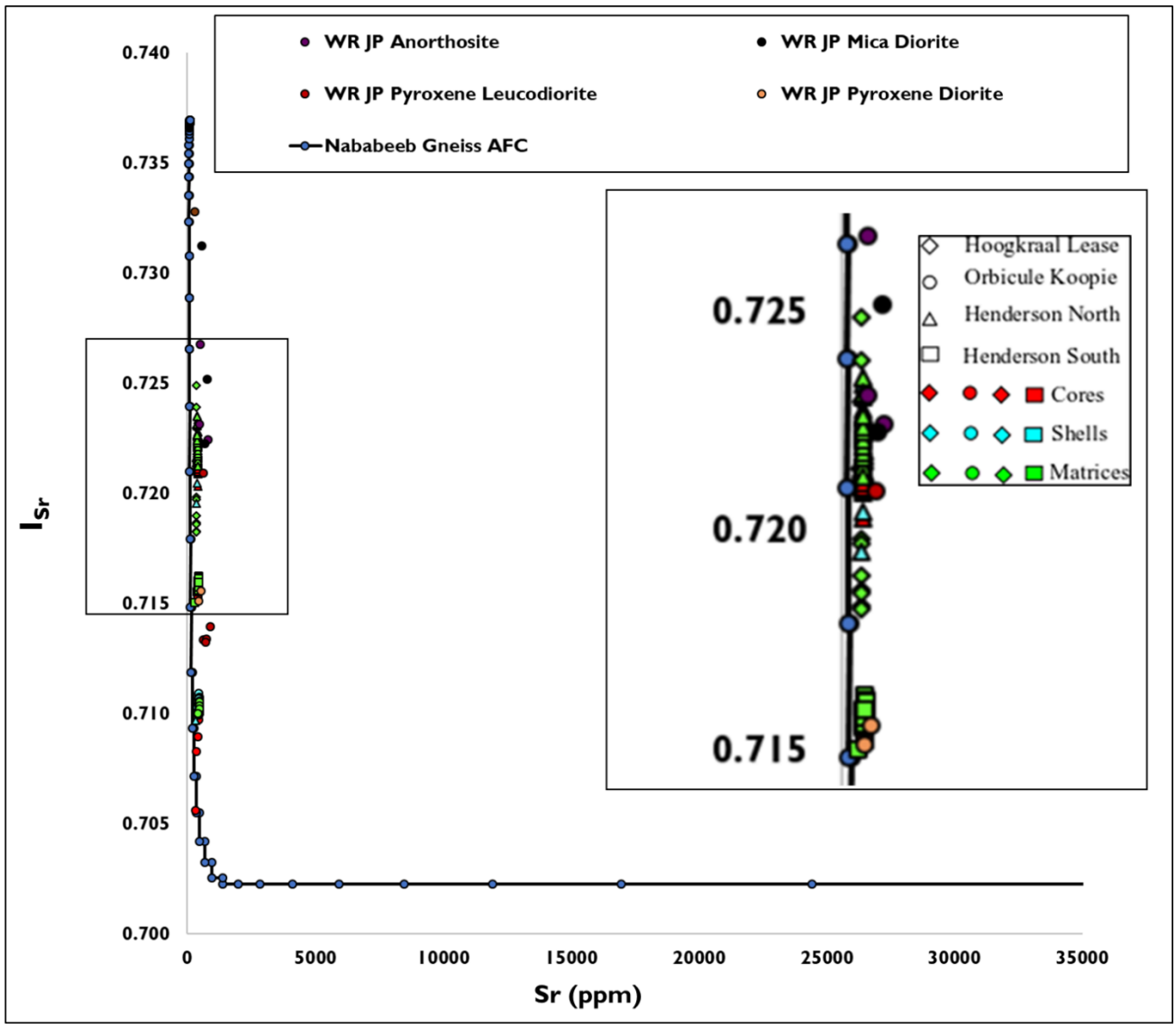


Figure 120: *An energy constrained MCS model simulating AFC using the Cascade arc basalt composition, the Nababeep Gneiss and the Concordia Granite wallrock at 6 kbar.*

Case 4: Recharge–assimilation of wallrock anatectic melts – Fractional Crystallization (RAFC) with the Concordia Granite and the Nababeep Gneiss.

The chemical and thermal parameters that were successful in the arc basalt (1.5 kbar pressure), the Concordia Granite and the Nababeep Gneiss scenarios, were then applied to the RAFC scenarios (Figure 121). The predominant aim of this modelling iteration is to reproduce the initial Sr isotopic

compositions and concentrations from RAFC. The recharge event from the RFC case were imposed on the two AFC cases (the Concordia Granite and the Nababeep Gneiss; Table 19).

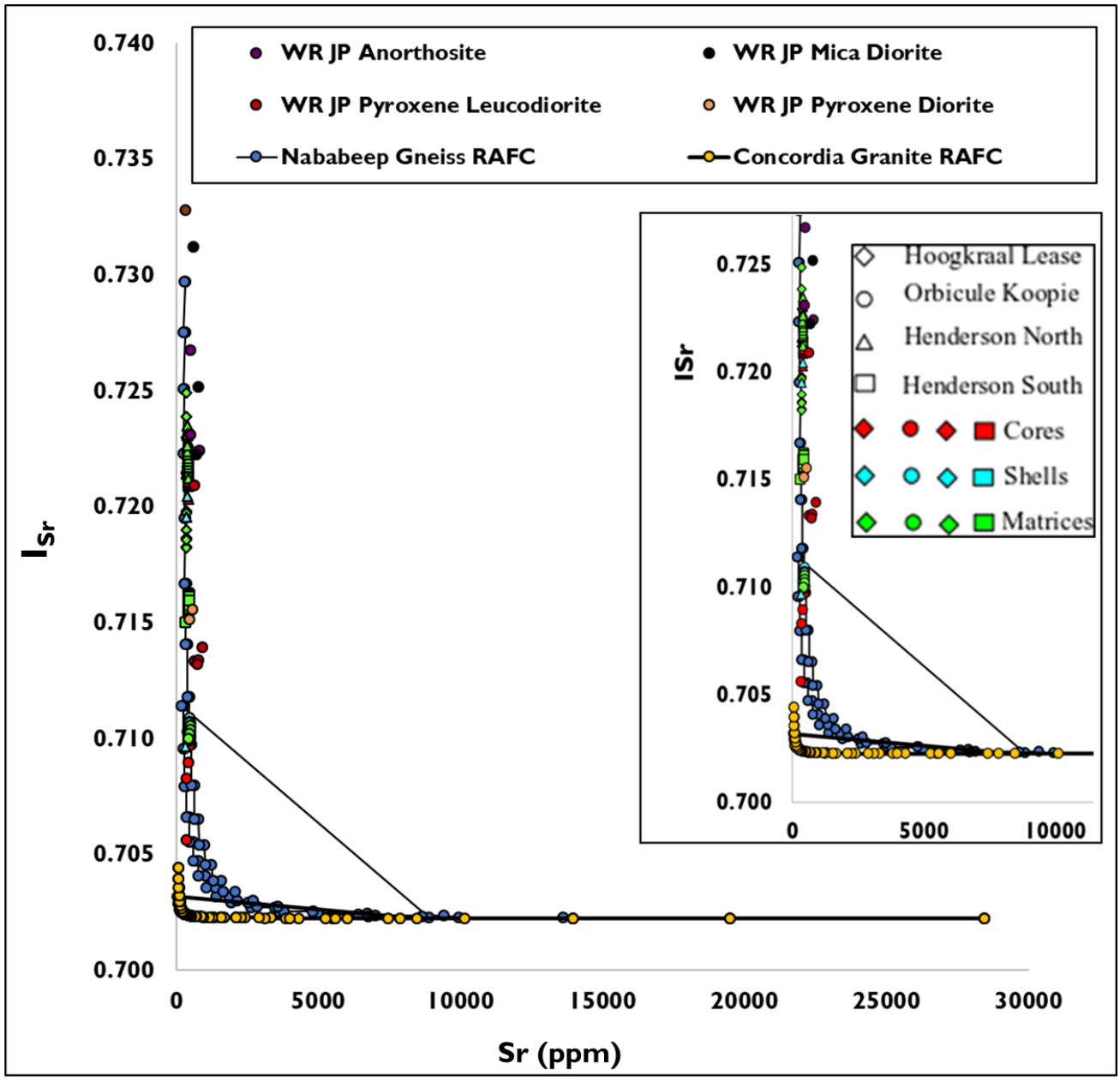


Figure 121*: An energy constrained MCS model simulating RAFC using the Cascade arc basalt composition, the Nababeep Gneiss and the Concordia Granite wallrock at 1.5 kbar.*

For the recharge event, like in the RFC simulation, the recharge magma initial ratio is 0.75 m.u. and the temperature of the recharge magma at the instance for recharge is 1130 ^{o}C. The recharge magma is 100 wt. % melt in both the RAFC cases. In the case of the Nababeep Gneiss RAFC simulation, assimilation begins at magma temperature of 1163 ^{o}C as in the AFC run, by the time the new magma is introduced in the system, the resident magma subsystem had assimilated 13 wt. % anatectic melt. When hybridizing an arc basalt magma that has an initial temperature of 1195 ^{o}C with the Nababeep Gneiss (at equilibrium) and introducing a new magma of the same composition, the levels of assimilation were up to 60 %, as implied by the MSC calculations. When the matrices of Hoogkraal Lease and Henderson North were crystallizing, the level of assimilation was at 50 %.

In the case of the Concordia Granite RAFC simulation, assimilation begins at magma temperature similar to that of the AFC run. By the time the new magma is introduced in the system, the resident magma subsystem had assimilated 13 wt. % anatectic melt. When hybridizing an arc basalt magma

that has an initial temperature of 1195 ^{o}C with the Concordia Granite (at equilibrium) and introducing a new magma of the same composition, the levels of assimilation were up to 50 %.

Similar to AFC, RAFC (assimilating the Concordia Granite) at any given pressure cannot reproduce the isotopic compositions and concentrations exhibited by the Koperberg Suite orbicules (Figure 121). However, the RAFC modelling assimilating the Nababeep Gneiss does reproduce the array and does account for both the isotopic compositions and concentrations exhibited by the orbicules (Figure 121). However, the levels of assimilation (up to 50 %) as implied by the MCS are considered unlikely. Hence, the "best fit" model with reasonable degrees of assimilation is the AFC model (up to 32 % degree of assimilation) as RAFC requires far too much assimilation (up to 50 %).

8.4.2.1. A conclusion on modelling

The behavior of open systems is thought to be characterized by crystal fractionation, magma mixing, and the interaction of magmas with their host environments through partial melting and stoping of wallrock, based an analysis of igneous system features. The Koperberg Suite magmas that formed the orbicules were no different. However, the important task of petrologists and geochemists includes deciphering the most crucial RAFC processes through quantification and temporal ordering.

In conclusion, simple fractional crystallization, magma mixing, and recharge-assimilation-fractional crystallization modelling fail to reproduce the isotopic signatures observed in the Koperberg Suite, within reasonable physiochemical bounds. Based on the modelling we present here, moderate amounts of assimilation (up to 32 %) combined with fractional crystallization produce the isotopic ratios in the Koperberg Suite rocks in general and in the orbicules investigated. Assimilation of mainly the Nababeep Gneiss terrane, with fractional crystallization at pressures between 1.5 and 5 kbar (or 3 and 14 km depth) is the operative mechanism. These quantitative supports previous assertions by Brandiss and Cawthorn (1996) and Van Zwieten et al. (1996). Although the Concordia Granite is an appropriate terrane to assimilate with Koperberg magmas, any kind of assimilation of these compositions cannot reproduce the array and isotopic compositions exhibited by the Koperberg Suite orbicules. This further supports Brandiss and Cawthorn (1996) and Van Zwieten et al. (1996) conclusions that the Concordia Granite cannot be considered a suitable contaminant because of its low and less radiogenic initial $^{87}Sr/^{86}Sr$ ratio (0.709 at 1030 Ma).

The modelling illustrates how the chemistry of the intruding magmas may have been produced, but assimilation and magma mixing (during ascent) may not have played a significant role in the formation of the orbicular textures themselves, as this is likely to be related to a physical, crystallization related process. Now that the formation and emplacement of the orbicule-forming magmas have been addressed, how do these textures form? This is addressed in the following section.

8.5. Formation of orbicules in the Koperberg Suite and the Diana's Pool area

The processes described and modelled in the previous section (crustal assimilation and magma mixing) occurred prior to the formation of the Koperberg Suite orbicules. The orbicules formed at depth, after the Koperberg Suite magmas were contaminated and hybridized, prior to emplacement along the steep structures. This is consistent with the deformation features observed in the Diana's Pool and Orbicule

Koppie orbicules. It is also important to emphasize that the formation of these rocks in not dependent on the specific magma composition, however, it is process related. How were these concentric shells formed around the cores to create the orbicules in both the Diana's Pool and the Koperberg Suite? Before addressing this question, different magmatic processes have been put forward as mechanisms in the formation of orbicular rocks in the preceding sections. Did they also play a role in the formation of both the Koperberg Suite and Diana's Pool orbicules? As mentioned in the preceding chapters, many petrologists have emphasized and supported the magmatic origin of orbicules. However, there are different magmatic processes proposed, and they are not always applicable in one specific orbicular body, and they may not be applicable in both the Koperberg Suite and Diana's Pool orbicules. As previously mentioned, the different magmatic processes include processes such as fractional crystallization, reactive nucleation, assimilation or incorporation of new material in the magma, liquid immiscibility, superheating and subsequent undercooling, incomplete mixing and mingling between magmas of different compositions, oscillatory crystallization process through rhythmic supersaturation of excessive crystallization of feldspar and mafic components, fluctuations of melt about a eutectic due to temperature and pressure variations, magma quenching, and magma reactions with xenoliths.

The formation of orbicular rocks by liquid immiscibility would require the occurrence of contrasting magma compositions (e.g., Lapin and Vartiainen, 1983) and the typical immiscible globules would be < 50 μm in diameter (Owen, 1992). This is not the case in both the Koperberg Suite and Diana's Pool orbicules, where the matrix and core compositions are comparable and the orbicules are greater than 50 μm in diameter. Some orbicules have a biotite-rich layer in between the mafic and felsic shells (e.g., Hoogkraal Lease, Diana's Pool and Henderson North), which is similar to what is seen in many magmatic mafic enclaves and reflects a reaction between two lithologies that are not in thermal or chemical equilibrium (Zhang and Lee, 2021). As truly, immiscible liquids would be in thermal and chemical equilibrium and the existence of biotite-rich concentric layers rule out strict liquid immiscibility (e.g., Zhang and Lee, 2021). In addition, the differences in grain sizes between the cores and shells does not support liquid immiscibility (e.g., Zhang and Lee, 2021). In addition, based on the MCS modelling in the preceding chapter, magma mixing (recharge) was ruled out as a possible mechanism behind the strontium isotopic compositions exhibited by the Koperberg Suite orbicules. Although it is stated that there is evidence of magma mixing in the Koperberg Suite, the hybridization possibly took place prior to orbicular rock formation because evidence of mixing is also seen in massive Koperberg Suite rocks that do not exhibit orbicular textures.

This implies that liquid immiscibility and incomplete mixing and mingling between magmas of different compositional models are unlikely to be significant in the formation of these orbicules. The fundamental differences between orbicule types in an outcrop imply differing source rocks or xenoliths (Thompson and Giles, 1974). Compositions and mineral assemblages that are comparable in cores, shells and matrices characterize the Koperberg Suite and Diana's Pool orbicules. In addition, there are no differences in mineral assemblages of different cores in a single outcrop of a specific orbicule locality in the Koperberg Suite. Hence, the reaction between xenoliths and the magma model (e.g., Nockolds,1931) would fail to account for the petrogenesis of these rocks. This leaves superheating and subsequent undercooling, oscillatory crystallization process through rhythmic supersaturation of

excessive crystallization of feldspar and mafic components, and crustal contamination as the most plausible mechanisms or processes behind the formation of the Koperberg Suite and Diana's Pool orbicules.

The model proposed here is modified from that proposed by Vernon (1985), McCarthy and Müntener (2016), McCarthy et al. (2016) and Barbey et al. (2021).

8.5.1. Formation of Koperberg Suite and Diana's Pool orbicular cores

Medium- to coarse-grained granitic igneous rocks are often formed from a magma that slowly cooled in a magma chamber deep underground (Bevan and Bevan 2009). Minerals typically start to crystallize around nucleation sites when the magma cools. The relatively gradual and slow cooling process enables the steady precipitation of a series of minerals, which ultimately solidify into a rock body with a relatively even distribution of randomly arranged minerals. The nucleation sites may only consist of a small number of molecules, yet they act as seeds that "start off" the crystallization process. However, something different occurred in the Koperberg Suite and Diana's Pool when the orbicules were forming.

Orbicular rocks always contain central cores, which may be megacryst (e.g., Decitre et al., 2002), early-crystallized parts of the orbicular-forming magma (e.g., Lindh and Näsström, 2006), autoliths (e.g., Barbey et al., 2021), or xenoliths (e.g., Elliston, 1984). Orbicular cores that have comparable composition as the surrounding matrices characterize the different Koperberg Suite orbicular localities and the Diana's Pool orbicules; hence, they are most likely products of early crystallization within the Koperberg Suite and Diana's Pool orbicular-forming magmas. In addition to this, most of the undeformed and leucocratic Diana's Pool and Koperberg Suite orbicular cores are characterized by rounded shapes and this suggest their partial resorption by the host magma (e.g., McCarthy and Müntener, 2016; Barbey et al., 2021). In addition, Diana's Pool and Koperberg Suite orbicular cores comprise subhedral to euhedral plagioclase grains that form aggregates and exhibit An contents that show an almost complete overlap with An of plagioclase in shells and the host matrix (Figure 21; Figure 85). This implies that they are most likely autoliths, which are plagioclase-rich cumulates, or rim fragments reworked by new magma inputs or injections (McCarthy and Müntener, 2016; Barbey et al., 2021).

8.5.2. The formation of the Koperberg Suite and Diana's Pool shell (s)

Shells exhibit features making them distinct and unique from cores and the matrix. From hand sample and petrographic descriptions, together with *in-situ* mineral composition data, the shells are different from both the cores and the matrix in all Koperberg Suite and Diana's Pool orbicules. Contrary to the coarse-grained cores and matrix, shells are fine-grained and exhibit polygonal textures. In addition to this, the shells are dominated by biotite, quartz, magnetite and plagioclase in the case of Diana's Pool (Figure 11), Henderson North (Figure 66) and orbicule Koppie (Figure 43) orbicules and by hypersthene and plagioclase in Hoogkraal Lease (Figure 54), and Henderson South; however, they do not contain hornblende. These characteristics precludes the direct crystallization of shells from the magma/melt from which the cores and the matrix crystallized, and this probably implies periodic injection of variably evolved magma batches (e.g., McCarthy and Müntener, 2016; Barbey et al.,

2021). The presence of magnetite-, plagioclase- and biotite-dominated layers characterising the Diana's Pool shells and the hypersthene-dominated shells in Hoogkraal Lease and Henderson South orbicules are evidence of variations in mineralogy, which can be related to the tapping of melt of slightly variable chemistry, temperature, crystal and volatile content, implying that the individual layers represent individual melt pulses (e.g., McCarthy and Müntener, 2016). The differences between these orbicular structures also suggest that processes involving core-matrix formation and shell formation were distinct from one another. The mechanism that formed shells is likely to have involved sudden changes in the physico-chemical environment or conditions of crystallization in the magma leading to the formation of shells. This is also supported by the growth of a biotite-rich layer in Diana's Pool and Hoogkraal Lease orbicules, which may be the result of a change in physicochemical parameters, for instance, it may be a change in melt XH_2O increasing the stability field of biotite at the expenses of orthopyroxene in Hoogkraal Lease.The individual melt pulses model is also consistent with the sharp contacts between cores and shells (e.g., Vernon, 1985), which are interpreted as new melt injections (McCarthy and Müntener, 2016).

The growth of orbicules implies a nucleus free magma, with the exception of rocks fragments (cores) that serve as nuclei for heterogeneous crystallization of shells.The main process invoked in numerous studies regarding orbicular rock formation is the fact that the melt is superheated, which leads to resorption of pre-existing crystals or nuclei (Vernon, 1985), followed by undercooling, leading to comb-textured growth of residual solid structures (e.g., wall rock, xenoliths and xenocrysts; Swanson, 1997; Grosse et al., 2010; Ort, 1992) and the growth of orbicules. Three main mechanisms that trigger superheating have been put forward: (1) addition of volatiles into water-undersaturated melt (Vernon, 1985) or (2) adiabatic decompression associated with dykes in zones of pronounced melt extraction (McCarthy and Müntener, 2016; Barbey et al., 2021) or intrusion of a hotter and more mafic melt (1100-1300 ^{o}C) into a felsic melt (750-950 ^{o}C; Vernon, 1985). The involvement of a mafic magma in the formation of Diana's Pool orbicules would introduce elements such as Fe and Mg, which are necessary for the formation of mafic minerals (e.g., pyroxene and olivine). However, Diana's Pool orbicules lack such minerals, hence; the involvement of a mafic magma is not conceivable. In the case of Koperberg Suite, an addition of a mafic magma seems more plausible in forming the Koperberg Suite magmas. The superheating event that could have destroyed nuclei in the magmas that formed the Hoogkraal Lease, the Henderson North and Henderson South orbicules prior to the formation of orbicules could have been an intrusion of a hot and mafic magma (e.g., Smillie and Turnbull, 2013). This would be consistent with the $^{87}Sr/^{86}Sr$ initial isotopic ratios in these orbicules, and also in a study by Cawthorn and Meyer (1993), who proposed that there is evidence for multiple episodes of mafic magma intrusions in the Koperberg Suite, based on the high $^{87}Sr/^{86}Sr$ initial isotopic ratios in the Koperberg Suite orbicules. Evidence for this hybridization would also be consistent with the abundance of orthopyroxene in both the Hoogkraal Lease and the Henderson South orbicules and the discordance in Mg# of biotite and the An content of plagioclase, hence the more radiogenic strontium isotopic compositions. However, forming the orbicules is more depended on physical processes and not the magma composition. The models presented in the preceding sections also dispute an addition of a new magma during the physical formation process of orbicules.

Yes, it is true that the most popular model to account for superheating is introduction of volatiles (Vernon, 1985; Ort, 1992; Lindh and Näsström 2006; Grosse et al., 2010; Díaz-Alvarado et al., 2017). Water addition has been proposed as the easiest way to explain the destruction of previous nuclei and it is consistent with the disequilibrium form of many crystals, together with the alteration of the rock (e.g., altered hypersthene in Henderson South orbicules). An increase in water content initiates the crystallization of biotite, and this is consistent with the increase in biotite concentration from cores to shells in all the orbicular localities, especially in Orbicule Koppie (Figure 43), Diana's Pool (Figure 11) and Henderson North (Figure 66) orbicular shells. Oscillating water content in the magma could also explain the alternating layers of biotite-rich (e.g., Henderson North; Diana's Pool, and Hoogkraal Lease orbicules), and plagioclase and hypersthene-rich layers in Hoogkraal Lease (Figure 54) and Henderson South orbicules (Figure 76). However, this process is very difficult to demonstrate (Lindh and Näsström 2006) and appears a little bit like a *deus ex machina* (Barbey, pers. comm., 2023). An additional argument against addition of water in the case of Hoogkraal Lease and Henderson orbicules is the stability of hypersthene, which requires water-undersaturated melts, which is obviously contradictory to water injection (Barbey, pers. comm, 2023).

Morse (1980), Grove et al. (1992), McCarthy and Müntener (2016), and Barbey et al. (2021) stated that variations in pressure during decompression of magma pulses in dykes play a significant role on the stability of minerals. This would account for the change in ferromagnesian phases from the cores to the shells in both Koperberg Suite and Dina's Pool orbicules. This could also explain the absence of hornblende in Diana's Pool orbicular shells and the total absence of hypersthene in Orbicule Koppie orbicules, compared to the other three Koperberg Suite orbicular localities. In addition to this, magnetite (Diana's Pool) and hypersthene (Henderson North and Henderson South) crystals in the ferromagnesian shells are fine, branched, and comb-layered (radiating-textures), indicating disequilibrium conditions during orbicular crystallization and rapid growth in a fluid-rich environment (e.g., Lofgren and Donaldson, 1975). Smillie and Turnbull (2013), Barbey et al. (2021), Li et al (2021) and Zhang and Lee (2021) stated that this indicates a fast and unimpeded crystal growth in a highly undercooled magma under non-equilibrium conditions. A sudden and important temperature variation is not conceivable in a plutonic environment; hence, the most likely process for rapid supersaturation is volatile exsolution upon decompression, displacing liquidus temperatures (McCarthy and Müntener, 2016; Barbey et al., (2021). Here, the model invoked first by McCarthy and Müntener (2016) and then by Barbey et al. (2021), considering: (1) adiabatic decompression of magma pulses ascending in dykes leading to superheating and resorption of early solids, and (2) volatile exsolution, inducing undercooling, supersaturation, and the crystallization of shells around central cores is proposes. In addition, a third stage is needed to account for deformation of orbicules in Diana's Pool and Orbicule Koppie (removal from the zone of formation).

To form the orbicular shells in Diana's Pool and the Koperberg Suite orbicules, the superheating event triggered by adiabatic decompression of the Matopos granite and the Koperberg Suite magmas during ascent led to mineral resorption and destruction of nuclei, and this resulted in a decrease in water contents of the ascending melt due to partial resorption of anhydrous crystals. Adiabatic ascent of the melt was then followed by the remobilization of upper crystal mush and emplacement in sub-vertical conduits, along intra-plutonic contacts forming cores (e.g., McCarthy et al., 2016; McCarthy and

Müntener, 2016). At this point, degassing occurred as a result of volatile saturation during dyke emplacement and as the melt reached the water-saturated liquidus, heterogeneous nucleation was triggered, and shells started crystallizing subsequently on the pre-existing cores (e.g., McCarthy and Müntener, 2016). When the process of shell nucleation around the shells began, it became much faster and easier since less energy was required to nucleate on a solid (e.g., Bevan and Bevan, 2009). This is supported by Grosse et al. (2010), who proposed that the process of orbicular formation is relatively quick and takes about ten days.

All Diana's Pool and Koperberg Suite orbicular shells start with an innermost layer that is rich in plagioclase and some shells are a succession of plagioclase-dominated or plagioclase- and magnetite-dominated or biotite-dominated or hypersthene-dominated layers. This is an indication that plagioclase was the dominant phase that was crystallizing when orbicular growth began. In the case of Diana's Pool orbicules, plagioclase as a dominant crystallizing phase was then followed by crystallization of magnetite- and plagioclase-rich and biotite-rich shells. In Henderson South, it was followed by the crystallization of the hypersthene-dominated layers. In Hoogkraal Lease, it was followed by hypersthene-dominated, and biotite dominated layers. In Orbicule Koppie and Henderson North, biotite-dominated layers were followed the crystallization of plagioclase. The alternation and recurrence of these layers in the individual orbicular localities can be attributed to oscillatory crystallization, which is well illustrated by Zhang and Lee (2021).

A study by Zhang and Lee (2021) on orbicular granitoids acquired from the Boogardie quarry at Mount Magnet in Western Australia is in agreement with Smillie and Turnbull's (2013), Barbey et al. (2021) and Li et al. (2021) conclusions on these alternating mafic and felsic shells observed in different orbicular localities. According to Zhang and Lee (2021), a succession of concentric bands made up of a mafic (hornblende-rich) outer layer and a felsic (plagioclase-rich) inner layer, collectively known as doublets, define the orbicules they studied. Each band is made up of radially orientated crystals (hornblende), which are separated by more equant plagioclase crystals, similar to the Hoogkraal Lease and the Henderson South orbicules, which are made up of hypersthene and plagioclase bands. Zhang and Lee (2021) stated that we can gain a qualitative understanding of the genesis of doublet bands rich in plagioclase and hornblende using a kinetic model in which binary eutectic crystallization in this system may be approximated (Figure 122).

Disequilibrium crystallization can result in preferential crystallization of one phase over the other that is, crystallizing in proportions that exceed that defined by equilibrium crystallization stoichiometry if the initial melt composition is slightly off the eutectic. Figure 122 (Porter and Easterling, 2009; Zhang and Lee, 2001) use a binary phase diagram to demonstrate this idea. Based on Zhang and Lee (2021) and Figure 122, a melt (with an initial bulk composition A) that is initially somewhat off the eutectic (towards the hornblende-rich side) cools from an initial temperature of T_0 to a temperature T_1 below the eutectic. If cooling proceeds more quickly than crystallization, the system is said to have undercooled and is thus supersaturated in all the crystallizing phases. The degree of supersaturation for a specific phase will scale with the degree of undercooling and the difference between the temperature of the liquid T_1 and the temperature of the liquidus line (or metastable extensions of the liquidus) for each phase at bulk composition A can be used to estimate the degree of undercooling (Figure 122). For the bulk composition considered, supersaturation at T_1 is given by ΔT_{hb} (amphibole

supersaturation) and is greater than that of ΔTpl (plagioclase supersaturation). Both hornblende and plagioclase will crystallize, but because hornblende has a greater driving force than plagioclase, it will crystallize in excess compared to plagioclase. However, excessive hornblende crystallization will cause the residual melt within the crystallizing boundary layer to migrate towards the plagioclase-rich end-member (point B; Figure 122) as it becomes more enriched in plagioclase and less enriched in hornblende components.

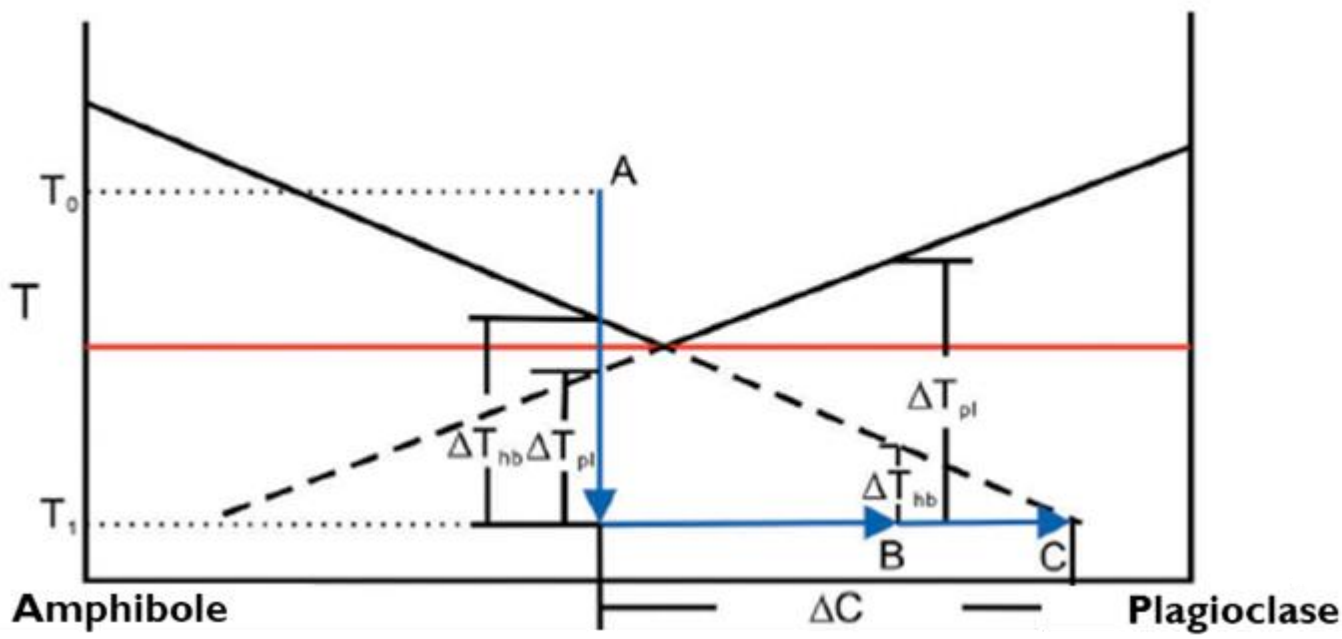


***Figure 122**: A schematic hornblende-plagioclase binary phase diagram showing how disequilibrium crystallization (undercooling) can cause oscillatory banding in the orbicules adapted from Zhang and Lee (2021).*

The remaining melt preferentially crystallizes plagioclase when the degree of plagioclase supersaturation exceeds the degree of hornblende supersaturation. The pattern is repeated until the local system returns to hornblende over-saturation as more cooling occurs, producing oscillating mafic-felsic doublets. This study and model are supported by a study by Li et al. (2021) on the Huangling orbicules, Yangtze Craton, China. The fact that the time frames of crystal formation, cooling and diffusion of key nutrients, such as Al (Acosta-Vigil et al., 2003), are comparable is crucial to the operation of this mechanism. The system will quench homogeneously if cooling rates are too high compared to chemical diffusion since there will not be enough time for boundary layer effects to develop. Chemical boundary layers will not form if cooling rates are too slow since crystallization will occur near equilibrium in such cases. Although Zhang and Lee's (2021) study focuses on hornblende and plagioclase, the same mechanism they apply is applicable and can be used to explain the alternating mafic (biotite) and intermediate (hypersthene and plagioclase) in Hoogkraal Lease (Figure 54) and Henderson North (Figure 69) shells and the hypersthene-plagioclase radial textures in the Henderson North, the Henderson South and Hoogkraal Lease orbicules. This mechanism can also explain the alteration between the mafic (biotite and magnetite) and felsic (feldspar-rich) layers in the Diana's Pool orbicules. From petrographic observations, biotite is distributed in successive layers or rings that crosscut the radiating texture perpendicularly in the Hoogkraal Lease orbicules (Figure 54).The

successive biotite layers suggest crystallization ruled by the fluctuation of biotite saturation in the magma (Grosse et al., 2010). The crystallization of biotite shells may have been sporadic, producing concentric layers (e.g., Grosse et al., 2010). Various layers of biotite that were deposited on the orbicule fronts were produced each time the saturation of biotite was reached (e.g., Grosse et al., 2010) and during this stage, the mafic biotite grew faster than plagioclase and hypersthene. Alternatively, the shift in phase stability from hypersthene to biotite and reversal, may be simply due to change in melt water saturation inducing the alternative crystallization of an anhydrous then a hydrous phase (Barbey, pers. comm, 2023).

Variations in the thickness of shells in all orbicular localities are also observed and oscillatory crystallization alone cannot account for this, and an additional mechanism is required. It may seem conceivable that periodic injection of more- or less-differentiated melts resulted in this variation (i.e., each layer corresponds to a specific liquid; Barbey et al., 2021). However, if decompression melting and superheating (inducing crystal-free liquids) is considered, significant differentiation during ascent of crustal melts generated at low pressure is not possible (e.g., Barbey et al., 2021) and not consistent with the constant composition of plagioclase observed in the different orbicular structures, in the case of Henderson South and Diana's Pool orbicules. Therefore, complementary to oscillatory crystallization. The author proposes that fluctuations in the nucleation and growth rates of plagioclase, biotite and magnetite in Diana's Pool; hypersthene, biotite and plagioclase in Hoogkraal Lease and Henderson South; and biotite, magnetite and plagioclase in Henderson North occurred in relation to the degrees of undercooling and supersaturation (e.g., Barbey et al., 2021). Crystal growth can exceed the diffusion rate at significant degrees of undercooling. This will result in a concentration of incompatible elements in front of growing crystals (Mollo and Hammer, 2017). At lower degrees of undercooling, growth rates become slower than the diffusion rate and crystal growth is interface limited (Mollo and Hammer, 2017). In the case of Diana's Pool orbicular shell formation (e.g., full orbicular sample BM14780F; Figure 11), rapid plagioclase growth resulted in a thin boundary layer rich in elements that are incompatible with the lattice of plagioclase (Mg and Fe). Supersaturation of these elements promoted the strong nucleation of magnetite, leading to a thin sheet of small magnetite grains (e.g., magnetite layer in between biotite layers; Figure 11). Conversely, if plagioclase growth is slower, but still faster than diffusion, a less concentrated, more diffuse and thicker boundary layer will result, favoring growth and leading to larger and fewer magnetite crystals (e.g., inner magnetite-rich layer in contact with the core; Figure 11). The same mechanism is applicable in the formation of biotite-dominated layers in this locality and can also explain variations in shell thickness in Hoogkraal Lease, Henderson South and Henderson North orbicules. The growth rates of plagioclase, magnetite, hypersthene and biotite in these different orbicular localities are attributed to variations in melt supersaturation related to variable volatile exsolution linked to the dynamics of the magma during ascent (e.g., Barbey et al., 2021).

8.5.3. The Formation of the Koperberg Suite and Diana's Pool matrices

Prolonged undercooling of the decompressed melt during ascent within the Matopos and the Koperberg Suite conduits led to homogeneous nucleation, orbicule growth ceased and the coarse-grained matrix started crystallizing (e.g., Blundy and Cashman, 2001). Judging from the sharp contacts

between shells and the matrices, this change must also have been abrupt (e.g., Vernon, 1985; Grosse et al., 2010; Sylvester, 2011). The matrix must have crystallized at a faster rate of growth or nucleation, and the grain size increased. The matrix is pegmatitic in some places in the Diana's Pool and Orbicule Koppie orbicules, implying that crystallization of the matrix was not uniform. This is further supported by the variation of selected oxides and $^{87}Sr/^{86}Sr$ ratios in plagioclase from different matrix samples in different orbicular localities. In addition to this, pegmatites represent the residual liquids formed after the extremely late-stage crystallization of the magma (Zhang and Lee, 2021), and the pegmatitic character of the matrix in some places in these localities further suggests that the matrix crystallized later, after the orbicules have formed, forming the groundmass and locking the orbicules in place.

The deformation of shells and cores (Figure 8) by the granitic matrix material in the Diana's Pool orbicules suggests a degree of plasticity within them, suggesting that the early orbicules were deformable but somewhat rigid, and they could move freely in the partially crystallized matrix material (e.g., Ray, 1952). This further suggests that the orbicules continued to evolve in the presence of a melt (matrix material) until they were emplaced in their present setting (e.g., Ray, 1952; Barbey et al., 2021). This is an example of magma that was constantly in motion during and after orbicule formation and consolidation (Sederhom, 1928). Alternatively, because of variations in temperature and pressure during the orbicular-forming process, is possible that during this stage, orbicules moved freely around in the magma, driven by convection currents. The orbicules that were partially crystallized may have settled through the fluid magma, and others may have accumulated at the bottom of the chamber while they were still relatively soft (e.g., Bevan and Bevan, 2009)

8.6. Mineralization in the Koperberg Suite orbicules

In the preceding sections (Section 7), it was stated the sulphide mineralization hosted in the Koperberg Suite also makes the Koperberg Suite orbicules unique from the Diana's Pool. It is also mentioned that there is no evidence of any mineralization in Diana's Pool orbicular samples that we studied or any orbicules described in published literature. In addition, the Koperberg Suite orbicules contain controversial sulphide mineralization that has stirred various debates and controversies, particularly regarding metallogenesis. In this section, interpretations and implications of petrographic, major element and trace element data of sulphides in the Koperberg Suite orbicules presented in Section 7 are presented.

8.6.1. The metallogenesis of sulphides in the Koperberg Suite orbicules

Wohlgemuth-Ueberwasser et al. (2013) stated that the final sulphide melt composition before full crystallization in a magmatic system should be close to the thermal minimum of the Ni/Cu/S system if sulphide melt composition is regulated by the fractionation of *mms* (monosulphide solid solution). This suggests that the atomic Cu/Fe ratio would be close to unity and that the dominant sulphide assemblage would include pyrrhotite, pentlandite, and chalcopyrite, which are typical of magmatic deposits (e.g., the Bushveld Complex; Wohlgemuth-Ueberwasser et al., 2013). However, there are other magmatic sulphide assemblages with bulk Cu/Fe ratios that are higher than the thermal Fe/Ni/Cu/S system. In these assemblages, bornite and digenite typically predominate, while pyrrhotite

and pentlandite, which are Fe/Ni phases, are relatively infrequent (Wohlgemuth-Ueberwasser et al., 2013) and this is what is observed in the Koperberg Suite orbicules (Figure 109).

The mineralization in the Koperberg Suite and the studied orbicules is considered magmatic; however, the occurrence of the bornite- and chalcopyrite-dominated sulphide assemblage (Figure 109) is atypical of magmatic sulphide deposits from elsewhere and the different models put forward to explain this unusual assemblage are explained in detail in Section 2.2.2. Similar to the source of the Koperberg Suite magmas, and the genesis of orbicules, the presence of this bornite + chalcopyrite + magnetite assemblages in the Koperberg Suite orbicules poses questions and controversies on sulphide metallogenesis. The polyhedral and granular textures between oxides, sulphides and silicates in the orbicules (Figure 109a) are atypical of magmatic deposits that form from immiscible sulphides (e.g., Cawthorn and Meyer, 1993; Van Zwieten et al., 1996), which usually form in interstitial areas (since the sulphide phase solidifies last in basic rocks; Cawthorn and Meyer, 1993; Van Zwieten et al., 1996). The modal abundance or proportions of magnetite to sulphides in the Jubilee Pit orbicules (Figure 109) is too high, implying that magnetite could not have been derived from a normal immiscible liquid (e.g., Cawthorn and Meyer, 1993; Van Zwieten et al., 1996). Similar assemblages or mineralization have been documented in the Upper Middle Zone of the Skaergaard intrusion (Wager et al., 1957; Andersen, 2006) and Phalaborwa copper deposits (Le Bras et al., 2021; 2021), and different mechanisms have been put forward to explain the high modal abundances of bornite in these different deposits (refer to section 2.2.2).

The present mineralogy as well as major and trace element geochemistry of the sulphides hosted in in the Koperberg Suite orbicules argue unequivocally against these sulphides being primary magmatic. The rare and atypical bornite + chalcopyrite + magnetite assemblage hosted in the orbicules and the sulphides themselves are chemically atypical of magmatic sulphides. Based on the major element (Table 33) and trace element data (Table5), both bornite and chalcopyrite have extremely high Cu over S contents. Hence, these sulphides exhibit high Cu/S ratios. The average Cu/S ratio in chalcopyrite is 1.0 and ~2.6 in bornite and the Cu/S ratio in bornite is anomalously high compared to known magmatic sulphides and corresponds to pure bornite (e.g., Van Zwieten et al., 1996). This is evident in the atypical bornite + magnetite + chalcopyrite assemblage and the absence of pyrrhotite and pentlandite in the orbicules. From the major elements, the Ni content (< 1 wt. %; Table 33) in the orbicules is lower than the Cu content. In addition, based on the trace element data, Ni concentrations ($\overline{x}$ < 20 ppm; Table5) are lower than the Cu concentrations ($\overline{x}$ = 425572 ppm; Table5). This implies that the Cu/Ni ratios in the sulphides are higher than in other typical magmatic sulphide deposits (e.g., Van Zwieten et al., 1996). The primary magmatic model fails to explain the high Cu/Ni ratios observed in the sulphides (e.g., Cu/Ni of ~ 63 in Jubilee Pit bornite; Maier et al., 2000) and I consider it unlikely and not plausible in explaining the bornite + magnetite + chalcopyrite assemblage and the unusual Cu/Ni ratios in the orbicules.

The assimilation of a Cu-rich contaminant at depth, where there is an involvement of a hydrothermal component in ore formation can well explain the high Cu/Ni ratios, the breakdown of orthopyroxene to chlorite and actinolite (e.g., Henderson South), saussurization of plagioclase and the abundance of mica in the orbicules. This model works more effectively if there was partial assimilation of a deep-

seated Cu-bearing country rock (e.g., a porphyry Cu-deposit, such as Eburnian-aged rocks north of O'okiep) in an ascending basic magma (e.g., Maier, 2000). However, this model is unlikely because the copper mineralization is hosted mainly in the mafic rocks, in this case, the Jubilee Pit orbicules. Similar to the primary magmatic model, this model is difficult to constrain with the data I present here.

The metamorphic desulphidization of a primary magmatic ore model proposed by Cawthorn and Meyer (1993) and Boer et al. (1994) seems less plausible in explaining the metallogenesis of the sulphides in the Koperberg Suite orbicules as it fails to explain the low Ni concentrations and the high Cu/Ni ratios in the Koperberg Suite rocks and in the studied orbicules. In addition, Cawthorn and Meyer's (1993) model is questionable as it is only applicable to a limited number of deposits and not all magmatic deposits are subjected to high-grade metamorphism. In addition, this model does not account for the atypical Cu enrichment of the sulphides in the Koperberg Suite and in the orbicules.

Proposing a resistic origin of a pyroxenite model by Maier (2000) could address most of the unusual features of the sulphides in the orbicules as well as their high-grade granulite-facies metamorphic setting. However, this model proposes there is ascent and emplacement of a crystal mush enriched in Cu-sulphides, apatite, and magnetite. However, this is deemed geologically unrealistic, and a more definitive judgement must await more data (e.g., PGE data). Studies on the concentration and distribution patterns of the PGE would also shed some more light on the IOCG model in explaining the origin of the sulphides in the Koperberg Suite and in the orbicular rocks. Andersen (2006) asserts that the lack of studies in which Cu-rich sulphides have been synthesized using basaltic magma compositions adds to the mystery surrounding the presence of bornite in magmatic sulphide deposits.

The primary components of *mss* are pyrrhotite and pentlandite, both of which are dominated by Fe^{2+} (De Villiers, 2002). As a result of the Ni-rich sulphide melts crystallizing to create *mss*, the $Fe^{3+}/\Sigma Fe$ ratio of the remaining Cu-rich sulphide melt increases. As Maier et al. (2012) suggested that the sulphides in the Koperberg Suite are considered to have crystallized from a Cu-rich residual sulphide melt, such a mechanism is plausible in explaining the sulphides in the orbicules of the Koperberg Suite. The presence of variable quantities of Ag, Se, Bi, Cd, In, Sn and Pb and the low contents of Co and Ni (Table5) characteristic of the sulphides in the orbicular rocks are consistent with trace elements assemblage typical of Cu-rich sulphide melt fractionated from a Ni-rich *mss* sulphide melt (Dare et al., 2011; Caraballo et al., 2022). Magmatic sulphides typically exhibit variable Ni contents (Cawthorn and Meyer, 1993). However, the Koperberg Suite orbicules contain relatively low Ni (<20 ppm; Figure 111; Table5).

In these orbicules, the lowest Ni concentrations are recorded in chalcopyrite and the highest concentrations are recorded in bornite ($\overline{x}$ = 18 ppm; Figure 111f; Table5). Moreover, these relatively low concentrations of Ni in the orbicule sulphides in comparison to known magmatic sulphide deposits associated with igneous rocks is intriguing. Barnes and Lightfoot (2005) stated that Co and Ni partition into *mss* relative to the melt of sulphide and because of this, the content of Ni is expected to increase in Cu-rich sulphide melt, which segregates from *mss*. The low Ni and Co contents in the sulphides support the generation of the sulphide phases hosted in the Koperberg Suite orbicules from such a Cu-rich sulphide melt. In addition, the segregation of a Ni-rich sulphide melt extraction at a deeper crustal level, presumably analogous to the Hondekloof deposit, is supported by trace element systematics.

This is consistent with the Maier et al. (2012) IOCG model. The Hondekloof deposit in the Kliprand region, some 160 km southeast of Springbok, similar to the O'okiep Copper District in age (1048–12 Ma; Bailie et al., 2019), is distinguished by its Ni- and Cu-rich sulphide mineralization, but low Cu concentrations (Hamman et al., 1996; Maier et al., 2012). The Koperberg Suite orbicular rock's low Ni and Co contents (< 20 ppm; Table5) and high quantities of elements that partition into Cu-rich sulphide melts in comparison to Ni-rich *mss* serve as indicators of this segregation of a Ni-rich sulphide melt extraction at a deeper crustal level. Mungall et al. (2006) states that Ni ($D^{iss/sulphide\ melt}$ of 1) partitions into sulphide melt relative to *iss*. Therefore, the Ni content of a sulphide melt is expected to increase with sulphide fractionation (Barnes and Lightfoot, 2005). The higher contents of Ni ($\overline{x}$ = 18 ppm) in bornite hosted in the Jubilee Pit orbicules can be attributed to the crystallization of bornite from a significantly fractionated melt. Conversely, the Ni content is lower and below the detection limit in bornite and chalcopyrite hosted in the more felsic orbicules (Table5). This is consistent with the derivation of bornite and chalcopyrite from a less fractionated sulphide melt (Marima, 2022).

Other chalcophile elements (e.g., Bi) are not uniform and their concentrations vary in both chalcopyrite and bornite. This is explained by how their substitution in sulphides is affected by the sulphide melt-shifting oxidation (Helmy et al., 2010). The LA-ICP-MS study by Cook et al. (2011) on bornite and chalcocite presents bornite and chalcocite that are poor in Co (0.01-115 ppm) and Ni (0.01-62.3 ppm), Ga (0.01-47 ppm) and Ge (0.41-19.5 ppm), similar to what is observed in the Koperberg Suite orbicules. In line with the behavior of Ni and Co in other common sulphides, Cook et al. (2011) assumes that there must be a degree of substitution of the two elements into the Fe site within bornite and chalcocite. Compared to the Koperberg Suite bornite (where Ag ranges between 15.42 and 111.82; Figure 111a; Bi ranges between 90.69 and 128.42; Figure 111b), the Cretaceous skarn, epithermal and porphyry deposits studied by Cook et al. (2011) exhibit higher Ag (121 to 1698 ppm) and Bi (134 to 7666 ppm) contents. Bi (618-3045) and Ag (282 to 8078 ppm) contents are even higher in the late Proterozoic metamorphosed veins they also studied. Based on the high concentrations of Ag and Bi in bornite, Cook et al. (2011) concluded that these chalcophile elements are clearly in solid solution and that bornite is an excellent host for both these trace elements and they state that when high-temperature bornite cools, Bi is preferentially partitioned into bornite. In the orbicular sulphides, bismuth, Ni and Se in these sulphides appear to partition into bornite while Ag, In, Cd, Sn, Mn, Ge and Co partition into chalcopyrite (Figure 111), consistent with trace elements assemblage typical of Cu-rich sulphide melt fractionated from a Ni-rich *mss* sulphide melt (Caraballo et al., 2022). Sulphide fractionation increases a sulphide melt's copper content (Naldrett, 2004). The Jubilee Pit orbicules exhibit higher Cu contents in bornite, which results in higher Cu/S ratios than in the more felsic orbicules. This can be attributed to the formation of a sulphide melt from a more fractionated melt and is consistent with the magmatic oxidation of a sulphide melt, in which the remaining sulphide melt eventually becomes richer in Cu and crystallizes into a bornite-*iss* assemblage. Fractionation of the Cu-rich melt sulphide melt (segregated from *mss*) also tends to enrich the residual sulphide melts in Se as seen in these sulphides (Table5; Marima 2022).

The Latsky (1942) and Van Zyl (1967) differentiation model is more in line with the patterns in trace elements that are discussed here. Based on this model, the Koperberg Suite bodies are devoid of post-intrusive differentiation. Additionally, the felsic members were emplaced first, with the more mafic

phases following later. This indicates that there was substantial differentiation in a deep-seated magma chamber prior to emplacement (Latsky, 1942; Lombaard et al., 1986). Van Zyl (1967) recognized the intrusive nature of the Koperberg Suite and attributed its development to magmatic differentiation in a deep-seated magma chamber where multiple pulses of different compositions of magma were emplaced. As a result, it has been said that the Koperberg Suite was emplaced by tapping from the top of a differentiated magma reservoir and sequential emplacement of progressively more basic fractions. In the Koperberg Suite and the studied orbicules, the more mafic and least fractionated members (e.g., orthopyroxenites and the Jubilee Pit pyroxene-bearing diorite) comprise bornite-dominated assemblages. Conversely, the more felsic and more fractionated members and orbicules of the Koperberg Suite (e.g., anorthosites and Henderson North and Hoogkraal Lease orbicules) do not host any sulphide mineralization and if there is any, it is mostly chalcopyrite.

The Koperberg Suite and the studied orbicules show an inverse relationship to what was described by Shapovalova et al. (2020) in their study on the Khangai Upland massif PGE-CU-Ni deposits in Mongolia. The differentiation process by Latsky (1942) and Van Zyl (1967) most likely promotes silicate melt fractionation and sulphide melt simultaneously and this is well seen in the Khangai deposits in Mongolia. The Mankhan massif, which includes gabbros and gabbronorites, is the least fractionated late intrusion in this deposit, and it has the usual *iss* chalcopyrite and pyrrhotite composition. The bornite-cubanite-chalcopyrite assemblage is found in the most fractionated Mongol massifs (anorthosites and leucogabbroids), which are also the oldest (Mao et al., 2018). The bornite-cubanite-chalcopyrite assemblage is the outcome of the increasing fractionation of the magma's sulphide melt's Cu content, which replaced the *iss* assemblage (Shapanova et al., 2020). The Koperberg Suite, however, shows the exact opposite of this. Magmatic oxidation of the sulphide melt by fractionation of Fe^{2+}- dominated silicate and fractional crystallization of the *mss* is the mechanism that is attributed to result in Cu-enriched sulphide melt, resulting in crystallization of the bornite-*iss* assemblage and is the most plausible. The Cu-sulphide mineralization patterns observed in the orbicules and the Koperberg Suite, in general, can be summarized in the following:

(a) Injection of a magma comprising a Cu-rich sulphide melt segregated from a prior *mss* fractionation event (e.g., IOCG model, Maier et al., 2012) into a deep-seated magma.

(b) In a stratified magma, the fractionation of a silicate melt by the gradual crystallization of a Fe^{2+} - dominated phase (pyroxene and biotite) was followed by the oxidation and Cu enrichment of a sulphide melt. The mafic melts were confined to the bottom portions of the magma chamber, while the felsic melts were concentrated in the top portions.

(c) Migration of the denser sulphide melt. With gradual crystallization and an increase in the viscosity of the silicate melt, the migration of sulphide droplets would be less effective (Chung and Mungall, 2009). In this instance, a small modal amount of sulphide melt would have been present in the silicate melt in the upper section of the magma.

(d) Emplacement and crustal contamination of the most fractionated and poorly mineralized felsic melt along steep structures in the O'okiep Copper District,

forming anorthosites and the felsic orbicules (e.g. Orbicule Koppie). The contamination of the silicate melt resulted in the obscured isotopic signatures exhibited by the felsic orbicules.

(e) Emplacement and crustal contamination of a silicate magma alongside the least fractionated, least oxidized, Cu-poor, and S-rich sulphide melt that gave rise to the assemblage of chalcopyrite and pyrrhotite (Narrap-type). These silicate magmas gave rise to the less mineralized and felsic orbicules (e.g. Henderson North and Hoogkraal Lease).

(f) Emplacement and crustal contamination of moderately fractionated intermediate and dioritic magma that produces chalcopyrite and generally poor bornite assemblages (e.g., Henderson South orbicules).

(g) Emplacement and crustal contamination of the mafic silicate melt beside the most evolved and oxidized sulphide melt, which was significantly enriched in copper and S-poor, resulting in an ore with a bornite-dominated composition (e.g., Jubilee Pit orbicules). This is consistent with the consensus that the more mafic Koperberg Suite members in the O'okiep Copper District and the orbicules host the most economically advantageous Cu-mineralization (Benedict et al., 1964).

8.7. The link between the genesis of orbicular rocks and sulphide metallogenesis in the Koperberg Suite

The Koperberg Suite magma pulses were emplaced at different times and as different pulses alongside the Cu-poor and S-rich sulphide melt that gave rise to the assemblage of bornite and chalcopyrite. This means that sulphides formed before the formation of orbicules (which formed after the emplacement and contamination of the sulphide-bearing magmas) as evidenced by the initial $^{87}Sr/^{86}Sr$ ratios of the orbicules. In addition, Cu-mineralization is prevalent in the matrices (Figure 109). This may be because the orbicule (core and shells) forming processes are short-lived (~10 days, Grosse et al., 2010) and the sulphides did not have enough time to be entrapped and crystallize in cores and shells during such a rapid time intervals. However, by the time the matrices crystallized and solidified, the sulphide would have had enough time to solidify since the sulphide phase solidifies last in mafic rocks. The mineralization is more prevalent in the more mafic Jubilee Pit orbicules than in the more felsic Orbicule Koppie orbicules and this has been explained in the preceding chapters. In addition, the segregation of a Ni-rich sulphide melt extraction at a deeper crustal level, presumably analogous to the Hondekloof deposit, is supported by trace element systematics. The Koperberg Suite orbicular rock's low Ni and Co contents (< 20 ppm; Table5) and high quantities of elements that partition into Cu-rich sulphide melts in comparison to Ni-rich *mss*, serve as indicators of this segregation of a Ni-rich sulphide melt extraction at a deeper crustal level. The fact that Ni-rich sulphides were extracted at deeper levels further suggests that the sulphur saturation that resulted in the formation of sulphides was already attained before the magmas were deposited along the steep structures, prior to orbicular texture formation, as these rocks formed after the emplacement along the steep structures (consistent with the east-west deformation trends in some of the Orbicule Koppie orbicules; Benedict et al., 1964;

Lombaard et al., 1986) and contamination of the Koperberg Suite magmas (Brandriss and Cawthorn, 1996; Van Zwieten et al., 1996).

In summary, the oxidation and Cu-enrichment of a sulphide melt that formed the mineralization in the orbicules and Koperberg Suite more generally began prior to the emplacement of the silicate Koperberg Suite magmas that formed the orbicules, suggesting no link between orbicule genesis and sulphide metallogenesis.

9. Conclusions

Formation of the Koperberg Suite and Diana's Pool orbicules has previously been attributed to metasomatic processes. However, varieties of textural and geochemical constraints rule out a metasomatic origin. These include chemical similarity between orbicules and the magmatic matrices, as well as a variety of synmagmatic textures. This, along with isotopic data, indicate that distinct pulses of orbicule-forming magmas make up the Koperberg Suite, where variable amounts of magma mixing, mingling and assimilation occurred. These differentiation processes took place during magma ascent and emplacement, triggering the ideal conditions for orbicule formation.

Based on hand sample descriptions field observation, petrological and *in-situ* mineral chemistry data presented here, Diana's Pool and the Koperberg Suite orbicules are of magmatic origin that involved two stages: (1) adiabatic decompression of melts in dykes or conduits, which led to superheating and resorption of solids, followed by a delay in nucleation and (2) volatile exsolution, inducing undercooling, supersaturation, and the crystallization of shells on existing cores/autoliths, forming orbicules. At a later stage, orbicule growth ceased and the coarse-grained matrix began to crystallize by homogenous nucleation as evidenced by the coarse-grained textures of the matrix. Based on the deformation features exhibited by the Diana's Pool and Orbicule Koppie orbicules, these orbicules formed in deeper areas of the crust and were later emplaced in their present setting. They were most likely dragged by the inter-orbicular magma during a repeated sequential process.

Sulphide mineralization is only present in the Koperberg Suite orbicules. The magmatic oxidation of a sulphide melt, which produces a Cu-rich and S-poor melt that later crystallizes to an *iss*-bornite assemblage, can be used to explain the bornite-dominated assemblage in the Koperberg Suite orbicules. This also explains why the Carolusberg-type (bornite, magnetite, and chalcopyrite) assemblage dominates the mafic orbicules and the Narrap-type (chalcopyrite) assemblage dominates the felsic orbicules. The least fractionated silicate melt, which contained a Cu-poor and S-rich sulphide melt that later gave rise to the Narrap-type assemblage, is likely to be that produced the felsic orbicules. In contrast, the most fractionated Cu-rich and S-poor sulphide melt is thought to have generated the mafic orbicules and the bornite-dominated assemblage. In addition, the sulphides in the orbicules have high concentrations of Ag, Se, Bi, Zn, Pb, and In and low concentrations of Ni and Co. This is typical of sulphides that segregated from a Ni-rich sulphide-rich component at an earlier stage followed by crystallization from a Cu-rich sulphide melt. This is comparable with the Hondekloof deposit, which is characterized by Ni- and Co-rich mineralization with low Cu-contents, and the formation of the Cu-rich O'okiep Copper District sulphide melts from a deep-seated magma reservoir (Maier et al., 2012).

10. Recommendations for future research

Several analyses in both orbicular rocks and the sulphides could not be completed due to time restrictions. Therefore, the subsequent geochemical analyses might be beneficial in further research:

- Analysis of oxygen isotopes in the orbicules, compared to the mantle derived ratios (5.3-6.0‰; Boer et al., 1994) to further constrain the origin of the Koperberg Suite and the orbicules.
- Crustal contamination is one of the main mechanisms that results in the attainment of S saturation in mantle-derived magmas in Ni-Cu-PGE sulphide deposits (Ripley and Li, 2013). The S isotope composition of the contaminated magma is altered when uncontaminated mantle-derived magmas interact with a sulphur reservoir or contaminant that has a $\delta^{34}S$ signature that is unusual for the mantle, and the magmas that result from these interactions will have $\delta^{34}S$ values that are outside the range of values for mantle-derived rocks (0 ± 2‰; Peters et al., 2010). Hence, the origins of sulphur in magmatic sulphide deposits are traced using $\delta^{34}S$ isotopic fingerprints (Ohmoto, 1986). Therefore, analyzing sulphur isotopes in the sulphides can better constrain their origin.
- Analyzing and using Nd isotopes on the MCS modelling can better constrain the other simulations that were unsuccessful.
- The fractionation of Cu and Fe isotopes during sulphide differentiation and the oxidation states of these two elements are controlled by magmatic oxidation of sulphide melt (Zhao et al., 2019). Cu^{2+} and Fe^{3+} tend to be abundant in oxidized sulphide melts that create Cu-Fe sulphides, which are characterized by relatively greater $\delta^{65}Cu$ and lower $\delta^{56}Fe$ values (Zhao et al., 2019). In order to evaluate the magmatic oxidation of sulphide melt as a process for the creation of the sulphide assemblage seen in the Koperberg Suite orbicules as postulated here, more Cu and Fe isotope studies on sulphides in the Koperberg Suite should be tested.
- High precision geochronology, driven by CA-ID-TIMS, might be an effective method to understand the overall emplacement history of the Koperberg Suite, particularly whether the orbicular granites are early/late/in the middle of the suite as a whole.

11. References

Abdel-Rahman, A.F.M., 1994. Nature of biotites from alkaline, calc-alkaline, and peraluminous magmas. Journal of Petrology, 35, 525–541.

Acosta-Vigil, A., London, D., Morgan, G.B. and Dewers, T.A., 2003. Solubility of excess alumina in hydrous granitic melts in equilibrium with peraluminous minerals at 700–800° C and 200 MPa, and applications of the aluminum saturation index. Contributions to Mineralogy and Petrology, 146, 100–119.

Amm, F. L., 1940. The geology of the country rocks around Bulawayo. Southern Rhodesia Geological Survey Bulletin. 35, 1-307.

Andersen, J.C., 2006. Postmagmatic sulphur loss in the Skaergaard intrusion: implications for the formation of the Platinova Reef. Lithos, 92, 198–221.

Andersen, T., Andersson, U.B., Graham, S., Åberg, G. and Simonsen, S.L., 2009. Granitic magmatism by melting of juvenile continental crust: new constraints on the source of Palaeoproterozoic granitoids in Fennoscandia from Hf isotopes in zircon. Journal of the Geological Society, 166, 233–247.

Andersen, T., Elburg, M.A., van Niekerk, H.S. and Ueckermann, H. 2018. Successive sedimentary recycling regimes in southwestern Gondwana: Evidence from detrital zircons in Neoproterozoic to Cambrian sedimentary rocks in southern Africa. Earth-Science Reviews, 181, 43–60.

Andreoli, M.A., Hart, R.J., Ashwal, L.D. and Coetzee, H., 2006. Correlations between U, Th content and metamorphic grade in the western Namaqualand Belt, South Africa, with implications for radioactive heating of the crust. Journal of Petrology, 47, 1095–1118.

Asimow, P.D. and Ghiorso, M.S., 1998. Algorithmic modifications extending MELTS to calculate subsolidus phase relations. American Mineralogist, 83, 1127–1132.

Bacon, C.R., Bruggman, P.E., Christiansen, R.L., Clynne, M.A., Donnelly-Nolan, J.M. and Hildreth, W., 1997. Primitive magmas at five Cascade volcanic fields; melts from hot, heterogeneous sub-arc mantle. The Canadian Mineralogist, 35, 397–423.

Bailie, R., Abrahams, G., Bokana, R., van Bever Donker, J., Frei, D. and le Roux, P., 2019. The geochemistry and geochronology of the upper granulite facies Kliprand dome: comparison of the southern and northern parts of the Bushmanland Domain of the Namaqua Metamorphic Province, southern Africa and clues to its evolution. Precambrian Research, 330, 58–100.

Ballhaus, C., Fonseca, R.O., Münker, C., Kirchenbaur, M. and Zirner, A., 2015. Spheroidal textures in igneous rocks–Textural consequences of H_2O saturation in basaltic melts. Geochimica et Cosmochimica Acta, 167, 241–252.

Ballhaus, C., Tredoux, M. and Späth, A., 2001. Phase relations in the Fe–Ni–Cu–PGE–S system at magmatic temperature and application to massive sulphide ores of the Sudbury igneous complex. Journal of Petrology, 42, 1911–1926.

Barnes, S.J. and Lightfoot, P.C., 2005. Formation of magmatic nickel sulfide deposits and processes affecting their copper and platinum group element contents. In: J.W. Hedenquist, J.F.H.

Thompson, R.J. Goldfarb and J.P. Richards (Editors) One Hundredth Anniversary Volume. Society of Economic Geologists, 179–213.

Barbey, P., Grandprat, M. and Faure, F., 2021. Cordierite-bearing orbicules record bulk assimilation and the pulsating nature of magma ascent: The Lafaye Orbicular Granite (France). Journal of Petrology, 62, egab063.

Barrière, M., Chauris, L., Cotten, J., 1971. Premières données sur un faciès orbiculaire dans le massif granitique de 1'Aber-Ildut (Finistère, France). Bulletin de Minéralogie, 94, 402.

Benedict, P., Wiid, D. de N. and Cornelissen, A. Staff., 1964. Progress report on the geology of the O'okiep Copper District. The Geology of some Ore Deposits in Southern Africa. Geological Society of South Africa II, 239–302.

Bevan, J. and Bevan, A., 2009. Nature and origin of the orbicular granodiorite from Boogardie Station, Western Australia: An ornamental stone of monumental proportions. The Australian Gemmologist, 23, 373–432.

Black, L.P., Kamo, S.L., Allen, C.M., Aleinikoff, J.N., Davis, D.W., Korsch, R.J. and Foudoulis, C., 2003. TEMORA 1: a new zircon standard for Phanerozoic U–Pb geochronology. Chemical Geology, 200, 155–170.

Blundy, J., and Cashman, K., 2001. Ascent-driven crystallization of dacite magmas at Mount St Helens, 1980–1986, Contrib. Mineral. Petrol., 140 (6), 631–650, doi: 10.1007/s004100000219.

Boer, R., Meyer, F. and Cawthorn, R.G., 1994. Stable isotopic evidence for crustal contamination and desulfidation of the cupriferous Koperberg Suite, Namaqualand, South Africa. Geochimica et Cosmochimica Acta, 58, 2677–2687.

Bohrson, W.A. and Spera, F.J., 2001. Energy-constrained open-system magmatic processes II: application of energy-constrained assimilation–fractional crystallization (EC-AFC) model to magmatic systems. Journal of Petrology, 42, 1019–1041.

Bohrson, W.A., Spera, F.J., Ghiorso, M.S., Brown, G.A., Creamer, J.B. and Mayfield, A., 2014. Thermodynamic model for energy-constrained open-system evolution of crustal magma bodies undergoing simultaneous recharge, assimilation and crystallization: The magma chamber simulator. Journal of Petrology, 55, 1685–1717.

Bohrson, W.A., Spera, F.J., Heinonen, J.S., Brown, G.A., Scruggs, M.A., Adams, J.V., Takach, M.K., Zeff, G. and Suikkanen, E., 2020. Diagnosing open-system magmatic processes using the Magma Chamber Simulator (MCS): part I—major elements and phase equilibria. Contributions to Mineralogy and Petrology, 175, 1–29.

Bourdeau, J., Hayes, B., Zhang, S., Logue, A. and Bybee, G., 2022. Origin and significance of noritic blocks in layered anorthosites in the Bushveld Complex, South Africa. Contributions to Mineralogy and Petrology, 177, 1–26.

Brandriss, M. and Cawthorn, R., 1996. Formation of anorthosite and leucotonalite during magma hybridization in the Koperberg Suite of Namaqualand, South Africa. South African Journal of Geology, 99, 135–151.

Broderick, T. and Hubbard, P., 2016. The Matobo Hills of Zimbabwe: A perfect blend of geology, scenery and human history. IN: Anhaeusser, C. R., Viljoen, M. J., Viljoen, R. P., (eds) 2016. Africa's Top Geological Sites.Stuik Nature, Cape Town.312pp.

Bybee, G.M., 2014. High-pressure megacrysts and lower crustal contamination: probing a mantle source for Proterozoic massif-type anorthosites. PhD. University of the Witwatersrand, South Africa.

Campbell, I., Compston, D., Richards, J., Johnson, J. and Kent, A., 1998. Review of the application of isotopic studies to the genesis of Cu-Au mineralization at Olympic Dam and Au mineralization at Porgera, the Tennant Creek district and Yilgarn Craton. Australian Journal of Earth Sciences, 45, 201–218.

Caraballo, E., Dare, S. and Beaudoin, G., 2022. Variation of trace elements in chalcopyrite from worldwide Ni-Cu sulfide and Reef-type PGE deposits: implications for mineral exploration. Mineralium Deposita, 57, 1293–1321.

Ceuleneer, G. and Nicolas, A., 1985. Structures in podiform chromite from the Maqsad district (Sumail ophiolite, Oman). Mineralium Deposita, 20, .177-184.

Cawthorn, R.G. and Meyer, F.M., 1993. Petrochemistry of the Okiep copper district basic intrusive bodies, northwestern Cape Province, South Africa. Economic Geology, 88, 590–605.

Chung, H. and Mungall, J.E. 2009. Physical constraints on the migration of immiscible fluids through partially molten silicates, with special reference to magmatic sulfide ores. Earth and Planetary Science Letters, 286, 14–22.

Clifford, T.N. and Barton, E.S., 2012. The O'okiep Copper District, Namaqualand, South Africa: a review of the geology with emphasis on the petrogenesis of the cupriferous Koperberg Suite. Mineralium Deposita, 47, 837–857.

Clifford, T.N., Barton, E.S., Retief, E.A., Rex, D.C. and Fanning, C.M., 1995. A Crustal Progenitor for the Intrusive Anorthosite—Charnockite Kindred of the Cupriferous Koperberg Suite, O'okiep District, Namaqualand, South Africa; New Isotope Data for the Country Rocks and the Intrusives. Journal of Petrology, 36, 231–258.

Clifford, T.N., Barton, E.S., Stern, R.A. and Duchesne, J.C., 2004. U–Pb zircon calendar for Namaquan (Grenville) crustal events in the granulite-facies terrane of the O'okiep copper district of South Africa. Journal of Petrology, 45, 669–691.

Clifford, T., Gronow, J., Rex, D. and Burger, A., 1975. Geochronological and petrogenetic studies of high-grade metamorphic rocks and intrusives in Namaqualand, South Africa. Journal of Petrology, 16, 154–188.

Clifford, T.N., Stumpfl, E.F., Burger, A.J., McCarthy, T.S. and Rex, D.C., 1981. Mineral-chemical and isotopic studies of Namaqualand granulites, South Africa: a Grenville analogue. Contributions to Mineralogy and Petrology, 77, 225–250.

Conradie, J. and Schoch, A., 1988. Rare earth element geochemistry of an anorthosite-diorite suite, Namaqua mobile belt, South Africa. Earth and Planetary Science Letters, 87, 409–422.

Conradie, J.A. and Schoch, A.E., 1986. Petrographical characteristics of the Koperberg Suite, South Africa—an analogy to massif-type anorthosites?. *Precambrian Research*, *31*(2), pp.157-188.

Cook, N.J., Ciobanu, C.L., Danyushevsky, L.V. and Gilbert, S., 2011. Minor and trace elements in bornite and associated Cu–(Fe)-sulfides: A LA-ICP-MS study of bornite mineral chemistry. Geochimica et Cosmochimica Acta, 75, 6473–6496.

Cornell, D., Thomas, R.J., Gibson, R., Moen, H., Reid, D., Moore, J. and Gibson, R., 2006. The Namaqua-Natal Province. In: Geological Society of South Africa.

Couturié, J.P., 1973. Un nouveau gisement de granite orbiculaire dans le Massif Central français: le granite du Signal de Randon (Lozère). Contributions to Mineralogy and Petrology, 42(4), 305-312.

Dare, S.A., Barnes, S.J., Prichard, H.M. and Fisher, P.C., 2011. Chalcophile and platinum-group element (PGE) concentrations in the sulfide minerals from the McCreedy East deposit, Sudbury, Canada, and the origin of PGE in pyrite. Mineralium Deposita, 46, 381–407.

De Villiers, J. The Composition and Crystal Structures of Pyrrhotite: A Common but Poorly Understoo MineralAvailableonline: http://www.mintek.co.za/Mintek75/Proceedings/L01DeVilliers.pdf (accessed on 19 June 2022).

Decitre, S., Gasquet, D. and Marignac, C., 2002. Genesis of orbicular granitic rocks from the Ploumanac'h Plutonic Complex (Brittany, France): petrographical, mineralogical and geochemical constraints. European Journal of Mineralogy, 14, 715–731.

Deer, W., Howie, R., and Zussman, J., 1992. An introduction to the rock-forming minerals. Longman London, UK

DePaolo, D. and Wasserburg, G., 1976. Inferences about magma sources and mantle structure from variations of 143Nd/144Nd. Geophysical Research Letters, 3, 743–746.

DePaolo, D.J., 1981. Trace element and isotopic effects of combined wallrock assimilation and fractional crystallization. Earth and Planetary Science Letters, 53, 189–202.

Díaz-Alvarado, J., Rodríguez, N., Rodríguez, C., Fernández, C. and Constanzo, Í., 2017. Petrology and geochemistry of the orbicular granitoid of Caldera, northern Chile. Models and hypotheses on the formation of radial orbicular textures. Lithos, 284, 327–346.

Donaldson, C.H., 1975. Ultrabasic Breccias in layered intrusions: The Rhum Complex. The Journal of Geology, 83, 33–45.

Donnelly, C.L., Griffin, W.L., Yang, J.-H., O'Reilly, S.Y., Li, Q.L., Pearson, N.J. and Li, X.H., 2012. In situ U–Pb dating and Sr–Nd isotopic analysis of perovskite: constraints on the age and petrogenesis of the Kuruman Kimberlite Province, Kaapvaal Craton, South Africa. Journal of Petrology, 53, 2497–2522.

Duchesne, J.C., Auwera, J.V., Liégeois, J.P., Barton, E.S. and Clifford, T.N., 2007. Geochemical constraints of the petrogenesis of the O'okiep Koperberg Suite and granitic plutons in Namaqualand, South Africa: A crustal source in Namaquan (Grenville) times. Precambrian Research, 153, 116–142.

Durant, D.G. and Fowler, A.D., 2002. Origin of reverse zoning in branching orthopyroxene and acicular plagioclase in orbicular diorite, Fisher Lake, California. Mineralogical Magazine, 66, 1003–1019.

Edelman, N., 1983. *Boulder of orbicular rapakivi in Taivassalo, southwestern Finland*. Åbo akademi.

Eglington, B.M., 2006. Evolution of the Namaqua-Natal Belt, southern Africa – A geochronological and isotope geochemical review. Journal of African Earth Sciences, 46, 93–111.

Elburg, M., Vroon, P., van der Wagt, B. and Tchalikian, A., 2005. Sr and Pb isotopic composition of five USGS glasses (BHVO-2G, BIR-1G, BCR-2G, TB-1G, NKT-1G). Chemical Geology, 223, 196–207.

Elliston, J.N., 1984. Orbicules: An indication of the crystallization of hydrosilicates, I. Earth-Science Reviews, 20, 265–344.

Enz, R.D., Kudo, A.M. and Brookins, D.G., 1979. Igneous origin of the Orbicular Rocks of the Sandia Mountains, New Mexico. Geological Society of America Bulletin, 90, 349–380.

Enzman, R.D., 1953. *The mode of occurrence and origin of orbicular bodies in the O'okiep district of Namaqualand.* M.Sc. thesis, University of the Witwatersrand, Johannesburg.

Eskola, P., 1938. On the Esboitic Crystallization of Orbicular Rocks. The Journal of Geology, 46, 448–485.Feely, M., McCarthy, W., Costanzo, A., Leake, B.E. and Yardley, B.W., 2022. The Late Silurian to Upper Devonian Galway Granite Complex (GGC). In *A Field Guide to the Geology of Western Ireland: The Birth and Death of an Ocean* (pp. 303-362). Cham: Springer International Publishing.

Gadd-Claxton, D., 1981. The economic geology of the Okiep copper deposits, Namaqualand, South Africa. M.Sc thesis, Rhodes University, Grahamstown, 93pp.

Garson, M.S., 1995. The geology of the Bulawayo greenstone belt and the surrounding granitic terrain. Zimbabwe Geological Survey Bulletin, 93-294.

Garvie, O. G., 1969. A note on the orbicular granite in the Diana's Pool area, Matopos. Rhodesia. Quarterly News Bulletin Geological Society of South Africa, 12. No. 4. 11-12.

Garvie, O.G., 1971. Stop 14. Nsezi River. Stop 15. Diana's Pool. In: Excursion Guidebook. Symposium on the granites, gneisses and related rocks. Compiled by E.R. Morrison and J.F. Wilson. Geological Society of South Africa, Rhodesian Branch, 11-14.

George, L.L., Cook, N.J., Crowe, B.B. and Ciobanu, C.L., 2018. Trace elements in hydrothermal chalcopyrite. Mineralogical Magazine, 82, 59-88

Geringer, G., Botha, BJV &. Slabbert, M.J., 1988. The Keimoes Suite-a composite granitoid batholith along the eastern margin of the Namaqua mobile belt, South Africa. South African Journal of Geology, 91, 465–476.

Geringer, G., Botha, B., Pretorius, J. and Ludick, D., 1986. Calc-alkaline volcanism along the eastern margin of the Namaqua Mobile Belt, South Africa-a possible middle Proterozoic volcanic arc.

Ghiorso, M.S. and Gualda, G.A., 2015. An H_2O–CO_2 mixed fluid saturation model compatible with rhyolite-MELTS. Contributions to Mineralogy and Petrology, 169, 1–30.

Ghiorso, M.S., Hirschmann, M.M., Reiners, P.W. and Kress III, V.C., 2002. The pMELTS: A revision of MELTS for improved calculation of phase relations and major element partitioning related to partial melting of the mantle to 3 GPa. Geochemistry, Geophysics, Geosystems, 3, 1–35.

Ghiorso, M.S. and Sack, R.O., 1995. Chemical mass transfer in magmatic processes IV. A revised and internally consistent thermodynamic model for the interpolation and extrapolation of liquid-

solid equilibria in magmatic systems at elevated temperatures and pressures. Contributions to Mineralogy and Petrology, 119, 197–212.

Gibson, R., Robb, L., Kisters, A. and Cawthorn, R., 1996. Regional setting and geological evolution of the Okiep Copper District, Namaqualand, South Africa. South African Journal of Geology, 99, 107–120.

Grosse, P., Toselli, A.J. and Rossi, J.N., 2010. Petrology and geochemistry of the orbicular granitoid of Sierra de Velasco (NW Argentina) and implications for the origin of orbicular rocks. Geological Magazine, 147, 451–468.

Grove, T. L., R. J. Kinzler, and Bryan, W. B., 1992. Fractionation of Mid-Ocean Ridge Basalt (MORB), in Mantle Flow and Melt Generation at Mid-Ocean Ridges, edited, pp. 281-310, AGU, Washington, D. C., doi: 10.1029/GM071p0281.

Gualda, G.A., Ghiorso, M.S., Lemons, R.V. and Carley, T.L., 2012. Rhyolite-MELTS: a modified calibration of MELTS optimized for silica-rich, fluid-bearing magmatic systems. Journal of Petrology, 53, 875–890.

Hamman, J., Rozendaal, A. and Jordaan, W., 1996. Gabbro-norite-hosted Ni-Cu-(Co)-sulphide mineralization in southern Namaqualand and its relationship to the cupriferous Koperberg Suite of the Okiep Copper District, South Africa. South African Journal of Geology, 99, 153–168.

Harpum, J.R., 1963, Petrographic classification of granitic rocks in Tanganyika by partial chemical analyses: Records of the Geological Survey of Tanganyika, v. 10, p. 80–86

Harrison, T.M. and Watson, E.B., 1984. The behavior of apatite during crustal anatexis: Equilibrium and kinetic considerations. Geochimica et Cosmochimica Acta, 48, 1467–1477.

Hayes, B., Bybee, G.M., Mawela, M., Nex, P.A. and van Niekerk, D., 2018. Residual melt extraction and out-of-sequence differentiation in the Bushveld Complex, South Africa. Journal of Petrology, 59, 2413–2434.

Heinonen, J.S., Spera, F.J. and Bohrson, W.A., 2022. Thermodynamic limits for assimilation of silicate crust in primitive magmas. Geology, 50, 81–85.

Helmy, H.M., Ballhaus, C., Wohlgemuth-Ueberwasser, C., Fonseca, R.O. and Laurenz, V., 2010. Partitioning of Se, As, Sb, Te and Bi between monosulfide solid solution and sulfide melt–application to magmatic sulfide deposits. Geochimica et Cosmochimica Acta, 74, 6174–6179.

Howard III, J.H., 1977. Geochemistry of selenium: formation of ferroselite and selenium behavior in the vicinity of oxidizing sulfide and uranium deposits. Geochimica et Cosmochimica Acta, 41, 1665–1678.

Huhma, H., 2012. Geological Survey of Finland. *Special Paper*, *54*, 74-175.

Jackson, S.E., Pearson, N.J., Griffin, W.L. and Belousova, E.A., 2004. The application of laser ablation-inductively coupled plasma-mass spectrometry to in situ U–Pb zircon geochronology. Chemical Geology, 211, 47–69.

Jochum, K.P., Nohl, U., Herwig, K., Lammel, E., Stoll, B. and Hofmann, A.W., 2005. GeoReM: a new geochemical database for reference materials and isotopic standards. Geostandards and Geoanalytical Research, 29, 333–338.

Jochum, K.P., Weis, U., Schwager, B., Stoll, B., Wilson, S.A., Haug, G.H., Andreae, M.O. and Enzweiler, J., 2016. Reference values following ISO guidelines for frequently requested rock reference materials. Geostandards and Geoanalytical Research, 40, 333–350.

Joubert, P., 1986. Namaqualand-a model of Proterozoic accretion? South African Journal of Geology, 89, 79–96.

Jogee, B. A., 2019. *Unravelling the Petrogenesis of mafic orbicules of the Koperberg Suite and their metallogenic link to Cu mineralization.* Unpublished. B.Sc. (Honours) thesis. University of the Witwatersrand.

Kisters, A.F., Charlesworth, E.G., Gibson, R.L. and Anhaeusser, C.R., 1996. Steep structure formation in the Okiep Copper District, South Africa: bulk inhomogeneous shortening of a high-grade metamorphic granite-gneiss sequence. Journal of Structural Geology, 18, 735–751.

Kisters, A.F., Potgieter, J.E., Charlesworth, E.G., Anhaeusser, C.R., Gibson, R.L. and Watkeys, M.K., 1994. Emplacement features of cupriferous noritoids in the Okiep copper district, Namaqualand, South Africa. Exploration and Mining Geology, 3, 297–310.

Kisters, A.F., Stevens, G., Dziggel, A. and Armstrong, R.A., 2003. Extensional detachment faulting and core-complex formation in the southern Barberton granite–greenstone terrain, South Africa: evidence for a 3.2 Ga orogenic collapse. Precambrian Research, 127, 355–378.

Lahti, S.I., Raivio, P. and Laitakari, I., 2005. Orbicular rocks in Finland. Geological Survey of Finland.

Laitakari, I., Rämö, T., Suominen, V., Niin, M., Stepanov, K. and Amantov, A., 1996. Subjotnian: Rapakivi granites and related rocks in the surroundings of the Gulf of Finland. Special Paper-Geological Survey of Finland, 59–98.

Lapin, A.V. and Vartiainen, H., 1983. Orbicular and spherulitic carbonatites from Sokli and Vuorijärvi. Lithos, 16, 53–60.

Latsky, R., 1942. The magmatic copper ores of Mamaqualand. South African Journal of Geology, 45, 109–150.

Le Bras, L.Y., Bolhar, R., Bybee, G.M., Nex, P.A., Guy, B.M., Moyana, T. and Lourens, P., 2021. Platinum-group and trace elements in Cu-sulfides from the Loolekop pipe, Phalaborwa: implications for ore-forming processes. Mineralium Deposita, 56, 161–177.

Leach, A.M. and Hieftje, G.M., 2000. Methods for shot-to-shot normalization in laser ablation with an inductively coupled plasma time-of-flight mass spectrometerPresented at the 2000 Winter Conference on Plasma Spectrochemistry, Fort Lauderdale, FL, USA, January 10–15, 2000. Journal of Analytical Atomic Spectrometry, 15, 1121–1124.

Leake, B.E., 2011. Stoping and the mechanisms of emplacement of the granites in the Western Ring Complex of the Galway granite batholith, western Ireland. Earth and Environmental Science Transactions of the Royal Society of Edinburgh, 102(1), pp.1-16.

Leveson, D.J., 1963. Orbicular Rocks of the Lonesome Mountain Area, Beartooth Mountains, Montana and Wyoming. Geological Society of America Bulletin, 74, 1015.

Leveson, D.J., 1966. Orbicular Rocks: A Review. Geological Society of America Bulletin, 77, 409.

Leveson, D.J., 1973. Origin of Comb Layering and Orbicular Structure, Sierra Nevada Batholith, California: Discussion. Geological Society of America Bulletin, 84, 4005–4006.

Li, Y., Zheng, J. and Satish-Kumar, M., 2021. Combining zircon texture, REE patterns and U-Pb-Hf isotopes to decipher the formation process of orbicular rocks: A case study from Huangling orbicular granodiorite, Yangtze craton, China. Lithos, 386, 106026.

Lindh, A. and Nasstrom, H., 2006. Crystallization of orbicular rocks exemplified by the Slättemossa occurrence, southeastern Sweden. Geological Magazine, 143, 713–722.

Lofgren, G.E. and Donaldson, C.H., 1975. Curved branching crystals and differentiation in comb-layered rocks. Contributions to Mineralogy and Petrology, 49, 309–319.

Lombaard, A.F. and Schreuder, F.J.G., 1978. Distribution pattern and general geological features of steep structures, megabreccias and basic rocks in the Okiep Copper District. In: W.J. Verwoerd (Editor) Mineralization in Metamorphic Terranes. Geological Society of South Africa Special Publication, 4, 522–523.

Lombaard, A.F. And the exploration staff of the O' okiep Copper Company Limited (1986). The copper deposits of the Okiep district, Namaqualand. In: Anhaeusser, C.R. & Maske, S. (Eds.), Mineral Deposits of Southern Africa, Geological Society of South Africa, II, 1421-144.

Longerich, H.P., Jackson, S.E. and Günther, D., 1996. Inter-laboratory note. Laser ablation inductively coupled plasma mass spectrometric transient signal data acquisition and analyte concentration calculation. Journal of Analytical Atomic Spectrometry, 11, 899–904.

Luttinen, A.V. and Furnes, H., 2000. Flood basalts of vestfjella: Jurassic magmatism across an Archaean–Proterozoic lithospheric boundary in Dronning Maud Land, Antarctica. Journal of Petrology, 41, 1271–1305.

Macey, P., Bailie, R., Miller, J., Thomas, R., De Beer, C., Frei, D. and Le Roux, P., 2018. Implications of the distribution, age and origins of the granites of the Mesoproterozoic Spektakel Suite for the timing of the Namaqua Orogeny in the Bushmanland Subprovince of the Namaqua-Natal Metamorphic Province, South Africa. Precambrian Research, 312, 68–98.

Macey, P.H., Thomas, R.J., Kisters, A.F.M., Diener, J.F.A., Angombe, M., Doggart, S., Groenewald, C.A., Lambert, C.W., Miller, J.A., Minnaar, H., Smith, H., Moen, H.F.G., Muvangua, E., Nguno, A., Shifotoka, G., Indongo, J., Frei, D., Spencer, C., Le Roux, P., Armstrong, R.A. and Tinguely, C., 2022. A continental back-arc setting for the Namaqua belt: Evidence from the Kakamas Domain. Geoscience Frontiers, 13, 101408.

Macgregor, A.M., 1951. Some milestones in the Precambrian of Southern Africa. Proc. Geological. Society of South Africa 54, 27–71

Maier, W.D., 2000. Platinum-group elements in Cu-sulphide ores at Carolusberg and East Okiep, Namaqualand, South Africa. Mineralium Deposita, 35, 422–429.

Maier, W.D., Andreoli, M.A., Groves, D. and Barnes, S.J., 2012. Petrogenesis of Cu-Ni sulphide ores from O'okiep and Kliprand, Namaqualand, South Africa: constraints from chalcophile metal contents. South African Journal of Geology, 115, 499–514.

Maier, W.D. and Barnes, S.J., 1996. Unusually high concentrations of magnetite at Caraiba and other Cu-sulfide deposits in the Curaca Valley, Bahia, Brazil. Canadian Mineralogist, 34, 717–731.

Maier, W.D. and Barnes, S.J., 1999. The origin of Cu sulfide deposits in the Curaca Valley, Bahia, Brazil; evidence from Cu, Ni, Se, and platinum-group element concentrations. Economic Geology, 94, 165–183

Makutu, M.N., Kanika, M., Bwanga, N., Nguangu, K., Mpoyi, K., 2004. Petrology and geochemistry of igneous rocks from Noqui Alkaline Complex. Bulletin du Centre de Recherches Géologiques et Minières, 5 (1), 28-39.

Marais, J., Agenbacht, A., Prinsloo, M. and Basson, W., 2001. The geology of the Springbok area. Council for Geosciences, South Africa, 103.

Marima, E., 2022. Trace element and sulphur isotope variations of sulphides in the Koperberg Suite, O'okiep Copper District, Namaqualand, South Africa; implications for formation of sulphides and the role of crustal sulphur assimilation. M.Sc. Rhodes University, South Africa.

Mao, Y.J., Dash, B., Qin, K.-Z., Bujinlkham, B. and Tang, D.M., 2018. Comparisons among the Oortsog, Dulaan, and Nomgon mafic–ultramafic intrusions in central Mongolia and Ni–Cu deposits in NW China: implications for economic Ni–Cu–PGE ore exploration in central Mongolia. Russian Geology and Geophysics, 59, 1–18.

McBirney, A.R., 1963. Geology of a Part of the Central Guatemalan Cordillera. University of California Press

McCarthy, T., 1976. Chemical interrelationships in a low-pressure granulite terrain in Namaqualand. South Africa and their bearing on granite genesis and the composition of the lower crust. Geochimica et Cosmochimica Acta, 40, 1057–1068.

McCarthy, A. and Müntener, O., 2016. Comb layering monitors decompressing and fractionating hydrous mafic magmas in subvolcanic plumbing systems (Fisher Lake, Sierra Nevada, USA): Petrology of Fisher Lake Comb Layers. Journal of Geophysical Research: Solid Earth, 121, 8595–8621.

Mclver, J., McCarthy, T. and Packham, B. de V., 1983. The copper-bearing basic rocks of Namaqualand, South Africa. Mineralium Deposita, 18, 135–160.

Mennell, F., 1902. Contributions to South African Petrography. Geological Magazine, 9, 356–366.

Mennell, F., 1904. The Average Composition of the Igneous Rocks. 1. Geological Magazine, 1, 263–264

Minnitt, R., 1986. Porphyry copper-molybdenum mineralization at Haib River, South West Africa/Namibia. In: Anhaeusser and Maske (Eds.) Mineral Deposits of Southern Africa 1567–1585.

Mollo, S. and Hammer, J. E., 2017. Dynamic crystallization in magmas. EMU Notes in Mineralogy 16, 373–418.

Monod, O., Pérez-Segura, E., Richard, D. and Calmus, T., 1995. Orbicular granite sills in the Mazatan core complex, Sonora, Mexico. Revista Mexicana de Ciencias Geologicas, 12, 9–16.

Moore, J.G. and Lockwood, J.P., 1973. Origin of Comb Layering and Orbicular Structure, Sierra Nevada Batholith, California. Geological Society of America Bulletin, 84, 1–20.

Mouri, H., Andreoli, M., Kienast, J., Guiraud, M. and De Waal, S., 2003. First occurrence of the rare ‘corundum+ quartz’assemblage in the high-grade zone from the Namaqualand Metamorphic Complex, South Africa: evidence for higher-P, T metamorphism? Mineralogical Magazine, 67, 1015–1021.

Morse S.A., 1991. Basaltic magma from the crust is not a free option. Eos Trans. Am Geophysics Union 72:161.

Morse, S. A., 1980. Basalts and Phase Diagrams: An Introduction to the Quantitative Use of Phase Diagrams in Igneous Petrology, 493 pp., Springer, New York.

Mungall, J.E., Hanley, J.J., Arndt, N.T. and Debecdelievre, A., 2006. Evidence from meimechites and other low-degree mantle melts for redox controls on mantle-crust fractionation of platinum-group elements. Proceedings of the National Academy of Sciences, 103, 12695–12700.

Nachit, H., Ibhi, A. and Ohoud, M.B., 2005. Discrimination between primary magmatic biotites, reequilibrated biotites and neoformed biotites. Comptes Rendus Geoscience, 337, 1415–1420.

Nicolaysen, L.O. and Burger, A.J., 1965. Note on an extensive zone of 1000 million-year old metamorphic and igneous rocks in southern Africa. Sciences de la Terre, 10, 497–516.

Nockolds, S.R., 1931. On an Orbicular Diorite from the Island of Alderney. Geological Magazine, 68, 499–506.

Norris, A. and Danyushevsky, L., 2018. Towards estimating the complete uncertainty budget of quantified results measured by LA-ICP-MS. Goldschmidt, Boston. MA, USA.

Ohmoto, H., 1986. Stable isotope geochemistry of ore deposits. In: J.W. Valley, H.P. Taylor and J.R. O'Neil (Eds.) Stable Isotopes in High Temperature Geological Processes. 491–559.

Ort, M.H., 1992. Orbicular volcanic rocks of Cerro Panizos: Their origin and implications for orb formation. Geological Society of America Bulletin, 104, 1048–1058.

Owen, J.V., 1992. Geochemistry of orbicular diorite from the Grenville Front zone, eastern Labrador. Mineralogical Magazine, 56, 451–458.

Palmer, D.F., Bradley, J. and Prebble, W.M., 1967. Orbicular Granodiorite from Taylor Valley, South Victoria Land, Antarctica. Geological Society of America Bulletin, 78, 1423–1428.

Peck, D.C. and Keays, R.R., 1990. Insights into the behavior of precious metals in primitive, S-undersaturated magmas; evidence from the Heazlewood River complex, Tasmania. The Canadian Mineralogist, 28, 553–577.

Pertunnen, V., 1983. Orbicular quartz diorite in Kemi, NW Finland. Bulletin of the Geological Society of Finland, 55, 51–6.

Peters, M., Strauss, H., Farquhar, J., Ockert, C., Eickmann, B. and Jost, C.L., 2010. Sulfur cycling at the Mid-Atlantic Ridge: A multiple sulfur isotope approach. Chemical Geology, 269, 180–196.

Porter, D.A. and Easterling, K.E., 2009. Phase transformations in metals and alloys (revised reprint). CRC press

Powell, R. and Holland, T., 1988. An internally consistent dataset with uncertainties and correlations: 3. Applications to geobarometry, worked examples and a computer program. Journal of Metamorphic Geology, 6, 173–204.

Powell, R. and Holland, T., 1994. Optimal geothermometry and geobarometry. American Mineralogist, 79, 120–133.

Powell, R., Holland, T. and Worley, B., 1998. Calculating phase diagrams involving solid solutions via non-linear equations, with examples using THERMOCALC. Journal of Metamorphic Geology, 16, 577–588.

Raith, J. and Harley, S., 1998. Low-P/high-T metamorphism in the Okiep Copper District, western Namaqualand, South Africa. Journal of Metamorphic Geology, 16, 281–305.

Rasbury, E.T., Present, T.M., Northrup, P., Tappero, R.V., Lanzirotti, A., Cole, J.M., Wooton, K.M. and Hatton, K., 2021. Tools for uranium characterization in carbonate samples: case studies of natural U–Pb geochronology reference materials. Geochronology, 3, 103–122.

Ray, R.G., 1952. Orbicular diorite from southern Alaska. American Journal of Science, 250, 57.

Read, H. H., 1951. Metamorphism and granitization. Alex. L. du Toit Memorial Lecture, No. 2. Trans. Proc. Geological Society of South Africa. Annex. 54, 1-17.

Reid, D.L., 1977. *Geochemistry of Precambrian igneous rocks in the lower Orange River region* (Doctoral dissertation, University of Cape Town).

Reid, D.L., 1979. Total rock RbSr and U-Th-Pb isotopic study of Precambrian metavolcanic rocks in the lower Orange River region, southern Africa. Earth and Planetary Science Letters, 42, 368–378.

Reid, D.L., 1997. Sm-Nd age and REE geochemistry of Proterozoic arc-related igneous rocks in the Richtersveld subprovince, Namaqua Mobile Belt, Southern Africa. Journal of African Earth Sciences, 24, 621–633.

Reid, D., Ransome, I., Onstott, T.C. and Adams, C., 1991. Time of emplacement and metamorphism of Late Precambrian mafic dykes associated with the Pan-African Gariep orogeny, Southern Africa: implications for the age of the Nama Group. Journal of African Earth Sciences (and the Middle East), 13, 531–541.

Ripley, E.M. and Li, C., 2013. Sulfide saturation in mafic magmas: Is external sulfur required for magmatic Ni-Cu-(PGE) ore genesis? Economic Geology, 108, 45–58.

Roberts, N. M. W., Rasbury, E. T., Parrish, R. R., 2017. A Calcite Reference Material for LA-ICP-MS U-Pb Geochronology. *Geochemistry, Geophysics, Geosystems*,18 (7):2807–2814.

Robb, L.J., Armstrong, R.A. and Waters, D.J., 1999. The history of granulite-facies metamorphism and crustal growth from single zircon U–Pb geochronology: Namaqualand, South Africa. *Journal of Petrology*, *40*(12), pp.1747-1770.

Salters, V.J. and Stracke, A., 2004. Composition of the depleted mantle. Geochemistry, Geophysics, Geosystems, 5.

Schoch, A.E. and Conradie, J.A., 1990. Petrochemical and mineralogical relationships in the Koperberg suite, Namaqualand, South Africa. American Mineralogist, 75, 27–36.

Scoon, R.N., Costin, G., Mitchell, A.A. and Moine, B., 2020. Non-sequential injection of PGE-rich ultramafic sills in the Platreef Unit at Akanani, Northern Limb of the Bushveld Complex: Evidence from Sr and Nd isotopic systematics. Journal of Petrology, 61, egaa032.

Sederholm, J.J., 1928. On orbicular Granites.Geological Society of Finland Bulletin, 83, 80–81.

Sederholm J.J., 1928. On orbicular granites, spotted and nodular granites etc. and on the rapakivi texture. Geological Society of Finland Bulletin, 83,105 pp.

Sithole, M., 2018. A study into the Main Structural Features of the Namaqua Region and their Relation to the Intrusion of the Keimoes Suite, MSc. thesis, University of Cape Town, Cape Town, South Africa, p.1-85

Shapovalova, M., Tolstykh, N., Shelepaev, R. and Kalugin, V., 2020. PGE-Cu-Ni mineralization of mafic-ultramafic massifs of the Khangai Upland, Western Mongolia. Minerals, 10, 942.

Shelley, D., 1993. Igneous and metamorphic rocks under the microscope: classification, textures, microstructures and mineral preferred-orientations. Springer.

Smillie, R.W. and Turnbull, R.E., 2013. Field and petrographical insight into the formation of orbicular granitoids from the Bonney Pluton, southern Victoria Land, Antarctica. Geological Magazine, 151, 534–549.

Smith, C.G. and Fripp, R.E.P., 1973. The northern contact facies of the Matopos granite, Rhodesia. Geological Society of South Africa Special Publication, 3, 447–53.

Smith C. C., 1968. *Some aspects of the geology of the Matopos.* Unpublished. B.Sc. (Special Honours) thesis. University College of Rhodesian.

Spera, F.J. and Bohrson, W.A., 2001. Energy-constrained open-system magmatic processes I: General model and energy-constrained assimilation and fractional crystallization (EC-AFC) formulation. Journal of Petrology, 42, 999–1018.

Stern, R.A., Bodorkos, S., Kamo, S.L., Hickman, A.H. and Corfu, F., 2009. Measurement of SIMS instrumental mass fractionation of Pb isotopes during zircon dating. Geostandards and Geoanalytical Research, 33, 145–168.

Stumpfl, E., Clifford, T., Burger, A. and Van Zyl, D., 1976. The copper deposits of the O'okiep district, South Africa: new data and concepts. Mineralium Deposita, 11, 46–70.

Sylvester, A.G., 2011. The nature and polygenetic origin of orbicular granodiorite in the Lower Castle Creek pluton, northern Sierra Nevada batholith, California. Geosphere, 7, 1134–1142.

Symes, R.F., Bevan, J.C. and Qasim Jan, M., 1987. The nature and origin of orbicular rocks from near Deshai, Swat Kohistan, Pakistan. Mineralogical Magazine, 51, 635–647.

Swanson, S. E., 1977. Relation of nucleation and crystal growth rate to the development of granitic textures. American Mineralogist 62, 966–978.

Taylor Jr, H.P., 1980. The effects of assimilation of country rocks by magmas on $^{18}O/^{16}O$ and 87Sr/86Sr systematics in igneous rocks. Earth and Planetary Science Letters, 47, 243–254.

Taylor Jr, H.P., 1974. Oxygen and hydrogen isotope evidence for large-scale circulation and interaction between ground waters and igneous intrusions, with particular reference to the San Juan volcanic field, Colorado.

Thomas, R., Cornell, D.H., Moore, J.M., and Jacobs, J., 1994. Crustal evolution of the Namaqua-Natal metamorphic province, Southern Africa. South African Journal of Geology, 97, 8–14.

Thomas, R., De Beer, C. and Bowring, S., 1996. A comparative study of the Mesoproterozoic late orogenic porphyritic granitoids of southwest Namaqualand and Natal, South Africa. Journal of African Earth Sciences, 23, 485–508.

Thompson, T.B. and Giles, D.L., 1974. Orbicular Rocks of the Sandia Mountains, New Mexico. Geological Society of America Bulletin, 85, 911–916.

Van Zwieten, A., McCarthy, T. and Cawthorn, R., 1996. A petrogenetic model for the Koperberg Suite: evidence from the Jubilee Mine, Namaqualand, South Africa. South African Journal of Geology, 99, 121–134.

Van Zyl, D., 1967. The geology of the O'Okiep Copper Mine, Namaqualand. Annals University of Stellenbosch Series A 42(1), 58.

Vernon, R.H., 1985. Possible role of superheated magma in the formation of orbicular granitoids. Geology, 13, 843–845.

Vigneresse, J.L., 2015. Textures and melt-crystal-gas interactions in granites. Geoscience Frontiers, 6, 635–663.

Von Buch, F.L., 1802 Geognostische Beobachtungen auf Reisen durch Deutschland und Italien. Bei Haude und Spener.

Wager, L.R., Vincent, E.A. and Smales, A.A., 1957. Sulphides in the Skaergaard intrusion, east Greenland. Economic Geology, 52, 855–903.

Waters, D., 1986. Metamorphic zonation and thermal history of pelitic gneisses from western Namaqualand, South Africa. South African Journal of Geology, 89, 97–102.

Waters, D., 1989. Metamorphic evidence for the heating and cooling path of Namaqualand granulites. Geological Society, London, Special Publications, 43, 357–363.

Wiedenbeck, M., Alle, P., Corfu, F., Griffin, W., Meier, M., Oberli, F. v, Quadt, A. von, Roddick, J. and Spiegel, W., 1995. Three natural zircon standards for U-Th-Pb, Lu-Hf, trace element and REE analyses. Geostandards newsletter, 19, 1–23.

Wohlgemuth-Ueberwasser, C.C., Fonseca, R.O., Ballhaus, C. and Berndt, J., 2013. Sulfide oxidation as a process for the formation of copper-rich magmatic sulfides. Mineralium Deposita, 48, 115–127.

Zhang, J. and Lee, C.T.A., 2021. Disequilibrium crystallization and rapid crystal growth: a case study of orbicular granitoids of magmatic origin. International Geology Review, 63, 900–916.

Zhao, Y., Xue, C., Liu, S. A., Mathur, R., Zhao, X., Yang, Y., Dai, J., Man, R. and Liu, X., 2019. Redox reactions control Cu and Fe isotope fractionation in a magmatic Ni–Cu mineralization system. Geochimica et Cosmochimica Acta, 249, 42–58.

Appendices

Appendix A: Diana's Pool EPMA and $^{87}Sr/^{86}$ Sr data

Appendix B: Koperberg Suite EPMA and $^{87}Sr/^{86}Sr$ data

Appendix C: Major element data in sulphides

Appendix A: Diana's Pool Data

Table 20: *Diana's Pool Plagioclase data*

Point	Sample	C/M/S	SiO_2	TiO_2	$Al2O_3$	$Cr2O_3$	FeO	MnO	MgO	CaO	BaO	Na_2O	K_2O	**Total**	**An**
P61/1	BM14780D	Core	60.69	0.01	24.05	0.00	0.07	0.02	0.00	4.91	0.00	9.36	0.13	**99.25**	**22.32**
P66/1	BM14780D	Core	60.84	0.00	24.32	0.01	0.14	0.00	0.00	5.26	0.01	8.86	0.23	**99.67**	**24.38**
P67/1	BM14780D	Core	59.47	0.00	24.56	0.00	0.08	0.00	0.00	5.81	0.00	8.87	0.13	**98.93**	**26.37**
P71/1	BM14780D	Core	60.77	0.00	24.17	0.00	0.01	0.02	0.00	5.07	0.00	9.25	0.15	**99.43**	**23.05**
P73/1	BM14780D	Core	61.19	0.00	24.22	0.02	0.02	0.00	0.00	5.03	0.00	9.32	0.10	**99.89**	**22.84**
P75/1	BM14780D	Core	59.59	0.00	24.68	0.00	0.03	0.01	0.00	5.66	0.02	8.69	0.19	**98.89**	**26.19**
P5/1	BM14780F	Core	57.40	0.01	27.41	0.02	0.10	0.00	0.00	5.52	0.00	8.46	0.23	**99.15**	**26.15**
P6/1	BM14780F	Core	57.29	0.02	26.78	0.02	0.10	0.01	0.00	5.21	0.00	8.84	0.32	**98.59**	**24.14**
P8/1	BM14780F	Core	57.04	0.02	27.13	0.00	0.06	0.00	0.00	5.55	0.02	8.63	0.35	**98.81**	**25.71**
P10/1	BM14780F	Core	58.05	0.00	27.26	0.00	0.04	0.00	0.00	4.96	0.02	9.01	0.14	**99.49**	**23.13**
P11/1	BM14780F	Core	57.33	0.00	27.79	0.01	0.14	0.00	0.00	5.56	0.00	7.49	0.14	**98.46**	**28.84**
P12/1	BM14780F	Core	57.66	0.01	27.62	0.00	0.08	0.00	0.00	5.43	0.00	8.86	0.09	**99.75**	**25.19**
P14/1	BM14780F	Core	58.19	0.00	27.42	0.03	0.07	0.00	0.00	4.90	0.00	9.09	0.13	**99.83**	**22.79**
P15/1	BM14780F	Core	56.78	0.01	27.76	0.00	0.08	0.00	0.00	5.73	0.00	7.43	0.22	**98.02**	**29.47**
P16/1	BM14780F	Core	57.57	0.00	27.66	0.00	0.08	0.01	0.00	5.33	0.00	8.89	0.17	**99.72**	**24.67**
P18/1	BM14780E	Shell	60.75	0.00	24.23	0.02	0.11	0.00	0.00	5.76	0.00	9.06	0.26	**100.19**	**25.65**

Table 21(continued)

Point	Sample	C/M/S	SiO_2	TiO_2	$Al2O_3$	$Cr2O_3$	FeO	MnO	MgO	CaO	BaO	Na_2O	K_2O	**Total**	**An**
P20/1	BM14780E	Shell	60.97	0.00	23.62	0.00	0.08	0.00	0.00	5.75	0.00	9.43	0.24	**100.10**	**24.89**
P22/1	BM14780E	Shell	60.05	0.00	23.53	0.01	0.09	0.00	0.00	5.75	0.00	8.80	0.30	**98.53**	**25.11**
P26/1	BM14780E	Shell	61.16	0.00	24.14	0.02	0.08	0.00	0.00	5.74	0.01	9.33	0.20	**100.68**	**25.11**
P27/1	BM14780E	Shell	61.35	0.05	24.30	0.01	0.06	0.00	0.00	5.89	0.00	7.25	0.26	**99.17**	**30.46**
P28/1	BM14780E	Shell	61.67	0.03	22.72	0.02	0.10	0.03	0.00	5.68	0.00	9.37	0.26	**99.87**	**30.46**
P29/1	BM14780E	Shell	60.81	0.07	24.13	0.00	0.11	0.00	0.00	5.82	0.00	7.26	0.35	**98.55**	**30.01**
P30/1	BM14780E	Shell	60.65	0.00	24.25	0.00	0.09	0.00	0.00	5.87	0.01	9.37	0.30	**100.54**	**25.30**
P31/1	BM14780E	Shell	60.97	0.04	23.63	0.01	0.06	0.01	0.00	5.85	0.00	8.95	0.17	**99.69**	**26.31**
P32/1	BM14780E	Shell	61.24	0.04	24.33	0.00	0.06	0.02	0.00	5.97	0.02	9.12	0.16	**100.96**	**26.34**
P33/1	BM14780E	Shell	61.28	0.00	23.93	0.00	0.09	0.00	0.00	5.74	0.00	6.76	0.30	**98.10**	**31.30**
P34/1	BM14780E	Shell	61.56	0.00	24.08	0.00	0.09	0.00	0.00	5.72	0.00	9.27	0.34	**101.06**	**24.97**
P23/1	BM14780 F	Shell	57.95	0.01	27.35	0.00	0.16	0.01	0.00	5.06	0.00	8.80	0.11	**99.45**	**23.95**
P24/1	BM14780 F	Shell	57.24	0.00	26.88	0.02	0.09	0.02	0.00	5.19	0.00	9.05	0.20	**98.69**	**23.81**
P27/1	BM14780 F	Shell	57.20	0.02	26.69	0.01	0.12	0.00	0.00	5.11	0.00	9.03	0.22	**98.42**	**23.53**
P28/1	BM14780 F	Shell	57.79	0.00	26.69	0.00	0.11	0.00	0.00	5.10	0.00	8.87	0.28	**98.85**	**23.74**
P29/1	BM14780 F	Shell	57.50	0.00	26.67	0.02	0.12	0.00	0.00	5.05	0.00	8.50	0.16	**98.02**	**24.50**

Table 21(continued)

Point	Sample	C/M/S	SiO_2	TiO_2	$Al2O_3$	$Cr2O_3$	FeO	MnO	MgO	CaO	BaO	Na_2O	K_2O	**Total**	**An**
P31/1	BM14780 F	Shell	57.31	0.01	26.54	0.04	0.11	0.02	0.00	5.11	0.00	8.95	0.22	**98.31**	**23.70**
P41/1	BM14780 F	Shell	57.20	0.01	26.53	0.03	0.12	0.02	0.00	5.11	0.00	9.10	0.24	**98.37**	**23.37**
P42/1	BM14780 F	Shell	57.50	0.00	26.78	0.00	0.12	0.03	0.00	5.00	0.00	8.28	0.29	**98.02**	**24.60**
P44/1	BM14780 F	Shell	57.18	0.03	26.46	0.00	0.09	0.02	0.00	5.06	0.01	9.07	0.18	**98.10**	**23.35**
P45/1	BM14780 F	Shell	57.13	0.00	27.11	0.00	0.09	0.01	0.00	5.52	0.00	8.31	0.18	**98.36**	**26.57**
P46/1	BM14780 F	Shell	57.41	0.03	26.49	0.00	0.11	0.00	0.00	5.00	0.00	9.16	0.25	**98.45**	**22.88**
P50/1	BM14780 F	Shell	57.45	0.01	26.82	0.00	0.16	0.00	0.00	5.01	0.01	9.06	0.21	**98.72**	**23.11**
P64/1	BM14780 F	Shell	57.05	0.00	26.35	0.03	0.08	0.00	0.00	5.17	0.02	9.18	0.13	**98.01**	**23.56**
P66/1	BM14780 F	Shell	57.06	0.00	26.48	0.03	0.16	0.02	0.00	5.10	0.01	9.27	0.21	**98.34**	**23.07**
P82/1	BM14780 G	Shell	57.52	0.00	26.49	0.01	0.14	0.02	0.00	5.35	0.01	8.53	0.27	**98.35**	**25.35**
P84/1	BM14780 G	Shell	57.27	0.00	26.45	0.00	0.11	0.01	0.00	5.16	0.00	8.80	0.37	**98.18**	**23.95**
P86/1	BM14780 G	Shell	58.05	0.08	27.45	0.00	0.18	0.02	0.00	5.18	0.00	8.82	0.28	**100.07**	**24.12**
P88/1	BM14780 G	Shell	57.45	0.00	26.79	0.01	0.14	0.00	0.00	5.24	0.00	8.90	0.15	**98.68**	**24.36**
P3/1	BM14780A	Matrix	60.87	0.04	23.81	0.01	0.06	0.00	0.00	4.87	0.00	9.32	0.19	**99.16**	**22.18**
P13/1	BM14780A	Matrix	59.64	0.02	24.39	0.00	0.07	0.00	0.00	5.47	0.00	8.65	0.46	**98.71**	**25.23**
P33 / 1	BM14780A	Matrix	60.77	0.00	24.13	0.00	0.02	0.00	0.00	4.86	0.00	9.47	0.08	**99.33**	**21.98**

Table 21 (continued)

Point	Sample	C/M/S	SiO_2	TiO_2	$Al2O_3$	$Cr2O_3$	FeO	MnO	MgO	CaO	BaO	Na_2O	K_2O	**Total**	**An**
P39 / 1	BM14780A	Matrix	61.11	0.01	24.68	0.00	0.08	0.03	0.00	5.01	0.01	9.18	0.25	**100.35**	**22.84**
P51 / 1	BM14780A	Matrix	61.09	0.00	23.93	0.00	0.07	0.00	0.00	4.82	0.00	9.53	0.12	**99.57**	**21.71**
P1 / 1	BM14780A	Matrix	62.82	0.00	23.68	0.01	0.08	0.03	0.00	6.13	0.01	7.75	0.18	**100.70**	**30.09**
P2 / 1	BM14780A	Matrix	61.37	0.00	23.68	0.03	0.10	0.00	0.00	6.34	0.00	9.39	0.38	**101.29**	**26.64**
P3 / 1	BM14780A	Matrix	61.92	0.00	23.43	0.00	0.07	0.00	0.00	6.09	0.02	8.33	0.20	**100.08**	**26.64**
P4 / 1	BM14780A	Matrix	61.50	0.03	23.55	0.00	0.06	0.02	0.00	6.40	0.00	9.19	0.21	**100.96**	**27.50**
P5 / 1	BM14780A	Matrix	61.78	0.06	23.39	0.00	0.04	0.02	0.00	6.02	0.00	8.67	0.18	**100.16**	**27.45**
P6 / 1	BM14780A	Matrix	62.32	0.02	22.90	0.00	0.15	0.02	0.00	5.57	0.00	9.52	0.24	**100.74**	**24.13**
P7 / 1	BM14780A	Matrix	60.77	0.00	24.93	0.00	0.05	0.01	0.00	6.59	0.00	8.02	0.23	**100.60**	**30.82**
P68/1	BM14780F	Matrix	57.76	0.01	26.63	0.02	0.07	0.00	0.00	5.08	0.00	9.08	0.25	**98.91**	**23.28**
P70/1	BM14780F	Matrix	56.37	0.04	27.90	0.01	0.04	0.00	0.00	6.00	0.00	7.66	1.15	**99.18**	**28.26**
P71/1	BM14780F	Matrix	57.95	0.00	26.92	0.04	0.17	0.02	0.00	5.16	0.00	7.89	0.15	**98.31**	**26.30**
P72/1	BM14780F	Matrix	58.79	0.00	26.48	0.00	0.11	0.00	0.00	4.61	0.01	8.77	0.23	**99.01**	**22.19**
P73/1	BM14780F	Matrix	56.95	0.00	27.64	0.00	0.08	0.00	0.00	5.63	0.00	8.25	0.26	**98.82**	**26.97**
P74/1	BM14780F	Matrix	57.56	0.01	27.21	0.01	0.10	0.01	0.00	5.21	0.00	8.93	0.13	**99.16**	**24.22**
P75/1	BM14780F	Matrix	59.09	0.00	26.68	0.02	0.08	0.00	0.00	4.90	0.02	8.76	0.12	**99.65**	**23.45**

Table 21: *Microprobe analysis of biotite in Diana's Pool orbicules.*

Dataset/Point	58 / 1	59 / 1	2 / 1	15 / 1	33 / 1
Sample	BM14780 D	BM14780 D	BM14780D	BM14780D	BM14780D
C/S/M	C	C	C	C	C
SiO_2	43.93	42.00	36.84	38.62	39.36
TiO_2	2.37	2.28	2.83	2.11	2.33
Al_2O_3	13.79	13.62	18.03	17.29	16.38
Cr_2O_3	0.00	0.02	0.02	0.00	0.02
MgO	4.53	4.87	5.24	5.72	4.36
CaO	0.16	0.18	0.01	0.00	0.01
MnO	0.32	0.33	0.45	0.32	0.36
FeO	21.48	22.63	24.12	24.31	25.00
Na_2O	0.24	0.10	0.05	0.02	0.08
K_2O	9.32	8.61	9.63	8.87	9.33
BaO	0.06	0.04	0.04	0.07	0.07
F	0.29	0.52	0.12	0.10	0.08
Cl	0.30	0.28	0.40	0.22	0.37
Li	0.02	0.06	0.01	0.00	0.00
H_2O	3.84	3.66	3.81	3.89	3.85
Total	**100.66**	**99.20**	**101.59**	**101.54**	**101.60**
Number of cations based on 24 oxygens					
Si	6.50	6.33	5.57	5.80	5.94
Ti	0.26	0.26	0.32	0.24	0.26
AlI^{V}	1.50	1.67	2.43	2.20	2.06
Al^{VI}	0.91	0.74	0.78	0.86	0.85
Cr	0.00	0.00	0.00	0.00	0.00
Mg	1.00	1.09	1.18	1.28	0.98
Ca	0.03	0.03	0.00	0.00	0.00
Mn	0.04	0.04	0.06	0.04	0.05
Fe^{2+}	2.66	2.85	3.05	3.05	3.15
Na	0.07	0.03	0.01	0.00	0.02

K	1.76	1.66	1.86	1.70	1.79
Ba	0.01	0.01	0.00	0.01	0.01
F	0.14	0.25	0.06	0.05	0.04
Cl	0.08	0.07	0.10	0.06	0.09
Li*	0.01	0.02	0.00	0.00	0.00
OH^-	3.79	3.68	3.84	3.90	3.87
Mg/(Mg + Fe)	**0.27**	**0.28**	**0.28**	**0.30**	**0.24**

Table 22 continued

Point	5 / 1	6 / 1	7 / 1	9 / 1	10 / 1	11 / 1	12 / 1	13 / 1	14 / 1	15 / 1	16 / 1	17 / 1	19 / 1
Sample	BM14780F	BM14780F	BM14780F	BM14780F	BM14780F	BM14780F	BM14780F	BM14780F	BM14780F	BM14780F	BM14780F	BM14780F	BM14780F
C/S/M	S	S	S	S	S	S	S	S	S	S	S	S	S
SiO_2	36.01	36.06	36.22	36.66	38.01	37.85	38.20	37.50	38.37	37.53	38.46	37.57	37.85
TiO_2	3.03	2.56	3.29	2.57	2.35	2.69	2.99	2.17	2.83	2.15	2.22	2.62	2.37
Al_2O_3	15.45	15.73	15.34	15.73	15.87	15.01	15.60	15.56	15.59	15.13	15.80	15.56	15.72
Cr_2O_3	0.00	0.00	0.00	0.00	0.01	0.00	0.01	0.00	0.01	0.00	0.00	0.02	0.02
MgO	3.13	3.20	3.02	3.51	3.20	3.60	3.33	3.38	3.51	3.51	3.89	2.22	2.38
CaO	0.00	0.00	0.00	0.00	0.00	0.00	0.19	0.02	0.00	0.02	0.00	0.00	0.00
MnO	0.32	0.33	0.34	0.31	0.29	0.36	0.30	0.32	0.35	0.28	0.37	0.28	0.27
FeO	26.28	26.74	25.98	25.11	26.16	25.03	26.04	25.62	25.92	26.15	25.49	27.04	26.13
Na_2O	0.07	0.02	0.07	0.07	0.04	0.08	0.10	0.10	0.10	0.03	0.08	0.09	0.09
K_2O	10.06	10.33	10.30	10.20	10.31	10.06	10.26	9.85	10.39	9.71	10.20	10.10	10.36
BaO	0.06	0.04	0.03	0.06	0.02	0.04	0.03	0.04	0.04	0.05	0.06	0.03	0.05
F	0.21	0.32	0.13	0.46	0.18	0.25	0.25	0.32	0.24	0.28	0.21	0.16	0.09
Cl	0.25	0.24	0.21	0.30	0.23	0.30	0.24	0.26	0.21	0.28	0.26	0.13	0.18

Li	0.01	0.03	0.01	0.05	0.01	0.02	0.02	0.03	0.02	0.02	0.01	0.01	0.00
H_2O	3.61	3.58	3.66	3.53	3.73	3.64	3.73	3.61	3.75	3.62	3.74	3.71	3.73
Total	**98.50**	**99.20**	**98.59**	**98.54**	**100.42**	**98.94**	**101.28**	**98.78**	**101.32**	**98.77**	**100.80**	**99.54**	**99.24**

Number of ions based on 24 oxygens (O, OH, F, Cl)

Si	5.72	5.69	5.76	5.75	5.88	5.92	5.85	5.87	5.88	5.89	5.90	5.90	5.95
Ti	0.36	0.30	0.39	0.30	0.27	0.32	0.35	0.26	0.33	0.25	0.26	0.31	0.28
Al^{IV}	2.28	2.31	2.24	2.25	2.12	2.08	2.15	2.13	2.12	2.11	2.10	2.10	2.05
Al^{VI}	0.61	0.62	0.63	0.66	0.78	0.68	0.67	0.75	0.69	0.69	0.76	0.78	0.86
Cr	0.00	0.00	0.00	0.00	0.00	0.00	0.00	0.00	0.00	0.00	0.00	0.00	0.00
Mg	0.74	0.75	0.71	0.82	0.74	0.84	0.76	0.79	0.80	0.82	0.89	0.52	0.56
Ca	0.00	0.00	0.00	0.00	0.00	0.00	0.03	0.00	0.00	0.00	0.00	0.00	0.00
Mn	0.04	0.04	0.05	0.04	0.04	0.05	0.04	0.04	0.04	0.04	0.05	0.04	0.04
Fe^{2+}	3.49	3.53	3.45	3.30	3.39	3.27	3.34	3.36	3.32	3.43	3.27	3.55	3.43
Na	0.02	0.01	0.02	0.02	0.01	0.03	0.03	0.03	0.03	0.01	0.02	0.03	0.03
K	2.04	2.08	2.09	2.04	2.04	2.01	2.00	1.97	2.03	1.95	2.00	2.02	2.08
Ba	0.01	0.00	0.00	0.01	0.00	0.00	0.00	0.01	0.01	0.01	0.01	0.00	0.01
F	0.11	0.16	0.06	0.23	0.09	0.13	0.12	0.16	0.12	0.14	0.10	0.08	0.04
Cl	0.07	0.06	0.06	0.08	0.06	0.08	0.06	0.07	0.05	0.07	0.07	0.04	0.05
Li*	0.00	0.01	0.00	0.02	0.00	0.01	0.01	0.01	0.01	0.01	0.00	0.00	0.00
OH-	3.82	3.77	3.88	3.69	3.85	3.79	3.81	3.77	3.83	3.79	3.83	3.89	3.91

Mg/(Mg+ Fe)	**0.18**	**0.18**	**0.17**	**0.20**	**0.18**	**0.20**	**0.19**	**0.19**	**0.19**	**0.19**	**0.21**	**0.13**	**0.14**

Table 22 continued

Point	20 / 1	21 / 1	22 / 1	23 / 1	24 / 1	26 / 1	27 / 1	28 / 1	30 / 1	32 / 1	33 / 1	34 / 1	35 / 1
Sample	BM14780F	BM14780F	BM14780F	BM14780F	BM14780F	BM14780F	BM14780F	BM14780F	BM14780F	BM14780F	BM14780F	BM14780F	BM14780F
C/S/M	S	S	S	S	S	S	S	S	S	S	S	S	S
SiO_2	37.41	38.29	38.13	37.87	38.15	38.59	38.52	38.69	37.86	38.20	38.17	38.45	38.10
TiO_2	2.42	2.72	2.38	3.16	3.15	2.51	2.28	2.70	2.83	2.90	2.59	3.18	2.55
Al_2O_3	15.79	15.54	15.56	15.31	15.48	15.56	15.67	15.31	15.45	15.49	15.15	15.15	16.18
$Cr2O_3$	0.05	0.02	0.00	0.02	0.00	0.04	0.01	0.00	0.03	0.04	0.04	0.00	0.00
MgO	3.00	2.43	2.44	3.22	3.17	3.66	3.61	3.61	3.07	3.08	3.55	3.23	1.87
CaO	0.00	0.00	0.00	0.00	0.00	0.00	0.01	0.00	0.00	0.00	0.00	0.00	0.03
MnO	0.31	0.33	0.33	0.29	0.33	0.34	0.31	0.33	0.30	0.29	0.33	0.31	0.29
FeO	26.29	26.05	26.23	26.10	25.84	25.47	25.45	25.22	26.60	25.86	25.37	25.63	25.77
Na_2O	0.05	0.10	0.07	0.04	0.07	0.10	0.06	0.04	0.05	0.07	0.02	0.06	0.09
K_2O	10.30	10.29	10.22	10.11	10.09	10.04	10.01	10.11	9.58	10.18	9.95	10.11	10.09
BaO	0.07	0.07	0.03	0.04	0.04	0.05	0.06	0.03	0.03	0.03	0.05	0.04	0.07
F	0.06	0.00	0.10	0.09	0.22	0.36	0.41	0.29	0.17	0.14	0.21	0.15	0.08
Cl	0.16	0.17	0.16	0.30	0.32	0.31	0.30	0.32	0.21	0.26	0.30	0.31	0.14
Li	0.00	0.00	0.00	0.00	0.01	0.03	0.04	0.02	0.01	0.01	0.01	0.01	0.00
H_2O	3.75	3.80	3.74	3.74	3.71	3.67	3.64	3.69	3.73	3.74	3.68	3.73	3.75

Total	**99.67**	**99.81**	**99.39**	**100.31**	**100.56**	**100.73**	**100.39**	**100.35**	**99.90**	**100.30**	**99.43**	**100.36**	**99.03**
Number of ions based on 24 (O, OH, F, Cl)													
Si		5.87	5.98	5.97	5.88	5.88	5.90	5.91	5.94	5.89	5.91	5.94	5.93	5.97
Ti		0.29	0.32	0.28	0.37	0.37	0.29	0.26	0.31	0.33	0.34	0.30	0.37	0.30
Al^{IV}		2.13	2.02	2.03	2.12	2.12	2.10	2.09	2.06	2.11	2.09	2.06	2.07	2.03
Al^{VI}		0.79	0.84	0.85	0.68	0.69	0.71	0.74	0.71	0.72	0.74	0.71	0.69	0.96
Cr		0.00	0.00	0.00	0.00	0.00	0.00	0.00	0.00	0.00	0.00	0.00	0.00	0.00
Mg		0.70	0.56	0.57	0.74	0.73	0.83	0.83	0.83	0.71	0.71	0.82	0.74	0.44
Ca		0.00	0.00	0.00	0.00	0.00	0.00	0.00	0.00	0.00	0.00	0.00	0.00	0.01
Mn		0.04	0.04	0.04	0.04	0.04	0.04	0.04	0.04	0.04	0.04	0.04	0.04	0.04
Fe^{2+}		3.45	3.40	3.44	3.39	3.33	3.26	3.26	3.24	3.46	3.35	3.30	3.31	3.38
Na		0.02	0.03	0.02	0.01	0.02	0.03	0.02	0.01	0.02	0.02	0.01	0.02	0.03
K		2.06	2.05	2.04	2.00	1.98	1.96	1.96	1.98	1.90	2.01	1.97	1.99	2.02
Ba		0.01	0.01	0.00	0.01	0.00	0.01	0.01	0.00	0.00	0.00	0.01	0.00	0.01
F		0.03	0.00	0.05	0.05	0.10	0.17	0.20	0.14	0.08	0.07	0.10	0.07	0.04
Cl		0.04	0.04	0.04	0.08	0.08	0.08	0.08	0.08	0.05	0.07	0.08	0.08	0.04
Li*		0.00	0.00	0.00	0.00	0.00	0.01	0.01	0.01	0.00	0.00	0.00	0.00	0.00
OH-		3.93	3.96	3.91	3.88	3.81	3.75	3.72	3.78	3.86	3.86	3.82	3.84	3.92
Mg/(Mg +Fe)		**0.17**	**0.14**	**0.14**	**0.18**	**0.18**	**0.20**	**0.20**	**0.20**	**0.17**	**0.18**	**0.20**	**0.18**	**0.11**

Table 22continued

Point	36 / 1	38 / 1	39 / 1	40 / 1	41 /	44 / 1	45 / 1	46 / 1	47 / 1	48 / 1	49 / 1	50 / 1	51 / 1
Sample	BM14780F	BM14780F	BM14780F	BM14780F	BM14780F	BM14780F	BM14780F	BM14780F	BM14780F	BM14780G	BM14780G	BM14780G	BM14780G
C/S/M	S	S	S	S	S	S	S	S	S	S	S	S	S
SiO_2	38.28	36.93	37.38	36.70	36.86	36.94	36.81	42.89	37.19	38.57	37.95	38.03	37.73
TiO_2	2.61	2.66	2.78	2.57	3.63	2.72	2.88	1.62	3.51	2.78	3.10	3.02	2.73
Al_2O_3	15.91	15.78	15.49	15.90	15.66	15.15	15.45	15.10	14.89	15.42	15.21	15.52	15.66
Cr_2O_3	0.04	0.02	0.00	0.04	0.05	0.00	0.00	0.00	0.03	0.00	0.00	0.00	0.00
MgO	1.79	2.06	2.42	2.27	2.85	3.34	2.80	1.94	3.23	3.45	3.28	3.14	2.98
CaO	0.02	0.02	0.00	0.01	0.00	0.02	0.02	0.09	0.00	0.00	0.00	0.01	0.00
MnO	0.29	0.30	0.32	0.33	0.32	0.35	0.26	0.22	0.31	0.36	0.35	0.37	0.34
FeO	25.96	27.15	25.84	26.64	25.96	25.95	26.27	23.71	25.67	25.17	25.61	25.86	25.76
Na_2O	0.07	0.07	0.10	0.05	0.03	0.04	0.06	0.11	0.06	0.08	0.10	0.05	0.11
K_2O	10.09	10.09	10.35	10.24	10.34	10.16	10.39	9.12	10.44	10.25	10.21	10.22	10.19
BaO	0.05	0.04	0.07	0.06	0.08	0.07	0.04	0.02	0.06	0.05	0.04	0.03	0.04
F	0.10	0.19	0.10	0.00	0.16	0.34	0.39	0.06	0.20	0.30	0.27	0.28	0.22
Cl	0.12	0.16	0.19	0.13	0.23	0.29	0.26	0.18	0.22	0.25	0.27	0.24	0.20
Li	0.00	0.01	0.00	0.00	0.01	0.03	0.04	0.00	0.01	0.02	0.02	0.02	0.01
H20	3.75	3.67	3.70	3.73	3.70	3.58	3.57	3.86	3.68	3.70	3.68	3.69	3.69
Total	**99.07**	**99.14**	**98.74**	**98.66**	**99.89**	**98.97**	**99.24**	**98.92**	**99.50**	**100.42**	**100.09**	**100.48**	**99.67**

Number of ions based on 24 (O, OH, F, Cl)

Si	6.00	5.84	5.91	5.84	5.76	5.81	5.78	6.54	5.83	5.93	5.88	5.87	5.88
Ti	0.31	0.32	0.33	0.31	0.43	0.32	0.34	0.19	0.41	0.32	0.36	0.35	0.32
Al^{IV}	2.00	2.16	2.09	2.16	2.24	2.19	2.22	1.46	2.17	2.07	2.12	2.13	2.12
Al^{VI}	0.94	0.77	0.79	0.83	0.65	0.61	0.64	1.25	0.58	0.72	0.65	0.69	0.75
Cr	0.00	0.00	0.00	0.00	0.00	0.00	0.00	0.00	0.00	0.00	0.00	0.00	0.00
Mg	0.42	0.48	0.57	0.54	0.66	0.78	0.66	0.44	0.75	0.79	0.76	0.72	0.69
Ca	0.00	0.00	0.00	0.00	0.00	0.00	0.00	0.01	0.00	0.00	0.00	0.00	0.00
Mn	0.04	0.04	0.04	0.04	0.04	0.05	0.03	0.03	0.04	0.05	0.05	0.05	0.05
Fe^{2+}	3.40	3.59	3.42	3.55	3.39	3.41	3.45	3.02	3.37	3.23	3.32	3.34	3.36
Na	0.02	0.02	0.03	0.02	0.01	0.01	0.02	0.03	0.02	0.02	0.03	0.01	0.03
K	2.02	2.03	2.09	2.08	2.06	2.04	2.08	1.77	2.09	2.01	2.02	2.01	2.02
Ba	0.01	0.00	0.01	0.01	0.01	0.01	0.00	0.00	0.01	0.01	0.00	0.00	0.01
F	0.05	0.09	0.05	0.00	0.08	0.17	0.19	0.03	0.10	0.15	0.13	0.14	0.11
Cl	0.03	0.04	0.05	0.03	0.06	0.08	0.07	0.05	0.06	0.07	0.07	0.06	0.05
Li*	0.00	0.00	0.00	0.00	0.00	0.01	0.01	0.00	0.00	0.01	0.01	0.01	0.00
OH-	3.92	3.86	3.90	3.97	3.86	3.75	3.74	3.93	3.84	3.79	3.80	3.80	3.84
Mg/(Mg +Fe)	**0.11**	**0.12**	**0.14**	**0.13**	**0.16**	**0.19**	**0.16**	**0.13**	**0.18**	**0.20**	**0.19**	**0.18**	**0.17**

Table 22 Continued

Dataset/Point	54 / 1	55 / 1	56 / 1	57 / 1	58 / 1	59 / 1	60 / 1	61 / 1	63 / 1	64 / 1	65 / 1	66 / 1	67 / 1
Sample	BM14780G	BM14780G	BM14780G	BM14780G	BM14780G	BM14780G	BM14780G	BM14780G	BM14780G	BM14780G	BM14780G	BM14780G	BM14780G
C/S/M	S	S	S	S	S	S	S	S	S	S	S	S	S
SiO_2	37.37	37.35	38.28	37.93	38.10	37.89	37.54	38.06	37.49	38.16	38.50	38.06	38.42
TiO_2	2.69	3.16	3.16	3.47	2.13	2.36	3.12	2.79	2.66	2.78	2.90	2.77	2.73
Al_2O_3	15.65	15.02	14.94	15.02	15.41	15.63	15.27	15.30	15.11	15.18	15.00	15.28	15.66
Cr_2O_3	0.02	0.00	0.01	0.01	0.02	0.00	0.01	0.02	0.00	0.00	0.01	0.00	0.00
MgO	2.95	3.32	3.23	3.20	3.40	3.47	3.07	3.13	3.30	3.21	3.53	3.15	3.20
CaO	0.00	0.01	0.01	0.00	0.02	0.00	0.00	0.00	0.02	0.01	0.02	0.00	0.00
MnO	0.32	0.39	0.31	0.34	0.33	0.34	0.39	0.35	0.36	0.30	0.34	0.31	0.26
FeO	26.31	26.05	25.20	25.69	25.13	25.25	26.00	25.75	25.39	25.66	25.94	26.03	25.43
Na_2O	0.08	0.06	0.05	0.06	0.09	0.06	0.02	0.07	0.14	0.09	0.06	0.08	0.07
K_2O	10.20	9.73	10.05	10.14	9.92	10.00	10.11	10.07	10.03	10.11	10.16	10.03	10.11
BaO	0.03	0.03	0.01	0.05	0.01	0.04	0.04	0.06	0.05	0.06	0.03	0.04	0.03
F	0.14	0.25	0.38	0.18	0.32	0.32	0.21	0.38	0.18	0.36	0.39	0.32	0.30
Cl	0.18	0.23	0.22	0.24	0.24	0.25	0.20	0.23	0.29	0.25	0.25	0.18	0.24
Li	0.01	0.02	0.04	0.01	0.03	0.03	0.01	0.04	0.01	0.03	0.04	0.03	0.02
H_20	3.72	3.65	3.63	3.72	3.63	3.64	3.69	3.64	3.65	3.64	3.66	3.67	3.69
Total	**99.67**	**99.27**	**99.53**	**100.03**	**98.78**	**99.27**	**99.68**	**99.88**	**98.68**	**99.84**	**100.82**	**99.96**	**100.17**

Number of ions based on 24 (O, OH, F, Cl)

Si	5.85	5.84	5.93	5.89	5.95	5.89	5.86	5.89	5.90	5.91	5.90	5.90	5.92
Ti	0.32	0.37	0.37	0.41	0.25	0.28	0.37	0.33	0.32	0.32	0.33	0.32	0.32
Al^{IV}	2.15	2.16	2.07	2.11	2.05	2.11	2.14	2.11	2.10	2.09	2.10	2.10	2.08
Al^{VI}	0.74	0.61	0.66	0.64	0.78	0.76	0.67	0.69	0.70	0.68	0.62	0.69	0.76
Cr	0.00	0.00	0.00	0.00	0.00	0.00	0.00	0.00	0.00	0.00	0.00	0.00	0.00
Mg	0.69	0.77	0.75	0.74	0.79	0.80	0.71	0.72	0.77	0.74	0.81	0.73	0.74
Ca	0.00	0.00	0.00	0.00	0.00	0.00	0.00	0.00	0.00	0.00	0.00	0.00	0.00
Mn	0.04	0.05	0.04	0.04	0.04	0.04	0.05	0.05	0.05	0.04	0.04	0.04	0.03
Fe^{2+}	3.44	3.41	3.26	3.33	3.28	3.28	3.39	3.33	3.34	3.32	3.33	3.38	3.28
Na	0.02	0.02	0.02	0.02	0.03	0.02	0.01	0.02	0.04	0.03	0.02	0.02	0.02
K	2.04	1.94	1.99	2.01	1.98	1.98	2.01	1.99	2.01	2.00	1.99	1.98	1.99
Ba	0.00	0.00	0.00	0.01	0.00	0.00	0.00	0.01	0.01	0.01	0.00	0.01	0.00
F	0.07	0.12	0.19	0.09	0.16	0.15	0.11	0.19	0.09	0.18	0.19	0.15	0.15
Cl	0.05	0.06	0.06	0.06	0.06	0.07	0.05	0.06	0.08	0.07	0.06	0.05	0.06
Li*	0.00	0.01	0.01	0.00	0.01	0.01	0.00	0.01	0.00	0.01	0.01	0.01	0.01
OH-	3.88	3.81	3.75	3.85	3.78	3.78	3.84	3.76	3.83	3.76	3.74	3.80	3.79
Mg/(Mg+ Fe)	**0.17**	**0.18**	**0.19**	**0.18**	**0.19**	**0.20**	**0.17**	**0.18**	**0.19**	**0.18**	**0.19**	**0.18**	**0.18**

Table 22 Continued

Dataset/Point	68 / 1	69 / 1	70 / 1	71 / 1	72 / 1	73 / 1	74 / 1	76 / 1	77 / 1	80 / 1	81 / 1
Sample	BM14780GS	BM14780GS	BM14780GS	BM14780GS	BM14780GS	BM14780GS	BM14780GS	BM14780GS	BM14780GS	BM14780GS	BM14780GS
C/S/M	S	S	S	S	S	S	S	S	S	S	S
SiO_2	38.35	38.72	38.71	38.01	38.36	36.99	38.44	38.66	38.53	37.69	37.61
TiO_2	3.51	2.86	2.04	2.39	2.46	2.38	2.75	4.07	2.46	2.95	3.23
Al_2O_3	14.94	15.54	15.75	15.61	15.64	15.69	15.13	14.83	15.34	15.84	15.25
Cr_2O_3	0.00	0.00	0.00	0.00	0.00	0.00	0.01	0.00	0.01	0.00	0.00
MgO	3.18	3.49	3.56	3.32	2.68	2.85	3.43	3.13	3.40	2.67	2.75
CaO	0.22	0.00	0.00	0.00	0.00	0.08	0.03	0.00	0.05	0.02	0.01
MnO	0.31	0.35	0.36	0.34	0.33	0.24	0.32	0.36	0.31	0.30	0.31
FeO	24.93	25.04	25.31	25.33	25.98	27.31	24.86	25.15	25.41	25.80	25.70
Na_2O	0.11	0.05	0.06	0.09	0.06	0.08	0.13	0.08	0.16	0.11	0.09
K_2O	9.78	10.15	10.14	10.11	10.30	9.02	10.00	10.01	9.82	9.96	9.86
BaO	0.05	0.08	0.05	0.06	0.02	0.02	0.03	0.02	0.04	0.05	0.03
F	0.22	0.42	0.36	0.27	0.13	0.20	0.29	0.12	0.06	0.04	0.03
Cl	0.29	0.24	0.24	0.26	0.22	0.19	0.29	0.29	0.29	0.23	0.26
Li	0.02	0.04	0.03	0.02	0.01	0.01	0.02	0.01	0.00	0.00	0.00
H20	3.69	3.67	3.68	3.67	3.74	3.66	3.66	3.77	3.76	3.76	3.73
Total	**99.62**	**100.66**	**100.30**	**99.47**	**99.93**	**98.73**	**99.39**	**100.49**	**99.64**	**99.41**	**98.87**

Number of ions based on 24 (O, OH, F, Cl)

Si	5.94	5.91	5.94	5.91	5.96	5.83	5.96	5.95	5.98	5.89	5.92
Ti	0.41	0.33	0.24	0.28	0.29	0.28	0.32	0.47	0.29	0.35	0.38
Al^{IV}	2.06	2.09	2.06	2.09	2.04	2.17	2.04	2.05	2.02	2.11	2.08
Al^{VI}	0.66	0.71	0.79	0.77	0.83	0.75	0.72	0.63	0.79	0.81	0.74
Cr	0.00	0.00	0.00	0.00	0.00	0.00	0.00	0.00	0.00	0.00	0.00
Mg	0.73	0.80	0.82	0.77	0.62	0.67	0.79	0.72	0.79	0.62	0.65
Ca	0.04	0.00	0.00	0.00	0.00	0.01	0.00	0.00	0.01	0.00	0.00
Mn	0.04	0.05	0.05	0.04	0.04	0.03	0.04	0.05	0.04	0.04	0.04
Fe^{2+}	3.23	3.20	3.25	3.29	3.38	3.60	3.22	3.24	3.30	3.38	3.38
Na	0.03	0.02	0.02	0.03	0.02	0.02	0.04	0.02	0.05	0.03	0.03
K	1.93	1.98	1.99	2.00	2.04	1.81	1.98	1.96	1.95	1.99	1.98
Ba	0.01	0.01	0.01	0.01	0.00	0.00	0.00	0.00	0.01	0.01	0.00
F	0.11	0.20	0.17	0.13	0.07	0.10	0.14	0.06	0.03	0.02	0.02
Cl	0.08	0.06	0.06	0.07	0.06	0.05	0.08	0.07	0.08	0.06	0.07
Li*	0.00	0.01	0.01	0.01	0.00	0.00	0.01	0.00	0.00	0.00	0.00
OH-	3.81	3.73	3.76	3.80	3.88	3.85	3.78	3.87	3.90	3.92	3.92
Mg/(Mg+ Fe)	**0.19**	**0.20**	**0.20**	**0.19**	**0.16**	**0.16**	**0.20**	**0.18**	**0.19**	**0.16**	**0.16**

Table 22 continued

Dataset/point	2 / 1	11 / 1	12 / 1	14 / 1	17 / 1	18 / 1	20 / 1	26 / 1	28 / 1	29 / 1	31 / 1	34 / 1	38 / 1
Sample	BM14780A	BM14780A	BM14780A	BM14780A	BM14780A	BM14780A	BM14780A	BM14780A	BM14780A	BM14780A	BM14780A	BM14780A	BM14780A
C/S/M	M	M	M	M	M	M	M	M	M	M	M	M	M
SiO_2	36.94	39.01	40.38	40.07	40.45	41.48	40.88	40.81	40.75	40.23	41.06	38.81	41.99
TiO_2	3.35	1.78	2.02	2.26	1.91	2.08	3.31	3.97	2.27	1.94	1.80	3.25	2.58
Al_2O_3	16.80	18.26	14.58	14.59	13.98	13.89	14.44	12.87	14.08	14.66	14.63	13.97	14.33
Cr_2O_3	0.02	0.01	0.00	0.01	0.00	0.00	0.02	0.02	0.00	0.00	0.03	0.00	0.00
MgO	4.84	4.33	4.81	4.87	4.74	5.86	4.20	4.45	4.43	4.68	4.57	4.91	4.58
CaO	0.01	0.08	0.02	0.05	0.06	0.12	0.34	0.00	0.03	0.09	0.10	0.01	0.07
MnO	0.32	0.20	0.27	0.28	0.23	0.24	0.23	0.29	0.23	0.22	0.25	0.27	0.24
FeO	25.88	26.17	24.71	25.90	24.17	23.07	23.93	24.67	24.49	25.07	24.66	23.61	23.10
Na_2O	0.05	0.06	0.08	0.06	0.05	0.19	0.04	0.08	0.07	0.11	0.06	0.07	0.16
K2O	8.12	6.02	8.61	7.96	8.46	9.17	8.81	10.02	9.41	7.68	7.85	10.33	9.71
BaO	0.09	0.10	0.09	0.12	0.13	0.12	0.08	0.08	0.07	0.07	0.10	0.05	0.10
F	0.18	0.06	0.18	0.17	0.25	0.14	0.13	0.30	0.14	0.08	0.16	0.51	0.10
Cl	0.10	0.09	0.25	0.13	0.18	0.27	0.22	0.21	0.21	0.18	0.14	0.16	0.18
Li	0.01	0.00	0.01	0.01	0.02	0.01	0.01	0.02	0.01	0.00	0.01	0.06	0.00
H_2O	3.81	3.93	3.79	3.83	3.73	3.85	3.85	3.78	3.81	3.82	3.82	3.62	3.90
Total	**100.52**	**100.10**	**99.79**	**100.31**	**98.35**	**100.47**	**100.48**	**101.58**	**99.99**	**98.83**	**99.24**	**99.64**	**101.05**

Number of ions based on 24 (O, OH, F, Cl)

Si	5.65	5.88	6.16	6.10	6.24	6.25	6.18	6.16	6.22	6.18	6.26	5.96	6 .30
Ti	0.39	0.20	0.23	0.26	0.22	0.24	0.38	0.45	0.26	0.22	0.21	0.38	0.29
Al^{IV}	2.35	2.12	1.84	1.90	1.76	1.75	1.82	1.84	1.78	1.82	1.74	2.04	1.70
Al^{VI}	0.68	1.13	0.78	0.71	0.78	0.71	0.75	0.45	0.76	0.84	0.88	0.49	0.83
Cr	0.00	0.00	0.00	0.00	0.00	0.00	0.00	0.00	0.00	0.00	0.00	0.00	0.00
Mg	1.10	0.97	1.09	1.10	1.09	1.32	0.95	1.00	1.01	1.07	1.04	1.12	1.02
Ca	0.00	0.01	0.00	0.01	0.01	0.02	0.05	0.00	0.00	0.01	0.02	0.00	0.01
Mn	0.04	0.03	0.03	0.04	0.03	0.03	0.03	0.04	0.03	0.03	0.03	0.04	0.03
Fe^{2+}	3.31	3.30	3.15	3.30	3.12	2.91	3.02	3.11	3.13	3.22	3.14	3.03	2.90
Na	0.01	0.02	0.02	0.02	0.01	0.05	0.01	0.02	0.02	0.03	0.02	0.02	0.05
K	1.58	1.16	1.67	1.55	1.66	1.76	1.70	1.93	1.83	1.51	1.53	2.02	1.86
Ba	0.01	0.01	0.01	0.01	0.02	0.01	0.01	0.01	0.01	0.01	0.01	0.01	0.01
F	0.09	0.03	0.09	0.08	0.12	0.07	0.06	0.14	0.07	0.04	0.08	0.25	0.05
Cl	0.03	0.02	0.06	0.03	0.05	0.07	0.06	0.05	0.05	0.05	0.04	0.04	0.05
Li*	0.00	0.00	0.00	0.00	0.01	0.00	0.00	0.01	0.00	0.00	0.00	0.02	0.00
OH^-	3.88	3.95	3.85	3.88	3.83	3.87	3.88	3.80	3.88	3.91	3.89	3.71	3.91
Mg/(Mg + Fe)	**0.25**	**0.23**	**0.26**	**0.25**	**0.26**	**0.31**	**0.24**	**0.24**	**0.24**	**0.25**	**0.25**	**0.27**	**0.26**

Table 22 continued

Dataset/Point	39 / 1	40 / 1	41 / 1	43 / 1	45 / 1	46 / 1	52 / 1
Sample	BM14780 A	BM14780 A	BM14780 A	BM14780 A	BM14780 A	BM14780 A	BM14780 A
C/S/M	M	M	M	M	M	M	M
SiO_2	38.98	43.97	36.54	39.71	40.17	40.36	40.50
TiO_2	4.00	3.09	1.81	3.26	2.77	3.20	3.26
Al_2O_3	13.28	13.05	13.77	13.28	13.61	13.10	13.53
Cr_2O_3	0.02	0.02	0.00	0.00	0.01	0.04	0.00
MgO	4.91	4.11	4.34	4.56	4.64	4.92	4.36
CaO	1.46	0.19	0.13	0.00	0.00	0.00	0.00
MnO	0.26	0.28	0.23	0.25	0.29	0.26	0.24
FeO	23.67	22.38	32.19	25.02	24.20	24.40	23.69
Na2O	0.20	0.07	0.09	0.06	0.07	0.11	0.06
K2O	7.13	8.44	6.03	9.83	9.85	9.81	10.01
BaO	0.09	0.09	0.10	0.10	0.12	0.12	0.11
F	0.31	0.13	0.18	0.14	0.27	0.28	0.18
Cl	0.12	0.14	0.09	0.16	0.15	0.20	0.23
Li	0.03	0.01	0.01	0.01	0.02	0.02	0.01
H2O	3.71	3.91	3.67	3.79	3.75	3.75	3.78
Total	**98.17**	**99.87**	**99.15**	**100.18**	**99.90**	**100.57**	**99.96**

Number of ions based on 24 oxygens (O, OH, F, Cl)

Si	6.02	6.57	5.80	6.11	6.16	6.15	6.19
Ti	0.47	0.35	0.22	0.38	0.32	0.37	0.38
Al^{IV}	1.98	1.43	2.20	1.89	1.84	1.85	1.81
Al^{VI}	0.44	0.87	0.38	0.52	0.61	0.50	0.63
Cr	0.00	0.00	0.00	0.00	0.00	0.00	0.00
Mg	1.13	0.92	1.03	1.05	1.06	1.12	0.99
Ca	0.24	0.03	0.02	0.00	0.00	0.00	0.00
Mn	0.03	0.04	0.03	0.03	0.04	0.03	0.03
Fe^{2+}	3.06	2.80	4.27	3.22	3.10	3.11	3.03
Na	0.06	0.02	0.03	0.02	0.02	0.03	0.02
K	1.40	1.61	1.22	1.93	1.93	1.91	1.95
Ba	0.01	0.01	0.01	0.01	0.01	0.01	0.01
F	0.15	0.06	0.09	0.07	0.13	0.13	0.09
Cl	0.03	0.03	0.02	0.04	0.04	0.05	0.06
Li*	0.01	0.00	0.00	0.00	0.01	0.01	0.00
OH-	3.82	3.90	3.89	3.89	3.83	3.81	3.85
Mg/(Mg+ Fe)	**0.27**	**0.25**	**0.19**	**0.25**	**0.25**	**0.26**	**0.25**

Table 22: *In-situ initial $^{87}Sr/^{86}Sr$ isotopic compositions of the Diana's Pool orbicules.*

Sample	C/S/M	$^{87}Sr/^{86}Sr$	1σ	$^{87}Rb/^{86}Sr$	2σ	I_{Sr}	1σ
BM14780F-1	Core	0.705601	0.000169	0.006550	0.000068	0.705350	0.000172
BM14780F-2	Core	0.702259	0.000134	0.003836	0.000049	0.702111	0.000136
BM14780F-3	Core	0.701294	0.000163	0.001692	0.000040	0.701229	0.000164
BM14780F-4	Core	0.701619	0.000174	0.002003	0.000046	0.701542	0.000176
BM14780F-5	Core	0.702176	0.000181	0.007305	0.000207	0.701896	0.000189
BM14780F-6	Core	0.702285	0.000173	0.002073	0.000187	0.702205	0.000180
BM14780F-7	Core	0.701767	0.000175	0.003211	0.000059	0.701644	0.000177
BM14780F-8	Core	0.701655	0.000175	0.001658	0.000064	0.701591	0.000177
BM14780F-9	Core	0.701779	0.000173	0.002744	0.000060	0.701674	0.000175
BM14780D-2	Core	0.702708	0.000167	0.013408	0.000167	0.702194	0.000173
BM14780D-1	Core	0.701518	0.000161	0.000831	0.000046	0.701486	0.000163
BM14780D-3	Core	0.702449	0.000163	0.001116	0.000039	0.702407	0.000164
BM14780D-4	Core	0.701784	0.000198	0.034085	0.001310	0.700477	0.000247
BM14780D-5	Core	0.702057	0.000186	0.010417	0.000458	0.701658	0.000203
BM14780D-6	Core	0.701697	0.000168	0.003551	0.000059	0.701561	0.000170
BM14780D-8	Core	0.702340	0.000176	0.002510	0.000067	0.702243	0.000179
BM14780D-9	Core	0.701868	0.000166	0.003741	0.000127	0.701725	0.000171
BM14780D-10	Core	0.702826	0.000172	0.055716	0.001340	0.700690	0.000222
BM14780F-10	Shell	0.702851	0.000179	0.002578	0.000049	0.702752	0.000181
BM14780F-11	Shell	0.702888	0.000169	0.003072	0.000065	0.702770	0.000171
BM14780F-12	Shell	0.703502	0.000171	0.002054	0.000041	0.703423	0.000173
BM14780F-13	Shell	0.702295	0.000173	0.002638	0.000046	0.702194	0.000175
BM14780F-14	Shell	0.702283	0.000164	0.000862	0.000044	0.702250	0.000166
BM14780F-15.	Shell	0.702039	0.000172	0.003413	0.000045	0.701908	0.000174

BM14780F-17	Shell	0.701736	0.000183	0.002450	0.000046	0.701642	0.000185
BM14780F-18	Shell	0.702242	0.000177	0.001455	0.000045	0.702187	0.000179
BM14780F-19	Shell	0.702676	0.000181	0.002106	0.000055	0.702595	0.000183
BM14780F-20	Shell	0.701852	0.000166	0.002049	0.000049	0.701773	0.000168
BM14780F-21	Shell	0.702790	0.000166	0.002151	0.000046	0.702707	0.000168
BM14780F-22	Shell	0.702903	0.000183	0.001160	0.000048	0.702858	0.000185
BM14780F-23	Shell	0.701984	0.000178	0.002546	0.000050	0.701886	0.000180
BM14780E-1	Shell	0.702140	0.000184	0.015470	0.000307	0.701547	0.000196
BM14780E-2	Shell	0.702175	0.000182	0.002087	0.000056	0.702095	0.000184
BM14780E-3	Shell	0.702271	0.000176	0.003224	0.000057	0.702147	0.000178
BM14780E-4	Shell	0.702731	0.000172	0.005139	0.000237	0.702534	0.000181
BM14780E-5	Shell	0.702381	0.000194	0.004119	0.000052	0.702223	0.000196
BM14780E-6	Shell	0.702991	0.000182	0.006095	0.000115	0.702758	0.000186
BM14780E-7	Shell	0.702139	0.000173	0.002076	0.000042	0.702059	0.000175
BM14780E-8	Shell	0.701899	0.000183	0.002406	0.000043	0.701807	0.000185
BM14780E-9	Shell	0.701816	0.000198	0.001504	0.000057	0.701759	0.000200
BM14780E-10	Shell	0.702478	0.000204	0.006213	0.000143	0.702240	0.000209
BM14780E-11	Shell	0.702076	0.000187	0.001159	0.000042	0.702031	0.000189
BM14780F-24	Matrix	0.703442	0.000311	0.071454	0.000957	0.700701	0.000347
BM14780A-2	Matrix	0.701217	0.000255	0.001779	0.000070	0.701148	0.000258
BM14780A-4	Matrix	0.701772	0.000242	0.003024	0.000069	0.701656	0.000245
BM14780A-5	Matrix	0.702935	0.000249	0.022552	0.000329	0.702071	0.000261
BM14780A-6	Matrix	0.701848	0.000281	0.004774	0.000090	0.701664	0.000284
BM14780A-7	Matrix	0.702120	0.000286	0.003047	0.000077	0.702003	0.000289
BM14780A-8	Matrix	0.703293	0.000274	0.002748	0.000089	0.703188	0.000277
BM14780A-9	Matrix	0.705127	0.000399	0.102917	0.001570	0.701181	0.000458
BM14780A-10	Matrix	0.702700	0.000311	0.006202	0.000166	0.702462	0.000317

BM14780A-11	Matrix	0.703371	0.000310	0.005074	0.000131	0.703177	0.000315

Appendix B: Koperberg Suite Data

Table 23: *Koperberg Suite country rocks plagioclase data. OK=Orbicule Koppie, HL=Hoogkraal Lease, HS=Henderson South and HN=Henderson North*

Data	Sample	Lithology	Locality	SiO2	TiO_2	Al_2O_3	Cr_2O_3	FeO	MnO	MgO	CaO	BaO	Na_2O	K_2O	**Total**	**An**
1 / 1	SD-32-15A	Anorthosite	OK	54.71	0.03	27.83	0.02	0.11	0.00	0.00	9.22	0.00	6.11	0.53	**98.55**	**44.10**
3 / 1	SD-32-15A	Anorthosite	OK	55.01	0.01	28.57	0.00	0.15	0.00	0.00	9.77	0.03	6.04	0.35	**99.92**	**46.27**
6 / 1	SD-32-15A	Anorthosite	OK	55.84	0.01	26.74	0.00	0.16	0.02	0.00	8.35	0.10	5.25	1.76	**98.24**	**41.86**
7 / 1	SD-32-15A	Anorthosite	OK	55.05	0.00	28.93	0.00	0.09	0.01	0.00	10.09	0.00	6.06	0.35	**100.59**	**46.99**
8 / 1	SD-32-15A	Anorthosite	OK	54.80	0.00	27.89	0.00	0.29	0.00	0.01	9.37	0.05	6.00	0.79	**99.19**	**44.27**
9 / 1	SD-32-15A	Anorthosite	OK	53.97	0.04	27.70	0.02	0.24	0.00	0.00	9.85	0.06	6.07	0.82	**98.78**	**45.17**
10 / 1	SD-32-15A	Anorthosite	OK	55.41	0.00	28.50	0.03	0.09	0.00	0.00	9.78	0.04	6.32	0.40	**100.56**	**45.10**
11 / 1	SD-32-15A	Anorthosite	OK	54.46	0.03	28.37	0.05	0.17	0.00	0.00	10.88	0.00	6.19	0.41	**100.55**	**48.24**
12 / 1	SD-32-15A	Anorthosite	OK	54.47	0.06	28.15	0.00	0.38	0.05	0.06	10.79	0.02	5.84	0.80	**100.62**	**48.34**
13 / 1	SD-32-15A	Anorthosite	OK	55.05	0.00	28.77	0.00	0.22	0.00	0.04	9.18	0.04	5.88	0.91	**100.09**	**43.91**
14 / 1	SD-32-15A	Anorthosite	OK	55.66	0.05	28.67	0.00	0.09	0.04	0.00	9.70	0.00	6.17	0.47	**100.86**	**45.28**
18 / 1	SD-32-15A	Anorthosite	OK	55.46	0.00	28.57	0.03	0.10	0.02	0.00	9.63	0.01	6.10	0.40	**100.32**	**45.55**
22 / 1	SD-32-15A	Anorthosite	OK	53.51	0.73	27.82	0.01	0.14	0.00	0.00	10.29	0.03	5.84	0.54	**98.92**	**47.84**
24 / 1	SD-32-15A	Anorthosite	OK	53.83	0.02	28.26	0.00	0.11	0.03	0.00	10.02	0.00	5.95	0.43	**98.65**	**47.05**
25 / 1	SD-32-15A	Anorthosite	OK	55.49	0.00	28.43	0.01	0.04	0.00	0.00	9.58	0.01	5.94	0.41	**99.93**	**46.01**
32 / 1	SD-32-15A	Anorthosite	OK	52.21	0.69	26.87	0.03	2.28	0.06	1.60	9.35	0.04	5.18	0.90	**99.23**	**47.25**
34 / 1	SD-32-15A	Anorthosite	OK	54.38	0.33	28.20	0.00	1.46	0.02	0.57	9.52	0.01	5.60	0.72	**100.82**	**46.44**
40 / 1	SD-5-1	Diorite	OK	54.30	0.02	27.63	0.02	0.16	0.00	0.00	9.64	0.01	5.60	0.33	**97.71**	**47.81**
41 / 1	SD-5-1	Diorite	OK	54.73	0.01	28.10	0.00	0.09	0.01	0.00	9.23	0.04	5.58	0.56	**98.37**	**46.14**
42 / 1	SD-5-1	Diorite	OK	54.99	0.00	28.47	0.00	0.16	0.00	0.00	9.67	0.03	5.65	0.44	**99.41**	**47.36**
43 / 1	SD-5-1	Diorite	OK	54.88	0.00	27.92	0.00	0.14	0.02	0.00	9.76	0.02	5.71	0.41	**98.85**	**47.44**
44 / 1	SD-5-1	Diorite	OK	53.67	0.00	27.55	0.00	0.15	0.00	0.00	9.95	0.02	5.70	0.62	**97.67**	**47.39**
45 / 1	SD-5-1	Diorite	OK	55.48	0.00	28.72	0.04	0.14	0.01	0.00	9.95	0.01	5.86	0.32	**100.52**	**47.55**
46 / 1	SD-5-1	Diorite	OK	50.54	0.03	26.21	0.02	3.28	0.01	2.48	8.47	0.02	4.81	1.17	**97.04**	**45.60**

Table 24 continued

Data	Sample	Lithology	Locality	SiO2	TiO_2	Al_2O3	Cr2O3	FeO	MnO	MgO	CaO	BaO	Na2O	K2O	**Total**	**An**
57 / 1	SD-5-1	Diorite	OK	55.03	0.03	28.54	0.00	0.29	0.00	0.00	10.22	0.04	5.54	0.42	**100.11**	**49.24**
58 / 1	SD-5-1	Diorite	OK	56.69	0.02	27.21	0.00	0.22	0.00	0.00	9.02	0.00	5.24	0.33	**98.74**	**47.76**
61 / 1	SD-5-1	Diorite	OK	53.24	0.00	28.81	0.05	0.55	0.03	0.00	10.89	0.01	5.94	0.42	**99.95**	**49.19**
66 / 1	SD-5-1	Diorite	OK	50.33	2.80	27.35	0.00	3.08	0.03	0.00	10.11	0.00	5.56	0.42	**99.69**	**48.89**
67 / 1	SD-5-1	Diorite	OK	54.11	0.00	29.59	0.00	0.16	0.02	0.00	10.60	0.01	6.06	0.35	**100.88**	**48.23**
68 / 1	SD-5-1	Diorite	OK	51.72	0.37	28.16	0.06	2.62	0.00	0.93	10.42	0.03	5.39	0.48	**100.18**	**50.21**
69 / 1	SD-5-1	Diorite	OK	53.82	0.00	29.18	0.00	0.08	0.01	0.00	11.62	0.04	5.58	0.68	**101.00**	**51.59**
72 / 1	SD-5-1	Diorite	OK	54.67	0.00	29.39	0.00	0.18	0.00	0.00	10.74	0.00	5.72	0.52	**101.22**	**49.48**
74 / 1	SD-5-1	Diorite	OK	53.69	0.03	28.84	0.01	0.11	0.04	0.00	10.62	0.02	5.70	0.29	**99.37**	**49.89**
126 / 1	SD-49-22	Anorthosite	HS	52.83	0.00	30.92	0.02	0.22	0.05	0.07	11.09	0.01	5.08	1.06	**101.35**	**51.47**
129 / 1	SD-49-22	Anorthosite	HS	52.94	0.03	29.92	0.02	0.07	0.02	0.00	11.20	0.02	5.44	0.62	**100.28**	**51.41**
132 / 1	SD-49-22	Anorthosite	HS	52.11	0.05	30.73	0.00	0.18	0.00	0.00	12.05	0.01	4.85	0.83	**100.82**	**55.24**
133 / 1	SD-49-22	Anorthosite	HS	50.37	0.08	29.66	0.03	0.08	0.01	0.00	13.51	0.01	5.02	0.76	**99.52**	**57.49**
134 / 1	SD-49-22	Anorthosite	HS	53.50	0.00	30.43	0.00	0.18	0.02	0.00	10.97	0.00	5.29	0.76	**101.15**	**51.13**
137 / 1	SD-49-22	Anorthosite	HS	53.33	0.00	28.63	0.01	0.12	0.20	0.07	9.23	0.04	5.28	0.73	**97.65**	**46.94**
141 / 1	SD-49-22	Anorthosite	HS	53.37	0.69	28.26	0.02	0.17	0.00	0.00	12.22	0.00	5.04	0.77	**100.54**	**54.90**
142 / 1	SD-49-22	Anorthosite	HS	53.34	0.00	29.71	0.00	0.14	0.00	0.00	11.72	0.01	5.17	0.26	**100.35**	**54.83**
144 / 1	SD-49-22	Anorthosite	HS	53.83	0.02	29.66	0.03	0.10	0.02	0.00	11.64	0.01	5.38	0.24	**100.94**	**53.74**
148 / 1	SD-49-22	Anorthosite	HS	53.42	0.04	30.11	0.00	0.18	0.00	0.00	11.74	0.03	5.44	0.25	**101.20**	**53.64**
150 / 1	SD-49-22	Anorthosite	HS	54.35	0.01	29.82	0.00	0.19	0.00	0.00	11.05	0.00	5.26	0.40	**101.08**	**52.51**
151 / 1	SD-49-22	Anorthosite	HS	54.49	0.00	28.82	0.03	0.22	0.03	0.06	9.21	0.02	5.36	0.93	**99.16**	**46.03**
154 / 1	SD-49-22	Anorthosite	HS	53.80	0.01	29.10	0.00	0.17	0.00	0.03	10.24	0.00	5.25	0.46	**99.05**	**50.47**
155 / 1	SD-49-22	Anorthosite	HS	54.08	0.00	29.66	0.00	0.13	0.02	0.00	11.20	0.02	5.16	0.49	**100.76**	**53.05**
80 / 1	SD-48-21	Diorite	HS	50.33	0.26	29.41	0.04	1.25	0.00	0.50	11.55	0.05	4.66	0.67	**98.71**	**55.58**

Table 24 continued

Data	Sample	Lithology	Locality	SiO2	TiO_2	Al_2O_3	Cr_2O_3	FeO	MnO	MgO	CaO	BaO	Na_2O	K_2O	**Total**	**An**
94 / 1	SD-48-21	Diorite	HS	52.74	0.01	30.36	0.00	0.11	0.00	0.00	12.03	0.06	5.10	0.28	**100.69**	**55.73**
98 / 1	SD-48-21	Diorite	HS	50.96	0.27	29.41	0.01	1.13	0.01	0.29	11.70	0.00	5.01	0.39	**99.18**	**55.11**
100 / 1	SD-48-21	Diorite	HS	51.22	0.38	30.26	0.07	0.99	0.02	0.13	12.38	0.01	4.85	0.29	**100.59**	**57.58**
101 / 1	SD-48-21	Diorite	HS	52.59	0.00	29.90	0.02	0.72	0.02	0.20	11.44	0.01	4.90	0.66	**100.46**	**54.25**
111 / 1	SD-48-21	Diorite	HS	52.79	0.03	30.32	0.00	0.11	0.00	0.00	12.11	0.00	5.19	0.32	**100.87**	**55.35**
113 / 1	SD-48-21	Diorite	HS	53.18	0.01	29.96	0.00	0.10	0.00	0.00	12.27	0.00	5.11	0.26	**100.88**	**56.24**
117 / 1	SD-48-21	Diorite	HS	52.35	0.00	29.82	0.02	0.09	0.03	0.00	11.92	0.00	5.17	0.24	**99.65**	**55.30**
118 / 1	SD-48-21	Diorite	HS	52.39	0.00	30.14	0.00	0.10	0.00	0.00	12.08	0.03	5.53	0.38	**100.64**	**53.61**
119 / 1	SD-48-21	Diorite	HS	52.15	0.00	30.09	0.02	0.14	0.03	0.00	12.07	0.01	5.23	0.27	**100.01**	**55.22**
122 / 1	SD-48-21	Diorite	HS	52.06	0.03	30.12	0.00	0.10	0.00	0.00	12.09	0.03	4.98	0.35	**99.77**	**56.16**
123 / 1	SD-48-21	Diorite	HS	47.46	0.60	28.41	0.02	4.37	0.01	0.90	12.00	0.02	4.32	0.79	**98.89**	**57.83**
124 / 1	SD-48-21	Diorite	HS	54.66	0.54	27.07	0.04	2.26	0.00	0.93	9.17	0.00	3.92	0.34	**98.92**	**55.06**
73 / 1	SD-20-10	Anorthosite	HL	49.59	0.02	29.19	0.00	0.19	0.04	0.00	12.98	0.01	5.76	0.21	**97.99**	**54.89**
74 / 1	SD-20-10	Anorthosite	HL	52.30	0.00	27.15	0.00	0.30	0.00	0.33	9.40	0.06	5.34	2.66	**97.54**	**42.30**
77 / 1	SD-20-10	Anorthosite	HL	51.76	0.02	30.01	0.00	0.11	0.00	0.00	12.81	0.01	5.73	0.24	**100.69**	**54.58**
82 / 1	SD-20-10	Anorthosite	HL	52.19	0.02	29.38	0.01	0.10	0.02	0.00	11.96	0.02	6.21	0.37	**100.27**	**50.60**
83 / 1	SD-20-10	Anorthosite	HL	52.43	0.00	29.83	0.00	0.07	0.00	0.00	12.16	0.00	6.45	0.36	**101.30**	**50.13**
92 / 1	SD-20-10	Anorthosite	HL	51.35	0.00	30.57	0.00	0.04	0.02	0.00	12.60	0.00	5.93	0.30	**100.81**	**53.21**
94 / 1	SD-20-10	Anorthosite	HL	50.22	0.00	29.85	0.00	0.08	0.04	0.00	12.75	0.00	6.01	0.21	**99.16**	**53.39**
96 / 1	SD-20-10	Anorthosite	HL	50.41	0.06	29.49	0.00	0.16	0.00	0.00	13.89	0.02	5.48	0.31	**99.81**	**57.46**
97 / 1	SD-20-10	Anorthosite	HL	51.56	0.02	29.05	0.01	0.11	0.03	0.00	13.23	0.00	5.82	0.36	**100.20**	**54.68**
98 / 1	SD-20-10	Anorthosite	HL	51.57	0.00	29.57	0.00	0.14	0.03	0.00	11.94	0.02	6.12	0.38	**99.77**	**50.87**
100 / 1	SD-20-10	Anorthosite	HL	48.92	0.00	30.51	0.00	0.11	0.00	0.00	14.27	0.04	5.40	0.22	**99.48**	**58.71**
1 / 1	SD-19-9	Diorite	HL	52.45	0.00	29.70	0.00	0.08	0.00	0.00	11.96	0.00	6.35	0.27	**100.80**	**50.33**
3 / 1	SD-19-9	Diorite	HL	52.53	0.01	29.05	0.00	0.05	0.00	0.00	11.85	0.00	6.24	0.12	**99.86**	**50.88**

Table 24 continued

Data	Sample	Lithology	Locality	SiO2	TiO_2	Al_2O_3	Cr_2O_3	FeO	MnO	MgO	CaO	BaO	Na_2O	K_2O	**Total**	**An**
177 / 1	SD-35-17	Anorthosite	HN	53.49	0.00	29.47	0.00	0.09	0.00	0.00	11.33	0.01	6.70	0.21	**101.29**	**47.81**
178 / 1	SD-35-17	Anorthosite	HN	53.20	0.00	29.08	0.01	0.09	0.03	0.00	11.00	0.00	6.56	0.35	**100.31**	**47.23**
188 / 1	SD-35-17	Anorthosite	HN	52.55	0.02	30.51	0.01	0.01	0.00	0.00	11.23	0.01	6.46	0.19	**101.01**	**48.53**
192 / 1	SD-35-17	Anorthosite	HN	52.40	0.00	28.85	0.00	0.07	0.00	0.00	12.00	0.00	6.44	0.21	**99.99**	**50.18**
193 / 1	SD-35-17	Anorthosite	HN	53.13	0.02	28.76	0.00	0.11	0.01	0.00	12.16	0.04	6.40	0.23	**100.85**	**50.66**
194 / 1	SD-35-17	Anorthosite	HN	52.56	0.04	29.62	0.00	0.09	0.01	0.00	11.49	0.00	6.40	0.28	**100.50**	**49.07**
195 / 1	SD-35-17	Anorthosite	HN	53.30	0.00	28.62	0.00	0.09	0.00	0.00	11.58	0.00	6.53	0.28	**100.41**	**48.80**
196 / 1	SD-35-17	Anorthosite	HN	52.89	0.00	29.59	0.01	0.07	0.00	0.00	11.43	0.00	6.38	0.26	**100.63**	**49.08**
197 / 1	SD-35-17	Anorthosite	HN	52.16	0.00	29.07	0.00	0.07	0.03	0.00	11.22	0.01	6.31	0.26	**99.13**	**48.89**
199 / 1	SD-35-17	Anorthosite	HN	53.53	0.00	28.58	0.01	0.07	0.00	0.00	11.26	0.02	6.52	0.19	**100.19**	**48.35**
200 / 1	SD-35-17	Anorthosite	HN	53.70	0.00	28.61	0.00	0.08	0.02	0.00	11.19	0.02	6.59	0.19	**100.41**	**47.94**
201 / 1	SD-35-17	Anorthosite	HN	52.95	0.03	29.43	0.00	0.07	0.01	0.00	11.04	0.00	6.24	0.30	**100.05**	**48.66**
202 / 1	SD-35-17	Anorthosite	HN	52.71	0.00	29.72	0.01	0.08	0.00	0.00	11.15	0.00	6.62	0.29	**100.57**	**47.50**
203 / 1	SD-35-17	Anorthosite	HN	53.37	0.05	28.77	0.00	0.09	0.03	0.00	11.14	0.03	6.61	0.31	**100.40**	**47.48**
204 / 1	SD-35-17	Anorthosite	HN	53.45	0.07	29.07	0.00	0.13	0.00	0.00	11.39	0.00	6.65	0.25	**100.99**	**48.03**
205 / 1	SD-35-17	Anorthosite	HN	53.68	0.02	28.72	0.00	0.09	0.01	0.00	11.47	0.00	6.45	0.19	**100.61**	**49.11**
206 / 1	SD-35-17	Anorthosite	HN	51.89	0.00	28.74	0.00	0.04	0.00	0.00	11.20	0.00	6.37	0.27	**98.51**	**48.58**
207 / 1	SD-35-17	Anorthosite	HN	52.95	0.00	29.31	0.03	0.11	0.00	0.00	11.63	0.00	6.30	0.34	**100.67**	**49.63**
208 / 1	SD-35-17	Anorthosite	HN	53.51	0.05	28.60	0.00	0.05	0.01	0.00	11.10	0.02	6.64	0.28	**100.26**	**47.35**
209 / 1	SD-35-17	Anorthosite	HN	52.53	0.00	29.82	0.05	0.08	0.00	0.00	11.05	0.01	6.77	0.33	**100.64**	**46.62**
210 / 1	SD-35-17	Anorthosite	HN	52.90	0.00	29.43	0.00	0.13	0.00	0.00	11.56	0.00	6.51	0.18	**100.71**	**49.05**
211 / 1	SD-35-17	Anorthosite	HN	53.81	0.02	29.63	0.00	0.06	0.01	0.00	10.33	0.01	6.50	0.65	**101.03**	**45.17**
212 / 1	SD-35-17	Anorthosite	HN	53.54	0.00	29.68	0.00	0.12	0.02	0.00	11.23	0.00	6.57	0.27	**101.43**	**47.89**
101 / 1	SD-33-16	Diorite	HN	51.92	0.00	30.83	0.00	0.05	0.03	0.00	12.45	0.00	5.82	0.25	**101.35**	**53.49**
102 / 1	SD-33-16	Diorite	HN	52.20	0.01	29.93	0.02	0.08	0.02	0.00	12.60	0.01	5.89	0.26	**101.00**	**53.46**

Table 24 continued

Data	Sample	Lithology	Locality	SiO2	TiO_2	Al_2O_3	Cr_2O_3	FeO	MnO	MgO	CaO	BaO	Na_2O	K_2O	**Total**	**An**
105 / 1	SD-33-16	Diorite	HN	52.01	0.01	29.14	0.00	0.05	0.01	0.00	12.45	0.03	5.94	0.29	**99.92**	**52.89**
106 / 1	SD-33-16	Diorite	HN	52.54	0.04	29.46	0.00	0.10	0.00	0.00	12.49	0.00	6.03	0.31	**100.97**	**52.58**
107 / 1	SD-33-16	Diorite	HN	52.27	0.04	29.60	0.01	0.07	0.05	0.00	12.56	0.01	5.99	0.32	**100.93**	**52.85**
108 / 1	SD-33-16	Diorite	HN	52.51	0.00	29.32	0.00	0.07	0.02	0.00	12.37	0.00	6.02	0.22	**100.52**	**52.57**
109 / 1	SD-33-16	Diorite	HN	49.49	0.00	29.58	0.00	0.12	0.02	0.00	12.94	0.00	5.76	0.22	**98.13**	**54.76**
110 / 1	SD-33-16	Diorite	HN	49.69	0.00	29.60	0.00	0.13	0.00	0.00	12.91	0.01	5.81	0.23	**98.39**	**54.47**
112 / 1	SD-33-16	Diorite	HN	52.25	0.02	29.17	0.00	0.08	0.02	0.00	12.53	0.01	5.98	0.34	**100.40**	**52.74**
114 / 1	SD-33-16	Diorite	HN	52.02	0.00	29.76	0.01	0.07	0.00	0.00	12.50	0.03	6.32	0.24	**100.96**	**51.60**
117 / 1	SD-33-16	Diorite	HN	52.29	0.00	29.20	0.00	0.10	0.00	0.00	12.46	0.00	5.90	0.30	**100.25**	**53.03**
118 / 1	SD-33-16	Diorite	HN	50.87	0.01	29.28	0.00	0.08	0.01	0.00	12.84	0.03	6.09	0.21	**99.42**	**53.24**
119 / 1	SD-33-16	Diorite	HN	50.97	0.00	29.67	0.00	0.16	0.04	0.00	12.58	0.02	5.89	0.29	**99.62**	**53.35**
123 / 1	SD-33-16	Diorite	HN	49.97	0.04	29.04	0.00	0.05	0.00	0.00	12.33	0.04	5.92	0.28	**97.67**	**52.74**
124 / 1	SD-33-16	Diorite	HN	49.73	0.00	29.55	0.03	0.15	0.00	0.00	12.77	0.02	6.04	0.27	**98.56**	**53.17**
125 / 1	SD-33-16	Diorite	HN	50.60	0.06	29.37	0.02	0.11	0.01	0.00	12.46	0.02	6.03	0.30	**98.98**	**52.52**
126 / 1	SD-33-16	Diorite	HN	50.67	0.00	29.64	0.03	0.09	0.00	0.00	12.49	0.00	6.04	0.31	**99.27**	**52.51**
127 / 1	SD-33-16	Diorite	HN	50.58	0.00	28.63	0.00	0.13	0.01	0.00	12.91	0.02	5.91	0.25	**98.44**	**54.00**
128 / 1	SD-33-16	Diorite	HN	49.86	0.02	29.85	0.00	0.09	0.00	0.00	12.91	0.00	5.82	0.26	**98.82**	**54.35**
129 / 1	SD-33-16	Diorite	HN	51.51	0.02	30.09	0.02	0.05	0.00	0.00	13.02	0.03	6.16	0.20	**101.11**	**53.34**
130 / 1	SD-33-16	Diorite	HN	50.06	0.03	29.81	0.00	0.10	0.01	0.00	12.81	0.02	6.06	0.19	**99.09**	**53.37**
131 / 1	SD-33-16	Diorite	HN	49.53	0.03	28.60	0.01	0.11	0.00	0.00	12.74	0.01	5.92	0.30	**97.25**	**53.52**
137 / 1	SD-33-16	Diorite	HN	50.49	0.00	31.77	0.00	0.12	0.01	0.00	11.71	0.02	5.86	0.32	**100.31**	**51.62**
139 / 1	SD-33-16	Diorite	HN	51.83	0.01	31.13	0.00	0.07	0.00	0.00	11.57	0.04	5.38	0.35	**100.39**	**53.25**
141 / 1	SD-33-16	Diorite	HN	50.94	0.02	31.77	0.00	0.11	0.00	0.00	11.67	0.04	5.78	0.35	**100.69**	**51.77**

Table 24: *Orbicule Koppie plagioclase data.*

Point	Sample	C/M/S	SiO_2	TiO_2	$Al2O_3$	Cr_2O_3	FeO	MnO	MgO	CaO	BaO	Na_2O	K_2O	**Total**	**An**
P153 / 1	SD-10-6B	Core	55.50	0.00	28.12	0.02	0.07	0.00	0.00	8.67	0.03	6.05	0.20	**98.65**	**43.64**
P156 / 1	SD-10-6B	Core	56.41	0.00	28.18	0.04	0.01	0.02	0.00	8.43	0.03	5.90	0.25	**99.25**	**43.64**
P157 / 1	SD-10-6B	Core	55.06	0.00	28.42	0.00	0.03	0.00	0.00	8.80	0.01	5.99	0.17	**98.48**	**44.35**
P165 / 1	SD-10-6B	Core	56.93	0.01	28.08	0.01	0.05	0.05	0.00	8.37	0.02	5.90	0.25	**99.67**	**43.24**
P168 / 1	SD-10-6B	Core	56.14	0.02	27.80	0.00	0.10	0.00	0.00	8.30	0.01	5.76	0.28	**98.41**	**43.55**
P169 / 1	SD-10-6B	Core	56.33	0.00	27.90	0.02	0.03	0.01	0.00	8.38	0.00	5.77	0.19	**98.63**	**43.97**
P171 / 1	SD-10-6B	Core	52.00	0.02	24.99	0.00	0.02	0.02	0.00	13.07	0.05	5.68	1.26	**97.11**	**52.60**
P172 / 1	SD-10-6B	Core	56.15	0.00	28.62	0.00	0.06	0.00	0.00	8.83	0.00	5.97	0.27	**99.89**	**44.27**
P178 / 1	SD-10-6B	Core	56.81	0.00	27.63	0.02	0.06	0.01	0.00	7.95	0.00	5.66	0.30	**98.46**	**42.83**
P181 / 1	SD-10-6B	Core	57.19	0.00	28.21	0.00	0.07	0.00	0.00	8.19	0.00	6.11	0.21	**99.98**	**42.02**
P183 / 1	SD-10-6B	Core	56.28	0.02	28.24	0.01	0.06	0.00	0.00	8.63	0.00	5.92	0.24	**99.41**	**43.98**
P184 / 1	SD-10-6B	Core	56.55	0.00	28.68	0.01	0.05	0.00	0.00	8.71	0.02	5.71	0.28	**100.01**	**44.96**
P185 / 1	SD-10-6B	Core	57.14	0.02	28.45	0.00	0.04	0.01	0.00	8.45	0.02	5.84	0.37	**100.35**	**43.43**
P1 / 1	SD-10-6A	Shell	56.26	0.01	27.93	0.00	0.06	0.00	0.00	9.75	0.00	5.92	0.22	**100.16**	**47.04**
P3 / 1	SD-10-6A	Shell	57.65	0.01	29.18	0.00	0.07	0.03	0.00	8.59	0.01	6.00	0.31	**101.85**	**43.31**
P5 / 1	SD-10-6A	Shell	56.61	0.00	28.83	0.01	0.04	0.02	0.00	8.92	0.02	5.75	0.25	**100.45**	**45.43**

Table 25 Continued

Point	Sample	C/M/S	SiO_2	TiO_2	$Al2O_3$	Cr_2O_3	FeO	MnO	MgO	CaO	BaO	Na_2O	K_2O	**Total**	**An**
P8 / 1	SD-10-6A	Shell	55.32	0.00	29.01	0.02	0.06	0.00	0.00	9.41	0.01	5.56	0.15	**99.54**	**47.88**
P9 / 1	SD-10-6A	Shell	56.20	0.01	28.22	0.00	0.06	0.01	0.00	8.58	0.00	5.89	0.31	**99.28**	**43.73**
P14 / 1	SD-10-6A	Shell	57.30	0.02	28.61	0.00	0.08	0.00	0.00	8.66	0.00	5.91	0.23	**100.83**	**44.11**
P15 / 1	SD-10-6A	Shell	55.91	0.01	28.59	0.01	0.08	0.00	0.00	8.63	0.01	5.92	0.27	**99.42**	**43.89**
P16 / 1	SD-10-6A	Shell	55.93	0.00	28.48	0.00	0.07	0.01	0.00	8.74	0.01	5.73	0.22	**99.19**	**45.10**
P19 / 1	SD-10-6A	Shell	56.75	0.01	28.33	0.03	0.07	0.00	0.00	8.77	0.00	5.87	0.23	**100.06**	**44.58**
P20 / 1	SD-10-6A	Shell	56.40	0.03	28.46	0.01	0.04	0.01	0.00	8.69	0.00	5.75	0.23	**99.62**	**44.88**
P21 / 1	SD-10-6A	Shell	57.04	0.00	28.53	0.00	0.04	0.01	0.00	8.69	0.01	5.90	0.17	**100.40**	**44.42**
P23 / 1	SD-10-6A	Shell	56.80	0.01	28.78	0.00	0.09	0.02	0.00	8.72	0.00	5.76	0.25	**100.43**	**44.85**
P24 / 1	SD-10-6A	Shell	56.48	0.00	28.22	0.01	0.06	0.01	0.00	8.71	0.01	5.83	0.27	**99.61**	**44.47**
P25 / 1	SD-10-6A	Shell	57.52	0.02	28.95	0.00	0.04	0.02	0.00	8.49	0.00	6.00	0.17	**101.21**	**43.43**
P28 / 1	SD-10-6A	Shell	56.52	0.00	28.01	0.00	0.06	0.00	0.00	8.97	0.01	5.81	0.27	**99.65**	**45.27**
P31 / 1	SD-10-6A	Shell	57.29	0.00	28.96	0.02	0.10	0.01	0.00	8.82	0.00	5.73	0.18	**101.11**	**45.45**
P32 / 1	SD-10-6A	Shell	56.97	0.00	28.32	0.00	0.08	0.01	0.00	8.34	0.01	6.09	0.18	**100.00**	**42.60**
P33 / 1	SD-10-6A	Shell	57.43	0.00	28.60	0.00	0.06	0.00	0.00	8.63	0.00	5.89	0.28	**100.90**	**43.96**
P34 / 1	SD-10-6A	Shell	57.24	0.01	28.64	0.00	0.10	0.00	0.00	8.70	0.00	5.80	0.27	**100.76**	**44.57**
P35 / 1	SD-10-6A	Shell	56.27	0.00	28.13	0.00	0.11	0.01	0.00	8.51	0.00	5.77	0.28	**99.06**	**44.12**

Table 25 Continued

Point	Sample	C/M/S	SiO_2	TiO_2	$Al2O_3$	Cr_2O_3	FeO	MnO	MgO	CaO	BaO	Na_2O	K_2O	**Total**	**An**
P36 / 1	SD-10-6A	Shell	56.17	0.03	28.16	0.01	0.04	0.00	0.00	8.73	0.01	5.75	0.28	**99.18**	**44.87**
P37 / 1	SD-10-6A	Shell	56.68	0.00	28.26	0.00	0.03	0.00	0.00	8.63	0.02	5.83	0.24	**99.70**	**44.33**
P38 / 1	SD-10-6A	Shell	55.94	0.00	28.20	0.01	0.08	0.03	0.00	8.74	0.00	5.66	0.26	**98.91**	**45.31**
P40 / 1	SD-10-6A	Shell	55.94	0.02	28.61	0.04	0.10	0.00	0.00	8.67	0.00	5.82	0.25	**99.46**	**44.47**
P41 / 1	SD-10-6A	Shell	57.29	0.04	28.69	0.00	0.07	0.02	0.00	8.54	0.00	5.82	0.30	**100.77**	**43.95**
P42 / 1	SD-10-6A	Shell	57.01	0.00	28.39	0.00	0.05	0.01	0.00	8.54	0.00	5.96	0.19	**100.15**	**43.69**
P43 / 1	SD-10-6A	Shell	57.30	0.01	27.24	0.02	0.07	0.00	0.00	7.89	0.02	6.22	0.23	**99.00**	**40.63**
P45 / 1	SD-10-6A	Shell	56.65	0.00	28.73	0.00	0.08	0.00	0.00	8.82	0.01	5.68	0.27	**100.24**	**45.40**
P47 / 1	SD-10-6A	Shell	57.30	0.00	29.08	0.03	0.04	0.00	0.00	8.78	0.01	5.94	0.22	**101.39**	**44.38**
P48 / 1	SD-10-6A	Shell	56.19	0.00	28.40	0.01	0.02	0.00	0.00	8.45	0.00	5.75	0.17	**98.99**	**44.34**
P49 / 1	SD-10-6A	Shell	57.41	0.02	28.70	0.00	0.08	0.00	0.00	8.57	0.00	5.78	0.29	**100.84**	**44.21**
P50 / 1	SD-10-6A	Shell	56.40	0.03	28.57	0.01	0.07	0.00	0.00	8.60	0.00	5.83	0.21	**99.72**	**44.30**
P51 / 1	SD-10-6A	Shell	57.03	0.04	28.59	0.00	0.08	0.00	0.00	8.81	0.02	5.63	0.25	**100.45**	**45.66**
P52 / 1	SD-10-6A	Shell	57.40	0.00	29.12	0.01	0.06	0.00	0.00	8.81	0.00	5.89	0.23	**101.52**	**44.63**
P55 / 1	SD-10-6A	Shell	56.02	0.02	28.00	0.00	0.05	0.02	0.00	9.39	0.00	5.74	0.29	**99.52**	**46.68**
P57 / 1	SD-10-6A	Shell	57.21	0.03	28.47	0.01	0.07	0.01	0.00	8.16	0.02	5.92	0.38	**100.29**	**42.22**
P60 / 1	SD-10-6A	Shell	56.91	0.03	28.89	0.02	0.07	0.00	0.00	8.72	0.01	5.66	0.22	**100.53**	**45.34**

Table 25 *Continued*

Point	Sample	C/M/S	SiO_2	TiO_2	$Al2O_3$	Cr_2O_3	FeO	MnO	MgO	CaO	BaO	Na_2O	K_2O	**Total**	**An**
P61 / 1	SD-10-6A	Shell	56.93	0.01	28.51	0.01	0.09	0.00	0.00	8.57	0.00	5.82	0.21	**100.16**	**44.25**
P63 / 1	SD-10-6A	Shell	57.74	0.00	28.50	0.00	0.08	0.00	0.00	8.53	0.00	5.95	0.27	**101.08**	**43.49**
P64 / 1	SD-10-6A	Shell	56.65	0.00	28.37	0.01	0.06	0.01	0.00	8.36	0.02	5.82	0.11	**99.39**	**43.98**
P65 / 1	SD-10-6A	Shell	56.49	0.00	28.11	0.00	0.04	0.00	0.00	8.27	0.01	5.84	0.14	**98.91**	**43.48**
P66 / 1	SD-10-6A	Shell	57.73	0.02	28.50	0.01	0.04	0.00	0.00	8.63	0.00	5.81	0.24	**100.99**	**44.42**
P67 / 1	SD-10-6A	Shell	56.94	0.03	28.72	0.00	0.17	0.00	0.00	9.37	0.02	5.69	0.26	**101.21**	**46.93**
P68 / 1	SD-10-6A	Shell	56.64	0.00	28.07	0.00	0.10	0.02	0.00	8.49	0.02	5.84	0.28	**99.45**	**43.79**
P72 / 1	SD-10-6A	Shell	56.67	0.00	28.11	0.00	0.06	0.00	0.00	8.54	0.00	5.70	0.25	**99.33**	**44.59**
P74 / 1	SD-10-6A	Shell	56.31	0.01	28.00	0.00	0.07	0.00	0.00	8.38	0.00	5.62	0.29	**98.69**	**44.36**
P76 / 1	SD-10-6A	Shell	56.49	0.00	28.49	0.00	0.05	0.00	0.00	8.77	0.02	5.90	0.20	**99.93**	**44.55**
P77 / 1	SD-10-6A	Shell	57.06	0.03	28.74	0.00	0.06	0.01	0.00	8.53	0.00	5.93	0.14	**100.48**	**43.93**
P1 / 1	SD-10-6C	Matrix	55.20	0.02	30.60	0.02	0.15	0.00	0.00	10.74	0.00	4.62	0.28	**101.63**	**55.24**
P2 / 1	SD-10-6C	Matrix	53.41	0.01	29.92	0.00	0.07	0.00	0.00	11.09	0.00	4.83	0.20	**99.54**	**55.24**
P3 / 1	SD-10-6C	Matrix	54.66	0.00	30.15	0.00	0.08	0.00	0.00	11.00	0.02	4.87	0.21	**100.99**	**54.81**
P4 / 1	SD-10-6C	Matrix	52.56	0.02	29.55	0.00	0.06	0.00	0.00	11.02	0.00	4.76	0.17	**98.14**	**55.53**
P5 / 1	SD-10-6C	Matrix	55.46	0.00	30.34	0.00	0.06	0.00	0.00	11.13	0.02	4.69	0.18	**101.89**	**56.11**
P8 / 1	SD-10-6C	Matrix	54.90	0.05	30.14	0.00	0.04	0.01	0.00	10.86	0.02	4.84	0.21	**101.06**	**54.66**

Table 25 *Continued*

Point	Sample	C/M/S	SiO_2	TiO_2	$Al2O_3$	Cr_2O_3	FeO	MnO	MgO	CaO	BaO	Na_2O	K_2O	**Total**	**An**
P9 / 1	SD-10-6C	Matrix	54.26	0.02	30.28	0.00	0.07	0.01	0.00	11.32	0.00	4.87	0.24	**101.06**	**55.43**
P10 / 1	SD-10-6C	Matrix	53.22	0.01	29.21	0.00	0.09	0.03	0.00	10.86	0.00	4.71	0.30	**98.45**	**55.00**
P11 / 1	SD-10-6C	Matrix	53.59	0.00	29.03	0.00	0.05	0.00	0.00	10.93	0.00	4.73	0.21	**98.54**	**55.36**
P12 / 1	SD-10-6C	Matrix	56.71	0.00	28.43	0.00	0.08	0.00	0.00	10.28	0.03	4.57	0.26	**100.38**	**54.49**
P13 / 1	SD-10-6C	Matrix	54.98	0.03	30.11	0.00	0.06	0.00	0.00	10.90	0.00	4.88	0.26	**101.24**	**54.36**
P16 / 1	SD-10-6C	Matrix	53.07	0.00	29.17	0.02	0.08	0.00	0.00	10.83	0.02	4.85	0.27	**98.30**	**54.38**
P17 / 1	SD-10-6C	Matrix	53.81	0.00	28.67	0.00	0.06	0.02	0.00	10.80	0.01	4.82	0.22	**98.40**	**54.63**
P18 / 1	SD-10-6C	Matrix	54.67	0.00	30.47	0.02	0.08	0.01	0.00	11.04	0.00	4.81	0.25	**101.35**	**55.10**
P19 / 1	SD-10-6C	Matrix	53.92	0.02	29.50	0.02	0.09	0.05	0.00	10.80	0.00	4.77	0.22	**99.38**	**54.84**
P20 / 1	SD-10-6C	Matrix	54.83	0.00	28.50	0.00	0.05	0.00	0.00	10.62	0.01	4.71	0.12	**98.84**	**55.07**
P21 / 1	SD-10-6C	Matrix	57.06	0.01	28.42	0.01	0.08	0.00	0.00	10.82	0.01	4.72	0.17	**101.30**	**55.28**
P22 / 1	SD-10-6C	Matrix	55.63	0.00	28.47	0.01	0.06	0.00	0.00	10.68	0.00	4.75	0.21	**99.81**	**54.67**
P23 / 1	SD-10-6C	Matrix	53.35	0.00	29.76	0.00	0.06	0.01	0.00	10.79	0.00	4.85	0.20	**99.01**	**54.48**
P24 / 1	SD-10-6C	Matrix	53.43	0.00	29.92	0.02	0.05	0.02	0.00	11.24	0.00	4.86	0.23	**99.76**	**55.33**
P25 / 1	SD-10-6C	Matrix	55.60	0.00	28.35	0.00	0.07	0.00	0.00	10.92	0.01	4.46	0.19	**99.60**	**56.82**
P28 / 1	SD-10-6C	Matrix	52.71	0.00	29.47	0.02	0.06	0.00	0.00	10.68	0.01	4.91	0.32	**98.19**	**53.53**
P29 / 1	SD-10-6C	Matrix	54.11	0.00	29.11	0.02	0.06	0.00	0.00	10.63	0.01	4.95	0.21	**99.10**	**53.60**

Table 25 Continued

Point	Sample	C/M/S	SiO_2	TiO_2	Al_2O_3	Cr_2O_3	FeO	MnO	MgO	CaO	BaO	Na_2O	K_2O	**Total**	**An**
P30 / 1	SD-10-6C	Matrix	52.81	0.01	28.71	0.00	0.05	0.02	0.00	11.34	0.01	4.82	0.24	**98.01**	**55.73**
P31 / 1	SD-10-6C	Matrix	53.03	0.00	28.56	0.00	0.03	0.00	0.00	11.41	0.01	4.77	0.30	**98.11**	**55.94**
P32 / 1	SD-10-6C	Matrix	56. 57	0.03	27.74	0.00	0.29	0.01	0.00	11.03	0.03	4.53	0.35	**100.58**	**56.11**
P33 /1	SD-10-6C	Matrix	53.73	0.00	28.50	0.01	0.03	0.00	0.00	11.38	0.00	4.73	0.22	**98.61**	**56.35**
P35 / 1	SD-10-6C	Matrix	57.01	0.03	27.93	0.00	0.00	0.00	0.00	10.99	0.00	4.70	0.23	**100.89**	**55.63**
P37 / 1	SD-10-6C	Matrix	52.82	0.02	28.97	0.02	0.06	0.00	0.00	11.03	0.01	4.95	0.25	**98.12**	**54.40**
P38 / 1	SD-10-6C	Matrix	53.89	0.01	28.87	0.00	0.12	0.01	0.00	11.13	0.02	4.64	0.26	**98.95**	**56.14**
P39 / 1	SD-10-6C	Matrix	55.18	0.00	29.36	0.01	0.09	0.00	0.00	11.43	0.01	4.93	0.20	**101.22**	**55.51**
P40 / 1	SD-10-6C	Matrix	54.93	0.00	28.09	0.00	0.11	0.01	0.00	10.84	0.02	4.79	0.22	**99.01**	**54.86**
P43 / 1	SD-10-6C	Matrix	55.27	0.00	29.17	0.03	0.06	0.03	0.00	10.33	0.01	4.97	0.37	**100.24**	**52.27**
P45 / 1	SD-10-6C	Matrix	56.61	0.00	28.32	0.00	0.06	0.02	0.00	9.72	0.01	4.78	0.36	**99.88**	**51.72**
P50 / 1	SD-10-6C (2)	Matrix	59.39	0.00	27.43	0.00	0.09	0.01	0.02	9.33	0.02	4.84	0.38	**101.51**	**50.32**
P51 / 1	SD-10-6C (2)	Matrix	56.96	0.00	28.79	0.01	0.04	0.00	0.00	10.82	0.00	4.89	0.28	**101.79**	**54.10**
P52 / 1	SD-10-6C (2)	Matrix	58.74	0.00	26.98	0.01	0.05	0.00	0.01	10.66	0.01	4.56	0.30	**101.31**	**55.33**
P53 / 1	SD-10-6C (2)	Matrix	57.87	0.01	26.24	0.00	0.07	0.00	0.00	9.97	0.00	4.63	0.26	**99.06**	**53.41**
P55 / 1	SD-10-6C (2)	Matrix	58.64	0.00	25.96	0.01	0.01	0.00	0.00	9.86	0.00	4.73	0.25	**99.47**	**52.70**
P59 / 1	SD-10-6C (2)	Matrix	54.65	0.01	31.44	0.00	0.05	0.00	0.00	9.25	0.01	4.78	0.24	**100.42**	**50.90**

Table 25: *Microprobe analysis of biotites from the Orbicule Koppie orbicules. C= core, S= shells and M= matrix.*

Point	52	53	54	55	56	58	59	62	65	67	74	77	79
Sample	SD-10-6B	SD-10-6B	SD-10-6B	SD-10-6B	SD-10-6B	SD-10-6B	SD-10-6B	SD-10-6B	SD-10-6B	SD-10-6B	SD-10-6B	SD-10-6B	SD-10-6B
C/S/M	C	C	C	C	C	C	C	C	C	C	C	C	C
SiO2	39.25	38.85	38.98	37.28	37.77	37.31	39.02	36.67	36.91	38.20	38.06	37.44	38.40
TiO2	2.93	1.58	2.62	3.14	2.79	1.15	1.78	2.11	2.49	2.21	2.01	1.03	2.81
Al_2O_3	14.32	17.49	14.75	15.05	14.75	17.24	15.71	14.79	14.55	16.00	14.10	16.74	13.99
Cr_2O_3	0.01	0.04	0.04	0.05	0.02	0.05	0.01	0.03	0.03	0.02	0.07	0.00	0.02
MgO	15.02	18.29	15.85	16.47	16.27	19.32	18.39	16.67	16.63	17.98	16.96	20.04	16.30
CaO	0.25	0.08	0.69	0.13	0.19	0.23	0.13	0.04	0.03	0.12	0.04	0.08	0.03
MnO	0.06	0.09	0.08	0.09	0.08	0.11	0.08	0.06	0.06	0.09	0.04	0.11	0.08
FeO	10.46	11.37	10.21	10.77	10.31	10.49	11.16	10.28	10.93	11.20	10.39	11.47	10.08
Na_2O	0.05	0.03	0.03	0.09	0.05	0.02	0.12	0.06	0.07	0.06	0.07	0.06	0.09
K_2O	12.87	8.19	12.30	12.54	13.71	8.76	9.17	12.12	12.95	10.52	12.44	6.39	12.74
BaO	0.24	0.13	0.22	0.27	0.25	0.12	0.17	0.24	0.27	0.18	0.22	0.12	0.24
F	1.01	0.66	1.18	1.18	1.15	0.99	1.03	1.01	1.11	1.09	1.32	0.71	1.06
Cl	0.16	0.08	0.15	0.18	0.14	0.10	0.12	0.15	0.16	0.15	0.15	0.08	0.17
Li	0.18	0.09	0.23	0.23	0.22	0.17	0.19	0.18	0.21	0.20	0.28	0.10	0.19
H2O	3.62	3.91	3.59	3.55	3.57	3.71	3.72	3.52	3.52	3.68	3.46	3.80	3.57
Total	**100.40**	**100.86**	**100.86**	**100.97**	**101.21**	**99.72**	**100.72**	**97.91**	**99.86**	**101.65**	**99.54**	**98.12**	**99.74**

Number of ions based on 24 oxygens (O, OH, F, Cl)													
Si	5.68	5.49	5.59	5.38	5.46	5.32	5.52	5.45	5.41	5.41	5.53	5.40	5.59
Ti	0.32	0.17	0.28	0.34	0.30	0.12	0.19	0.24	0.27	0.24	0.22	0.11	0.31
Al^{IV}	2.32	2.51	2.41	2.56	2.51	2.68	2.48	2.55	2.51	2.59	2.42	2.60	2.40
Al^{VI}	0.12	0.40	0.08	0.00	0.00	0.22	0.15	0.04	0.00	0.08	0.00	0.25	0.00
Cr	0.00	0.00	0.00	0.00	0.00	0.00	0.00	0.00	0.00	0.00	0.01	0.00	0.00
Mg	3.24	3.85	3.39	3.54	3.50	4.11	3.88	3.69	3.63	3.79	3.68	4.31	3.54
Ca	0.04	0.01	0.11	0.02	0.03	0.04	0.02	0.01	0.00	0.02	0.01	0.01	0.01
Mn	0.01	0.01	0.01	0.01	0.01	0.01	0.01	0.01	0.01	0.01	0.01	0.01	0.01
Fe^{2+}	1.27	1.34	1.22	1.30	1.25	1.25	1.32	1.28	1.34	1.33	1.26	1.38	1.23
Na	0.01	0.01	0.01	0.03	0.01	0.01	0.03	0.02	0.02	0.02	0.02	0.02	0.03
K	2.38	1.48	2.25	2.31	2.53	1.60	1.66	2.30	2.42	1.90	2.31	1.18	2.37
Ba	0.03	0.01	0.02	0.03	0.03	0.01	0.02	0.03	0.03	0.02	0.03	0.01	0.03
F	0.46	0.30	0.54	0.54	0.53	0.45	0.46	0.47	0.51	0.49	0.61	0.32	0.49
Cl	0.04	0.02	0.04	0.04	0.03	0.02	0.03	0.04	0.04	0.03	0.04	0.02	0.04
Li*	0.05	0.03	0.07	0.07	0.06	0.05	0.05	0.05	0.06	0.06	0.08	0.03	0.06
OH^-	3.50	3.69	3.43	3.42	3.44	3.53	3.51	3.49	3.45	3.48	3.36	3.66	3.47
Mg/(Mg + Fe)	**0.72**	**0.74**	**0.73**	**0.73**	**0.74**	**0.77**	**0.75**	**0.74**	**0.73**	**0.74**	**0.74**	**0.76**	**0.74**

Table 26 continued

Dataset/Point	1	3	4	7	8	10	11	16	17	18	19	20	21
Sample	SD-10-6A	SD-10-6A	SD-10-6A	SD-10-6A	SD-10-6A	SD-10-6A	SD-10-6A	SD-10-6A	SD-10-6A	SD-10-6A	SD-10-6A	SD-10-6A	SD-10-6A
C/S/M	S	S	S	S	S	S	S	S	S	S	S	S	S
SiO_2	39.85	37.48	38.29	37.04	37.88	39.39	39.43	39.54	38.76	38.86	37.75	37.51	39.13
TiO_2	4.18	2.55	2.77	2.12	1.20	2.92	1.71	2.69	2.70	0.87	2.62	2.75	2.11
Al_2O_3	15.29	16.09	15.27	17.12	17.53	14.98	17.00	14.47	14.42	17.00	14.53	16.26	15.84
Cr_2O_3	0.02	0.04	0.05	0.04	0.04	0.01	0.01	0.02	0.07	0.02	0.06	0.03	0.04
MgO	15.34	17.50	16.20	19.25	19.06	15.17	19.01	15.70	16.90	19.39	18.05	14.81	18.31
CaO	6.30	0.03	1.22	1.31	0.10	0.19	0.04	0.07	1.54	0.17	0.00	0.07	0.85
MnO	0.06	0.10	0.10	0.09	0.10	0.08	0.08	0.12	0.07	0.08	0.07	0.06	0.09
FeO	8.04	10.65	10.00	10.78	10.67	10.06	11.32	10.88	10.05	10.96	10.37	10.17	9.78
Na_2O	0.07	0.05	0.06	0.04	0.07	0.04	0.06	0.07	0.03	0.04	0.05	0.09	0.07
K_2O	7.41	10.12	10.05	8.48	7.86	12.68	7.33	11.63	10.16	6.38	10.46	13.38	9.26
BaO	0.10	0.18	0.14	0.12	0.11	0.21	0.16	0.21	0.21	0.11	0.23	0.21	0.18
F	1.14	1.20	0.92	0.96	0.72	1.09	0.94	0.91	1.24	0.80	1.49	1.02	1.13
Cl	0.09	0.17	0.18	0.11	0.08	0.15	0.13	0.13	0.18	0.08	0.14	0.17	0.12
Li	0.22	0.24	0.15	0.17	0.10	0.20	0.16	0.15	0.25	0.12	0.34	0.18	0.22
H_2O	3.76	3.57	3.66	3.77	3.83	3.63	3.82	3.69	3.56	3.81	3.44	3.60	3.69
Total	**101.87**	**99.99**	**99.05**	**101.39**	**99.35**	**100.80**	**101.19**	**100.27**	**100.14**	**98.69**	**99.62**	**100.31**	**100.81**

Number of ions based on 24 oxygens (O, OH, F, Cl)

Si	5.53	5.37	5.55	5.23	5.42	5.65	5.50	5.71	5.54	5.53	5.42	5.45	5.51
Ti	0.44	0.27	0.30	0.23	0.13	0.32	0.18	0.29	0.29	0.09	0.28	0.30	0.22
Al^{IV}	2.47	2.63	2.45	2.77	2.58	2.35	2.50	2.29	2.43	2.47	2.46	2.55	2.49
Al^{VI}	0.03	0.08	0.16	0.08	0.37	0.18	0.29	0.17	0.00	0.39	0.00	0.24	0.14
Cr	0.00	0.00	0.00	0.00	0.00	0.00	0.00	0.00	0.01	0.00	0.00	0.00	0.00
Mg	3.17	3.74	3.50	4.05	4.06	3.24	3.95	3.38	3.60	4.12	3.86	3.21	3.84
Ca	0.94	0.00	0.19	0.20	0.02	0.03	0.01	0.01	0.24	0.03	0.00	0.01	0.13
Mn	0.01	0.01	0.01	0.01	0.01	0.01	0.01	0.01	0.01	0.01	0.01	0.01	0.01
Fe^{2+}	0.93	1.28	1.21	1.27	1.28	1.21	1.32	1.31	1.20	1.31	1.24	1.24	1.15
Na	0.02	0.01	0.02	0.01	0.02	0.01	0.02	0.02	0.01	0.01	0.01	0.03	0.02
K	1.31	1.85	1.86	1.53	1.43	2.32	1.30	2.14	1.85	1.16	1.91	2.48	1.66
Ba	0.01	0.02	0.02	0.01	0.01	0.02	0.02	0.02	0.02	0.01	0.03	0.02	0.02
F	0.50	0.55	0.42	0.43	0.32	0.49	0.41	0.41	0.56	0.36	0.68	0.47	0.51
Cl	0.02	0.04	0.04	0.03	0.02	0.04	0.03	0.03	0.04	0.02	0.03	0.04	0.03
Li*	0.06	0.07	0.05	0.05	0.03	0.06	0.04	0.04	0.07	0.04	0.10	0.05	0.06
OH^-	3.48	3.41	3.53	3.54	3.66	3.47	3.56	3.56	3.40	3.62	3.29	3.49	3.47
Mg/(Mg + Fe)	**0.77**	**0.75**	**0.74**	**0.76**	**0.76**	**0.73**	**0.75**	**0.72**	**0.75**	**0.76**	**0.76**	**0.72**	**0.77**

Table 26 continued

Point	22	23	24	25	27	28	29	30	31	32	33	35	36
Sample	SD-10-6A	SD-10-6A	SD-10-6A	SD-10-6A	SD-10-6A	SD-10-6A	SD-10-6A	SD-10-6A	SD-10-6A	SD-10-6A	SD-10-6A	SD-10-6A	SD-10-6A
C/S/M	S	S	S	S	S	S	S	S	S	S	S	S	S
SiO_2	39.17	39.73	38.04	36.97	35.11	35.90	38.11	37.50	36.91	39.01	36.74	35.82	35.65
TiO_2	2.37	3.34	3.09	1.68	3.23	3.29	2.48	1.76	2.37	2.47	2.96	2.97	3.23
Al_2O_3	14.64	14.08	14.64	14.96	15.02	14.35	15.92	15.29	15.66	15.46	15.34	14.78	14.39
Cr_2O_3	0.05	0.05	0.03	0.04	0.02	0.04	0.04	0.05	0.04	0.06	0.05	0.04	0.03
MgO	16.59	16.62	16.26	18.89	16.18	16.52	17.19	18.90	17.81	16.32	17.53	16.84	16.33
CaO	0.25	0.01	0.03	0.28	1.02	0.01	0.47	0.02	0.00	0.23	0.00	0.20	0.00
MnO	0.11	0.11	0.09	0.10	0.07	0.10	0.03	0.08	0.10	0.09	0.10	0.06	0.09
FeO	10.16	10.40	11.10	10.20	10.53	10.83	11.03	10.50	10.81	10.29	10.89	10.67	10.43
Na_2O	0.06	0.04	0.05	0.03	0.06	0.03	0.04	0.09	0.09	0.06	0.04	0.04	0.05
K_2O	12.83	10.29	10.49	11.20	13.10	13.82	11.07	10.70	10.43	11.94	10.78	13.79	13.81
BaO	0.21	0.24	0.22	0.16	0.22	0.28	0.22	0.26	0.26	0.19	0.29	0.27	0.27
F	1.00	1.23	1.21	1.21	1.23	1.24	1.13	1.70	1.41	1.16	1.12	1.44	1.32
Cl	0.14	0.14	0.16	0.10	0.15	0.15	0.14	0.22	0.18	0.14	0.16	0.16	0.16
Li	0.18	0.25	0.24	0.24	0.25	0.25	0.22	0.42	0.31	0.23	0.21	0.32	0.28
H_2O	3.68	3.59	3.52	3.54	3.44	3.45	3.65	3.38	3.46	3.63	3.57	3.40	3.39
Total	**101.43**	**100.11**	**99.16**	**99.60**	**99.63**	**100.25**	**101.75**	**100.87**	**99.85**	**101.28**	**99.77**	**100.81**	**99.42**

Number of ions based on 24 (O, OH, F, Cl)

Si	5.61	5.66	5.51	5.36	5.19	5.28	5.41	5.31	5.30	5.55	5.32	5.22	5.27
Ti	0.26	0.36	0.34	0.18	0.36	0.36	0.26	0.19	0.26	0.26	0.32	0.33	0.36
Al^{IV}	2.39	2.34	2.49	2.55	2.61	2.49	2.59	2.55	2.65	2.45	2.62	2.54	2.51
Al^{VI}	0.08	0.03	0.02	0.00	0.00	0.00	0.07	0.00	0.00	0.15	0.00	0.00	0.00
Cr	0.00	0.00	0.00	0.00	0.00	0.00	0.00	0.00	0.00	0.00	0.00	0.00	0.00
Mg	3.54	3.53	3.51	4.08	3.56	3.62	3.64	3.99	3.81	3.46	3.79	3.66	3.60
Ca	0.04	0.00	0.01	0.04	0.16	0.00	0.07	0.00	0.00	0.04	0.00	0.03	0.00
Mn	0.01	0.01	0.01	0.01	0.01	0.01	0.00	0.01	0.01	0.01	0.01	0.01	0.01
Fe^{2+}	1.22	1.24	1.35	1.24	1.30	1.33	1.31	1.24	1.30	1.23	1.32	1.30	1.29
Na	0.02	0.01	0.01	0.01	0.02	0.01	0.01	0.03	0.03	0.02	0.01	0.01	0.02
K	2.34	1.87	1.94	2.07	2.47	2.59	2.00	1.93	1.91	2.17	1.99	2.56	2.60
Ba	0.02	0.03	0.02	0.02	0.03	0.03	0.02	0.03	0.03	0.02	0.03	0.03	0.03
F	0.45	0.55	0.56	0.56	0.58	0.58	0.51	0.76	0.64	0.52	0.51	0.66	0.62
Cl	0.03	0.03	0.04	0.02	0.04	0.04	0.03	0.05	0.04	0.03	0.04	0.04	0.04
Li*	0.05	0.07	0.07	0.07	0.07	0.07	0.06	0.12	0.09	0.07	0.06	0.09	0.08
OH^-	3.51	3.41	3.41	3.42	3.39	3.39	3.46	3.19	3.31	3.44	3.45	3.30	3.34
Mg/(Mg + Fe)	**0.74**	**0.74**	**0.72**	**0.77**	**0.73**	**0.73**	**0.74**	**0.76**	**0.75**	**0.74**	**0.74**	**0.74**	**0.74**

Table 26 continued

Point	37	38	39	40	41	42	43	46	47	49	50	51
Sample	SD-10-6A	SD-10-6A	SD-10-6A	SD-10-6A	SD-10-6A	SD-10-6A	SD-10-6A	SD-10-6A	SD-10-6A	SD-10-6A	SD-10-6A	SD-10-6A
C/S/M	S	S	S	S	S	S	S	S	S	S	S	S
SiO2	35.01	38.65	38.97	40.39	38.21	37.90	38.33	36.86	40.16	37.99	37.26	42.86
TiO2	3.08	2.90	3.10	1.84	3.31	2.24	2.75	2.15	3.17	1.92	2.50	1.33
Al2O3	14.67	13.19	13.84	14.86	14.61	14.97	15.08	16.02	14.71	18.37	18.20	15.68
Cr2O3	0.00	0.05	0.06	0.06	0.01	0.04	0.02	0.04	0.03	0.04	0.04	0.04
MgO	16.00	15.03	15.90	17.05	17.28	17.82	17.51	17.47	15.76	15.61	15.81	18.30
CaO	0.01	0.00	0.00	0.15	0.05	0.37	0.07	0.34	0.02	0.06	0.00	0.39
MnO	0.07	0.08	0.07	0.09	0.12	0.09	0.12	0.11	0.08	0.09	0.11	0.09
FeO	11.05	9.94	10.46	10.19	10.51	10.14	10.19	11.38	11.16	9.58	10.43	10.10
Na2O	0.05	0.04	0.03	0.05	0.07	0.06	0.04	0.05	0.04	0.08	0.03	0.02
K2O	13.31	12.90	13.27	10.34	10.46	9.87	10.24	10.14	10.65	11.97	11.72	7.64
BaO	0.31	0.26	0.31	0.18	0.33	0.24	0.25	0.17	0.24	0.18	0.22	0.12
F	0.97	0.93	0.91	0.99	1.01	1.43	1.17	0.83	1.09	1.02	0.98	0.79
Cl	0.16	0.16	0.15	0.13	0.17	0.16	0.15	0.11	0.15	0.15	0.13	0.07
Li	0.17	0.16	0.15	0.17	0.18	0.32	0.23	0.13	0.20	0.18	0.17	0.12
H2O	3.48	3.55	3.67	3.71	3.64	3.46	3.59	3.69	3.68	3.69	3.71	3.96
Total	**98.35**	**97.83**	**100.89**	**100.21**	**99.97**	**99.12**	**99.73**	**99.50**	**101.13**	**100.92**	**101.32**	**101.50**

Number of ions based on 24 (O, OH, F, Cl)

Si	5.27	5.75	5.65	5.75	5.50	5.44	5.50	5.37	5.69	5.41	5.32	5.91
Ti	0.35	0.32	0.34	0.20	0.36	0.24	0.30	0.24	0.34	0.21	0.27	0.14
Al^{IV}	2.60	2.25	2.35	2.25	2.48	2.53	2.50	2.63	2.31	2.59	2.68	2.09
Al^{VI}	0.00	0.07	0.01	0.24	0.00	0.00	0.04	0.12	0.15	0.49	0.37	0.46
Cr	0.00	0.00	0.00	0.00	0.00	0.00	0.00	0.00	0.00	0.00	0.00	0.00
Mg	3.59	3.33	3.44	3.62	3.71	3.82	3.74	3.79	3.33	3.31	3.36	3.76
Ca	0.00	0.00	0.00	0.02	0.01	0.06	0.01	0.05	0.00	0.01	0.00	0.06
Mn	0.01	0.01	0.01	0.01	0.01	0.01	0.01	0.01	0.01	0.01	0.01	0.01
Fe^{2+}	1.39	1.24	1.27	1.21	1.27	1.22	1.22	1.39	1.32	1.14	1.24	1.16
Na	0.01	0.01	0.01	0.01	0.02	0.02	0.01	0.02	0.01	0.02	0.01	0.00
K	2.55	2.45	2.45	1.88	1.92	1.81	1.87	1.88	1.93	2.17	2.13	1.34
Ba	0.04	0.03	0.04	0.02	0.04	0.03	0.03	0.02	0.03	0.02	0.02	0.01
F	0.46	0.44	0.42	0.45	0.46	0.65	0.53	0.38	0.49	0.46	0.44	0.34
Cl	0.04	0.04	0.04	0.03	0.04	0.04	0.04	0.03	0.04	0.04	0.03	0.02
Li*	0.05	0.05	0.04	0.05	0.05	0.09	0.07	0.04	0.06	0.05	0.05	0.03
OH^-	3.50	3.52	3.55	3.52	3.50	3.31	3.43	3.59	3.48	3.50	3.53	3.64
Mg/(Mg + Fe)	**0.72**	**0.73**	**0.73**	**0.75**	**0.75**	**0.76**	**0.75**	**0.73**	**0.72**	**0.74**	**0.73**	**0.76**

Table 26 continued

Point	82 / 1	84 / 1	85 / 1	86 / 1	87 / 1	88 / 1	90 / 1	91 / 1	93 / 1	95 / 1	96 / 1	97 / 1	98 / 1
Sample	SD-10-6C	SD-10-6C	SD-10-6C	SD-10-6C	SD-10-6C	SD-10-6C	SD-10-6C	SD-10-6C	SD-10-6C	SD-10-6C	SD-10-6C	SD-10-6C	SD-10-6C
C/S/M	M	M	M	M	M	M	M	M	M	M	M	M	M
SiO_2	38.06	39.37	37.47	39.09	41.41	39.05	38.29	38.24	38.59	37.67	41.24	38.63	38.33
TiO_2	2.63	1.85	2.69	2.26	1.54	2.33	2.02	5.05	2.80	2.53	2.23	2.66	2.18
Al_2O_3	13.22	15.33	14.85	17.91	18.81	14.86	15.48	13.87	15.41	15.39		15.68	14.20
Cr_2O_3	0.04	0.03	0.06	0.04	0.04	0.02	0.03	0.03	0.03	0.06	0.02	0.05	0.03
MgO	16.92	17.99	16.84	14.96	10.79	15.79	16.47	15.74	17.59	17.10	16.86	16.83	15.67
CaO	0.00	0.04	0.01	4.34	9.19	0.06	0.16	3.88	0.00	1.25	0.00	0.02	0.01
MnO	0.08	0.12	0.07	0.03	0.05	0.06	0.07	0.07	0.06	0.07	0.06	0.08	0.11
FeO	9.75	11.15	10.22	8.62	6.98	10.17	9.53	9.63	10.14	9.47	9.54	10.17	10.12
Na_2O	0.14	0.07	0.06	0.09	0.05	0.08	0.16	0.06	0.07	0.10	0.09	0.08	0.13
K_2O	13.54	10.49	13.19	8.91	7.54	12.09	13.44	8.41	10.30	12.09	10.19	10.28	12.74
BaO	0.18	0.15	0.24	0.15	0.14	0.11	0.12	0.12	0.22	0.16	0.21	0.24	0.22
F	1.22	1.11	1.24	1.01	0.96	1.06	1.22	1.16	1.29	1.14	1.30	1.34	1.18
Cl	0.21	0.16	0.20	0.12	0.11	0.17	0.18	0.15	0.18	0.15	0.19	0.18	0.17
Li	0.24	0.21	0.25	0.18	0.17	0.20	0.25	0.23	0.27	0.22	0.27	0.29	0.23
H_2O	3.47	3.69	3.52	3.77	3.84	3.60	3.55	3.62	3.57	3.60	3.59	3.53	3.49
Total	**99.70**	**101.75**	**100.91**	**101.47**	**101.61**	**99.64**	**100.96**	**100.25**	**100.52**	**100.98**	**100.25**	**100.06**	**98.81**

Number of ions based on 24 oxygens (O, OH, F, Cl)

Si	5.56	5.55	5.41	5.47	5.74	5.65	5.50	5.45	5.47	5.40	5.80	5.49	5.63
Ti	0.29	0.20	0.29	0.24	0.16	0.25	0.22	0.54	0.30	0.27	0.24	0.28	0.24
Al^{IV}	2.28	2.45	2.53	2.53	2.26	2.35	2.50	2.33	2.53	2.60	2.20	2.51	2.37
Al^{VI}	0.00	0.10	0.00	0.43	0.81	0.19	0.12	0.00	0.05	0.00	0.20	0.12	0.08
Cr	0.00	0.00	0.00	0.00	0.00	0.00	0.00	0.00	0.00	0.00	0.00	0.00	0.00
Mg	3.69	3.78	3.62	3.12	2.23	3.41	3.52	3.35	3.72	3.65	3.54	3.57	3.43
Ca	0.00	0.01	0.00	0.65	1.36	0.01	0.03	0.59	0.00	0.19	0.00	0.00	0.00
Mn	0.01	0.01	0.01	0.00	0.01	0.01	0.01	0.01	0.01	0.01	0.01	0.01	0.01
Fe^{2+}	1.19	1.31	1.23	1.01	0.81	1.23	1.14	1.15	1.20	1.14	1.12	1.21	1.24
Na	0.04	0.02	0.02	0.03	0.01	0.02	0.04	0.02	0.02	0.03	0.02	0.02	0.04
K	2.52	1.89	2.43	1.59	1.33	2.23	2.46	1.53	1.86	2.21	1.83	1.86	2.39
Ba	0.02	0.02	0.03	0.02	0.01	0.01	0.01	0.01	0.02	0.02	0.02	0.03	0.03
F	0.56	0.49	0.57	0.45	0.42	0.49	0.55	0.52	0.58	0.52	0.58	0.60	0.55
Cl	0.05	0.04	0.05	0.03	0.03	0.04	0.04	0.04	0.04	0.04	0.04	0.04	0.04
Li*	0.07	0.06	0.07	0.05	0.05	0.06	0.07	0.06	0.08	0.06	0.08	0.08	0.07
OH^-	3.39	3.47	3.38	3.52	3.55	3.47	3.40	3.44	3.38	3.45	3.37	3.35	3.41
Mg/(Mg + Fe)	**0.76**	**0.74**	**0.75**	**0.76**	**0.73**	**0.73**	**0.76**	**0.74**	**0.76**	**0.76**	**0.76**	**0.75**	**0.73**

Table 26 continued

Point	99	102	104	105	107	108	109	110	112	114	117	120	121
Sample	SD-10-6C	SD-10-6C	SD-10-6C	SD-10-6C	SD-10-6C	SD-10-6C	SD-10-6C	SD-10-6C	SD-10-6C	SD-10-6C	SD-10-6C	SD-10-6C	SD-10-6C
C/S/M	M	M	M	M	M	M	M	M	M	M	M	M	M
SiO_2	37.33	38.61	39.59	37.66	36.45	38.72	38.23	39.08	37.26	39.39	37.47	38.84	37.47
TiO_2	2.40	2.56	2.19	2.76	2.37	2.61	2.61	2.62	2.47	2.48	2.56	2.14	2.80
Al_2O_3	15.13	15.16	14.64	13.98	15.16	14.18	13.94	14.03	15.37	14.28	14.63	14.87	15.32
Cr_2O_3		0.04	0.06	0.03	0.02	0.02	0.04	0.05	0.02	0.05	0.02	0.05	0.01
MgO	17.69	17.34	16.78	16.71	17.96	16.57	16.89	16.32	16.69	16.51	17.25	16.10	17.07
CaO	0.10	0.04	0.01	0.00	0.01	0.00	0.00	0.00	0.00	0.00	0.00	0.02	0.62
MnO	0.07	0.08	0.09	0.05	0.03	0.07	0.07	0.08	0.07	0.06	0.07	0.06	0.10
FeO	9.98	10.27	9.50	10.20	10.20	10.31	10.08	10.12	10.32	10.04	9.98	9.84	9.97
Na_2O	0.08	0.07	0.04	0.05	0.04	0.06	0.07	0.04	0.04	0.06	0.07	0.02	0.05
K_2O	12.75	10.42	12.74	13.45	13.62	13.60	13.06	13.39	13.49	13.33	13.34	12.10	12.79
BaO	0.24	0.22	0.18	0.24	0.26	0.25	0.24	0.17	0.20	0.23	0.22	0.20	0.24
F	1.32	1.53	1.23	1.18	1.38	1.21	1.10	1.33	1.14	0.96	1.38	1.14	1.13
Cl	0.16	0.18	0.19	0.20	0.17	0.17	0.20	0.18	0.17	0.19	0.17	0.16	0.12
Li	0.28	0.35	0.25	0.23	0.30	0.24	0.21	0.28	0.22	0.17	0.30	0.22	0.22
H2O	3.51	3.46	3.58	3.51	3.47	3.56	3.56	3.51	3.56	3.67	3.47	3.55	3.61
Total	**101.07**	**100.34**	**101.08**	**100.25**	**101.45**	**101.59**	**100.28**	**101.21**	**101.00**	**101.41**	**100.94**	**99.31**	**101.51**

Number of ions based on 24 (O, OH, F, Cl)

Si	5.36	5.47	5.64	5.48	5.25	5.55	5.55	5.60	5.39	5.65	5.40	5.63	5.38
Ti	0.26	0.27	0.23	0.30	0.26	0.28	0.29	0.28	0.27	0.27	0.28	0.23	0.30
Al^{IV}	2.56	2.53	2.36	2.40	2.57	2.40	2.39	2.37	2.61	2.35	2.48	2.37	2.59
Al^{VI}	0.00	0.01	0.10	0.00	0.00	0.00	0.00	0.00	0.01	0.07	0.00	0.17	0.00
Cr	0.00	0.00	0.00	0.00	0.00	0.00	0.00	0.00	0.00	0.00	0.00	0.00	0.00
Mg	3.78	3.66	3.56	3.63	3.85	3.54	3.65	3.48	3.60	3.53	3.70	3.48	3.65
Ca	0.01	0.01	0.00	0.00	0.00	0.00	0.00	0.00	0.00	0.00	0.00	0.00	0.09
Mn	0.01	0.01	0.01	0.01	0.00	0.01	0.01	0.01	0.01	0.01	0.01	0.01	0.01
Fe^{2+}	1.20	1.22	1.13	1.24	1.23	1.24	1.22	1.21	1.25	1.20	1.20	1.19	1.20
Na	0.02	0.02	0.01	0.01	0.01	0.02	0.02	0.01	0.01	0.02	0.02	0.01	0.01
K	2.33	1.88	2.31	2.50	2.50	2.49	2.42	2.45	2.49	2.44	2.45	2.24	2.34
Ba	0.03	0.02	0.02	0.03	0.03	0.03	0.03	0.02	0.02	0.03	0.02	0.02	0.03
F	0.60	0.68	0.55	0.55	0.63	0.55	0.51	0.60	0.52	0.44	0.63	0.52	0.51
Cl	0.04	0.04	0.04	0.05	0.04	0.04	0.05	0.04	0.04	0.05	0.04	0.04	0.03
Li*	0.08	0.10	0.07	0.07	0.09	0.07	0.06	0.08	0.06	0.05	0.09	0.06	0.06
OH-	3.36	3.27	3.40	3.41	3.33	3.41	3.45	3.35	3.44	3.52	3.33	3.44	3.46
Mg/(Mg + Fe)	**0.76**	**0.75**	**0.76**	**0.74**	**0.76**	**0.74**	**0.75**	**0.74**	**0.74**	**0.75**	**0.76**	**0.74**	**0.75**

Table 26 continued

Point	172	173	174	175	176	177	178	180	181	182	183	184	185 /	186
Sample	SD-10-6C (2)	SD-10-6C (2)	SD-10-6C (2)	SD-10-6C (2)	SD-10-6C (2)	SD-10-6C (2)	SD-10-6C (2)	SD-10-6C (2)	SD-10-6C (2)	SD-10-6C (2)	SD-10-6C (2)	SD-10-6C (2)	SD-10-6C (2)	SD-10-6C (2)
C/S/M	M	M	M	M	M	M	M	M	M	M	M	M	M	M
SiO_2	37.58	38.67	39.63	38.82	39.15	38.35	39.27	38.13	38.17	37.15	37.33	37.78	39.77	37.82
TiO_2	2.91	2.80	2.82	2.87	3.63	3.03	2.65	2.86	3.12	2.57	5.55	2.74	2.79	2.25
Al_2O_3	14.57	13.85	14.06	13.89	15.01	14.31	14.07	13.98	15.03	14.62	15.20	15.67	14.63	15.19
Cr_2O_3	0.05	0.04	0.00	0.00	0.04	0.03	0.04	0.05	0.00	0.03	0.00	0.03	0.06	0.01
MgO	16.47	15.97	15.50	15.59	15.89	15.06	15.70	14.95	17.12	16.36	14.73	16.27	16.01	15.97
CaO	0.06	0.03	0.13	0.07	2.74	0.36	0.10	0.07	0.16	0.02	7.43	0.84	0.15	0.00
MnO	0.10	0.06	0.11	0.08	0.07	0.06	0.07	0.11	0.04	0.07	0.06	0.05	0.07	0.12
FeO	10.40	9.66	10.03	10.45	10.10	10.10	10.13	10.36	10.93	10.32	7.44	10.76	9.77	9.72
Na_2O	0.08	0.08	0.11	0.11	0.07	0.06	0.09	0.07	0.06	0.07	0.09	0.07	0.04	0.11
K_2O	13.15	12.91	12.79	12.61	8.22	12.74	13.05	13.09	10.35	13.31	7.26	10.37	13.10	13.39
BaO	0.24	0.23	0.22	0.20	0.16	0.27	0.21	0.18	0.22	0.24	0.11	0.18	0.19	0.14
F	1.09	1.12	1.08	1.00	0.73	1.04	0.96	1.02	1.13	1.11	1.21	0.94	1.05	1.25
Cl	0.19	0.20	0.21	0.16	0.12	0.17	0.18	0.19	0.19	0.18	0.11	0.14	0.18	0.25
Li	0.20	0.21	0.20	0.18	0.11	0.19	0.17	0.18	0.22	0.21	0.24	0.16	0.19	0.26
H_2O	3.57	3.53	3.60	3.59	3.81	3.56	3.63	3.53	3.60	3.52	3.63	3.66	3.67	3.47
Total	**100.67**	**99.38**	**100.48**	**99.61**	**99.85**	**99.32**	**100.34**	**98.77**	**100.36**	**99.79**	**100.41**	**99.67**	**101.65**	**99.95**

Number of ions based on 24 oxygens (O, OH, F, Cl)

Si	5.45	5.64	5.71	5.67	5.61	5.61	5.69	5.63	5.47	5.44	5.29	5.47	5.67	5.49
Ti	0.32	0.31	0.31	0.32	0.39	0.33	0.29	0.32	0.34	0.28	0.59	0.30	0.30	0.25
Al^{IV}	2.49	2.36	2.29	2.33	2.39	2.39	2.31	2.37	2.53	2.52	2.54	2.53	2.33	2.51
Al^{VI}	0.00	0.02	0.10	0.06	0.14	0.08	0.10	0.07	0.00	0.00	0.00	0.14	0.12	0.09
Cr	0.00	0.00	0.00	0.00	0.00	0.00	0.00	0.00	0.00	0.00	0.00	0.00	0.00	0.00
Mg	3.56	3.47	3.33	3.39	3.39	3.29	3.39	3.29	3.65	3.57	3.11	3.51	3.40	3.46
Ca	0.01	0.00	0.02	0.01	0.42	0.06	0.02	0.01	0.02	0.00	1.13	0.13	0.02	0.00
Mn	0.01	0.01	0.01	0.01	0.01	0.01	0.01	0.01	0.01	0.01	0.01	0.01	0.01	0.01
Fe^{2+}	1.26	1.18	1.21	1.28	1.21	1.24	1.23	1.28	1.31	1.27	0.88	1.30	1.16	1.18
Na	0.02	0.02	0.03	0.03	0.02	0.02	0.02	0.02	0.02	0.02	0.03	0.02	0.01	0.03
K	2.43	2.40	2.35	2.35	1.50	2.38	2.41	2.47	1.89	2.49	1.31	1.91	2.38	2.48
Ba	0.03	0.03	0.02	0.02	0.02	0.03	0.02	0.02	0.03	0.03	0.01	0.02	0.02	0.02
F	0.50	0.52	0.49	0.46	0.33	0.48	0.44	0.48	0.51	0.51	0.54	0.43	0.47	0.57
Cl	0.05	0.05	0.05	0.04	0.03	0.04	0.05	0.05	0.05	0.05	0.03	0.03	0.04	0.06
Li*	0.06	0.06	0.06	0.05	0.03	0.06	0.05	0.05	0.06	0.06	0.07	0.05	0.05	0.07
OH-	3.45	3.43	3.46	3.50	3.64	3.48	3.51	3.47	3.44	3.44	3.43	3.54	3.48	3.36
Mg/(Mg + Fe)	**0.74**	**0.75**	**0.73**	**0.73**	**0.74**	**0.73**	**0.73**	**0.72**	**0.74**	**0.74**	**0.78**	**0.73**	**0.74**	**0.75**

***Table 26**: Hoogkraal Lease EPMA plagioclase data.*

Point	Sample	C/M/S	SiO_2	TiO_2	Al_2O_3	$Cr2O_3$	FeO	MnO	MgO	CaO	BaO	Na_2O	K_2O	**Total**	**An**
P79 / 1	SD-27-14	Core	54.82	0.01	27.19	0.00	0.07	0. 00	0.00	10.72	0.02	6.23	0.44	**99.51**	**47.63**
P80 / 1	SD-27-14	Core	54.70	0.00	26.99	0.02	0.14	0.00	0.00	10.53	0.04	6.37	0.43	**99.22**	**46.65**
P81 / 1	SD-27-14	Core	54.84	0.01	27.61	0.01	0.07	0.01	0.00	10.63	0.00	6.14	0.42	**99.74**	**47.83**
P82 / 1	SD-27-14	Core	54.74	0.00	27.29	0.02	0.05	0.00	0.00	10.63	0.03	6.41	0.42	**99.60**	**46.76**
P83 / 1	SD-27-14	Core	55.51	0.04	27.42	0.00	0.05	0.00	0.00	10.47	0.03	6.45	0.41	**100.37**	**46.25**
P84 / 1	SD-27-14	Core	55.38	0.00	27.15	0.01	0.15	0.00	0.00	10.36	0.01	6.56	0.40	**100.03**	**45.61**
P85 / 1	SD-27-14	Core	55.59	0.00	27.16	0.00	0.09	0.00	0.00	10.30	0.01	5.67	0.43	**99.26**	**48.88**
P86 / 1	SD-27-14	Core	55.05	0.01	27.10	0.00	0.08	0.00	0.00	10.66	0.03	6.47	0.39	**99.79**	**46.70**
P87 / 1	SD-27-14	Core	54.79	0.00	26.97	0.01	0.09	0.00	0.00	10.42	0.00	6.07	0.38	**98.72**	**47.68**
P88 / 1	SD-27-14	Core	54.12	0.03	27.61	0.00	0.09	0.00	0.00	10.95	0.02	6.38	0.39	**99.60**	**47.68**
P89 / 1	SD-27-14	Core	54.32	0.00	27.92	0.00	0.11	0.00	0.00	11.50	0.03	5.87	0.35	**100.11**	**50.99**
P91 / 1	SD-27-14	Core	56.15	0.00	27.53	0.05	0.13	0.02	0.00	10.05	0.02	6.28	0.40	**100.63**	**45.91**
P92 / 1	SD-27-14	Core	55.17	0.00	28.00	0.02	0.14	0.04	0.00	10.68	0.00	6.55	0.37	**100.96**	**46.49**
P93 / 1	SD-27-14	Core	55.44	0.00	27.51	0.00	0.21	0.02	0.00	10.22	0.07	6.00	0.93	**100.39**	**46.08**
P94 / 1	SD-27-14	Core	55.72	0.04	27.22	0.02	0.07	0.03	0.00	10.02	0.01	6.93	0.31	**100.36**	**43.68**
P95 / 1	SD-27-14	Core	54.19	0.01	27.00	0.00	0.13	0.00	0.00	10.08	0.01	6.19	0.39	**97.99**	**46.37**
P96 / 1	SD-27-14	Core	53.58	0.00	27.45	0.00	0.12	0.03	0.00	11.27	0.04	6.08	0.40	**98.98**	**49.54**

Table 27 continued

Point	Sample	C/M/S	SiO_2	TiO_2	Al_2O_3	$Cr2O_3$	FeO	MnO	MgO	CaO	BaO	Na_2O	K_2O	**Total**	**An**
P97 / 1	SD-27-14	Core	54.67	0.01	27.66	0.00	0.13	0.02	0.00	10.79	0.00	5.85	0.43	**99.56**	**49.33**
P98 / 1	SD-27-14	Core	54.56	0.00	27.43	0.01	0.13	0.00	0.00	10.68	0.01	6.33	0.42	**99.57**	**47.21**
P111 / 1	SD-27-14	Core	53.96	0.00	27.16	0.00	0.18	0.02	0.00	10.71	0.00	5.49	0.49	**98.01**	**50.49**
P112 / 1	SD-27-14	Core	54.59	0.00	27.47	0.00	0.13	0.02	0.00	10.58	0.01	6.67	0.21	**99.69**	**46.18**
P113 / 1	SD-27-14	Core	54.07	0.00	26.86	0.03	0.10	0.00	0.00	10.70	0.04	6.25	0.43	**98.48**	**47.51**
P114 / 1	SD-27-14	Core	54.11	0.01	27.10	0.00	0.11	0.00	0.00	10.96	0.01	6.13	0.41	**98.83**	**48.64**
P115 / 1	SD-27-14	Core	53.27	0.00	27.12	0.00	0.10	0.01	0.00	10.83	0.00	6.25	0.37	**97.94**	**47.97**
P117 / 1	SD-27-14	Core	54.22	0.00	27.16	0.01	0.10	0.02	0.00	10.86	0.02	6.29	0.38	**99.06**	**47.87**
P1 / 1	SD-22-11C	Core	55.46	0.00	28.65	0.00	0.04	0.00	0.00	9.15	0.00	6.63	0.47	**100.40**	**42.16**
P2 / 1	SD-22-11C	Core	52.93	0.02	30.12	0.00	0.10	0.00	0.00	10.38	0.02	5.70	0.43	**99.70**	**48.93**
P3 / 1	SD-22-11C	Core	54.76	0.00	27.84	0.00	0.06	0.01	0.00	8.43	0.01	7.06	0.45	**98.62**	**38.79**
P4 / 1	SD-22-11C	Core	53.68	0.00	31.38	0.04	0.09	0.02	0.00	9.04	0.00	6.34	0.47	**101.06**	**42.90**
P5 / 1	SD-22-11C	Core	52.12	0.00	31.56	0.01	0.08	0.00	0.00	9.66	0.02	6.19	0.45	**100.08**	**45.18**
P6 / 1	SD-22-11C	Core	52.35	0.02	31.63	0.01	0.09	0.01	0.00	9.75	0.02	6.05	0.41	**100.35**	**46.03**
P7 / 1	SD-22-11C	Core	52.69	0.03	30.18	0.03	0.06	0.01	0.00	8.75	0.00	6.73	0.47	**98.97**	**40.72**
P8 / 1	SD-22-11C	Core	52.95	0.04	30.00	0.00	0.10	0.01	0.00	8.60	0.00	6.78	0.35	**98.83**	**40.72**
P9 / 1	SD-22-11C	Core	52.93	0.01	30.46	0.00	0.18	0.02	0.00	8.94	0.00	6.66	0.41	**99.61**	**41.63**

Table 27 continued

Point	Sample	C/M/S	SiO_2	TiO_2	Al_2O_3	$Cr2O_3$	FeO	MnO	MgO	CaO	BaO	Na_2O	K_2O	**Total**	**An**
P10 / 1	SD-22-11C	Core	52.70	0.00	30.11	0.00	0.13	0.00	0.00	8.82	0.01	6.48	0.26	**98.50**	**42.32**
P11 / 1	SD-22-11C	Core	52.52	0.00	29.81	0.03	0.03	0.00	0.00	8.65	0.00	6.71	0.49	**98.25**	**40.45**
P12 / 1	SD-22-11C	Core	52.87	0.00	29.83	0.01	0.06	0.03	0.00	8.84	0.01	6.40	0.51	**98.55**	**42.01**
P13 / 1	SD-22-11C	Core	51.83	0.00	30.25	0.00	0.09	0.00	0.00	9.16	0.01	6.38	0.44	**98.16**	**43.11**
P15 / 1	SD-22-11C	Core	53.38	0.00	29.59	0.00	0.12	0.00	0.00	9.14	0.01	6.63	0.33	**99.20**	**43.11**
P16 / 1	SD-22-11C	Core	52.81	0.01	29.35	0.00	0.10	0.04	0.00	9.11	0.00	6.46	0.37	**98.25**	**42.89**
P17 / 1	SD-22-11C	Core	53.39	0.02	29.78	0.00	0.08	0.01	0.00	9.24	0.00	6.42	0.31	**99.24**	**43.54**
P18 / 1	SD-22-11C	Core	54.38	0.01	28.95	0.00	0.10	0.01	0.00	8.59	0.02	6.68	0.52	**99.26**	**40.33**
P21 / 1	SD-22-11C	Core	54.31	0.03	28.88	0.01	0.05	0.00	0.00	8.61	0.00	6.91	0.30	**99.09**	**40.10**
P22 / 1	SD-22-11C	Core	53.47	0.03	29.20	0.00	0.11	0.01	0.00	9.04	0.02	6.35	0.48	**98.70**	**42.85**
P23 / 1	SD-22-11C	Core	53.22	0.00	28.91	0.02	0.11	0.00	0.00	9.07	0.01	6.50	0.46	**98.30**	**42.41**
P25 / 1	SD-22-11C	Core	52.91	0.00	29.50	0.01	0.06	0.01	0.00	9.20	0.03	6.06	1.05	**98.84**	**42.97**
P34 / 1	SD-22-11C	Core	54.77	0.00	29.18	0.04	0.11	0.00	0.00	9.11	0.02	6.37	0.47	**100.07**	**42.97**
P118 / 1	SD-27-14	Shell	53.28	0.00	27.70	0.00	0.13	0.00	0.00	11.40	0.00	6.00	0.38	**98.89**	**50.21**
P119 / 1	SD-27-14	Shell	55.49	0.00	27.38	0.00	0.12	0.04	0.00	10.40	0.00	6.30	0.39	**100.12**	**46.70**
P120 / 1	SD-27-14	Shell	54.86	0.00	27.30	0.01	0.07	0.04	0.00	10.40	0.02	6.56	0.44	**99.70**	**45.62**
P121 / 1	SD-27-14	Shell	54.94	0.01	27.39	0.03	0.16	0.00	0.00	10.58	0.00	5.08	0.33	**98.51**	**52.48**

Table 27 continued

Point	Sample	C/M/S	SiO_2	TiO_2	Al_2O_3	$Cr2O_3$	FeO	MnO	MgO	CaO	BaO	Na_2O	K_2O	**Total**	**An**
P122 / 1	SD-27-14	Shell	54.94	0.02	27.03	0.00	0.16	0.00	0.00	10.38	0.00	6.60	0.38	**99.50**	**45.59**
P123 / 1	SD-27-14	Shell	55.65	0.04	27.12	0.01	0.10	0.01	0.00	10.27	0.02	6.71	0.31	**100.24**	**45.08**
P124 / 1	SD-28-14	Shell	55.63	0.02	28.18	0.00	0.12	0.00	0.00	10.42	0.00	6.61	0.30	**101.27**	**45.81**
P125 / 1	SD-27-14	Shell	55.50	0.04	27.36	0.00	0.09	0.00	0.00	10.51	0.01	6.34	0.30	**100.14**	**47.04**
P126 / 1	SD-27-14	Shell	55.83	0.01	27.06	0.00	0.12	0.01	0.00	9.83	0.03	6.86	0.36	**100.11**	**43.36**
P127 / 1	SD-27-14	Shell	56.07	0.00	27.29	0.00	0.10	0.00	0.00	10.38	0.00	6.37	0.30	**100.51**	**46.64**
P128 / 1	SD-27-14	Shell	55.30	0.00	27.21	0.00	0.07	0.00	0.00	10.25	0.00	6.63	0.39	**99.85**	**45.15**
P129 / 1	SD-27-14	Shell	55.35	0.02	27.36	0.00	0.18	0.04	0.00	10.52	0.02	6.42	0.38	**100.29**	**46.57**
P130 / 1	SD-27-14	Shell	55.16	0.02	27.30	0.00	0.09	0.00	0.00	10.32	0.00	6.64	0.41	**99.94**	**45.23**
P131 / 1	SD-27-14	Shell	55.13	0.00	27.90	0.00	0.09	0.00	0.00	10.87	0.02	6.19	0.38	**100.59**	**48.26**
P132 / 1	SD-27-14	Shell	55.19	0.02	27.33	0.00	0.06	0.01	0.00	10.31	0.02	6.62	0.44	**100.00**	**45.21**
P133 / 1	SD-27-14	Shell	54.99	0.00	27.04	0.00	0.11	0.00	0.00	10.27	0.00	6.53	0.45	**99.39**	**45.39**
P134 / 1	SD-27-14	Shell	55.04	0.03	27.07	0.00	0.11	0.00	0.00	10.14	0.01	6.59	0.42	**99.42**	**44.92**
P135 / 1	SD-27-14	Shell	55.37	0.00	27.16	0.00	0.17	0.01	0.00	10.47	0.02	6.69	0.37	**100.27**	**45.47**
P136 / 1	SD-27-14	Shell	54.43	0.03	27.14	0.00	0.14	0.00	0.00	10.46	0.01	6.42	0.41	**99.04**	**46.36**
P137 / 1	SD-26-14	Shell	55.73	0.00	26.77	0.03	0.12	0.00	0.00	10.14	0.02	6.32	0.43	**99.56**	**45.92**
P138 / 1	SD-26-14	Shell	55.55	0.00	26.55	0.00	0.16	0.00	0.00	10.67	0.03	6.73	0.41	**100.09**	**45.71**

Table 27 continued

Point	Sample	C/M/S	SiO_2	TiO_2	Al_2O_3	$Cr2O_3$	FeO	MnO	MgO	CaO	BaO	Na_2O	K_2O	**Total**	**An**
P139 / 1	SD-27-14	Shell	56.56	0.02	27.62	0.00	0.06	0.01	0.00	9.95	0.00	6.42	0.37	**101.01**	**45.22**
P140 / 1	SD-27-14	Shell	56.20	0.03	27.59	0.01	0.10	0.00	0.00	9.92	0.00	6.86	0.33	**101.03**	**43.65**
P141 / 1	SD-27-14	Shell	56.20	0.00	27.42	0.00	0.10	0.00	0.00	9.96	0.00	6.32	0.36	**100.37**	**45.64**
P142 / 1	SD-27-14	Shell	55.64	0.02	27.46	0.00	0.07	0.00	0.00	9.88	0.00	6.76	0.28	**100.11**	**44.03**
P143 / 1	SD-27-14	Shell	56.18	0.03	28.00	0.00	0.11	0.00	0.00	10.32	0.02	6.56	0.35	**101.57**	**45.65**
P92 / 1	SD-22-11D	Matrix	54.57	0.00	28.48	0.01	0.30	0.01	0.14	7.60	0.00	7.42	0.41	**98.94**	**35.30**
P93 / 1	SD-22-11D	Matrix	57.60	0.01	28.33	0.00	0.03	0.00	0.00	7.51	0.03	7.40	0.56	**101.47**	**34.84**
P94 / 1	SD-22-11D	Matrix	56.85	0.04	28.78	0.00	0.09	0.02	0.00	8.01	0.01	6.97	0.45	**101.22**	**37.86**
P95 / 1	SD-22-11D	Matrix	55.80	0.01	28.73	0.02	0.07	0.00	0.00	8.82	0.01	6.72	0.38	**100.55**	**41.15**
P98 / 1	SD-22-11D	Matrix	56.63	0.00	28.94	0.00	0.08	0.02	0.00	8.29	0.01	7.08	0.40	**101.45**	**38.43**
P100 / 1	SD-22-11D	Matrix	54.22	0.01	29.68	0.00	0.21	0.03	0.06	8.46	0.00	6.89	0.47	**100.02**	**39.39**
P101 / 1	SD-22-11D	Matrix	54.19	0.00	29.44	0.01	0.11	0.00	0.00	8.48	0.01	6.95	0.42	**99.60**	**39.33**
P102 / 1	SD-22-11D	Matrix	54.98	0.02	29.00	0.00	0.05	0.01	0.00	7.68	0.00	7.31	0.50	**99.55**	**35.74**
P103 / 1	SD-22-11D	Matrix	54.70	0.01	28.73	0.02	0.07	0.02	0.00	7.87	0.00	7.15	0.53	**99.10**	**36.73**
P106 / 1	SD-22-11D	Matrix	55.51	0.00	27.78	0.00	0.05	0.02	0.00	8.14	0.02	6.73	0.56	**98.79**	**38.78**
P107 / 1	SD-22-11D	Matrix	55.47	0.00	28.14	0.00	0.05	0.00	0.00	8.17	0.00	6.69	0.56	**99.07**	**39.03**
P108 / 1	SD-22-11D	Matrix	55.61	0.02	27.96	0.00	0.08	0.01	0.00	8.46	0.02	6.73	0.50	**99.39**	**39.85**

Table 27 continued

Point	Sample	C/M/S	SiO_2	TiO_2	Al_2O_3	$Cr2O_3$	FeO	MnO	MgO	CaO	BaO	Na_2O	K_2O	**Total**	**An**
P109 / 1	SD-22-11D	Matrix	55.63	0.04	28.52	0.00	0.06	0.01	0.00	8.73	0.00	6.68	0.45	**100.13**	**40.86**
P110 / 1	SD-22-11D	Matrix	55.45	0.00	28.33	0.03	0.08	0.00	0.00	8.58	0.03	6.80	0.35	**99.65**	**40.27**
P111 / 1	SD-22-11D	Matrix	55.32	0.03	28.78	0.00	0.13	0.00	0.01	8.39	0.02	6.65	0.30	**99.62**	**40.39**
P112 / 1	SD-22-11D	Matrix	56.57	0.03	28.06	0.00	0.02	0.01	0.00	7.86	0.03	7.29	0.39	**100.25**	**36.51**
P115 / 1	SD-22-11D	Matrix	57.06	0.00	28.07	0.00	0.09	0.00	0.00	7.75	0.02	7.18	0.58	**100.76**	**36.13**
P117 / 1	SD-22-11D	Matrix	56.61	0.00	28.43	0.01	0.08	0.02	0.00	8.27	0.00	7.21	0.30	**100.91**	**38.16**
P118 / 1	SD-22-11D	Matrix	56.14	0.01	27.75	0.02	0.04	0.00	0.00	8.24	0.02	6.63	0.79	**99.64**	**38.88**
P121 / 1	SD-22-11D	Matrix	54.83	0.04	30.11	0.00	0.07	0.00	0.00	8.97	0.02	6.70	0.33	**101.08**	**41.75**
P135 / 1	SD-22-11D	Matrix	56.36	0.00	28.42	0.00	0.05	0.02	0.00	8.48	0.00	6.99	0.25	**100.57**	**39.56**
P136 / 1	SD-22-11D	Matrix	57.07	0.00	28.34	0.00	0.00	0.00	0.00	7.98	0.00	6.99	0.47	**100.86**	**37.66**
P137 / 1	SD-22-11D	Matrix	56.98	0.01	28.13	0.00	0.12	0.02	0.00	8.49	0.02	6.76	0.46	**100.99**	**39.93**
P153 / 1	SD-22-11D	Matrix	58.89	0.00	27.30	0.02	0.06	0.02	0.00	7.75	0.01	7.24	0.47	**101.74**	**36.20**
P154 / 1	SD-22-11D	Matrix	56.10	0.01	28.05	0.00	0.08	0.00	0.00	8.24	0.01	6.77	0.43	**99.71**	**39.24**
P155 / 1	SD-22-11D	Matrix	57.36	0.03	27.34	0.00	0.02	0.01	0.00	7.75	0.00	7.13	0.54	**100.18**	**36.38**
P156 / 1	SD-22-11D	Matrix	59.46	0.04	26.85	0.00	0.05	0.01	0.00	7.37	0.00	7.16	0.57	**101.51**	**35.09**
P157 / 1	SD-22-11D	Matrix	58.73	0.00	27.69	0.03	0.09	0.00	0.00	8.01	0.01	6.69	0.49	**101.74**	**38.71**
P158 / 1	SD-22-11D	Matrix	57.30	0.01	28.09	0.00	0.06	0.00	0.00	8.73	0.00	6.47	0.46	**101.11**	**41.61**

Table 27: *Microprobe analyses of biotite from Hoogkraal Lease. C= Core, S=Shell and M= Matrix.*

Point	1 / 1	2 / 1	4 / 1	5 / 1	6 / 1	8 / 1	9 / 1	10 / 1	11 / 1	12 / 1	13 / 1	14 / 1	16 / 1
Sample	SD-22-11C	SD-22-11C	SD-22-11C	SD-22-11C	SD-22-11C	SD-22-11C	SD-22-11C	SD-22-11C	SD-22-11C	SD-22-11C	SD-22-11C	SD-22-11C	SD-22-11C
C/S/M	C	C	C	C	C	C	C	C	C	C	C	C	C
SiO_2	37.40	36.94	37.63	38.22	36.98	36.87	37.48	36.71	36.37	37.77	38.15	38.31	37.37
TiO_2	1.97	1.75	1.90	2.08	2.13	1.80	2.14	1.77	1.72	1.67	1.76	1.74	2.13
Al_2O_3	13.47	15.03	14.11	14.03	13.84	14.01	14.30	13.84	13.80	13.76	14.29	14.06	14.01
Cr_2O_3	0.09	0.02	0.08	0.04	0.04	0.05	0.11	0.07	0.06	0.04	0.03	0.04	0.04
MgO	18.33	17.08	14.25	16.72	14.34	13.94	16.35	14.81	14.17	17.69	16.90	17.45	16.19
CaO	0.01	0.04	0.00	0.00	0.26	0.00	0.00	0.01	0.00	0.00	0.00	0.00	0.01
MnO	0.12	0.23	0.28	0.18	0.32	0.28	0.16	0.29	0.31	0.13	0.17	0.13	0.21
FeO	11.53	13.49	15.89	12.16	15.85	15.95	12.32	14.96	16.53	11.52	11.95	11.54	12.84
Na_2O	0.09	0.10	0.04	0.06	0.03	0.09	0.09	0.08	0.03	0.05	0.03	0.05	0.06
K_2O	11.09	10.06	10.18	10.77	10.47	9.76	10.73	10.49	10.10	11.01	10.69	10.87	10.34
BaO	0.21	0.22	0.17	0.19	0.19	0.29	0.13	0.17	0.14	0.14	0.16	0.14	0.16
F	2.89	2.31	2.11	2.61	2.05	1.84	2.72	2.47	1.98	2.88	2.58	3.11	2.54
Cl	0.26	0.26	0.23	0.23	0.19	0.22	0.18	0.21	0.19	0.19	0.20	0.21	0.23
Li	1.01	0.70	0.61	0.85	0.58	0.48	0.91	0.78	0.54	1.01	0.84	1.14	0.82
H2O	2.86	3.09	3.11	2.99	3.11	3.14	2.92	2.92	3.08	2.87	3.00	2.82	2.95
Total	**101.33**	**101.31**	**100.58**	**101.13**	**100.39**	**98.73**	**100.53**	**99.58**	**99.02**	**100.72**	**100.75**	**101.61**	**99.91**

Number of ions based on 24 oxygens (O, OH, F, Cl)

Si	5.22	5.21	5.42	5.35	5.36	5.43	5.28	5.31	5.36	5.29	5.36	5.28	5.32
Ti	0.21	0.19	0.21	0.22	0.23	0.20	0.23	0.19	0.19	0.18	0.19	0.18	0.23
Al^{IV}	2.22	2.50	2.39	2.32	2.37	2.43	2.37	2.36	2.40	2.27	2.36	2.29	2.35
Al^{VI}	0.00	0.00	0.00	0.00	0.00	0.00	0.00	0.00	0.00	0.00	0.00	0.00	0.00
Cr	0.01	0.00	0.01	0.00	0.00	0.00	0.01	0.01	0.00	0.00	0.00	0.00	0.00
Mg	3.81	3.59	3.06	3.49	3.10	3.06	3.43	3.19	3.11	3.69	3.54	3.59	3.43
Ca	0.00	0.01	0.00	0.00	0.04	0.00	0.00	0.00	0.00	0.00	0.00	0.00	0.00
Mn	0.01	0.03	0.03	0.02	0.04	0.04	0.02	0.03	0.04	0.02	0.02	0.02	0.03
Fe^{2+}	1.35	1.59	1.91	1.42	1.92	1.96	1.45	1.81	2.04	1.35	1.40	1.33	1.53
Na	0.02	0.03	0.01	0.01	0.01	0.03	0.02	0.02	0.01	0.01	0.01	0.01	0.02
K	1.97	1.81	1.87	1.92	1.94	1.83	1.93	1.94	1.90	1.97	1.91	1.91	1.88
Ba	0.02	0.02	0.02	0.02	0.02	0.03	0.01	0.02	0.02	0.02	0.02	0.02	0.02
F	1.27	1.03	0.96	1.16	0.94	0.86	1.21	1.13	0.92	1.27	1.15	1.36	1.14
Cl	0.06	0.06	0.06	0.05	0.05	0.05	0.04	0.05	0.05	0.05	0.05	0.05	0.06
Li*	0.28	0.20	0.18	0.24	0.17	0.14	0.26	0.23	0.16	0.28	0.24	0.32	0.23
OH-	2.66	2.91	2.98	2.79	3.01	3.09	2.75	2.82	3.03	2.68	2.81	2.59	2.80
Mg/(Mg + Fe)	**0.74**	**0.69**	**0.62**	**0.71**	**0.62**	**0.61**	**0.70**	**0.64**	**0.60**	**0.73**	**0.72**	**0.73**	**0.69**

Table 28 continued

Point	17 / 1	18 / 1	19 / 1	20 / 1	21 / 1	22 / 1	23 / 1	24 / 1	26 / 1	27 / 1	28 / 1	29 / 1	30 / 1
Sample	SD-22-11C	SD-22-11C	SD-22-11C	SD-22-11C	SD-22-11C	SD-22-11C	SD-22-11C	SD-22-11C	SD-22-11C	SD-22-11C	SD-22-11C	SD-22-11C	SD-22-11C
C/S/M	C	C	C	C	C	C	C	C	C	C	C	C	C
SiO_2	37.64	37.35	37.41	37.76	37.88	37.76	37.90	37.22	36.43	38.24	38.09	38.42	38.30
TiO_2	2.04	2.24	1.65	1.59	1.64	1.66	1.70	1.65	1.14	1.51	1.42	1.44	1.52
$Al2O_3$	14.31	13.63	14.10	14.30	14.39	14.16	14.73	14.34	14.02	14.47	14.20	14.40	14.40
Cr_2O_3	0.01	0.07	0.06	0.04	0.10	0.05	0.08	0.06	0.07	0.09	0.05	0.06	0.07
MgO	16.62	16.37	15.77	17.22	17.55	16.02	17.32	14.42	14.97	17.80	14.77	17.02	15.75
CaO	0.00	0.00	0.02	0.00	0.00	0.03	0.02	0.00	0.02	0.01	0.03	0.00	0.00
MnO	0.16	0.12	0.30	0.17	0.11	0.22	0.12	0.25	0.30	0.08	0.27	0.15	0.27
FeO	12.19	13.43	13.60	11.91	11.52	14.00	11.82	14.94	14.75	10.87	14.48	11.68	13.67
Na_2O	0.05	0.06	0.08	0.03	0.05	0.08	0.09	0.06	0.08	0.02	0.10	0.07	0.07
K_2O	10.85	10.72	10.48	10.97	10.91	10.25	10.61	10.47	9.93	10.81	9.44	10.78	10.42
BaO	0.14	0.13	0.13	0.16	0.17	0.12	0.17	0.13	0.18	0.22	0.12	0.16	0.14
F	2.25	2.81	2.65	2.75	2.62	2.44	2.83	2.47	2.04	2.92	2.26	2.86	2.88
Cl	0.21	0.22	0.20	0.23	0.22	0.20	0.24	0.20	0.30	0.24	0.27	0.23	0.24
Li	0.67	0.97	0.88	0.93	0.86	0.77	0.98	0.78	0.57	1.03	0.67	1.00	1.00
H_2O	3.10	2.87	2.91	2.92	2.99	3.02	2.92	2.95	3.02	2.89	3.03	2.90	2.88
Total	**100.25**	**100.98**	**100.23**	**100.98**	**101.01**	**100.77**	**101.53**	**99.95**	**97.84**	**101.21**	**99.21**	**101.17**	**101.62**

Number of ions based on 24 oxygens (O, OH, F, Cl)

Si	5.35	5.26	5.32	5.29	5.30	5.35	5.26	5.35	5.38	5.29	5.48	5.34	5.34
Ti	0.22	0.24	0.18	0.17	0.17	0.18	0.18	0.18	0.13	0.16	0.15	0.15	0.16
Al^{IV}	2.40	2.26	2.36	2.36	2.37	2.37	2.41	2.43	2.44	2.36	2.41	2.36	2.36
Al^{VI}	0.00	0.00	0.00	0.00	0.00	0.00	0.00	0.00	0.00	0.00	0.00	0.00	0.00
Cr	0.00	0.01	0.00	0.00	0.01	0.00	0.01	0.00	0.01	0.01	0.00	0.00	0.01
Mg	3.52	3.44	3.34	3.59	3.66	3.39	3.58	3.09	3.30	3.67	3.17	3.53	3.27
Ca	0.00	0.00	0.00	0.00	0.00	0.00	0.00	0.00	0.00	0.00	0.00	0.00	0.00
Mn	0.02	0.01	0.04	0.02	0.01	0.03	0.01	0.03	0.04	0.01	0.03	0.02	0.03
Fe^{2+}	1.45	1.58	1.62	1.39	1.35	1.66	1.37	1.80	1.82	1.26	1.74	1.36	1.59
Na	0.01	0.02	0.02	0.01	0.01	0.02	0.03	0.02	0.02	0.01	0.03	0.02	0.02
K	1.97	1.93	1.90	1.96	1.95	1.85	1.88	1.92	1.87	1.91	1.73	1.91	1.85
Ba	0.02	0.01	0.01	0.02	0.02	0.01	0.02	0.01	0.02	0.02	0.01	0.02	0.02
F	1.01	1.25	1.19	1.22	1.16	1.10	1.24	1.12	0.95	1.28	1.03	1.26	1.27
Cl	0.05	0.05	0.05	0.05	0.05	0.05	0.06	0.05	0.08	0.06	0.07	0.05	0.06
Li*	0.19	0.27	0.25	0.26	0.24	0.22	0.27	0.23	0.17	0.29	0.19	0.28	0.28
OH^-	2.94	2.70	2.76	2.73	2.79	2.86	2.70	2.83	2.97	2.67	2.91	2.69	2.67
Mg/(Mg + Fe)	**0.71**	**0.68**	**0.67**	**0.72**	**0.73**	**0.67**	**0.72**	**0.63**	**0.64**	**0.74**	**0.65**	**0.72**	**0.67**

Table 28 continued

Dataset/Point	83 / 1	84 / 1	85 / 1	86 / 1	87 / 1	89 / 1	93 / 1	94 / 1	95 / 1	96 / 1	97 / 1	98 / 1	99 / 1
Sample	SD-27-14	SD-27-1	SD-27-14	SD-27-14	SD-27-14	SD-27-14	SD-27-14	SD-27-1	SD-27-14	SD-27-14	SD-27-14	SD-27-14	SD-27-14
C/S/M	S	S	S	S	S	S	S	S	S	S	S	S	S
SiO_2	39.04	39.10	38.98	38.92	38.89	38.21	38.80	39.51	39.13	38.97	38.92	39.10	39.75
TiO_2	4.66	4.48	4.23	4.61	4.21	4.38	4.31	4.14	4.36	4.04	4.33	4.48	4.32
Al_2O_3	13.30	13.27	13.40	13.05	13.23	13.22	13.01	12.81	13.47	12.39	13.48	13.16	13.49
Cr_2O_3	0.08	0.05	0.09	0.11	0.08	0.10	0.09	0.08	0.09	0.05	0.06	0.07	0.08
MgO	15.85	15.90	15.49	15.92	15.59	16.01	15.79	15.11	15.43	15.23	15.61	15.71	15.72
CaO	0.00	0.00	0.00	0.00	0.00	0.04	0.07	0.04	0.00	0.02	0.00	0.00	0.00
MnO	0.06	0.10	0.09	0.10	0.08	0.05	0.08	0.12	0.03	0.08	0.06	0.09	0.08
FeO	12.25	12.65	12.32	12.34	12.62	12.07	12.17	12.89	12.17	13.68	12.08	11.86	11.83
Na_2O	0.07	0.05	0.04	0.08	0.06	0.09	0.11	0.07	0.10	0.11	0.12	0.05	0.08
K_2O	10.61	10.52	10.46	10.49	10.19	10.38	9.70	9.60	10.49	9.90	10.35	10.32	10.36
BaO	0.19	0.20	0.18	0.18	0.20	0.21	0.23	0.20	0.19	0.20	0.18	0.15	0.18
F	0.97	0.64	0.87	0.71	0.72	0.68	0.81	0.67	0.82	0.69	0.81	1.03	0.70
Cl	0.21	0.19	0.21	0.20	0.18	0.22	0.21	0.19	0.21	0.22	0.20	0.21	0.21
Li	0.17	0.08	0.14	0.10	0.10	0.09	0.13	0.09	0.13	0.10	0.13	0.19	0.10
H2O	3.67	3.80	3.67	3.75	3.73	3.72	3.67	3.74	3.70	3.69	3.70	3.61	3.78
Total	**101.12**	**101.03**	**100.18**	**100.56**	**99.87**	**99.46**	**99.19**	**99.24**	**100.34**	**99.38**	**100.03**	**100.04**	**100.68**

Number of ions based on 24 oxygens (O, OH, F, Cl)

Si	5.60	5.65	5.65	5.64	5.67	5.60	5.67	5.78	5.66	5.73	5.65	5.64	5.72
Ti	0.50	0.49	0.46	0.50	0.46	0.48	0.47	0.46	0.47	0.45	0.47	0.49	0.47
Al^{IV}	2.25	2.26	2.29	2.23	2.27	2.28	2.24	2.21	2.30	2.15	2.30	2.24	2.28
Al^{VI}	0.00	0.00	0.00	0.00	0.00	0.00	0.00	0.00	0.00	0.00	0.00	0.00	0.01
Cr	0.01	0.00	0.01	0.01	0.01	0.01	0.01	0.01	0.01	0.00	0.00	0.01	0.01
Mg	3.39	3.43	3.35	3.44	3.39	3.50	3.44	3.30	3.33	3.34	3.37	3.38	3.37
Ca	0.00	0.00	0.00	0.00	0.00	0.01	0.01	0.01	0.00	0.00	0.00	0.00	0.00
Mn	0.01	0.01	0.01	0.01	0.01	0.01	0.01	0.02	0.00	0.01	0.01	0.01	0.01
Fe^{2+}	1.47	1.53	1.49	1.50	1.54	1.48	1.49	1.58	1.47	1.68	1.47	1.43	1.42
Na	0.02	0.01	0.01	0.02	0.02	0.03	0.03	0.02	0.03	0.03	0.03	0.01	0.02
K	1.94	1.94	1.93	1.94	1.89	1.94	1.81	1.79	1.94	1.86	1.92	1.90	1.90
Ba	0.02	0.02	0.02	0.02	0.02	0.02	0.03	0.02	0.02	0.02	0.02	0.02	0.02
F	0.44	0.29	0.40	0.33	0.33	0.31	0.37	0.31	0.38	0.32	0.37	0.47	0.32
Cl	0.05	0.05	0.05	0.05	0.05	0.05	0.05	0.05	0.05	0.06	0.05	0.05	0.05
Li*	0.05	0.02	0.04	0.03	0.03	0.03	0.04	0.03	0.04	0.03	0.04	0.05	0.03
OH^-	3.51	3.66	3.55	3.62	3.62	3.63	3.57	3.65	3.57	3.62	3.58	3.48	3.63
Mg/(Mg + Fe)	**0.70**	**0.69**	**0.69**	**0.70**	**0.69**	**0.70**	**0.70**	**0.68**	**0.69**	**0.66**	**0.70**	**0.70**	**0.70**

Table 28 continued

Point	100 / 1	101 / 1	102 / 1	103 / 1	104 / 1	105 / 1	107 / 1	108 / 1	110 / 1	111 / 1	112 / 1	113 / 1	114 / 1
Sample	SD-27-14	SD-27-14	SD-27-14	SD-27-14	SD-27-14	SD-27-14	SD-27-14	SD-27-14	SD-27-14	SD-27-14	SD-27-14	SD-27-14	SD-27-14
C/S/M	S	S	S	S	S	S	S	S	S	S	S	S	S
SiO_2	39.88	39.33	40.65	38.32	39.62	38.17	38.00	40.00	38.39	39.09	38.33	38.48	39.33
TiO_2	4.68	4.55	4.67	4.25	4.30	4.31	4.38	4.26	4.41	4.61	4.55	4.55	4.55
Al_2O_3	13.50	13.19	12.95	13.14	12.77	13.17	13.12	12.85	13.19	12.84	13.18	13.15	13.20
Cr_2O_3	0.06	0.07	0.08	0.08	0.07	0.05	0.09	0.08	0.09	0.03	0.06	0.08	0.07
MgO	15.78	15.42	15.32	16.11	14.48	15.94	15.87	15.13	14.75	15.32	14.59	13.74	15.86
CaO	0.01	0.00	0.00	0.00	0.01	0.04	0.01	0.22	0.07	0.02	0.04	0.02	0.01
MnO	0.06	0.06	0.08	0.05	0.13	0.08	0.11	0.14	0.14	0.13	0.13	0.14	0.09
FeO	12.26	11.64	11.66	12.25	13.66	12.04	12.03	11.91	13.50	12.81	13.55	14.30	11.77
Na_2O	0.07	0.09	0.17	0.05	0.11	0.11	0.07	0.27	0.10	0.10	0.17	0.23	0.17
K_2O	10.40	10.43	10.26	10.69	10.31	9.82	9.72	9.83	9.96	10.34	10.18	9.95	10.30
BaO	0.21	0.19	0.17	0.26	0.22	0.20	0.24	0.21	0.21	0.18	0.22	0.19	0.19
F	0.66	0.81	0.94	0.67	0.54	0.98	0.87	0.92	0.87	0.73	0.68	0.63	0.56
Cl	0.19	0.19	0.20	0.20	0.22	0.22	0.14	0.21	0.21	0.20	0.24	0.24	0.23
Li	0.09	0.12	0.16	0.09	0.07	0.17	0.14	0.15	0.14	0.11	0.09	0.08	0.07
H2O	3.84	3.70	3.71	3.73	3.79	3.58	3.62	3.66	3.63	3.72	3.70	3.70	3.81
Total	**101.68**	**99.80**	**101.01**	**99.90**	**100.30**	**98.88**	**98.40**	**99.82**	**99.66**	**100.24**	**99.71**	**99.48**	**100.21**

Number of ions based on 24 (O, OH, F, Cl)

Si	5.70	5.70	5.79	5.61	5.79	5.58	5.60	5.78	5.62	5.69	5.63	5.68	5.71
Ti	0.50	0.50	0.50	0.47	0.47	0.47	0.48	0.46	0.49	0.50	0.50	0.51	0.50
Al^{IV}	2.27	2.26	2.17	2.27	2.20	2.27	2.28	2.19	2.28	2.20	2.28	2.29	2.26
Al^{VI}	0.00	0.00	0.00	0.00	0.00	0.00	0.00	0.00	0.00	0.00	0.00	0.00	0.00
Cr	0.00	0.01	0.01	0.01	0.01	0.00	0.01	0.01	0.01	0.00	0.00	0.01	0.01
Mg	3.36	3.33	3.25	3.51	3.15	3.48	3.48	3.26	3.22	3.32	3.20	3.03	3.43
Ca	0.00	0.00	0.00	0.00	0.00	0.01	0.00	0.03	0.01	0.00	0.01	0.00	0.00
Mn	0.01	0.01	0.01	0.01	0.02	0.01	0.01	0.02	0.02	0.02	0.02	0.02	0.01
Fe^{2+}	1.46	1.41	1.39	1.50	1.67	1.47	1.48	1.44	1.65	1.56	1.67	1.77	1.43
Na	0.02	0.03	0.05	0.01	0.03	0.03	0.02	0.08	0.03	0.03	0.05	0.06	0.05
K	1.90	1.93	1.86	2.00	1.92	1.83	1.83	1.81	1.86	1.92	1.91	1.88	1.91
Ba	0.02	0.02	0.02	0.03	0.03	0.02	0.03	0.02	0.02	0.02	0.03	0.02	0.02
F	0.30	0.37	0.42	0.31	0.25	0.45	0.41	0.42	0.40	0.34	0.32	0.29	0.26
Cl	0.05	0.05	0.05	0.05	0.05	0.06	0.04	0.05	0.05	0.05	0.06	0.06	0.06
Li*	0.03	0.04	0.05	0.03	0.02	0.05	0.04	0.04	0.04	0.03	0.03	0.02	0.02
OH-	3.66	3.58	3.53	3.64	3.69	3.49	3.56	3.53	3.55	3.61	3.62	3.65	3.69
Mg/(Mg + Fe)	**0.70**	**0.70**	**0.70**	**0.70**	**0.65**	**0.70**	**0.70**	**0.69**	**0.66**	**0.68**	**0.66**	**0.63**	**0.71**

Table 28 Continued

Point	43 / 1	44 / 1	45 / 1	46 / 1	47 / 1	48 / 1	49 / 1	50 / 1	51 / 1	52 / 1	53 / 1	54 / 1	55 / 1
Sample	SD-22-11D	SD-22-11D	SD-22-11D	SD-22-11D	SD-22-11D	SD-22-11D	SD-22-11D	SD-22-11D	SD-22-11D	SD-22-11D	SD-22-11D	SD-22-11D	SD-22-11D
C/S/M	M	M	M	M	M	M	M	M	M	M	M	M	M
SiO_2	36.92	37.43	36.98	36.86	36.89	37.77	36.97	37.01	36.82	37.25	36.64	36.40	37.81
TiO_2	3.19	3.66	3.05	3.21	3.12	2.73	2.74	3.08	3.07	2.93	3.01	2.92	2.58
Al_2O_3	14.93	14.75	14.82	14.40	14.79	14.90	14.52	14.22	14.53	14.71	14.14	14.18	14.51
Cr_2O_3	0.00	0.02	0.00	0.00	0.03	0.03	0.01	0.01	0.01	0.04	0.00	0.02	0.00
MgO	14.88	15.31	15.89	15.99	15.79	15.89	15.70	15.79	15.85	16.10	15.71	15.65	15.14
CaO	0.00	0.00	0.00	0.00	0.00	0.00	0.00	0.00	0.00	0.00	0.01	0.01	0.02
MnO	0.17	0.18	0.14	0.12	0.06	0.21	0.27	0.17	0.15	0.11	0.14	0.13	0.24
FeO	12.42	12.54	12.36	12.09	12.36	12.37	12.64	13.05	12.55	12.53	12.55	12.65	12.75
Na_2O	0.15	0.08	0.06	0.10	0.06	0.09	0.05	0.05	0.08	0.10	0.09	0.07	0.06
K_2O	10.46	10.65	10.58	10.73	10.67	10.56	10.70	10.65	10.82	10.75	10.83	10.43	10.18
BaO	0.12	0.17	0.19	0.16	0.15	0.15	0.14	0.16	0.18	0.18	0.17	0.14	0.17
F	2.48	2.21	2.40	2.32	2.49	2.45	2.73	2.62	2.44	2.31	2.13	2.22	2.07
Cl	0.25	0.23	0.20	0.22	0.21	0.22	0.21	0.24	0.26	0.20	0.21	0.22	0.22
Li	0.79	0.65	0.75	0.71	0.79	0.77	0.92	0.86	0.77	0.70	0.61	0.66	0.59
H2O	2.97	3.14	3.04	3.05	3.00	3.06	2.90	2.94	3.00	3.10	3.09	3.03	3.14
Total	**99.73**	**101.01**	**100.46**	**99.95**	**100.41**	**101.21**	**100.50**	**100.86**	**100.52**	**100.99**	**99.33**	**98.72**	**99.48**

Number of ions based on 24 oxygen (O, OH, F, Cl)

Si	5.26	5.29	5.24	5.26	5.22	5.30	5.22	5.23	5.23	5.26	5.29	5.27	5.42
Ti	0.34	0.39	0.33	0.34	0.33	0.29	0.29	0.33	0.33	0.31	0.33	0.32	0.28
Al^{IV}	2.51	2.46	2.47	2.42	2.47	2.46	2.42	2.37	2.43	2.45	2.41	2.42	2.45
Al^{VI}	0.00	0.00	0.00	0.00	0.00	0.00	0.00	0.00	0.00	0.00	0.00	0.00	0.00
Cr	0.00	0.00	0.00	0.00	0.00	0.00	0.00	0.00	0.00	0.00	0.00	0.00	0.00
Mg	3.16	3.23	3.36	3.40	3.33	3.32	3.31	3.32	3.35	3.39	3.38	3.38	3.24
Ca	0.00	0.00	0.00	0.00	0.00	0.00	0.00	0.00	0.00	0.00	0.00	0.00	0.00
Mn	0.02	0.02	0.02	0.01	0.01	0.03	0.03	0.02	0.02	0.01	0.02	0.02	0.03
Fe^{2+}	1.48	1.48	1.46	1.44	1.46	1.45	1.49	1.54	1.49	1.48	1.52	1.53	1.53
Na	0.04	0.02	0.02	0.03	0.02	0.02	0.01	0.01	0.02	0.03	0.03	0.02	0.02
K	1.90	1.92	1.91	1.95	1.93	1.89	1.93	1.92	1.96	1.94	2.00	1.93	1.86
Ba	0.01	0.02	0.02	0.02	0.02	0.02	0.02	0.02	0.02	0.02	0.02	0.02	0.02
F	1.12	0.99	1.08	1.05	1.12	1.09	1.22	1.17	1.10	1.03	0.97	1.02	0.94
Cl	0.06	0.06	0.05	0.05	0.05	0.05	0.05	0.06	0.06	0.05	0.05	0.05	0.05
Li*	0.23	0.19	0.21	0.20	0.23	0.22	0.26	0.24	0.22	0.20	0.18	0.19	0.17
OH^-	2.82	2.96	2.87	2.90	2.83	2.86	2.73	2.77	2.84	2.92	2.98	2.93	3.01
Mg/(Mg + Fe)	**0.68**	**0.69**	**0.70**	**0.70**	**0.69**	**0.70**	**0.69**	**0.68**	**0.69**	**0.70**	**0.69**	**0.69**	**0.68**

Table 28 continued

Point	56 / 1	57 / 1	58 / 1	59 / 1	60 / 1	61 / 1	62 / 1	63 / 1	64 / 1	65 / 1	80 / 1	81 / 1	82 / 1
Sample	SD-22-11D	SD-22-11D	SD-22-11D	SD-22-11D	SD-22-11D	SD-2211D	SD-22-11D	SD-22-11D	SD-22-11D	SD-22-11D	SD-22-11D	SD-22-11D	SD-22-11D
C/S/M	M	M	M	M	M	M	M	M	M	M	M	M	M
SiO_2	38.39	38.13	37.87	37.49	37.23	36.86	36.75	37.27	37.24	37.22	35.96	37.40	37.01
TiO_2	3.42	3.03	2.73	2.36	2.34	2.39	2.44	2.66	1.83	1.78	3.02	3.52	3.68
Al_2O_3	14.29	14.15	14.64	14.08	14.14	13.87	14.09	14.06	15.00	13.99	14.17	14.08	14.30
Cr_2O_3	0.00	0.00	0.00	0.01	0.05	0.00	0.02	0.02	0.01	0.00	0.01	0.00	0.02
MgO	14.88	15.50	14.85	16.54	16.41	16.59	15.86	15.84	14.58	16.18	12.82	15.39	14.33
CaO	0.00	0.00	0.04	0.00	0.00	0.00	0.00	0.00	0.00	0.00	0.01	0.02	0.00
MnO	0.13	0.20	0.23	0.15	0.23	0.18	0.18	0.15	0.28	0.11	0.27	0.15	0.23
FeO	13.05	12.55	13.00	12.32	12.09	11.46	12.67	12.40	13.27	12.65	15.71	12.39	13.68
Na_2O	0.08	0.05	0.09	0.07	0.05	0.08	0.06	0.11	0.10	0.05	0.13	0.10	0.09
K_2O	10.61	10.82	10.17	10.84	10.76	10.79	10.63	10.72	10.19	10.87	9.90	10.48	10.54
BaO	0.17	0.17	0.10	0.19	0.18	0.20	0.20	0.17	0.19	0.19	0.16	0.14	0.10
F	2.00	2.27	2.20	2.54	2.44	2.28	2.36	2.26	2.07	2.53	1.92	2.31	1.99
Cl	0.24	0.23	0.23	0.19	0.22	0.23	0.20	0.22	0.23	0.26	0.19	0.20	0.22
Li	0.55	0.68	0.64	0.82	0.77	0.69	0.73	0.68	0.58	0.81	0.52	0.70	0.55
H_2O	3.22	3.11	3.11	2.99	3.00	3.02	2.99	3.05	3.10	2.93	3.08	3.06	3.16
Total	**101.03**	**100.90**	**99.90**	**100.59**	**99.90**	**98.63**	**99.19**	**99.61**	**98.65**	**99.56**	**97.86**	**99.95**	**99.90**

Number of ions based on 24 oxygen (O, OH, F, Cl)

Si	5.44	5.39	5.40	5.30	5.30	5.32	5.29	5.34	5.40	5.32	5.35	5.33	5.34
Ti	0.37	0.32	0.29	0.25	0.25	0.26	0.26	0.29	0.20	0.19	0.34	0.38	0.40
Al^{IV}	2.39	2.36	2.46	2.34	2.37	2.36	2.39	2.37	2.56	2.36	2.48	2.36	2.43
Al^{VI}	0.00	0.00	0.00	0.00	0.00	0.00	0.00	0.00	0.00	0.00	0.00	0.00	0.00
Cr	0.00	0.00	0.00	0.00	0.00	0.00	0.00	0.00	0.00	0.00	0.00	0.00	0.00
Mg	3.14	3.27	3.16	3.49	3.48	3.57	3.40	3.38	3.15	3.45	2.84	3.27	3.08
Ca	0.00	0.00	0.01	0.00	0.00	0.00	0.00	0.00	0.00	0.00	0.00	0.00	0.00
Mn	0.02	0.02	0.03	0.02	0.03	0.02	0.02	0.02	0.03	0.01	0.03	0.02	0.03
Fe^{2+}	1.55	1.48	1.55	1.46	1.44	1.38	1.53	1.49	1.61	1.51	1.95	1.48	1.65
Na	0.02	0.01	0.03	0.02	0.01	0.02	0.02	0.03	0.03	0.01	0.04	0.03	0.02
K	1.92	1.95	1.85	1.95	1.95	1.99	1.95	1.96	1.89	1.98	1.88	1.91	1.94
Ba	0.02	0.02	0.01	0.02	0.02	0.02	0.02	0.02	0.02	0.02	0.02	0.02	0.01
F	0.90	1.01	0.99	1.13	1.10	1.04	1.08	1.03	0.95	1.14	0.90	1.04	0.91
Cl	0.06	0.06	0.06	0.05	0.05	0.06	0.05	0.05	0.06	0.06	0.05	0.05	0.05
Li*	0.16	0.19	0.18	0.23	0.22	0.20	0.21	0.20	0.17	0.23	0.15	0.20	0.16
OH-	3.05	2.93	2.95	2.82	2.85	2.90	2.88	2.92	2.99	2.79	3.05	2.91	3.04
Mg/(Mg + Fe)	**0.67**	**0.69**	**0.67**	**0.71**	**0.71**	**0.72**	**0.69**	**0.69**	**0.66**	**0.70**	**0.59**	**0.69**	**0.65**

Table 28 continued

Point	83 / 1	84 / 1	85 / 1	86 / 1	87 / 1	89 / 1	90 / 1	93 / 1	96 / 1	97 / 1	98 / 1	99 / 1	100 / 1
Sample	SD-22-11D	SD-22-11D	SD-22-11D	SD-22-11D	SD-22-11D	SD-22-11D	SD-22-11D	SD-22-11D	SD-22-11D	SD-22-11D	SD-22-11D	SD-22-11D	SD-22-11D
C/S/M	M	M	M	M	M	M	M	M	M	M	M	M	M
SiO_2	37.55	37.54	37.77	36.99	36.76	38.22	37.38	38.54	37.57	37.19	37.41	37.54	37.17
TiO_2	3.30	2.52	3.28	3.63	2.70	3.19	3.43	2.21	3.27	3.25	3.22	3.30	3.06
$Al2O_3$	14.12	15.90	13.98	14.05	17.36	15.62	15.54	17.63	15.53	15.19	15.45	15.55	15.46
Cr_2O_3	0.00	0.01	0.02	0.04	0.02	0.01	0.00	0.00	0.01	0.00	0.04	0.01	0.00
MgO	15.29	14.45	15.84	13.41	12.02	15.21	15.06	13.58	14.33	15.15	15.08	15.37	15.54
CaO	0.03	0.03	0.02	0.01	0.03	0.04	0.01	0.04	0.03	0.01	0.00	0.00	0.01
MnO	0.16	0.14	0.21	0.30	0.25	0.12	0.17	0.21	0.25	0.20	0.20	0.14	0.20
FeO	12.39	12.18	12.19	14.84	15.23	12.31	12.07	12.48	13.50	12.61	12.74	12.20	12.46
Na_2O	0.18	0.13	0.08	0.09	0.08	0.15	0.11	0.14	0.09	0.08	0.11	0.09	0.11
K_2O	10.09	8.90	10.52	10.05	8.35	9.96	10.32	8.56	9.57	10.34	10.68	10.73	10.26
BaO	0.14	0.13	0.10	0.15	0.10	0.14	0.15	0.09	0.11	0.14	0.13	0.16	0.17
F	2.12	2.15	2.27	1.92	1.36	2.14	2.14	1.62	2.23	2.51	2.23	1.89	1.99
Cl	0.21	0.21	0.21	0.23	0.18	0.24	0.25	0.21	0.22	0.23	0.24	0.24	0.21
Li	0.61	0.62	0.68	0.51	0.29	0.62	0.62	0.39	0.66	0.80	0.66	0.50	0.55
H_2O	3.12	3.10	3.09	3.15	3.39	3.20	3.16	3.39	3.12	3.01	3.14	3.28	3.22
Total	**99.32**	**98.03**	**100.28**	**99.37**	**98.13**	**101.18**	**100.40**	**99.10**	**100.50**	**100.71**	**101.33**	**101.00**	**100.40**

Number of ions based on 24 oxygens (O, OH, F, Cl)

Si	5.39	5.39	5.36	5.39	5.40	5.35	5.29	5.49	5.32	5.24	5.27	5.32	5.29
Ti	0.36	0.27	0.35	0.40	0.30	0.34	0.37	0.24	0.35	0.34	0.34	0.35	0.33
Al^{IV}	2.39	2.61	2.34	2.41	2.60	2.58	2.59	2.51	2.59	2.52	2.57	2.60	2.59
Al^{VI}	0.00	0.08	0.00	0.00	0.40	0.00	0.00	0.45	0.00	0.00	0.00	0.00	0.00
Cr	0.00	0.00	0.00	0.00	0.00	0.00	0.00	0.00	0.00	0.00	0.00	0.00	0.00
Mg	3.27	3.09	3.35	2.91	2.63	3.18	3.18	2.88	3.02	3.18	3.17	3.25	3.30
Ca	0.00	0.00	0.00	0.00	0.00	0.01	0.00	0.01	0.00	0.00	0.00	0.00	0.00
Mn	0.02	0.02	0.03	0.04	0.03	0.01	0.02	0.02	0.03	0.02	0.02	0.02	0.02
Fe^{2+}	1.49	1.46	1.45	1.81	1.87	1.44	1.43	1.49	1.60	1.49	1.50	1.45	1.48
Na	0.05	0.04	0.02	0.02	0.02	0.04	0.03	0.04	0.02	0.02	0.03	0.03	0.03
K	1.85	1.63	1.91	1.87	1.56	1.78	1.87	1.56	1.73	1.86	1.92	1.94	1.86
Ba	0.02	0.01	0.01	0.02	0.01	0.02	0.02	0.01	0.01	0.02	0.01	0.02	0.02
F	0.96	0.98	1.02	0.88	0.63	0.95	0.96	0.73	1.00	1.12	0.99	0.85	0.90
Cl	0.05	0.05	0.05	0.06	0.05	0.06	0.06	0.05	0.05	0.05	0.06	0.06	0.05
Li*	0.18	0.18	0.19	0.15	0.09	0.17	0.18	0.11	0.19	0.23	0.19	0.14	0.16
OH^-	2.98	2.97	2.93	3.06	3.32	2.99	2.98	3.22	2.95	2.83	2.95	3.10	3.05
Mg/(Mg + Fe)	**0.69**	**0.68**	**0.70**	**0.62**	**0.58**	**0.69**	**0.69**	**0.66**	**0.65**	**0.68**	**0.68**	**0.69**	**0.69**

Table 28: *Henderson North plagioclase data.*

Point	Sample	C/M/S	SiO_2	TiO_2	Al_2O_3	Cr_2O_3	FeO	MnO	MgO	CaO	BaO	Na_2O	K_2O	**Total**	**An**
P142 / 1	SD-36-18C	Core	57.05	0.00	27.56	0.01	0.09	0.00	0.00	11.86	0.02	3. 87	0.43	**100.88**	**61.19**
P143 / 1	SD-36-18C	Core	55.88	0.02	28.76	0.00	0.09	0.01	0.00	11.83	0.01	3.92	0.43	**100.95**	**60.88**
P144 / 1	SD-36-18C	Core	57.55	0.00	27.78	0.00	0.04	0.00	0.00	11.29	0.01	4.04	0.75	**101.47**	**57.94**
P145 / 1	SD-36-18C	Core	57.14	0.01	27.56	0.01	0.08	0.00	0.00	11.48	0.00	4.09	0.48	**100.86**	**59.01**
P146 / 1	SD-36-18C	Core	56.39	0.01	26.95	0.00	0.03	0.01	0.00	11.46	0.01	4.14	0.58	**99.59**	**58.33**
P147 / 1	SD-36-18C	Core	55.73	0.03	27.54	0.03	0.07	0.01	0.00	12.07	0.01	4.13	0.29	**99.91**	**60.69**
P148 / 1	SD-36-18C	Core	55.58	0.00	27.24	0.00	0.08	0.02	0.00	11.73	0.00	4.08	0.51	**99.23**	**59.50**
P149 / 1	SD-36-18C	Core	56.28	0.00	27.53	0.00	0.05	0.01	0.00	11.95	0.01	3.96	0.47	**100.25**	**60.76**
P150 / 1	SD-36-18C	Core	55.88	0.01	26.67	0.01	0.08	0.00	0.00	11.47	0.01	4.08	0.38	**98.59**	**59.40**
P151 / 1	SD-36-18C	Core	55.29	0.00	28.35	0.04	0.04	0.00	0.00	11.53	0.00	4.20	0.61	**100.06**	**58.07**
P152 / 1	SD-36-18C	Core	55.32	0.01	26.95	0.03	0.05	0.02	0.00	12.07	0.00	4.21	0.42	**99.09**	**59.76**
P155 / 1	SD-36-18C	Core	56.47	0.02	26.79	0.00	0.07	0.02	0.00	11.54	0.02	4.08	0.62	**99.62**	**58.69**
P157 / 1	SD-36-18C	Core	56.06	0.02	27.08	0.00	0.05	0.02	0.00	12.01	0.01	4.17	0.62	**100.05**	**59.15**
P158 / 1	SD-36-18C	Core	55.41	0.00	26.93	0.00	0.10	0.01	0.00	11.71	0.00	4.11	0.64	**98.91**	**58.84**
P159 / 1	SD-36-18C	Core	55.77	0.00	27.34	0.00	0.03	0.02	0.00	11.88	0.01	3.82	0.58	**99.45**	**61.01**
P161 / 1	SD-36-18C	Core	55.41	0.03	26.59	0.00	0.11	0.00	0.00	11.90	0.00	4.01	0.62	**98.69**	**59.79**
P163 / 1	SD-36-18C	Core	56.81	0.00	26.89	0.00	0.06	0.00	0.00	11.73	0.01	4.32	0.48	**100.31**	**58.32**

Table 29 Continued

Point	Sample	C/M/S	SiO_2	TiO_2	Al_2O_3	Cr_2O_3	FeO	MnO	MgO	CaO	BaO	Na_2O	K_2O	**Total**	**An**
P165 / 1	SD-36-18C	Core	55.22	0.01	27.03	0.00	0.04	0.02	0.00	11.79	0.01	3.98	1.07	**99.17**	**58.19**
P166 / 1	SD-36-18C	Core	54.92	0.00	27.14	0.00	0.09	0.00	0.00	12.21	0.00	4.09	0.68	**99.13**	**59.78**
P168 / 1	SD-36-18C	Core	56.71	0.00	27.28	0.00	0.12	0.00	0.00	11.82	0.00	4.06	0.72	**100.71**	**59.04**
P169 / 1	SD-36-18C	Core	54.12	0.03	28.29	0.00	0.08	0.01	0.00	11.83	0.01	4.19	0.64	**99.21**	**58.62**
P170 / 1	SD-36-18C	Core	54.43	0.00	29.13	0.01	0.07	0.00	0.00	11.85	0.00	4.33	0.58	**100.40**	**58.15**
P171 / 1	SD-36-18C	Core	53.68	0.00	28.06	0.01	0.07	0.00	0.00	11.41	0.00	4.21	0.49	**97.94**	**58.14**
P172 / 1	SD-36-18C	Core	53.12	0.00	28.25	0.00	0.09	0.00	0.00	12.01	0.00	4.26	0.60	**98.32**	**58.78**
P173 / 1	SD-36-18C	Core	57.78	0.02	26.45	0.00	0.09	0.00	0.00	11.29	0.01	3.84	0.73	**100.20**	**59.04**
P174 / 1	SD-36-18C	Core	54.97	0.04	28.34	0.00	0.08	0.00	0.00	11.47	0.00	4.23	0.61	**99.76**	**57.75**
P175 / 1	SD-36-18C	Core	55.43	0.03	27.66	0.00	0.05	0.01	0.00	11.93	0.02	4.01	0.61	**99.76**	**59.93**
P176 / 1	SD-36-18C	Core	55.91	0.05	26.72	0.00	0.10	0.00	0.00	11.31	0.01	4.06	0.67	**98.83**	**58.12**
P179 / 1	SD-36-18C	Core	56.02	0.01	27.41	0.00	0.06	0.00	0.00	12.12	0.00	3.86	0.50	**99.99**	**61.55**
P180 / 1	SD-36-18C	Core	55.76	0.00	27.46	0.02	0.10	0.01	0.00	11.84	0.01	4.12	0.64	**99.96**	**59.01**
P182 / 1	SD-36-18C	Core	55.98	0.01	27.32	0.01	0.04	0.00	0.00	11.59	0.02	4.28	0.59	**99.83**	**57.86**
P187 / 1	SD-36-18C	Core	56.99	0.03	27.13	0.00	0.07	0.01	0.00	11.71	0.00	3.99	0.66	**100.59**	**59.37**
P188 / 1	SD-36-18C	Core	55.57	0.00	26.78	0.00	0.17	0.00	0.00	12.17	0.00	3.72	0.52	**98.93**	**62.34**
P189 / 1	SD-36-18C	Core	57.97	0.01	27.15	0.01	0.09	0.01	0.00	11.54	0.01	4.03	0.60	**101.42**	**59.03**

Table 29 Continued

Point	Sample	C/M/S	SiO_2	TiO_2	Al_2O_3	Cr_2O_3	FeO	MnO	MgO	CaO	BaO	Na_2O	K_2O	**Total**	**An**
P190 / 1	SD-36-18C	Core	55.55	0.04	28.60	0.00	0.08	0.03	0.00	11.86	0.01	4.16	0.65	**100.97**	**58.80**
P191 / 1	SD-36-18C	Core	57.51	0.01	26.90	0.00	0.04	0.01	0.00	11.71	0.00	3.94	0.57	**100.68**	**60.02**
P193 / 1	SD-36-18C	Core	56.34	0.05	26.60	0.00	0.07	0.00	0.00	11.28	0.01	3.78	0.90	**99.03**	**58.80**
P194 /1	SD-36-18C	Core	53.88	0.00	28.18	0.00	0.06	0.00	0.00	11.71	0.01	4.28	0.70	**98.81**	**57.76**
P195 / 1	SD-36-18C	Core	57.67	0.00	26.89	0.03	0.06	0.01	0.00	11.40	0.00	3.97	0.70	**100.73**	**58.69**
P1 / 1	SD-36-18A	Shell	53.51	0.04	31.13	0.01	0.08	0.01	0.00	10.08	0.00	4.05	0.43	**99.34**	**56.24**
P3 / 1	SD-36-18A	Shell	58.15	0.01	29.38	0.00	0.07	0.00	0.00	9.51	0.01	3.89	0.40	**101.43**	**55.88**
P5 / 1	SD-36-18A	Shell	56.25	0.02	28.35	0.02	0.08	0.00	0.00	9.53	0.00	3.79	0.45	**98.49**	**56.31**
P6 / 1	SD-36-18A	Shell	55.84	0.00	28.85	0.02	0.04	0.00	0.00	9.42	0.00	3.88	0.43	**98.48**	**55.56**
P7 / 1	SD-36-18A	Shell	57.29	0.00	29.04	0.03	0.07	0.00	0.00	9.55	0.00	3.75	0.40	**100.14**	**56.80**
P8 / 1	SD-36-18A	Shell	56.44	0.00	28.80	0.00	0.08	0.02	0.00	9.59	0.01	3.99	0.51	**99.44**	**55.08**
P9 / 1	SD-36-18A	Shell	57.15	0.00	29.01	0.00	0.08	0.02	0.00	9.64	0.01	3.92	0.43	**100.24**	**55.92**
P11 / 1	SD-36-18A	Shell	56.58	0.00	28.34	0.00	0.17	0.00	0.00	9.36	0.00	3.88	0.49	**98.83**	**55.17**
P13 / 1	SD-36-18A	Shell	57.29	0.00	29.24	0.02	0.06	0.01	0.00	9.80	0.02	3.86	0.47	**100.78**	**56.48**
P14 / 1	SD-36-18A	Shell	57.18	0.02	29.29	0.00	0.08	0.01	0.01	9.72	0.00	3.71	0.42	**100.46**	**57.40**

Table 29 Continued

Point	Sample	C/M/S	SiO_2	TiO_2	$Al2O_3$	Cr_2O_3	FeO	MnO	MgO	CaO	BaO	Na_2O	K_2O	**Total**	**An**
P16 / 1	SD-36-18A	Shell	53.62	0.00	31.08	0.00	0.02	0.01	0.00	9.47	0.01	4.15	0.52	**98.89**	**53.77**
P18 / 1	SD-36-18A	Shell	55.33	0.00	31.32	0.00	0.03	0.01	0.00	9.43	0.00	3.90	0.49	**100.51**	**55.23**
P19 / 1	SD-36-18A	Shell	56.97	0.02	27.37	0.02	0.08	0.00	0.00	9.34	0.00	4.00	0.47	**98.27**	**54.51**
P20 / 1	SD-36-18A	Shell	56.44	0.00	29.12	0.01	0.03	0.00	0.00	9.71	0.02	4.08	0.33	**99.75**	**55.49**
P24 / 1	SD-36-18A	Shell	55.89	0.00	28.73	0.01	0.10	0.00	0.00	9.66	0.01	3.93	0.38	**98.70**	**56.12**
P26 / 1	SD-36-18A	Shell	56.45	0.01	28.55	0.00	0.13	0.00	0.00	8.79	0.00	3.87	0.48	**98.28**	**53.70**
P27 / 1	SD-36-18A	Shell	58.55	0.00	28.88	0.02	0.05	0.00	0.00	9.37	0.01	3.90	0.39	**101.18**	**55.45**
P28 / 1	SD-36-18A	Shell	55.45	0.01	28.82	0.00	0.09	0.00	0.00	9.83	0.02	3.91	0.40	**98.52**	**56.59**
P30 / 1	SD-36-18A	Shell	54.41	0.04	31.24	0.00	0.07	0.00	0.00	9.17	0.01	3.84	0.51	**99.29**	**54.81**
P31 / 1	SD-36-18A	Shell	56.05	0.00	28.28	0.01	0.05	0.00	0.00	9.47	0.02	3.90	0.49	**98.27**	**55.33**
P34 / 1	SD-36-18A	Shell	55.06	0.00	28.62	0.00	0.13	0.02	0.00	10.15	0.00	3.80	0.36	**98.14**	**58.17**
P35 / 1	SD-36-18A	Shell	57.54	0.00	29.08	0.00	0.09	0.00	0.00	9.61	0.01	3.91	0.39	**100.63**	**56.02**
P36 / 1	SD-36-18A	Shell	52.78	0.02	30.93	0.00	0.07	0.00	0.00	9.89	0.01	3.92	0.44	**98.07**	**56.48**
P38 / 1	SD-36-18A	Shell	56.66	0.03	29.11	0.00	0.05	0.02	0.00	9.66	0.00	4.02	0.52	**100.05**	**55.07**
P39 / 1	SD-36-18A	Shell	56.77	0.02	28.41	0.01	0.07	0.00	0.00	9.28	0.03	3.75	0.43	**98.77**	**55.94**

Table 29 Continued

Point	Sample	C/M/S	SiO_2	TiO_2	Al_2O_3	Cr_2O_3	FeO	MnO	MgO	CaO	BaO	Na_2O	K_2O	**Total**	**An**
P41 / 1	SD-36-18A	Matrix	56.22	0.03	28.49	0.04	0.09	0.01	0.00	9.80	0.00	3.94	0.44	**99.07**	**56.16**
P43 / 1	SD-36-18A	Matrix	57.02	0.01	28.95	0.02	0.07	0.00	0.00	9.44	0.01	3.73	0.53	**99.79**	**56.09**
P44 / 1	SD-36-18A	Matrix	56.08	0.01	28.59	0.00	0.07	0.01	0.00	9.53	0.01	3.90	0.48	**98.67**	**55.54**
P45 / 1	SD-36-18A	Matrix	56.00	0.01	28.45	0.00	0.05	0.00	0.00	9.54	0.00	3.84	0.40	**98.29**	**56.24**
P46 / 1	SD-36-18A	Matrix	55.66	0.01	28.73	0.00	0.06	0.00	0.00	9.94	0.00	3.90	0.44	**98.75**	**56.76**
P47 / 1	SD-36-18A	Matrix	54.43	0.00	30.56	0.02	0.08	0.01	0.00	9.28	0.00	3.69	0.40	**98.47**	**56.49**
P48 / 1	SD-36-18A	Matrix	57.00	0.02	29.02	0.04	0.06	0.00	0.00	9.50	0.00	3.93	0.44	**100.00**	**55.45**
P50 / 1	SD-36-18A	Matrix	55.67	0.00	28.50	0.00	0.06	0.00	0.00	9.41	0.02	3.82	0.53	**98.02**	**55.51**
P51 / 1	SD-36-18A	Matrix	56.71	0.04	29.28	0.01	0.07	0.00	0.00	9.70	0.00	3.74	0.43	**99.97**	**57.13**
P53 / 1	SD-36-18A	Matrix	56.95	0.01	28.94	0.03	0.08	0.03	0.00	9.60	0.02	3.97	0.45	**100.09**	**55.40**
P54 / 1	SD-36-18A	Matrix	57.80	0.01	29.64	0.00	0.09	0.00	0.00	9.51	0.00	3.99	0.39	**101.43**	**55.28**
P55 / 1	SD-36-18A	Matrix	54.55	0.00	30.75	0.00	0.04	0.00	0.00	9.59	0.00	3.83	0.49	**99.26**	**56.09**
P57 / 1	SD-36-18A	Matrix	54.46	0.00	31.04	0.00	0.07	0.00	0.00	9.23	0.00	3.67	0.44	**98.92**	**56.29**
P59 / 1	SD-36-18A	Matrix	55.95	0.05	28.72	0.00	0.07	0.01	0.00	9.45	0.01	3.82	0.41	**98.48**	**56.06**
P60 / 1	SD-36-18A	Matrix	56.73	0.00	27.98	0.00	0.09	0.01	0.00	10.24	0.02	3.68	0.37	**99.12**	**59.07**
P61 / 1	SD-36-18A	Matrix	56.62	0.00	28.76	0.01	0.04	0.00	0.00	9.82	0.00	3.82	0.24	**99.30**	**57.66**
P63 / 1	SD-36-18A	Matrix	56.79	0.01	28.04	0.00	0.09	0.03	0.00	9.29	0.02	3.82	0.44	**98.53**	**55.54**

Table 29 Continued

Point	Sample	C/M/S	SiO_2	TiO_2	Al_2O_3	$Cr2O_3$	FeO	MnO	MgO	CaO	BaO	Na_2O	K_2O	**Total**	**An**
P65 / 1	SD-36-18A	Matrix	57.25	0.01	28.52	0.01	0.04	0.01	0.00	9.43	0.01	3.89	0.45	**99.62**	**55.47**
P67 / 1	SD-36-18A	Matrix	57.94	0.01	29.11	0.02	0.02	0.02	0.00	9.41	0.00	3.98	0.45	**100.96**	**54.87**
P69 / 1	SD-36-18A	Matrix	56.76	0.02	28.75	0.00	0.13	0.03	0.00	9.28	0.00	3.95	0.40	**99.31**	**54.89**
P198 / 1	SD-40-19D	Matrix	57.36	0.00	27.16	0.02	0.08	0.00	0.00	11.55	0.01	4.22	0.68	**101.07**	**57.79**
P199 / 1	SD-40-19D	Matrix	55.89	0.01	28.17	0.00	0.15	0.00	0.00	13.44	0.00	3.72	0.45	**101.85**	**64.87**
P200 / 1	SD-40-19D	Matrix	54.93	0.00	28.86	0.00	0.06	0.00	0.00	13.29	0.01	3.69	0.46	**101.30**	**64.79**
P201 / 1	SD-40-19D	Matrix	53.89	0.02	29.35	0.00	0.07	0.00	0.00	13.92	0.01	3.73	0.50	**101.49**	**65.46**
202 / 1	SD-40-19D	Matrix	54.46	0.00	28.72	0.00	0.12	0.02	0.00	13.37	0.01	3.80	0.51	**101.02**	**64.14**
P203 / 1	SD-40-19D	Matrix	54.12	0.02	28.00	0.00	0.04	0.00	0.00	12.71	0.01	3.98	0.51	**99.38**	**61.92**
P204 / 1	SD-40-19D	Matrix	54.10	0.00	28.22	0.00	0.07	0.00	0.00	12.82	0.01	4.07	0.53	**99.82**	**61.60**
P205 / 1	SD-40-19D	Matrix	55.63	0.00	28.01	0.00	0.09	0.00	0.00	12.69	0.00	3.95	0.47	**100.86**	**62.19**
P208 / 1	SD-40-19D	Matrix	53.34	0.03	27.57	0.03	0.06	0.00	0.00	12.94	0.00	3.99	0.32	**98.27**	**63.02**
P209 / 1	SD-40-19D	Matrix	54.96	0.01	28.48	0.00	0.08	0.00	0.00	12.80	0.00	3.91	0.44	**100.68**	**62.75**
P210 / 1	SD-40-19D	Matrix	55.89	0.01	28.11	0.05	0.04	0.03	0.00	12.31	0.00	4.04	0.57	**101.07**	**60.65**
P211 / 1	SD-40-19D	Matrix	54.50	0.00	28.05	0.01	0.07	0.00	0.00	12.57	0.02	3.92	0.47	**99.61**	**62.19**
P212 / 1	SD-40-19D	Matrix	54.90	0.00	29.43	0.02	0.16	0.00	0.00	12.76	0.02	3.99	0.37	**101.66**	**62.50**
P213 / 1	SD-40-19D	Matrix	56.34	0.01	28.56	0.01	0.05	0.00	0.00	12.42	0.01	3.88	0.37	**101.66**	**62.49**

Table 29 Continued

Point	Sample	C/M/S	SiO_2	TiO_2	Al_2O_3	$Cr2O_3$	FeO	MnO	MgO	CaO	BaO	Na_2O	K_2O	**Total**	**An**
P214 / 1	SD-40-19D	Matrix	55.79	0.00	27.68	0.00	0.10	0.01	0.00	12.05	0.00	3.98	0.38	**100.00**	**61.16**
P215 / 1	SD-40-19D	Matrix	54.87	0.01	28.95	0.00	0.09	0.01	0.00	12.29	0.00	4.02	0.52	**100.77**	**60.87**
P216 / 1	SD-40-19D	Matrix	56.26	0.01	27.50	0.00	0.06	0.01	0.00	12.06	0.00	3.99	0.59	**100.49**	**60.35**
P217 / 1	SD-40-19D	Matrix	54.44	0.03	28.95	0.00	0.10	0.02	0.00	12.75	0.02	3.94	0.51	**100.75**	**62.23**
P218 / 1	SD-40-19D	Matrix	55.08	0.02	28.76	0.00	0.07	0.01	0.00	12.36	0.00	4.16	0.45	**100.91**	**60.53**
P219 / 1	SD-40-19D	Matrix	54.74	0.01	28.07	0.00	0.08	0.00	0.00	12.52	0.00	3.97	0.45	**99.83**	**61.89**
P220 / 1	SD-40-19D	Matrix	54.83	0.02	28.54	0.00	0.06	0.00	0.00	13.04	0.02	3.85	0.39	**100.75**	**63.67**
P221 / 1	SD-40-19D	Matrix	55.91	0.04	28.29	0.00	0.10	0.00	0.00	12.26	0.02	3.93	0.52	**101.08**	**61.30**
P222 / 1	SD-40-19D	Matrix	55.84	0.01	27.61	0.01	0.04	0.00	0.00	12.08	0.00	3.93	0.49	**100.01**	**61.04**
P223 / 1	SD-40-19D	Matrix	54.91	0.00	27.66	0.01	0.04	0.03	0.00	12.63	0.00	4.04	0.45	**99.78**	**61.66**
P224 / 1	SD-40-19D	Matrix	55.55	0.00	27.83	0.00	0.07	0.00	0.00	12.83	0.01	4.09	0.47	**100.86**	**61.69**
P225 / 1	SD-40-19D	Matrix	56.05	0.01	28.02	0.00	0.10	0.00	0.00	12.69	0.00	3.99	0.46	**101.32**	**62.05**
P230 / 1	SD-40-19D	Matrix	52.81	0.00	29.40	0.02	0.07	0.00	0.00	13.44	0.00	4.05	0.34	**100.12**	**63.48**
P231 / 1	SD-40-19D	Matrix	56.15	0.03	27.96	0.03	0.06	0.00	0.00	12.40	0.02	3.99	0.50	**101.14**	**61.32**
P233 / 1	SD-40-19D	Matrix	53.60	0.00	28.83	0.00	0.04	0.01	0.00	12.41	0.02	3.96	0.50	**99.37**	**61.49**
P234 / 1	SD-40-19D	Matrix	53.01	0.02	28.56	0.02	0.05	0.04	0.00	12.60	0.02	4.21	0.32	**98.85**	**61.17**
P235 / 1	SD-40-19D	Matrix	52.80	0.01	28.67	0.00	0.04	0.02	0.00	12.81	0.00	3.94	0.45	**98.74**	**62.60**

Table 29 Continued

Point	Sample	C/M/S	SiO_2	TiO_2	Al_2O_3	$Cr2O_3$	FeO	MnO	MgO	CaO	BaO	Na_2O	K_2O	**Total**	**An**
P236 / 1	SD-40-19D	Matrix	52.50	0.03	28.41	0.01	0.09	0.00	0.00	12.75	0.01	4.05	0.43	**98.27**	**61.92**
P237 / 1	SD-40-19D	Matrix	54.04	0.01	28.27	0.00	0.08	0.02	0.00	12.07	0.00	3.89	0.39	**98.78**	**61.63**
P238 / 1	SD-40-19D	Matrix	54.02	0.01	29.75	0.00	0.11	0.02	0.00	12.90	0.00	3.99	0.29	**101.10**	**63.02**
P239 / 1	SD-40-19D	Matrix	55.71	0.02	28.52	0.01	0.07	0.02	0.00	11.67	0.01	4.27	0.33	**100.63**	**59.01**
P240 / 1	SD-40-19D	Matrix	54.41	0.00	29.42	0.01	0.07	0.00	0.00	12.77	0.01	4.13	0.42	**101.24**	**61.56**
P241 / 1	SD-40-19D	Matrix	54.99	0.00	28.87	0.03	0.07	0.00	0.00	12.00	0.02	3.96	0.43	**100.37**	**61.00**
P242 / 1	SD-40-19D	Matrix	54.82	0.03	29.88	0.00	0.05	0.02	0.00	11.50	0.00	3.84	0.58	**100.71**	**60.13**
P243 / 1	SD-40-19D	Matrix	56.05	0.00	29.27	0.03	0.04	0.00	0.00	11.92	0.00	3.90	0.41	**101.62**	**61.21**
P245 / 1	SD-40-19D	Matrix	56.83	0.00	27.74	0.04	0.08	0.00	0.00	11.75	0.01	3.59	0.48	**100.50**	**62.46**
P246 / 1	SD-40-19D	Matrix	53.52	0.01	29.37	0.00	0.13	0.03	0.00	12.57	0.01	3.94	0.32	**99.89**	**62.59**
P247 / 1	SD-40-19D	Matrix	55.29	0.00	29.00	0.00	0.10	0.02	0.00	12.07	0.02	3.85	0.56	**100.92**	**61.25**
P248 / 1	SD-40-19D	Matrix	54.75	0.01	29.07	0.00	0.08	0.02	0.00	12.38	0.01	3.99	0.42	**100.72**	**61.61**
P249 / 1	SD-40-19D	Matrix	54.19	0.00	29.85	0.00	0.07	0.04	0.06	10.99	0.02	3.55	0.53	**99.31**	**60.86**
P250 / 1	SD-40-19D	Matrix	54.55	0.01	30.78	0.00	0.08	0.00	0.00	11.78	0.00	3.78	0.44	**101.41**	**61.53**
P251 / 1	SD-40-19D	Matrix	54.32	0.00	30.72	0.00	0.00	0.00	0.00	11.64	0.00	3.94	0.41	**101.05**	**60.41**
P252 / 1	SD-40-19D	Matrix	54.74	0.00	29.46	0.01	0.04	0.00	0.00	12.28	0.00	3.99	0.48	**101.00**	**61.20**

Table 29: *Microprobe analyses of biotites from the Henderson North Orbicules. C=core, S= Shells and M=matrix*

Point	175 / 1	178 / 1	179 / 1	180 / 1
Sample	SD-36-18C	SD-36-18C	SD-36-18C	SD-36-18C
C/S/M	C	C	C	C
SiO_2	39.95	40.96	41.00	40.42
TiO_2	2.39	1.88	2.43	2.27
Al_2O_3	12.68	12.67	12.25	12.40
Cr_2O_3	0.02	0.03	0.00	0.01
MgO	17.68	19.10	17.69	15.99
CaO	0.10	0.04	0.05	0.16
MnO	0.14	0.08	0.12	0.12
FeO	10.88	8.51	9.31	10.62
Na_2O	0.05	0.09	0.06	0.07
K_2O	12.99	12.04	12.32	12.30
BaO	0.15	0.13	0.12	0.13
F	0.62	0.86	0.75	0.72
Cl	0.05	0.06	0.06	0.06
Li	0.08	0.14	0.11	0.10
H_2O	3.84	3.76	3.77	3.72
Total	**101.63**	**100.34**	**100.06**	**99.10**

Number of ions based on 24 (O, OH, F, Cl)

Si	5.77	5.86	5.92	5.94
Ti	0.26	0.20	0.26	0.25
Al^{IV}	2.16	2.14	2.08	2.06
Al^{VI}	0.00	0.00	0.01	0.08
Cr	0.00	0.00	0.00	0.00
Mg	3.81	4.07	3.81	3.50
Ca	0.01	0.01	0.01	0.03
Mn	0.02	0.01	0.01	0.02
Fe^{2+}	1.31	1.02	1.12	1.30
Na	0.01	0.03	0.02	0.02
K	2.39	2.20	2.27	2.30
Ba	0.02	0.01	0.01	0.01
F	0.28	0.39	0.34	0.34
Cl	0.01	0.01	0.01	0.02
Li*	0.02	0.04	0.03	0.03
OH-	3.70	3.60	3.64	3.65
Mg/(Mg + Fe)	**0.74**	**0.80**	**0.77**	**0.73**

Table 30 continued

Point	109	112	113	118	120	126	127	128	132	133	134	136	141
Sample	SD-36-18A	SD-36-18A	SD-36-18A	SD-36-18A	SD-36-18A	SD-36-18A	SD-36-18A	SD-36-18A	SD-36-18A	SD-36-18A	SD-36-18A	SD-36-18A	SD-36-18A
C/S/M	S	S	S	S	S	S	S	S	S	S	S	S	S
SiO_2	39.80	42.44	39.36	37.18	39.19	38.17	39.61	38.42	39.15	39.71	37.58	40.01	40.69
TiO_2	2.06	2.39	2.47	2.11	2.15	2.40	2.16	1.98	2.18	2.31	2.23	2.35	2.17
Al_2O_3	14.67	19.78	14.90	14.69	14.96	12.94	12.58	13.21	12.92	12.59	12.36	12.15	12.04
Cr_2O_3	0.01	0.00	0.02	0.00	0.00	0.02	0.00	0.00	0.02	0.01	0.00	0.00	0.02
MgO	18.57	12.24	16.51	17.19	18.06	18.82	18.93	18.89	19.06	19.10	17.52	19.38	18.11
CaO	0.01	2.24	0.00	0.19	0.00	0.00	0.08	0.15	0.00	0.00	1.46	0.00	0.01
MnO	0.08	0.07	0.11	0.12	0.07	0.13	0.08	0.08	0.11	0.11	0.08	0.09	0.09
FeO	9.02	5.55	9.95	9.31	9.49	9.72	9.15	8.51	9.93	9.35	9.27	9.37	9.25
Na_2O	0.07	0.23	0.04	0.12	0.05	0.04	0.05	0.07	0.04	0.09	0.06	0.06	0.07
K_2O	12.15	7.53	12.31	10.94	12.52	13.23	12.59	12.01	12.60	12.70	11.42	13.00	12.36
BaO	0.21	0.11	0.24	0.20	0.21	0.23	0.16	0.18	0.23	0.24	0.23	0.25	0.24
F	1.15	0.21	0.72	0.83	1.06	0.80	0.99	1.08	0.95	0.99	0.87	1.06	0.92
Cl	0.07	0.09	0.07	0.09	0.07	0.08	0.09	0.07	0.07	0.10	0.08	0.06	0.08
Li	0.22	0.01	0.10	0.13	0.20	0.12	0.17	0.20	0.16	0.17	0.14	0.19	0.15
H_2O	3.68	4.09	3.79	3.60	3.69	3.70	3.66	3.56	3.69	3.68	3.56	3.68	3.69
Total	**101.76**	**97.00**	**100.59**	**96.70**	**101.71**	**100.38**	**100.29**	**98.42**	**101.11**	**101.15**	**96.86**	**101.64**	**99.88**

Number of ions based on 24 oxygens (O, OH, F, Cl)

Si	5.61	6.03	5.68	5.55	5.56	5.57	5.71	5.62	5.63	5.69	5.64	5.71	5.88
Ti	0.22	0.26	0.27	0.24	0.23	0.26	0.23	0.22	0.24	0.25	0.25	0.25	0.24
Al^{IV}	2.39	1.97	2.32	2.45	2.44	2.23	2.14	2.28	2.19	2.13	2.19	2.04	2.05
Al^{VI}	0.04	1.35	0.21	0.13	0.06	0.00	0.00	0.00	0.00	0.00	0.00	0.00	0.00
Cr	0.00	0.00	0.00	0.00	0.00	0.00	0.00	0.00	0.00	0.00	0.00	0.00	0.00
Mg	3.90	2.59	3.55	3.82	3.82	4.10	4.07	4.12	4.09	4.08	3.92	4.12	3.90
Ca	0.00	0.34	0.00	0.03	0.00	0.00	0.01	0.02	0.00	0.00	0.24	0.00	0.00
Mn	0.01	0.01	0.01	0.02	0.01	0.02	0.01	0.01	0.01	0.01	0.01	0.01	0.01
Fe^{2+}	1.06	0.66	1.20	1.16	1.13	1.19	1.10	1.04	1.19	1.12	1.16	1.12	1.12
Na	0.02	0.06	0.01	0.04	0.01	0.01	0.01	0.02	0.01	0.03	0.02	0.02	0.02
K	2.18	1.37	2.27	2.08	2.27	2.46	2.32	2.24	2.31	2.32	2.19	2.36	2.28
Ba	0.02	0.01	0.03	0.02	0.02	0.03	0.02	0.02	0.03	0.03	0.03	0.03	0.03
F	0.51	0.10	0.33	0.39	0.48	0.37	0.45	0.50	0.43	0.45	0.41	0.48	0.42
Cl	0.02	0.02	0.02	0.02	0.02	0.02	0.02	0.02	0.02	0.02	0.02	0.02	0.02
Li*	0.06	0.00	0.03	0.04	0.06	0.04	0.05	0.06	0.05	0.05	0.04	0.06	0.04
OH-	3.47	3.88	3.65	3.58	3.51	3.61	3.53	3.48	3.55	3.53	3.57	3.51	3.56
Mg/(Mg + Fe)	**0.79**	**0.80**	**0.75**	**0.77**	**0.77**	**0.78**	**0.79**	**0.80**	**0.77**	**0.78**	**0.77**	**0.79**	**0.78**

Table 30 continued

Point	143 / 1	144 / 1	145 / 1	146 / 1	147 / 1	148 / 1	151 / 1	154 / 1	155 / 1	156 / 1	158 / 1	159 / 1	160 / 1
Sample	SD-36-18A	SD-36-18A	SD-36-18A	SD-36-18A	SD-36-18A	SD-36-18A	SD-36-18A	SD-36-18A	SD-36-18A	SD-36-18A	SD-36-18A	SD-36-18A	SD-36-18A
C/S/M	S	S	S	S	S	S	S	S	S	S	S	S	S
SiO2	41.45	38.01	39.01	38.75	39.91	39.50	41.51	40.21	41.47	38.76	39.34	38.20	39.65
TiO2	2.44	1.94	1.91	1.86	2.22	2.33	2.15	1.85	2.53	2.16	2.16	3.63	2.12
Al2O3	12.55	11.67	12.51	12.45	11.87	12.26	12.48	12.49	12.41	12.10	11.98	11.31	12.34
Cr2O3	0.00	0.01	0.00	0.01	0.02	0.00	0.00	0.00	0.03	0.04	0.00	0.05	0.01
MgO	17.77	18.40	19.08	18.22	18.05	18.36	18.43	17.91	16.24	16.62	18.09	15.25	18.32
CaO	0.03	0.01	0.00	0.12	0.01	0.01	0.00	0.18	0.08	0.02	0.01	5.06	0.07
MnO	0.10	0.09	0.08	0.10	0.09	0.08	0.08	0.09	0.08	0.10	0.11	0.13	0.14
FeO	9.23	9.33	10.17	10.10	9.81	9.53	9.38	9.85	10.84	10.73	9.60	8.55	10.41
Na2O	0.06	0.05	0.04	0.05	0.03	0.06	0.05	0.04	0.03	0.06	0.06	0.09	0.04
K2O	12.70	12.86	12.01	12.23	12.37	12.97	12.61	12.44	12.51	12.55	12.79	9.28	12.33
BaO	0.19	0.20	0.19	0.19	0.22	0.23	0.23	0.19	0.22	0.22	0.21	0.18	0.22
F	0.89	1.07	1.13	0.87	0.85	0.85	0.94	0.89	0.83	0.86	0.83	1.04	0.76
Cl	0.06	0.08	0.07	0.06	0.09	0.06	0.08	0.06	0.08	0.07	0.08	0.08	0.06
Li	0.15	0.20	0.22	0.14	0.14	0.14	0.16	0.15	0.13	0.14	0.13	0.19	0.11
H2O	3.77	3.48	3.58	3.63	3.67	3.69	3.76	3.69	3.76	3.58	3.66	3.49	3.74
Total	**101.39**	**97.40**	**100.00**	**98.79**	**99.33**	**100.08**	**101.85**	**100.04**	**101.23**	**98.02**	**99.04**	**96.54**	**100.33**

Number of ions based on 24 (O, OH, F, Cl)

Si	5.90	5.68	5.65	5.71	5.83	5.75	5.88	5.83	5.95	5.78	5.79	5.71	5.76
Ti	0.26	0.22	0.21	0.21	0.24	0.25	0.23	0.20	0.27	0.24	0.24	0.41	0.23
Al^{IV}	2.10	2.06	2.13	2.16	2.04	2.10	2.08	2.13	2.05	2.13	2.08	1.99	2.11
Al^{VI}	0.00	0.00	0.00	0.00	0.00	0.00	0.00	0.00	0.05	0.00	0.00	0.00	0.00
Cr	0.00	0.00	0.00	0.00	0.00	0.00	0.00	0.00	0.00	0.00	0.00	0.00	0.00
Mg	3.77	4.10	4.12	4.00	3.93	3.98	3.89	3.87	3.47	3.70	3.97	3.40	3.97
Ca	0.00	0.00	0.00	0.02	0.00	0.00	0.00	0.03	0.01	0.00	0.00	0.81	0.01
Mn	0.01	0.01	0.01	0.01	0.01	0.01	0.01	0.01	0.01	0.01	0.01	0.02	0.02
Fe^{2+}	1.10	1.17	1.23	1.24	1.20	1.16	1.11	1.19	1.30	1.34	1.18	1.07	1.27
Na	0.02	0.01	0.01	0.01	0.01	0.02	0.01	0.01	0.01	0.02	0.02	0.03	0.01
K	2.30	2.45	2.22	2.30	2.31	2.41	2.28	2.30	2.29	2.39	2.40	1.77	2.29
Ba	0.02	0.02	0.02	0.02	0.03	0.03	0.03	0.02	0.03	0.03	0.02	0.02	0.02
F	0.40	0.51	0.52	0.40	0.39	0.39	0.42	0.41	0.38	0.41	0.38	0.49	0.35
Cl	0.02	0.02	0.02	0.02	0.02	0.02	0.02	0.01	0.02	0.02	0.02	0.02	0.02
Li*	0.04	0.06	0.06	0.04	0.04	0.04	0.05	0.04	0.04	0.04	0.04	0.06	0.03
OH-	3.58	3.47	3.47	3.58	3.59	3.59	3.56	3.58	3.60	3.57	3.60	3.49	3.64
Mg/(Mg + Fe)	**0.77**	**0.78**	**0.77**	**0.76**	**0.77**	**0.77**	**0.78**	**0.76**	**0.73**	**0.73**	**0.77**	**0.76**	**0.76**

Table 30 continued

Point	161 / 1	162 / 1	163 / 1	164 / 1	165 / 1	166 / 1	168 / 1	169 / 1	170 / 1	171 / 1	172 / 1	174 / 1
Sample	SD-36-18A	SD-36-18A	SD-36-18A	SD-36-18A	SD-36-18A	SD-36-18A	SD-36-18A	SD-36-18A	SD-36-18A	SD-36-18A	SD-36-18A	SD-36-18A
C/S/M	S	S	S	S	S	S	S	S	S	S	S	S
SiO_2	40.03	38.25	39.16	38.91	38.27	37.64	38.45	39.74	40.21	40.17	38.73	38.77
TiO_2	2.33	2.98	2.29	2.41	2.22	2.09	2.12	2.58	2.16	2.35	2.08	2.09
Al_2O_3	12.00	12.15	11.97	12.13	11.84	11.97	12.18	12.45	12.87	12.38	12.34	12.12
Cr_2O_3	0.00	0.02	0.00	0.01	0.01	0.00	0.00	0.03	0.00	0.01	0.02	0.01
MgO	18.85	17.16	17.78	18.78	17.65	17.99	17.52	17.60	16.19	17.52	16.70	17.67
CaO	0.00	2.44	0.00	0.02	0.00	0.00	0.00	0.13	0.00	0.00	0.01	0.17
MnO	0.10	0.07	0.10	0.11	0.08	0.09	0.07	0.10	0.13	0.11	0.11	0.11
FeO	9.48	9.56	9.49	9.31	9.52	9.84	10.22	10.30	10.63	9.90	10.85	9.38
Na_2O	0.05	0.06	0.05	0.07	0.06	0.08	0.04	0.05	0.04	0.07	0.07	0.07
K_2O	12.87	10.95	12.45	13.19	12.46	12.53	12.16	12.28	12.96	12.79	12.76	12.39
BaO	0.24	0.21	0.24	0.23	0.27	0.24	0.27	0.25	0.24	0.23	0.23	0.25
F	1.04	0.92	1.08	1.18	0.93	1.09	0.80	0.92	0.93	0.67	0.91	1.00
Cl	0.05	0.08	0.07	0.06	0.06	0.08	0.07	0.07	0.08	0.09	0.07	0.07
Li	0.19	0.15	0.20	0.23	0.16	0.20	0.12	0.15	0.16	0.09	0.15	0.18
H_2O	3.66	3.60	3.53	3.55	3.54	3.46	3.61	3.68	3.66	3.77	3.58	3.55
Total	**100.87**	**98.61**	**98.40**	**100.21**	**97.05**	**97.31**	**97.62**	**100.32**	**100.25**	**100.16**	**98.60**	**97.81**

Number of ions based on 24 oxygens (O, OH, F, Cl)

Si	5.75	5.64	5.76	5.64	5.74	5.63	5.75	5.76	5.84	5.85	5.75	5.75
Ti	0.25	0.33	0.25	0.26	0.25	0.24	0.24	0.28	0.24	0.26	0.23	0.23
Al^{IV}	2.03	2.11	2.07	2.07	2.09	2.11	2.14	2.13	2.16	2.12	2.16	2.12
Al^{VI}	0.00	0.00	0.00	0.00	0.00	0.00	0.00	0.00	0.05	0.00	0.00	0.00
Cr	0.00	0.00	0.00	0.00	0.00	0.00	0.00	0.00	0.00	0.00	0.00	0.00
Mg	4.04	3.77	3.90	4.06	3.95	4.01	3.90	3.80	3.51	3.80	3.70	3.91
Ca	0.00	0.38	0.00	0.00	0.00	0.00	0.00	0.02	0.00	0.00	0.00	0.03
Mn	0.01	0.01	0.01	0.01	0.01	0.01	0.01	0.01	0.02	0.01	0.01	0.01
Fe^{2+}	1.14	1.18	1.17	1.13	1.19	1.23	1.28	1.25	1.29	1.21	1.35	1.16
Na	0.01	0.02	0.01	0.02	0.02	0.02	0.01	0.01	0.01	0.02	0.02	0.02
K	2.36	2.06	2.34	2.44	2.38	2.39	2.32	2.27	2.40	2.37	2.42	2.34
Ba	0.03	0.02	0.03	0.03	0.03	0.03	0.03	0.03	0.03	0.03	0.03	0.03
F	0.47	0.43	0.50	0.54	0.44	0.52	0.38	0.42	0.43	0.31	0.43	0.47
Cl	0.01	0.02	0.02	0.02	0.02	0.02	0.02	0.02	0.02	0.02	0.02	0.02
Li*	0.05	0.05	0.06	0.07	0.05	0.06	0.04	0.04	0.05	0.03	0.05	0.05
OH^-	3.52	3.55	3.48	3.44	3.54	3.46	3.61	3.56	3.56	3.67	3.55	3.52
Mg/(Mg + Fe)	**0.78**	**0.76**	**0.77**	**0.78**	**0.77**	**0.77**	**0.75**	**0.75**	**0.73**	**0.76**	**0.73**	**0.77**

Table 30 continued

Dataset/Point	71 / 1	78 / 1	80 / 1	81 / 1	82 / 1	83 / 1	84 / 1	85 / 1	86 / 1	87 / 1	88 / 1	89 / 1	90 / 1
Sample	SD-10-36A	SD-10-36A	SD-10-36A	SD-10-36A	SD-10-36A	SD-10-36A	SD-10-36A	SD-10-36A	SD-10-36A	SD-10-36A	SD-10-36A	SD-10-36A	SD-10-36A
C/S/M	M	M	M	M	M	M	M	M	M	M	M	M	M
SiO_2	37.58	37.79	38.01	35.60	36.86	36.39	36.76	37.92	37.02	36.47	35.65	37.65	36.90
TiO_2	2.00	2.21	2.29	1.87	1.94	2.24	2.26	2.38	2.37	2.31	1.79	2.32	2.22
Al_2O_3	15.69	14.69	15.20	15.10	14.98	14.25	15.20	14.59	14.61	14.22	15.73	14.42	14.41
Cr_2O_3	0.02	0.00	0.01	0.03	0.01	0.01	0.01	0.01	0.03	0.00	0.00	0.02	0.01
MgO	18.82	16.80	17.96	18.86	17.98	16.41	19.20	18.78	16.78	17.50	19.14	17.91	17.75
CaO	2.59	0.01	0.00	0.14	0.12	0.00	0.02	0.16	0.00	0.02	0.26	0.02	0.08
MnO	0.08	0.08	0.07	0.11	0.08	0.13	0.08	0.11	0.12	0.11	0.12	0.11	0.10
FeO	9.28	10.12	9.92	9.73	10.31	10.77	9.95	9.59	10.49	9.80	10.81	10.25	10.67
Na_2O	0.03	0.04	0.03	0.06	0.08	0.03	0.06	0.06	0.06	0.05	0.03	0.05	0.06
K_2O	9.61	12.47	12.61	11.07	12.84	12.61	12.42	12.87	13.00	12.63	10.58	12.94	13.21
BaO	0.09	0.14	0.16	0.16	0.15	0.18	0.13	0.17	0.16	0.16	0.11	0.17	0.13
F	0.78	0.77	0.92	0.55	0.86	0.60	0.69	0.99	0.78	0.85	0.71	0.79	0.88
Cl	0.06	0.09	0.08	0.08	0.05	0.08	0.08	0.08	0.07	0.07	0.04	0.08	0.08
Li	0.12	0.11	0.15	0.07	0.14	0.08	0.10	0.17	0.12	0.14	0.10	0.12	0.14
H_2O	3.80	3.68	3.71	3.71	3.67	3.65	3.78	3.69	3.66	3.59	3.71	3.72	3.64
Total	**100.55**	**99.00**	**101.13**	**97.14**	**100.06**	**97.43**	**100.73**	**101.56**	**99.27**	**97.92**	**98.77**	**100.57**	**100.28**

Number of ions based on 24 (O, OH, F, Cl)

Si	5.38	5.57	5.46	5.35	5.40	5.51	5.34	5.43	5.48	5.45	5.26	5.48	5.41
Ti	0.21	0.25	0.25	0.21	0.21	0.26	0.25	0.26	0.26	0.26	0.20	0.25	0.24
Al^{IV}	2.62	2.43	2.54	2.65	2.59	2.49	2.60	2.46	2.52	2.50	2.74	2.48	2.49
Al^{VI}	0.03	0.12	0.04	0.02	0.00	0.05	0.00	0.00	0.03	0.00	0.00	0.00	0.00
Cr	0.00	0.00	0.00	0.00	0.00	0.00	0.00	0.00	0.00	0.00	0.00	0.00	0.00
Mg	4.02	3.69	3.85	4.22	3.93	3.70	4.16	4.01	3.70	3.90	4.21	3.89	3.88
Ca	0.40	0.00	0.00	0.02	0.02	0.00	0.00	0.02	0.00	0.00	0.04	0.00	0.01
Mn	0.01	0.01	0.01	0.01	0.01	0.02	0.01	0.01	0.02	0.01	0.01	0.01	0.01
Fe^{2+}	1.11	1.25	1.19	1.22	1.26	1.36	1.21	1.15	1.30	1.22	1.33	1.25	1.31
Na	0.01	0.01	0.01	0.02	0.02	0.01	0.02	0.02	0.02	0.02	0.01	0.01	0.02
K	1.76	2.34	2.31	2.12	2.40	2.43	2.30	2.35	2.46	2.41	1.99	2.40	2.47
Ba	0.01	0.02	0.02	0.02	0.02	0.02	0.01	0.02	0.02	0.02	0.01	0.02	0.02
F	0.35	0.36	0.42	0.26	0.40	0.29	0.32	0.45	0.37	0.40	0.33	0.36	0.41
Cl	0.02	0.02	0.02	0.02	0.01	0.02	0.02	0.02	0.02	0.02	0.01	0.02	0.02
Li*	0.03	0.03	0.04	0.02	0.04	0.02	0.03	0.05	0.04	0.04	0.03	0.04	0.04
OH^-	3.63	3.62	3.56	3.72	3.59	3.69	3.66	3.54	3.62	3.58	3.66	3.62	3.57
Mg/(Mg + Fe)	**0.78**	**0.75**	**0.76**	**0.78**	**0.76**	**0.73**	**0.77**	**0.78**	**0.74**	**0.76**	**0.76**	**0.76**	**0.75**

Table 30 continued

Dataset/Point	91 / 1	92 / 1	94 / 1	102 / 1	187 / 1	191 / 1	193 / 1	194 / 1	195 / 1	196 / 1	197 / 1	198 / 1	200 / 1
Sample	SD-10-36A	SD-10-36A	SD-10-36A	SD-10-36A	SD-40-19D	SD-40-19D	SD-40-19D	SD-40-19D	SD-40-19D	SD-40-19D	SD-40-19D	SD-40-19D	SD-40-19D
C/S/M	M	M	M	M	M	M	M	M	M	M	M	M	M
SiO_2	36.22	37.03	38.83	39.18	38.88	39.15	40.78	40.28	41.00	39.42	39.56	37.72	39.32
TiO_2	1.90	2.11	2.05	2.44	2.26	2.36	2.27	2.43	2.47	2.34	2.35	2.16	2.39
Al_2O_3	15.07	15.29	14.94	15.25	12.49	12.00	12.22	12.37	12.45	12.55	12.30	12.35	12.69
Cr_2O_3	0.00	0.00	0.00	0.00	0.00	0.03	0.00	0.01	0.00	0.01	0.02	0.00	0.00
MgO	17.64	18.28	17.69	17.17	16.49	17.12	16.78	18.00	17.45	18.16	17.43	18.76	18.49
CaO	0.12	0.37	0.01	0.00	0.07	0.05	0.04	0.01	0.01	0.00	0.11	0.00	0.00
MnO	0.08	0.09	0.09	0.11	0.07	0.13	0.08	0.11	0.09	0.09	0.11	0.11	0.09
FeO	9.63	10.55	9.79	10.04	10.56	9.79	10.20	9.49	10.01	9.88	10.16	9.58	9.73
Na_2O	0.03	0.02	0.05	0.07	0.05	0.08	0.06	0.10	0.05	0.07	0.08	0.05	0.04
K_2O	11.29	12.92	12.50	12.70	12.40	12.56	12.47	12.74	12.43	12.80	12.30	12.80	13.19
BaO	0.13	0.13	0.13	0.10	0.25	0.27	0.22	0.23	0.22	0.22	0.24	0.22	0.23
F	0.74	0.78	0.89	0.68	0.96	1.07	0.96	0.96	0.82	0.88	0.90	1.01	1.20
Cl	0.08	0.07	0.08	0.08	0.07	0.10	0.09	0.09	0.07	0.08	0.07	0.07	0.07
Li	0.11	0.12	0.14	0.09	0.17	0.20	0.17	0.17	0.13	0.14	0.15	0.18	0.24
H_2O	3.62	3.75	3.73	3.85	3.56	3.52	3.65	3.68	3.77	3.69	3.65	3.55	3.58
Total	**96.66**	**101.52**	**100.94**	**101.75**	**98.29**	**98.43**	**99.99**	**100.66**	**100.97**	**100.33**	**99.43**	**98.56**	**101.26**

Number of ions based on 24 (O, OH, F, Cl)

Si	5.44	5.36	5.58	5.61	5.76	5.77	5.90	5.80	5.88	5.72	5.78	5.58	5.64
Ti	0.22	0.23	0.22	0.26	0.25	0.26	0.25	0.26	0.27	0.26	0.26	0.24	0.26
Al^{IV}	2.56	2.61	2.42	2.39	2.18	2.09	2.09	2.10	2.11	2.15	2.12	2.15	2.14
Al^{VI}	0.11	0.00	0.11	0.18	0.00	0.00	0.00	0.00	0.00	0.00	0.00	0.00	0.00
Cr	0.00	0.00	0.00	0.00	0.00	0.00	0.00	0.00	0.00	0.00	0.00	0.00	0.00
Mg	3.95	3.94	3.79	3.66	3.64	3.76	3.62	3.86	3.73	3.93	3.80	4.14	3.95
Ca	0.02	0.06	0.00	0.00	0.01	0.01	0.01	0.00	0.00	0.00	0.02	0.00	0.00
Mn	0.01	0.01	0.01	0.01	0.01	0.02	0.01	0.01	0.01	0.01	0.01	0.01	0.01
Fe^{2+}	1.21	1.28	1.18	1.20	1.31	1.21	1.24	1.14	1.20	1.20	1.24	1.19	1.17
Na	0.01	0.01	0.01	0.02	0.01	0.02	0.02	0.03	0.02	0.02	0.02	0.01	0.01
K	2.16	2.39	2.29	2.32	2.34	2.36	2.30	2.34	2.28	2.37	2.29	2.42	2.41
Ba	0.02	0.02	0.01	0.01	0.03	0.03	0.03	0.03	0.02	0.03	0.03	0.03	0.03
F	0.35	0.36	0.40	0.31	0.45	0.50	0.44	0.44	0.37	0.40	0.42	0.47	0.54
Cl	0.02	0.02	0.02	0.02	0.02	0.02	0.02	0.02	0.02	0.02	0.02	0.02	0.02
Li*	0.03	0.03	0.04	0.03	0.05	0.06	0.05	0.05	0.04	0.04	0.04	0.05	0.07
OH^-	3.63	3.62	3.58	3.67	3.53	3.48	3.54	3.54	3.61	3.58	3.57	3.51	3.44
Mg/(Mg + Fe)	**0.77**	**0.76**	**0.76**	**0.75**	**0.74**	**0.76**	**0.75**	**0.77**	**0.76**	**0.77**	**0.75**	**0.78**	**0.77**

Table 30 continued

Point	201 / 1	202 / 1	203 / 1	204 / 1	206 / 1	208 / 1	211 / 1	213 / 1	215 / 1	217 / 1	218 / 1	219 / 1	220 / 1
Sample	SD-40-19D	SD-40-19D	SD-40-19D	SD-40-19D	SD-40-19D	SD-40-19D	SD-40-19D	SD-40-19D	SD-40-19D	SD-40-19D	SD-40-19D	SD-40-19D	SD-40-19D
C/S/M	M	M	M	M	M	M	M	M	M	M	M	M	M
SiO2	39.52	37.97	40.05	39.76	39.45	39.38	39.74	40.21	40.22	40.18	39.82	40.29	39.01
TiO2	2.35	2.33	2.35	1.99	2.12	2.03	2.22	2.50	2.30	2.32	2.23	2.28	1.75
Al2O3	12.19	12.25	12.44	12.57	12.25	12.41	12.48	12.72	12.59	12.38	12.06	12.47	13.22
Cr2O3	0.05	0.00	0.00	0.02	0.01	0.00	0.00	0.02	0.00	0.00	0.04	0.04	0.02
MgO	18.12	17.47	17.56	19.38	18.16	18.03	18.73	18.50	18.26	18.55	17.51	18.30	18.27
CaO	0.00	0.02	0.00	0.00	0.02	0.10	0.00	0.00	0.00	0.00	0.03	0.00	1.75
MnO	0.12	0.10	0.10	0.09	0.11	0.10	0.12	0.08	0.15	0.05	0.09	0.10	0.09
FeO	9.11	9.72	9.99	9.21	9.51	9.56	9.53	9.30	8.84	9.56	9.63	9.84	10.68
Na2O	0.06	0.04	0.10	0.06	0.06	0.09	0.04	0.07	0.07	0.06	0.07	0.07	0.04
K2O	12.73	12.77	12.69	12.66	12.89	12.31	12.76	12.81	12.36	12.82	12.73	12.64	8.97
BaO	0.24	0.23	0.24	0.20	0.20	0.22	0.23	0.26	0.27	0.26	0.22	0.23	0.14
F	0.71	0.96	1.00	1.21	0.82	0.99	0.90	1.03	0.97	0.97	0.90	1.14	0.76
Cl	0.06	0.05	0.09	0.09	0.09	0.07	0.07	0.07	0.07	0.07	0.09	0.06	0.06
Li	0.10	0.17	0.18	0.24	0.13	0.17	0.15	0.19	0.17	0.17	0.15	0.22	0.11
H2O	3.73	3.53	3.64	3.60	3.68	3.61	3.71	3.69	3.67	3.69	3.64	3.63	3.73
Total	**99.09**	**97.61**	**100.43**	**101.08**	**99.50**	**99.05**	**100.68**	**101.45**	**99.94**	**101.09**	**99.21**	**101.31**	**98.59**

Number of ions based on 24 oxygen (O, OH, F, Cl)

Si	5.80	5.68	5.79	5.67	5.77	5.76	5.73	5.73	5.80	5.76	5.83	5.75	5.69
Ti	0.26	0.26	0.26	0.21	0.23	0.22	0.24	0.27	0.25	0.25	0.25	0.24	0.19
Al^{IV}	2.11	2.16	2.12	2.11	2.11	2.14	2.12	2.14	2.14	2.09	2.08	2.10	2.27
Al^{VI}	0.00	0.00	0.00	0.00	0.00	0.00	0.00	0.00	0.00	0.00	0.00	0.00	0.00
Cr	0.00	0.00	0.00	0.00	0.00	0.00	0.00	0.00	0.00	0.00	0.00	0.00	0.00
Mg	3.97	3.89	3.78	4.12	3.96	3.93	4.03	3.93	3.92	3.97	3.82	3.89	3.97
Ca	0.00	0.00	0.00	0.00	0.00	0.02	0.00	0.00	0.00	0.00	0.00	0.00	0.27
Mn	0.01	0.01	0.01	0.01	0.01	0.01	0.01	0.01	0.02	0.01	0.01	0.01	0.01
Fe^{2+}	1.12	1.21	1.21	1.10	1.16	1.17	1.15	1.11	1.07	1.15	1.18	1.17	1.30
Na	0.02	0.01	0.03	0.02	0.02	0.02	0.01	0.02	0.02	0.02	0.02	0.02	0.01
K	2.38	2.43	2.34	2.31	2.41	2.29	2.35	2.33	2.27	2.35	2.38	2.30	1.67
Ba	0.03	0.03	0.03	0.02	0.02	0.03	0.03	0.03	0.03	0.03	0.02	0.03	0.02
F	0.33	0.45	0.46	0.54	0.38	0.46	0.41	0.46	0.44	0.44	0.42	0.51	0.35
Cl	0.01	0.01	0.02	0.02	0.02	0.02	0.02	0.02	0.02	0.02	0.02	0.01	0.02
Li*	0.03	0.05	0.05	0.07	0.04	0.05	0.04	0.05	0.05	0.05	0.04	0.06	0.03
OH^-	3.65	3.53	3.52	3.43	3.60	3.53	3.57	3.52	3.54	3.54	3.56	3.47	3.63
Mg/(Mg + Fe)	**0.78**	**0.76**	**0.76**	**0.79**	**0.77**	**0.77**	**0.78**	**0.78**	**0.79**	**0.78**	**0.76**	**0.77**	**0.75**

Table 30: *Henderson South plagioclase data.*

Point	Sample	C/M/S	SiO_2	TiO_2	Al_2O_3	Cr_2O_3	FeO	MnO	MgO	CaO	BaO	Na_2O	K_2O	**Total**	**An**
P1 / 1	SD-55-24C	Core	53.61	0.00	30.38	0.00	0.12	0.02	0.00	11.91	0.01	4.26	0.40	**100.71**	**59.31**
P2 / 1	SD-55-24C	Core	55.18	0.00	30.12	0.00	0.16	0.00	0.00	11.81	0.00	4.12	0.33	**101.72**	**60.06**
P3 /	SD-55-24C	Core	53.56	0.00	30.80	0.00	0.12	0.01	0.00	11.47	0.00	4.43	0.40	**100.79**	**57.47**
P4 / 1	SD-55-24C	Core	53.89	0.03	30.54	0.00	0.16	0.02	0.00	10.84	0.00	4.21	0.42	**100.11**	**57.19**
P5 / 1	SD-55-24C	Core	54.37	0.00	29.68	0.00	0.08	0.00	0.00	10.96	0.02	4.41	0.36	**99.88**	**56.59**
P6 / 1	SD-55-24C	Core	53.77	0.00	30.14	0.04	0.08	0.00	0.00	10.87	0.00	4.26	0.31	**99.47**	**57.37**
P8 / 1	SD-55-24C	Core	55.71	0.02	29.22	0.01	0.14	0.00	0.00	10.58	0.00	4.34	0.36	**100.37**	**56.09**
P9 / 1	SD-55-24C	Core	54.34	0.00	29.70	0.00	0.15	0.00	0.00	10.37	0.02	4.27	0.38	**99.23**	**55.95**
P12 / 1	SD-55-24C	Core	54.93	0.00	29.47	0.01	0.13	0.00	0.00	10.75	0.01	4.24	0.37	**99.90**	**57.00**
P13 / 1	SD-55-24C	Core	54.59	0.00	29.80	0.00	0.09	0.01	0.00	10.82	0.00	4.35	0.34	**99.99**	**56.66**
P14 / 1	SD-55-24C	Core	54.27	0.00	29.96	0.02	0.17	0.00	0.00	11.64	0.00	4.25	0.30	**100.61**	**59.10**
P15 / 1	SD-55-24C	Core	54.59	0.03	30.14	0.00	0.10	0.01	0.00	10.74	0.00	4.31	0.34	**100.26**	**56.69**
P19 / 1	SD-55-24C	Core	53.67	0.00	29.98	0.00	0.08	0.01	0.00	10.62	0.02	4.50	0.41	**99.27**	**55.18**
P20 / 1	SD-55-24C	Core	55.69	0.00	28.97	0.01	0.10	0.00	0.00	10.26	0.01	4.34	0.42	**99.79**	**55.10**
P21 / 1	SD-55-24C	Core	54.55	0.00	28.99	0.00	0.10	0.00	0.00	10.54	0.01	4.51	0.27	**98.97**	**55.42**
P36 / 1	SD-55-24C	Core	55.91	0.00	28.67	0.01	0.10	0.01	0.00	10.44	0.01	4.16	0.36	**99.67**	**56.72**
P37 / 1	SD-55-24C	Core	55.01	0.02	29.53	0.03	0.08	0.03	0.00	10.63	0.02	4.26	0.38	**99.99**	**56.58**

Table 31 continued

Point	Sample	C/M/S	SiO_2	TiO_2	Al_2O_3	Cr_2O_3	FeO	MnO	MgO	CaO	BaO	Na_2O	K_2O	**Total**	**An**
P38 / 1	SD-55-24C	Core	55.34	0.00	29.76	0.00	0.10	0.00	0.00	10.96	0.01	4.35	0.40	**100.91**	**56.78**
P40 / 1	SD-55-24C	Core	54.82	0.00	30.30	0.00	0.16	0.01	0.00	9.72	0.00	4.02	1.51	**100.55**	**51.72**
P41 / 1	SD-55-24C	Core	55.68	0.02	29.35	0.01	0.08	0.01	0.00	10.62	0.02	4.36	0.49	**100.64**	**55.64**
43 / 1	SD-55-24C	Core	54.48	0.00	29.59	0.01	0.12	0.00	0.00	10.79	0.00	4.32	0.37	**99.67**	**56.63**
P44 / 1	SD-55-24C	Core	55.26	0.00	29.36	0.01	0.17	0.02	0.00	10.64	0.01	4.11	0.37	**99.95**	**57.48**
P45 / 1	SD-55-24C	Core	55.64	0.00	29.92	0.03	0.12	0.00	0.00	10.89	0.02	4.46	0.37	**101.45**	**56.16**
P46 / 1	SD-55-24C	Core	55.18	0.00	29.80	0.00	0.09	0.02	0.00	11.01	0.00	4.09	0.32	**100.50**	**58.62**
P47 / 1	SD-55-24C	Core	55.41	0.01	29.55	0.00	0.08	0.00	0.00	10.57	0.03	4.29	0.37	**100.31**	**56.28**
P48 / 1	SD-55-24C	Core	53.36	0.00	30.01	0.00	0.14	0.01	0.00	10.83	0.02	4.28	0.42	**99.05**	**56.78**
P49 / 1	SD-55-24C	Core	54.54	0.00	29.70	0.00	0.11	0.00	0.00	11.16	0.00	4.38	0.38	**100.27**	**57.12**
P50 / 1	SD-55-24C	Core	53.77	0.00	29.88	0.04	0.14	0.00	0.00	10.70	0.01	4.21	0.39	**99.15**	**56.95**
P53 / 1	SD-55-24C	Core	55.04	0.02	29.57	0.00	0.15	0.01	0.00	10.60	0.01	4.36	0.41	**100.16**	**55.84**
P57 / 1	SD-55-24C	Core	55.62	0.01	29.20	0.00	0.12	0.00	0.00	10.50	0.01	4.56	0.32	**100.35**	**54.86**
P58 / 1	SD-55-24C	Core	54.67	0.00	29.59	0.00	0.09	0.01	0.00	10.78	0.00	4.16	0.35	**99.66**	**57.54**
P60 / 1	SD-55-24C	Core	55.72	0.00	29.51	0.01	0.09	0.00	0.00	10.72	0.01	4.35	0.38	**100.79**	**56.27**
P61 / 1	SD-55-24C	Core	54.43	0.00	29.39	0.01	0.14	0.00	0.00	10.78	0.03	4.05	0.35	**99.17**	**58.22**

Table 31 continued

Point	Sample	C/M/S	SiO_2	TiO_2	Al_2O_3	Cr_2O_3	FeO	MnO	MgO	CaO	BaO	Na_2O	K_2O	**Total**	**An**
P63 / 1	SD-55-24C	Core	55.17	0.00	29.23	0.00	0.13	0.00	0.00	10.87	0.01	4.20	0.37	**99.98**	**57.48**
P65 / 1	SD-55-24C	Core	55.26	0.04	29.27	0.00	0.10	0.00	0.00	11.16	0.00	4.26	0.41	**100.51**	**57.65**
P66 / 1	SD-55-24C	Core	55.93	0.02	29.02	0.01	0.10	0.01	0.00	10.68	0.01	4.12	0.40	**100.31**	**57.40**
P68 / 1	SD-55-24C	Core	54.61	0.00	28.94	0.01	0.09	0.02	0.00	10.47	0.00	4.20	0.38	**98.72**	**56.55**
P69 / 1	SD-55-24C	Core	54.62	0.02	30.00	0.02	0.14	0.01	0.00	11.00	0.00	4.09	0.34	**100.24**	**58.49**
P70 / 1	SD-55-24C	Core	55.99	0.00	30.02	0.00	0.08	0.01	0.00	10.91	0.01	4.16	0.29	**101.47**	**58.05**
P71 / 1	SD-55-24C	Core	54.86	0.00	30.39	0.04	0.13	0.00	0.00	11.40	0.01	4.28	0.26	**101.37**	**58.63**
P72 / 1	SD-55-24C	Core	54.01	0.02	30.18	0.00	0.12	0.01	0.00	10.69	0.01	4.37	0.27	**99.69**	**56.49**
P73 / 1	SD-55-24C	Core	55.18	0.00	29.01	0.00	0.13	0.00	0.00	11.00	0.02	4.19	0.29	**99.82**	**58.10**
P74 / 1	SD-55-24C	Core	53.77	0.00	30.45	0.03	0.12	0.01	0.00	10.93	0.02	4.39	0.36	**100.06**	**56.63**
P75 / 1	SD-55-24C	Core	55.35	0.01	29.69	0.02	0.13	0.00	0.00	10.59	0.03	4.24	0.38	**100.43**	**56.55**
P76 / 1	SD-55-24C	Core	53.62	0.00	30.92	0.00	0.17	0.02	0.00	11.25	0.02	4.28	0.29	**100.57**	**58.17**
P77 / 1	SD-55-24C	Core	55.32	0.00	30.39	0.01	0.15	0.00	0.00	11.32	0.00	4.02	0.33	**101.55**	**59.59**
P78 / 1	SD-55-24C	Core	54.18	0.01	30.02	0.00	0.08	0.00	0.00	10.65	0.00	4.38	0.40	**99.72**	**55.90**
P79 / 1	SD-55-24C	Core	54.79	0.01	29.96	0.01	0.09	0.00	0.00	10.83	0.01	3.97	0.36	**100.04**	**58.74**

Table 31 continued

Point	Sample	C/M/S	SiO_2	TiO_2	Al_2O_3	Cr_2O_3	FeO	MnO	MgO	CaO	BaO	Na_2O	K_2O	**Total**	**An**
P94 / 1	SD-55-24B	Core	54.95	0.00	28.90	0.00	0.10	0.03	0.00	10.26	0.01	4.53	0.21	**98.99**	**54.83**
P97 / 1	SD-55-24B	Core	53.54	0.03	29.81	0.00	0.12	0.01	0.00	11.31	0.03	4.04	0.27	**99.15**	**59.70**
P98 / 1	SD-55-24B	Core	54.99	0.00	28.94	0.02	0.13	0.01	0.00	10.70	0.03	4.32	0.25	**99.38**	**56.88**
P101 / 1	SD-55-24B	Core	54.93	0.00	28.15	0.01	0.10	0.00	0.00	12.43	0.02	3.99	0.29	**99.93**	**62.14**
P103 / 1	SD-55-24B	Core	54.62	0.03	29.61	0.00	0.13	0.00	0.00	10.78	0.00	4.55	0.38	**100.11**	**55.36**
P104 / 1	SD-55-24B	Core	54.91	0.00	29.56	0.00	0.08	0.00	0.00	10.70	0.00	4.45	0.32	**100.01**	**55.95**
P106 / 1	SD-55-24B	Core	55.38	0.03	29.53	0.00	0.11	0.02	0.00	10.56	0.00	4.27	0.32	**100.21**	**56.58**
P107 / 1	SD-55-24B	Core	53.78	0.00	29.32	0.00	0.10	0.02	0.00	10.86	0.00	4.52	0.32	**98.92**	**55.92**
P108 / 1	SD-55-24B	Core	54.46	0.00	29.16	0.00	0.16	0.00	0.00	10.71	0.02	4.19	0.43	**99.12**	**56.97**
P109 / 1	SD-55-24B	Core	54.39	0.01	29.54	0.02	0.13	0.01	0.00	10.80	0.02	4.44	0.41	**99.76**	**55.90**
P110 / 1	SD-55-24B	Core	55.23	0.01	29.65	0.00	0.11	0.02	0.00	10.69	0.01	4.41	0.34	**100.48**	**56.02**
P111 / 1	SD-55-24B	Core	55.88	0.00	28.41	0.00	0.08	0.01	0.00	10.35	0.00	4.42	0.44	**99.58**	**54.87**
P115 / 1	SD-55-24B	Core	55.93	0.02	29.28	0.01	0.12	0.00	0.00	10.60	0.00	4.23	0.69	**100.88**	**55.57**
P116 / 1	SD-55-24B	Core	54.32	0.00	29.40	0.02	0.10	0.00	0.00	10.66	0.00	4.44	0.33	**99.27**	**55.84**
P117 / 1	SD-55-24B	Core	54.76	0.00	28.05	0.00	0.07	0.00	0.00	10.56	0.01	4.06	0.35	**97.86**	**57.62**
P124 / 1	SD-55-24B	Core	55.19	0.00	28.99	0.01	0.12	0.00	0.00	10.61	0.01	4.22	0.45	**99.61**	**56.50**

Table 31 continued

Point	Sample	C/M/S	SiO_2	TiO_2	Al_2O_3	Cr_2O_3	FeO	MnO	MgO	CaO	BaO	Na_2O	K_2O	**Total**	**An**
P126 / 1	SD-55-24B	Core	54. 04	0.00	29.80	0.02	0.13	0.00	0.00	10.97	0.00	4.30	0.38	**99.65**	**57.13**
P8 / 1	SD-55-24A	Matrix	53.33	0.01	30.45	0.00	0.15	0.00	0.00	10.06	0.00	4.22	0.33	**98.57**	**55.59**
P9 / 1	SD-55-24A	Matrix	54.31	0.00	29.09	0.01	0.10	0.00	0.00	10.88	0.03	4.36	0.35	**99.12**	**56.73**
P10 / 1	SD-55-24A	Matrix	54.76	0.01	28.94	0.01	0.12	0.01	0.00	10.18	0.01	4.25	0.44	**98.72**	**55.37**
P11 / 1	SD-55-24A	Matrix	55.45	0.00	29.63	0.00	0.10	0.00	0.00	10.94	0.01	4.40	0.31	**100.83**	**56.76**
P13 / 1	SD-55-24A	Matrix	55.12	0.00	28.92	0.03	0.11	0.01	0.00	10.60	0.00	4.35	0.41	**99.54**	**55.95**
P14 / 1	SD-55-24A	Matrix	55.13	0.00	28.09	0.00	0.08	0.00	0.00	10.29	0.01	4.32	0.34	**98.25**	**55.59**
P16 / 1	SD-55-24A	Matrix	54.49	0.00	29.37	0.01	0.15	0.00	0.00	10.35	0.00	4.28	0.36	**99.02**	**55.87**
P19 / 1	SD-55-24A	Matrix	54.37	0.00	29.29	0.01	0.15	0.01	0.00	11.03	0.01	4.24	0.34	**99.44**	**57.74**
P20 / 1	SD-55-24A	Matrix	53.40	0.03	29.83	0.03	0.13	0.01	0.00	10.91	0.00	4.15	0.38	**98.88**	**57.80**
P21 / 1	SD-55-24A	Matrix	54.45	0.00	28.17	0.00	0.10	0.00	0.00	10.85	0.01	4.00	0.35	**97.93**	**58.65**
P22 / 1	SD-55-24A	Matrix	54.52	0.00	28.56	0.00	0.07	0.00	0.00	10.54	0.00	4.14	0.41	**98.22**	**56.94**
P23 / 1	SD-55-24A	Matrix	54.03	0.00	28.66	0.02	0.07	0.02	0.00	10.46	0.01	4.38	0.44	**98.07**	**55.32**
P24 / 1	SD-55-24A	Matrix	53.13	0.00	29.72	0.02	0.06	0.02	0.00	10.75	0.00	4.24	0.39	**98.31**	**56.92**
P26 / 1	SD-55-24A	Matrix	54.76	0.00	28.27	0.00	0.07	0.00	0.00	10.22	0.00	4.26	0.40	**97.98**	**55.55**
P27 / 1	SD-55-24A	Matrix	54.23	0.00	29.21	0.00	0.14	0.01	0.00	11.03	0.02	4.30	0.34	**99.29**	**57.41**

Table 31 continued

Point	Sample	C/M/S	SiO_2	TiO_2	Al_2O_3	Cr_2O_3	FeO	MnO	MgO	CaO	BaO	Na_2O	K_2O	**Total**	**An**
P30 / 1	SD-55-24A	Matrix	54.18	0.00	28.80	0.02	0.07	0.00	0.00	10.21	0.02	4.43	0.30	**98.03**	**54.95**
P75 / 1	SD-55-24B	m	52.97	0.00	29.46	0.01	0.12	0.00	0.00	11.24	0.01	4.10	0.34	**98.25**	**58.98**
P76 / 1	SD-55-24B	Matrix	54.24	0.01	28.93	0.00	0.09	0.02	0.00	10.99	0.00	3.90	0.33	**98.51**	**59.61**
P77 / 1	SD-55-24B	Matrix	53.91	0.00	29.39	0.00	0.13	0.00	0.00	11.08	0.02	4.13	0.36	**99.02**	**58.36**
P78 / 1	SD-55-24B	Matrix	54.43	0.00	29.13	0.01	0.10	0.00	0.00	10.72	0.01	4.20	0.43	**99.03**	**56.94**
P79 / 1	SD-55-24B	Matrix	54.13	0.00	29.22	0.02	0.20	0.03	0.05	10.30	0.00	4.61	0.26	**98.81**	**54.34**
P81 / 1	SD-55-24B	Matrix	54.10	0.00	30.22	0.02	0.13	0.01	0.00	11.23	0.01	4.23	0.38	**100.32**	**58.07**
P84 / 1	SD-55-24B	Matrix	53.39	0.01	29.07	0.02	0.12	0.00	0.00	10.98	0.01	4.09	0.36	**98.05**	**58.38**
P85 / 1	SD-55-24B	Matrix	53.64	0.02	30.09	0.00	0.12	0.02	0.00	11.13	0.01	4.20	0.36	**99.59**	**58.08**
P86 / 1	SD-55-24B	Matrix	53.52	0.03	28.10	0.00	0.10	0.00	0.00	10.28	0.01	4.18	0.38	**96.60**	**56.19**
P87 / 1	SD-55-24B	Matrix	53.46	0.00	30.26	0.02	0.18	0.00	0.00	11.05	0.02	4.07	0.36	**99.41**	**58.64**
P88 / 1	SD-55-24B	Matrix	54.75	0.00	29.17	0.01	0.08	0.00	0.00	10.80	0.00	4.45	0.38	**99.64**	**55.93**
P89 / 1	SD-55-24B	Matrix	53.86	0.02	30.18	0.00	0.11	0.00	0.00	10.90	0.00	4.19	0.38	**99.63**	**57.53**
P90 / 1	SD-55-24B	Matrix	53.93	0.00	29.29	0.00	0.15	0.01	0.00	10.87	0.01	4.11	0.37	**98.74**	**57.98**
P128 / 1	SD-55-24B	Matrix	55.17	0.00	29.70	0.00	0.10	0.01	0.00	11.11	0.01	4.21	0.34	**100.67**	**58.06**
P130 / 1	SD-55-24B	Matrix	55.51	0.00	30.08	0.00	0.12	0.03	0.06	10.89	0.02	4.21	0.54	**101.48**	**56.87**

Table 31 continued

Point	Sample	C/M/S	SiO_2	TiO_2	Al_2O_3	Cr_2O_3	FeO	MnO	MgO	CaO	BaO	Na_2O	K_2O	**Total**	**An**
P132 / 1	SD-55-24B	Matrix	54.75	0.02	28.71	0.01	0.14	0.00	0.00	10.68	0.01	3.97	0.37	**98.66**	**58.37**
P133 / 1	SD-55-24B	Matrix	55.29	0.03	29.91	0.00	0.11	0.01	0.00	11.46	0.00	4.12	0.33	**101.28**	**59.31**
P134 / 1	SD-55-24B	Matrix	55.01	0.00	29.77	0.00	0.12	0.02	0.00	10.99	0.00	4.10	0.37	**100.37**	**58.31**
P135 / 1	SD-55-24B	Matrix	54.67	0.00	29.82	0.00	0.14	0.00	0.00	10.80	0.00	4.36	0.30	**100.09**	**56.73**
P136 / 1	SD-55-24B	Matrix	54.30	0.00	29.67	0.01	0.12	0.01	0.00	10.17	0.01	4.09	0.32	**98.71**	**56.68**
P2 / 1	SD-55-24A	Matrix	53.88	0.00	32.05	0.00	0.05	0.01	0.00	10.40	0.01	4.20	0.34	**100.94**	**56.49**
P3 / 1	SD-55-24A	Matrix	53.62	0.02	30.29	0.03	0.12	0.00	0.00	10.62	0.00	4.49	0.39	**99.59**	**55.29**
P4 / 1	SD-55-24A	Matrix	53.15	0.00	29.98	0.00	0.06	0.00	0.00	10.81	0.00	4.24	0.34	**98.58**	**57.25**
P5 / 1	SD-55-24A	Matrix	55.63	0.00	30.43	0.01	0.09	0.02	0.00	11.04	0.01	4.32	0.36	**101.90**	**57.25**
P6 / 1	SD-55-24A	Matrix	53.21	0.00	29.74	0.01	0.10	0.02	0.00	10.46	0.01	4.19	0.35	**98.08**	**56.67**
P34 / 1	SD-55-24B	Matrix	53.26	0.00	29.54	0.03	0.12	0.00	0.00	10.76	0.02	4.14	0.31	**98.17**	**57.82**
P35 / 1	SD-55-24B	Matrix	54.38	0.00	30.08	0.00	0.09	0.00	0.00	11.55	0.01	4.31	0.29	**100.71**	**58.65**
P36 / 1	SD-55-24B	Matrix	54.40	0.01	30.66	0.01	0.08	0.00	0.00	11.13	0.00	4.10	0.28	**100.66**	**58.94**
P37 / 1	SD-55-24B	Matrix	53.45	0.00	30.21	0.02	0.12	0.00	0.00	11.12	0.02	4.30	0.31	**99.55**	**57.69**
P38 / 1	SD-55-24B	Matrix	54.43	0.01	30.41	0.01	0.09	0.00	0.00	11.16	0.00	4.13	0.31	**100.56**	**58.76**
P42 / 1	SD-55-24B	Matrix	53.47	0.03	29.46	0.03	0.09	0.00	0.00	10.48	0.01	4.23	0.36	**98.16**	**56.44**
P43 / 1	SD-55-24B	Matrix	53.94	0.00	29.11	0.00	0.12	0.00	0.00	10.85	0.00	4.18	0.64	**98.85**	**56.58**

Table 31 continued

Point	Sample	C/M/S	SiO_2	TiO_2	Al_2O_3	Cr_2O_3	FeO	MnO	MgO	CaO	BaO	Na_2O	K_2O	**Total**	**An**
P44 / 1	SD-55-24B	Matrix	53.56	0.00	30.43	0.00	0.17	0.01	0.00	11.38	0.02	4.15	0.30	**100.02**	**59.09**
P45 / 1	SD-55-24B	Matrix	55.13	0.00	27.87	0.00	0.14	0.02	0.00	10.37	0.01	4.13	0.29	**97.97**	**56.98**
P46 / 1	SD-55-24B	Matrix	54.41	0.00	30.07	0.00	0.11	0.03	0.00	11.47	0.01	4.20	0.24	**100.54**	**59.28**
P48 / 1	SD-55-24B	Matrix	53.49	0.00	29.79	0.00	0.12	0.00	0.00	10.97	0.00	4.15	0.34	**98.86**	**58.09**
P49 / 1	SD-55-24B	Matrix	53.80	0.01	29.67	0.00	0.14	0.02	0.00	11.31	0.00	4.16	0.28	**99.38**	**59.02**
P51 / 1	SD-55-24B	Matrix	55.14	0.01	28.82	0.00	0.16	0.00	0.00	10.39	0.00	4.34	0.24	**99.11**	**56.05**
P54 / 1	SD-55-24B	Matrix	54.18	0.00	28.48	0.01	0.13	0.00	0.00	10.68	0.01	4.23	0.32	**98.03**	**57.09**
P55 / 1	SD-55-24B	Matrix	54.91	0.00	28.10	0.00	0.10	0.02	0.00	10.69	0.00	4.10	0.33	**98.26**	**57.78**
P56 / 1	SD-55-24B	Matrix	54.04	0.01	29.22	0.00	0.08	0.00	0.00	10.68	0.01	4.41	0.30	**98.75**	**56.18**
P57 / 1	SD-55-24B	Matrix	54.68	0.00	29.32	0.01	0.10	0.00	0.00	11.49	0.00	4.00	0.30	**99.90**	**60.23**
P58 / 1	SD-55-24B	Matrix	53.50	0.00	29.40	0.01	0.14	0.00	0.00	10.84	0.00	4.23	0.39	**98.52**	**57.17**
P59 / 1	SD-55-24B	Matrix	55.79	0.01	28.51	0.00	0.09	0.03	0.00	10.38	0.01	4.39	0.30	**99.50**	**55.58**
P62 / 1	SD-55-24B	Matrix	54.05	0.00	28.76	0.01	0.09	0.00	0.00	10.35	0.01	4.32	0.42	**98.01**	**55.47**
P63 / 1	SD-55-24B	Matrix	54.25	0.02	29.02	0.01	0.10	0.03	0.00	10.59	0.00	4.26	0.34	**98.62**	**56.63**
P65 / 1	SD-55-24B	Matrix	55.75	0.00	29.54	0.05	0.13	0.02	0.00	11.31	0.01	4.05	0.36	**101.22**	**59.30**
P66 / 1	SD-55-24B	Matrix	55.83	0.02	28.26	0.00	0.08	0.00	0.00	10.27	0.01	4.15	0.34	**98.98**	**56.45**
P67 / 1	SD-55-24B	Matrix	53.52	0.00	29.31	0.00	0.32	0.02	0.02	10.53	0.01	4.34	0.31	**98.38**	**56.15**

Table 31 continued

Point	Sample	C/M/S	SiO_2	TiO_2	Al_2O_3	Cr_2O_3	FeO	MnO	MgO	CaO	BaO	Na_2O	K_2O	**Total**	**An**
P69 / 1	SD-55-24B	Matrix	55.30	0.04	28.90	0.00	0.19	0.00	0.00	10.44	0.00	3.84	0.37	**99.08**	**58.58**
P71 / 1	SD-55-24B	Matrix	54.17	0.00	30.16	0.01	0.15	0.00	0.00	11.08	0.01	4.06	0.33	**99.97**	**58.90**
P72 / 1	SD-55-24B	Matrix	53.58	0.01	29.71	0.00	0.05	0.01	0.00	10.95	0.01	4.24	0.37	**98.93**	**57.44**
P73 / 1	SD-55-24B	Matrix	53.77	0.01	30.01	0.01	0.13	0.00	0.00	10.64	0.00	4.43	0.40	**99.41**	**55.61**
P101 / 1	SD-55-24D	Matrix	55.43	0.00	29.52	0.00	0.09	0.00	0.00	10.76	0.01	4.35	0.31	**100.47**	**56.64**
P102 / 1	SD-55-24D	Matrix	52.99	0.04	30.78	0.00	0.11	0.00	0.00	11.59	0.00	4.28	0.31	**100.10**	**58.80**
P103 / 1	SD-55-24D	Matrix	54.53	0.00	30.60	0.00	0.14	0.02	0.00	11.24	0.01	4.13	0.29	**100.96**	**59.01**
P104 / 1	SD-55-24D	Matrix	53.28	0.03	29.69	0.00	0.14	0.00	0.00	11.10	0.01	4.16	0.32	**98.72**	**58.40**
P105 / 1	SD-55-24D	Matrix	54.98	0.00	30.86	0.01	0.07	0.00	0.00	11.30	0.03	4.22	0.35	**101.83**	**58.39**
P106 / 1	SD-55-24D	Matrix	54.66	0.00	28.89	0.01	0.06	0.00	0.00	10.45	0.00	4.21	0.35	**98.62**	**56.55**
P108 / 1	SD-55-24D	Matrix	54.96	0.01	29.21	0.00	0.07	0.00	0.00	11.00	0.02	4.09	0.33	**99.69**	**58.54**
P109 / 1	SD-55-24D	Matrix	54.92	0.01	29.20	0.00	0.08	0.00	0.00	10.57	0.01	4.26	0.29	**99.35**	**56.75**
P110 / 1	SD-55-24D	Matrix	55.37	0.02	29.88	0.01	0.11	0.00	0.00	10.97	0.01	4.19	0.32	**100.87**	**57.98**
P111 / 1	SD-55-24D	Matrix	54.99	0.00	29.95	0.00	0.10	0.01	0.00	11.16	0.01	4.24	0.31	**100.76**	**58.13**
P112 / 1	SD-55-24D	Matrix	55.17	0.00	29.44	0.00	0.15	0.01	0.00	11.11	0.01	4.02	0.30	**100.22**	**59.27**
P113 / 1	SD-55-24D	Matrix	55.98	0.01	29.33	0.00	0.05	0.01	0.00	10.59	0.00	4.31	0.35	**100.62**	**56.30**

Table 31 continued

Point	Sample	C/M/S	SiO_2	TiO_2	Al_2O_3	Cr_2O_3	FeO	MnO	MgO	CaO	BaO	Na_2O	K_2O	**Total**	**An**
P115 / 1	SD-55-24D	Matrix	55.02	0.00	28.84	0.00	0.11	0.00	0.00	10.41	0.01	4.28	0.35	**99.02**	**56.08**
P117 / 1	SD-55-24D	Matrix	52.89	0.00	30.37	0.00	0.08	0.01	0.00	10.68	0.02	4.59	0.50	**99.14**	**54.54**
P118 / 1	SD-55-24D	Matrix	55.70	0.01	29.57	0.03	0.06	0.00	0.00	10.81	0.02	4.07	0.33	**100.60**	**58.20**
P119 / 1	SD-55-24D	Matrix	55.05	0.00	29.61	0.00	0.08	0.00	0.00	11.05	0.00	4.25	0.30	**100.34**	**57.86**
P120 / 1	SD-55-24D	Matrix	55.09	0.01	29.65	0.00	0.15	0.00	0.00	10.64	0.02	4.12	0.36	**100.03**	**57.48**
P121 / 1	SD-55-24D	Matrix	55.82	0.02	28.79	0.00	0.09	0.01	0.00	10.47	0.02	4.34	0.37	**99.92**	**55.79**
P122 / 1	SD-55-24D	Matrix	53.73	0.01	29.80	0.02	0.09	0.01	0.00	10.35	0.02	4.28	0.40	**98.70**	**55.71**
P123 / 1	SD-55-24D	Matrix	55.55	0.00	29.65	0.00	0.16	0.01	0.00	10.68	0.01	4.34	0.37	**100.78**	**56.26**
P124 / 1	SD-55-24D	Matrix	53.95	0.00	30.14	0.00	0.11	0.00	0.00	10.59	0.00	4.54	0.38	**99.70**	**54.99**
P125 / 1	SD-55-24D	Matrix	55.49	0.00	29.92	0.00	0.16	0.02	0.00	10.67	0.00	4.47	0.45	**101.18**	**55.30**
P126 / 1	SD-55-24D	Matrix	55.69	0.03	29.96	0.01	0.07	0.00	0.00	10.38	0.02	4.35	0.38	**100.91**	**55.49**
P127 / 1	SD-55-24D	Matrix	54.78	0.00	29.45	0.00	0.11	0.00	0.00	10.65	0.01	4.37	0.36	**99.72**	**56.08**
P128 / 1	SD-55-24D	Matrix	54.09	0.00	30.40	0.00	0.09	0.00	0.00	10.56	0.01	4.36	0.39	**99.89**	**55.85**
P129 / 1	SD-55-24D	Matrix	53.18	0.00	30.10	0.02	0.10	0.00	0.00	10.68	0.01	4.37	0.34	**98.82**	**56.19**
P130 / 1	SD-55-24D	Matrix	55.81	0.00	29.67	0.02	0.07	0.00	0.00	10.66	0.02	4.23	0.35	**100.84**	**56.90**
P131 / 1	SD-55-24D	Matrix	52.37	0.00	30.55	0.00	0.12	0.00	0.00	11.38	0.02	4.42	0.33	**99.18**	**57.58**

Table 31 continued

Point	Sample	C/M/S	SiO_2	TiO_2	Al_2O_3	Cr_2O_3	FeO	MnO	MgO	CaO	BaO	Na_2O	K_2O	**Total**	**An**
P134 / 1	SD-55-24D	Matrix	54.65	0.02	28.40	0.01	0.11	0.02	0.00	10.11	0.02	4.29	0.38	**98.00**	**55.17**
P136 / 1	SD-55-24D	Matrix	55.70	0.00	30.43	0.00	0.12	0.00	0.00	11.08	0.02	4.27	0.31	**101.93**	**57.78**
P137 / 1	SD-55-24D	Matrix	53.53	0.00	29.26	0.01	0.05	0.00	0.00	11.16	0.00	3.96	0.31	**98.29**	**59.67**
P138 / 1	SD-55-24D	Matrix	55.71	0.00	28.58	0.00	0.09	0.02	0.00	10.40	0.02	4.20	0.40	**99.41**	**56.28**
P139 / 1	SD-55-24D	Matrix	55.95	0.02	29.00	0.00	0.08	0.01	0.00	10.50	0.00	4.50	0.36	**100.42**	**55.08**
P140 / 1	SD-55-24D	Matrix	55.66	0.00	30.40	0.01	0.06	0.01	0.00	11.14	0.00	4.05	0.32	**101.66**	**59.10**
P141 / 1	SD-55-24D	Matrix	55.18	0.02	30.18	0.00	0.07	0.00	0.00	11.25	0.00	4.38	0.28	**101.34**	**57.66**
P228 / 1	SD-55-24D	Matrix	55.56	0.00	29.55	0.04	0.06	0.01	0.00	10.87	0.01	4.35	0.32	**100.77**	**56.84**
P230 / 1	SD-55-24D	Matrix	55.99	0.00	28.89	0.00	0.08	0.01	0.00	10.40	0.02	4.50	0.24	**100.13**	**55.25**
P231 / 1	SD-55-24D	Matrix	54.71	0.03	28.53	0.01	0.12	0.00	0.00	10.49	0.00	4.32	0.39	**98.60**	**55.88**
P232 / 1	SD-55-24D	Matrix	55.77	0.00	27.92	0.00	0.10	0.00	0.00	10.13	0.04	4.33	0.38	**98.66**	**55.03**
P233 / 1	SD-55-24D	Matrix	54.40	0.06	28.48	0.00	0.06	0.00	0.00	11.02	0.02	4.36	0.32	**98.71**	**57.10**
P234 / 1	SD-55-24D	Matrix	55.78	0.00	29.37	0.00	0.09	0.03	0.00	10.83	0.02	4.30	0.31	**100.73**	**57.05**
P235 / 1	SD-55-24D	Matrix	55.98	0.01	29.52	0.03	0.17	0.00	0.00	11.25	0.00	4.23	0.26	**101.45**	**58.54**
P236 / 1	SD-55-24D	Matrix	56.41	0.00	28.32	0.00	0.10	0.00	0.00	10.67	0.00	4.32	0.27	**100.08**	**56.75**
P237 / 1	SD-55-24D	Matrix	55.97	0.01	28.72	0.00	0.12	0.00	0.00	11.19	0.01	4.38	0.36	**100.75**	**57.27**

Table 31 continued

Point	Sample	C/M/S	SiO_2	TiO_2	Al_2O_3	Cr_2O_3	FeO	MnO	MgO	CaO	BaO	Na_2O	K_2O	**Total**	**An**
P239 / 1	SD-55-24D	Matrix	55.49	0.00	28.79	0.02	0.09	0.00	0.00	10.51	0.00	4.54	0.27	**99.72**	**55.16**
P240 / 1	SD-55-24D	Matrix	56.48	0.01	28.15	0.00	0.08	0.02	0.00	10.30	0.00	4.26	0.35	**99.65**	**55.90**
P241 / 1	SD-55-24D	Matrix	54.60	0.00	29.48	0.00	0.08	0.00	0.00	10.77	0.01	4.31	0.30	**99.55**	**56.91**
P242 / 1	SD-55-24D	Matrix	57.26	0.00	29.09	0.00	0.13	0.00	0.00	10.49	0.01	4.43	0.33	**101.75**	**55.50**
P243 / 1	SD-55-24D	Matrix	55.44	0.02	29.27	0.02	0.07	0.00	0.00	11.01	0.02	4.29	0.33	**100.46**	**57.45**
P244 / 1	SD-55-24D	Matrix	55.12	0.01	29.01	0.01	0.13	0.03	0.00	10.84	0.01	4.20	0.29	**99.63**	**57.72**
P245 / 1	SD-55-24D	Matrix	55.32	0.00	29.78	0.00	0.13	0.00	0.00	11.00	0.00	4.11	0.27	**100.63**	**58.65**
P246 / 1	SD-55-24D	Matrix	57.43	0.00	28.73	0.00	0.08	0.00	0.00	10.56	0.01	4.41	0.28	**101.50**	**55.97**
P247 / 1	SD-55-24D	Matrix	56.37	0.00	28.49	0.01	0.04	0.00	0.00	10.43	0.00	4.40	0.25	**99.99**	**55.85**

Table 31: *Microprobe analyses of biotite from Henderson South orbicules.*

Dataset/Point	36 / 1	69 / 1	71 / 1	72 / 1	7 3 / 1	74 / 1	77 / 1	78 / 1	81 / 1	82 / 1	88 / 1
Sample	SD-55-24B	SD-5-24C	SD-5-24C	SD-5-24C	SD-5-24C	SD-5-24C	SD-5-24C	SD-5-24C	SD-5-24C	SD-5-24C	SD-5-24C
C/S/M	C	C	C	C	C	C	C	C	C	C	C
SiO2	37.50	39.08	37.26	37.37	38.05	38.77	37.30	37.59	37.70	37.43	38.55
TiO2	2.91	3.13	3.08	3.24	3.63	3.08	2.59	3.06	2.82	2.67	2.97
Al2O3	14.40	12.44	13.10	13.12	13.23	12.21	13.80	12.56	13.15	14.27	14.80
Cr2O3	0.04	0.00	0.00	0.04	0.07	0.00	0.00	0.00	0.03	0.00	0.00
MgO	16.71	15.37	14.52	14.83	16.10	15.59	14.64	15.28	15.19	14.62	12.81
CaO	0.43	0.04	0.02	0.06	0.01	0.00	0.03	0.40	0.06	0.16	0.00
MnO	0.18	0.10	0.17	0.16	0.09	0.17	0.16	0.19	0.23	0.21	0.22
FeO	16.20	14.43	15.47	15.59	14.56	14.67	15.66	16.65	15.98	16.74	16.78
Na2O	0.08	0.09	0.11	0.11	0.10	0.14	0.09	0.08	0.06	0.08	0.08
K2O	7.26	9.07	9.20	9.30	9.42	9.52	9.21	7.84	8.32	8.40	8.70
BaO	0.30	0.41	0.40	0.41	0.45	0.40	0.41	0.39	0.23	0.36	0.41
F	0.93	0.68	0.67	0.71	0.85	1.04	0.59	0.73	0.76	0.43	0.72
Cl	0.11	0.11	0.13	0.10	0.11	0.10	0.08	0.10	0.09	0.08	0.08
Li	0.16	0.09	0.09	0.10	0.14	0.19	0.08	0.11	0.11	0.04	0.10
H2O	3.68	3.70	3.62	3.64	3.68	3.56	3.69	3.64	3.63	3.80	3.71
Total	**100.89**	**98.77**	**97.84**	**98.80**	**100.47**	**99.45**	**98.34**	**98.61**	**98.36**	**99.29**	**99.94**

Number of ions based on 24 oxygen (O, OH, F, Cl)

Si	5.43	5.79	5.62	5.59	5.56	5.71	5.61	5.62	5.63	5.58	5.67
Ti	0.32	0.35	0.35	0.37	0.40	0.34	0.29	0.34	0.32	0.30	0.33
Al^{IV}	2.45	2.17	2.33	2.31	2.28	2.12	2.39	2.21	2.31	2.42	2.33
Al^{VI}	0.00	0.00	0.00	0.00	0.00	0.00	0.05	0.00	0.00	0.09	0.24
Cr	0.00	0.00	0.00	0.00	0.01	0.00	0.00	0.00	0.00	0.00	0.00
Mg	3.60	3.39	3.27	3.31	3.50	3.42	3.28	3.41	3.38	3.25	2.81
Ca	0.07	0.01	0.00	0.01	0.00	0.00	0.01	0.06	0.01	0.03	0.00
Mn	0.02	0.01	0.02	0.02	0.01	0.02	0.02	0.02	0.03	0.03	0.03
Fe^{2+}	1.96	1.79	1.95	1.95	1.78	1.81	1.97	2.08	2.00	2.09	2.07
Na	0.02	0.03	0.03	0.03	0.03	0.04	0.03	0.02	0.02	0.02	0.02
K	1.34	1.71	1.77	1.78	1.76	1.79	1.77	1.49	1.58	1.60	1.63
Ba	0.03	0.05	0.05	0.05	0.05	0.05	0.05	0.05	0.03	0.04	0.05
F	0.42	0.32	0.32	0.34	0.39	0.48	0.28	0.34	0.36	0.20	0.34
Cl	0.03	0.03	0.03	0.03	0.03	0.03	0.02	0.03	0.02	0.02	0.02
Li*	0.01	0.01	0.01	0.01	0.01	0.01	0.00	0.01	0.01	0.00	0.01
OH^-	3.55	3.65	3.65	3.64	3.58	3.49	3.70	3.63	3.62	3.78	3.64
Mg/(Mg + Fe)	**0.65**	**0.66**	**0.63**	**0.63**	**0.66**	**0.65**	**0.63**	**0.62**	**0.63**	**0.61**	**0.58**

Table 32 continued

Dataset/Point	41 / 1	48 / 1	59 / 1	60 / 1	61 / 1	67 / 1	98 / 1	99 / 1
Sample	SD-55-24B	SD-55-24B	SD-55-24A	SD-55-24A	SD-55-24A	SD-55-24A	SD-55-24C	SD-55-24C
C/S/M	S	S	S	S	S	S	S	S
SiO2	37.93	38.33	37.41	38.57	37.74	38.11	39.63	37.29
TiO2	2.65	3.18	3.33	3.37	3.52	2.13	2.74	4.37
Al2O3	13.92	14.14	12.86	12.71	12.36	13.47	15.68	14.13
Cr2O3	0.00	0.04	0.03	0.02	0.00	0.00	0.00	0.00
MgO	14.66	14.56	14.74	13.87	13.61	15.05	14.45	14.07
CaO	0.19	0.03	0.44	0.14	0.04	0.03	1.26	1.34
MnO	0.19	0.22	0.20	0.19	0.21	0.22	0.23	0.20
FeO	15.73	16.26	16.20	16.93	16.67	16.81	14.29	16.13
Na2O	0.10	0.10	0.05	0.03	0.08	0.08	0.56	0.07
K2O	8.52	9.41	8.76	9.76	9.53	8.78	7.14	8.21
BaO	0.27	0.33	0.34	0.38	0.39	0.34	0.21	0.22
F	0.81	0.57	0.65	0.58	0.68	0.40	0.51	0.93
Cl	0.11	0.11	0.10	0.11	0.12	0.07	0.09	0.14
Li	0.12	0.07	0.09	0.07	0.09	0.04	0.06	0.16
H2O	3.63	3.80	3.67	3.75	3.62	3.81	3.91	3.64
Total	**98.84**	**101.16**	**98.85**	**100.48**	**98.68**	**99.34**	**100.76**	**100.89**

Number of ions based on 24 (O, OH, F, Cl)

Si	5.62	5.61	5.60	5.72	5.69	5.69	5.69	5.44
Ti	0.30	0.35	0.37	0.38	0.40	0.24	0.30	0.48
Al^{IV}	2.38	2.39	2.27	2.22	2.20	2.31	2.31	2.43
Al^{VI}	0.06	0.05	0.00	0.00	0.00	0.06	0.35	0.00
Cr	0.00	0.00	0.00	0.00	0.00	0.00	0.00	0.00
Mg	3.24	3.18	3.29	3.06	3.06	3.35	3.09	3.06
Ca	0.03	0.01	0.07	0.02	0.01	0.01	0.19	0.21
Mn	0.02	0.03	0.03	0.02	0.03	0.03	0.03	0.02
Fe^{2+}	1.95	1.99	2.03	2.10	2.10	2.10	1.72	1.97
Na	0.03	0.03	0.02	0.01	0.02	0.02	0.16	0.02
K	1.61	1.76	1.67	1.85	1.83	1.67	1.31	1.53
Ba	0.03	0.04	0.04	0.04	0.05	0.04	0.02	0.02
F	0.38	0.26	0.31	0.27	0.33	0.19	0.23	0.43
Cl	0.03	0.03	0.02	0.03	0.03	0.02	0.02	0.03
Li*	0.01	0.00	0.00	0.00	0.01	0.00	0.00	0.01
OH^-	3.59	3.71	3.67	3.70	3.64	3.79	3.74	3.54
Mg/(Mg + Fe)	**0.62**	**0.61**	**0.62**	**0.59**	**0.59**	**0.61**	**0.64**	**0.61**

Table 32 continued

Point	3 / 1	4 / 1	12 / 1	14 / 1	16 / 1	19 / 1	51 / 1	52 / 1	108 / 1	113 / 1	114 / 1	117 / 1	118 / 1
Sample	SD-55-24B	SD-55-24B	SD-55-24B	SD-55-24B	SD-55-24B	SD-55-24B	SD-55-24A	SD-55-24A	SD-55-24C	SD-55-24C	SD-55-24C	SD-55-24C	SD-55-24C
C/S/M	M	M	M	M	M	M	M	M	M	M	M	M	M
SiO_2	37.25	36.20	37.68	39.33	36.38	37.41	37.04	38.28	39.13	38.57	39.69	39.10	38.49
TiO_2	2.96	3.30	3.94	2.96	3.57	2.83	5.14	3.84	2.92	3.43	3.97	2.87	3.37
Al_2O_3	13.60	14.22	13.85	13.37	13.08	13.23	13.20	13.35	13.56	13.16	12.99	14.18	13.27
Cr_2O_3	0.04	0.01	0.02	0.02	0.03	0.01	0.06	0.00	0.00	0.03	0.02	0.01	0.02
MgO	15.62	14.99	13.32	13.17	13.16	17.38	15.41	14.35	13.90	14.23	13.24	15.20	12.94
CaO	0.02	0.76	0.03	0.03	0.01	0.51	0.05	2.34	0.16	0.07	0.05	0.36	0.31
MnO	0.15	0.18	0.25	0.22	0.15	0.14	0.16	0.21	0.22	0.23	0.17	0.21	0.18
FeO	15.66	15.81	17.40	16.74	16.89	15.19	14.26	16.18	16.57	17.17	16.42	16.07	16.47
Na_2O	0.11	0.08	0.22	0.07	0.14	0.05	0.10	0.04	0.05	0.09	0.13	0.06	0.05
K_2O	9.25	8.36	9.37	9.37	9.66	6.76	8.82	6.64	8.76	9.35	9.57	7.98	9.14
BaO	0.46	0.30	0.27	0.36	0.39	0.29	0.41	0.14	0.26	0.29	0.36	0.24	0.30
F	0.67	0.87	0.57	0.58	0.75	0.65	0.82	0.55	0.67	0.66	0.68	0.52	0.57
Cl	0.10	0.13	0.15	0.14	0.13	0.07	0.09	0.08	0.13	0.11	0.15	0.08	0.15
Li	0.09	0.14	0.07	0.07	0.11	0.09	0.13	0.07	0.09	0.09	0.09	0.06	0.07
H_2O	3.70	3.58	3.75	3.75	3.55	3.72	3.65	3.80	3.73	3.75	3.76	3.86	3.71
Total	**99.68**	**98.94**	**100.90**	**100.17**	**98.01**	**98.33**	**99.33**	**99.89**	**100.15**	**101.24**	**101.29**	**100.80**	**99.05**

Number of ions based on 24 oxygen (O, OH, F, Cl)

Si	5.53	5.39	5.57	5.81	5.54	5.54	5.46	5.62	5.75	5.66	5.79	5.68	5.75
Ti	0.33	0.37	0.44	0.33	0.41	0.31	0.57	0.42	0.32	0.38	0.44	0.31	0.38
Al^{IV}	2.38	2.50	2.41	2.19	2.35	2.31	2.30	2.31	2.25	2.27	2.21	2.32	2.25
Al^{VI}	0.00	0.00	0.00	0.13	0.00	0.00	0.00	0.00	0.10	0.00	0.02	0.11	0.09
Cr	0.00	0.00	0.00	0.00	0.00	0.00	0.00	0.00	0.00	0.00	0.00	0.00	0.00
Mg	3.46	3.33	2.93	2.90	2.99	3.84	3.39	3.14	3.04	3.11	2.88	3.29	2.88
Ca	0.00	0.12	0.00	0.01	0.00	0.08	0.01	0.37	0.03	0.01	0.01	0.06	0.05
Mn	0.02	0.02	0.03	0.03	0.02	0.02	0.02	0.03	0.03	0.03	0.02	0.03	0.02
Fe^{2+}	1.94	1.97	2.15	2.07	2.15	1.88	1.76	1.99	2.04	2.11	2.00	1.95	2.06
Na	0.03	0.02	0.06	0.02	0.04	0.01	0.03	0.01	0.01	0.03	0.04	0.02	0.01
K	1.75	1.59	1.77	1.77	1.88	1.28	1.66	1.24	1.64	1.75	1.78	1.48	1.74
Ba	0.05	0.04	0.03	0.04	0.05	0.03	0.05	0.02	0.03	0.03	0.04	0.03	0.04
F	0.32	0.41	0.27	0.27	0.36	0.31	0.38	0.26	0.31	0.31	0.31	0.24	0.27
Cl	0.02	0.03	0.04	0.03	0.03	0.02	0.02	0.02	0.03	0.03	0.04	0.02	0.04
Li*	0.01	0.01	0.00	0.00	0.01	0.00	0.01	0.00	0.00	0.00	0.00	0.00	0.00
OH^-	3.66	3.56	3.69	3.70	3.60	3.68	3.60	3.72	3.66	3.67	3.65	3.74	3.69
Mg/(Mg + Fe)	**0.64**	**0.63**	**0.58**	**0.58**	**0.58**	**0.67**	**0.66**	**0.61**	**0.60**	**0.60**	**0.59**	**0.63**	**0.58**

Table 32 continued

Point	120 / 1	122 / 1	125 / 1	127 / 1	131 / 1	140 / 1	141 / 1	147 / 1	150 / 1	159 / 1	161 / 1	169 / 1	170 / 1
Sample	SD-55-24C	SD-55-24D	SD-55-24D	SD-55-24D	SD-55-24D	SD-55-24D	SD-55-24D	SD-55-24D	SD-55-24D	SD-55-24D	SD-55-24D	SD-55-24D	SD-55-24D
C/S/M	M	M	M	M	M	M	M	M	M	M	M	M	M
SiO_2	38.72	38.04	37.42	39.49	38.74	38.94	37.99	35.82	36.48	38.25	36.86	37.37	39.11
TiO_2	4.22	4.77	2.45	2.74	3.47	3.93	1.08	4.11	3.25	2.38	2.02	2.27	2.86
Al_2O_3	12.84	12.65	15.12	13.29	14.04	13.60	14.52	15.31	15.33	14.90	13.84	15.16	13.62
Cr_2O_3	0.01	0.02	0.00	0.05	0.00	0.03	0.02	0.00	0.04	0.00	0.00	0.00	0.00
MgO	12.32	14.39	15.50	15.90	13.02	13.90	17.17	15.47	15.53	13.71	19.71	16.29	14.85
CaO	0.03	0.52	0.48	0.29	0.16	0.60	0.31	0.86	0.37	0.24	0.34	0.08	0.31
MnO	0.22	0.20	0.25	0.16	0.19	0.20	0.21	0.21	0.19	0.22	0.19	0.23	0.21
FeO	16.99	16.81	16.48	16.84	16.76	16.68	16.34	17.20	17.15	16.08	16.00	17.60	16.55
Na_2O	0.08	0.12	0.08	0.09	0.08	0.08	0.04	0.05	0.05	0.13	0.29	0.15	0.15
K_2O	9.69	8.01	6.54	6.96	9.75	8.56	7.14	7.70	7.22	8.56	7.43	6.02	8.06
BaO	0.38	0.27	0.20	0.29	0.35	0.26	0.22	0.19	0.29	0.29	0.25	0.23	0.34
F	0.67	0.73	0.77	0.74	0.56	0.68	0.73	0.65	0.85	0.57	0.50	0.55	0.74
Cl	0.11	0.10	0.09	0.10	0.13	0.09	0.07	0.08	0.10	0.10	0.13	0.08	0.13
Li	0.09	0.11	0.11	0.11	0.07	0.09	0.11	0.09	0.13	0.07	0.06	0.07	0.11
H_2O	3.69	3.71	3.70	3.77	3.79	3.78	3.73	3.78	3.69	3.75	3.86	3.81	3.74
Total	**100.08**	**100.44**	**99.18**	**100.83**	**101.12**	**101.45**	**99.68**	**101.53**	**100.67**	**99.23**	**101.48**	**99.92**	**100.78**

Number of ions based on 24 oxygens (O, OH, F, Cl)

Si	5.75	5.59	5.49	5.71	5.69	5.66	5.56	5.23	5.32	5.66	5.35	5.47	5.69
Ti	0.47	0.53	0.27	0.30	0.38	0.43	0.12	0.45	0.36	0.26	0.22	0.25	0.31
Al^{IV}	2.25	2.19	2.51	2.26	2.31	2.33	2.44	2.63	2.64	2.34	2.37	2.53	2.31
Al^{VI}	0.00	0.00	0.11	0.00	0.12	0.00	0.07	0.00	0.00	0.27	0.00	0.08	0.02
Cr	0.00	0.00	0.00	0.00	0.00	0.00	0.00	0.00	0.00	0.00	0.00	0.00	0.00
Mg	2.73	3.15	3.39	3.43	2.85	3.01	3.75	3.36	3.38	3.03	4.27	3.55	3.22
Ca	0.00	0.08	0.07	0.05	0.02	0.09	0.05	0.13	0.06	0.04	0.05	0.01	0.05
Mn	0.03	0.02	0.03	0.02	0.02	0.03	0.03	0.03	0.02	0.03	0.02	0.03	0.03
Fe^{2+}	2.11	2.06	2.02	2.04	2.06	2.03	2.00	2.10	2.09	1.99	1.94	2.15	2.01
Na	0.02	0.03	0.02	0.02	0.02	0.02	0.01	0.02	0.01	0.04	0.08	0.04	0.04
K	1.84	1.50	1.22	1.28	1.83	1.59	1.33	1.43	1.34	1.62	1.38	1.12	1.50
Ba	0.04	0.03	0.02	0.03	0.04	0.03	0.03	0.02	0.03	0.03	0.03	0.03	0.04
F	0.31	0.34	0.36	0.34	0.26	0.31	0.34	0.30	0.39	0.27	0.23	0.26	0.34
Cl	0.03	0.02	0.02	0.03	0.03	0.02	0.02	0.02	0.02	0.02	0.03	0.02	0.03
Li*	0.00	0.01	0.01	0.01	0.00	0.01	0.01	0.00	0.01	0.00	0.00	0.00	0.01
OH^-	3.66	3.63	3.62	3.64	3.71	3.66	3.64	3.68	3.59	3.71	3.74	3.72	3.63
Mg/(Mg + Fe)	**0.56**	**0.60**	**0.63**	**0.63**	**0.58**	**0.60**	**0.65**	**0.62**	**0.62**	**0.60**	**0.69**	**0.62**	**0.62**

$^{87}Sr/^{86}Sr$ Data

Table 32: *In-situ initial $^{87}Sr/^{86}Sr$ isotopic compositions of the Koperberg Suite orbicules and surrounding rocks.OK=Orbicule Koppie, HS=Henderson South, HN=Henderson North and HL=Hoogkraal Lease*

Sample	**C/S/M**	**Locality**	**$^{87}Sr/^{86}Sr$**	**1SE**	**$^{87}Rb/^{86}Sr$**	**1SE**	**I_{Sr}**
SD-27-14.	Core	HL	0.712458	0.000067	0.000350	0.000017	0.712453
SD-27-14.	Core	HL	0.712553	0.000072	0.004228	0.000074	0.712490
SD-27-14.	Core	HL	0.712611	0.000071	0.000555	0.000022	0.712603
SD-27-14.	Core	HL	0.712723	0.000074	0.000866	0.000022	0.712710
SD-27-14.	Core	HL	0.713242	0.000066	0.004017	0.000054	0.713183
SD-27-14.	Core	HL	0.713062	0.000071	0.000615	0.000019	0.713053
SD-27-14.	Core	HL	0.713052	0.000077	0.014885	0.000244	0.712833
SD-27-14.	Core	HL	0.712850	0.000077	0.001234	0.000038	0.712832
SD-27-14.	Core	HL	0.712969	0.000072	0.000600	0.000019	0.712960
SD-27-14.	Core	HL	0.713350	0.000063	0.001196	0.000016	0.713332
SD-27-14.	Core	HL	0.713499	0.000069	0.001806	0.000026	0.713472
SD-27-14.	Core	HL	0.713398	0.000071	0.001094	0.000017	0.713382
SD-27-14.	Core	HL	0.713461	0.000074	0.002794	0.000048	0.713420
SD-27-14.	Core	HL	0.713236	0.000137	0.052525	0.000939	0.712462
SD-27-14.	Core	HL	0.713585	0.000070	0.001426	0.000021	0.713564
SD-22-11C	Core	HL	0.718378	0.000118	0.002833	0.000029	0.718337
SD-22-11C	Core	HL	0.719624	0.000116	0.005129	0.000031	0.719548
SD-22-11C	Core	HL	0.718917	0.000115	0.024644	0.001030	0.718554
SD-22-11C	Core	HL	0.718462	0.000123	0.003395	0.000032	0.718412
SD-22-11C	Core	HL	0.717672	0.000300	0.125175	0.001400	0.715827
SD-22-11C	Core	HL	0.717829	0.000126	0.003221	0.000027	0.717782
SD-22-11C	Core	HL	0.718158	0.000125	0.002211	0.000030	0.718126
SD-22-11C	Core	HL	0.718457	0.000119	0.011169	0.000084	0.718292
SD-22-11C	Core	HL	0.718554	0.000133	0.004632	0.000036	0.718486
SD-27-14.	Shells	HL	0.714449	0.000070	0.001121	0.000032	0.714433
SD-27-14.	Shells	HL	0.713702	0.000073	0.001371	0.000020	0.713681
SD-27-14.	Shells	HL	0.713863	0.000071	0.003028	0.000031	0.713819

SD-27-14.	Shells	HL	0.714862	0.000064	0.009845	0.000251	0.714717
SD-27-14.	Shells	HL	0.714550	0.000067	0.001193	0.000017	0.714533
SD-27-14.	Shells	HL	0.714429	0.000073	0.002173	0.000026	0.714397
SD-27-14.	Shells	HL	0.715873	0.000073	0.001159	0.000018	0.715855
SD-27-14.	Shells	HL	0.713373	0.000071	0.001305	0.000017	0.713354
SD-27-14.	Shells	HL	0.713954	0.000071	0.001391	0.000015	0.713933
SD-27-14.	Shells	HL	0.717301	0.000068	0.000988	0.000018	0.717286
SD-27-14.	Shells	HL	0.714143	0.000074	0.001578	0.000016	0.714119
RSD-22-11D	Matrix	HL	0.721831	0.000144	0.024406	0.000616	0.721472
RSD-22-11D	Matrix	HL	0.723146	0.000183	0.115442	0.001870	0.721445
RSD-22-11D	Matrix	HL	0.719670	0.000158	0.046516	0.001610	0.718985
RSD-22-11D	Matrix	HL	0.718411	0.000132	0.007984	0.000068	0.718293
RSD-22-11D	Matrix	HL	0.718420	0.000128	0.012690	0.000062	0.718233
RSD-22-11D	Matrix	HL	0.724043	0.000144	0.072808	0.001840	0.722971
RSD-22-11D	Matrix	HL	0.724067	0.000138	0.011494	0.000100	0.723898
RSD-22-11D	Matrix	HL	0.724997	0.000151	0.006271	0.000108	0.724905
RSD-22-11D	Matrix	HL	0.721605	0.000149	0.026046	0.000199	0.721222
RSD-22-11D	Matrix	HL	0.718728	0.000144	0.004864	0.000048	0.718656
RSD-22-11D	Matrix	HL	0.719921	0.000147	0.006867	0.000169	0.719820
RSD-22-11D	Matrix	HL	0.719829	0.000140	0.007219	0.000054	0.719723
RSD-22-11D	Matrix	HL	0.718881	0.000143	0.020132	0.000169	0.718585
SD-10-6B	Core	OK	0.710405	0.000059	0.001721	0.000031	0.710380
SD-10-6B	Core	OK	0.710463	0.000176	0.147197	0.016200	0.708294
SD-10-6B	Core	OK	0.710532	0.000050	0.012450	0.000151	0.710349
SD-10-6B	Core	OK	0.710525	0.000059	0.006075	0.000059	0.710435
SD-10-6B	Core	OK	0.710961	0.000054	0.037254	0.000475	0.710412
SD-10-6B	Core	OK	0.710575	0.000060	0.010873	0.000411	0.710415
SD-10-6B	Core	OK	0.710476	0.000056	0.015296	0.000421	0.710251
SD-10-6B	Core	OK	0.710394	0.000056	0.011834	0.000483	0.710220
SD-10-6B	Core	OK	0.710726	0.000081	0.052660	0.000993	0.709951
SD-10-6B	Core	OK	0.710723	0.000087	0.009863	0.000277	0.710578
SD-10-6B	Core	OK	0.714346	0.000121	0.365313	0.006660	0.708963

SD-10-6B	Core	OK	0.711704	0.000055	0.135195	0.000698	0.709713
SD-10-6B	Core	OK	0.711243	0.000055	0.089475	0.000868	0.709925
SD-10-6B	Core	OK	0.715144	0.000256	0.647201	0.014500	0.705608
SD-10-6B	Core	OK	0.713829	0.000053	0.259006	0.002810	0.710013
SD-10-6A	Shells	OK	0.711091	0.000062	0.019331	0.000271	0.710806
SD-10-6A	Shells	OK	0.710864	0.000058	0.011964	0.000459	0.710688
SD-10-6A	Shells	OK	0.710946	0.000058	0.050687	0.000350	0.710200
SD-10-6A	Shells	OK	0.710943	0.000055	0.001981	0.000046	0.710914
SD-10-6A	Shells	OK	0.710414	0.000057	0.004051	0.000055	0.710354
SD-10-6A	Shells	OK	0.710546	0.000063	0.006807	0.000118	0.710445
SD-10-6A	Shells	OK	0.710704	0.000049	0.012030	0.000215	0.710526
SD-10-6A	Shells	OK	0.710656	0.000056	0.002709	0.000104	0.710616
SD-10-6A	Shells	OK	0.710767	0.000053	0.005853	0.000244	0.710680
SD-10-6A	Shells	OK	0.710795	0.000050	0.004627	0.000040	0.710726
SD-10-6A	Shells	OK	0.710927	0.000051	0.024769	0.000351	0.710562
SD-10-6A	Shells	OK	0.710603	0.000053	0.026892	0.000801	0.710207
SD-10-6A	Shells	OK	0.710729	0.000051	0.002926	0.000201	0.710686
SD-10-6A	Shells	OK	0.710698	0.000052	0.027759	0.000369	0.710289
SD-10-6A	Shells	OK	0.710343	0.000055	0.001346	0.000017	0.710323
SD-10-6A	Shells	OK	0.710409	0.000050	0.001304	0.000023	0.710390
SD-10-6A	Shells	OK	0.710431	0.000055	0.001285	0.000013	0.710412
SD-10-6A	Shells	OK	0.711121	0.000100	0.057186	0.002810	0.710278
SD-10-6A	Shells	OK	0.710625	0.000053	0.004208	0.000194	0.710563
SD-10-6A	Shells	OK	0.710558	0.000051	0.006895	0.000128	0.710457
SD-10-6A	Shells	OK	0.710776	0.000052	0.007525	0.000124	0.710665
SD-10-6A	Shells	OK	0.710430	0.000059	0.002723	0.000095	0.710390
SD-10-6C(1)	Matrix	OK	0.710394	0.000053	0.003596	0.000102	0.710341
SD-10-6C(1)	Matrix	OK	0.710330	0.000047	0.001406	0.000011	0.710309
SD-10-6C(1)	Matrix	OK	0.710444	0.000047	0.001273	0.000012	0.710425
SD-10-6C(1)	Matrix	OK	0.711269	0.000056	0.086653	0.000614	0.709993
SD-10-6C(1)	Matrix	OK	0.710318	0.000045	0.001638	0.000011	0.710294
SD-10-6C(1)	Matrix	OK	0.710356	0.000055	0.003095	0.000056	0.710310

SD-10-6C(1)	Matrix	OK	0.710049	0.000049	0.001801	0.000012	0.710023
SD-10-6C(1)	Matrix	OK	0.711163	0.000051	0.065750	0.000517	0.710194
SD-10-6C(1)	Matrix	OK	0.710910	0.000052	0.050323	0.000741	0.710168
SD-10-6C(1)	Matrix	OK	0.710731	0.000056	0.024417	0.000387	0.710371
SD-10-6C(1)	Matrix	OK	0.710287	0.000054	0.008102	0.000142	0.710168
SD-10-6C(1)	Matrix	OK	0.710318	0.000057	0.001457	0.000012	0.710297
SD-10-6C(1)	Matrix	OK	0.710294	0.000054	0.003660	0.000110	0.710240
SD-10-6C(1)	Matrix	OK	0.710579	0.000053	0.001190	0.000012	0.710561
SD-10-6C(1)	Matrix	OK	0.710246	0.000054	0.002825	0.000073	0.710205
SD-10-6C(1)	Matrix	OK	0.710154	0.000053	0.002664	0.000066	0.710115
SD-10-6C(1)	Matrix	OK	0.710328	0.000054	0.002641	0.000081	0.710289
SD-10-6C(2)	Matrix	OK	0.710585	0.000048	0.005596	0.000085	0.710503
SD-10-6C(2)	Matrix	OK	0.710980	0.000049	0.063848	0.000707	0.710039
SD-10-6C(2)	Matrix	OK	0.710596	0.000052	0.003587	0.000069	0.710543
SD-10-6C(2)	Matrix	OK	0.710305	0.000048	0.004785	0.000199	0.710235
SD-10-6C(2)	Matrix	OK	0.710773	0.000053	0.027406	0.001620	0.710369
SD-10-6C(2)	Matrix	OK	0.710433	0.000048	0.014570	0.000476	0.710218
SD-10-6C(2)	Matrix	OK	0.710235	0.000076	0.015721	0.001160	0.710003
SD-55-24C	Core	HS	0.716038	0.000080	0.020525	0.000201	0.715736
SD-55-24C	Core	HS	0.716241	0.000070	0.019983	0.000230	0.715946
SD-55-24C	Core	HS	0.715808	0.000068	0.000339	0.000017	0.715803
SD-55-24C	Core	HS	0.715833	0.000074	0.000149	0.000017	0.715830
SD-55-24C	Core	HS	0.716073	0.000080	0.005653	0.000185	0.715990
SD-55-24C	Core	HS	0.715841	0.000063	0.000187	0.000013	0.715838
SD-55-24C	Core	HS	0.716419	0.000060	0.043122	0.000458	0.715784
SD-55-24C	Core	HS	0.715910	0.000068	0.000174	0.000013	0.715907
SD-55-24C	Core	HS	0.715573	0.000066	0.000193	0.000013	0.715570
SD-55-24C	Core	HS	0.715952	0.000059	0.000175	0.000012	0.715950
SD-55-24C	Core	HS	0.716205	0.000064	0.000802	0.000049	0.716193
SD-55-24C	Core	HS	0.715690	0.000064	0.000216	0.000013	0.715686
SD-55-24C	Core	HS	0.715685	0.000065	0.000147	0.000013	0.715683
SD-55-24C	Core	HS	0.715760	0.000067	0.008519	0.000071	0.715635

SD-55-24C	Core	HS	0.715869	0.000056	0.000218	0.000017	0.715865
SD-55-24C	Core	HS	0.716118	0.000064	0.012204	0.000129	0.715938
SD-55-24C	Core	HS	0.715754	0.000066	0.000413	0.000015	0.715748
SD-55-24C	Core	HS	0.715820	0.000071	0.000060	0.000013	0.715819
SD-55-24C	Core	HS	0.715851	0.000067	0.002106	0.000163	0.715820
SD-55-24C	Core	HS	0.715862	0.000067	0.000168	0.000014	0.715859
SD-55-24B	Core	HS	0.716352	0.000066	0.045085	0.000408	0.715688
SD-55-24B	Core	HS	0.715882	0.000071	0.008359	0.000088	0.715759
SD-55-24B	Core	HS	0.716765	0.000069	0.095283	0.001970	0.715361
SD-55-24B	Core	HS	0.715981	0.000077	0.002677	0.000032	0.715942
SD-55-24B	Core	HS	0.715844	0.000074	0.002531	0.000038	0.715806
SD-55-24B	Core	HS	0.716700	0.000070	0.099882	0.000948	0.715228
SD-55-24B	Core	HS	0.715616	0.000074	0.000120	0.000017	0.715614
SD-55-24B	Core	HS	0.715752	0.000062	0.000159	0.000017	0.715750
SD-55-24B	Shells	HS	0.715878	0.000075	0.002304	0.000042	0.715844
SD-55-24B	Shells	HS	0.715819	0.000070	0.003067	0.000025	0.715773
SD-55-24B	Shells	HS	0.716217	0.000069	0.026620	0.000194	0.715825
SD-55-24B	Shells	HS	0.715809	0.000073	0.000225	0.000016	0.715806
SD-55-24B	Shells	HS	0.715948	0.000074	0.011334	0.000265	0.715781
SD-55-24B	Shells	HS	0.715808	0.000073	0.000291	0.000016	0.715804
SD-55-24B	Shells	HS	0.715773	0.000085	0.016325	0.000732	0.715532
SD-55-24A	Shells	HS	0.715912	0.000057	0.000217	0.000013	0.715909
SD-55-24A	Shells	HS	0.716284	0.000061	0.022617	0.000716	0.715951
SD-55-24A	Shells	HS	0.715745	0.000064	0.006668	0.000169	0.715647
SD-55-24A	Shells	HS	0.715988	0.000062	0.000381	0.000027	0.715982
SD-55-24A	Shells	HS	0.716020	0.000061	0.000220	0.000013	0.716017
SD-55-24A	Shells	HS	0.715740	0.000065	0.000364	0.000017	0.715735
SD-55-24A	Shells	HS	0.716065	0.000069	0.035182	0.000531	0.715546
SD-55-24A	Shells	HS	0.715653	0.000060	0.002326	0.000090	0.715619
SD-55-24A	Shells	HS	0.715797	0.000062	0.001047	0.000015	0.715781
SD-55-24A	Shells	HS	0.716063	0.000065	0.031993	0.000445	0.715592
SD-55-24A	Matrix	HS	0.715868	0.000064	0.000207	0.000015	0.715865

SD-55-24A	Matrix	HS	0.715831	0.000069	0.001761	0.000021	0.715805
SD-55-24A	Matrix	HS	0.715971	0.000071	0.000306	0.000015	0.715966
SD-55-24A	Matrix	HS	0.716033	0.000065	0.003091	0.000065	0.715988
SD-55-24A	Matrix	HS	0.715984	0.000062	0.002688	0.000035	0.715944
SD-55-24B	Matrix	HS	0.716162	0.000063	0.000193	0.000013	0.716159
SD-55-24B	Matrix	HS	0.716044	0.000060	0.000381	0.000013	0.716038
SD-55-24B	Matrix	HS	0.715878	0.000067	0.000150	0.000015	0.715876
SD-55-24B	Matrix	HS	0.716248	0.000066	0.000166	0.000014	0.716246
SD-55-24B	Matrix	HS	0.715832	0.000065	0.003576	0.000150	0.715779
SD-55-24B	Matrix	HS	0.715071	0.000375	0.004370	0.000153	0.715006
SD-55-24B	Matrix	HS	0.715958	0.000069	0.000031	0.000015	0.715958
SD-55-24B	Matrix	HS	0.715677	0.000067	0.002089	0.000066	0.715646
SD-55-24B	Matrix	HS	0.715994	0.000068	0.026132	0.000355	0.715609
SD-55-24B	Matrix	HS	0.715692	0.000067	0.001327	0.000107	0.715673
SD-55-24D	Matrix	HS	0.715780	0.000060	0.001817	0.000096	0.715753
SD-55-24D	Matrix	HS	0.715927	0.000058	0.006457	0.000320	0.715832
SD-55-24D	Matrix	HS	0.715894	0.000059	0.000474	0.000024	0.715887
SD-55-24D	Matrix	HS	0.716587	0.000061	0.046828	0.000860	0.715897
SD-55-24D	Matrix	HS	0.715983	0.000068	0.019133	0.000172	0.715701
SD-55-24D	Matrix	HS	0.715724	0.000059	0.000110	0.000015	0.715722
SD-55-24D	Matrix	HS	0.715915	0.000059	0.000557	0.000016	0.715906
SD-55-24D	Matrix	HS	0.718002	0.000072	0.162305	0.001620	0.715611
SD-55-24D	Matrix	HS	0.717713	0.000057	0.104896	0.000677	0.716168
SD-55-24D	Matrix	HS	0.715702	0.000059	0.000676	0.000021	0.715692
SD-55-24D	Matrix	HS	0.715821	0.000064	0.000260	0.000017	0.715817
SD-55-24D	Matrix	HS	0.716311	0.000070	0.019536	0.000252	0.716023
SD-55-24D	Matrix	HS	0.715599	0.000060	0.000284	0.000017	0.715595
SD-55-24D	Matrix	HS	0.715760	0.000061	0.000605	0.000015	0.715751
SD-55-24D	Matrix	HS	0.716217	0.000062	0.005922	0.000161	0.716130
SD-55-24D	Matrix	HS	0.715982	0.000059	0.002197	0.000020	0.715949
SD-36-18C	Core	HN	0.722638	0.000076	0.080847	0.000379	0.721447
SD-36-18C	Core	HN	0.721884	0.000072	0.006820	0.000342	0.721784

SD-36-18C	Core	HN	0.721448	0.000077	0.004871	0.000066	0.721376
SD-36-18C	Core	HN	0.721578	0.000080	0.008725	0.000363	0.721449
SD-36-18C	Core	HN	0.721876	0.000080	0.019638	0.000339	0.721586
SD-36-18C	Core	HN	0.721968	0.000076	0.112424	0.002400	0.720312
SD-36-18C	Core	HN	0.721530	0.000076	0.027686	0.000278	0.721122
SD-36-18C	Core	HN	0.721697	0.000066	0.019858	0.000168	0.721405
SD-36-18C	Core	HN	0.721140	0.000068	0.004589	0.000057	0.721072
SD-36-18C	Core	HN	0.720969	0.000069	0.005644	0.000050	0.720886
SD-36-18C	Core	HN	0.721616	0.000074	0.032447	0.000626	0.721137
SD-36-18C	Core	HN	0.721301	0.000064	0.001325	0.000018	0.721282
SD-36-18C	Core	HN	0.721245	0.000078	0.001878	0.000022	0.721218
SD-36-18C	Core	HN	0.721035	0.000071	0.001576	0.000024	0.721012
SD-36-18C	Core	HN	0.721222	0.000081	0.011166	0.000044	0.721058
SD-36-18C	Core	HN	0.721213	0.000073	0.017108	0.000188	0.720961
SD-36-18C	Core	HN	0.721377	0.000074	0.003032	0.000034	0.721332
SD-36-18C	Core	HN	0.721200	0.000071	0.005580	0.000084	0.721118
SD-36-18C	Core	HN	0.721182	0.000072	0.012440	0.000102	0.720998
SD-36-18C	Core	HN	0.721147	0.000077	0.003227	0.000031	0.721099
SD-36-18C	Core	HN	0.721503	0.000078	0.001486	0.000017	0.721481
SD-10-36A	Shells	HN	0.721835	0.000087	0.000686	0.000019	0.721825
SD-10-36A	Shells	HN	0.722125	0.000089	0.112575	0.000454	0.720466
SD-10-36A	Shells	HN	0.721648	0.000072	0.004040	0.000104	0.721589
SD-10-36A	Shells	HN	0.721539	0.000078	0.001758	0.000023	0.721513
SD-10-36A	Shells	HN	0.722209	0.000090	0.008959	0.000226	0.722077
SD-10-36A	Shells	HN	0.721519	0.000077	0.000505	0.000019	0.721511
SD-10-36A	Shells	HN	0.721786	0.000088	0.013086	0.000276	0.721594
SD-10-36A	Shells	HN	0.722290	0.000091	0.023155	0.000135	0.721948
SD-40-19B	Shells	HN	0.722463	0.000074	0.002097	0.000017	0.722432
SD-40-19B	Shells	HN	0.722916	0.000078	0.010133	0.000296	0.722766
SD-40-19B	Shells	HN	0.722444	0.000074	0.009865	0.000498	0.722298
SD-40-19B	Shells	HN	0.722122	0.000079	0.003869	0.000109	0.722065
SD-40-19B	Shells	HN	0.722499	0.000086	0.001685	0.000022	0.722474

SD-40-19B	Shells	HN	0.722445	0.000076	0.016562	0.000278	0.722201
SD-40-19B	Shells	HN	0.723386	0.000079	0.001842	0.000036	0.723358
SD-40-19B	Shells	HN	0.722235	0.000078	0.001627	0.000019	0.722211
SD-40-19B	Shells	HN	0.722760	0.000076	0.036520	0.000545	0.722222
SD-40-19B	Shells	HN	0.722614	0.000081	0.001535	0.000023	0.722591
SD-40-19B	Shells	HN	0.721769	0.000075	0.001779	0.000021	0.721743
SD-40-19B	Shells	HN	0.721991	0.000084	0.003621	0.000117	0.721938
SD-40-19B	Shells	HN	0.719969	0.000602	0.698730	0.025700	0.709675
SD-40-19B	Shells	HN	0.722628	0.000084	0.001759	0.000019	0.722602
SD-40-19B	Shells	HN	0.721957	0.000147	0.163797	0.000184	0.719544
SD-40-19B	Shells	HN	0.722219	0.000082	0.004329	0.000131	0.722155
SD-40-19B	Shells	HN	0.722687	0.000122	0.085440	0.007380	0.721428
SD-40-19B	Shells	HN	0.721778	0.000084	0.004368	0.000042	0.721714
SD-40-19B	Shells	HN	0.721672	0.000082	0.002651	0.000028	0.721633
SD-40-19B	Shells	HN	0.721657	0.000092	0.008439	0.000156	0.721533
SD-40-19D	Matrix	HN	0.721644	0.000074	0.001432	0.000017	0.721623
SD-40-19D	Matrix	HN	0.721737	0.000082	0.005005	0.000024	0.721664
SD-40-19D	Matrix	HN	0.721888	0.000069	0.038713	0.000543	0.721318
SD-40-19D	Matrix	HN	0.721383	0.000072	0.003842	0.000032	0.721327
SD-40-19D	Matrix	HN	0.721848	0.000077	0.001597	0.000020	0.721824
SD-40-19D	Matrix	HN	0.721696	0.000082	0.002071	0.000050	0.721666
SD-40-19D	Matrix	HN	0.721760	0.000068	0.001686	0.000018	0.721735
SD-40-19D	Matrix	HN	0.722310	0.000070	0.001765	0.000018	0.722284
SD-40-19D	Matrix	HN	0.722332	0.000075	0.060031	0.000739	0.721447
SD-40-19D	Matrix	HN	0.723286	0.000077	0.077458	0.001570	0.722145
SD-40-19D	Matrix	HN	0.721483	0.000074	0.002642	0.000037	0.721444
SD-40-19D	Matrix	HN	0.721877	0.000075	0.027621	0.000272	0.721470
SD-40-19D	Matrix	HN	0.721279	0.000083	0.003011	0.000064	0.721234
SD-40-19D	Matrix	HN	0.721808	0.000082	0.008016	0.000190	0.721689
SD-40-19D	Matrix	HN	0.721879	0.000081	0.012183	0.000528	0.721700
SD-40-19D	Matrix	HN	0.722625	0.000077	0.001823	0.000031	0.722599
SD-40-19D	Matrix	HN	0.721925	0.000073	0.007769	0.000146	0.721810

SD-40-19D	Matrix	HN	0.721969	0.000081	0.001855	0.000021	0.721942
SD-40-19D	Matrix	HN	0.722557	0.000075	0.007291	0.000225	0.722449
SD-40-19D	Matrix	HN	0.722136	0.000083	0.002141	0.000023	0.722104
SD-40-19D	Matrix	HN	0.722876	0.000085	0.013383	0.000266	0.722678
SD-40-19D	Matrix	HN	0.722558	0.000087	0.013474	0.000161	0.722359
SD-40-19D	Matrix	HN	0.722730	0.000085	0.005136	0.000037	0.722654
SD-40-19D	Matrix	HN	0.723636	0.000087	0.008045	0.000134	0.723517
SD-40-19D	Matrix	HN	0.723866	0.000093	0.107842	0.002210	0.722277
SD-40-19D	Matrix	HN	0.722628	0.000088	0.004082	0.000101	0.722568
SD-40-19D	Matrix	HN	0.722743	0.000087	0.009459	0.000201	0.722603
SD-40-19D	Matrix	HN	0.723093	0.000082	0.002445	0.000021	0.723057
SD-40-19D	Matrix	HN	0.723548	0.000094	0.003178	0.000025	0.723501
SD-40-19D	Matrix	HN	0.723228	0.000084	0.004043	0.000038	0.723169
SD-40-19D	Matrix	HN	0.722471	0.000088	0.005682	0.000100	0.722387
SD-40-19D	Matrix	HN	0.723261	0.000094	0.008541	0.000090	0.723135
SD-40-19D	Matrix	HN	0.726749	0.000089	0.278144	0.002310	0.722651
SD-10-36A	Matrix	HN	0.722876	0.000085	0.013383	0.000266	0.722678
SD-10-36A	Matrix	HN	0.722558	0.000087	0.013474	0.000161	0.722359
SD-10-36A	Matrix	HN	0.722730	0.000085	0.005136	0.000037	0.722654
SD-10-36A	Matrix	HN	0.723636	0.000087	0.008045	0.000134	0.723517
SD-10-36A	Matrix	HN	0.723866	0.000093	0.107842	0.002210	0.722277
SD-10-36A	Matrix	HN	0.722628	0.000088	0.004082	0.000101	0.722568
SD-10-36A	Matrix	HN	0.722743	0.000087	0.009459	0.000201	0.722603
SD-10-36A	Matrix	HN	0.723093	0.000082	0.002445	0.000021	0.723057
SD-10-36A	Matrix	HN	0.723548	0.000094	0.003178	0.000025	0.723501
SD-10-36A	Matrix	HN	0.723228	0.000084	0.004043	0.000038	0.723169

SD-10-36A	Matrix	HN	0.722471	0.000088	0.005682	0.000100	0.722387
SD-10-36A	Matrix	HN	0.723261	0.000094	0.008541	0.000090	0.723135
SD-10-36A	Matrix	HN	0.726749	0.000089	0.278144	0.002310	0.722651

SD-35-17.	HN Anorthosite	0.722239	0.000107	0.001972	0.000035	0.722210
SD-35-17.	HN Anorthosite	0.722742	0.000121	0.011931	0.000437	0.722566
SD-35-17.	HN Anorthosite	0.722381	0.000126	0.000775	0.000034	0.722370
SD-35-17.	HN Anorthosite	0.722779	0.000106	0.013174	0.000268	0.722585
SD-35-17.	HN Anorthosite	0.722366	0.000115	0.001147	0.000030	0.722349
SD-35-17.	HN Anorthosite	0.722146	0.000114	0.002826	0.000049	0.722105
SD-35-17.	HN Anorthosite	0.722719	0.000119	0.053688	0.002530	0.721928
SD-35-17.	HN Anorthosite	0.723673	0.000119	0.059216	0.000907	0.722800
SD-35-17.	HN Anorthosite	0.722307	0.000119	0.014642	0.000101	0.722092
SD-35-17.	HN Anorthosite	0.722833	0.000129	0.005749	0.000142	0.722748
SD-35-17.	HN Anorthosite	0.722596	0.000149	0.004307	0.000133	0.722532
SD-35-17.	HN Anorthosite	0.722195	0.000120	0.003527	0.000175	0.722143
SD-35-17.	HN Anorthosite	0.722578	0.000135	0.000649	0.000036	0.722568
SD-33-16.	HN Diorite	0.717595	0.000086	0.000576	0.000025	0.717587
SD-33-16.	HN Diorite	0.717164	0.000096	0.000556	0.000022	0.717156
SD-33-16.	HN Diorite	0.717429	0.000089	0.007086	0.000150	0.717325
SD-33-16.	HN Diorite	0.717454	0.000094	0.025499	0.000114	0.717078
SD-33-16.	HN Diorite	0.717117	0.000094	0.000902	0.000029	0.717104
SD-33-16.	HN Diorite	0.717648	0.000100	0.037182	0.000273	0.717100

SD-33-16.	HN Diorite	0.717527	0.000085	0.006958	0.000093	0.717424
SD-33-16.	HN Diorite	0.717765	0.000100	0.014928	0.000233	0.717545
SD-33-16.	HN Diorite	0.717740	0.000094	0.005224	0.000155	0.717663
SD-33-16.	HN Diorite	0.717295	0.000083	0.001946	0.000043	0.717267
SD-33-16.	HN Diorite	0.706913	0.000016	0.000001	0.000002	0.706913
SD-33-16.	HN Diorite	0.717202	0.000096	0.012273	0.000107	0.717021
SD-33-16.	HN Diorite	0.717684	0.000092	0.014194	0.000173	0.717475
SD-33-16.	HN Diorite	0.711294	0.000072	0.073327	0.000314	0.710213
SD-33-16.	HN Diorite	0.710839	0.000075	0.007469	0.000161	0.710729
SD-33-16.	HN Diorite	0.710617	0.000083	0.001485	0.000032	0.710595
SD-20-10.	HL Anorthosite	0.720023	0.000091	0.001296	0.000025	0.720004
SD-20-10.	HL Anorthosite	0.717344	0.000095	0.001482	0.000031	0.717322
SD-20-10.	HL Anorthosite	0.715533	0.000101	0.001202	0.000039	0.715516
SD-20-10.	HL Anorthosite	0.715231	0.000104	0.002321	0.000036	0.715196
SD-20-10.	HL Anorthosite	0.717612	0.000097	0.123522	0.001070	0.715792
SD-20-10.	HL Anorthosite	0.716876	0.000102	0.001923	0.000022	0.716848
SD-20-10.	HL Anorthosite	0.718549	0.000101	0.001380	0.000028	0.718528
SD-20-10.	HL Anorthosite	0.716127	0.000096	0.008264	0.000073	0.716005
SD-20-10.	HL Anorthosite	0.717302	0.000099	0.007098	0.000055	0.717197
SD-20-10.	HL Anorthosite	0.717584	0.000118	0.004129	0.000036	0.717523
SD-20-10.	HL Anorthosite	0.715449	0.000122	0.025912	0.000283	0.715067
SD-20-10.	HL Anorthosite	0.717313	0.000108	0.008954	0.000152	0.717181
SD-20-10.	HL Anorthosite	0.715935	0.000098	0.009335	0.000059	0.715798
SD-19-9-2.	HL Diorite	0.718165	0.000090	0.000176	0.000021	0.718162

SD-19-9-2.	HL Diorite	0.718314	0.000089	0.008574	0.000317	0.718188
SD-19-9-2.	HL Diorite	0.717971	0.000084	0.000769	0.000034	0.717960
SD-19-9-2.	HL Diorite	0.718265	0.000086	0.001208	0.000088	0.718247
SD-19-9-2.	HL Diorite	0.718272	0.000083	0.004159	0.000217	0.718210
SD-19-9-2.	HL Diorite	0.718329	0.000093	0.027771	0.000697	0.717920
SD-19-9-2.	HL Diorite	0.718289	0.000089	0.002814	0.000093	0.718248
SD-19-9-2.	HL Diorite	0.718275	0.000086	0.011546	0.000129	0.718104
SD-19-9-2.	HL Diorite	0.718006	0.000083	0.001217	0.000033	0.717988
SD-19-9-2.	HL Diorite	0.718185	0.000092	0.000794	0.000030	0.718174
SD-19-9-2.	HL Diorite	0.718212	0.000082	0.004080	0.000081	0.718152
SD-49-22.	HS Anorthosite	0.717474	0.000258	0.191501	0.008350	0.714652
SD-49-22.	HS Anorthosite	0.717625	0.000373	0.235437	0.013000	0.714156
SD-49-22.	HS Anorthosite	0.717443	0.000101	0.000420	0.000025	0.717437
SD-49-22.	HS Anorthosite	0.717374	0.000103	0.033755	0.001730	0.716877
SD-49-22.	HS Anorthosite	0.717343	0.000093	0.001713	0.000045	0.717318
SD-49-22.	HS Anorthosite	0.717490	0.000109	0.002013	0.000088	0.717461
SD-49-22.	HS Anorthosite	0.717125	0.000103	0.000811	0.000026	0.717113
SD-49-22.	HS Anorthosite	0.717454	0.000111	0.001052	0.000037	0.717439
SD-49-22.	HS Anorthosite	0.717122	0.000117	0.000432	0.000027	0.717115
SD-49-22.	HS Anorthosite	0.717341	0.000108	0.000821	0.000027	0.717329
SD-49-21.	HS Diorite	0.713901	0.000089	0.005673	0.000057	0.713818
SD-49-21.	HS Diorite	0.714288	0.000092	0.000660	0.000020	0.714278
SD-49-21.	HS Diorite	0.713887	0.000112	0.028397	0.000080	0.713469
SD-49-21.	HS Diorite	0.713585	0.000086	0.000973	0.000022	0.713571

SD-49-21.	HS Diorite	0.713764	0.000085	0.000538	0.000021	0.713756
SD-49-21.	HS Diorite	0.713990	0.000089	0.001263	0.000021	0.713971
SD-49-21.	HS Diorite	0.713950	0.000085	0.003350	0.000076	0.713901
SD-49-21.	HS Diorite	0.714031	0.000087	0.001101	0.000031	0.714015
SD-49-21.	HS Diorite	0.714096	0.000094	0.001088	0.000030	0.714080
SD-49-21.	HS Diorite	0.713744	0.000101	0.000861	0.000021	0.713732
SD-49-21.	HS Diorite	0.713942	0.000093	0.000700	0.000025	0.713931
SD-49-21.	HS Diorite	0.714218	0.000098	0.000549	0.000021	0.714210
SD-49-21.	HS Diorite	0.713819	0.000092	0.003871	0.000079	0.713762
SD-32-15A	OK Anorthosite	0.710971	0.000069	0.007739	0.000152	0.710857
SD-32-15A	OK Anorthosite	0.710818	0.000073	0.009994	0.000060	0.710671
SD-32-15A	OK Anorthosite	0.710881	0.000077	0.015389	0.000193	0.710654
SD-32-15A	OK Anorthosite	0.711134	0.000075	0.026091	0.000281	0.710749
SD-32-15A	OK Anorthosite	0.710892	0.000072	0.000904	0.000017	0.710878
SD-32-15A	OK Anorthosite	0.710672	0.000062	0.002667	0.000030	0.710632
SD-32-15A	OK Anorthosite	0.711055	0.000071	0.000932	0.000019	0.711041
SD-32-15A	OK Anorthosite	0.711312	0.000076	0.008380	0.000317	0.711188
SD-32-15A	OK Anorthosite	0.710762	0.000067	0.001198	0.000029	0.710745
SD-32-15A	OK Anorthosite	0.710734	0.000081	0.002387	0.000090	0.710699
SD-32-15A	OK Anorthosite	0.710981	0.000066	0.001206	0.000020	0.710963
SD-32-15A	OK Anorthosite	0.710804	0.000076	0.004420	0.000113	0.710739
SD-32-15A	OK Anorthosite	0.710830	0.000079	0.018102	0.000603	0.710563
SD-5-1B	OK Diorite	0.710330	0.000123	0.022858	0.001120	0.709994
SD-5-1B	OK Diorite	0.710375	0.000066	0.001056	0.000020	0.710360

SD-5-1B	OK Diorite	0.710930	0.000074	0.024578	0.000510	0.710568
SD-5-1B	OK Diorite	0.710146	0.000065	0.001225	0.000015	0.710128
SD-5-1B	OK Diorite	0.710561	0.000070	0.007416	0.000253	0.710452
SD-5-1B	OK Diorite	0.710191	0.000067	0.010038	0.000146	0.710043
SD-5-1B	OK Diorite	0.710414	0.000073	0.015985	0.000289	0.710178
SD-5-1B	OK Diorite	0.710541	0.000069	0.015663	0.000197	0.710310
SD-5-1B	OK Diorite	0.710449	0.000067	0.008791	0.000113	0.710320
SD-5-1B	OK Diorite	0.711200	0.000068	0.043775	0.000444	0.710555

Appendix C: Major element data in sulphides

Table 33: *Major and trace element results in bornite and chalcopyrite from the Koperberg Suite orbicules. CCP=Chalcopyrite, Bn= Bornite, OK=Orbicule Koppie, JP=Jubilee pit, HN=Henderson North and HS=Henderson South. Co As Se Pb Bi Ag Cd Sn Sb Te Mn and Zn are all trace elements in this table,*

Spot analysis	Locality	Structure	S	Fe	Co	Ni	Cu	As	Se	Pb	Bi	Ag	Cd	Sn	Sb	Te	Mn	Zn	Total
SD-10-6B_CCP1	OK	Core	35.05	29.84	0.00	0.00	34.10	0.00	0.02	0.01	0.00	0.01	0.03	0.01	0.00	0.02	0.00	0.05	**99.15**
SD-10-6B_CCP2	OK	Core	33.33	29.83	0.01	0.01	34.11	0.00	0.00	0.01	0.03	0.02	0.07	0.00	0.00	0.02	0.00	0.00	**97.45**
SD-10-6A_CCP1	OK	Matrix	34.14	29.94	0.01	0.01	34.00	0.00	0.02	0.00	0.03	0.00	0.02	0.00	0.00	0.01	0.00	0.03	**98.22**
SD-10-6A_CCP2	OK	Matrix	34.52	29.76	0.00	0.00	34.11	0.00	0.00	0.00	0.00	0.00	0.00	0.00	0.00	0.01	0.00	0.02	**98.44**
SD-10-6A_CCP3	OK	Matrix	34.26	29.74	0.00	0.00	34.03	0.00	0.00	0.00	0.02	0.00	0.03	0.01	0.00	0.01	0.00	0.03	**98.14**
SD-10-6A_CCP4	OK	Matrix	34.43	29.64	0.00	0.00	34.05	0.00	0.01	0.00	0.01	0.01	0.00	0.00	0.00	0.02	0.00	0.03	**98.21**
SD-10-6A_CCP5	OK	Matrix	34.56	28.41	0.00	0.00	31.93	0.01	0.00	0.00	0.00	0.00	0.02	0.00	0.00	0.01	0.00	0.00	**94.95**
SD-10-6C_CCP2	OK	Matrix	34.82	29.76	0.00	0.00	34.20	0.01	0.00	0.00	0.00	0.00	0.00	0.00	0.00	0.00	0.00	0.00	**98.80**
SD-10-6C_CCP3	OK	Matrix	34.79	29.84	0.00	0.01	34.01	0.00	0.01	0.00	0.00	0.00	0.01	0.01	0.00	0.01	0.00	0.01	**98.71**
SD-10-6C_CCP1	OK	Matrix	34.56	29.70	0.00	0.00	34.06	0.00	0.03	0.00	0.00	0.00	0.01	0.03	0.00	0.02	0.00	0.04	**98.45**
SD-10-6C_CCP7	OK	Matrix	34.64	29.85	0.00	0.03	33.98	0.00	0.00	0.00	0.00	0.02	0.00	0.00	0.00	0.01	0.00	0.02	**98.55**
SD-10-6C_CCP8	OK	Matrix	34.60	29.90	0.00	0.00	34.07	0.00	0.01	0.00	0.02	0.00	0.07	0.00	0.00	0.00	0.00	0.01	**98.68**
SD-10-6C_CCP4	OK	Matrix	34.77	29.73	0.00	0.00	34.00	0.00	0.02	0.01	0.03	0.00	0.02	0.00	0.02	0.02	0.00	0.00	**98.64**
SD-10-6C_CCP5	OK	Matrix	34.99	29.66	0.00	0.00	33.97	0.00	0.01	0.01	0.00	0.02	0.00	0.00	0.00	0.00	0.01	0.03	**98.69**
SD-10-6C_CCP6	OK	Matrix	34.42	29.89	0.00	0.01	33.95	0.00	0.01	0.00	0.01	0.00	0.00	0.01	0.00	0.00	0.00	0.01	**98.31**
AJ-19-4B_CCP3	JP	Matrix	34.46	29.62	0.00	0.02	33.94	0.00	0.01	0.00	0.02	0.00	0.01	0.00	0.00	0.02	0.00	0.00	**98.10**
AJ-19-4B_CCP4	JP	Matrix	34.56	29.83	0.00	0.00	34.22	0.00	0.00	0.00	0.00	0.00	0.00	0.02	0.01	0.04	0.00	0.00	**98.68**
AJ-19-4B_CCP5	JP	Matrix	34.48	29.66	0.01	0.01	34.18	0.00	0.00	0.01	0.00	0.01	0.00	0.00	0.00	0.00	0.00	0.00	**98.37**
AJ-19-4B_CCP2	JP	Matrix	34.78	29.84	0.00	0.02	34.37	0.00	0.00	0.00	0.01	0.00	0.00	0.02	0.00	0.00	0.00	0.00	**99.04**
AJ-19-4B_CCP1	JP	Matrix	34.35	29.71	0.00	0.00	34.19	0.00	0.01	0.02	0.01	0.00	0.00	0.01	0.00	0.00	0.00	0.02	**98.31**

Table 34 (Continued)

Spot analysis	Locality	Structure	S	Fe	Co	Ni	Cu	As	Se	Pb	Bi	Ag	Cd	Sn	Sb	Te	Mn	Zn	Total
AJ-19-4B_Bn3	JP	Matrix	25.34	10.55	0.00	0.00	63.74	0.00	0.00	0.00	0.02	0.03	0.02	0.00	0.02	0.04	0.00	0.00	**99.76**
AJ-19-4B_Bn4	JP	Matrix	25.53	10.40	0.01	0.02	63.94	0.00	0.01	0.00	0.01	0.00	0.04	0.00	0.00	0.01	0.00	0.00	**99.96**
AJ-19-4B_Bn5	JP	Matrix	25.43	10.42	0.01	0.00	63.96	0.00	0.00	0.00	0.00	0.04	0.01	0.00	0.00	0.03	0.00	0.00	**99.89**
AJ-19-4B_Bn1	JP	Matrix	25.51	11.14	0.01	0.00	61.11	0.00	0.00	0.00	0.03	0.01	0.02	0.00	0.00	0.00	0.00	0.00	**97.84**
AJ-19-4B_Bn2	JP	Matrix	25.70	10.32	0.00	0.00	63.08	0.00	0.02	0.00	0.03	0.00	0.01	0.00	0.00	0.02	0.00	0.00	**99.19**
AJ-19-3B_Bn2	JP	Matrix	24.49	10.04	0.00	0.00	67.10	0.00	0.01	0.00	0.03	0.01	0.03	0.00	0.00	0.06	0.00	0.00	**101.77**
AJ-19-3B_Bn1	JP	Matrix	25.24	10.60	0.00	0.00	64.78	0.01	0.01	0.00	0.00	0.02	0.01	0.01	0.00	0.00	0.00	0.00	**100.70**
AJ-19-3B_Bn3	JP	Matrix	24.87	10.97	0.01	0.01	63.00	0.00	0.00	0.00	0.02	0.03	0.04	0.01	0.00	0.04	0.00	0.00	**98.99**
AJ-19-3B_Bn4	JP	Matrix	25.78	10.96	0.00	0.00	62.42	0.00	0.01	0.00	0.05	0.02	0.02	0.00	0.00	0.03	0.00	0.00	**99.30**
AJ-19-3B_Bn5	JP	Matrix	25.53	11.02	0.00	0.00	62.66	0.00	0.00	0.00	0.00	0.00	0.03	0.00	0.00	0.02	0.00	0.00	**99.26**
AJ-19-3B_Bn6	JP	Matrix	25.58	10.73	0.00	0.00	62.41	0.00	0.00	0.00	0.01	0.00	0.02	0.00	0.00	0.05	0.01	0.00	**98.82**
SD-55-24D_CCP1	HS	Matrix	34.43	29.58	0.00	0.00	34.40	0.00	0.00	0.00	0.01	0.01	0.00	0.00	0.00	0.01	0.00	0.00	**98.45**
SD-55-24D_Bn1	HS	Matrix	24.91	8.28	0.00	0.00	65.58	0.00	0.00	0.00	0.01	0.02	0.00	0.00	0.00	0.03	0.00	0.00	**98.83**
SD-55-24D_Bn2	HS	Matrix	24.61	9.71	0.00	0.00	66.44	0.00	0.00	0.00	0.01	0.02	0.03	0.00	0.02	0.02	0.00	0.00	**100.86**
SD-55-24D_CCP3	HS	Matrix	34.06	29.49	0.00	0.00	34.08	0.00	0.02	0.02	0.05	0.00	0.00	0.01	0.01	0.00	0.00	0.00	**97.73**
SD-40-19D_CCP3	HN	Matrix	34.45	29.80	0.00	0.00	34.00	0.00	0.01	0.00	0.00	0.01	0.01	0.01	0.00	0.03	0.01	0.00	**98.33**
SD-40-19D_CCP1	HN	Matrix	34.76	29.68	0.00	0.01	34.15	0.00	0.01	0.00	0.00	0.00	0.00	0.00	0.00	0.01	0.00	0.00	**98.62**
SD-40-19D_CCP2	HN	Matrix	34.61	29.75	0.00	0.01	34.02	0.00	0.00	0.02	0.00	0.00	0.02	0.03	0.00	0.01	0.00	0.00	**98.47**
SD-40-19D_CCP4	HN	Matrix	35.03	29.88	0.01	0.00	33.98	0.00	0.01	0.00	0.00	0.00	0.03	0.00	0.00	0.01	0.00	0.03	**98.98**